Proceedings of

RAGtime 20–22: Workshops on black holes and neutron stars

15–19 October / 16–20 September /
19–23 October / '18/'19/'20
Opava, Czech Republic

Editors:
Z. Stuchlík, G. Török,
V. Karas

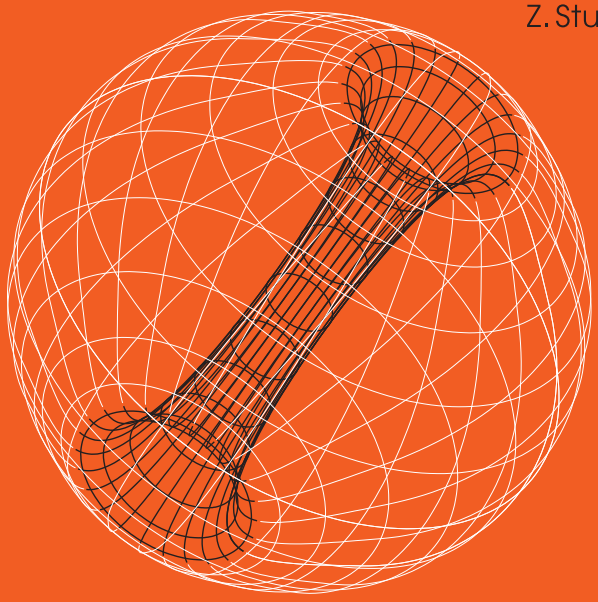

SILESIAN UNIVERSITY IN OPAVA

Publications of the Institute of Physics in Opava No. 9

Proceedings of RAGtime 20–22: Workshops on black holes and neutron stars 15–19 Oct., 16–20 Sept., 19–23 Oct. 2018/2019/2020 Opava Czech Republic

Z. Stuchlík, G. Török and V. Karas, editors

Opava 2020

Annotation: In this Proceedings, the talks presented during workshops *RAGtime 20–22: Workshops on black holes and neutron stars, 15–19 Oct., 16–20 Sept., 19–23 Oct. 2018/2019/2020, Opava, Czech Republic* are collected.

ISBN 978-80-7510-432-8

PREFACE

RAGtime – the series of the Relativistic Astrophysics Group workshops and proceedings – which started in 1999 at Institute of Physics in Opava, the Institute of Physics in Opava of the Silesian University in Opava, Czech Republic, has become after two decades of its existence a well-established and respected meeting with a strong tradition mainly devoted to relativistic astrophysics, but recently expanding also to some additional areas related to the relativistic and more generally also theoretical physics. This volume presents an edition of the workshop proceedings associated with a triad of annual events organised during the years 2018, 2019, and 2020. The progress of research at this period has been rather outstanding. Just after the celebrations of the Centenary of the Einstein's General Theory of Relativity *and*, it demonstrates spectacular achievements in both theory and related observations, this time concentrated on direct observations of the closest neighbourhood of the black hole event horizon in the large observational projects such as the Event Horizon Telescope and GRAVITY, which in a fascinating way confirm the theoretical predictions in the area of the strongest gravity effects. Naturally, there are a number of additional, very important achievements in the area of both theory and observations, which confirm the expectations based on general relativity, and sometimes further challenge the research at the borderline of the modern theoretical physics, astrophysics, and particle physics. It is a great pleasure to say that the present edition of proceeding papers brings a significant contribution to most up-to-date research activities carried out in these fields.

The present volume is focused on the processes taking place in strong gravitational and electromagnetic fields in the vicinity of black holes and neutron stars, or various types of even more exotic compact objects. The solutions of general relativity are extended to viable alternatives, such as string theories and supersymmetry, or to the cases combining general relativity with possible variants of non-linear electrodynamics that are able to predict the so-called regular black holes, which do not contain a central physical singularity. The astrophysical processes are treated in the test-particle or fluid-configuration approximations. One of the central points are the observable optical phenomena and their most relevant demonstrations, namely the high-frequency quasi-periodic oscillations observed in the low-mass X-ray binaries containing accreting black holes or neutron stars, or in the case of supermassive black holes in active galactic nuclei, and furthermore also optical phenomena connected to the appearance of the spectroscopy and polarimetry of the emerging radiation signal. Special attention has been devoted to complex structures of corotating and counterrotating fluid tori around supermassive rotating black holes. Important studies are related to the acceleration ultra-high energy cosmic rays, or to the relation of chaos and regularity in the motion of matter in gravo-magnetic fields around black holes. The equilibrium of charged fluid tori has been investigated within the analytical and numerical frameworks in situations related to the magnetized compact objects. Black holes have been considered in the context of cosmology and neutron stars in the context of hybrid configurations combining the neutron and quark matter, or in the context of a charged fluid. In addition to the standard variety of works in the field of relativistic physics, this proceedings also includes a study relating the ideas of the so-called soliton solutions as applied to quantum informatics and to molecules relevant for the replications of DNA.

Most of the presented contributions have been obtained thanks to the collaboration of the research groups at the Silesian University in Opava, the Astronomical Institute of the Czech Academy of Science, the Faculty of Mathematics and Physics of the Charles University in Prague, and furthermore our colleagues at many other foreign institutions. The RAGtime participants from a wide international community have represented Observatoire de Paris, The Joint Institute for Nuclear Research in Dubna, The International Space Science Institute in Bern, Osservatorio Astronomico di Roma, University of Cologne, University of Oxford, The Ulugh Beg Astronomical Institute in Tashkent and others.

We thank the Editorial Board members for their valuable advice and assistance, and all the authors for the careful preparation of their contributions. We are also indebted to the Ministry of Education of the Czech Republic and the European Social Fund in the Czech Republic for providing the financial support for the workshops and participants' activities, namely within the INTER-EXCELLENCE project No. LTI17018, the ESF projects No.CZ.02.2.69/0.0/0.0/18_058/0010238, CZ.02.2.69/0.0/0.0/18_056/0013364, CZ.02.2.69/0.0/0.0/18_054/0014696, and the internal grants of the Silesian University in Opava No. SGS/13,14/2019 and IP/15/19.

Opava, December 2020

Z. Stuchlík, G. Török and V. Karas
editors

CONTENTS

Proceedings of *RAGtime 20–22, 15–19 Oct., 16–20 Sept., 19–23 Oct., 2018/2019/2020, Opava, Czech Republic*
Z. Stuchlík, G. Török and V. Karas, editors, Silesian University in Opava, 2020, pp. i–v

Zdeněk Stuchlík in the pursuit of beauty

Marek Abramowicz

Göteborg University, Sweden, Silesian University, Opava, Czech Republic,
and N. Copernicus Astronomical Centre, Warsaw, Poland
marek.abramowicz@physics.gu.se

Zdeněk Stuchlík is a very successful, award-winning, university educator, adored by generations of students and peers for his role as a professor, lecturer, supervisor of doctoral theses and as a long-time proficient Dean of the Faculty of Philosophy and Science and the Director of the Institute of Physics at the Silesian University in Opava. He is widely recognized as the creator and leader of a distinctly original and productive circle of assistants and collaborators that he established in Opava. Working together with foreign visitors to Opava and colleagues abroad, Stuchlík and his Opavian team have spent the best part of three decades spearheading research into Einstein's General Relativity, most impressive in its scope and scale. Indeed, to the global community of physicists and astrophysicists, Zdeněk Stuchlík is simply a Czech scientist, a well-known and respected black hole theorist from Opava. And yes, many of them know that in addition Stuchlík sometimes goes awol, takes pictures and even shows them at exhibitions in respected art galleries and museums.

Because his photography is so fine and neatly sophisticated, people outside of the community of physicists, who attend these exhibitions, usually consider Stuchlík as somebody whose main occupation is solely photography. They assume that a Czech with his artistic talent must obviously belong to the world-esteemed mob of legendary Czech photographers, and are surprised to discover that he is not *also* — but *primarily* — a well renowned respected scientist.

Stuchlík is, of course, connected institutionally to Opava's world-famous *Institut tvůrčí fotografie* (The Institute of Creative Photography), where Jindřich Štreit, and other best known contemporary Czech photographers, work and teach. Stuchlík and Štreit are close friends; they were among a small team of visionary pioneers who created out of nothingness the Silesian University in Opava — at times of the great optimism and hope just after the Velvet Revolution. Today, their University is considered to be the best among all provincial universities in the Republic.

So many papers written and countless labours of love, all in the pursuit of exploring stunning beauties of reality — physical, mathematical and intellectual — all gorgeously presented in scholarly attempts to share these excitements with others!

During the years, I have witnessed Zdeněk's sure and brilliant acting in many of his distinguished social roles, but I see him, most of all, as my darling friend and a classy gentlemen, whom I trust in important matters of life and profession.

Happy birthday, Zdeněk.

978-80-7510-432-8

1 STUCHLÍK THE ARTIST: SMOOTHER PEBBLES AND PRETTIER SHELLS.

An internal pre-requisite that compels those like Stuchlík to undertake so many different intellectual activities, has been metaphorically described in the profoundly modest words by Sir Isaac Newton:

– I do not know what I may appear to the world, but to myself I seem to have been only like a boy playing on the sea-shore, and diverting myself in now and then finding a smoother pebble or a prettier shell than ordinary, whilst the great ocean of truth lay all undiscovered before me.

Zdeněk has been exhibiting his photographs of smoother pebbles and prettier shells in Opava, Prague and other Czech cities, as well as in Wrocław, Warsaw, Vilnius, Riga, Trieste, Frankfurt and Oxford. His artistic creations have been already discussed in books, including one devoted solely to him. One of his quite often displayed photos, paints my silhouette portrait in a hotel window, against the background of the famous Copacabana beach in Rio de Janeiro. Thank you, Zdenku, for the *Macho in the window*.

Here in Opava, in January-February 2015, he had an exhibition *Neurčitý prostor* (Undefined space) together with Jerzy Olek, a top Polish artist-photographer and art theoretician. I wrote an introduction to its *Catalogue*, saying that the joint exhibition of photos taken by these friends of mine showed their utterly dissimilar ways of perceiving reality. Such striking differences cannot be explained through sole recourse to the stereotypical assumption that a scientist surveys the world by number, weight and measure, applying a cool eye to things and phenomena, whereas an artist sees reality in a way which is subjective, emotional and altogether irrational. There, at this exhibition, the stereotype was simply false. The unaware viewer would never have been able to guess which photos were taken by the "artist" and which ones by the "scientis".

Indeed, Zdeněk Stuchlík as an artist simply accepts the world along with its amazing complexity. He does not try to explain or even tentatively order reality. He does not strive to improve it. His photos represent faithful, unprocessed images of specific things. Some unyielding and eternal as seas, rocks or castles, others registered in a snapshot, and noticed exclusively by him. All Stuchlik's "things and voyages" constitute his own private catalogues of reality wherein he can accommodate portraits of his friends, views of Rio de Janeiro, as well as abstract light reflections in the fogs over the Gulf of Trieste. Stuchlík shows to us the beauty of the reality which is boundless, unique and inexplicable. He does his job humbly. He does not try to educate. Instead, he arranges his photographs in sequences whose deliberate lack of order imitates the puzzling and confusing randomness of the real world.

2 STUCHLÍK THE SCIENTIST: NAKED SINGULARITIES.

In its 19th December 2020 issue, *The Spectator* published a remarkable interview with Sir Roger Penrose by Dr Thomas Fink. In the interview, Penrose says that the Nobel Committee in Stockholm may have jumped the gun stating that they awarded him the Prize "for the discovery that black hole formation is a robust prediction of the general theory of relativity".

– I never proved black holes could be there, generically – smiles Penrose – *What I proved was that singularities had to be there.*

In the interview, Penrose carefully corrects this surprisingly common, and quite old, misconception that he has proved the existence of black holes, i.e. the existence of compact objects with the event horizon. No, he has not — and nobody ever has. Neither has he proven his own cosmic censor hypothesis, stating that singularities are always hidden inside event horizons, so that they cannot be visible from the outside. His original 1965 singularity theorem is quite remarkable, for it is based only on a few very general assumptions: it does not need even to assume Einstein's field equations! Indeed, a scrupulous and accurate student of the theorem would notice that all Roger Penrose needed for his proof was:

(1) The existence of the 4D space-time $\mathbb{M}$ with a Lorentzian metric.
(2) An existence in $\mathbb{M}$ of a compact, 2D *trapped surface* $\mathbb{T}$ such that both the ingoing and outgoing congruences of null geodesics emerging from $\mathbb{T}$ converge, in the sense of the negative expansion invariant, $\theta < 0$.
(3) The gravity is attractive in the sense that along any congruence of null geodesics, $\mathrm{d}\theta/\mathrm{d}\mu < 0$, where μ is the affine parameter along the congruence.
(4) There exists a non-compact Cauchy surface (this is roughly equivalent to say that the space-time has a trivial topology, for example it is not wrapped in space into a cylinder).

Note that usually instead of (3) one assumes the weak energy condition $R_{ab}X^aX^b > 0$, with X^a being a null vector and then one uses the Raychaudhuri equation, together with $\omega = 0$, in order to conclude that $\mathrm{d}\theta/\mathrm{d}\mu < 0$. Note also that $\omega = 0$ is not an extra assumption, as it must be $\omega = 0$ at the trapped surface $\mathbb{T}$ for the congruence in question (the congruence emerges from the surface $\mathbb{T}$ orthogonally) and thus, from the Newman Penrose equation for $\mathrm{d}\omega/\mathrm{dit}$ follows that $\omega = 0$ everywhere along this congruence.

I prefer to use the assumption $\mathrm{d}\theta/\mathrm{d}\mu < 0$ rather than $R_{ab}X^aX^b > 0$, as it avoids (seemingly only, but this is all right) the murky subject of the energy condition, the cosmological question of Λ, and so on.

One should be aware of the important point here: the Penrose theorem is far more general than most of the commentators, even those with a Ph.D. in physics, say (or know). The theorem works in *all Lorentzian*, and *not only strictly Einsteinian*, space-times in which gravity is attractive, which admit trapped surfaces, and which have a trivial topology (non-compact Cauchy surfaces). In such space-times singularities, *defined as null geodesic incompleteness*, are unavoidable. The Einstein field equations play no role in the proof when one assumes $\mathrm{d}\theta/\mathrm{d}\mu < 0$ instead of the usual $R_{ab}X^aX^b > 0$.

The space times and circumstances considered by Penrose are far more general than those strictly consistent with Einstein's theory. This was, perhaps still another reason for Penrose's delicate smile when he quoted Nobel Committee's wording of their explanation why they awarded him the Prize...

Nobody has proved that the Penrose cosmic censor hypothesis holds even in the standard Einstein's relativity. Could it therefore be so, that in our Universe the naked singularities are present? And if they are present, what would be their observable signatures? This is one of a few fundamental questions that have occupied Stuchlík's mind for a long time. Even

years before the Event Horizon Telescope time he and his collaborators in Opava were calculating images of naked singularities that would be in principle eventually possible to observe.

They found that the naked singularity images have features that are qualitatively (topologically) different than those that black holes may be consistent with. This is independent of all uncertainties with the emissivity properties of matter that surrounds these objects and is the source of photons emitted there, which are eventually detected by the EHT. Today the resolution is still too weak to dig out these features, but it will quickly, in a matter of a few years, improve.

I have only mentioned the naked singularities here, because they are so closely connected to this year's Nobel Prize in physics. But Stuchlík and colleagues are studying other possibilities as well: wormholes, strange stars, horizontless objects in alternative gravity theories... All these subjects belong to new, the brave and marvellous, future of physics. Very near future. Observations by EHT, Ligo-Virgo, Gravity and other astrophysical instruments alike, together with the purely theoretical insight coming from the directions that Zdeněk Stuchlík pioneered long ago and which are now the main subject of many, will soon open the flood gates. I hope to see successful and direct observational testing of the sweet dreams of XX and XXI century physics: *you better watch out — quantum gravity is coming to town!*

3 STUCHLÍK THE EDUCATOR.

Theoretical physics is not a profession like others, but almost an existential condition, a necessity of life. It requires a passionate commitment to conduct research, continuous and persistent self-education and joyful teaching of students at all university levels. The latter aspect is as important as the two first. Every theorist must be personally involved in education: preparing solid and interesting lectures, even when teaching is not an obligation arising from his university employment.

Dennis Sciama, John Wheeler, Richard Feynman and Lev Landau were probably the most charismatic and successful teachers of university physics in the XX century. I had the privilege to spent many years in Sciama's group, first in Oxford and then in Trieste, and two years in Wheeler's group in Austin, Texas. I have experienced first hand their tradition and attitude towards teaching physics, the quality of their courses and their unique style of shaping friendly and helpful master-student relations. To me, it is obvious that the way of teaching physics at Opava under Zdeněk, compares well with these best-in-class examples. Stuchlík has been able to create the school in which, at all stages of education, students are in the safe hands of their professors who offer each of them an individual plan to learn. Students enjoy academic freedom, but at the same time have well defined duties, and are involved not only in learning, but also, step by step, in participating in the Department's research and even in some administrative work. Stuchlík devotes a lot of extra- curricular time, giving himself personal tutorials to all students who need help.

And, of course, everyday we all go together for lunches, often for dinners, and sometimes to the *Slezské divadlo* (‘ ‘it's an opera”).

4 ZDENĚK, MY CZECH REFERENCE POINT.

To conclude, let me say something rather personal. I am a Pole who does not speak Czech, but who throughout his whole adult life, was fascinated by Czech culture, literature, way of life and customs. When I think of the personalities important in Czech culture and science who influenced me most of all, I remember, of course, Johannes Kepler, Jehuda Löw, Jan Hus, Franz Kafka, Christian Doppler, Alfons Mucha, Egon Erwin Kisch, Karel Čapek, Emil Zátopek, Bohumil Hrabal, Milan Kundera, Václav Havel, Marta Kubišová, Miloš Forman, Helena Vondráčkova, Jiří Bičák and Jara Cimrman... Then *Praga magica* where once I lived alone in a large, nice apartment at Malá Strana, through all seasons of the year changing one after the other. And, of course, Zdeněk Stuchlík who is my most important Czech reference point.

One day, Zdeněk and I enjoyed an evening in *U Krbu* , our favourite restaurant in Opava, in the company of a few colleagues, mostly from the University, and a few students. We all were a bit drunk. Not much, of course, just a tiny bit. – *Zdenku* – I asked – *tell me please, taking into account just everything you could think of: which country in Europe would you consider to be the best to live a happy life?*
– *The Czech Republic.* – he replied immediately
– *Really? And why not Switzerland?* – I expressed my surprise.
– *Because our mountains are smaller.*

Zdeněk Stuchlík, *Macho in the Window* (Rio de Janeiro, 2003)

This book is especially dedicated to Professor Zdeněk Stuchlík and his work as a celebration of his 70th birthday.

Zdeněk Stuchlík: *The Message* (Berlin, 2007)

Zdeněk Stuchlík: *The Corridor of Ethernity* (Opava, 2003)

Man in Fire
(NYC, 2011)

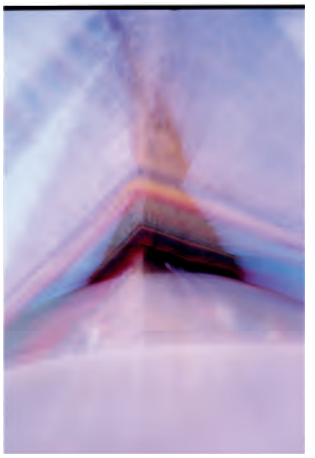

The Temple
(Kathmandu, 2010)

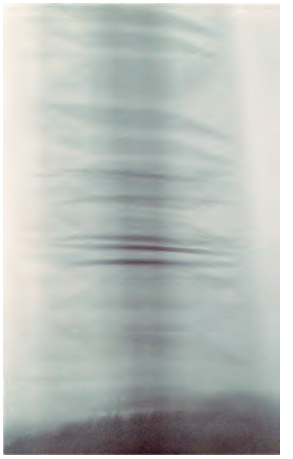

Jet to Heaven
(Opava, 2007)

Zdeněk Stuchlík: *Triangle* (Paris, 2009)

Zdeněk Stuchlík: *Goodes* (Kathmandu 2008)

Zdeněk Stuchlík: *Night Watch*
(Kathmandu 2020)

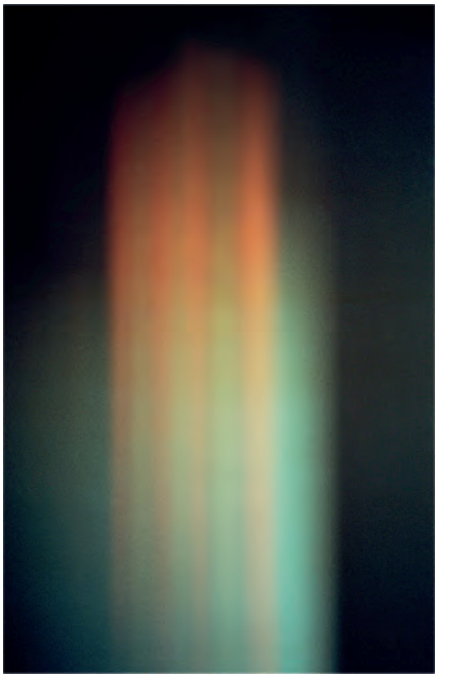

Zdeněk Stuchlík: *Arising of Stars*
(Frankfurt an der Oder, 2016)

Zdeněk Stuchlík: *Return of a Lady* (Opava, 2011)

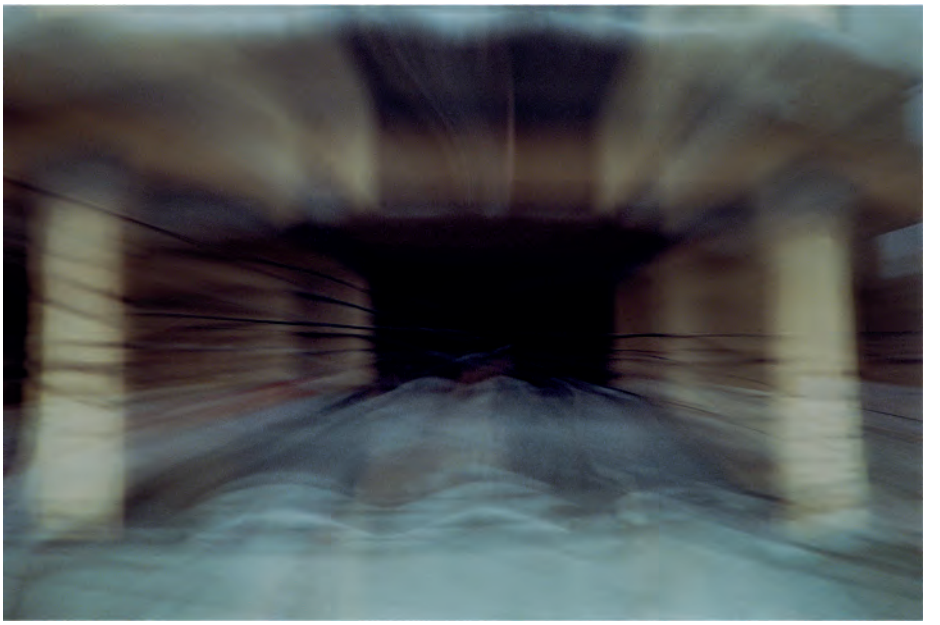

Zdeněk Stuchlík: *Way to a Black Hole* (Kathmandu 2010)

Proceedings of *RAGtime 20–22, 15–19 Oct., 16–20 Sept., 19–23 Oct., 2018/2019/2020, Opava, Czech Republic*
Z. Stuchlík, G. Török and V. Karas, editors, Silesian University in Opava, 2020, pp. 1–9

Charged particle dynamics in the vicinity of Reissner-Nordström black hole

Madina Boboqambarova[1,a] Bobur Turimov[1,2]
and Bobomurat Ahmedov[1]

[1]Ulugh Beg Astronomical Institute, Astronomicheskaya 33, Tashkent 100052, Uzbekistan
[2]Research Centre for Theoretical Physics and Astrophysics, Institute of Physics,
Silesian University in Opava, Bezručovo nám. 13, CZ-74601 Opava, Czech Republic
[a]asmik96@astrin.uz

ABSTRACT
The charged particle motion in Reissner-Nordström spacetime has been discussed. Equation of motion for charged particle around electrically (ECBH) and magnetically (MCBH) charged black holes has been considered by using the Hamilton-Jacobi formalism. The parameters of the innermost stable circular orbit (ISCO) such as energy, angular momentum, and position of particle have been explicitly investigated. The dependences of the energy efficiency, the velocity of charged particle, and the capture cross-section of charged particle by RN black hole on the charge coupling parameter are shown.

Keywords: Reissner-Nordström spacetime – black hole – charged particle

1 INTRODUCTION

New data from observations of black holes provide new motivations for studying the dynamics of particles in the framework of the General relativity. Because the motion of the test particles clearly describes the properties of the spacetime of the black hole and the hidden singularity. The motion of uncharged and spinless sample particles is controlled only by geodesic equations and directly determines the geodesic structure of spacetime. However, charged test particles can experience not only gravitational, but also an electromagnetic field, and accordingly can provide information about the electromagnetic properties of a black hole. In this work, we studied the circular motion of charged test particles around spherically symmetric, electrically and magnetically charged non-rotating black holes. By using the Hamilton-Jacobi formalism, we obtain the basic equations governing the innermost stability of circular orbits and the associated energies, angular moments, and also the particle velocities in these orbits.

The detailed analyses of neutral particle motion Pugliese et al. (2011a), dynamics charged of particle Bini et al. (2007); Pugliese et al. (2011b, 2017); Das et al. (2017) in Reissner-Nordström spacetime has been studied. In the Ref. Grunau and Kagramanova

978-80-7510-432-8

(2011) geodesics of electrically and magnetically charged test particles in the Reissner-Nordström spacetime has been investigated. The capture cross-section of massless and massive particles by the charged black hole has been investigated in Zakharov (1994). The innermost stable circular orbits of charged spinning test particles have been analyzed in Zhang and Liu (2019). In Ref. Zaslavskii (2010) the effect of charged particles acceleration by the black holes in Reissner-Nordström spacetime has been studied. In Refs. Zaječek et al. (2018); Ghosh et al. (2020) the significance of the electric and magnetic charge of the astrophysical black hole has been discussed. In Ref. Stuchlík et al. (2020) dynamical motion of charged particle in the vicinity of rotating black hole in the presence of external magnetic field has been investigated.

In the present research, we are interested in investigating of charged particle motion around electrically (ECBH) and magnetically (MCBH) charged black holes. One of the simple candidates for such black holes is described by the Reissner-Nordström metric as

$$\mathrm{d}s^2 = -f(r)\mathrm{d}t^2 + \frac{\mathrm{d}r^2}{f(r)} + r^2\left(\mathrm{d}\theta^2 + \sin^2\theta\mathrm{d}\phi^2\right), \qquad f(r) = 1 - \frac{2M}{r} + \frac{Q^2}{r^2}, \tag{1}$$

where M is the gravitational mass of a black hole, Q is its total charge which can be either the *electric charge* ($Q = Q_e$) or *magnetic charge* ($Q = Q_m$). In these cases, the components of the associated vector potential of the electromagnetic fields are given as

$$A_t = -\frac{Q_e}{r}, \qquad A_\phi = Q_m\cos\theta, \tag{2}$$

Note that the metric (1) together with (2) are, fully, satisfied the Einstein-Maxwell field equations. The radius of outer spacelike horizon can be calculated, from equation $f = 0$, as $r_+ = M^2 + \sqrt{M^2 - Q^2}$. Notice that throughout the paper, we use system of a geometrized units, $G = c = 1$.

2 HAMILTON-JACOBI EQUATION

The Hamilton-Jacobi equation for charged particle of mass m and charge q is given by

$$g^{\alpha\beta}\left(\frac{\partial S}{\partial x^\alpha} - qA_\alpha\right)\left(\frac{\partial S}{\partial x^\beta} - qA_\beta\right) = -m^2, \tag{3}$$

with solution, $S = -Et + L\phi + S_r + S_\theta$, then

$$-\frac{1}{f}\left(E + \frac{qQ_e}{r}\right)^2 + f\left(\frac{\partial S_r}{\partial r}\right)^2 + \frac{1}{r^2}\left(\frac{\partial S_\theta}{\partial\theta}\right)^2 + \frac{(L - qQ_m\cos\theta)^2}{r^2\sin^2\theta} = -m^2\,. \tag{4}$$

where E, L are the energy and angular momentum of test particle at the infinity, respectively. S_r and S_θ are the radial and angular functions. Here one can see that equation (4) is fully separable into radial and angular parts. Hereafter performing simple algebraic

manipulations, one can show that

$$S_r = \int \frac{\mathrm{d}r}{f} \sqrt{\left(E + \frac{qQ_e}{r}\right)^2 - f\left(m^2 + \frac{K}{r^2}\right)}, \tag{5}$$

$$S_\theta = \int \mathrm{d}\theta \sqrt{K - \frac{(L - qQ_m \cos\theta)^2}{\sin^2\theta}}, \tag{6}$$

where K is the Carter constant of motion.

Before go further, we introduce the following useful notations:

$$\mathcal{E} = \frac{E}{m}, \quad \mathcal{L} = \frac{L}{mM}, \quad \mathcal{K} = \frac{K}{(mM)^2}, \quad \mathcal{Q} = \frac{Q}{M}, \tag{7}$$

and the radial coordinate is normalized as $r \to r/M$. Now we write components of momentum as $p^\alpha = g^{\alpha\beta}(\partial S/\partial x^\beta)$, on the other hand $p^\alpha = m\dot{x}^\alpha = m(dx^\alpha/d\lambda)$, where λ is an affine parameter. Finally, taking into account all facts above, equations of motion can be written as

$$\dot{t} = \frac{1}{f}\left(\mathcal{E} + \frac{\sigma_e}{r}\right), \qquad \dot{\phi} = \frac{\mathcal{L} - \sigma_m \cos\theta}{r^2 \sin^2\theta}, \tag{8}$$

$$\dot{r}^2 = \left(\mathcal{E} + \frac{\sigma_e}{r}\right)^2 - f\left(1 + \frac{\mathcal{K}}{r^2}\right) \equiv \frac{R(r)}{r^4}, \qquad R(r) \geq 0, \tag{9}$$

$$\dot{\theta}^2 = \frac{1}{r^4}\left[\mathcal{K} - \frac{(\mathcal{L} - \sigma_m \cos\theta)^2}{\sin^2\theta}\right] \equiv \frac{T(\theta)}{r^4}, \qquad T(\theta) \geq 0, \tag{10}$$

where the charge coupling parameters are defined as

$$\sigma_e = \frac{qQ_e}{mM}, \qquad \sigma_m = \frac{qQ_m}{mM}\,. \tag{11}$$

According to Refs. Shapiro and Teukolsky (1983); Misner et al. (1973), the spatial components of velocity of particle measured by a local observer can be determined as

$$v_{\hat{r}} = \sqrt{-\frac{g_{rr}}{g_{tt}}}\frac{\mathrm{d}r}{\mathrm{d}t} = \sqrt{1 - f\frac{r^2 + \mathcal{K}}{(r\mathcal{E} + \sigma_e)^2}}, \tag{12}$$

$$v_{\hat{\theta}} = \sqrt{-\frac{g_{\theta\theta}}{g_{tt}}}\frac{\mathrm{d}\theta}{\mathrm{d}t} = \frac{\sqrt{f}}{r\mathcal{E} + \sigma_e}\sqrt{\mathcal{K} - \frac{(\mathcal{L} - \sigma_m \cos\theta)^2}{\sin^2\theta}}, \tag{13}$$

$$v_{\hat{\phi}} = \sqrt{-\frac{g_{\phi\phi}}{g_{tt}}}\frac{\mathrm{d}\phi}{\mathrm{d}t} = \frac{\sqrt{f}}{r\mathcal{E} + \sigma_e}\frac{\mathcal{L} - \sigma_m \cos\theta}{\sin\theta}, \tag{14}$$

which allows to write

$$\mathcal{E} = \frac{\sqrt{f}}{\sqrt{1 - v^2}} - \frac{\sigma_e}{r}, \qquad v^2 = v_{\hat{r}}^2 + v_{\hat{\theta}}^2 + v_{\hat{\phi}}^2\,. \tag{15}$$

Notice that near the horizon i.e. $f = 0$, the radial velocity will be $v_{\hat{r}} = 1$, while angular componets vanish $v_{\hat{\theta}} = v_{\hat{\phi}} = 0$.

3 INNERMOST STABLE CIRCULAR ORBIT (ISCO)

It is important to compute the radius of the stable circular orbit of test particle so-called innermost stable circular orbit (ISCO) radius. In order to find the ISCO radius for test particle one can use the following conditions:

$$R(r)=0, \qquad \frac{\mathrm{d}R(r)}{\mathrm{d}r}=0, \qquad \frac{\mathrm{d}^2R(r)}{\mathrm{d}r^2}=0, \tag{16}$$

$$T(\theta)=0, \qquad \frac{\mathrm{d}T(\theta)}{\mathrm{d}\theta}=0, \qquad \frac{\mathrm{d}^2T(\theta)}{\mathrm{d}\theta^2}=0, \tag{17}$$

where the first equations in (16) and (17) provide the particle motion to be in the circular orbit (i.e. $\dot{r}=\dot{\theta}=0$), while the first order derivatives with respect to coordinates (r,θ) represent the stationary points of the functions $R(r), T(\theta)$. Finally, the last conditions in (16) and (17) correspond the minimum of the radial and angular functions. For simplicity, assume that black hole charge is negligibly small to change background spacetime, ($Q^2\to 0$, so that the lapse function will be $f(r)=1-2M/r$), however, contribution of the interaction terms are large enough in dynamics particle orbiting around black hole.

3.1 Charged particle in the vicinity MCBH

We first discuss charged particle motion around MCBH with $\sigma_m\neq 0$ and $\sigma_e=0$. Hereafter using the conditions (17), we obtain

$$\theta_0=\tan^{-1}\left(\frac{\sigma_m}{\mathcal{L}},\pm\frac{\sqrt{\mathcal{L}^2-\sigma_m^2}}{\mathcal{L}}\right), \qquad \mathcal{K}=\mathcal{L}^2-\sigma_m^2\,. \tag{18}$$

Then after eliminating the Carter constant, the radial function takes a form:

$$R(r)=\left(\mathcal{E}^2-1\right)r^4+2r^3-\left(\mathcal{L}^2-\sigma_m^2\right)r^2+2\left(\mathcal{L}^2-\sigma_m^2\right)r, \tag{19}$$

Recalling the conditions (16), and performing simple algebraic manipulations, one can obtain

$$\mathcal{E}=f\sqrt{\frac{r}{r-3}}, \qquad \mathcal{L}=\sqrt{\frac{r^2}{r-3}+\sigma_m^2}, \qquad r=6, \tag{20}$$

Finally, parameters of the ISCO such as the energy $\mathcal{E}_0$, angular momentum $\mathcal{L}_0$, angle θ_0 and radius r_0 for charged particle orbiting around MCBH take the form:

$$\mathcal{E}_0=\frac{2\sqrt{2}}{3}, \quad \mathcal{L}_0=\sqrt{12+\sigma_m^2}, \quad \theta_0=\tan^{-1}\left(\pm\frac{2\sqrt{3}}{\sigma_m}\right), \qquad r_0=6\,. \tag{21}$$

As one can see from equation (21) a position of the ISCO for charged particle orbiting around MCBH is located at $r_{\rm ISCO}=6$ and $\theta_{\rm ISCO}=\tan^{-1}\left(2\sqrt{3}/\sigma_m\right)$. Figure 1 draws dependence of ISCO positions from the charge coupling parameter.

On the other hand, it is easy to show that the orbital velocity measured by the local observer at the ISCO will be independent of coupling parameter σ_m, and it equals half of the speed of light, i.e. $v = 1/2$ as for neutral particle.

It is also an interesting task to demonstrate capture cross-section of charged particle by the black hole. According to Ref. Zakharov (1994), the impact parameter of a massive particle, b, can be found as,

$$b^2 = \alpha \mathcal{L}^2, \qquad \alpha = \frac{1}{\mathcal{E}^2 - 1}, \tag{22}$$

which allows to determine capture cross section $\sigma = \pi b^2$. Taking into account definition (22), the radial functions can be rewritten as, $\mathcal{R} = \alpha R/r$, or

$$\mathcal{R}(r) = r^3 + 2\alpha r^2 - \left(b^2 - \alpha\sigma_m^2\right) r + 2\left(b^2 - \alpha\sigma_m^2\right), \tag{23}$$

The existence condition for multiple roots is equivalent to vanishing of the discriminant of cubic equation (23), after simple calculations, one can obtain the explicit expressions for the impact parameter of charged particle orbiting around MCBH .... in the form:

$$b^2 = \frac{1}{2}\left[27 + 18\alpha - \alpha^2 + (\alpha + 9)\sqrt{(\alpha + 9)(\alpha + 1)}\right] + \alpha\sigma_m^2, \tag{24}$$

In comparison with the expression for impact parameter in Ref. Zakharov (1994), there is additional term in equation (24) given as $\alpha\sigma_m^2$ which arises due to the electromagnetic interaction between the black hole and particle. From here one can conclude that capture cross-section of charged particle by MCBH increases for $\alpha > 0$, while it decreases for $\alpha < 0$ in comparison with that for a neutral particle.

3.2 Charged particle in the vicinity ECBH

Now we focus on charged particle motion around ECBH with $\sigma_e \neq 0$, $\sigma_m = 0$. Again after using the conditions in (17), one can find that particle is located in an equatorial plane with $\theta_0 = \pi/2$ and $\mathcal{K} = \mathcal{L}^2$. Then the radial function takes a form:

$$R(r) = \left(\mathcal{E}^2 - 1\right) r^4 + 2\left(1 - \mathcal{E}\sigma_e\right) r^3 - \left(\mathcal{L}^2 - \sigma_e^2\right) r^2 + 2\mathcal{L}^2 r, \tag{25}$$

Hereafter using conditions (16), one can obtain

$$\mathcal{E} = f\sqrt{\frac{r}{r-3} + \frac{\sigma_e^2}{4(r-3)^2}} - \frac{1}{2}\sigma_e \frac{r-4}{r(r-3)}, \tag{26}$$

$$\mathcal{L}_{\pm}^2 = \frac{r^2}{r-3}\left[1 \pm \sigma_e f\sqrt{\frac{r}{r-3} + \frac{\sigma_e^2}{4(r-3)^2}} + \frac{1}{2}\sigma_e^2 f\frac{1}{r-3}\right], \tag{27}$$

and

$$\left(r^2 - 4r + 6\right)\sigma_e^2 \pm (r-6)(r-2)\,\sigma_e\sqrt{4r(r-3) + \sigma_e^2} - 2r(r-3)(r-6) = 0, \tag{28}$$

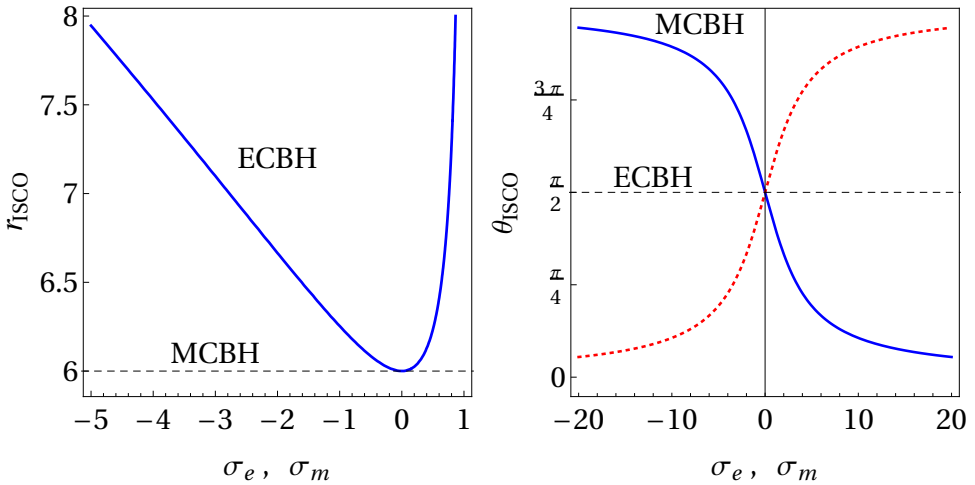

Figure 1. Dependence of the ISCO positions for charged particle orbiting around ECBH and MCBH on the charge coupling parameters $(\sigma_e, \sigma_m) \equiv (Q_e, Q_m)(q/mM)$.

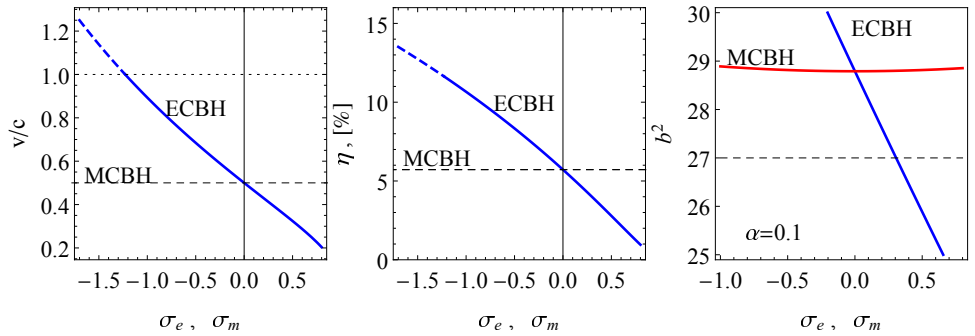

Figure 2. Dependence of the orbital velocity (left panel), the energy efficiency (centeral panel) and the impact parameter (right panel) of charged particle orbiting around ECBH and MCBH on the charge coupling parameters $(\sigma_e, \sigma_m) \equiv (Q_e, Q_m)(q/mM)$.

which allows finding the ISCO radius for charged particle. Unfortunatly, it is difficult to find analytical solution of the equation (28). However, careful numerical analyzes show that the ISCO for charged particle orbiting around will be always greater than that for neutral particle. Figure 1 draws dependence of the ISCO radius on the charge coupling parameters (σ_e, σ_m).

The orbital velocity measured by the local observer at the ISCO will be dependent on coupling parameter σ_e, and this dependence is expressed as follows:

$$v = \frac{\sqrt{f}\mathcal{L}}{r\mathcal{E} + \sigma_e}\,. \tag{29}$$

Figure 2 illustrates the dependence of the orbital velocity of charged particle measured by a local observer at the ISCO on the coupling parameter σ_e. It shows that for the positive value of the coupling parameter orbital velocity at the ISCO will be smaller than a half of the speed of light, $v = 1/2$, (which is responsible for neutral particle), and it decreases up to value $v \sim 0.16$, while for a negative value of coupling parameter it increases almost linearly and becomes larger than the speed of light for $\sigma_e < -1.23$, which corresponds to so-called superluminal motion. However, from the physical point of view, a massive particle can not move faster than the speed of light that is why at a sudden value of velocity charged particle starts to radiate and loses its energy.

In order to determine capture cross-section of particle by ECBH, we again write the radial function in the form:

$$\mathcal{R}(r) = r^3 + 2\left(\alpha - \sigma_e\sqrt{\alpha(1+\alpha)}\right)r^2 - \left(b^2 - \alpha\sigma_e^2\right)r + 2b^2\,. \tag{30}$$

As we mentioned before that the discriminant of the equation above should vanishes. Since the expression for the impact parameter is not simple, we decided to solve numerically. Figure 2 shows the dependence of the impact parameter on the charge coupling parameter for the case when α is equal to 0.1. The graph shows that the capture cross-section of charged particle by ECBH strongly depends on the charge coupling parameter, and increases with decreasing it.

3.3 Energy efficiency

It is also interesting to analyze the energy efficiency of the test particle, the ratio of the binding energy $mc^2 - E_{\rm ISCO}$, and the rest energy mc^2, can be found as, $\eta = 1 - \mathcal{E}_0$. As we show before that the ISCO energy for charged particle orbiting around MCBH is the same as for neutral particle, which means the energy efficiency should be the same. So that one can obtain $\eta_{\rm MCBH} \sim 6\%$. On other hand, the detailed analyses show that the energy efficiency for charged particle orbiting around ECBH strongly depends on the charged coupling parameter σ_e, that can reach a maximal value of $\sim 12\%$ as shown in Fig.2.

4 CONCLUSIONS AND FUTURE OUTLOOK

We investigated charged test particle motion in Reissner-Nordstrom spacetime. Using the Hamiltonian formalism, equation of motion for charged particle orbiting around both ECBH and MCBH has been explicitly derived. It is shown that the charge coupling parameter dramatically changes the behavior of particle in the vicinity of the black hole.

The parameters of the innermost stable circular orbit (ISCO) such as specific energy, specific angular momentum, and position of particle have been explicitly discussed. It is shown that the ISCO position for charged particle is located in an equatorial plane and will be greater than that for a neutral particle in the vicinity of ECBH, while in the vicinity of MCBH, it is the same as that for a neutral particle, but displaced from the equatorial plane. It is also shown that charged particle at the ISCO moves around MCBH with half of the speed of light, independently from the coupling parameter σ_m, like a neutral particle. However, the orbital velocity of charged particle moving at the ISCO around ECBH strongly

depends on the charge coupling constant. It increases with decreasing couple parameter, even becomes than the speed of light for the value $\sigma_e < -1.23$, which corresponds to so-called superluminal motion. However, from the physical point of view, a massive particle can not move faster than the speed of light that is why at a sudden value of velocity charged particle stars to radiate and loses its energy.

It has been shown that the dependence of capture cross-section on the charge coupling parameter, it can be seen that capture cross-section of charged particle by MCBH depends on square of the charge coupling parameter, and it decreases by decreasing α parameter. But, unlike the case for MCBH, the capture cross-section of charged particle by ECBH depends from the charge coupling parameter, and detailed analyses showed that this dependence will be stronger by increasing of the energy parameter α.

It is also shown that the energy efficiency of charged particle orbiting around MCBH will be independent of charge parameter, i.e $\eta_{\rm MCBH} \simeq 6\%$, while in the vicinity of ECBH, it strongly depends on charged parameter, σ_e, that can reach a maximal value of $\eta_{\rm ECBH} \sim 12\%$.

ACKNOWLEDGEMENTS

The present work is supported by the internal student grant SGS/12/2019 of Silesian University in Opava, Czech republic.

REFERENCES

Bini, D., Geralico, A. and Ruffini, R. (2007), On the equilibrium of a charged massive particle in the field of a Reissner Nordström black hole, *Physics Letters A*, **360**(4-5), pp. 515–517, arXiv: gr-qc/0608139.

Das, P., Sk, R. and Ghosh, S. (2017), Motion of charged particle in Reissner-Nordström spacetime: a Jacobi-metric approach, *European Physical Journal C*, **77**(11), 735, arXiv: 1609.04577.

Ghosh, D., Thalapillil, A. and Ullah, F. (2020), Astrophysical hints for magnetic black holes, *arXiv e-prints*, arXiv:2009.03363.

Grunau, S. and Kagramanova, V. (2011), Geodesics of electrically and magnetically charged test particles in the Reissner-Nordström space-time: Analytical solutions, *Phys. Rev. D*, **83**(4), 044009, arXiv: 1011.5399.

Misner, C. W., Thorne, K. S. and Wheeler, J. A. (1973), *Gravitation*, W. H. Freeman, San Francisco.

Pugliese, D., Quevedo, H. and Ruffini, R. (2011a), Circular motion of neutral test particles in Reissner-Nordström spacetime, *Phys. Rev. D*, **83**(2), 024021, arXiv: 1012.5411.

Pugliese, D., Quevedo, H. and Ruffini, R. (2011b), Motion of charged test particles in Reissner-Nordström spacetime, *Phys. Rev. D*, **83**(10), 104052, arXiv: 1103.1807.

Pugliese, D., Quevedo, H. and Ruffini, R. (2017), General classification of charged test particle circular orbits in Reissner-Nordström spacetime, *European Physical Journal C*, **77**(4), 206, arXiv: 1304.2940.

Shapiro, S. L. and Teukolsky, S. A. (1983), *Black Holes, White Dwarfs, and Neutron Stars*, John Wiley & Sons, New York.

Stuchlík, Z., Kološ, M., Kovář, J., Slaný, P. and Tursunov, A. (2020), Influence of Cosmic Repulsion and Magnetic Fields on Accretion Disks Rotating around Kerr Black Holes, *Universe*, **6**(2), p. 26.

Zajaček, M., Tursunov, A., Eckart, A. and Britzen, S. (2018), On the charge of the Galactic centre black hole, *Mon.Not.R.A.S*, **480**(4), pp. 4408–4423, arXiv: 1808.07327.

Zakharov, A. F. (1994), Particle capture cross sections for a Reissner–Nordström black hole, *Classical and Quantum Gravity*, **11**(4), pp. 1027–1033.

Zaslavskii, O. B. (2010), Acceleration of particles by nonrotating charged black holes?, *Soviet Journal of Experimental and Theoretical Physics Letters*, **92**(9), pp. 571–574, arXiv: 1007.4598.

Zhang, M. and Liu, W.-B. (2019), Innermost stable circular orbits of charged spinning test particles, *Physics Letters B*, **789**, pp. 393–398, arXiv: 1812.10115.

Proceedings of *RAGtime 20–22, 15–19 Oct., 16–20 Sept., 19–23 Oct., 2018/2019/2020, Opava, Czech Republic*
Z. Stuchlík, G. Török and V. Karas, editors, Silesian University in Opava, 2020, pp. 11–17

Flux ropes in SANE disks

Miljenko Čemeljić,[1,2,3,a] Feng Yuan[1] and Hai Yang[1]

[1]Shanghai Astronomical Observatory, Chinese Academy of Sciences,
80 Nandan Road, Shanghai 200030, China
[2]Nicolaus Copernicus Astronomical Center, Polish Academy of Sciences,
Bartycka 18, 00-716 Warsaw, Poland
[3]Academia Sinica, Institute of Astronomy and Astrophysics,
P.O. Box 23-141, Taipei 106, Taiwan
[a]miki@camk.edu.pl

ABSTRACT
Three-dimensional numerical simulations of a hot accretion flow around a supermassive black hole are performed using the general relativity magneto-hydrodynamic (GRMHD) code Athena++. We focus on the case of SANE, with the initial magnetic field consisting of multiple loops with oppositely directed poloidal magnetic field in the torus. Using the simulation data, we investigate the formation of flux ropes, follow the forming of flux ropes atop the disk, and their release into corona.

Keywords: accretion, accretion discs – black hole – MHD

1 INTRODUCTION

In the accreting systems, large scale jets are usually steady, while episodic jets are sometimes related to flares, which are observed on the smaller scale. One such example is Sgr A*, a massive black hole in the Galactic centre, where we observe radio, infrared and X-ray flares several times a day. It was concluded that delays in peaks in the light curves at different wavebands and their fast rise and slow decay in the brightness and polarisation are related to the ejection and expansion of plasmoids from the accretion flow. Knots in the jets are also observed, e.g. in 3C 120 and M87, and could be related to episodic emission. There are models, like e.g. Blandford and Znajek (1977) and Blandford and Payne (1982) for continuous jets, but we still do not have a viable model for episodic jets. In Yuan et al. (2009), such a model was proposed, in analogy with Coronal Mass Ejections (CMEs) in the Sun, with the closed magnetic field lines emerging from the main body of the accretion flow, expelled to the corona region: The foot-points of the magnetic loops are positioned in the turbulent accretion flow, and their twisting results in magnetic reconnection, forming the flux ropes. Because of the ongoing reconnection below such a flux rope, the magnetic tension force weakens, and the initial equilibrium between the magnetic tension and the magnetic pressure is not maintained. The flux ropes will be accelerated outwards, forming the episodic jet. The flares, observed from such jets, are from the emission originating from the electrons accelerated by the reconnection. In Shende et al. (2019), another model

978-80-7510-432-8

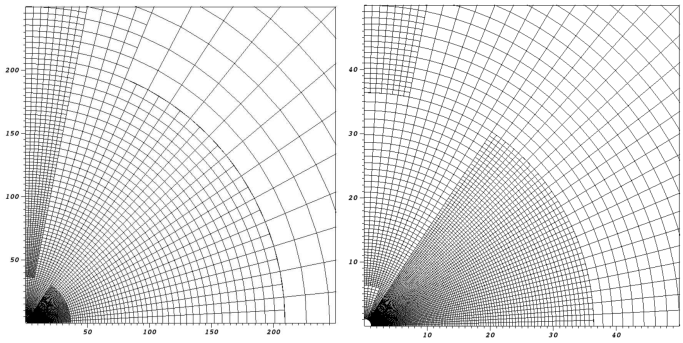

Figure 1. We use static mesh refinement for the grid, to obtain largest resolution where it is most needed. Resolution is $R \times \theta \times \varphi = (288 \times 128 \times 64)$ grid cells in spherical coordinates, in a physical domain reaching to 1200 gravitational radii. The different refinements used in this grid are shown.

was proposed, in analogy with Toroidal Instability from tokamak research and also used to model the CMEs.

Nathanail et al. (2020) present results of two-dimensional (2D) GRMHD simulations with the Black Hole Accretion Code (BHAC, Porth et al. (2019)), with Adaptive Mesh Refinement (AMR) of both Magnetically Arrested and Standard and Normal Evolution (MAD and SANE) discs. Different initial magnetic field configurations and resolutions are chosen. They find the formation of copious plasmoids and describe their outward motion. Similar simulations based on the same code, but with the physical resistivity included, are presented in Ripperda et al. (2020). They show no difference in results between the ideal and weakly resistive simulations. They conclude that 2D ideal MHD simulations, with only the numerical resistivity dissipating the magnetic field, can capture the physics.

In this work, we perform 3D GRMHD simulations to investigate the formation of magnetic flux ropes, checking the scenario proposed by Yuan et al. (2009).

2 NUMERICAL SIMULATIONS SETUP

We perform numerical simulations using the GRMHD code Athena++ (White et al., 2016) in full 3D, solving the ideal MHD equations in the Kerr metrics, in Kerr-Schild (horizon penetrating) coordinates. Resolution is $R \times \theta \times \varphi = (288 \times 128 \times 64)$ grid cells in spherical coordinates, in a physical domain reaching to 1200 gravitational radii, $r_g = GM/c^2$. We use different refinements in this grid, as shown in Fig. 1. The staggered mesh Constrained Transport (CT) method is applied to maintain the divergence-free magnetic field. Static mesh refinement is used for the grid, to obtain largest resolution where it is most needed. Initial configuration of density and magnetic field in our SANE simulation is shown in Fig. 2. The central object is not rotating.

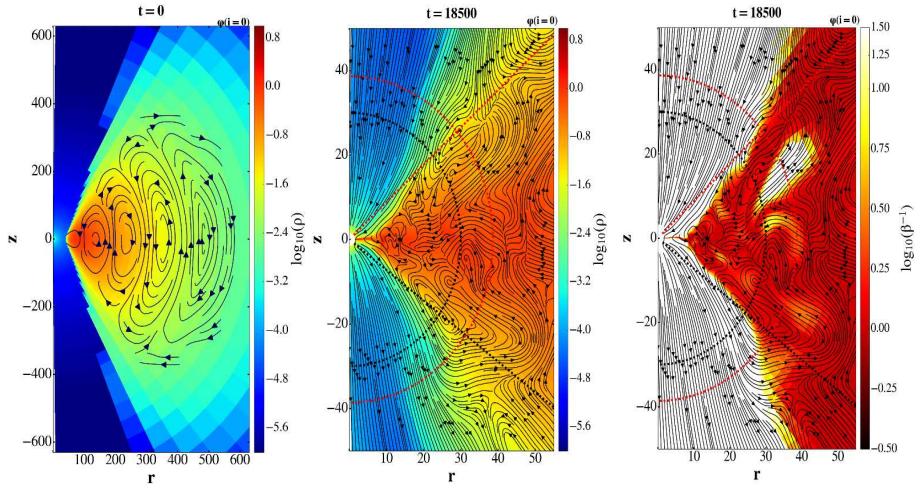

Figure 2. Left panel: The initial setup in our SANE simulation. The color denotes the density, solid lines denote the poloidal magnetic field with arrows showing the field direction. Middle panel: a zoomed-in snapshot in the result after $t = 18500\ r_g/c$. The positions of two magnetic islands are marked with the cross of two dotted black lines and two dotted red lines, respectively. Right panel: Same with the middle panel, but the color shows the plasma $\beta = P_{\rm gas}/P_{\rm mag}$. The two magnetic islands are located at the surface with plasma $\beta \sim 1$.

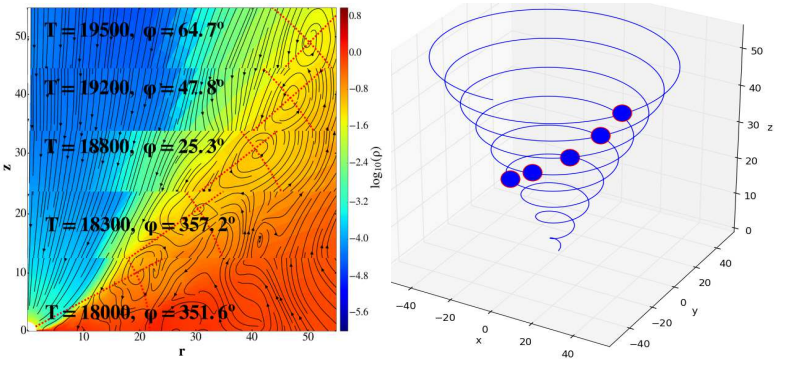

Figure 3. Left panel: Outward motion of the magnetic island in our simulation, in different colatitudinal planes. Right panel: Spiralling-out of the magnetic island in a schematic plot of the trajectory in 3D. Positions of the blue circles are chosen to approximately represent magnetic islands from the left panel.

3 FORMATION AND MOTION OF THE FLUX ROPE

Interchanging directions of the initial magnetic field in the torus prevent the field to grow too large, and magneto-rotational instability can provide the dissipation for successful

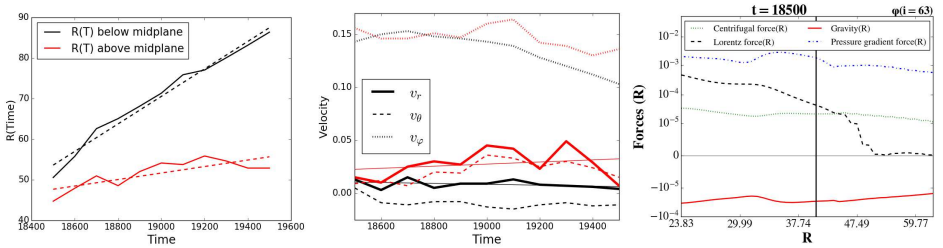

Figure 4. Time evolution of the position of the center of magnetic island (left panel) and velocity of the material near the center of magnetic island (middle panel) for two magnetic islands from Fig. 2. Slopes of the least square fits shown in dashed lines in the left panel are 0.03 c and 0.01 c for the black and red lines, respectively. In the middle panel, least square fits of the radial velocity components are shown by the corresponding color thin solid lines. In the right panel are shown forces, along the radial direction, on the material in the flux rope above the disk mid-plane, near the center of the magnetic island at $t = 18500\ r_g/c$.

accretion of material towards the central object. We perform our simulation until $t = 40000\ r_g/c$. A snapshot at $t = 18500\ r_g/c$ during the evolution of the accretion flow is shown in Fig. 2. We find magnetic islands in the colatitudinal (R, θ) planes, at different azimuths φ, after the relaxation from the initial conditions and stabilization of the flows. Such magnetic islands start forming after about $t = 15000\ r_g/c$. They periodically emerge from the disk surface at similar radii (azimuthal angle φ changes with the rotation of the disk), with period of about $t = 1000\ r_g/c$. The magnetic islands are extended in the azimuthal direction, forming magnetic flux ropes of various lengths. We trace the extension of the flux ropes in φ direction, which is typically about 120° or less, and perform slices in the middle of their length at different times–as shown in Fig. 3. In the same Figure we give a sketch in 3D of the counter-clockwise spiral trajectory of the indicated flux rope cross-sections. To understand the launching and motion of the flux rope, we measure positions of the magnetic islands and velocity of the material near their centers in time–see Fig. 4. Forces acting on the material in the magnetic islands in radial direction are also shown. The pressure gradient and Lorentz forces push the rope radially outwards.

The launching of the flux rope is caused by the reconnection in the disk, near the disk surface, as shown in the left panel Fig. 5. In the right panels in the same Figure is shown the reconnection signature in the magnetic field and velocity components perpendicular to the reconnection layer: all three magnetic field components and both poloidal velocity components change sign. Reconnection occurs throughout the disk and in the corona, but its effect on the matter depends on the value of plasma $\beta = P_{\rm gas}/P_{\rm mag}$. Only in the locations where it is about unity, material from the disk will be pushed by reconnection. In the rarefied corona, plasma β is much smaller, and in the dense disk, it is much larger than unity.

Inside the disk, which is accreting because of magneto-rotational instability (MRI) providing the sufficient dissipation, reconnection layers which are brought close to the disk surface, can result in the formation of flux rope and its further ejection into the corona.

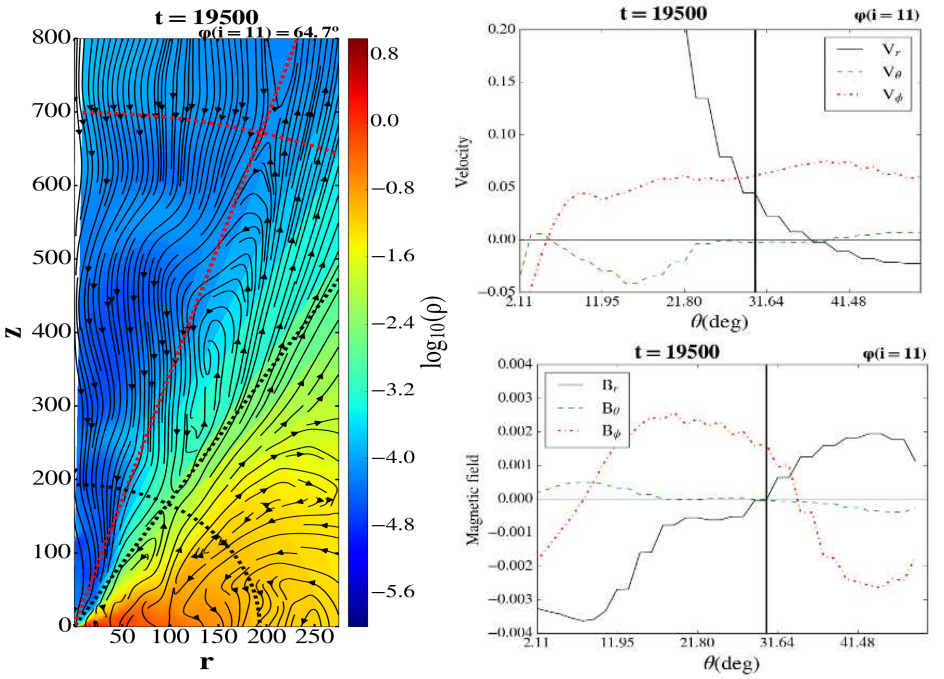

Figure 5. Two reconnection layers with a magnetic island between them in a snapshot at $t = 19500\ r_g/c$ in our simulation are marked with the black and red dotted lines in the left panel. In the right panels are shown the velocity and magnetic field components at the same time, along a part of the black dotted line circle passing through the reconnection layer. A signature of reconnection, change in the direction of poloidal velocity and all three components of magnetic field, is visible in the projections in θ-direction. A similar signature is obtained in the reconnection layer positioned at the intersection of red dotted lines.

Once lifted into the rarefied corona, the flux rope can be expelled outwards or break. In both cases it would be observed as episodic emission from the vicinity of the black hole.

In addition to the reconnection layer below the magnetic flux rope, there is another reconnection layer, above the magnetic flux rope in our simulations–see Fig. 5. It helps the opening of the magnetic field lines and ejection of the flux rope.

4 CONCLUSIONS

We have performed 3D ideal GRMHD numerical simulations of a hot accretion flow around a black hole, to study formation and motion of flux ropes. During the time-evolution until $t = 40000\ r_g/c$, magnetic flux ropes of the azimuthal extension of about 120° or less are formed, which show as magnetic islands in 2D slices in colatitudinal planes at different azimuthal angles. These flux ropes are created by reconnection close to the disk surface, where the plasma β, defined as the ratio of the gas to magnetic pressure, is close to unity.

Because of the reconnection and disk differential rotation, the flux ropes are twisted and pushed radially outwards and launched into the corona, spiralling-out from the central object. The radial velocity of their outward propagation is of the order of 0.01 c.

Ejection of the flux ropes from the disk surface repeats periodically in our simulation, with the period of about 1000 $r_{\rm g}/c$. It could cause episodic flaring from the vicinity of the disk around a black hole.

In addition to the reconnection layer near the disk surface, which forms the flux rope, another reconnection layer above the flux rope can form, helping its outward launch.

ACKNOWLEDGEMENTS

MČ was supported by CAS President's International Fellowship for Visiting Scientists (grant No. 2020VMC0002), and the Polish NCN grant 2019/33/B/ST9/01564. FY and HY are supported in part by the National Key Research and Development Program of China (Grant No. 2016YFA0400704), the Natural Science Foundation of China (grants 11633006), and the Key Research Program of Frontier Sciences of CAS (No. QYZDJSSW-SYS008). This work made use of the High Performance Computing Resource in the Core Facility for Advanced Research Computing at Shanghai Astronomical Observatory. We thank the referee for constructive questions and suggestions.

REFERENCES

Blandford, R. D. and Payne, D. G. (1982), Hydromagnetic flows from accretion disks and the production of radio jets., *Mon. Not. R. Astron Soc.*, **199**, pp. 883–903.

Blandford, R. D. and Znajek, R. L. (1977), Electromagnetic extraction of energy from Kerr black holes., *Mon. Not. R. Astron Soc.*, **179**, pp. 433–456.

Nathanail, A., Fromm, C. M., Porth, O., Olivares, H., Younsi, Z., Mizuno, Y. and Rezzolla, L. (2020), Plasmoid formation in global GRMHD simulations and AGN flares, *Mon. Not. R. Astron Soc.*, **495**(2), pp. 1549–1565, arXiv: 2002.01777.

Porth, O., Koushik, C., Ramesh, N. and et al. (2019), The Event Horizon General Relativistic Magnetohydrodynamic Code Comparison Project, *The Astrophysical Journal Supplement*, **243**(2), 26, arXiv: 1904.04923.

Ripperda, B., Bacchini, F. and Philippov, A. A. (2020), Magnetic Reconnection and Hot Spot Formation in Black Hole Accretion Disks, *The Astrophysical Journal*, **900**(2), 100, arXiv: 2003.04330.

Shende, M. B., Subramanian, P. and Sachdeva, N. (2019), Episodic Jets from Black Hole Accretion Disks, *The Astrophysical Journal*, **877**(2), 130, arXiv: 1904.10870.

White, C. J., Stone, J. M. and Gammie, C. F. (2016), An Extension of the Athena++ Code Framework for GRMHD Based on Advanced Riemann Solvers and Staggered-mesh Constrained Transport, *The Astrophysical Journal Supplement*, **225**(2), 22, arXiv: 1511.00943.

Yuan, F., Lin, J., Wu, K. and Ho, L. C. (2009), A magnetohydrodynamical model for the formation of episodic jets, *Mon. Not. R. Astron Soc.*, **395**(4), pp. 2183–2188, arXiv: 0811.2893.

Proceedings of *RAGtime 20–22, 15–19 Oct., 16–20 Sept., 19–23 Oct., 2018/2019/2020, Opava, Czech Republic*
Z. Stuchlík, G. Török and V. Karas, editors, Silesian University in Opava, 2020, pp. 19–28

Characteristic orbits of charged particles around charged black holes

Aleksandra Demyanova[1,a] Ozodbek Rakhimov[1,b]
Yunus Turaev[1,c] Nuriddin Kurbonov[1,d]
and Javlon Rayimbaev[1,2,e]

[1]Ulugh Beg Astronomical Institute, Tashkent, 100052,Uzbekistan
[2]National University of Uzbekistan, Tashkent 100174,Uzbekistan
[a]demyanova@astrin.uz
[b]rahimov@astrin.uz [c]yunus@astrin.uz
[d]nuriddin@astrin.uz
[e]javlon@astrin.uz

ABSTRACT
We have explored the dynamics of test particles around electrically charged Reissner-Nordström (RN) nonrotating black hole (BH). Particularly, we have studied the motion of charged particles around charged RN BH. It was found that there are two boundary conditions for specific angular momentum of stable circular orbits corresponding to innermost stable circular orbits (ISCO) and outermost stable circular orbits (OSCO). We have also shown that the accretion disk is originated between these two orbits. It was obtained the upper and lower limits for the values of the electric charge of the matter in the accretion disk around the extreme charged Reissner Nordström BH.

Keywords: Reissner-Nordström spacetime – black hole – test charged particle – particle dynamics –ISCO –OSCO

1 INTRODUCTION

Just after the discovery of general relativity two exact solutions of the Einstein field equation have been obtained by Schwarzschild describing non-rotating point-like massive object – black hole (BH) and by Reissner and Nordström independently describing the electrically and magnetically charged non-rotating black hole. However, these solutions have singularity at the center of the black hole ($r = 0$), which cannot be resolved within the theory. Other electrically and magnetically charged regular black hole solutions avoiding the singularity have been obtained within the framework of general relativity coupled to non-linear electrodynamics by several authors Bardeen (1968); Ayon-Beato (1999); Wang and Maartens (2010).

978-80-7510-432-8

a From astrophysical point of view the study the charged particles motion around charged BH and/or BH in external magnetic field is one of the important task. Recently, the motion of charged Rayimbaev et al. (2020); Turimov et al. (2020); Stuchlík et al. (2020); Tursunov et al. (2016), magnetized Rayimbaev (2016); de Felice and Sorge (2003); Abdujabbarov et al. (2020); Vrba et al. (2020); Rayimbaev et al. (2020) particles around black holes with different parameters in an external asymptotically uniform magnetic field in various theories of gravity have been studied. Particularly, the charged particle motion around Reissner-Nordström black hole has been studied in Pugliese et al. (2010, 2011).

In this paper we study the charged particle orbits around RN BH. The paper is organized as follow: in Sec. 2 we have considered charged particle motion in the spacetime of a charged black hole. In Sec. 3 we summarize the obtained results.

Throughout the work we use spacelike signature $(-,+,+,+)$ for the space-time and system of units where $G = 1 = c$. Latin indices run from 1 to 3 and Greek ones from 0 to 3.

2 MOTION OF CHARGED PARTICLES AROUND REISSNER-NORDSTRÖM BLACK HOLE

The geometry of the spacetime around electrically and magnetically charged RN BH in spherical coordinates ($x^\alpha = \{t, r, \theta, \phi\}$) is given in the following form

$$\mathrm{d}s^2 = -f\mathrm{d}t^2 + f^{-1}\mathrm{d}r^2 + r^2\left[\mathrm{d}\theta^2 + \sin^2\theta\mathrm{d}\phi^2\right], \tag{1}$$

with the following gravitational metric function

$$f = 1 - \frac{2M}{r} + \frac{Q^2}{r^2}, \tag{2}$$

and associated with the four vector potential of the electromagnetic field around the electrically charged BH

$$A_\alpha = \frac{Q}{r}\Big\{1, 0, 0, 0\Big\}, \tag{3}$$

where M and Q are the total mass and electric charge of the RN BH, .

Here we study the charged particle with rest mass m and electric charge e around charged BH. The Lagrangian for the charged particle in the electromagnetic field in the BH environment has the following form

$$\mathcal{L} = \frac{1}{2}mg_{\mu\nu}u^\mu u^\nu + eu^\mu A_\mu. \tag{4}$$

The conserved energy and angular momentum can be found by

$$g_{tt}\dot{t} + qA_t = \mathcal{E}, \tag{5}$$

$$g_{\phi\phi}\dot{\phi} = \mathcal{L}, \tag{6}$$

where $\mathcal{E} = E/m$ and $\mathcal{L} = L/m$ are the specific energy and angular momentum of the particle, respectively, $q = e/(mc)$ is the specific electric charge of the particle with mass m and electric charge e.

The equation of motion for charged particles with the Lagrangian (4) can be found using the Euler-Lagrange equation Pugliese et al. (2010)

$$u^{\mu}\nabla_{\mu}u^{\nu} = qF^{\nu}_{\sigma}u^{\sigma}, \tag{7}$$

where $F_{\mu\sigma} = A_{\sigma,\mu} - A_{\mu,\sigma}$ is the electromagnetic field tensor. Using the equations (5-7) one may easily find the equation of motion of the charged particles at the equatorial plane ($\theta = \pi/2$) in the following form:

$$\begin{aligned}
\dot{t} &= \frac{1}{f}\left(\mathcal{E} - \frac{qQ}{r}\right),\\
\dot{r}^2 &= \left(\mathcal{E} - \frac{qQ}{r}\right)^2 - f\left(1 + \frac{\mathcal{L}^2}{r^2}\right),\\
\dot{\phi} &= \frac{\mathcal{L}}{r^2}.
\end{aligned} \tag{8}$$

The effective potential for charged particle in the equatorial plane (where $\theta = \pi/2$ and $\dot{\theta} = 0$) can be found solving equation $\mathcal{E} = V_{\rm eff}$ ($\dot{r} = 0$):

$$V^{\pm}_{\rm eff}(r) = \frac{qQ}{r} \pm \sqrt{f\left(1 + \frac{\mathcal{L}^2}{r^2}\right)}. \tag{9}$$

Now we will study the positive root of the effective potential $V^{+}_{\rm eff}$: (i) In the case of $\left|\frac{qQ}{r}\right| < \sqrt{f\left(1 + \frac{\mathcal{L}^2}{r^2}\right)}$ the second root of the effective potential V^{-}_{eff} will be negative and (ii) in the case of $\left|\frac{qQ}{r}\right| > \sqrt{f\left(1 + \frac{\mathcal{L}^2}{r^2}\right)}$ the effective potential V^{-}_{eff} has neither maximum nor minimum.

Figure 1 illustrates the charged and neutral particles trajectories in similar bounded states with the same initial conditions $r_0 = 7M$ and $\theta_0 = 1.6$. In this figure, the grey area implies the hypothetical surface of the BH–horizon of the BH and dashed line for the region where bounded circular orbits are allowed. Here, we have aimed to show the bounded orbits for the different (charged and neutral) particles, by changing the angular momentum of the particles. One can easily see that for the neutral particle (black solid orbits at the middle row in Fig.1) the bounded orbits exists with specific angular momentum $\mathcal{L} = 3.5$ and energy $\mathcal{E} = 0.95$, while the orbits of positively charged particles $q = 1$ are bounded for the values: $\mathcal{L} = 4.33$ and $\mathcal{E} = 0.93$, and orbits of negatively charged particles $p = 1$ are bound for the values $\mathcal{L} = 2.53$ and $\mathcal{E} = 0.98$ due to the different feature of Coulomb interaction.

Stable circular orbits

Here we will study the stable circular orbits using following standard conditions

$$V_{\rm eff} = \mathcal{E}\,, \qquad V'_{\rm eff} = 0\,, \qquad V''_{\rm eff} = 0. \tag{10}$$

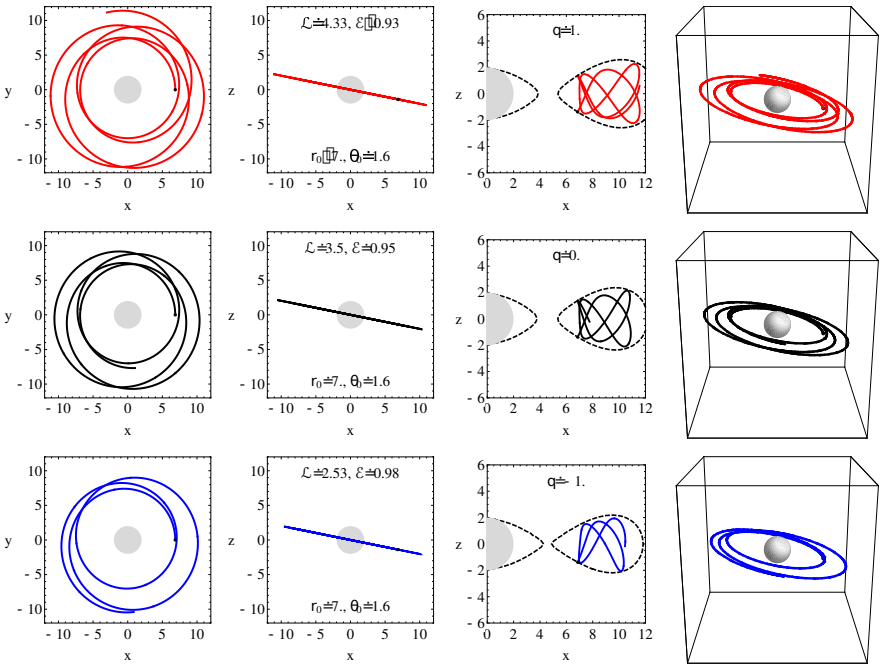

Figure 1. Trajectories of charged particles around Reissner-Nordström black hole with $Q = 0.5M$.

At the equatorial plane the circular orbits can be stable for the critical value of angular momentum $\mathcal{L}_{cr}$ which is the solution of the equation $V'_{\text{eff}} = 0$ and have the following form:

$$\mathcal{L}^2_{\pm} = \frac{1}{2\left(r\left(r-3M\right)+2Q^2\right)^2}\Big[Q^2r^3\left(\left(q^2-2\right)r-2M\left(q^2-5\right)\right)+2Mr^4(r-3M) \\ +\left(q^2-4\right)Q^4r^2 \pm qQr^2\left(r\left(r-2M\right)+Q^2\right)\sqrt{4r(r-3M)+\left(q^2+8\right)Q^2}\Big]. \tag{11}$$

One can see from equation (11) that for positive charges $\mathcal{L}^2_+ < \mathcal{L}^2_-$ and for negative charges $\mathcal{L}^2_- > \mathcal{L}^2_+$. We also have

$$\mathcal{L}^2_+|_{q<0} = \mathcal{L}^2_-|_{q>0} < \mathcal{L}^2_+|_{q>0} = \mathcal{L}^2_-|_{q<0}\,. \tag{12}$$

This can be interpreted as follow: the circular orbits exist at the values of angular momentum for positive charge with angular momentum in the range $\mathcal{L}^2_- \le \mathcal{L}^2 \le \mathcal{L}^2_+$ and negative charge with angular momentum in the range $\mathcal{L}^2_- \ge \mathcal{L}^2 \ge \mathcal{L}^2_+$. The value of critical angular momentum for neutral particles ($q = 0$) has the following form

$$\mathcal{L}^2_{\pm} = \frac{r^2\left(Mr-Q^2\right)}{r\left(r-3M\right)+2Q^2}, \tag{13}$$

and in the case when $Q = 0$, we will get the Schwarzschild solution and the angular momentum takes the standard form

$$\mathcal{L}_{\pm}^2 = \frac{Mr^2}{r - 3M}. \tag{14}$$

Now we will analyze the solution (11) and look for the condition where both $\mathcal{L}_{\pm}^2$ are real. For this we require the expression inside the square root to be non-negative:

$$\left(q^2 + 8\right) Q^2 - 4r(3M - r) \geq 0\,. \tag{15}$$

Thus, for the critical value of specific angular momentum $\mathcal{L}$ we consider two cases:

Case 1 – since $\left(q^2 + 8\right) Q^2$ is always positive, then the we require the condition $r > 3M0$ for all values of q, including neutral particles ($q = 0$).

Case 2 – for the case when $r < 3M$ we require the condition $\left(q^2 + 8\right) Q^2 > 4r\,(3M - r)$ which will be satisfied for a large values of electric charge.

From the condition (15) one may get the lower limit for radius of the circular orbit of particle (at the same time the radius equals to the radius of photon circular orbits) when $\mathcal{L}$ is still real

$$r_{\rm crit} = \frac{3}{2} M \left(1 + \sqrt{1 - \frac{(q^2 + 8)}{9} \frac{Q^2}{M^2}}\right)\,. \tag{16}$$

In expression (16), in order to have real value for $r_{\rm crit}$ we require the expression under the square root to be non-negative: $9M^2 - \left(q^2 + 8\right) Q^2 \geq 0$. This will give us the interval for the allowed values of the electric charge of the particles:

$$-\frac{\sqrt{9 - 8\frac{Q^2}{M^2}}}{Q/M} \leq q \leq \frac{\sqrt{9 - 8\frac{Q^2}{M^2}}}{Q/M}\,. \tag{17}$$

Expression (17) indicates the allowed value of the charge of the test particle required for circular stable orbits.

Figure 2 illustrates the dependence of the value of the radius of photon circular orbits from the electric charge of the BH Q for the different values of the particle charge q. One can see that the radius decreases with the increase of the value of Q. From the Figure 2 one can also see that for the neutral test particle we get $r_{\rm crit} = 3M$ (the Scwarzchild case). It can be also seen from the figure that for the large values of Q and q, the photon sphere radius decreases very fast, depending both black hole and particles charge. The critical radius decreases with the increase of the black hole charge and reaches the value of $2M$ for $Q = M$ for neutral particle.

Now we will study the radius of stable circular orbits using the condition $V''_{\rm eff} \geq 0$. There are bounds for stable circular orbits corresponding to two roots of $\mathcal{L}^2$. One of them called innermost stable circular orbits (ISCO) and the other one called outermost stable circular orbits (OSCO). Inner stable circular orbits requires large angular moments, while outer ones requires smaller angular momentum. Obviously, according to equation (12), $\mathcal{L}_{+}^2$ for negative charges and $\mathcal{L}_{-}^2$ for positively charged particles correspond to OSCO and $\mathcal{L}_{+}^2$ for positively charged particles and $\mathcal{L}_{-}^2$ for negatively charged particles correspond to ISCO.

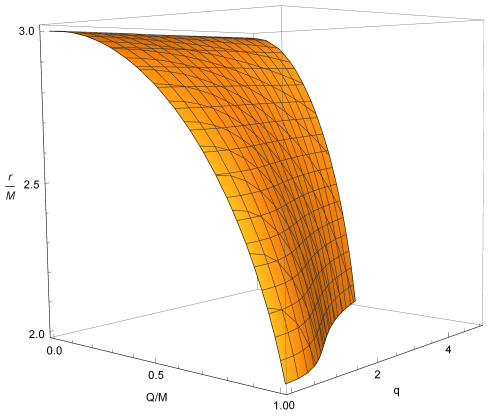

Figure 2. The dependence of radius of photon circular orbits on the charge of BH Q for the different values of the particle charge, q.

Taking into account above estimations we can calculate ISCO and OSCO equations using condition for circular stable orbits (10) in the following form

$$2q\,Q - \frac{\left(r^2\left(\mathcal{L}_\pm^2+Q^2\right)+2\mathcal{L}_\pm^2Q^2-Mr^3-3\mathcal{L}_\pm^2Mr\right)^2}{r\left(\mathcal{L}_\pm^2+r^2\right)^{3/2}\left(r(r-2M)+Q^2\right)^{3/2}} + \frac{3r^2\left(\mathcal{L}_\pm^2+Q^2\right)+10\mathcal{L}_\pm^2Q^2-2Mr^3-12\mathcal{L}_\pm^2Mr}{r\sqrt{\left(\mathcal{L}_\pm^2+r^2\right)\left[r(r-2M)+Q^2\right]}} \geq 0 \tag{18}$$

So, within the range $r_{\rm isco} \leq r \leq r_{\rm osco}$ there is an accretion disk contains the charged particles with the different specific angular momentum.

Now, we will analyze ISCO and OSCO radius for both positively and negatively charged particles.

Figure 3 illustrates the dependence of the ISCO and OSCO radius on the charge of the RN black hole charge for positively charged particles. One can see that in both cases $q = 1.4$ and $q = 0.8$ ISCO radius decreases with the increase the value of black hole charge. In case when $q = 0.8$ the radius of OSCO decreases with the increase of Q, while when $q = 1.4$ increases and tends to infinity at some upper values of $(qQ)_{\rm upper}$ due to domination of the Coulomb interaction.

Figure 4 illustrates the dependence of ISCO and OSCO radius on black charge for negatively charged particles. One can see that in both case $q = -1.4$ and $q = -0.8$ ISCO radius decreases with the increase of the value of black hole charge. The behavior of the radius of OSCO differs from the case of positive charge: for all negative charge of particles the radius of OSCO increases with the increase of the module of the charge.

[h]

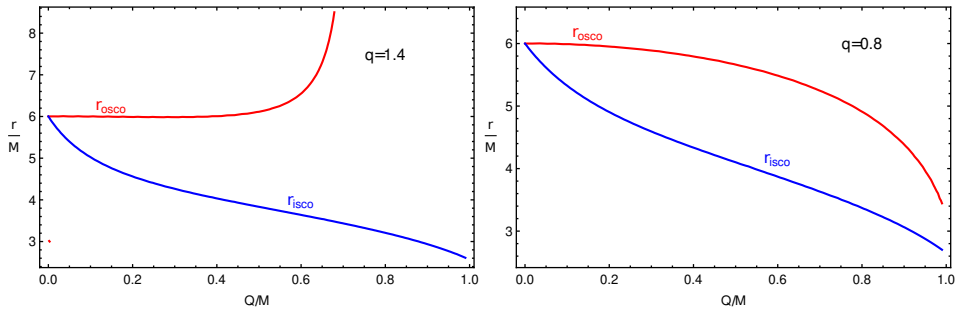

Figure 3. ISCO and OSCO radius as a function of black hole charge for positively charged particles.

[h!]

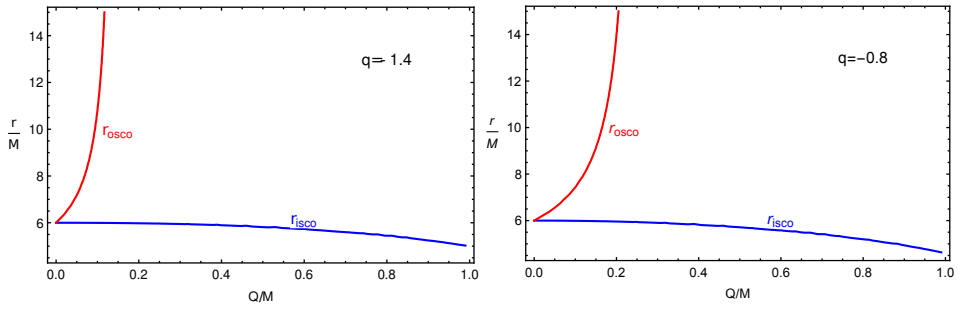

Figure 4. ISCO and OSCO radius as a function of black hole charge for negatively charged particles.

[h!]

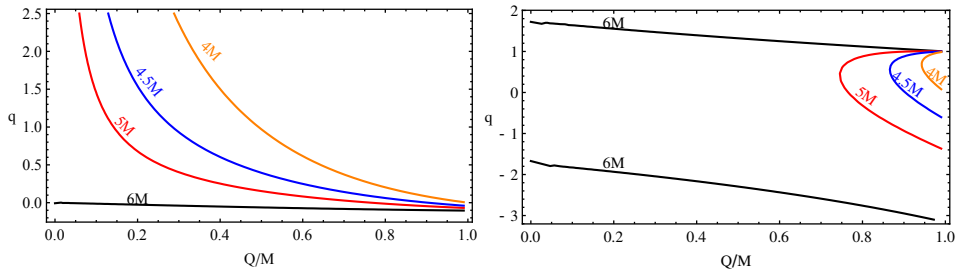

Figure 5. $q - Q$ diagram for different values of ISCO (left panel) and OSCO (right panel) radius of a charged particle.

In Figure 5 we present the relation between the particle's and the black hole's charges for the fixed values of ISCO and OSCO. One can see from the diagram that OSCO may not exist below the radius $6M$ from the central object for negatively charged particles and for positively charged particles with value more than $q = 2$. One can also see from the right panel of the Figure 5 OSCO radius (at the range $4M \leq r_{\rm osco} \leq 6M$) can be the same for different charged particles ($2 \leq q \leq -3$) for the fixed value of black hole charge.

Now we study thed istance between ISCO and OSCO corresponding to the size of accretion disk $\Delta r = r_{\rm osco} - r_{\rm isco}$.

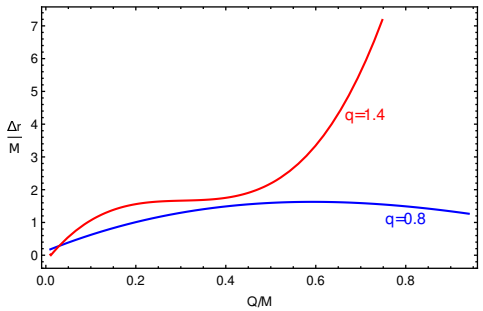

Figure 6. The dependence of the accretion disk size on black hole charge

In Figure 6 we show the relation between black hole charge, Q, and the size of the accretion disk which contains positively charged particles with values $q = 0.8$ and $q = 1.4$. From the Figure 6 one can see that size of accretion disk for the charge with the value $q < 1$ is always less than one in the case when $q > 1$. As it was shown in Figure 6 in case of when $q = 0.8$ the size Δr increases with the increase of Q, reaches its maximum then starts to decrease. However, the size increases with the increase of Q up to $\approx 0.45M$ then starts to increase due to increase the Coulomb force. Moreover, one can see that the delta r increases with increasing the particle charge. In the other words, the as sizeable specific charge of particles as wider the width of their allowed circular orbits in the accretion disk.

3 CONCLUSION

In this work, we have studied circular motion of charged particles around Reissner-Nordström black hole and the following main results are obtained:

- Upper and lower limits for the value of charged particle at circular orbits for the given value of RN black hole charge have been found.
- It was shown that the critical radius of circular orbits depends on particle charge.
- It was found that there are two critical values for the specific angular momentum for charged particles. One of them corresponds to the lower boundary and the other to the upper boundary of the stable circular orbits.

• It was shown that OSCO radius of positively charged particles increases with the increase of Q for $q > 1$ and it decreases with the increase of Q fr $q < 1$. However, OSCO radius for negatively charged particles increases with the increase of the black hole charge Q.

ACKNOWLEDGEMENTS

This research is supported by Grants No. VA-FA-F-2-008, No. MRB-AN-2019-29 and No. YFA-Ftech-2018-8 of the Uzbekistan Ministry for Innovational Development, and by the Abdus Salam International Centre for Theoretical Physics through Grant No. OEA-NT-01.

REFERENCES

Abdujabbarov, A., Rayimbaev, J., Turimov, B. and Atamurotov, F. (2020), Dynamics of magnetized particles around 4-D Einstein Gauss-Bonnet black hole, *Physics of the Dark Universe*, **30**, 100715.

Ayon-Beato, E. (1999), New regular black hole solution from nonlinear electrodynamics, *Physics Letters B*, **464**, pp. 25–29, arXiv: hep-th/9911174.

Bardeen, J. (1968), in C. DeWitt and B. DeWitt, editors, *Proceedings of GR5*, p. 174, Tbilisi, USSR, Gordon and Breach.

de Felice, F. and Sorge, F. (2003), Magnetized orbits around a Schwarzschild black hole, *Classical and Quantum Gravity*, **20**, pp. 469–481.

Pugliese, D., Quevedo, H. and Ruffini, R. (2010), Circular motion in Reissner-Nordstr\"om spacetime, *ArXiv e-prints*, arXiv: 1003.2687.

Pugliese, D., Quevedo, H. and Ruffini, R. (2011), Motion of charged test particles in Reissner-Nordström spacetime, *Phys. Rev. D*, **83**(10), 104052, arXiv: 1103.1807.

Rayimbaev, J., Abdujabbarov, A., Jamil, M., Ahmedov, B. and Han, W.-B. (2020), Dynamics of test particles around renormalization group improved schwarzschild black holes, *Phys. Rev. D*, **102**, p. 084016, URL https://link.aps.org/doi/10.1103/PhysRevD.102.084016.

Rayimbaev, J., Figueroa, M., Stuchlík, Z. and Juraev, B. (2020), Test particle orbits around regular black holes in general relativity combined with nonlinear electrodynamics, *Phys. Rev. D*, **101**(10), 104045.

Rayimbaev, J. R. (2016), Magnetized particle motion around non-Schwarzschild black hole immersed in an external uniform magnetic field, *Astrophys Space Sc*, **361**, 288.

Stuchlík, Z., Kološ, M., Kovář, J., Slaný, P. and Tursunov, A. (2020), Influence of Cosmic Repulsion and Magnetic Fields on Accretion Disks Rotating around Kerr Black Holes, *Universe*, **6**(2), p. 26.

Turimov, B., Rayimbaev, J., Abdujabbarov, A., Ahmedov, B. and Stuchlík, Z. c. v. (2020), Test particle motion around a black hole in einstein-maxwell-scalar theory, *Phys. Rev. D*, **102**, p. 064052, URL https://link.aps.org/doi/10.1103/PhysRevD.102.064052.

Tursunov, A., Stuchlík, Z. and Kološ, M. (2016), Circular orbits and related quasiharmonic oscillatory motion of charged particles around weakly magnetized rotating black holes, *Phys. Rev. D*, **93**(8), 084012, arXiv: 1603.07264.

Vrba, J., Abdujabbarov, A., Kološ, M., Ahmedov, B., Stuchlík, Z. and Rayimbaev, J. (2020), Charged and magnetized particles motion in the field of generic singular black holes governed by general relativity coupled to nonlinear electrodynamics, *Phys.Rev.D*, **101**(12), 124039.

Wang, A. and Maartens, R. (2010), Cosmological perturbations in Horava-Lifshitz theory without detailed balance, *Phys. Rev. D*, **81**(2), 024009, arXiv: 0907.1748.

Proceedings of *RAGtime 20–22, 15–19 Oct., 16–20 Sept., 19–23 Oct., 2018/2019/2020, Opava, Czech Republic*
Z. Stuchlík, G. Török and V. Karas, editors, Silesian University in Opava, 2020, pp. 29–37

Electrostatic effects on the hydrostatic equilibrium of compact stars

Sudipta Hensh,[1,a] Arman Tursunov,[1,b] Martin Urbanec[2] and Zdeněk Stuchlík[1]

[1]Research Centre for Theoretical Physics and Astrophysics, Institute of Physics, Silesian University in Opava, Bezručovo nám. 13, CZ-746 01 Opava, Czech Republic
[2]Research Centre for Computational Physics and Data Processing, Institute of Physics, Silesian University in Opava, Bezručovo nám. 13, CZ-746 01 Opava, Czech Republic
[a]sudiptahensh2009@gmail.com, f170656@fpf.slu.cz
[b]arman.tursunov@physics.slu.cz

ABSTRACT
We consider electrostatic effect on the fluid distribution of compact star. We modify the energy-momentum tensor including the electric field and current density terms and get a set of hydrostatic equilibrium equations which are an extended version of Tolman-Openheimer-Volkoff (TOV) equations. We expect that solutions of set of hydrostatic equations will lead to a mass-radius relation of the compact star configuration.

Keywords: electrostatic effect – modified energy momentum tensor –charge fluid configuration – charged neutron star

1 INTRODUCTION

Compact stellar objects such as neutron stars are the laboratories for study the physics in extreme conditions, being the crossroad of various disciplines of the contemporary physics. In the recent years, using the multi-wavelength and multi-messenger observations of neutron stars a large amount of data has been collected, stimulating an interest in testing various theories and theoretical models. The direct detection of gravitational waves in the event GW170817, from a binary neutron star merger (Abbott et al., 2017) opened up a new avenue in the investigation of these remarkable objects, on the other hand, restricting the applicability of some of the theories (see, e.g. Radice et al., 2018).

Neutron stars are compact stars with tremendously high densities, in which most of protons and electrons fuse together producing neutrons. However, closer to the surface of the neutron star, where the densities are expected to be less than in the center, some portion of charged particles, like protons and electrons may survive under certain conditions, so the local charge neutrality cannot be imposed (Rotondo et al., 2011). In this contribution

978-80-7510-432-8

we focus on the possibility of the neutron star to have non-negligible electric charge and corresponding electric field, which eventually modifies the conditions for the relativistic hydrostatic equilibrium.

The net charge contribution in case of the neutron stars is often neglected in the literature, justified by lack of astrophysical mechanisms for charging of this object to such values, for which the energy-momentum tensor of electromagnetic field would become comparable with those of the gravitational field of the neutron star. This problem is quite similar to the fact that the Reissner-Nordström spacetime metric for compact objects like black holes is not often used in realistic models. Neglecting the charge also simplifies the equations governing the hydrostatic equilibrium of neutron stars known as the Tolman-Oppenheimer-Volkoff (TOV) equation. However, in addition to the purely conceptual interest in studying charged compact star configurations, one can point out at least two realistic mechanisms of charging of compact stars, which we briefly summarize below.

The first mechanism is based on Arthur Eddington's idea formulated in Eddington (1926). Difference of masses of protons and electrons by a factor of almost 2×10^3 leads to the charge separation in the stellar atmosphere. Therefore, stars should possess a small and positive electric charge to prevent protons and electrons from further separation. Eddington estimated the charge of a star of the order of 100 C per solar mass. Later in 1978, Eddington's idea was generalized by Bally and Harrison (1978), concluding that any macroscopic cosmic body, including galaxies, stars and also the neutron stars bear a positive electric charge of the order of 100 C per solar mass. In this case, the positive charges of cosmic objects are compensated by negatively charged particles, i.e. electrons distributed in the intergalactic and interstellar media. Indeed, for ordinary stars, the density of charge obtained in this mechanism is negligibly small due to large stellar surface. However, due to compactness of neutron stars, having relatively small surface area, the charge density corresponding even to 100 C per solar mass might have some non-negligible impact. Moreover, similar charging mechanism has been recently applied also to black holes (see, e.g. Zaječek et al., 2018; Zajacek and Tursunov, 2019). It has been shown that the charge in case of black hole is not only measurable, but has quite important astrophysical consequences related to the acceleration of cosmic rays (Tursunov et al., 2020a; Tursunov and Dadhich, 2019) and interpretation of observational data of black holes (Tursunov et al., 2020b).

In addition to the above mentioned mechanism, the presence of the charge in neutron stars can be justified by using relativistic approach. Neutron stars are strongly magnetized with the strength of magnetic fields reaching up to 10^{18} G. If the highly magnetized neutron star is rotating (which is often the case, as observed e.g. in pulsars), this causes the induction of non-zero electric charge density, known as the Goldreich-Julian charge density, given by the relation

$$\rho_{\rm GJ} = \frac{1}{2\pi c}\Omega B, \tag{1}$$

where Ω is the angular velocity of the star (Goldreich and Julian, 1969). The relativistic rotation of a neutron star in the presence of strong and highly ordered magnetic field aligned with the rotation axis induces an electric field as in the case of the classical Faraday's unipolar dynamo, which causes charge separation in the neutron star matter leading to subsequent electric charge density given by Eq. (1).

At a high density of matter of a neutron star, the kinetic energy of electrons may become very high, so that it allows them to escape from the surface of the neutron star. The limit on this charge, thus, should be given by the electro-hydro-static equilibrium equations. Therefore, in both Newtonian and relativistic approaches neutron stars bear non-zero electric charge, motivating us to seek for corresponding modifications of the TOV equations.

The modifications of TOV equations by the presence of an electric charge of the neutron star have been previously studied by several authors. We briefly introduce some of these works. Bekenstein (1971) have shown that the metric corresponding to the spherical distribution of charged perfect fluid matches with the standard exterior Reissner-Nordström spacetime metric. Malheiro et al. (2004); Ray et al. (2006) found that strongly charged neutron star configurations (charge tending to its maximal limit) is possible, although such configuration is likely leads to the collapse of the star and subsequent formation of charged black hole. Bhatia et al. (1969) estimated the electric field on the surface of the star by the value of around $\sim 120\,\mathrm{V/cm}$ by solving the hydrostatic equilibrium equations including electrostatic interaction. Lemos et al. (2015) solved electrically modified TOV equation with an assumption of proportionality of the charge to the energy density distributions. Our approach somewhat follows the work of Lemos et al. (2015) with the difference that we include an additional interaction term in the stress-energy tensor expressed in terms of the four-current density and electromagnetic four-potential. When we neglect the additional term, resulting modified TOV equations match with those obtained by Lemos et al. (2015).

2 RELATIVISTIC BACKGROUND

The metric of the static spherically symmetric star can be written in the following general form

$$\mathrm{d}s^2 = -f(r)c^2\mathrm{d}t^2 + l(r)\mathrm{d}r^2 + r^2\left(\mathrm{d}\theta^2 + \sin^2\theta\mathrm{d}\phi^2\right). \tag{2}$$

Here, $f(r)$ and $l(r)$ are the function of a radial coordinate only, due to the spherical symmetry of the central object. The hydrostatic equation that we derive should be in accordance with the Einstein-Maxwell equations, which read

$$G_{\mu\nu} = \frac{8\pi G}{c^4}T_{\mu\nu}, \qquad \nabla_\nu F^{\mu\nu} = \frac{4\pi}{c}j^\mu, \tag{3}$$

where $G_{\mu\nu} = R_{\mu\nu} - \frac{1}{2}g_{\mu\nu}R$ is the Einstein tensor and $F_{\mu\nu} = \partial_\mu A_\nu - \partial_\nu A_\mu$ is the Faraday-Maxwell tensor written in the terms of the electromagnetic potential A_μ. Here $j^\mu = \rho_c u^\mu$ is the four-current of an electromagnetic field, where ρ_c is the charge density and u^μ is the four-velocity normalized by the condition $u_\mu u^\mu = -c^2$, which we can write as $u_\mu = (c\sqrt{-g_{tt}}, 0, 0, 0)$ in the static case. Note, that we use physical units throughout the paper.

We assume a static neutron star configuration with non-vanishing net charge density of the star, so that the four-current can be written as

$$j^\mu = \left(c\rho_c\sqrt{-g^{tt}}, 0, 0, 0\right). \tag{4}$$

2.1 Energy-momentum tensor

The total energy-momentum tensor can be represented as the sum of two terms

$$T_{\mu\nu} = T^{M}_{\mu\nu} + T^{EM}_{\mu\nu}, \tag{5}$$

where $T^{M}_{\mu\nu}$ corresponds to the energy-momentum tensor of a matter and $T^{EM}_{\mu\nu}$ is an electromagnetic energy-momentum tensor. In the present paper we consider a matter to be a perfect fluid with the total mass density ρ, pressure P, and four-velocity u_μ. Then the matter energy-momentum tensor $T^{M}_{\mu\nu}$ takes the form

$$T^{M}_{\mu\nu} = \left(\rho + P/c^2\right) u_\mu u_\nu + P g_{\mu\nu}. \tag{6}$$

The energy-momentum tensor responsible for the electromagnetic part can be found by variation of the action

$$S = \frac{1}{c}\int \mathcal{L}_{EM}\sqrt{-g}\mathrm{d}^4x, \tag{7}$$

with respect to the metric, where the Lagrangian is given by

$$\mathcal{L}_{EM} = \frac{1}{16\pi}F_{\mu\nu}F^{\mu\nu} + A_\mu j^\mu. \tag{8}$$

Here the first term of Eq. (8) is the pure contribution due to the electromagnetic field and the second term is responsible for the interaction of charged particles with an electromagnetic field. For the interaction term of the Lagrangian, one can find the corresponding energy-momentum tensor by using the Noether's theorem (Noether, 1971). It basically states that for each differentiable symmetry of the action of a physical system associates a conservation law. Generalization of the Noether's theorem to non-local field theories was studied in Krivoruchenko and Tursunov (2019). For the first term, describing the field, the energy-momentum tensor is calculated in a standard manner by variation of the action Eq. (7) with respect to $g_{\mu\nu}$ and putting on the boundaries $\delta g^{\mu\nu} = 0$, which gives

$$\frac{1}{2}\sqrt{-g}T_{\mu\nu} = \frac{\partial\sqrt{-g}\mathcal{L}}{\partial g^{\mu\nu}} - \frac{\partial}{\partial x^\lambda}\frac{\partial\sqrt{-g}\mathcal{L}}{\partial g^{\mu\nu}_{,\lambda}}. \tag{9}$$

Thus, one can write the total energy-momentum tensor for electromagnetic field with the interaction in the following form

$$T^{EM}_{\mu\nu} = \frac{1}{4\pi}\left(F^{\cdot\gamma}_{\mu}F_{\nu\gamma} - \frac{1}{4}g_{\mu\nu}F_{\gamma\beta}F^{\gamma\beta}\right) + A_\mu j_\nu. \tag{10}$$

One should note, that the symmetric property of the energy-momentum tensor requires that in the last term of Eq. (10) both A_μ and j_ν correspond to the same source.

Due to the spherical symmetry of the star, only nonzero component of an electric field should be E_r which implies that the nonzero components of a tensor of electromagnetic field are $F^{tr} = -F^{rt}$. Thus, the non vanishing components of the total energy-momentum

tensor Eq. (5) take the form

$$T_{tt} = \rho c^2 f(r) + \frac{1}{8\pi} l^{-1}(r) F_{rt}^2 + A_t(r) j_t(r), \tag{11}$$

$$T_{rr} = Pl(r) - \frac{1}{8\pi} f^{-1}(r) F_{rt}^2, \tag{12}$$

$$T_{\theta\theta} = r^2 \left(P + \frac{1}{8\pi} f^{-1}(r) l^{-1}(r) F_{rt}^2 \right), \tag{13}$$

$$T_{\phi\phi} = r^2 \left(P + \frac{1}{8\pi} f^{-1}(r) l^{-1}(r) F_{rt}^2 \right) \sin^2\theta. \tag{14}$$

Now, let us rewrite the Maxwell equation given in Eq. (3) as

$$\partial_\nu \left(\sqrt{-g} F^{\mu\nu} \right) = \frac{4\pi}{c} j^\mu \sqrt{-g} \, . \tag{15}$$

Here g is the determinant of metric tensor $g_{\mu\nu}$. If we solve the Maxwell equation then we get

$$\begin{aligned} \partial_r \left(\sqrt{l(r) f(r)} r^2 F^{tr} \right) &= 4\pi \rho_c r^2 \sqrt{l(r)}, \\ \Rightarrow F^{tr} &= \frac{Q(r)}{r^2 \sqrt{l(r) f(r)}}. \end{aligned} \tag{16}$$

The above equation can be rewritten as,

$$\frac{\mathrm{d}A_t(r)}{\mathrm{d}r} = \frac{Q(r)}{r^2} \sqrt{f(r) l(r)} \, , \tag{17}$$

where

$$\frac{\mathrm{d}Q(r)}{\mathrm{d}r} = 4\pi r^2 \rho_c \sqrt{l(r)} \, . \tag{18}$$

3 HYDROSTATIC EQUATIONS

Let us assume the function $l(r)$ in the spacetime metric satisfies the following relation

$$\frac{1}{l(r)} = 1 - \frac{2Gm(r)}{c^2 r} + \frac{GQ^2(r)}{c^4 r^2}, \tag{19}$$

which coincides with the external Reissner-Nordström metric.

Now we try to find the differential equation concerning mass of the stellar object considering F^{tr} from Eq. (16). Einstein equation for $G_{tt} = (8\pi G/c^4) T_{tt}$ is given by

$$\frac{f(r) \left(r l'(r) + l^2(r) - l(r) \right)}{r^2 l^2(r)} = \frac{8\pi G}{c^4} f(r) \rho(r) c^2 + \frac{G f(r) Q^2(r)}{c^4 r^4} + \frac{8\pi G}{c^4} A_t(r) j_t(r) \, . \tag{20}$$

Using the form of metric as per expression Eq. (19) we get,

$$\frac{\mathrm{d}m}{\mathrm{d}r} = 4\pi r^2\rho(r) + \frac{Q(r)}{c^2 r}\frac{\mathrm{d}Q(r)}{\mathrm{d}r} + \frac{4\pi r^2 A_t(r) j_t(r)}{c^2 f(r)} \,. \tag{21}$$

Taking the solution of Maxwell equation, F^{tr} from Eq. (16), we write Einstein equation for $G_{rr} = (8\pi G/c^4)T_{rr}$ as

$$\frac{rf'(r) - f(r)l(r) + f(r)}{r^2 f(r)} = \frac{8\pi G}{c^4} l(r)P(r) - \frac{Gl(r)Q^2(r)}{c^4 r^4} \,. \tag{22}$$

By manipulating above equation we get,

$$\frac{\mathrm{d}f(r)}{\mathrm{d}r} = \frac{8\pi G}{c^4} rf(r)l(r)P(r) - \frac{f(r)}{r} + \frac{f(r)l(r)}{r} - \frac{Gf(r)l(r)Q^2(r)}{c^4 r^3} \,. \tag{23}$$

Now we are interested to see the radial dependence of pressure inside the star. For this we introduce the energy-momentum conservation equation as

$$\nabla_\mu T^{\mu\nu} = 0 \,. \tag{24}$$

For $\nu = 1$ we get,

$$\frac{\mathrm{d}P(r)}{\mathrm{d}r} = -\frac{\Big(\rho(r)c^2 + P(r)\Big) f'(r)}{2f(r)} + \frac{Q(r)}{4\pi r^4}\frac{\mathrm{d}Q(r)}{\mathrm{d}r} - \frac{A_t(r) j_t(r) f'(r)}{2f^2(r)} \,. \tag{25}$$

Eqs. (17), (18), (21), (23), and (25) are the set of five governing equations which we have to solve simultaneously in order to obtain mass-radius relation.

3.1 Set of equations to be solved

Using Eq. (19) we can simplify Eq. (23) as follows

$$\frac{\mathrm{d}f(r)}{\mathrm{d}r} = \frac{f(r)\Big(\frac{8\pi GrP(r)}{c^4} + \frac{2Gm(r)}{c^2 r^2} - \frac{2GQ^2(r)}{c^4 r^3}\Big)}{\Big(1 - \frac{2Gm(r)}{c^2 r} + \frac{GQ^2(r)}{c^4 r^2}\Big)}. \tag{26}$$

From Eq. (4) we can write

$$j_t = c\rho_c(r) g_{tt}\sqrt{-g^{tt}} = -c\rho_c(r)\sqrt{f(r)} \,, \tag{27}$$

and substituting Eqs. (18), (26) and (27) into the pressure equation Eq. (25) we get

$$\begin{aligned}\frac{\mathrm{d}P(r)}{\mathrm{d}r} = &-\frac{\Big(\rho(r)c^2 + P(r)\Big)\Big(\frac{4\pi GrP(r)}{c^4} + \frac{Gm(r)}{c^2 r^2} - \frac{GQ^2(r)}{c^4 r^3}\Big)}{\Big(1 - \frac{2Gm(r)}{c^2 r} + \frac{GQ^2(r)}{c^4 r^2}\Big)} \\ &+ \rho_c \frac{Q(r)/r^2}{\sqrt{1 - \frac{2Gm(r)}{c^2 r} + \frac{GQ^2(r)}{c^4 r^2}}} + \frac{c\rho_c A_t(r)\Big(\frac{4\pi GrP(r)}{c^4} + \frac{Gm(r)}{c^2 r^2} - \frac{GQ^2(r)}{2c^4 r^3}\Big)}{\sqrt{f(r)}}.\end{aligned} \tag{28}$$

Below we summarize a set of equations which we have to solve in order to describe the configuration

$$\frac{\mathrm{d}A_t(r)}{\mathrm{d}r} = \frac{Q(r)}{r^2}, \tag{29}$$

$$\frac{\mathrm{d}Q(r)}{\mathrm{d}r} = \frac{4\pi r^2 \rho_c}{\sqrt{1 - \frac{2Gm(r)}{c^2 r} + \frac{GQ^2(r)}{c^4 r^2}}}, \tag{30}$$

$$\frac{\mathrm{d}m}{\mathrm{d}r} = 4\pi r^2 \rho(r) + \frac{4\pi r \rho_c Q(r)}{c^2 \sqrt{1 - \frac{2Gm(r)}{c^2 r} + \frac{GQ^2(r)}{c^4 r^2}}} - \frac{4\pi r^2 \rho_c A_t(r)}{c\sqrt{f(r)}}, \tag{31}$$

$$\frac{\mathrm{d}f(r)}{\mathrm{d}r} = \frac{f(r)\left(\frac{8\pi G r P(r)}{c^4} + \frac{2Gm(r)}{c^2 r^2} - \frac{2GQ^2(r)}{c^4 r^3}\right)}{\left(1 - \frac{2Gm(r)}{c^2 r} + \frac{GQ^2(r)}{c^4 r^2}\right)}, \tag{32}$$

$$\begin{aligned}\frac{\mathrm{d}P(r)}{\mathrm{d}r} = &- \frac{\left(\rho(r)c^2 + P(r)\right)\left(\frac{4\pi G r P(r)}{c^4} + \frac{Gm(r)}{c^2 r^2} - \frac{GQ^2(r)}{c^4 r^3}\right)}{\left(1 - \frac{2Gm(r)}{c^2 r} + \frac{GQ^2(r)}{c^4 r^2}\right)} \\ &+ \rho_c \frac{Q(r)/r^2}{\sqrt{1 - \frac{2Gm(r)}{c^2 r} + \frac{GQ^2(r)}{c^4 r^2}}} \\ &+ \frac{c\rho_c A_t(r)\left(\frac{4\pi G r P(r)}{c^4} + \frac{Gm(r)}{c^2 r^2} - \frac{GQ^2(r)}{2c^4 r^3}\right)}{\sqrt{f(r)}}.\end{aligned} \tag{33}$$

3.2 Density profile of mass and charge

We have five differential equations to be solved to find $A_t(r)$, $Q(r)$, $m(r)$, $f(r)$, $P(r)$, $\rho(r)$ and $\rho_c(r)$. So we have to get rid of two unknowns to close the system. At first we calculate for constant density inside distribution i.e.

$$\rho(r) = \text{constant}\,. \tag{34}$$

We assume

$$\rho_c(r) = \beta\rho(r)\,, \tag{35}$$

where β is a dimensionless parameter describing the charge fraction in the distribution.

As now we know $\rho(r)$ and $\rho_c(r)$ from Eqs. (34) and (35), we finally have five equations for five unknowns. Therefore the system is closed.

3.3 Initial and boundary conditions

At the center of the star we can consider that $m(0) = 0$, $Q(0) = 0$, $A_t(0) = 0$ and $l(0) = 1$. We also consider that $P(0) = P_0$, $\rho(0) = \rho_0$ and $\rho_c(0) = \rho_{c0}$ where P_c is the central pressure, ρ_0 is the central mass density and ρ_{c0} is the central charge density.

We have to consider the pressure of the distribution vanish at the surface i.e. $P(R) = 0$, where R is the radius of the star. Apart from that it must be taken into account that the electric field at infinity is zero, i.e. $r \to \infty$, $A_t \to 0$ and the spacetime is asymptotically flat which means $r \to \infty$, $f \to 1$.

Following these initial and boundary conditions if we solve system of equations numerically then we can find mass-radius relation and maximum mass that can be supported by this configuration. We leave the numerical calculations for further studies.

4 SUMMARY

We revisited the problem of charged neutron star which might be realistic and astrophysically relevant. We have derived modified TOV Eqs. (29) - (33), governing quantities of our interest. These equations together with Eqs. (34) and (35) can be simultaneously solved numerically, which we will complete in the future work, where we also plan to use realistic equations of state.

5 ACKNOWLEDGMENT

S.H. acknowledges the support from the internal student Grant No. SGS/12/2019 of SU. Authors would like to acknowledge the institutional support of the Institute of Physics, Silesian University in Opava. M.U. was supported by LTT17003.

REFERENCES

Abbott, B. P., et. al, LIGO Scientific Collaboration and Virgo Collaboration (2017), GW170817: Observation of Gravitational Waves from a Binary Neutron Star Inspiral, *PhysRevLett.*, **119**(16), 161101, arXiv: 1710.05832.

Bally, J. and Harrison, E. R. (1978), The electrically polarized universe., *The Astrophysical Journal*, **220**, p. 743.

Bekenstein, J. D. (1971), Hydrostatic Equilibrium and Gravitational Collapse of Relativistic Charged Fluid Balls, *Phys. Rev. D*, **4**(8), pp. 2185–2190.

Bhatia, M. S., Bonazzola, S. and Szamosi, G. (1969), Electric Field in Neutron Stars, *Astron. Astrophys.*, **3**, p. 206.

Eddington, A. S. (1926), *The Internal Constitution of the Stars*.

Goldreich, P. and Julian, W. H. (1969), Pulsar Electrodynamics, *The Astrophysical Journal*, **157**, p. 869.

Krivoruchenko, M. and Tursunov, A. (2019), Noether's Theorem in Non-Local Field Theories, *Symmetry*, **12**(1), p. 35, arXiv: 1602.03074.

Lemos, J. P. S., Lopes, F. J., Quinta, G. and Zanchin, V. T. (2015), Compact stars with a small electric charge: the limiting radius to mass relation and the maximum mass for incompressible matter, *European Physical Journal C*, **75**, 76, arXiv: 1408.1400.

Malheiro, M., Picanço, R., Ray, S., Lemos, J. P. S. and Zanchin, V. T. (2004), Of Charged Stars and Charged Black Holes, *International Journal of Modern Physics D*, **13**(7), pp. 1375–1379.

Noether, E. (1971), Invariant variation problems, *Transport Theory and Statistical Physics*, **1**(3), p. 186–207, ISSN 1532-2424, URL http://dx.doi.org/10.1080/00411457108231446.

Radice, D., Perego, A., Zappa, F. and Bernuzzi, S. (2018), GW170817: Joint Constraint on the Neutron Star Equation of State from Multimessenger Observations, *Astrophysical Journal Letters*, **852**(2), L29, arXiv: 1711.03647.

Ray, S., Malheiro, M., Lemos, J. P. S. and Zanchin, V. T. (2006), Electrically Charged Compact Stars, in *The Tenth Marcel Grossmann Meeting. On recent developments in theoretical and experimental general relativity, gravitation and relativistic field theories*, p. 1361, arXiv: nucl-th/0604039.

Rotondo, M., Rueda, J. A., Ruffini, R. and Xue, S. S. (2011), The self-consistent general relativistic solution for a system of degenerate neutrons, protons and electrons in β-equilibrium, *Physics Letters B*, **701**(5), pp. 667–671, arXiv: 1106.4911.

Tursunov, A. and Dadhich, N. (2019), Fifty Years of Energy Extraction from Rotating Black Hole: Revisiting Magnetic Penrose Process, *Universe*, **5**(5), p. 125, arXiv: 1905.05321.

Tursunov, A., Stuchlík, Z., Kološ, M., Dadhich, N. and Ahmedov, B. (2020a), Supermassive Black Holes as Possible Sources of Ultrahigh-energy Cosmic Rays, *The Astrophysical Journal*, **895**(1), 14, arXiv: 2004.07907.

Tursunov, A., Zajaček, M., Eckart, A., Kološ, M., Britzen, S., Stuchlík, Z., Czerny, B. and Karas, V. (2020b), Effect of Electromagnetic Interaction on Galactic Center Flare Components, *The Astrophysical Journal*, **897**(1), 99, arXiv: 1912.08174.

Zajacek, M. and Tursunov, A. (2019), The Electric Charge of Black Holes: Is It Really Always Negligible, *The Observatory*, **139**, pp. 231–236, arXiv: 1904.04654.

Zajaček, M., Tursunov, A., Eckart, A. and Britzen, S. (2018), On the charge of the Galactic centre black hole, *Mon. Not. R. Astron Soc.*, **480**(4), pp. 4408–4423, arXiv: 1808.07327.

Proceedings of *RAGtime 20–22, 15–19 Oct., 16–20 Sept., 19–23 Oct., 2018/2019/2020, Opava, Czech Republic*
Z. Stuchlík, G. Török and V. Karas, editors, Silesian University in Opava, 2020, pp. 39–53

Propagation of waves in polytropic disks

Jiří Horák

Astronomical Institute, Academy of Sciences, Boční II 141 31 Prague, Czech Republic

ABSTRACT
We derive an analytic dispersion relation for waves in three-dimensional polytropic disks. The problem can be separated to two one-dimensional problems of radial and vertical wave propagation. For the vertical problem, we use and generalize first-order perturbation method for waves near the vertical resonance introduced previously by several authors. Based on comparison of the analytical solutions with numerical integration, we find a surprisingly large region of validity of our dispersion relation including both p-mode and g-mode oscillations.

Keywords: perturbation methods – disk dynamics

1 INTRODUCTION

One of the most prominent observation features of galactic black-hole candidates is a rapid and strong X-ray variability. Apart from the chaotic fluctuations, the signal occasionally also contains relatively coherent discrete features known as the quasi-periodic oscillations (QPOs) superimposed on a broad-band noise continuum in the power density spectra. In addition to the most prominent QPOs observed at low frequencies (from 0.1Hz to 30Hz), the accreting objects also occasionally show a variability at frequencies of few hundreds Hz that correponds to dynamical timescales of the flow in the vicinity of the central black hole.

Perhaps the most advanced theoretical models of high-frequency QPOs are based on the relativistic diskoseismology that deals with oscillation modes and wave propagation in geometrically thin accretion flows (Kato, 2001; Kato et al., 2008; Wagoner, 2008). Different types of oscillation modes are most easily discussed with the aid of the local dispersion relation for vertically isothermal accretion disks (Okazaki et al., 1987),

$$\tilde{\omega}^2 c_{\rm s}^2 k_r^2 - \left(\tilde{\omega}^2 - \kappa^2\right)\left(\tilde{\omega}^2 - j\Omega_\perp^2\right) = 0. \tag{1}$$

Here, the background flow has sound speed $c_{\rm s}$ and orbital velocity Ω, a particular mode is described by its oscillation frequency ω, azimuthal wavenumber m and vertical quantum number j, the oscillation frequency with respect to the flow is given by $\tilde{\omega} = \omega - m\Omega$, and finally κ and $\Omega_\perp$ are the radial and vertical epicyclic frequencies determined by the gravity of the central object. For given values of ω, m and j, the dispersion relation (1) gives value of the squared radial wavevector k_r^2. The oscillations can radially propagate as free waves when $k_r^2 > 0$. The case $k_r^2 < 0$ corresponds to evanescent waves. It is obvious from

978-80-7510-432-8

equation (1) that for $j \geq 1$ there exist two types of freely propagating waves: g-modes for which $\tilde{\omega}^2 < \kappa^2$ and p-modes with $\tilde{\omega}^2 > j\Omega_\perp^2$. For $j = 0$, there exists only p-modes with $\tilde{\omega}^2 > 0$. The terminology is derived from the nature of the main restoring forces: in the case of p-modes, it is pressure gradient, and therefore they are essentially acoustic waves, in the case of g-modes it is mostly gravity and inertial forces. The dispersion relation also reveals three important resonances where k_r either vanish, or is infinite. The Lindblad resonance correspond to radii where $\tilde{\omega} = \pm\kappa$. In the case of the vertical resonances $\tilde{\omega} = \pm\sqrt{j}\Omega_\perp$. Finally, the corotation resonance occurs at the radius where oscillation frequency matches the local orbital frequency, and thus $\tilde{\omega} = 0$.

In this note, we will derive a dispersion relation similar to equation (1) describing the waves propagating in polytropic disks. This subject has been touched by several authors already. Korycansky and Pringle (1995) studied propagation of axisymmetric waves in polytropic disks with vertical stratification of the entropy. The authors derive numerical dispersion relation. Ortega-Rodríguez et al. (2002) investigated p-modes in relativistic disks and introduced the perturbation method that is used here. The same method was also used by Kato (2010) to study nearly vertical $m = 2$ disk oscillations.

The plan of the paper is as follows. In section 2 we introduce the separation to the radial and vertical problems. Section 3 deals with the vertical problem and its solution in some special cases. The main results of this work are in section 4 that deals with the approximate solution of the vertical problem for a general polytropic index. The last section 5 is devoted to conclusions.

2 RADIAL AND VERTICAL WAVE PROPAGATION

The problem of adiabatic linear oscillations of a purely rotating inviscid flows leads to a single linear partial differential equation for the enthalpy perturbations h,

$$\frac{\partial}{\partial r}\left(\frac{r\rho}{D}\frac{\partial h}{\partial r}\right) - \frac{r}{\tilde{\omega}^2}\frac{\partial}{\partial z}\left(\rho\frac{\partial h}{\partial z}\right) - \left[\frac{r\rho}{c_\mathrm{s}^2} + \frac{m^2\rho}{rD} + \frac{2m}{\tilde{\omega}}\frac{\partial}{\partial r}\left(\frac{\rho\Omega}{D}\right)\right]h = 0. \tag{2}$$

Here the cylindrical coordinates $\{r, \phi, z\}$ are employed and the equilibrium state of the disk is described by the density $\rho(r, z)$, the sound speed $c_\mathrm{s}(r, z)$ and the angular velocity $\Omega(r)$. The perturbation is assumed to depend on the time and azimuthal angle through the factor $\exp[\mathrm{i}(m\phi - \omega t)]$, where m is the azimuthal wave number and ω is the angular frequency of the perturbation with respect to static observers. The angular frequency with respect to the flow is Doppler-shifted to the value $\tilde{\omega} = \omega - m\Omega$ and $D = \kappa^2 - \tilde{\omega}^2$ is the determinant of the $r\phi$ block of the Euler equations with κ being the radial epicyclic frequency. Equation (2) is valid for arbitrary angular momentum distribution. In the case of geometrically thick (toroidal) flows, the substitution $W = h/\tilde{\omega}$ leads to the well-known Papaloizou-Pringe equation (Papaloizou and Pringle, 1984).

In the case of cold geometrically thin Keplerian disks, the radial pressure gradient is negligible with respect to inertial forces. Consequently, the equilibrium structure of the flow varies slowly in the radial direction while it changes quickly in the vertical one. The ratio of the horizontal to vertical pressure gradients are typically of the order of r/H, where r is the radial coordinate and $H \sim c_{\mathrm{s}0}/\Omega \ll r$ is the vertical scale-high of the disk and $c_{\mathrm{s}0}$

is the equatorial value of the sound speed. On the other hand, a typical wavelength of the perturbation is of the order of c_{s0}/Ω and therefore it is comparable with the scale-height H. Under these circumstances, the equation (2) is nearly separable and the problem is tractable using a radial WKBJ approximation.

To outline this procedure, in the following we adopt the two-scale approach. In addition to the 'slow' radial coordinate r, we introduce 'fast' radial scale $\theta(r)$ (WKBJ 'phase') describing the fast radial variations of the perturbation on the scale $\sim H$. While the quantities describing the unperturbed disk depend solely on slow scale r, the enthalpy perturbation is allowed to vary on both of them, $h = h(\theta, r)$. Consequently, we rewrite the radial derivative as

$$\frac{\partial h}{\partial r} \to \frac{\mathrm{d}\theta}{\mathrm{d}r}\frac{\partial h}{\partial \theta} + \frac{\partial h}{\partial r}. \tag{3}$$

A particular functional dependence $\theta = \theta(r)$ will be fixed later, here we just assume that $\partial h/\partial\theta \sim r(\partial h/\partial r)$ and therefore the strong radial gradient of the perturbation is transferred to gradient of the variable θ. The approximation works as long as the two scales are well separated, that is $r\theta' \gg 1$. The equation (2) becomes

$$\underbrace{\theta'^2\frac{\partial^2 h}{\partial\theta^2}}_{O(h\theta'^2)} + \underbrace{\sqrt{\frac{D\theta'}{r\rho}}\frac{\partial}{\partial r}\left(\sqrt{\frac{r\rho\theta'}{D}}\frac{\partial h}{\partial\theta}\right)}_{O(h\theta'/r)} + \underbrace{\frac{D}{r\rho}\frac{\partial}{\partial r}\left(\frac{r\rho}{D}\frac{\partial h}{\partial r}\right)}_{O(h/r^2)}$$
$$- \underbrace{\frac{2m\Omega}{r\tilde{\omega}}\frac{\partial}{\partial r}\left(\ln\frac{\rho\Omega}{D}\right)h}_{O(h/r^2)} - \underbrace{\frac{m^2}{r^2}h}_{O(h/r^2)} - \underbrace{\frac{Dh}{c_s^2}}_{O(h/H^2)} - \underbrace{\frac{D}{\rho H^2\tilde{\omega}^2}\frac{\partial}{\partial y}\left(\rho\frac{\partial h}{\partial y}\right)}_{O(h/H^2)} = 0, \tag{4}$$

where $y \equiv z/H$. In this work, we assume that $\tilde{\omega} \sim \Omega$ and $D \sim \Omega^2$ what corresponds to radii sufficiently far away from the corotation and Lindblad resonances. Magnitudes of individual terms in this case are indicated in equation (4). Clearly, the last two terms dominate the preceding three because $H \ll r$. Similarly, the first term dominates the second one because $r\theta' \gg 1$. Therefore we demand θ' to be of the order of $1/H$. Then the leading order terms (the first and the last two) are of the order of $O(h/H^2)$, the second term is by factor of $\sim H/r$ smaller and the rest is smaller by factor of $\sim (H/r)^2$. We will look for the solution in the form of successive approximations,

$$h(\theta, r) = h^{(0)}(\theta, r) + h^{(1)}(\theta, r) + h^{(2)}(\theta, r) + \ldots, \tag{5}$$

where similarly $h^{(n)} = O[(H/r)^n]$. The leading and first-order approximation are governed by

$$\theta'^2\frac{\partial^2 h^{(0)}}{\partial\theta^2} - \frac{Dh^{(0)}}{c_s^2} - \frac{D}{\rho H^2\tilde{\omega}^2}\frac{\partial}{\partial y}\left(\rho\frac{\partial h^{(0)}}{\partial y}\right) = 0, \tag{6}$$

$$\theta'^2\frac{\partial^2 h^{(1)}}{\partial\theta^2} - \frac{Dh^{(1)}}{c_s^2} - \frac{D}{\rho H^2\tilde{\omega}^2}\frac{\partial}{\partial y}\left(\rho\frac{\partial h^{(1)}}{\partial y}\right) = -\sqrt{\frac{D\theta'}{r\rho}}\frac{\partial}{\partial r}\left(\sqrt{\frac{r\rho\theta'}{D}}\frac{\partial h^{(0)}}{\partial\theta}\right). \tag{7}$$

The equation (6) is separable in the variables θ and y because the quantities describing the stationary disk (ρ and c_s) are functions of r and y only. Hence, putting

$$h^{(0)}(\theta, y, r) = f^{(0)}(\theta, r)g(y, r), \tag{8}$$

we find

$$\frac{\theta'^2}{f^{(0)}}\frac{\partial^2 f^{(0)}}{\partial\theta^2} = \frac{D}{c_\mathrm{s}^2} - \frac{D}{H^2\tilde{\omega}^2\rho g}\frac{\partial}{\partial y}\left(\rho\frac{\partial g}{\partial y}\right) \equiv k_r^2(r), \tag{9}$$

where $k_r^2(r)$ is a slowly changing separation variable. Equation (9) introduces radial and vertical problem. The radial part $f^{(0)}$ is governed by

$$\theta'^2\frac{\partial^2 f^{(0)}}{\partial\theta^2} - k_r^2 f^{(0)} = 0. \tag{10}$$

This equation has a particularly simple solution when we fix the variation of the function $\theta(r)$ so that $\theta' = k_r$. Then we get

$$f^{(0)}(\theta, r) = a_0(r)\mathrm{e}^{-\mathrm{i}\theta} + b_0(r)\mathrm{e}^{\mathrm{i}\theta}, \quad \theta = \int^r k_r(r)dr \tag{11}$$

with a_0 and b_0 being yet undetermined functions of r only. This result shows physical meaning of the functions $\theta(r)$ and k_r: $\theta(r)$ is a quickly changing WKBJ phase and $k_r(r)$ is the local radial wavevector of the perturbations. The case $k_r^2 > 0$ corresponds to freely radially propagating waves. When $k_r^2 < 0$, the solution consists of growing and decaying exponentials describing evanescent waves. Actual value of k_r for given frequency of oscillations arises as an eigenvalue of the vertical problem. Before determining it, we discuss the solution of the first-order equation (7).

Substituting solution (11) into equation (7), we find

$$k_r^2\frac{\partial^2 h^{(1)}}{\partial\theta^2} - \frac{Dh^{(1)}}{c_\mathrm{s}^2} - \frac{D}{\rho H^2\tilde{\omega}^2}\frac{\partial}{\partial y}\left(\rho\frac{\partial h^{(1)}}{\partial y}\right) = \\ = \mathrm{i}\sqrt{\frac{Dk_r}{r\rho}}\left[\frac{\partial}{\partial r}\left(a_0\sqrt{\frac{r\rho k_r}{D}}\right)\mathrm{e}^{-\mathrm{i}\theta} - \frac{\partial}{\partial r}\left(b_0\sqrt{\frac{r\rho k_r}{D}}\right)\mathrm{e}^{\mathrm{i}\theta}\right]g(y, r). \tag{12}$$

Making the ansatzs

$$h^{(1)}(\theta, y, r) = f^{(1)}(\theta, r)g(y, r), \quad \rho(r, y) = \Sigma(r)\rho_y(y), \tag{13}$$

where $\Sigma(r)$ is the column density and $\rho_y(y)$ describes the vertical density profile. We find that the vertical part $g(y, r)$ can be factorized out and we are left with

$$\frac{\partial^2 f^{(1)}}{\partial\theta^2} - f^{(1)} = \mathrm{i}\sqrt{\frac{Dk_r}{r\Sigma}}\left[\frac{\partial}{\partial r}\left(a_0\sqrt{\frac{r\Sigma k_r}{D}}\right)\mathrm{e}^{-\mathrm{i}\theta} - \frac{\partial}{\partial r}\left(b_0\sqrt{\frac{r\Sigma k_r}{D}}\right)\mathrm{e}^{\mathrm{i}\theta}\right]. \tag{14}$$

Since the right-hand side contains terms varying as $\mathrm{e}^{\pm\mathrm{i}\theta}$, the solution would vary as $\theta\mathrm{e}^{\pm\mathrm{i}\theta}$ causing non-uniformity of the expansion (5) when $\theta \sim (r/H)$. Nevertheless, these terms can be eliminated by putting

$$a_0\sqrt{\frac{r\Sigma k_r}{D}} = \mathrm{const} \equiv a, \quad b_0\sqrt{\frac{r\Sigma k_r}{D}} = \mathrm{const} \equiv b. \tag{15}$$

This way the functions $a_0(r)$ and $b_0(r)$ in the zero-th order approximation are determined and we also find that $f^{(1)}(\theta, r) = 0$. Hence, the zeroth order approximation

$$f^{(0)}(\theta, r) = \sqrt{\frac{D}{r\Sigma k_r}}\left[a\mathrm{e}^{-\mathrm{i}\theta} + b\mathrm{e}^{\mathrm{i}\theta}\right] \tag{16}$$

solves the problem even up to the first order in H/r.

3 VERTICAL PROBLEM AND DISPERSION RELATIONS

As follows from equation (9), the vertical part g of the perturbation is governed by

$$\frac{1}{\rho}\frac{\partial}{\partial y}\left(\rho\frac{\partial g}{\partial y}\right) + \frac{\tilde{\omega}^2 H^2}{c_\mathrm{s}^2}\left(1 + \frac{c_\mathrm{s}^2 k_r^2}{D}\right)g = 0. \tag{17}$$

The equation (17) should be supplied with appropriate boundary conditions at the surface of the disk. Typically, we require the Lagrangian pressure variations Δp to vanish at the surface of the flow (a free surface boundary),

$$\Delta p = 0 \quad \text{as} \quad p \to 0. \tag{18}$$

For fixed r and $\tilde{\omega}$, the equation (17) represents the eigenvalue problem for distinct values of k_r. The algebraic relation $\phi(\tilde{\omega}, k_r, r) = 0$ is the dispersion relation.

3.1 Isothermal case

In the simplest case of a vertically isothermal accretion disk the sound speed does not vary with height $c_\mathrm{s}(r, y) = c_{\mathrm{s}0}(r)$ and the density profile is Gaussian, $\rho(r, y) = \rho_0(r)\exp(-y^2/2)$. The vertical thickness of the disk is given by $H \equiv c_{\mathrm{s}0}/\Omega_\perp$, where $\Omega_\perp$ is the vertical epicyclic frequency. The equation (17) takes the form of Hermite differential equation

$$\frac{\partial^2 g}{\partial y^2} - y\frac{\partial g}{\partial y} + Cg = 0, \quad C \equiv \frac{\tilde{\omega}^2}{\Omega_\perp^2}\left(1 + \frac{c_\mathrm{s}^2 k_r^2}{D}\right) \tag{19}$$

and the boundary condition (18) translates to

$$\left(g - \frac{\tilde{\omega}^2}{\Omega_\perp^2} y\frac{\partial g}{\partial y}\right)\mathrm{e}^{-y^2/2} \to 0 \quad \text{as} \quad y \to \pm\infty. \tag{20}$$

When $|y| \to \infty$, a general solution of equation (19) behaves as $g(y) \sim ay^C + b\mathrm{e}^{y^2/2}$ with a and b being constants. The boundary condition is satisfied when $b = 0$ on both sides. This happen only for particular values of C, given by non-negative integer values, $C \equiv j = 0, 1, 2, \ldots$. We therefore recover the dispersion relation (1). The eigenfunctions are Hermite polynomials, $g(y) = \mathrm{He}_j(y)$.

3.2 Incompresible case

In the incompressible limit, the density is constant $\rho(r, y) = \rho_0(r)$ for $|y| \leq 1$, pressure varies as $p(r, y) = p_0(r)(1 - y^2)$ and sound speed is infinite. The vertical thickness H is a free parameter of the model. The equation (17) takes a remarkably simple form,

$$\frac{\partial^2 g}{\partial y^2} + k_z^2 g = 0, \quad k_z^2 \equiv \frac{\tilde{\omega}^2 k_r^2}{D}, \tag{21}$$

where k_z is the vertical wavenumber. A general solution when $k_z^2 > 0$ reads

$$g(y) = a \cos(k_z y) + b \sin(k_z y) \tag{22}$$

and the boundary condition (18) becomes

$$g \mp \frac{\tilde{\omega}^2}{\Omega_\perp^2} \frac{\partial g}{\partial y} = 0 \quad \text{at} \quad y = \pm 1. \tag{23}$$

Both boundary conditions are satisfied when

$$\left(\frac{\tilde{\omega}^2}{\Omega_\perp^2} k_z - \mathrm{ctg} k_z\right)\left(\frac{\tilde{\omega}^2}{\Omega_\perp^2} k_z - \mathrm{tg} k_z\right) = 0, \tag{24}$$

what, after substituting for k_z from equation (21), becomes the dispersion relation. The first term and second term in equation (24) corresponds to even and odd modes, respectively. In the case $k_z^2 < 0$, the equation (21) with boundary conditions (23) gives only trivial solutions. Consequently, p-modes for which $D < 0$ are absent in the incompressible flows and only modes with $D > 0$ (g-modes) may exist.

3.3 General polytropic case

Both isothermal and incompresible flows are special (and singular) cases of more general flows made by polytropic gas governed by equation of state of the form $p \propto \rho^{1+1/n}$, where n is the polytropic index. The isothermal case corresponds to the limit $n \to \infty$, while incompresible flow corresponds to $n = 0$. In the case of a general polytropic index, the density and sound speed vary as $\rho(r, y) = \rho_0(r)\left(1 - y^2\right)^n$ and $c_s^2(r, y) = c_{s0}^2(r)(1 - y^2)$. The half-thickness of the disk is $H = \sqrt{2n} c_{s0}/\Omega_\perp$. The equation (17) becomes

$$\left(1 - y^2\right) \frac{\partial^2 g}{\partial y^2} - 2ny \frac{\partial g}{\partial y} + \left[A + B\left(1 - y^2\right)\right] g = 0 \tag{25}$$

with

$$A \equiv \frac{2n\tilde{\omega}^2}{\Omega_\perp^2}, \quad B \equiv \frac{c_s^2 k_r^2}{D} A \tag{26}$$

and the boundary condition (18) reads

$$\left(1 - y^2\right)^n \left(g - \frac{A}{2n} \frac{\partial g}{\partial y}\right) \to 0 \quad \text{as} \quad y \to \pm 1. \tag{27}$$

The behavior of a general solution of equation (25) close to singularities at $y = \pm 1$ is $g(y) \sim a + b(y \mp 1)^{1-n}$. The boundary condition (27) therefore selects the solutions with $b = 0$. This can be done on both sides only for particular values of the parameter A. Unfortunately, for nonzero values of B, the equation (25) does not represent any well known type of eigenvalue problem, for which solution is known in a closed form. However, we will attempt to find its approximate solution in the next section.

4 APPROXIMATE SOLUTION

4.1 Qualitative discussion based on WKBJ approximation

Because the parameters A and B are connected to the oscillation frequency $\tilde{\omega}$ and radial wavevector k_r through definitions (26), it is good to remind that for real-valued $\tilde{\omega}$, A cannot be negative. The limiting case $A = 0$ corresponds to the corrotation resonance where $\tilde{\omega} = 0$. At Lindblad resonances we have $D = \kappa^2 - \tilde{\omega}^2 = 0$ corresponding to $A = 2n\kappa^2/\Omega_\perp^2$. Finally, the vertical resonances occurs when $B = 0$. The waves can propagate freely in the radial direction when the squared radial wavevector k_r^2 is positive, i.e. when B and D have the same signs. The case $B < 0$, $A > 2n\kappa/\Omega_\perp$ correponds to p-modes, while $B > 0$ and $A < 2n\kappa/\Omega_\perp$ for g-modes. In the remaining regions the waves are evanescent.

In the equation (25), the first-derivative term can be eliminated by a substitution

$$g(y) = (1 - y^2)^{-n/2}\tilde{g}(y). \tag{28}$$

Then the equation (25) becomes suitable for WKBJ approximation,

$$\frac{\partial^2 \tilde{g}}{\partial y^2} + k_z^2(y)\tilde{g} = 0, \quad k_z^2(y) = -\frac{n(n-2)}{(1-y^2)^2} + \frac{A + n(n-1)}{1-y^2} + B. \tag{29}$$

Here k_z^2 is the squared vertical wavevector. The perturbation can propagate as a wave in the vertical direction when $k_z^2 > 0$, when $k_z^2 < 0$ the perturbation is evanescent. Depending on the values of the parameters A and B and polytropic index, one of five possible situations occurs (see Figure 1).

For $n < 2$, the singularity at the surface of the disk ($y = 1$) is in the wave-propagation region. The function $k_z^2(y)$ is monotonic in the range $0 \le y < 1$. In the mid-plane ($y = 0$) we have $k_z^2(0) = A + B + n$. Therefore, when $B < -A - n$ the mid-plane is in the evanescent region and there is a turning point at

$$y_{t1} = \left[1 + x + \sqrt{x^2 + n(n-2)/B}\right]^{1/2}, \quad x \equiv \frac{A + n(n-1)}{2B}. \tag{30}$$

This case will be further referred as the case ①. When $B < -A - n$ the waves can propagate in entire domain corresponding to the case ②. Because $A > 0$ (being a product of positive quantities), case ① corresponds to oscillations with $B < 0$ and therefore $D < 0$. Therefore, the case ① describes p-modes. Their oscillations are concentrated mostly close to the surface of the disk. On the other hand, g-modes with $D > 0$ and $B > 0$ correspond to the case ② and one may expect variability in the whole vertical range of the disk. The parameter space for $n > 2$ is shown in the upper-right panel in Figure 1 using gray color.

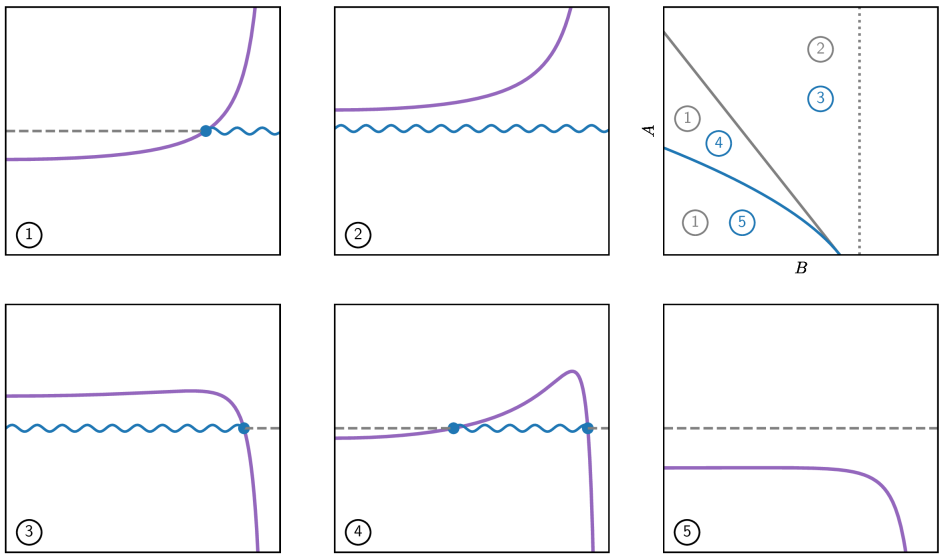

Figure 1. Five possible cases of vertical propagation of perturbations in a disk with general polytropic index n. The first and second row corresponds to $n < 2$ and $n > 2$, respectively. Each panel shows the squared vertical WKBJ wavevector $k_z^2(y)$ by purple line. Due to the mid-plane symmetry, only range $0 \le y < 1$ is shown. The wave-propagation regions, where $k_z^2(y)$ is positive are indicated by blue wavy lines. The locations of the turning points are given by equations (30) and (31) (see text). The upper-right panel shows domains of each case in the (A, B)-plane. The gray and blue symbols correspond to $n < 2$ and $n > 2$, respectively. The separating curves are given by $B = -A - n$ (gray) and $B = -[A + n(n-1)]^2/[4n(n-2)]$ (blue). The vertical dotted line corresponds to $B = 0$.

The situation is more complex for $n > 2$. In that case, the surface of the disk is in the wave-evanescent region. The mid-plane is in the wave-propagation region when $B > -A - n$. In addition, when $A > n(n-3)$, the function $k_z^2(y)$ has a local maximum between $y = 0$ and 1. Therefore, the function $k_z^2(y)$ may in principle change sign in zero, one or two points in each half of the disk, depending on the actual values of the parameters A, B and n.

When $B > -A - n$, the function $k_z^2(y)$ has a single root in the range $0 \le y < 1$ corresponding to a single turning point separating wave-propagating and wave-evanescent regions. This is the case ③ that describes mostly all g-modes and also p-modes near the vertical resonances. The location of the turning point is given by

$$y_{t2} = \left[1 + x - \sqrt{x^2 + n(n-2)/B}\right]^{1/2}, \tag{31}$$

where x is defined in equation (30). The oscillations can freely propagate around the mid-plane being evanescent in the vicinity of the disk surface. Because the radiation emerging from the disk has to pass through the evanescent region, this fact could have some impact on the observability of the oscillations in this case.

When $-[A + n(n-1)]^2/[4n(n-2)] < B < -A - n$, function $k_z^2(y)$ has two roots in the range $0 \le y < 1$ corresponding to the case ④. This corresponds to limited ranges of free wave propagation, surrounded by evansescent regions around the mid-plane and the surface. Locations of the turning points are given by equations (30) and (31). This case is relevant for p-modes with high negative B (i.e. for those far from the vertical resonances).

Finally, when $B < -[A + n(n-1)]^2/[4n(n-2)]$, the function $k_z^2(y)$ has no root in the range $0 \le y < 1$ and whole disk is in the wave-evanescent region corresponding to the case ⑤. Consequently, no oscillation modes exist.

Although the local WKBJ approximations is very helpful to get a qualitative insight in the vertical propagation of oscillations, it does not give any quantitative results. In particular, it does not provide the dispersion relation $\phi(A, B) = 0$, from which allowed values of the radial wave-vector arises. To find them, one needs to solve global vertical problem (25) together with boundary conditions (27). One way would be to use global WKBJ approximation as Perez et al. (1997) did. This approach needs a special treatment at the singularity at the surface of the disk and turning points. Another way is to use the exact solution of the equation (25) for $B = 0$ expressible in terms of the Gegenbauer polynomials, and extend it for non-zero values of B perturbatively. This approach has been adopted by Ortega-Rodríguez et al. (2002) and later by Kato (2010) for the lowest order modes. In the following section, we will adopt the latter way and generalize it to modes of arbitrary order.

4.2 Approximation using Gegenbauer polynomials

The equation (25) can be written in the form

$$\hat{L}g + \left(\tilde{A} - By^2\right) g = 0, \quad \hat{L} \equiv \left(1 - y^2\right) \frac{d^2}{dy^2} - 2ny\frac{d}{dy}, \quad \tilde{A} = A + B. \tag{32}$$

The operator $\hat{L}$ is self-adjoint with respect to the scalar product

$$\langle g_1 | g_2 \rangle \equiv \int_{-1}^{1} g_1 g_2 \left(1 - y^2\right)^{n-1} dy. \tag{33}$$

for any smooth functions that obey boundary conditions (27). When $B = 0$, equation (32) coincides with the Gegenbauer differential equation, $\hat{L}g + \tilde{A}g = 0$, for which solutions satisfying boundary conditions (27) are known to be

$$\tilde{A}_j \equiv \tilde{A}_j^{(0)} = j(j + 2n - 1), \quad g_j(y) \equiv g_j^{(0)}(y) = a_j C_j^{(n-1/2)}(y). \tag{34}$$

Here j is non-negative integer labeling the modes (vertical quantum numbers), $C_j^{(\lambda)}$ are the Gegenbauer polynomials and a_j are normalization constants such that $\langle g_j^{(0)} | g_k^{(0)} \rangle = \delta_{jk}$,

$$a_j = \frac{2^{n-1}\Gamma(n - 1/2)}{\sqrt{\pi}} \left[\frac{j!(j + n - 1/2)}{\Gamma(j + 2n - 1)} \right]^{1/2}. \tag{35}$$

The vertical quantum number describes number of nodes (‘zeros’) of the eigenfunctions in the vertical direction.

In the following, we apply a standard perturbation technique to the equation (32) with parameter B being a small expansion parameter as outlined bellow. We look for the solutions $(\tilde{A}_j, g_j)$ in terms of power series

$$\tilde{A}_j = \tilde{A}_j^{(0)} + B\tilde{A}_j^{(1)} + B^2\tilde{A}_j^{(2)} + \ldots, \tag{36}$$

$$g_j = g_j^{(0)} + Bg_j^{(1)} + B^2 g_j^{(2)} + \ldots. \tag{37}$$

By substituting these expansions to equation (32) and comparing the coefficients of the same powers of B, we obtain a sequence of equations governing the s-th approximations $A_j^{(s)}$ and $g_j^{(s)}$

$$\hat{L}g_j^{(s)} + \tilde{A}_j^{(0)}h_j^{(s)} = -\sum_{i=1}^{s} \tilde{A}_j^{(i)} g_j^{(s-i)} + y^2 g_j^{(s-1)}. \tag{38}$$

Next, we expand the s-th approximation in the basis of the zeroth-order eigenfunctions as

$$g_j^{(s)} = \sum_k \alpha_{jk}^{(s)} h_k^{(0)}, \tag{39}$$

with $\alpha_{jk}^{(s)}$ being the coordinates of the s-th approximation of the eigenfunction of the j-th oscillation mode with respect to the basis $\{g_k^{(0)}\}$. The result is further projected on the eigenfunctions $g_m^{(0)}$. This way we find an algebraic equation determining the successive approximations $A_j^{(s)}$, $\alpha_{jm}^{(s)}$,

$$\left(\tilde{A}_j^{(0)} - \tilde{A}_m^{(0)}\right)\alpha_{jm}^{(s)} = -\sum_{i=1}^{s} \tilde{A}_j^{(i)}\alpha_{jm}^{(s-i)} + \sum_k \alpha_{jk}^{(s-1)} \left\langle g_m^{(0)} | y^2 g_k^{(0)} \right\rangle. \tag{40}$$

The scalar product in the second term on the right-hand side can be found using well-known recurrence relations for the Gegenbauer polynomials Thompson (2011),

$$\left\langle g_m^{(0)} | y^2 g_k^{(0)} \right\rangle = q_k\delta_{mk-2} + d_k\delta_{mk} + q_{k+2}\delta_{mk+2}, \tag{41}$$

where

$$q_j \equiv \langle h_{j-2}^{(0)} | y^2 h_j^{(0)} \rangle = \left[\frac{j(j-1)(j+2n-2)(j+2n-3)}{(2j+2n-1)(2j+2n-3)^2(2j+2n-5)}\right]^{1/2}, \tag{42}$$

$$d_j \equiv \langle h_j^{(0)} | y^2 h_j^{(0)} \rangle = \frac{2j(j+2n-1)+2n-3}{4j(j+2n-1)+(2n+1)(2n-3)}. \tag{43}$$

The equation (40) then reduces to algebraic equation for $A_j^{(s)}$ and $h_j^{(s)}$,

$$\left(\tilde{A}_j^{(0)} - \tilde{A}_m^{(0)}\right)\alpha_{jm}^{(s)} = -\sum_{i=1}^{s} \tilde{A}_j^{(i)}\alpha_{jm}^{(s-i)} + q_m\alpha_{jm-2}^{(s-1)} + d_m\alpha_{jm}^{(s-1)} + q_{m+2}\alpha_{jm+2}^{(s-1)}. \tag{44}$$

Putting $s = 1$ and remembering that $\alpha_{jm}^{(0)} = \delta_{jm}$, the equation (44) becomes

$$\left(\tilde{A}_j^{(0)} - \tilde{A}_m^{(0)}\right)\alpha_{jm}^{(1)} = -\left(\tilde{A}_j^{(1)} - d_m\right)\delta_{jm} + q_m\delta_{jm-2} + q_{m+2}\delta_{jm+2}. \tag{45}$$

When $m = j$ we find the first-order correction to the eigenvalues, $A_j^{(1)} = d_j$, while for $m \neq j$, we obtain the correction to the eigenfunctions,

$$\alpha_{jm}^{(1)} = \frac{q_j}{\tilde{A}_j^{(0)} - \tilde{A}_{j-2}^{(0)}}\delta_{mj-2} - \frac{q_{j+2}}{\tilde{A}_{j+2}^{(0)} - \tilde{A}_j^{(0)}}\delta_{mj+2}. \tag{46}$$

The coefficient $\alpha_{jj}^{(1)}$ remains undetermined, however it affects only normalization of the eigenfunction of the perturbed problem. Consequently, we may put $\alpha_{jj}^{(1)} = 0$ without lose of generality. In principle, one may continue this procedure to higher orders, however already the first-order correction provides very good results as will be demonstrated in the next section.

4.3 First-order dispersion relation

The first-order solution of the eigenvalue problem reads

$$A_j = A_j^{(0)} + \Big(d_j - 1\Big)\, B. \tag{47}$$

Figure 2 shows the analytic relations (47) for four lowest-order modes along with the solutions obtained by direct numerical integration of equation (25) combined with a simple shooting method to find the eigenvalues A_j. The value of the polytropic index is $n = 3$ what corresponds to a radiative pressure dominated flow. Positions of resonances separating the regions of evanescent and freely propagating waves are shown by dashed lines. Not surprisingly, our analytic formula (47) (shown by dotted line) gives exact values A_j at the vertical resonances where $B = 0$. However, we find also a very good agreement for g-modes trapped between two Lindbblad resonances and even for p-modes not too far from the vertical resonances.

Using relations (26), (32) and (34), the dispersion relation (47) can be written in a more familiar form,

$$\beta_j \left(\tilde{\omega}^2 - \kappa^2\right)\left[\tilde{\omega}^2 - \frac{j\,(j+2n-1)}{2n}\Omega_\perp^2\right] = \tilde{\omega}^2 c_{s0}^2 k_r^2 \tag{48}$$

with

$$\beta_j = \frac{4j(j+2n-1) + (2n+1)(2n-3)}{2j(j+2n-1) + 2n(2n-3)}. \tag{49}$$

Coefficient β_j is positive for $j \geq 0$ and $n \geq 0$. For fixed j and $n \to \infty$, the coefficient $\beta_j \to 1$ and the dispersion relation coincides with the one for the isothermal case. The waves propagate freely when $k_r^2 > 0$, what corresponds to either

$$m\Omega - \kappa \leq \omega \leq m\Omega + \kappa, \tag{50}$$

for g-modes with $j \geq 1$, or

$$\omega \leq m\Omega - \left[\frac{j\,(j+2n-1)}{2n}\right]^{1/2}\Omega_\perp \quad \text{or} \quad \omega \geq m\Omega + \left[\frac{j\,(j+2n-1)}{2n}\right]^{1/2}\Omega_\perp \tag{51}$$

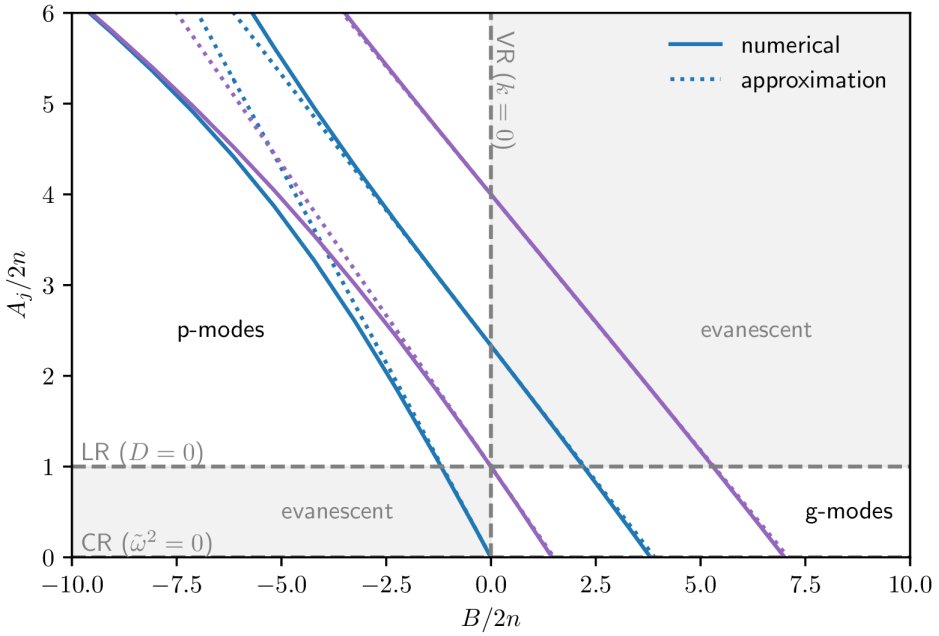

Figure 2. Dependence of the eigenvalues A_j on the parameter B for four lowest order modes with $j = 0, 1, 2$ and 3 (from left to right) for a polytropic disk with $n = 3$. Analytic first-order approximations are shown by dotted lines, numerical solutions correspond to solid lines. Domains of p-mode and g-modes are separated from regions where the waves are evanescent by Lindblad ('LR') and vertical ('VR') resonances. The Lindblad resonances occur for $A = 2n\kappa/\Omega_\perp$. Here we put $\kappa = \Omega_\perp$ what corresponds to Newtonian disks. In the case of relativistic disks, Lindblad resonances are shifted to $A < 1$ because $\kappa < \Omega_\perp$. The line $A = 0$ denotes the corrotation ('CR') resonance. The analytic approximations provides very good results in entire g-mode domain and for p-modes of not too high frequencies.

for p-modes with $j \geq 1$, or

$$\omega \leq m\Omega - \kappa \quad \text{or} \quad \omega \geq m\Omega + \kappa, \tag{52}$$

for p-modes with $j = 0$.

4.4 Vertical eigenfunctions

The eigenfunctions are labeled by the vertical number j giving number of the nodes of $g_j(y)$ in full range $-1 < y < 1$. According to equations (37), (39) and (46), the first-order

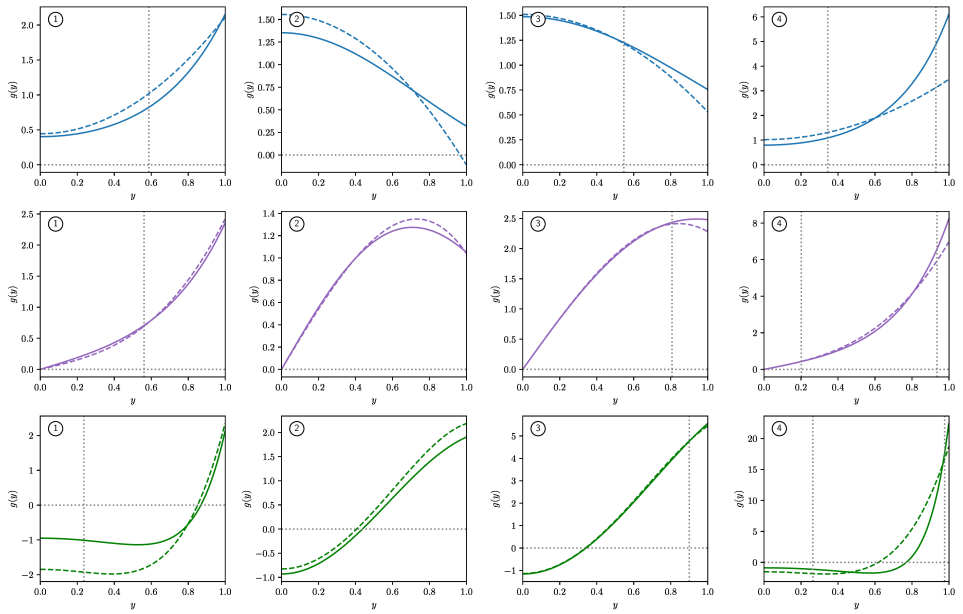

Figure 3. Vertical enthalpy perturbations $g(y)$ for different values of parameters B and n and vertical mode number j. In each panel, the result of numerical calculations is shown by the solid line, the analytic first-order approximation is shown by the dashed line. Each column corresponds to a different case according to classification introduced in Sec. 4.1, particular case is indicated. The first two columns correspond to the value of the polytropic index $n = 3/2$, the latter two are for $n = 3$. The first, second and the third raw are for $j = 0, 1$ and 2. Positions of the turning points are indicated by vertical dotted lines.

eigenfunctions can be expressed as

$$g_j = g_j^{(0)} + \frac{1}{2}B\left\{\left[\frac{j(j-1)(j+2n-2)(j+2n-3)}{(2j+2n-1)(2j+2n-3)^4(2j+2n-5)}\right]^{1/2} g_{j-2}^{(0)} - \left[\frac{(j+2)(j+1)(j+2n)(j+2n-1)}{(2j+2n+3)(2j+2n+1)^4(2j+2n-1)}\right]^{1/2} g_{j+2}^{(0)}\right\} \tag{53}$$

In particular, the eigenfunctions of the fundamental ($j = 0$) mode and the first overtone ($j = 1$) are

$$g_0 = a_0\left[1 + \frac{1-(2n+1)y^2}{2(2n+1)^2}B\right], \quad g_1 = a_1(2n-1)y\left[1 + \frac{3-(2n+3)y^2}{2(2n+3)^2}B\right]. \tag{54}$$

In figure 3 the first-order vertical eigenfunctions $g_j(y)$ are compared with those obtained by direct numerical integration for $j = 0, 1, 2$. First two columns correspond to the gas-pressure dominated disk with $n = 3/2$, the latter two are for radiation-pressure dominated

disk with $n = 3$. In each panel, the parameter B has been chosen so that the eigenfunctions correspond to particular cases according to classification introduced in Sec. 4.1. Its highest value $B = -70$ corresponds to the case ④ of the $j = 2$ mode. Interestingly, the first-order approximation gives acceptable results even for such high value of the parameter B. Generally, the accuracy of the approximation improves with increasing n and j.

5 DISCUSSION AND CONCLUSIONS

In this work, we have reviewed the problem of wave propagations in polytropic disks. We have concentrated on cold geometrically-thin Keplerian disks, where significant difference between radial and vertical scales on which properties of the flow vary allows to find the solution in the separable form. The separation has been done using the method of two scales. The radial problem can be treated with aid of the WKBJ approximation because the perturbation typically vary on much shorter scales than the equilibrium flow. The vertical problem resembles the Sturm-Liouville eigenvalue problem from which the squared radial wave-vector k_r^2 arises as the eigenvalue and the shape of the enthalpy perturbarion in the vertical direction as the eigenfunction.

We have discussed basic characteristics of the vertical propagation of the enthalpy perturbations using local WKBJ approximation. We have identified 5 possible types based on occurence of the wave-propagation and evanescent regions. We have also generalized the analytic perturbation method used by Ortega-Rodríguez et al. (2002) and Kato (2010) to arbitrary order of the mode j. This allowed us to construct a general dispersion relation (48) describing propagation of waves of arbitrary vertical number j in three-dimensional polytropic disks.

ACKNOWLEDGEMENTS

The author thanks the organizers of the RAGtime meeting for excellent conference and interesting discussions.

REFERENCES

Kato, S. (2001), Basic Properties of Thin-Disk Oscillations [1], *PASJ*, **53**(1), pp. 1–24.

Kato, S. (2010), Trapped, Two-Armed, Nearly Vertical Oscillations in Polytropic Disks, *PASJ*, **62**, p. 635, arXiv: 1004.0503.

Kato, S., Fukue, J. and Mineshige, S. (2008), *Black-Hole Accretion Disks — Towards a New Paradigm*.

Korycansky, D. G. and Pringle, J. E. (1995), Axisymmetric waves in polytropic accretion discs, *Mounthly Notices Roy.Astronom.Soc.*, **272**(3), pp. 618–624.

Okazaki, A. T., Kato, S. and Fukue, J. (1987), Global trapped oscillations of relativistic accretion disks., *PASJ*, **39**, pp. 457–473.

Ortega-Rodríguez, M., Silbergleit, A. S. and Wagoner, R. V. (2002), Relativistic Diskoseismology. III. Low-Frequency Fundamental p-Modes, *Astrophys.J.*, **567**(2), pp. 1043–1056, arXiv: astro-ph/0611010.

Papaloizou, J. C. B. and Pringle, J. E. (1984), The dynamical stability of differentially rotating discs with constant specific angular momentum, *Mounthly Notices Roy.Astronom.Soc.*, **208**, pp. 721–750.

Perez, C. A., Silbergleit, A. S., Wagoner, R. V. and Lehr, D. E. (1997), Relativistic Diskoseismology. I. Analytical Results for "Gravity Modes", *Astrophys.J.*, **476**(2), pp. 589–604, arXiv: `astro-ph/9601146`.

Thompson, I. (2011), NIST Handbook of Mathematical Functions, edited by Frank W.J. Olver, Daniel W. Lozier, Ronald F. Boisvert, Charles W. Clark, *Contemporary Physics*, **52**(5), pp. 497–498.

Wagoner, R. V. (2008), Relativistic and Newtonian diskoseismology, *New Astronomy Reviews*, **51**(10-12), pp. 828–834.

Proceedings of *RAGtime 20–22, 15–19 Oct., 16–20 Sept., 19–23 Oct., 2018/2019/2020, Opava, Czech Republic*
Z. Stuchlík, G. Török and V. Karas, editors, Silesian University in Opava, 2020, pp. 55–71

Quantum information in biomolecules: Transcription and replication of DNA using a soliton model

Ivan Hubač,[1,a] Filip Blaschke,[2,3,b] Ondřej Nicolas Karpíšek,[1,c] Miloslav Švec[4,d] and Stephen Wilson[5,*]

[1]Institute of Physics, Silesian University in Opava, Bezručovo nám. 1150/13, 746 01 Opava, Czech Republic.
[2]Research Centre for Theoretical Physics and Astrophysics, Institute of Physics, Silesian University in Opava, Bezručovo nám. 1150/13, 746 01 Opava, Czech Republic
[3]Institute of Experimental and Applied Physics, Czech Technical University in Prague, Husova 240/5, 110 00 Prague 1, Czech Republic
[4]Physics Department, Dawson College, Montreal, Quebec, Canada H3Z 1A4
[5]Theoretical Chemistry Group, South Parks Road, Oxford OX1 3TG, UK
[a]belaxx@gmail.com
[b]filip.blaschke@fpf.slu.cz
[c]karponius@gmail.com
[d]svec@hep.physics.mcgill.ca
[*]Passed away on September 2nd, 2020

ABSTRACT
By performing a Majorana transformation on the total molecular Hamiltonian operator for electrons adiabatically following nuclear motion, the electrons in a hydrogen bond in DNA can be treated as a chain of quasiparticles resulting in a Kitaev chain with a delocalized fermion state. Delocalized fermions define Majorana qubits which can give rise to entanglement and form the foundation of molecular quantum information processes. During transcription and replication of DNA hydrogen bonds are severed. This process can be investigated by employing the soliton model for DNA proposed by Peyrard and Bishop. The effects of solitons in the DNA double helix are studied and, in particular, their effects on decoherence.

Keywords: Quantum information – Majorana fermions – hydrogen bonds – solitons – DNA – transcription and replication of DNA

1 INTRODUCTION

The nature of the life and what distinguishes it from the inanimate is notoriously difficult to identify with any precision (Schrödinger, 1944; Cleland and Chyba, 2002; Tirard et al., 2010; Benner, 2010; Prossr, 2012). In his famous lectures delivered in Dublin in

1943, Schrödinger (Schrödinger, 1944) put the problem succinctly with the question "How can the events in space and time which take place within the spatial boundary of a living organism be accounted for by physics and chemistry?"

Today, whilst the relationship between the mathematical and physical sciences, on the one hand, and the life and mind sciences, on the other, has elucidated much of the complexity of living processes and the dynamical chemical reactions underpinning them, as Nurse (Nurse, 2008) has observed, a "comprehensive understanding of many higher-level biological phenomena remains elusive". There is, however, an emerging consensus that information is a key property of the life phenomenon (Szathmáry, 1989; Küppers, 1990; Yockey, 2002; Davies, 2005; Hazen et al., 2007; Walker and Davies, 2013; Walker et al., 2017; Davies and Walker, 2016; Davies, 2019). There has also been renewal of interest in quantum biology (see, for example Marais et al. (2018); Jim Al-Khalili (2016)) a field of research begun in 1965 by Löwdin (Löwdin, 1963) as a "field of research which describes the life processes and the functioning of the cell on a molecular and submolecular level" (Löwdin, 1963). Here we continue to develop our suggestion (Hubač et al., 2017) on the role of quantum information in biomolecules.

In this paper, we suggest the potential exploitation of *quantum* information in living processes and, in particular, the role of emergent quasiparticles called Majorana fermions associated with the hydrogen bonds in the DNA molecule. This paper builds on our previous study Hubač et al. (2017) of quantum information in biomolecules by investigating transcription and replication of DNA using a soliton model.

In section 2, Majorana fermions are associated with the hydrogen bonds in DNA and associated with the possibility of quantum information being exploited in biomolecules. In section 3, the transcription and replication of DNA is considered using a soliton model. Specifically, we use the Peyrard-Bishop model (Peyrard and Bishop, 1989) and make a small amplitude expansion.

2 MAJORANA FERMIONS AND QUANTUM INFORMATION IN DNA

Recent years have witnessed renewed interest in Majorana fermions and their realization in condensed matter systems has been intensively studied (Wilczek, 2009; Franz, 2013; Leijnse and Flensberg, 2012; Elliott and Franz, 2014; Alicea, 2012). Although initially introduced over 80 years ago by Etore Majorana (Majorana, 1937) as solutions of the Dirac equation (Dirac and Fowler, 1928) describing a neutral spin $\frac{1}{2}$ particle which is its own antiparticle and distinct from the Dirac solutions, for a long time Majorana fermions were regarded as rather abstract entities. (A review of the original work of Majorana is given in the recent volume by Esposito (Esposito, 2014).) Majorana fermion has been extensively investigated in nuclear and particle physics. Over the past decade, Majorana fermions have been realized as emergent quasiparticles (Wilczek, 2009; Franz, 2013; Leijnse and Flensberg, 2012; Elliott and Franz, 2014) in certain condensed matter systems. Specifically, they were studied in p-wave superconductivity by Leijense and Flensberg (Leijnse and Flensberg, 2012), using the Kitaev chain (Kitaev, 2007). The Kitaev chain is a one–dimensional model of a topological superconductor developed by Kitaev in 2001 and illustrated in Figure 2.

As can be seen from this Figure, the Kitaev chain is chain of fermions, which are strongly delocalized. This delocalization is an important property which makes the study of Majorana fermions very interesting. The Kitaev chain or delocalized Majorana fermions is very stable system. However, the delocalization can be lost by decoherence. The stability of the Kitaev chain makes it interesting for quantum information. If we are able to construct a qubit from these delocalized Majorana fermions, the system is very stable and has the potential play an important role in quantum information. The delocalization property of Majorana fermions were studied in connection with non-adiabatic processes by Scheurer and Shnirman (Scheurer and Shnirman, 2013).

In this paper, we use the delocalization property of the hydrogen bonds in the DNA (Deoxyribonucleic acid) molecule and try to use Majorana fermions as a source of quantum information in biomolecules. DNA is the information storage medium for most organisms. Genetic information is encoded in a sequence of pairs of nitrogenous bases which are held together via hedrogen bonds: adenine - thymine (A-T) and guanine - cytosine (G-C). Each base is attached to a five-carbon sugar forming a nucleoside which in turn is attached to a phosphate group creating a nucleotide. Nucleotides are arranged in two antiparallel strands of polynucleotides in a right-handed double-helix structure. In a given DNA molecule each polynucleotide strand is held in place by interactions between complementary base pairs. Genetic information is copied when the strands separate during DNA replication and in transcription, which is the first step in protein synthesis. DNA opens locally allowing only a segment of the sequence to be copied by a ribonucleic acid (RNA), messenger RNA (mRNA). The sense strand of the DNA molecule has the same sequence as the mRNA (mRNA) whilst the antisense strand provides its template. The sequence of nucleotides in mRNA is identical to that in the sense strand of the corresponding DNA except that uracil is used instead of thymine. In both replication and transcription processes the hydrogen bonds between the bases are severed. The area of partially separated DNA strands is known as the denaturation bubble.

The study of replication or transcription of DNA at a quantum mechanical level is a difficult problem because of the complexity of DNA molecule. Progress can be made by constructing low-resolution model descriptions of DNA, which facilitate computationally tractable schemes for investigating these phenomena. One popular choice is a mechanical model of DNA in which the nucleotides are represented by point masses.

The key advantage of such simplified models is that the dynamics of DNA are rendered solvable numerically and can be used to investigate non-linear phenomena, which might gain us some insight into how the denaturation bubble (a precursor for RNA transcription) might form. a staple of non-linear phenomena is the presence of solitons, which are particle-like non-linear waves representing a moving pattern of highly concentrated energy.

In our recent paper Hubač et al. (2017) (see also Hubač and Svrček (1988, 1992b,a); Hubač and Wilson (2008)), we introduced the non-adiabatic Hamiltonian for molecular systems. The relation between this molecular Hamiltonian and the solid state non-adiabatic Hamiltonian was also explored. Our derivation is based on a supersymmetric transformation. We began with a 'crude' adiabatic Hamiltonian, then we introduced new creation and annihilation operators which were functions of the normal coordinates B. Furthermore, we made these new operators functions of the corresponding momentum $\tilde{B}$.

$$\bar{a}_p = \sum_q C_{pq}\left(B, \tilde{B}\right) a_q \tag{1}$$

$$\bar{a}_p^\dagger = \sum_q C_{pq}\left(B, \tilde{B}\right) a_q^\dagger. \tag{2}$$

$$\bar{a}_p = \frac{1}{2}\left(\gamma_{p,1} + \mathrm{i}\gamma_{r,2}\right) \tag{3}$$

$$\bar{a}_p^\dagger = \frac{1}{2}\left(\gamma_{p,1} - \mathrm{i}\gamma_{r,2}\right), \tag{4}$$

We see that the creation and annihilation operators correspond to delocalized fermions; delocalization being realized through B and $\tilde{B}$. We identify these delocalized operators with Majorana fermions. A similar approach was followed by Scheurer and Shnirman (Scheurer and Shnirman, 2013) in their study of non-adiabatic processes in condensed matter systems. We focus our attention on the hydrogen bonds in the DNA molecule. There are several studies which describe the hydrogen bonds in DNA as a non-adiabatic system, with the hydrogen bonds being strongly delocalized (McKenzie, 2014). We therefore found it interesting to apply the quasiparticle concept of Majorana fermions to the hydrogen bond. We investigate Majorana fermions which have been discussed widely in the condensed matter and solid state literature (Wilczek, 2009; Leijnse and Flensberg, 2012; Franz, 2013; Elliott and Franz, 2014; Zuo and Mourik, 2016; Kitaev, 2007; Finck et al., 2012; Nadj-Perge et al., 2014; Bunkov and Gazizulin, 2015; Williams et al., 2012; Rokhinson et al., 2012; Deng et al., 2012; Das et al., 2012; Knez et al., 2012), as emergent quasi–particles in quantum molecular systems and, in particular, associated with the hydrogen bonds in the DNA biomolecule.

The hydrogen bond in DNA is characterized by double-well potential such as that shown in Figure 1. In early work in the field of quantum biology, Löwdin (Löwdin, 1963) constructed double-well potentials for the hydrogen bonds in DNA by a superposition of two Morse potentials. Delocalization occurs between the two minima and we, therefore, place the Majorana fermions, γ_1 and γ_N, into these minima. In some respect this is Kitaev chain between γ_1 and γ_N. By this concept we were able to define qubits and entangled states (Hubač et al., 2017).

There is extensive discussion in literature about proton tunnelling between two double-well minima (see, for example Löwdin (1963); Godbeer et al. (2015)). It is assumed that proton tunnelling can play a role in both mutation and replication of DNA. But even recent sophisticated calculations (Godbeer et al., 2015) using density functional theory (DFT) to model the double-well potential, did not support the role of proton tunnelling. The lack of evidence for proton tunneling supports our assumption that it is not, in fact, a proton but a highly delocalized fermionic quasiparticle which constitutes each of the hydrogen bonds between the DNA strands.

In this paper, we study the effect of solitons on the Majorana fermions associated with the hydrogen bonds in DNA and their possible role in mutation and replication. As described in our previous work Hubač et al. (2017), two hydrogen bonds in DNA represent one qubit and three hydrogen bonds give rise to entangled states. We were therefore able to introduce

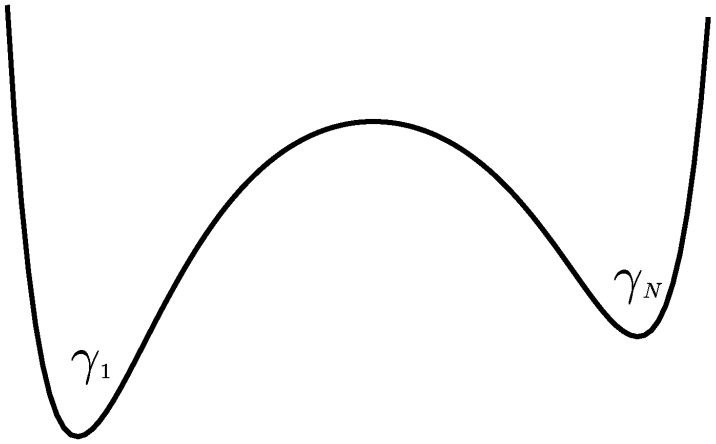

Figure 1. Double-well potential representation of the hydrogen bond. Asymmetric double-well potential obtained by superposition of two Morse potentials. Majorana fermions γ_1 and γ_N are associated with the two minima.

quantum entropy and quantum information. In the present work, we show that solitons can push the delocalized Majorana fermions close to each other leading to decoherence and to a decoupling of the strong electron-phonon interaction. We note that decoherence on a double well potential was demonstrated in the recent work of Marais *et al.* (Marais et al., 2018) (see their Figure 2 on the photosystem II reaction centre in higher plants).
In this way the quantum information associated with the Majorana fermions can be changed. We note that the question of the role of information flow in the cell and and how information is communicated was recently addressed by Nurse (Nurse, 2008).

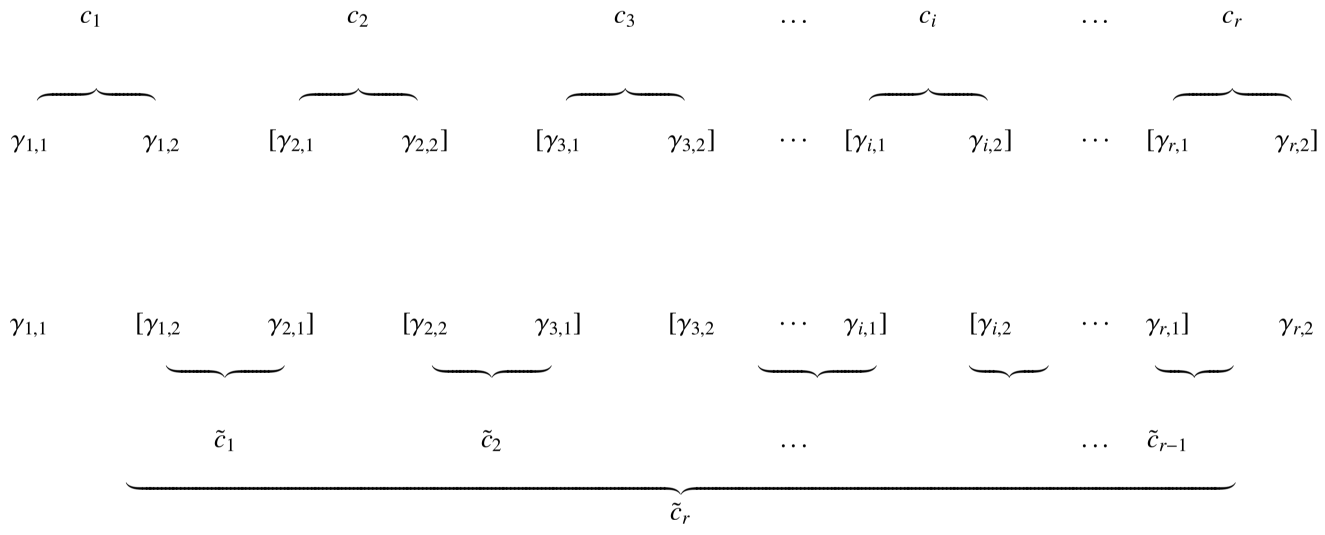

Figure 2. A Kitaev chain. In a product of fermion operators $c_1 c_2 \dots c_i \dots c_r$ each operator is written as a sum of two Majorana operators $\gamma_{i,1}$ and $\gamma_{i,2}$. The Majorana operators are then recoupled so as to leave the isolated γ operators $\gamma_{1,1}$ and $\gamma_{r,2}$ at either end of the chain.

3 SOLITONS ON DNA

An advantage of the drastic simplification adopted in this work is that the dynamics of DNA becomes (at least numerically) solvable and we can look for non-linear phenomena, which might gain us some insight into how the denaturation bubble (a precursor for RNA transcription) might form. A staple of non-linear phenomena is the presence of solitons, which are particle-like non-linear waves representing a moving pattern of highly concentrated energy. Furthermore, solitons are ubiquitous in all media where dispersion can be compensated by non-linear effects. As such, DNA can be also regarded as non-linear medium and both existence and utility of solitons has been anticipated a long time ago (Englander et al., 1980). In particular, the role of solitons in emergence of denaturation bubbles has been studied extensively (Tabi, 2016) (for fuller description see the report by Manghi and Destainville (Manghi and Destainville, 2015a) and references therein).

Many approximate models of DNA were proposed over the years in order to illuminate the role and importance of non-linear excitations (solitons) on DNA processes.
Yakushevich (Yakushevich, 2006) presented a hierarchy of important models. In these models, the focus is on torsion modes. In the continuous limit, the equations governing these models transform into either the famous sine-Gordon (sG) equation or equations related to it. As is well known, sG equation has analytic solitonic solutions. A complementary model, the so-called Peyrard-Bishop model (Peyrard and Bishop, 1989) has also attracted considerable attention and many studies have been devoted to its properties (see Zdravkovic (2011) and references therein).

In this paper, we propose that solitons may be also critical for quantum information specifically regarding braiding of qubits on the hydrogen bonds. As we mentioned, solitons in DNA has been studied for their capacity of promoting local openings, *i.e.* denaturation bubbles. However, they can also serve in the opposite way of creating small depressions where the strands of DNA are squeezed together. In particular, here we focus on collisions of solitons with regard to this issue. A squeezing of DNA strands may result in braiding of the qubits on hydrogen bonds, giving us a basic form of quantum computing. Quantum computing based on Majorana fermions is discussed in recent paper by Robinson *et al.* (Robinson et al., 2019). Our Majorana model of DNA is very similar to quantum computation model presented in Figure 2 of that paper (Robinson et al., 2019). Left vertical bubbles correspond to a A-T base pair (*i.e.* two hydrogen bonds). Horizontal bubbles correspond to a C-G base pair (*i.e.* entangled states) and right bubbles correspond to a T-A base pair (*i.e.* two hydrogen bonds).

As this is all highly speculative, in the following subsection we will work in the simplest setting possible to make our presentation concise. To that end, we will work within the Peyrard-Bishop model in the continuous limit. We first demonstrate the existence of solitons using Renormalization Group (RG) perturbation expansion technique developed by Chen, Goldenfeld and Oono (Chen et al., 1994). Then we discuss their properties and in the last subsection we show our numerical results regarding their collisions.

3.1 Peyrard-Bishop model

In the Peyrard-Bishop (PB) model, DNA strands are represented as two parallel chains of point masses. Along each chain the points are coupled together via harmonic force representing covalent bonds between nucleotides, while the hydrogen bonds between the strands is modelled via the Morse potential. Since the masses of the different nucleotides (*i.e.* with different bases A, T, C and G) do not differ from each other dramatically (about 4% (Zdravkovic, 2011)), it is convenient to adopt only the mean mass for every nucleotide. Moreover, since the covalent bonds are far stronger than the hydrogen bonds, the PB model assumes only transversal motion disregarding longitudinal and torsion movements which effectively reduces the problem to a single dimension.

Indeed, if we denote the deviation form the equilibrium distance of the two strands at the n-th site as y_n the PB model can be written as

$$H = \sum_n \left\{ \frac{m}{2}\dot{y}_n^2 + \frac{k}{2}(y_n - y_{n-1})^2 + D\Big(\mathrm{e}^{-a\sqrt{2}y_n} - 1\Big)^2 \right\} . \tag{5}$$

From here on we adopt the following values for the parameters of PB model (taken from Zdravkovic (2011))

$$k = 12\frac{\mathrm{N}}{\mathrm{m}} \approx 0.74892\frac{\mathrm{eV}}{\mathrm{\AA}^2} , \quad m = 307.2 \text{ a.m.u.} , \tag{6}$$

$$a = 1.2\,\mathrm{\AA}^{-1} , \quad D = 0.07\mathrm{eV} , \quad l = 3.4\,\mathrm{\AA} . \tag{7}$$

Here, k is the spring constant for harmonic potential, m is the average mass of the nucleotides, a and D are the inverse length and depth of the Morse potential, respectively. Lastly, l is the distance between adjacent sites along the strands.

The equation of motion reads

$$m\ddot{y}_n = k\,(y_{n+1} + y_{n-1} - 2y_n) + 2\sqrt{2}aD\Big(\mathrm{e}^{-\sqrt{2}ay_n} - 1\Big)\mathrm{e}^{-\sqrt{2}ay_n} . \tag{8}$$

Being both discrete and non-linear this equation is very difficult to solve. However, since we only want to illustrate how solitons could lead to decoherence of qubits we will take a continuous limit to simplify matters as much as possible. Hence, we take the distance between sites l to zero, while we keep $\tilde{k} \equiv kl^2$ finite (and numerically equal to $\tilde{k} = 8.6575$ eV). Further, let us denote the continuous variable tracing the distance along strands as $nl \to x$ and the field variable which replaces transversal motion at the n-th side as $y_n(t) \sim y(nl, t) \to y(x, t)$. In this way, the equations of motion becomes

$$m\partial_t^2 y - \tilde{k}\partial_x^2 y = 2\sqrt{2}a\,D\Big(\mathrm{e}^{-a\sqrt{2}y} - 1\Big)\mathrm{e}^{-a\sqrt{2}y} . \tag{9}$$

In the dimensionless units defined as

$$t \equiv \frac{\sqrt{m}}{2a\sqrt{D}}\tilde{t} \approx 28\,\tilde{t}\,[\mathrm{ps}] , \qquad x \equiv \frac{\sqrt{\tilde{k}}}{2a\sqrt{D}}\tilde{x} \approx 4.63\,\tilde{x}\,[\mathrm{\AA}] , \tag{10}$$

$$y = \frac{\tilde{y}}{a\sqrt{2}} \approx 0.59\,\tilde{y}\,[\mathrm{\AA}] , \tag{11}$$

the equation takes especially simple form

$$\partial^2 y = (\mathrm{e}^{-y} - 1)\,\mathrm{e}^{-y}\,, \tag{12}$$

where we dropped all˜ signs for brevity and where we used relativistic notation $\partial^2 \equiv \partial_\mu \partial^\mu = \partial_t^2 - \partial_x^2$. For future purposes it is advantageous to use substitution $y = \log(1+u)$, which transforms (12) into

$$(1+u)\,\partial^2 u - \partial_\mu u \partial^\mu u + u = 0\,. \tag{13}$$

3.2 Small amplitude expansion

Let us study small amplitude perturbations of Eq. (13). Inserting a series expansion

$$u = \varepsilon\left(u_0 + \varepsilon u_1 + \varepsilon^2 u_2 + \ldots\right), \tag{14}$$

where ε is a bookkeeping parameter which we assume to be small $|\varepsilon| \ll 1$, we obtain a hierarchy of equations

$$H_0 u_{n+1} = \sum_{k=0}^{n}\left(\partial_\mu u_{n-k}\partial^\mu u_k - u_{n-k}\partial^2 u_k\right), \tag{15}$$

where $H_0 = \partial^2 + 1$.

For the zero order, let us start with a monochromatic wave, *i.e.*

$$u_0 = A_0 \mathrm{e}^{\mathrm{i}\theta} + \text{c.c.}\,, \quad \theta \equiv qx - \omega t\,, \tag{16}$$

with $\omega = \sqrt{q^2+1}$.

Solving the hierarchy up to the second order we get

$$u_1 = 4\,|A_0|^2\,, \tag{17}$$

$$u_2 = -2A_0\,|A_0|^2\,\mathrm{e}^{\mathrm{i}\theta}\left(\xi\bar{\theta}^2 + \mathrm{i}\,(1-\xi)\,\theta\right) + \text{c.c.} \tag{18}$$

Here, ξ is an arbitrary constant and we have introduced an auxiliary variable $\bar{\theta} \equiv \omega x - qt$, which appears in u_2 as a part of the so-called secular term. This term is a sign of resonance phenomena and arise due to the identity

$$\frac{1}{\partial^2+1}\mathrm{e}^{\mathrm{i}\theta} = -\frac{1}{2}\mathrm{e}^{\mathrm{i}\theta}\left(\xi\bar{\theta}^2 + \mathrm{i}\,(1-\xi)\,\theta + c\right), \tag{19}$$

where c is an arbitrary constant.

The presence of secular term is a bad news for our perturbation series since – as the name indicates – secular term quickly outgrow any other terms with increasing t (or x) casting a doubt on the convergence of our series.

In order to eliminate terms like u_2 we employ Renormalization Group (RG) method developed by Chen, Goldenfeld and Oono (Chen et al., 1994). This method calls for introduction of artificial renormalization scales θ_0 and $\bar{\theta}_0$ via innocuous shifts in the secular term:

$$\bar{\theta}^2 \to \bar{\theta}^2 - \bar{\theta}_0^2 + \bar{\theta}_0^2\,, \qquad \theta \to \theta - \theta_0 + \theta_0\,. \tag{20}$$

Now we redefine the so-called 'bare' amplitude A_0 in terms of 'dressed' amplitude A in such a way that the dependence on the second instances of θ_0 and $\bar{\theta}_0$ disappears:

$$A_0 = \left(1 + 2\varepsilon^2 |A|^2 \left(\xi\bar{\theta}_0^2 + \mathrm{i}\,(1-\xi)\,\theta_0\right) + O\left(\varepsilon^4\right)\right) A\,, \tag{21}$$

In other words, the renormalization scales only shows up in the combinations $\theta - \theta_0$ and $\bar{\theta}^2 - \bar{\theta}_0^2$. This is important, since, as we will see, we want to ultimately set $\theta_0 = \theta$ and $\bar{\theta}_0 = \bar{\theta}$. Because the renormalization scales are completely artificial, meaning that the solution does not depend on them, we can make this identification. However, since $A \equiv A(\theta_0, \bar{\theta}_0)$ can be in principle an arbitrary function of renormalization scales we must enforce the independence of the solution by ensuring that

$$\frac{\partial u}{\partial \theta_0} = \frac{\partial u}{\partial \bar{\theta}_0} = 0\,, \quad \forall x, t\,, \tag{22}$$

holds. These conditions gives us the Renormalization Group Equations (RGE's):

$$\frac{\partial A}{\partial \theta_0} = -2\mathrm{i}\varepsilon^2 a\ |A|^2\,(1-\xi) + O(\varepsilon^4)\,, \tag{23}$$

$$\frac{\partial A}{\partial \bar{\theta}_0} = -2\varepsilon^2 a\ |A|^2\,\xi\bar{\theta}_0 + O(\varepsilon^4)\,. \tag{24}$$

However, solving these equations would give us wrong global behaviour since these are not *slow motion* equations, meaning that the derivatives can get arbitrary large. A proper RGE is therefore a differential consequence of these equations, which is the famous non-linear Schrödinger (NLS) equation:

$$\mathrm{i}\frac{\partial A}{\partial \theta_0} - \frac{1}{2}\frac{\partial^2 A}{\partial \bar{\theta}_0^2} = 2\varepsilon^2 a\ |A|^2 + O(\varepsilon^4)\,. \tag{25}$$

Solving NLS equation and plugging it into the expansion we arrive at a single soliton solution in the form

$$u_R = \frac{u_0}{\cosh\left(\frac{u_0}{\sqrt{2}}\frac{x - V_E t}{\sqrt{1-V_E^2}}\right)} \cos\left(\left(1 - \frac{u_0^2}{4}\right)\frac{t - V_E x}{\sqrt{1-V_E^2}}\right) + \frac{u_0^2}{\cosh^2\left(\frac{u_0}{\sqrt{2}}\frac{x - V_E t}{\sqrt{1-V_E^2}}\right)}\,. \tag{26}$$

Several comments are in order:
i) This solution is independent on ε due to the fact that it can be rescaled away via scale invariance of NLS; however, the solution is still only valid for small u_0 – the core amplitude of the soliton. This is as it should be since ε was only a bookkeeping parameter and not a true parameter of the equation of motion.
ii) The parameter q has been replaced in favor of the envelope velocity via $q = V_E/\sqrt{1-V_E^2}$.
iii) This solution has a manifestly Lorentz symmetry structure, *i.e.* it is a boost of a standing wave solution with modulated amplitude. This is due to the underlying Lorentz symmetry of the equation of motion even though NLS is not Lorentz invariant.

iv) The width of the soliton is roughly $\sim 10\sqrt{2\left(1-V_E^2\right)}/u_0$, while its core height is $u_0+u_0^2$. Of course, not all values of u_0 is physically acceptable. In Zdravkovic (2011) it is argued that a typical length of a DNA segment participating in a transcription bubble is between 8 to 17 nucleotides. This translates into a typical width of the soliton between 27 to 58 Å. This means that the width of the soliton (in dimensionless units) is in the range $6-12$.
v) The energy of a single soliton (at leading order) is given as (in dimensionful units)

$$E = 2D\sqrt{\frac{2}{1-V_E^2}}u_0 + O\left(u_0^2\right), \tag{27}$$

which is again fully consistent with special relativity, making the solitons rest mass to be $\sqrt{2}Du_0$.

3.3 Scattering of solitons in the continuous PB model

In this subsection, we broadly outline key features of soliton scattering in continuous PB model. At least qualitatively, findings presented here should be the same to that of discrete PB model for reasons which we outline below.

In the continuous PB model the interesting thing about scattering of solitons is its mundaneness. We have performed numerous numerical simulations where initially well-separated solitons of various sizes (parametrized by u_0) are sent against each other with various speeds (controlled by V_E). From these studies it became clear that solitons interact with each other only minimally and after they pass through each other they rapidly regain their original shapes. The only impact of the interaction is a slight phase shift and delay compared with completely noninteracting solitons, as can be seen on Figure 3. Furthermore, these differences are less and less pronounced as the velocity increases due to the fact that for larger velocities the effective interaction time between the solitons becomes smaller.

This behaviour is paramount to scattering of solitons in integrable theories. As it is well known, NLS equation can be solved via the inverse scattering method (Zakharov and Shabat, 1972). The implication is that NLS equation is an integrable theory and soliton scattering has the features which makes solitons solitons, *i.e.* rapid shape recovery with only a phase shift gained through the interaction. On the other hand, in a generic, non-integrable model with solitons, we typically observe a wealth of interesting associated phenomena, such as soliton bouncing, formation of bound states and others (for details see a recent paper on collisions solitons in the Montonen-Sarker-Trullinger-Bishop (MSTB) model (Izquierdo, 2017) and references therein).

Our observations in the continuous PB model can be therefore explained as a result of an *approximate integrability* for small amplitudes, which is inherited from NLS. Since the solitons in discrete PB model are also governed by NLS equation we can thus claim that the same should be (and indeed is) observed in the discrete PB model.

Here, we are interested in assessing whether collision of solitons can lead to a substantial squeezing of DNA strands. To this end we will focus only on the case where the colliding solitons are of the same size and starts with the same phase, so that their internal oscillations positively interfere at the point of collision. Further, we explore the collisions for various

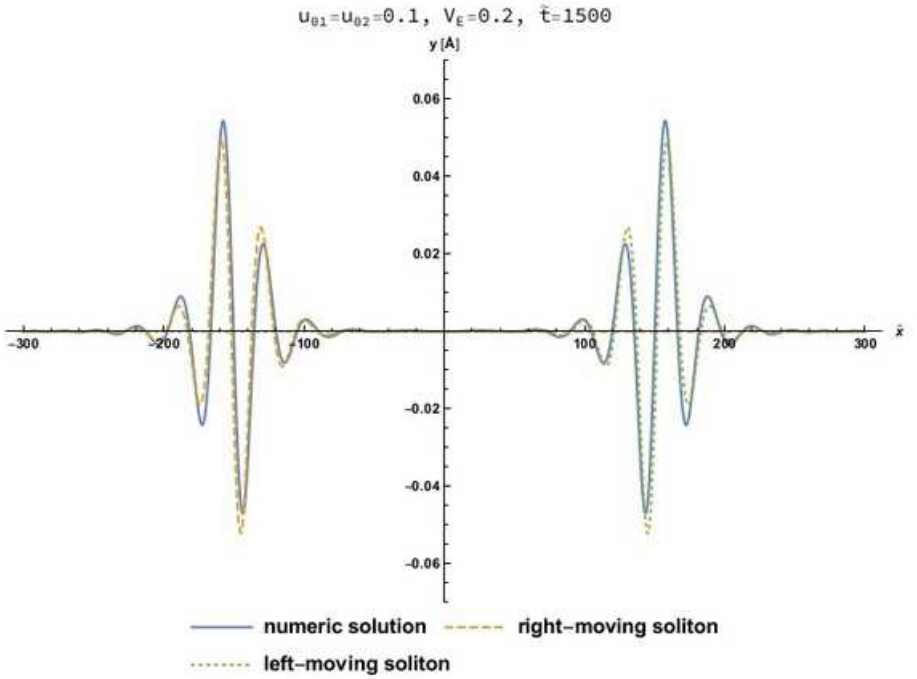

Figure 3. A typical outcome of soliton scattering where two well-separated but otherwise identical solitons are sent against each other with velocity V_E. Compared with noninteracting solitons (yellow dashed line and green dotted line) we see that the only marks of interaction are slight time delay.

sizes u_0 and envelope velocities V_E in order to pinpoint the best circumstances for the most negative values of y.

The results are sumarized in Figure 4. There, we show minimal values $y_{\min} \equiv \mathrm{Min}[y(0,t)]$ which the field reaches when the solitons collides. We show the results for initial sizes $u_0 = \{0, 1, 0.2, 0.3, 0.4\}$ and for various velocities V_E.

A minimal value of y for a single soliton is $\frac{1}{\sqrt{2}a}\log(1 - u_0 + u_0^2) + O(u_0^3)$. Therefore we expect that for two roughly non-interacting overlapping solitons the *theoretical* minimum is twice as low. Indeed, if $u_0 = 0.1$ this theoretical minimum is ≈ -0.11 Å which is almost reached for $V_E = 0.75$ and above. This is due to the fact that for larger velocities, the time for non-linear effects of PB model to kick in is smaller and solitons behaviour is more in accordance with the above expectations. As we increase the size, however, two effects grow in importance. First, the approximate initial solitonic solution becomes more unreliable and deformations start to develop even before the collision. Typically, the solitonic wave tend to settle into more accurate shape (described by higher-order corrections to the approximate solution) and, in the process, emit small waves. Second, as the field probes the negative half of the Morse potential it feels more of the exponential suppression to the negative

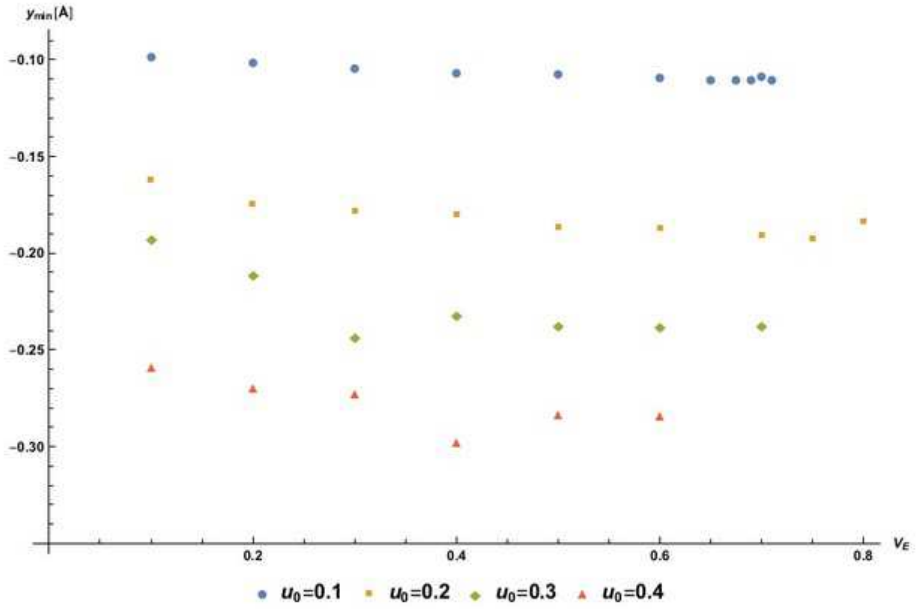

Figure 4. Minimal values of the field $y_{\min} \equiv \mathrm{Min}[y(0,t)]$ attained at the time of collision between equal solitons for various sizes u_0 and velocities V_E.

deviations compared with only polynomial suppression for positive deviations. Therefore, for higher u_0 solitons cannot attain even their theoretical minima. These expectations are fully manifested in Figure 4 as, for example, for $u_0 = 0.4$ the observed minimum $y_{\min}$ never approaches theoretical one ≈ -0.323 Å even at high velocities.

Our findings suggest that local squeezing of DNA strands is propagated by solitons and can be enhanced via soliton collisions. However, let us stress that we are talking about very small depressions, *e.g.* $|y| \leq 0.3$Å. We were not able to find larger depressions within the limitations of our approach. Nevertheless, it is quite possible that even a mild squeezing of DNA strands can influence the distance of minima of the double-well potential for hydrogen bonds sufficient to cause decoherence of associated Majorana fermions or to trigger braiding. To quantify this precisely is, however, far outside the scope of this work.

Furthermore, there are additional reasons to mistrust the picture of events we are painting here when deformations get larger. For instance, we have completely neglected rotational degrees of freedom. It is easy to imagine, that trying to squeeze DNA strands would at some point just result in rotation of the bases or slight twisting/untwisting of the double helix and would not manifest in reducing their distance. Another matter, which we completely neglect here, and which can heavily impact the dynamics of solitons is viscosity. It is clear, that viscosity would play a major role in the motion and lifetime of solitons, perhaps rendering soliton collisions untenable. Again, this is outside the scope of our study and we

recommend the paper by Manghi and Destainville (Manghi and Destainville, 2015b), where the impact of viscosity on mechanical models of DNA are summarized. Let us, however, say that for the small amplitudes to which our study is confined, it is quite plausible that the damped motion of sugar-phosphate backbone of DNA would not play as a significant role on small deformations of hydrogen bonds we are interested in.

4 CONCLUDING REMARKS

In this article, we have developed further our ideas about quantum information in biomolecules. These ideas are based on the observation that the hydrogen bonds in the DNA molecule are strongly delocalized systems characterized by double well potential. If this double well potential is described by the non-adiabatic Hamiltonian, fermion quasiparticles are obtained which we can identified with Majorana fermions. This result then allows us to introduce qubits. We found similarities between this fermion quasiparticles and Majorana quasiparticles. Both are emergent quasiparticles and are delocalized. Our idea is also supported by the fact that proton tunelling was not found. This is due to the effect of delocalization and coupling of electrons and vibrations (phonons). The two hydrogen bonds associated with the base pairs A-T or T-A represent one qubit and the three hydrogen bonds associated with C-G or G-C represent entangled states. In this way, we can introduce quantum information and quantum entropy.

It is expected that solitons play a role in the transcription and replication of DNA. We have, therefore, studied the effects of solitons on our model. Specifically, we have used the Peyrard and Bishop model of DNA. Solitons may be critical for quantum information, in particular, with regard to the braiding of qubits on the hydrogen bonds. Solitons can play a role in decoherence of delocalized Majorana fermions. We note that decoherence on a double well potential was demonstrated in the recent work of Marais *et al.* (Marais et al., 2018) (see their Figure 2). These effects may be important for quantum computation. We also studied solitons in DNA for their capacity of promoting local openings, *i.e.* denaturation bubbles. Our results are presented in Figures 3 and 4.

The solitons in the PB model are natural candidates for agents of quantum computation on DNA molecule because they are coherent, extended and stable wave patterns where energy is concentrated. Here, we have shown that during their collisions the strands of DNA do become closer compared with the isolated soliton if only for a brief time. If sufficiently large solitons participate in collision, the negative deviation can reach values such that braiding or decoherence of qubits on the hydrogen bonds may take place. As we have already mentioned, we have kept our analysis in the present work at the most basic level as a proof-of-concept.

Building on the emerging consensus that information is a key property of the life phenomenon, we have continued to develop our suggestion that quantum information has a role in biomolecules and, in particular, in DNA.

ACKNOWLEDGEMENTS

This work was supported by the Albert Einstein Centre for Gravitation and Astrophysics financed by the Czech Science Agency Grant No. 14-37086G (F.B.) and by the program of Czech Ministry of Education Youth and Sports INTER-EXCELLENCE Grant number LTT17018 (F.B.).

REFERENCES

Alicea, J. (2012), New directions in the pursuit of majorana fermions in solid state systems, *Reports on progress in physics. Physical Society (Great Britain)*, **75**, p. 076501.

Benner, S. (2010), Defining life, *Astrobiology*, **10**, pp. 1021–30.

Bunkov, Y. and Gazizulin, R. (2015), Majorana fermions: Direct observation in 3he.

Chen, L.-Y., Goldenfeld, N. and Oono, Y. (1994), Renormalization group theory for global asymptotic analysis, *Physical Review Letters*, **74**.

Cleland, C. and Chyba, C. (2002), Defining 'life'., *Origins of life and evolution of the biosphere : the journal of the International Society for the Study of the Origin of Life*, **32**, pp. 387–93.

Das, A., Ronen, Y., Most, Y., Oreg, Y., Heiblum, M. and Shtrikman, H. (2012), Zero-bias peaks and splitting in an al-inas nanowire topological superconductor as a signature of majorana fermions, *Nature Physics*, **8**, pp. 887–895.

Davies, P. (2005), A quantum recipe for life, *Nature*, **437**, p. 819.

Davies, P. (2019), *The Demon in the Machine: How Hidden Webs of Information Are Solving the Mystery of Life*, ISBN 9780226669700.

Davies, P. and Walker, S. (2016), The hidden simplicity of biology, *Reports on progress in physics. Physical Society (Great Britain)*, **79**, p. 102601.

Deng, M., Yu, C., Huang, G.-Y., Larsson, M., Caroff, P. and Xu, H. (2012), Anomalous zero-bias conductance peak in a nb-insb nanowire-nb hybrid device, *Nano letters*, **12**.

Dirac, P. A. M. and Fowler, R. H. (1928), The quantum theory of the electron, *Proceedings of the Royal Society of London. Series A, Containing Papers of a Mathematical and Physical Character*, **117**(778), pp. 610–624, arXiv: `https://royalsocietypublishing.org/doi/pdf/10.1098/rspa.1928.0023`, URL `https://royalsocietypublishing.org/doi/abs/10.1098/rspa.1928.0023`.

Elliott, S. and Franz, M. (2014), Colloquium: Majorana fermions in nuclear, particle and solid-state physics, *Reviews of Modern Physics*, **87**.

Englander, W., Kallenbach, N., Heeger, A., Krumhansl, J. and Litwin, S. (1980), Soliton-like states for opening in polynucleotide double helices, *Ferroelectrics*, **30**, pp. 167–167.

Esposito, S. (2014), *The physics of ettore majorana: Phenomenological, theoretical, and mathematical*.

Finck, A., Van Harlingen, D., Katal Mohseni, P., Jung, K. and Li, X. (2012), Anomalous modulation of a zero-bias peak in a hybrid nanowire-superconductor device, *Physical Review Letters*, **110**.

Franz, M. (2013), Majorana fermions: The race continues.

Godbeer, A., Al-Khalili, J. and Stevenson, P. (2015), Modelling proton tunnelling in the adenine–thymine base pair, *Physical chemistry chemical physics : PCCP*, **17**.

Hazen, R., Griffin, P., Carothers, J. and Szostak, J. (2007), Functional information and the emergence of biocomplexity, *Proceedings of the National Academy of Sciences*, **104**, pp. 8574–8581.

Hubač, Svec and Wilson (2017), Quantum entanglement and quantum information in biological systems (dna), *Proceedings of RAGtime17-19: Workshops on black holes and neutron stars*.

Hubač, I. and Svrček, M. (1988), The quasiparticle concept in vibrational–electronic problems in molecules. i. partitioning of the vibrational–electronic hamiltonian, *International Journal of Quantum Chemistry*, **33**.

Hubač, I. and Svrček, M. (1992a), *Many-Body Perturbation Theory for Vibrational Electronic Molecular Hamiltonian*, volume 293, pp. 471–512.

Hubač, I. and Svrček, M. (1992b), *The Many-Body Perturbation Theory of the Vibrational-Electronic Problem in Molecules*, volume 293, pp. 471–512.

Hubač, I. and Wilson, S. (2008), *The Non-Adiabatic Molecular Hamiltonian: A Derivation Using Quasiparticle Canonical Transformations*, pp. 403–428, ISBN 978-1-4020-8706-6.

Izquierdo, A. (2017), Reflection, transmutation, annihilation and resonance in two-component kink collisions, *Physical Review D*, **97**.

Jim Al-Khalili, J. M. (2016), Life on the edge: The coming of age of quantum biology.

Kitaev, A. (2007), Unpaired majorana fermions in quantum wires, *Physics-Uspekhi*, **44**, p. 131.

Knez, I., Du, R.-R. and Sullivan, G. (2012), Andreev reflection of helical edge modes in inas/gasb quantum spin hall insulator, *Physical review letters*, **109**, p. 186603.

Küppers, B.-O. (1990), *Information and the Origin of Life*.

Leijnse, M. and Flensberg, K. (2012), Introduction to topological superconductivity and majorana fermions, *Semiconductor Science and Technology*, **27**.

Löwdin, P.-O. (1963), Quantum genetics and the aperiodic solid, *Advances in quantum chemistry*, **2**.

Majorana, E. (1937), Teoria simmetrica dell'elettrone e del positrone, *Il Nuovo Cimento*, **14**, pp. 171–184.

Manghi, M. and Destainville, N. (2015a), Physics of base-pairing dynamics in dna, *Physics Reports*, **631**.

Manghi, M. and Destainville, N. (2015b), Physics of base-pairing dynamics in dna, *Physics Reports*, **631**.

Marais, A., Adams, B., Ringsmuth, A., Ferretti, M., Gruber, J., Hendrikx, R., Schuld, M., Smith, S., Sinayskiy, I., Krüger, T., Petruccione, F. and van Grondelle, R. (2018), The future of quantum biology, **15**, p. 20180640.

McKenzie, R. (2014), A diabatic state model for double proton transfer in hydrogen bonded complexes, *The Journal of chemical physics*, **141**.

Nadj-Perge, S., Drozdov, I., Li, J., Chen, H., Jeon, S., Seo, J., Macdonald, A., Bernevig, B. and Yazdani, A. (2014), Topological matter. observation of majorana fermions in ferromagnetic atomic chains on a superconductor, *Science (New York, N.Y.)*, **31**, p. 602.

Nurse, P. (2008), Life, logic and information, *Nature*, **454**, pp. 424–6.

Peyrard, M. and Bishop, A. (1989), Statistical mechanics of a nonlinear model for dna denaturation, *Physical review letters*, **62**, pp. 2755–2758.

Prossr, A. (2012), *What is Life?: How Chemistry Becomes Biology*, Oxford Landmark Science.

Robinson, N., Altland, A., Egger, R., Gergs, N., Li, W., Schuricht, D., Tsvelik, A., Weichselbaum, A. and Konik, R. (2019), Nontopological majorana zero modes in inhomogeneous spin ladders, *Physical Review Letters*, **122**.

Rokhinson, L., Liu, X. and Furdyna, J. (2012), The fractional a.c. josephson effect in a semiconductor-superconductor nanowire as a signature of majorana particles, *Nature Physics*, **8**, pp. 795–799.

Scheurer, M. and Shnirman, A. (2013), Non-adiabatic processes in majorana qubit systems, *Physical Review B*, **88**.

Schrödinger, E. (1944), *What is Life? The Physical Aspect of the Living Cell*, Cambridge University Press.

Szathmáry, E. (1989), The integration of the earliest genetic information, *Trends in ecology & evolution*, **4**, pp. 200–4.

Tabi, C. B. (2016), Bubble formation in helicoidal dna molecules, *Journal of Physical Chemistry & Biophysics*, **06**.

Tirard, S., Morange, M. and Lazcano, A. (2010), The definition of life: A brief history of an elusive scientific endeavor, *Astrobiology*, **10**, pp. 1003–9.

Walker, S. and Davies, P. (2013), The algorithmic origins of life, *Journal of the Royal Society, Interface / the Royal Society*, **10**, p. 20120869.

Walker, S., Davies, P. and Ellis, G. (2017), *From matter to life: Information and causality*.

Wilczek, F. (2009), Majorana returns, *Nature Physics*, **5**, pp. 614–618.

Williams, J., Bestwick, A., Gallagher, P., Hong, S., Cui, Y., Bleich, A., Fisher, I. and Goldhaber-Gordon, D. (2012), Unconventional josephson effect in hybrid superconductor-topological insulator devices, *Physical Review Letters*, **109**.

Yakushevich, L. (2006), Nonlinear physics of dna.

Yockey, H. (2002), Information theory, evolution, and the origin of life, *Inf. Sci.*, **141**, pp. 219–225.

Zakharov, V. and Shabat, A. (1972), Exact theory of two-dimensional self-focusing and one-dimensional self-modulation of waves in nonlinear media, *Soviet Physics Journal of Experimental and Theoretical Physics Letters*, **34**, pp. 62–69.

Zdravkovic, S. (2011), Helicoidal peyrardbishop model of dna dynamics.

Zuo, K. and Mourik, V. (2016), *Signatures of Majorana Fermions in Hybrid Superconductor-Semiconductor Nanowire Devices*, Ph.D. thesis.

Proceedings of *RAGtime 20–22, 15–19 Oct., 16–20 Sept., 19–23 Oct., 2018/2019/2020, Opava, Czech Republic*
Z. Stuchlík, G. Török and V. Karas, editors, Silesian University in Opava, 2020, pp. 73–82

Proton acceleration in the active galactic nuclei

Yakov Istomin[1] and Alexey Gunya[1,a]

[1]P.N. Lebedev Physical Institute, Leninsky Prospect 53, Moscow 119991, Russia
[a]aagunya@lebedev.ru

ABSTRACT

In this paper, the process of acceleration of an ultrahigh-energy proton in the active galactic nucleus is briefly considered. The full cycle of collisionless acceleration of a proton up to the maximum energy E_{max} includes the primary acceleration in the region of the light cylinder up to the energy $E_{max}^{2/3}$ and additional acceleration in the region of the relativistic jet base where the proton reaches its maximum energy E_{max}. Different regimes of acceleration of protons in a jet have been discovered, depending on the values of the amplitudes of the electric and magnetic fields. The obtained theoretical estimates were confirmed by the data of the Pierre Auger collaboration, as well as by the IceCube collaboration when evaluating the neutrino energy on a jet subparsec scale.

Keywords: Cosmic rays – active galactic nuclei – black holes

1 INTRODUCTION

High-energy protons make up up to 90% of the composition of ultra-high-energy cosmic rays. The most probable sources and mechanisms of origin of protons with energies $> 10^{19}$ eV has been an extensive discussion for decades. The detection of protons of such energies is hampered by the remoteness of objects, as well as by the natural dissipation of relic radiation by photons, called the Greisen-Zatsepin-Kuzmin effect. The most likely candidates for high-energy proton sources are active galactic nuclei (AGN), the astrophysical scales of which make it possible to form an optimal accelerating medium. It is assumed that the most likely mechanism responsible for the proton reaching such energies is stationary acceleration by an electric field in the vicinity of massive objects such as supermassive black holes (SMBH). This mechanism allows the proton to reach energies $> 10^{20}$ eV, due to the presence of weak magnetization with magnetic fields in the vicinity of the SMBH, as well as a large potential difference between the SMBH and the relativistic jet. The explanation of this mechanism is based on the Blandford-Znaek process (Blandford and Znajek (1977)). This is based on the assumption of extracting rotational energy from the SMBH. For comparison, Fermi acceleration of a proton on a shock wave can reach no more than 10^{15} eV (F. A. Aharonian. (2004)). The detection of high-energy protons is less bright and more difficult due to the much lower synchrotron losses compared to electrons. This is also an advantage when reaching the ultimate energies.

978-80-7510-432-8

The calculations used a kinetic approach to describe the motion of a charged particle. This is a key difference from MHD modeling, since in the kinetic approach, the action of inertial forces is important, especially in the area of the light cylinder.

2 ELECTROMAGNETIC FIELD

Acceleration process starts from the inner boundary of the ISCO disk (Istomin and Sol (2009)). Due to turbulent accretion the primary protons achieved 10-100 eV. With an increase in the accretion rate $\dot{M}$, a part of the accreting matter forms a jet propagating along the axis of rotation of the BH. In terms of the topology of the electromagnetic field, the SMBH has a uniform split-monopole structure. A toroidal field arises in the magnetosphere, which, due to the slower decay of $B_\phi \simeq r^{-1}$ in comparison with the poloidal field $B_r \simeq r^{-2}$, reaches a significant value in the region where matter reaches relativistic velocities namely light cylinder (Fig. 1). This specific area where the electric field becomes equal to the magnetic field $E = H$ and linear velocity v becomes equal to light velocity c. Due to centrifugal force the proton shifting to the light cylinder surface and its energy increase asymptotically. A similar structure is well known in neutron stars (Goldreich and Julian (1969)).

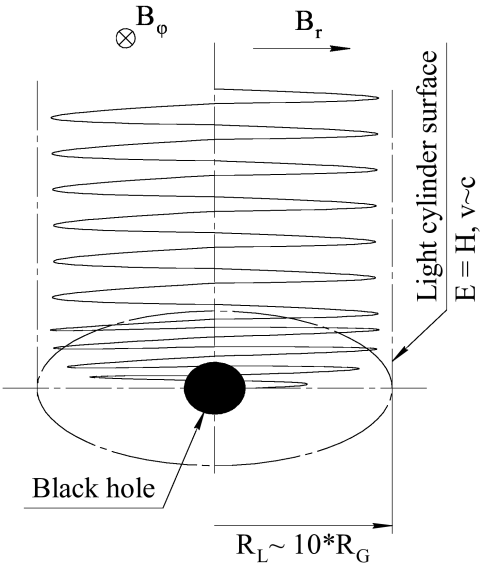

Figure 1. The magnetic field structure in the light cylinder

A relativistic jet is formed in the SMBH region of the corona above the surface of the light cylinder. In this region, the electromagnetic field is also inherited from the magnetosphere B_r, B_ϕ, E_θ into the jet B_z, B_ϕ, E_ρ. The structure of the magnetosphere electromag-

netic field is fully described in the work Istomin and Gunya (2020a), the structure of the jet electromagnetic field is fully described in the work Istomin and Gunya (2020b).

3 PARTICLE ACCELERATION

The trajectory of a full cycle of proton acceleration is the sum of the acceleration in the magnetosphere and the acceleration in the jet. The centrifugal force due to acceleration shifted the proton to the light cylinder with radius $R_L = \Omega_F/c$, where c is the speed of light, the magnetic field angular velocity Ω_F is determined by the angular velocity of the SMBH Ω_H as $\Omega_F \simeq \Omega_H/2$ (Blandford and Znajek (1977)). When the proton reaching the light cylinder, the energy increases to $\gamma_{max}^{(2/3)}$ asymptotically shifted to the boundary of the light cylinder and then leaves it, passing into the jet region. The pre-accelerated proton begins to increase its energy up to the maximum value $\gamma_{max}^{(1)}$ when it reaches the plane of intersection of the parabolic and conical jet profiles (Kovalev et al. (2020)). Upon reaching and crossing the jet boundary, the proton passes through the maximum potential difference, which gives the maximum energy.

The motion of particles with mass m and charge q in an electromagnetic field is described by the equations

$$\begin{aligned}\frac{\mathrm{d}\mathbf{p}}{\mathrm{d}t} &= q\left(\mathbf{E} + \frac{1}{c}[\mathbf{v},\mathbf{B}]\right),\\ \frac{\mathrm{d}\mathbf{r}}{\mathrm{d}t} &= \frac{\mathbf{p}}{m\gamma},\\ \gamma^2 &= 1 + \frac{p^2}{m^2c^2}.\end{aligned} \tag{1}$$

Here $\mathbf{r}$ and $\mathbf{p}$ are coordinates and momentum of a charged particle, γ is its Lorentz factor.

The motion of a proton in the magnetosphere (Istomin and Gunya (2020a)) is described by equations (3). Here $\mathbf{r}$ and $\mathbf{p}$ are the coordinate and the momentum of a particle, γ is its Lorentz factor. It is convenient for us to introduce dimensionless time, coordinates, velocity and momentum,

$$t' = \frac{\omega_c t}{\gamma_i},\ \mathbf{r}' = \frac{\mathbf{r}}{r_L},\ \mathbf{v}' = \frac{\mathbf{v}}{c},\ \mathbf{p}' = \frac{\mathbf{p}}{mc\gamma_i}. \tag{2}$$

The initial value of the Lorentz factor is γ_i, the nonrelativistic cyclotron frequency of a particle rotation in the B_0 field is $\omega_c = qB_0/mc$. Let us also introduce the value of the Lorentz factor relative to the initial energy, $\gamma' = \gamma/\gamma_i$. In these variables, the equations of

motion (3) in spherical coordinates r, θ, ϕ (primes are omitted) have the form

$$\begin{aligned}
\frac{\mathrm{d}p_r}{\mathrm{d}t} =& \frac{\kappa}{r\gamma}\left(p_\theta^2 + p_\phi^2\right) + \frac{s\alpha}{r\gamma}p_\theta,\\
\frac{\mathrm{d}p_\theta}{\mathrm{d}t} =& -\frac{\kappa}{r\gamma}\left(p_r p_\theta - p_\phi^2\cot\theta\right) - \frac{s}{r}\sin\theta + \frac{s}{r^2\gamma}p_\phi - \frac{s\alpha}{r\gamma}p_r,\\
\frac{\mathrm{d}p_\phi}{\mathrm{d}t} =& -\frac{\kappa}{r\gamma}\left(p_r + p_\theta\cot\theta\right)p_\phi - \frac{s}{r^2\gamma}p_\theta,\\
\frac{\mathrm{d}r}{\mathrm{d}t} =& \frac{\kappa}{\gamma}p_r,\\
\frac{\mathrm{d}\theta}{\mathrm{d}t} =& \frac{\kappa}{r\gamma}p_\theta.
\end{aligned} \tag{3}$$

Here $s = sign|z|$.

The equations of a proton motion in a jet (Istomin and Gunya (2020b)) is described by equations (5).

The dimensionless time, coordinates and variables

$$\begin{aligned}
t' =& \frac{c}{R_J}t,\ \rho' = \frac{\rho}{R_J},\ z' = \frac{z}{R_J},\\
\mathbf{p}' =& \frac{c}{\omega_c R_J}\frac{\mathbf{p}}{mc},\ \gamma' = \frac{c}{\omega_c R_J}\gamma.
\end{aligned} \tag{4}$$

The value of ω_c is the nonrelativistic frequency of rotation of a particle in the magnetic field. The relation c/ω_c is the cyclotron radius of a nonrelativistic particle. It is significantly smaller than the jet radius R_J, $c/\omega_c R_J << 1$. Omitting the primes, we move to the equations of particle motion in the fields $B_z = B_0$, B_ϕ, E_ρ

$$\begin{aligned}
\frac{\mathrm{d}p_\rho}{\mathrm{d}t} &= \frac{p_\phi^2}{\rho\gamma} + \frac{p_\phi}{\gamma} - \alpha\frac{p_z\rho(1-\rho)^2}{\gamma} + \beta\rho(1-\rho)^2,\\
\frac{\mathrm{d}p_\phi}{\mathrm{d}t} &= -\frac{p_\rho p_\phi}{\rho\gamma} - \frac{p_\rho}{\gamma},\\
\frac{\mathrm{d}p_z}{\mathrm{d}t} &= \alpha\frac{p_\rho\rho(1-\rho)^2}{\gamma},\\
\frac{\mathrm{d}\rho}{\mathrm{d}t} &= \frac{p_\rho}{\gamma},\\
\frac{\mathrm{d}\phi}{\mathrm{d}t} &= \frac{p_\theta}{\rho\gamma},\\
\frac{\mathrm{d}z}{\mathrm{d}t} &= \frac{p_z}{\gamma}.
\end{aligned} \tag{5}$$

The dimensionless equations (3) and (5) uncluding dimensionless parameters. Magnetic field parameter $\alpha = B_\phi/B_0$, where B_0 is the radial field B_r for the magnetosphere or the

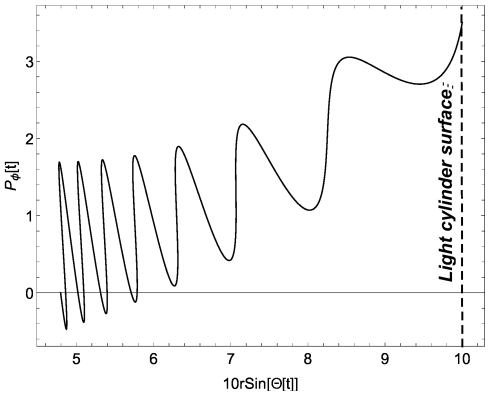

Figure 2. The magnetosphere toroidal momemtum versus the radial distance $r \sin\theta$. The numerical parameters considered as an example $\kappa = 10^{-2}$ and $\alpha = 10^{-2}$. The light cylinder surface is located at 10 on the abscissa axis.

longitudinal field B_z for the jet. The parameter of the electric field amplitude in the jet β and the magnetization parameter $\kappa = \Omega_F/\omega_c << 1$ in the magnetosphere, characterizing the cyclotron frequency of the particle ω_c much higher than the angular velocity of the magnetic field Ω_F.

Analysis of the toroidal moment P_ϕ on the figure (2) shows that centrifugal acceleration $P_\phi >> P_r + P_\theta$ is predominant in the area of the light cylinder R_L.

Analysis of the proton acceleration trajectory showed that the main energy increment occurs in the near-boundary region of the light cylinder (Fig. 3). The thickness of this area:

$$\Delta r = -\frac{s\kappa\gamma_{max}}{\sin^2\theta}\frac{p_r}{p_\theta}\,|_{r=1/\sin\theta}\,. \tag{6}$$

The calculation of the dependence of the proton energy on the distance to the light cylinder revealed that the proton leaves the acceleration region on the light cylinder when $\gamma_{max}^{(2/3)}$ is reached for the magnetosphere with a significant dominance of the toroidal field B_ϕ over poloidal B_r, which is typical for systems with AGN and a jet, and $\gamma_{max}^{(1/2)}$ for systems with an insignificant toroidal field, which is typical for inactive nuclei without a jet.

In a jet, the trajectory of displacement and the increment of energy occur mainly in the radial direction at different (Fig. 4).

Three acceleration regimes are determined depending on the values of the dimensionless amplitudes of the electric and magnetic fields.
(1) $\beta^2 - \alpha^2 > a_2^2 = 36$ – protons in the "untrapped" regime acquire the total energy $\gamma = \gamma_{max}$,
(2) $19 = a_1^2 < \beta^2 - \alpha^2 < a_2^2 = 36$ – protons in the "trapped" regime cyclically increase and lose energy, oscillating between the boundary and the axis of jet $\gamma = 0.74\gamma_{max}$,
(3) $\beta^2 - \alpha^2 < a_1^2 = 19$ – protons are not accelerated in the jet and move with the energy previously acquired in the magnetosphere, $\gamma = \gamma_{max}^{2/3}$ along the jet axis with insignificant oscillation.

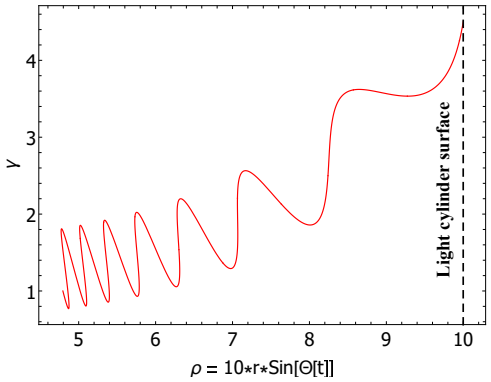

Figure 3. The magnetosphere Lorentz factor versus the radial distance $r \sin\theta$. The numerical parameters considered as an example $\kappa = 10^{-2}$ and $\alpha = 10^{-2}$. The light cylinder surface is located at 10 on the abscissa axis.

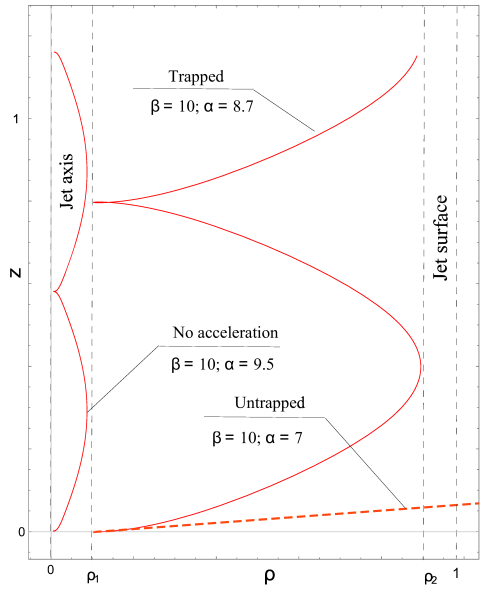

Figure 4. Particle trajectories on the plane (ρ, z). The figure shows particle trajectories in the regimes: untrapped, trapped and nonaccelerated.

4 AGN

The energy achieved in the magnetosphere and the jet, as well as the acceleration regime for a real AGN, is determined by the potential U generated by the SMBH and transferred along the magnetic field lines from the magnetosphere to the jet. Thus, the U is also the total potential difference between the region of the ergosphere of the SMBH in the

magnetosphere and the boundary of the jet. The SMBH potential (Thorne et al. (1986), Landau and Lifshitz (1984)) is

$$U = B_p r_g^2 \Omega_H / 2c. \tag{7}$$

The angular velocity of rotation of the black hole is proportional to the angular momentum of rotation of the black hole $J = j(M^2 G/c)$, where j is the specific angular momentum of the black hole, $j < 1$,

$$\Omega_H = \frac{2c}{r_g} \frac{j}{1 + (1 - j^2)^{1/2}}. \tag{8}$$

The quantity r_g is the gravitational radius of a SMBH with mass M,

$$r_g = \frac{2GM}{c^2} = 3 \cdot 10^5 \frac{M}{M_\odot} \text{ cm} = 3 \cdot 10^{14} M_9 \text{ cm}. \tag{9}$$

The value M_9 denotes the mass represented in units of $10^9 M_\odot$. Accordingly, $\Omega_H = 2 \cdot 10^{-4} M_9^{-1} j/[1 + (1 - j^2)^{1/2}]\ s^{-1}$.

The energies are defined as follows. For a proton accelerated in the "untrapped" regime, the energy is

$$E_{max}[\text{eV}] = 300 \cdot U[\text{cgs}]; \tag{10}$$

for a proton accelerated in the "trapped" regime, the energy is

$$E_{max}[\text{eV}] = 0.74 \cdot 300 \cdot U[\text{cgs}]; \tag{11}$$

and finally, for a proton moving in the "nonacceleration" regime

$$E_i[\text{eV}] = 0.94\,\text{GeV} \cdot \left(\frac{U[\text{eV}]}{0.94\,\text{GeV}} \right)^{2/3} \tag{12}$$

is the initial energy acquired in the magnetosphere. Parameters such as mass M_9, magnetic field B_4, specific angular momentum j, potential U, energies E_{max}, E_i.

5 SUMMARY

It has been proved that the main energy of the high-energy cosmic ray proton is accumulated in the region of the light cylinder R_L of the SMBH magnetosphere in the process of collisionless stationary electromagnetic acceleration. The astrophysical scales of the magnetosphere of the AGN core and its surroundings, including the jet and the inner boundary of the ISCO disk (Istomin and Sol (2009)), accelerate charged particles most effectively. The conversion of the rotational energy of the SMBH into the rotation of the magnetic field lines of the poloidal field B_p is possible thanks to the Blandford-Znajek process, direct numerical simulations of which (Komissarov (2001)), (Komissarov (2005)) confirmed the

Table 1. Enrgies and acceleration regimes in the AGNs

Object	E_{max} [eV]	E_i [eV]	regime
OQ 530	$3.6 \cdot 10^{19}$	$2.4 \cdot 10^{14}$	trap./untrapped
S5 2007+77	$5.1 \cdot 10^{19}$	$3.0 \cdot 10^{14}$	trap./untrapped
S4 0954+ 5	$8.4 \cdot 10^{19}$	$4.2 \cdot 10^{14}$	trap./untrapped
NGC 1275	$1.9 \cdot 10^{21}$	$3.3 \cdot 10^{15}$	untrap./trapped
NGC 4261	$1.4 \cdot 10^{20}$	$5.9 \cdot 10^{14}$	untrap./trapped
NGC 4486	$1.6 \cdot 10^{20}$	$6.4 \cdot 10^{14}$	untrap./trapped
3C 371	$1.3 \cdot 10^{21}$	$3.2 \cdot 10^{15}$	untrapped
3C 405	$9.6 \cdot 10^{20}$	$2.6 \cdot 10^{15}$	untrapped
NGC 6251	$2.9 \cdot 10^{21}$	$5.5 \cdot 10^{15}$	untrapped
3C 120	$4.0 \cdot 10^{21}$	$6.7 \cdot 10^{15}$	untrapped
BL Lac	$9.3 \cdot 10^{21}$	$1.2 \cdot 10^{16}$	untrapped
3C 273	$5.4 \cdot 10^{21}$	$6.7 \cdot 10^{15}$	untrapped
3C 390.3	$9.8 \cdot 10^{21}$	$1.2 \cdot 10^{16}$	untrapped
3C 454.3	$8.1 \cdot 10^{20}$	$1.9 \cdot 10^{15}$	trap./untrapped
1H 0323+342	$5.2 \cdot 10^{20}$	$1.7 \cdot 10^{15}$	untrapped
SS433	$6.7 \cdot 10^{20}$	$2.0 \cdot 10^{15}$	untrapped

efficiency and possibility of this process, as well as an immediate impact on the formation of a jet (Sob'yanin (2019)). The rotation of the poloidal magnetic field lines provides the generation of a polar electric field E_θ, which makes it possible to accelerate the proton to $\gamma_{max}^{(2/3)}$. The total potential difference U ends already at the jet boundary, where the radial electric field E_ρ is inherited from the initially generated SMBH polar field E_θ. In the "untrapped" regime, the proton escape out of the jet, accelerating to the limit value $\gamma_{max}^{(1)}$. In the table 1 shortly represented energies and regimes for diffrent real AGNs. The more complete set of parameters is presented in work Istomin and Gunya (2020b). The obtained data of the total energy E_{max} proton from table 1 also correspond to the data obtained from several sources by PA collaboration (Pierre Auger Collaboration and Abraham (2008)), (Abreu (2010)), (Nagar and Matulich (2008)), (Aab (2018)), (Zaw et al. (2009)). Note that due to natural constrains (Pierre Auger Collaboration and Abreu (2013)) named GZK-effect (Zatsepin and Kuz'min (1966)), not all sources can be associated with the predicted energies. Also according to IceCube results (Plavin (2020)), the neutrino energy in the subparsec region at the base of the jet corresponds to the maximum energy of colliding protons $E_p \simeq 10^{16} - 10^{17}$ eV, which corresponds to orders of magnitude energy acquired by protons in the region of the SMBH magnetosphere (third coloumn (Tab. 1)). Eventually the proton acceleration algorithm directly depends on the activity of the galactic nucleus (5).

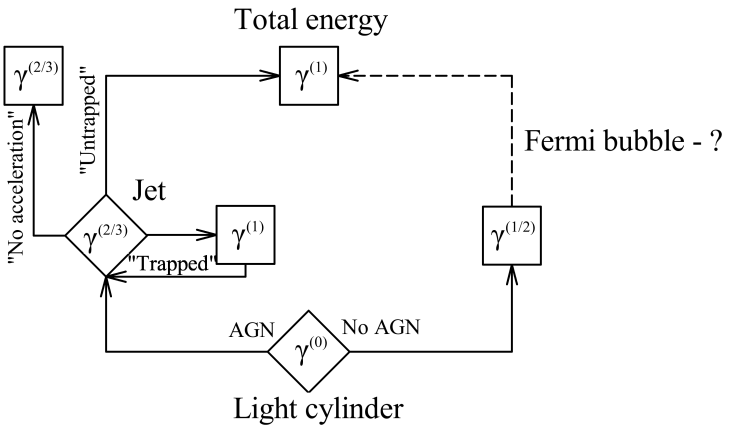

Figure 5. UHECR proton acceleration algorythm for diffrenet galaxyes activity

The acceleration of a proton in a non active nuclei to energy E^1_{max} is also assumed to possibly occur in a Fermi bubble, which will be considered by the authors in the next paper.

REFERENCES

Aab, A. e. a. (2018), An Indication of Anisotropy in Arrival Directions of Ultra-high-energy Cosmic Rays through Comparison to the Flux Pattern of Extragalactic Gamma-Ray Sources, *ApJ*, **853**(2), L29, arXiv: 1801.06160.

Abreu, P. e. a. P. (2010), Update on the correlation of the highest energy cosmic rays with nearby extragalactic matter, *Astroparticle Physics*, **34**(5), pp. 314–326, arXiv: 1009.1855.

Blandford, R. D. and Znajek, R. L. (1977), Electromagnetic extraction of energy from Kerr black holes., *MNRAS*, **179**, pp. 433–456.

F. A. Aharonian. (2004), High-energy particle acceleration in the shell of a supernova remnant, *Nature*, **432**(7013), pp. 75–77.

Goldreich, P. and Julian, W. H. (1969), Pulsar Electrodynamics, *ApJ*, **157**, p. 869.

Istomin, Y. N. and Gunya, A. A. (2020a), Centrifugal acceleration of protons by a supermassive black hole, *MNRAS*, **492**(4), pp. 4884–4891.

Istomin, Y. N. and Gunya, A. A. (2020b), Acceleration of high energy protons in agn relativistic jets, *Phys. Rev. D*, **102**, p. 043010, URL https://link.aps.org/doi/10.1103/PhysRevD.102.043010.

Istomin, Y. N. and Sol, H. (2009), Acceleration of particles in the vicinity of a massive black hole, *Astrophys. Space Sci.*, **321**, pp. 57–67.

Komissarov, S. S. (2001), Direct numerical simulations of the Blandford-Znajek effect, *MNRAS*, **326**(3), pp. L41–L44.

Komissarov, S. S. (2005), Observations of the Blandford-Znajek process and the magnetohydrodynamic Penrose process in computer simulations of black hole magnetospheres, *MNRAS*, **359**(3), pp. 801–808, arXiv: astro-ph/0501599.

Kovalev, Y. Y., Pushkarev, A. B., Nokhrina, E. E., Plavin, A. V., Beskin, V. S., Chernoglazov, A. V., Lister, M. L. and Savolainen, T. (2020), A transition from parabolic to conical shape as a common effect in nearby AGN jets, *Mon. Not. R. Astron. Soc.*, **495**(4), pp. 3576–3591.

Landau, L. D. and Lifshitz, E. M. (1984), *Course of Theoretical Physics. Vol. 8.*, Oxford.

Nagar, N. M. and Matulich, J. (2008), Ultra-high energy cosmic rays detected by the Pierre Auger observatory. First direct evidence, and its implications, that a subset originate in nearby radiogalaxies, *A&A*, **488**(3), pp. 879–885, arXiv: 0806.3220.

Pierre Auger Collaboration and Abraham, e. a. (2008), Correlation of the highest-energy cosmic rays with the positions of nearby active galactic nuclei, *Astroparticle Physics*, **29**(3), pp. 188–204, arXiv: 0712.2843.

Pierre Auger Collaboration and Abreu, P. e. (2013), Constraints on the Origin of Cosmic Rays above 10^{18} eV from Large-scale Anisotropy Searches in Data of the Pierre Auger Observatory, *ApJ*, **762**(1), L13, arXiv: 1212.3083.

Plavin (2020), Observational evidence for the origin of high-energy neutrinos in parsec-scale nuclei of radio-bright active galaxies, *Astrophys. J.*, **894**(2), 101.

Sob'yanin, D. N. (2019), Relativistic polytrope from the collimation and acceleration profiles of the M87 jet at subparsec scales and thermodynamic evidence for the Blandford-Znajek mechanism, *MNRAS*, **489**(1), pp. L7–L11, arXiv: 1908.05485.

Thorne, K. S., Price, R. H. and MacDonald, D. A. (1986), *Black Holes: the Membrane Paradigm.*, Yale University Press, New Haven.

Zatsepin, G. T. and Kuz'min, V. A. (1966), Upper Limit of the Spectrum of Cosmic Rays, *Soviet Journal of Experimental and Theoretical Physics Letters*, **4**, p. 78.

Zaw, I., Farrar, G. R. and Greene, J. E. (2009), Galaxies Correlating with Ultra-High Energy Cosmic Rays, *ApJ*, **696**(2), pp. 1218–1229, arXiv: 0806.3470.

Proceedings of *RAGtime 20–22, 15–19 Oct., 16–20 Sept., 19–23 Oct., 2018/2019/2020, Opava, Czech Republic*
Z. Stuchlík, G. Török and V. Karas, editors, Silesian University in Opava, 2020, pp. 83–95

Accretion induced black hole spin up in magnetized collapsars

Agnieszka Janiuk[1,a] and Dominika Ł. Król[2]

[1]Center for Theoretical Physics, Polish Academy of Sciences, Al. Lotnikow 32/46, P-02-668 Warsaw, Poland
[2]Jagiellonian University Astronomical Observatory, ul. Orla 171, P-30-244 Krakow, Poland
[a]agnes@cft.edu.pl

ABSTRACT

Black holes are the final stage of gravitational collapse process, and due to the cosmic censorhip conjecture, they are created inevitably if a trapped surface has formed in the space-time. The solutions of Schwarzschild and Kerr are describing the spacetime metric for the gravitational field of a spherically symmetric, or rotating black hole. Astrophysically, the rotating black holes of stellar mass are end products of stellar evolution, when the progenitor star was massive enough and possessed a substantial amount of angular momentum. They can be discovered when leaving behind a luminous transient in a form of gamma ray burst, which is followed by an afterglow emission at lower energies and associated with the emerging supernova-like spectra that trace the chemical composition of expanding shells from the explosion. The gravitational binding energy of the massive progenitor star is released in the supernova explosion, while the extraction of rotational energy of the newly formed black hole drives the gamma ray burst. In the latter, magnetic fields are the agent driving the process.

In this article, we study the gravitational collapse and formation of the Kerr black hole from the rotating progenitor star. We follow the evolution of black hole spin, coupled with its increasing mass. We study the effect of different level of rotation endowed in the progenitor's envelope, and we out some constraints on the final black hole parameters.

Our method is based on semi-analytical computations that involve stellar-evolution models of different progenitors. We also follow numerically the black hole evolution and spacetime metric changes during the collapse, via General Relativistic MHD modeling.

Keywords: Black hole physics – magnetic fields – accretion

1 INTRODUCTION

Stellar mass black holes reside in transient and persistent X-ray sources. Transient X-ray sources transform the gravitational potential energy of the black hole into radiation of

978-80-7510-432-8

the accretion disk, fed by the companion star. From the analysis of the orbital motion in the binary, astronomers obtain information about the gravitational mass, and an estimate of the mass of the black hole. The typical masses of these black holes are around 6-10 Solar mass, while the most massive electromagnetic black holes have masses of 20 $M_\odot$ (Reynolds, 2019). Various methods of spin estimates utilize the spectral analysis of radiation from the accretion disk, namely the continuum fitting method or the X-ray reflection spectrum modeling. These methods give consistent results but with a wide range of spin determinations for individual black holes, from $a = 0.3$ to $a \gtrsim 0.95$.

The newly born black holes are engines of gamma ray bursts. These very energetic events have a transient nature and are associated with a catastrophic collapse of the star. The accretion power is transformed to the bulk kinetic energy of the jet launched along the rotation axis of the black hole. This black hole must be at least moderately or very highly spinning $a \gtrsim 0.6 - 0.9$ in order to provide an efficient power generation for the jet.

Apart from electromagnetic observations, black holes in the Universe are detected via gravitational wave window. The existence of gravitational waves is predicted by General Relativity. The accelerating objects generate changes in the spacetime curvature which propagate outwards with the speed of light. These propagating ripples are called waves, and the observer on Earth will also find the spacetime distorted once such a wave reaches the Solar System. In the gravitational wave detectors, the strain is a measured displacement between the test masses, relative to the reference length. The analysis of the signal is done via numerical relativity methods, and it enables determination of the masses and projected spins of compact objects whose coalescence is being observed.

Since 2015, the binary compact object mergers, including stellar mass black holes, have been detected many times. These discoveries brought new information about the masses and estimated spins of the black holes produced from stellar progenitors. In LIGO data, a negative correlation between the black hole masses and the mean effective spins is found (Safarzadeh et al., 2020). In general, the LIGO measurements disfavour large spins. Typical spins are constrained to $a \lesssim 0.4$. For aligned spins, these constraints are tighter, and results suggest $a \sim 0.1$. On the other hand, masses of black holes detected through gravitational waves are systematically larger than previously known. Most of them seem to be around $20 - 30 M_\odot$, while the most massive event detected recently was fitted with two black holes weighing about 66 and 85 Solar masses (GW 190521).

In this contribution we are interested in quantifying the gravitational collapse of a massive star and determination of the mass and spin of the newly formed black hole. Our analysis shows that these two quantities are anti-correlated and depend on the angular momentum content in the collapsing envelope.

We build our study following a series of works that have been previously published (Janiuk and Proga, 2008; Janiuk et al., 2008, 2018; Murguia-Berthier et al., 2020). In particular, Janiuk and Proga (2008) and Janiuk et al. (2008) explored the problem of how fast the black hole can spin up via the collapse. This study addressed the long GRB as a luminous transient powered by the spinning black hole. Depending on the accretion scenario and the angular momentum content in the envelope, the maximum duration of the GRB event can be determined. Basic condition that has to be satified for a successful GRB, is that some part of the rotating envelope must contain enough angular momentum

to exceed the critical limit:

$$l_{\rm spec} = l_0 f(\theta) g(r) \tag{1}$$

where the normalization is scaled to $l_0/l_{\rm crit} = x$.

$$l_{\rm crit} = \frac{2GM}{c} \sqrt{2 - a \ + 2\sqrt{1 - A}} \tag{2}$$

where A is the black hole dimensionless spin parameter. The rotating torus and BH spin drive the GRB central engine, as long as the torus angular momentum is above the critical value (Janiuk et al., 2008).

Various authors (Lee and Ramirez-Ruiz, 2006; Barkov and Komissarov, 2010) studied the properties of rotating collapsar envelope in the context of long gamma ray bursts. In particular, also spin-up of the envelope by a companion can be a source of enhanced rotation to prolong the duration and/or provide more power to the transient. Some results suggest that the binary companion black hole merged with the collapsar's core might lead to a gravitational wave event accompanied by a bright gamma ray burst (Janiuk et al., 2017). On the contrary, other studies show that a certain fraction of massive O-type stars can vanish without a trace (i.e. without a bright luminous transient), if only the slow rotation of those stars prevents them from gaining an effective feedback from accretion disk (Murguia-Berthier et al., 2020).

2 THE MODEL SET-UP

To describe the process of collapse in a proper way, we would need to start from the matter distribution of an evolved star, and then follow gravitational collapse by solving the Einstein equations for matter-field evolution, until the massive Kerr black hole is finally formed and all matter is either accreted or expelled because of energy deposition, possible due to the shock waves or magnetic reconnections. Such computations are currently beyond the scope of theoretical and numerical astrophysics.

Some efforts have been made already to simulate a collapsar and involve the conservation equation for the stress–energy tensor. They include the fluid and radiation fields, and the metric evolution followed through the standard BSSN method. However, the black hole growth was not followed in these works and the simulations stopped after the core collapse (Ott et al., 2018). If the black hole was found and diagnosed by means of the baryon mass enclosed inside a certain radius, this radius was identified with the Schwarzschild radius, i.e. the black hole was by definition a non-rotating one. Its mass is then fixed and also the metric is frozen (Kuroda et al., 2018).

In our approach, we focus on the further evolution of the black hole parameters, namely its spin and mass, which are affecting also the Kerr metric changes. Our approach is therefore more precise than in the above cited works, as for the dynamical evolution studied in General Relativity. On the other hand, the cost of this approach is a big simplification of the matter field distribution. We are trying to tackle this problem in two ways.

2.1 Matter configuration

First, we adopt the density distribution that is resulting from physical model of the pre-supernova star, pre-calculated by means of the stellar evolution model. Second, we adopt a spherical density distribution resulting from the radial accretion problem (i.e. the Bondi solution). In both cases, we supply the collapsing cloud with a small angular momentum, concentrated on the equatiorial plane, so that the star is rotating. Furthermore, in the Bondi case, we equip the star with magnetic fields of a chosen geometry and strength. We study the gravitational collapse as the sequence of quasi-stationary Kerr solutions for a growing mass and changing spin of the black hole. The spin is changing because of rotating matter is adding the angular momentum after it is transmitted through the black hole horizon.

Computations of the self-similar solutions based on the pre-computed stellar evolution tables are performed with the numerical code adopted from (Janiuk and Proga, 2008). The magnetized Bondi case is studied by means of the full general relativistic magneto-hydrodynamical simulation, i.e. here the stress-energy tensor contains both matter and electromagnetic parts. Numerics is tackled here with the generic MHD algorithm adopted from the HARM code (Gammie et al., 2003) and further developed by (Janiuk et al., 2018). This code is working in the MPI-parallelized version on the supercomputing clusters and the evolutionary scheme is supplemented with the Kerr metric update embedded in the code, as developed in 2018 by our Warsaw group.

2.1.1 Density distribution in a pre-supernova star

We use the pre-supernova models from Woosley and Weaver (1995) and also newer ones from Heger et al. (2000); Woosley et al. (2002) and Heger et al. (2005). The ZAMS mass of the star is 25 $M_\odot$. First two of them did not take into account rotation during the stellar evolution modeling, and neglected magnetic fields. The initial metallicity was 10^{-4}, so the mass loss was negligible. The third star model is magnetized.

The density distribution in these pre-supernova models is shown in Fig. 1. Subsequent layers of elements synthesized in the stellar interior are traced by this density profile. The innermost layer, consisting of pure Iron, is forming the core that represents initial black hole born just at the start of collapse. The mass of this core is equal to 1.4 $M_\odot$. The thin Silikon shell located outside this layer accretes first. Further heavy shells are then made of Oxygen with some contribution of Neon, Magnesium and Carbon, and accrete on the newly born black hole. The outermost Helium shell accretes at the core at later times. The Hydrogen envelope, located above radius of $r \gtrsim 10^{11}$ cm, can be either accreted or expelled.

2.1.2 Spherically symmetric inflow

We assume initially that the angular momentum of accreted fluid is negligible and its velocity has a non-vanishing component only in the radial direction. The equation of continuity gives $4\pi r^2 \rho(r) u^r(r) = -\dot{M}$, where the constant on the right-hand side has a meaning of mass accretion rate.

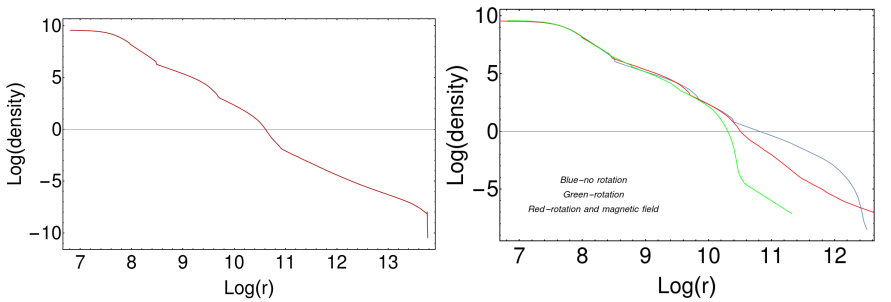

Figure 1. Density distribution in the pre-supernova stars used in our modeling. **Left:** Pre-SN spherically symmetric stellar model from Woosley and Weaver (1995) taken as initial condition for homologous collapse simulation of Janiuk and Proga (2008). **Right:** three othe pre-SN stellar models, taken from Heger et al. (2000); Woosley et al. (2002), and Heger et al. (2005). These latest models include rotation or magnetic fields in the stellar evolution calculations.

The distribution of density as the function of radius comes from the solution of transonic accretion flow in spherical geometry. The initial density profile and the radial component of the velocity (u^r) of the material is determined by the relativistic version of the Bernoulli equation (Hawley et al., 1984). In this formalism, the critical point (r_s), where the flow becomes supersonic, is set as a parameter. Here we take the value of $r_s = 80 r_g$. The fluid is considered a polytrope with a pressure $P = K\rho^\gamma$, where ρ is the density, $\gamma = 4/3$ is the adiabatic index, and K is the constant specific entropy. Once the critical point, r_s, is set, the velocity at that point is:

$$(u^r_s)^2 = \frac{GM}{2r_s}, \tag{3}$$

where r is the radial coordinate, M is the mass of the BH and the sound speed is:

$$c_s^2 = \frac{\gamma \frac{P_s}{\rho_s}}{1 + \frac{\gamma}{\gamma-1}\frac{P_s}{\rho_s}}. \tag{4}$$

The constant specific entropy can be obtained using the sound speed:

$$K = \frac{c_s^2}{\rho^{\gamma-1}\gamma} \tag{5}$$

The radial velocity profile is obtained by numerically solving the equation (Shapiro and Teukolsky, 1986):

$$\left(1 + \frac{\gamma}{\gamma-1}\frac{P}{\rho}\right)^2 \left(1 - \frac{2GM}{r} + (u^r)^2\right) = \text{constant} \tag{6}$$

The radial velocity is given by:

$$(u^r)^2 = \frac{GM}{2r}. \tag{7}$$

Finally, the accreting material is endowed with small angular momentum scaled to the one at the circularisation radius of $r_{\rm circ}$, being the ISCO radius (equal to 6 r_g for a non-rotating black hole; see (Janiuk et al., 2018)). It is also scaled with polar angle to have its maximum value on the equatorial plane, at $\theta = \pi/2$:

$$l = S\, l_{\rm isco} r^2 \sin^2\theta \tag{8}$$

where l is the specific angular momentum, defined as $l = u^\phi r^2$, $l_{\rm isco}$ is the specific angular momentum at the ISCO of the black hole, and θ is the polar coordinate.

3 STRONG GRAVITATIONAL FIELDS

Gravitational field of a black hole is described by Kerr metric, which can be written in the well-known Boyer-Lindquist coordinate system (t, r, θ, ϕ) and the metric element is given by:

$$\begin{aligned} {\rm d}s^2 = &-\left(1 - \frac{2Mr}{R^2}\right){\rm d}t^2 - \frac{4Mra\sin^2\theta}{R^2}\,{\rm d}t{\rm d}\phi + \\ &+\left(r^2 + a^2 + \frac{2Mra^2}{R^2}\sin^2\theta\right)\sin^2\theta\,{\rm d}\phi^2 + \frac{R^2}{\Delta}\,{\rm d}r^2 + R^2\,{\rm d}\theta^2 \end{aligned} \tag{9}$$

where $R^2 = r^2 + a^2\cos^2\theta$, $\Delta = r^2 - 2Mr + a^2$. The inner horizon is located at $r_{\rm H} = 1 + (1 - a^2)^{1/2}M$, with $a = J/M$, and the condition about the presence of the outer event horizon leads to the maximum value of the dimensionless spin, $|a \leq 1|$. Note that here the convention is used with $G = c = 1$. Here M denotes mass of the black hole, and the spin parameter a of the Kerr metric describes its rotation. This spacetime is asymptotically flat and the region far away from the ergosphere and event horizon experiences a negligible gravitational influence.

In Kerr metric the axial symmetry about the rotation axis is assumed and the metric elements are stationary in time. The very strong gravitational distorsion becomes infinite and forms a singularity below the event horizon.

3.1 Evolution of Kerr metric

The mass and spin of the black hole are rapidly changing during the collapse process. In the numerical simulations we update therefore the six non-trivial coefficients of the Kerr matric, according to the change of these quantities. We neglect however the self-gravity of the accreting fluid, and we assure that the only source of gravitational potential is the dynamically changing black hole mass, $M + \Delta M$:

$$\Delta M = \frac{M^t}{M^0} - 1 \tag{10}$$

Also, the black hole spin changes according to the inflow of angular momentum from the rotating enevelope. Hence,

$$\Delta a = \left(\frac{\dot{J}}{M^t} - \frac{a^{t-dt}}{M^t}\dot{E}\right)\Delta t \tag{11}$$

where M^t denotes the current black hole mass at time t, M^0 denotes initial black hole mass, and $\dot{J}$ and $\dot{E}$ are the flux of angular momentum and energy flux transmitted through the black hole horizon at a given time (Janiuk et al., 2018). The six non-trivial components of the Kerr metric, namely g_{tt}, g_{tr}, $g_{t\phi}$, g_{rr}, $g_{r\phi}$, $g_{\phi\phi}$, are updated at every time step and they get new values. This is a simplified treatment of the process, and new simulations with the self-gravity effects taken into account are planned to be the subject of our future work (Palit et al., in prep.).

4 MAGNETIC FIELDS

In order to initiate the numerical code we employ an initially parabolic magnetic field which is fully described by the only non-vanishing components of the four-potential,

$$A_\phi \propto (1 - \cos(\theta)) \tag{12}$$

in dimension-less Boyer-Lindquist coordinates. The magnetic field (and the associated electric component) are generated by currents flowing in the accreted medium far from the black hole, as the latter does not support its own magnetic field. The four-potential vector components define the structure of the electromagnetic tensor, $F_{\mu\nu} \equiv A_{[\mu,\nu]}$; by projecting onto a local observer frame one then obtains the electric and magnetic vectors $\boldsymbol{E}$ and $\boldsymbol{B}$. From the simple initial configuration, the numerical solution rapidly evolves into a complex entangled structure, with field lines turbulent within the accreting medium. At the end of the simulation, while the matter gets accreted into black hole and almost empty envelope remains, the field lines become more organized again.

5 RESULTS

5.1 Homologous mass accretion in collapsar

The original paper by Janiuk and Proga (2008) included four models of the angular momentum profile, but did not consider the black hole spin changes during the collapse. Then the subsequent work Janiuk et al. (2008) examined the black hole spin evolution, with the number of models of angular momentum distribution limited to two cases. Here we present the results of calculations for one of the models which was not included in the second paper, with the angular momentum profile described by the function:

$$f(\theta) \propto \sin^2(\theta). \tag{13}$$

with several normalizations with respect to the critical vaue, l_{crit} (see (2)): $x = 0.4$, $x = 1.0$ and $x = 1.4$. Note that the same values are used in GRMHD simulations presented in te next Section.

In this particular model we allowed for accretion of matter with super- and sub-critical angular momentum at the same time, thus referring to a homologus accretion scenario. We also did not terminate our calculations after there was no matter with sufficient amount of

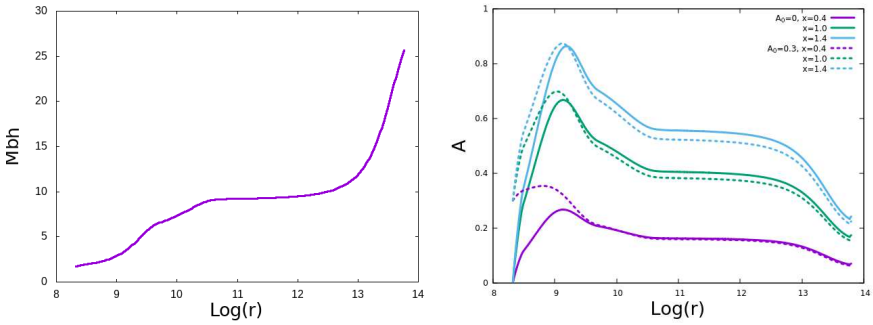

Figure 2. BH mass (left) and spin evolution (right) during collapse. Initial density distribution is taken from the 25 $M_\odot$ pre-supernova model of Woosley and Weaver (1995). Accretion scenario assumes homologous collapse with black hole spin-up, starting from either spin-less or moderately spinning core ($A_0 = 0$ or $A_0 = 0.3$). Initial core mass is $1.4M_\odot$. Angular momentum in the envelope is maximum at the equator, and scales with polar angle as $\sin^2\theta$, where $\theta = 0$ and $\theta = \pi$ refer to the poles. Normalisation of rotation with respect to the critical value, see (2), is denoted with $x = 0.4, 1.0$ and 1.4 (see blue, green and cyan lines in the right panel).

angular momentum to sustain the torus, so that no part of the Hydrogen envelope was expelled, and finally all the mass is accreted. We performed the calculations for two values of the initial black hole spin: $A_0 = 0$ and $A_0 = 0.3$. The spin and the black hole mass evolution are shown in Fig. 2. The black hole mass increase is the same for all the x normalization values, because matter with sub- and super critical angular momentum accrete togethter. The black hole spin evolution depends on both initial spin and initial angular momentum of the matter. In case of $x = 0.4$ maximal spin is significantly higher for $A_0 = 0.3$ than for a non-spinning black hole. The difference between maximal spin values in the models with $A_0 = 0.3$ and $A_0 = 0$ is smaller for higher x. In general, we note that the spin starts to increase immediately at the beginning of the calculations, and the lower x value is, the faster the spin reaches its maximum and then starts to decrease. The final spin value does not depend on the A_0.

5.2 MHD evolution of slowly-rotating inflow with Kerr metric update

In the *HARM* code GR MHD simulations, we set the outer boundary of the computational domain at the radius $10^3 r_g$, where the inflow is purely radial at initial time. The inner boundary is set at $\simeq 0.98 r_H$, i.e. at below the horizon radius for the corresponding value of spin a. The grid domain has been resolved at 256×256 points in (r, θ) coordinates. In MHD models, we renormalize the magnetic intensity to determine the plasma parameter $\beta = p_{gas}/p_{mag}$ (smaller β corresponds to a more magnetized plasma).

Because of the perfect conductivity and the force-free approximation (apart from the effective small-scale numerical dissipation), the magnetic field lines remain attached to plasma. During the evolution, the β-parameter is not uniform across the computational domain and it changes in time. In the limit of negligible magnetization ($\beta = \infty$) the grav-

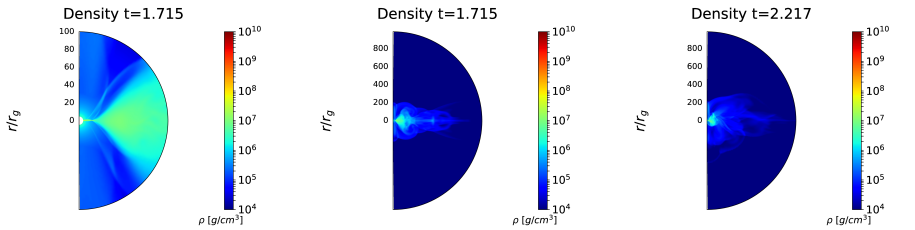

Figure 3. Density distribution in the late time of the simulation. Model parameters: black hole initial spin $A_0 = 0.5$, critical rotation parameter, $S = 1.0$. Model neglects magnetic fields. Rotationally supported disk-like structure is present for a long time in the equatorial plane. Note the different spatial scale of the left panel, which shows a zoom-in of the middle figure.

itational attraction of the black hole prevails. But in the case of equipartition between the magnetic and hydrodynamic pressure ($\beta \approx 1$) near the horizon the accretion rate is diminished (cf. Karas et al. (2020), *this Proceeding*).

Our collapsar simulations start from a spherically symmetric distribution of density of a purely radial infall, which is quickly broken by the imposed roation. The flow concentrates towards the equator, forming a mini-disk structure. The flow is supersonic near the black hole horizon, and in many cases, the multiple sonic surfaces are found with an aspherical shape (resembing an *eight-letter*). This feature refers to the inner sonic surface which after some time gets accreted. In the models with critical and supercritical roation ($S \gtrsim 1.0$), this initial transient shock is accompanied with some moderate variability of the accretion rate. Another sonic surphace, located initially at 80 r_g, expands outwards. The expanding shock velocity is typically much lower than the escape velocity at the shock radius.

The densest part of a roationally-supported mini-disk is enclosed within a small region of $r < 20r_g$ (cf. Murguia-Berthier et al. (2020)). The sub-critical models ($S \leq 1.0$) do not contain enough angular momentum to form a mini-disk bubble, and the material from both polar regions and equator can contribute to accretion and black hole mass grows more quickly in these models. In case of super-critical accretion, only material from polar regions accretes, while the angular momentum cannot be transported if magnetic fields are neglected. The accretion rate in this case is rather low for the first part of the simulation, while it grows later, when the bulk of material falling from the outer parts of the envelope reaches the mini-disk and is able to overpass it above and beow the equatorial plane. This phase (reached typicaly after $t > 0.8 - 1$ s, in physical time units) is also associated with large spikes in the accretion rate. The mini-disk is destroyed, nevertheless in many simulations we observe the existence of a long-living disk-like structure a the equatorial plane, which is sustained until the end of the simulations (typically $t_{end} = 2$ s). The detailed shape, and time for which the feature is preserved, depends also somewhat on the value of initial back hole spin A_0 (for the highets probed value, $A_0 = 0.85$, we found the longest timescale of disk structure, $t_f = 4.5$ s; see (Król and Janiuk, 2020)). In Fig. 3 we show the density distribution in the late phase of the simulation, for one exemplary model. Parameters of this model are $A_0 = 0.5$ and $S = 1.0$.

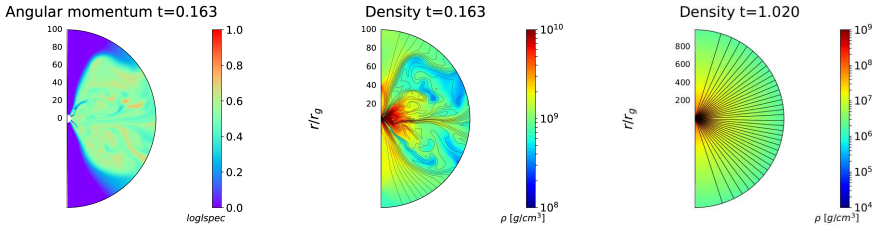

Figure 4. Results for magnetized model, with $\beta = 1$, initial black hole spin $A_0 = 0.5$ and critical rotation parameter, $S = 1.0$. Figures show angular momentum distribution and density field with overplotted magnetic field lines at the beginning of the simulation (left and middle panels) and the density structure, at the end of the simulation. Note the different spatial scale of the right panel, which shows a zoom-out of the middle figure.

The evolution of the black hole spin is non-linear, as the rotation of the black hole can both speed up and slow down, depending on the amount of angular momentum that is reaching the horizon. The maximum value of the spin reached during the collapse temporarily, as well as the final value, depends also on the assumed initial spin. For sub-critical rotation models, only for smallest value of $A_0 = 0.3$ we observed a temporal spin-up of the black hole (up to $A \sim 0.4$), while the end value was below the starting one ($A_f \sim 0.15$). For super-critical rotation, the black hole could even spin-up maximally for some period of time, but finally the spin was smaller. Typically $A \sim 0.7$ was reached in case of angular momentum in the envelope normalised to $S = 1.4$, which means that effectively the highly spinning black hole at $A_0 = 0.85$ did spin-down after the collapse.

The final black hole masses are oboviously limited by the total mass of he envelope, assumed always to be 25 $M_\odot$. They were between $M_{BH}^{end} = 11$ and 18 $M_\odot$ at the end of the simulation, and in non-magnetized models the largest back hole masses were obtained for sub-critical rotations, which also correlates with the smallest final spins. These values did not differ much between the models with various initial spins. For super-critical rotation of the envelope, the final black hole mass was smaller, and also decreased for large initial black hole spins.

In order to reveal the changes of the magnetic field near the black hole, we study the evolution of the strongly magnetized plasma, that is inflowing into the horizon. In Fig. 4 we present the MHD simulation results. Parameters of rotation in the envelope and initial black hole spin are the same as in Fig. 3, but now the model is magnetized, and the magnetic to gas pressure ratio in the accreting cloud is equal to $\beta = 1$.

As mentioned above, the initial configuration is the parabolic magnetic field solution, but this configuration starts quickly changing once the inflowing plasma arrives in the domain, while the magnetic field is coupled to matter. The purely poloidal field changes and develops a strong toroidal component (see Fig. 5).

We observe also that the magnetized jet wants to form in the polar regions, where the open field lines are visible in the early stage of evolved configuration, together with dense and turbulent torus structure in the equatorial plane (time $t \sim 0.1 - 0.15$ s). Nevertheless, because of large density in the envelope, the jet cannot break out of the collapsing star.

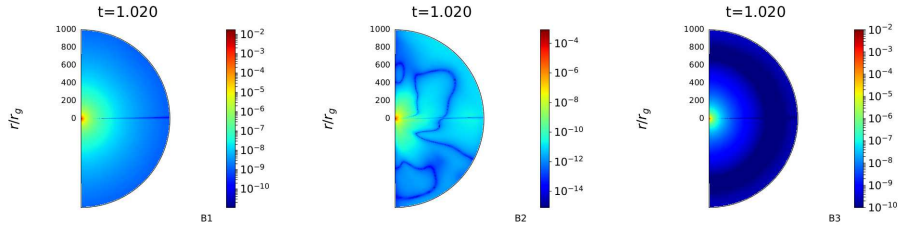

Figure 5. Components of magnetic field 3-vector, at the late stage of the simulation. Parameters of the run: $\beta = 1$, initial black hole spin $A_0 = 0.5$, envelope rotation $S = 1.0$

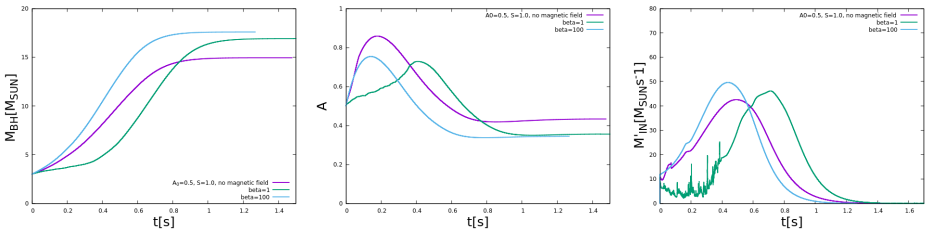

Figure 6. Evolution of the black hole mass, its spin, and accretion rate onto BH horizon, during the simulation. Parameters of the run: initial black hole spin $A_0 = 0.5$, envelope rotation parameter $S = 1.0$. Non-magnetized models are shown with purple lines. Magnetic field in magnetized model was parameterized with $\beta = 1$ (green lines) or $\beta = 100$ (cyan lines).

The polar funnels are baryon-polluted, and quickly change the magnetic field configuration back to radially-dominated, and the equatorial configuration of matter turns back to quasi-spherical (at time $t \sim 0.5$ s). We envisage, that full 3-dimensional simulations might be needed to overcome this problem and allow to sustain a long-living, dense and magnetized torus together with a jet-like funnel.

We also probed the effects of magnetic fields on the accretion rate, black hole spin, and mass in the collapsar models. In Fig. 6 we show the evolution of these quantites, for initial spin $A_0 = 0.5$ and the critical rotation parameter $S = 1.0$. Parabolic magnetic field was normalized to $\beta = 1$ or $\beta = 100$. For comparison, non-magnetized model of the same parameters but $\beta = \infty$ is presented in the Figure. The main quantitative difference is that the black hole spin is always smaller at its maximum in the magnetized models, than in the non-magnetized, for the same set of other parameters. The final black hole spin is also smaller if magnetic fields are included. On the other hand, the mass of the black hole achieved larger values. This is the result of angular momentum transport via magnetic fields, which allows matter to accrete not only from the polar regions, but also through the rotating disk. The variability of accretion rate is more visible in the weakly magnetized case ($\beta = 100$) than in the strongly magnetized. We suggest that this is an effect of a very strong magnetic barrier in the latter.

6 CONCLUSIONS

• We compute the collapsar model with slowly-rotating quasi spherical collapse with changing black hole spin and mass and Kerr metric update. We probed a range of angular momentum contents in the collapsars envelope, and range of initial black hole spins.
• Our method to follow collapse is fully GR MHD, while still not by exactly solving the Einsteins equations, but it gives a good approximation to this problem
• Our test models out some constraints on the angular momentum content of the collapsing progenitor star, with the resultant mass and spin of the BH.
• For supercritical rotation, we always observe spin up of the black hole at some stage of the simulation. The dependence on the initial black hole spin is however not monotonic, and at the end of simulation, the black hole can be effectively spun down with respect to the initial spin value.
• The strongly magnetized collapsars reach lower maximum black hole spins, and even for supercritical rotation in the envelope, the black hole may not reach the maximum Kerr parameter.
• The growth of the black hole mass is largest when the envelope rotation is slow, and when the black hole was at least moderately spinning initially.
• Two shock fronts were found with velocities are $0.014\,c$ and $0.022\,c$. For the models with sub critical envelope rotation we obtained higher velocities of the shock fronts: $0.04\,c$ and $0.044\,c$, depending on BH spin ($A_0 = 0.5, 0.85$). This trend seems opposite in comparison to Murguia-Berthier et al. (2020) who studied non-spinning BHs.

ACKNOWLEDGEMENTS

The authors thank Daniel Proga for helpful discussion. AJ was supported by grant no. 2019/35/B/ST9/04000 from the Polish National Science Center, and acknowledges computational resources of the Warsaw ICM through grant Gb79-9. DK was supported by Polish NSC grant 2016/22/E/ST9/00061.

REFERENCES

Barkov, M. V. and Komissarov, S. S. (2010), Close binary progenitors of gamma-ray bursts, *MNRAS*, **401**(3), pp. 1644–1656, arXiv: 0908.0695.

Gammie, C. F., McKinney, J. C. and Tóth, G. (2003), HARM: A Numerical Scheme for General Relativistic Magnetohydrodynamics, *ApJ*, **589**(1), pp. 444–457, arXiv: astro-ph/0301509.

Hawley, J. F., Smarr, L. L. and Wilson, J. R. (1984), A numerical study of nonspherical black hole accretion. I Equations and test problems, *ApJ*, **277**, pp. 296–311.

Heger, A., Langer, N. and Woosley, S. E. (2000), Presupernova Evolution of Rotating Massive Stars. I. Numerical Method and Evolution of the Internal Stellar Structure, *ApJ*, **528**(1), pp. 368–396, arXiv: astro-ph/9904132.

Heger, A., Woosley, S. E. and Spruit, H. C. (2005), Presupernova Evolution of Differentially Rotating Massive Stars Including Magnetic Fields, *ApJ*, **626**(1), pp. 350–363, arXiv: astro-ph/0409422.

Janiuk, A., Bejger, M., Charzyński, S. and Sukova, P. (2017), On the possible gamma-ray burst-gravitational wave association in GW150914, *NewA*, **51**, pp. 7–14, arXiv: 1604.07132.

Janiuk, A., Moderski, R. and Proga, D. (2008), On the Duration of Long GRBs: Effects of Black Hole Spin, *ApJ*, **687**(1), pp. 433–442, arXiv: 0807.2251.

Janiuk, A. and Proga, D. (2008), Low Angular Momentum Accretion in the Collapsar: How Long Can a Long GRB Be?, *ApJ*, **675**(1), pp. 519–527, arXiv: 0708.2711.

Janiuk, A., Sukova, P. and Palit, I. (2018), Accretion in a Dynamical Spacetime and the Spinning Up of the Black Hole in the Gamma-Ray Burst Central Engine, *ApJ*, **868**(1), 68, arXiv: 1810.05261.

Karas, V., Sapountzis, K. and Janiuk, A. (2020), Magnetically Ejected Disks: Equatorial Outflows Near Vertically Magnetized Black Hole, in *RAGtime 20-22: Workshops on Black Holes and Neutron Stars*, pp. 97–109.

Król, D. Ł.. and Janiuk, A. (2020), Accretion induced black hole spin up revised by numerical GR MHD simulations, *ApJ(submited)*.

Kuroda, T., Kotake, K., Takiwaki, T. and Thielemann, F.-K. (2018), A full general relativistic neutrino radiation-hydrodynamics simulation of a collapsing very massive star and the formation of a black hole, *MNRAS*, **477**(1), pp. L80–L84, arXiv: 1801.01293.

Lee, W. H. and Ramirez-Ruiz, E. (2006), Accretion Modes in Collapsars: Prospects for Gamma-Ray Burst Production, *ApJ*, **641**(2), pp. 961–971, arXiv: astro-ph/0509307.

Murguia-Berthier, A., Batta, A., Janiuk, A., Ramirez-Ruiz, E., Mandel, I., Noble, S. C. and Everson, R. W. (2020), On the Maximum Stellar Rotation to form a Black Hole without an Accompanying Luminous Transient, *ApJL*, **901**(2), L24, arXiv: 2005.10212.

Ott, C. D., Roberts, L. F., da Silva Schneider, A., Fedrow, J. M., Haas, R. and Schnetter, E. (2018), The Progenitor Dependence of Core-collapse Supernovae from Three-dimensional Simulations with Progenitor Models of 12-40 $M_{\odot}$, *ApJL*, **855**(1), L3, arXiv: 1712.01304.

Reynolds, C. S. (2019), Observing black holes spin, *Nature Astronomy*, **3**, pp. 41–47, arXiv: 1903.11704.

Safarzadeh, M., Farr, W. M. and Ramirez-Ruiz, E. (2020), A Trend in the Effective Spin Distribution of LIGO Binary Black Holes with Mass, *ApJ*, **894**(2), 129, arXiv: 2001.06490.

Shapiro, S. L. and Teukolsky, S. A. (1986), *Black Holes, White Dwarfs and Neutron Stars: The Physics of Compact Objects*.

Woosley, S. E., Heger, A. and Weaver, T. A. (2002), The evolution and explosion of massive stars, *Reviews of Modern Physics*, **74**(4), pp. 1015–1071.

Woosley, S. E. and Weaver, T. A. (1995), The Evolution and Explosion of Massive Stars. II. Explosive Hydrodynamics and Nucleosynthesis, *ApJS*, **101**, p. 181.

Proceedings of *RAGtime 20–22, 15–19 Oct., 16–20 Sept., 19–23 Oct., 2018/2019/2020, Opava, Czech Republic*
Z. Stuchlík, G. Török and V. Karas, editors, Silesian University in Opava, 2020, pp. 97–106

Particle ionization near a weakly charged black hole

Bakhtinur Juraev[1,a] and Arman Tursunov[1,b]

[1]Research Centre of Theoretical Physics and Astrophysics, Institute of Physics,
Silesian University in Opava, Bezručovo nám. 13, CZ-746 01 Opava, Czech Republic
[a]jur0173@slu.cz
[b]arman.tursunov@physics.slu.cz

ABSTRACT
In many astrophysical scenarios, the charge of the black hole is often neglected due to unrealistically large values of the charge required for the Reissner-Nordström spacetime metric. However, black holes may possess a small electric charge due to various selective accretion mechanisms. In this paper we investigate the process of ionization of a neutral particle in the vicinity of a weakly charged non-rotating black hole and calculate the energy of an ionized particle in a chosen scenario. High energy obtained by a charged particle after the ionization process can serve as a distinguishing signature of the weakly charged black holes.

Keywords: Black hole – Electric charge – Ionization – Particle acceleration

1 INTRODUCTION

Recently, it has been pointed out that the ionization or decay of neutral particles in the vicinity of a rotating Kerr black hole immersed into an external magnetic field can lead to the acceleration of ionized particles to ultra high energies, with the Lorentz γ-factors of particles exceeding 10^{12} (Tursunov et al., 2020a; Tursunov and Dadhich, 2019; Stuchlík et al., 2020). The formalism of accelerating mechanism is based on the magnetic Penrose process (Wagh et al., 1985; Parthasarathy et al., 1986) in its ultra-efficient regime (Tursunov et al., 2020a), in which the energy of an ionized particle drives away the rotational energy of the black hole through electromagnetic interaction. It was claimed that the driving engine of the process is in the induced electric field generated by the rotation of the black hole in the external magnetic field.

In this contribution we investigate whether the acceleration of ionized particles can be achieved in a more simplified setting, namely, in the vicinity of a non-rotating Schwarzschild black hole with a radial test electric field. By a *test* electric field we denote the field, whose energy-momentum tensor can be neglected in the description of the gravitational field of the black hole. This implies that the electric field influences the dynamics of charged particles only, being negligible for the geodesics of neutral particles.

978-80-7510-432-8

Such a simplified setup is motivated by the following reasons. First of all, the *no-hair theorem* states that the spacetime around black holes can be fully described by at most three metric parameters - black hole mass, spin and electric charge. The later is usually neglected in astrophysical scenarios, justified by unrealistically large values of the charge required for its visible effect on the spacetime metric. Indeed, one can compare the gravitational radius of a black hole with the characteristic length of the charge $Q_{\rm G}$ of the Reissner-Nordström black hole, which gives the maximum charge value

$$\sqrt{\frac{Q_{\rm G}^2 G}{c^4}} = \frac{2GM}{c^2}, \tag{1}$$

$$\Rightarrow Q_{\rm G} = 2G^{1/2}M \approx 10^{31}\frac{M}{10M_\odot}\ \text{Fr}. \tag{2}$$

This value of the charge is unattainable in any known astrophysically relevant scenario. Thus, the Reissner-Nordström spacetime metric is interesting, but astrophysically not viable.

On the other hand, there exist several astrophysical mechanisms based on a selective accretion, in which a black hole can be weakly charged. Since protons are about 1836 times more massive than electrons, the balance between the gravitational and Coulombic forces for the particles close to the surface of the compact object is obtained when the black hole acquires a positive net electric charge of the order of $Q \sim 3 \times 10^{11}$Fr per solar mass (Zajacek and Tursunov, 2019; Bally and Harrison, 1978). Moreover, matter surrounding black hole can be ionized and charged by the irradiating photons taking away some electrons (Weingartner et al., 2006). Perhaps the most famous mechanism of charging of black holes is based on the solution by Wald (1974), in which the charge is induced by the twisting of magnetic field lines due to the frame-dragging effect. As a result, both the black hole and surrounding magnetosphere should acquire an equal and opposite charge of the order of $Q \sim 10^{18}$Fr per solar mass (see, e.g. Tursunov et al., 2020b). In all cases, the charge of the black hole is much weaker than the maximal value (2) by many orders of magnitude (see, e.g. for the Galactic center supermassive black hole in Zaječek et al., 2018), therefore, the gravitational effect of the charge on the spacetime metric can be rightly neglected. One should also note that our consideration of a weakly charged Schwarzschild black hole in the current paper is reasonable and well justified unless the value of the black hole charge is comparable with its maximum limit (2).

Below we will show that even such a weak electric field ($Q \ll Q_{\rm G}$) cannot be neglected in the description of the motion of charged particles. Moreover, it plays a crucial role in the mechanism of acceleration of ionized particles. Hereafter we use the signature $(-,+,+,+)$, and the system of geometric units, in which $G = 1 = c$, unless the units are given explicitly in physical units.

2 DYNAMICS OF A CHARGED PARTICLE

2.1 Background setup & equations of motion

The Schwarzschild solution of the Einstein's field equations, corresponding to a spherically symmetric spacetime metric reads

$$ds^2 = -f(r)dt^2 + f^{-1}(r)dr^2 + r^2(d\theta^2 + \sin^2\theta d\phi^2), \tag{3}$$

where $f(r)$ is a lapse function parametrized by the black hole mass M as follows

$$f(r) = 1 - \frac{2M}{r}. \tag{4}$$

Let us assume the presence of the radial electric field with a corresponding small electric charge Q at the center. Then, the only non-zero covariant component of the electromagnetic potential $A_\mu = (A_t, 0, 0, 0)$ takes the following simple form

$$A_t = -\frac{Q}{r}. \tag{5}$$

The anti-symmetric tensor of the electromagnetic field $F_{\alpha\beta} = A_{\beta,\alpha} - A_{\alpha,\beta}$ has the only one independent nonzero component

$$F_{tr} = -F_{rt} = -\frac{Q}{r^2}. \tag{6}$$

Let us now consider the motion of a charged particle of mass m and charge q in the combined background of gravitational and electric fields. The motion of a charged particle is governed by the Lorentz equation in curved spacetime

$$\frac{\mathrm{d}u^\mu}{\mathrm{d}\tau} + \Gamma^\mu_{\alpha\beta}u^\alpha u^\beta - \frac{q}{m}F^\mu{}_\nu u^\nu = 0, \tag{7}$$

where u^μ is the four-velocity of the particle, τ is the proper time of the particle and $\Gamma^\mu_{\alpha\beta}$ – Christoffel symbols.

Due to symmetries of the background Schwarzschild metric, one can introduce two integrals of motion, corresponding to temporal and spatial components of the canonical four-momentum of the charged particle

$$\frac{P_t}{m} = -\mathcal{E} \equiv -\frac{E}{m} = u_t - \frac{qQ}{mr}, \tag{8}$$

$$\frac{P_\phi}{m} = \mathcal{L} \equiv \frac{L}{m} = u_\phi, \tag{9}$$

where $\mathcal{E}$ and $\mathcal{L}$ denote specific energy and specific angular momentum of the charged particle. Since both gravitational and electric fields are spherically symmetric and there is no preferred plane of the motion, one can fix the motion of the charged particle to the equatorial plane ($\theta = \pi/2$), without loss of generality. Thus, three non-vanishing components of

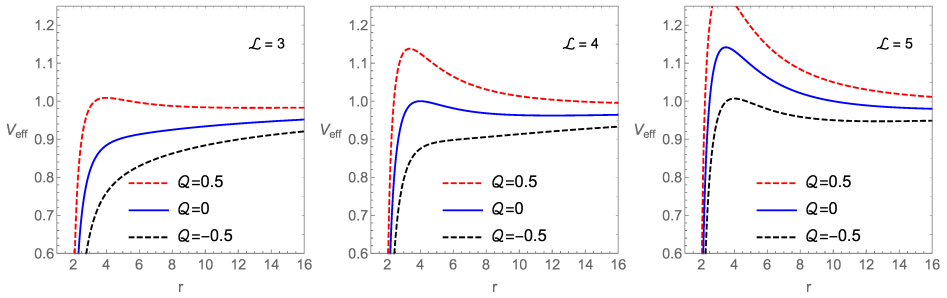

Figure 1. The radial dependence of the effective potential V_{eff} for a charged particle around weakly charged non-rotating black hole in the equatorial plane $\theta = \pi/2$ for different values of the parameters $\mathcal{L}$ and Q.

the equation of motion (7) can be found in the form

$$\frac{du^t}{d\tau} = \frac{u^r\left[Qr - 2M\left(er + Q\right)\right]}{r\left(r-2M\right)^2}, \tag{10}$$

$$\frac{du^r}{d\tau} = \frac{eQ}{r^2} + \frac{\mathcal{L}^2\left(r-2M\right)}{r^4} - \frac{M\left[e^2 - \left(u^r\right)^2\right]}{r\left(r-2M\right)}, \tag{11}$$

$$\frac{du^\phi}{d\tau} = -\frac{2\,\mathcal{L}\,u^r}{r^3}, \tag{12}$$

$$\text{where} \quad e = \mathcal{E} - \frac{qQ}{mr}. \tag{13}$$

Equations (10) - (12) are ordinary differential equations, which can be easily solved numerically.

2.2 Effective potential

Using the normalization condition for a massive particle $u^\mu u_\mu = -1$, one can derive the effective potential for the charged particle moving around a weakly charged Schwarzschild black hole in the form

$$V_{eff}(r) = \frac{Q}{r} + \sqrt{f(r)\left(1 + \frac{\mathcal{L}^2}{r^2}\right)}, \tag{14}$$

where $Q = Qq/m$ is a parameter characterizing the electric interaction between the charges of the particle and black hole. Without loss of generality, we set the mass of the black hole to be equal to unity, i.e. $M = 1$.

Since the right hand side of the effective potential (14) is always positive one can distinguish two qualitatively different situations depending on the sign of the parameter Q. When $Q > 0$, the charges of the particle and black hole have the same sign, so the electric interaction is repulsive. In the opposite case, when $Q < 0$, the charges of the particle and black

hole have different signs, so the electric interaction is attractive. The term $\mathcal{L}^2$ under the root of Eq.(14) means that the clockwise and counter-clockwise directions of the motion are equivalent.

The radial profile of the effective potential is shown in Figure 1. One can see that the effect of the charge parameter Q is similar to those of the angular momentum $\mathcal{L}$, i.e. increasing (or decreasing) both parameters Q and $\mathcal{L}$ one can increase (or decrease) the value of the effective potential. It is interesting to note that taking into account the parameter Q can mimic the effect of angular momentum (compare, e.g. red curve in the middle plot with a very similar blue curve on the right plot of the Figure 1).

The stationary points of the effective potential $V_{eff}(r)$ are given by the equation

$$\partial_r V_{eff}(r) = 0. \tag{15}$$

Note that in the case of a weakly charged Schwarzschild black hole all the local extrema of the effective potential V_{eff} are located in the equatorial plane $\theta = \pi/2$. Eq. (15) leads to a polynomial equation of the fourth order in the radial coordinate

$$r^2(J-1) + \mathcal{L}^2(r-3) = 0, \tag{16}$$

$$\text{where} \quad J = \frac{Q}{r}\sqrt{\frac{(r-2)\left(\mathcal{L}^2 + r^2\right)}{r}}. \tag{17}$$

A solution of the equation (16) has four roots of $\mathcal{L}$ with two of them being independent

$$\mathcal{L}^2_{\pm} = \frac{r}{(r-3)^2}\left(-Q^2 - 3r + \frac{Q^2 r}{2} + r^2 \pm Q\sqrt{Q^2 - 12r + 4r^2}\left(1 - \frac{r}{2}\right)\right), \tag{18}$$

2.3 Angular velocity measured at infinity

Noticing that in the equatorial plane the four velocity takes the form $u^\alpha = u^t(1, v, 0, \Omega)$, where $v = dr/dt$, $\Omega = d\phi/dt$ and using the normalization condition $u^\alpha u_\alpha = -k$, where $k = 1$ for massive particle and $k = 0$ for massless particle, we can obtain the following equation

$$(u^t)^2\left(f^{-1}(r)v^2 - f(r) + \Omega^2 r^2\right) = -k. \tag{19}$$

Simplifying the equation above, we can easily derive an equation for angular velocity measured by a static observer at infinity $\Omega = d\phi/dt$

$$\Omega = \pm\frac{1}{u_t r}\sqrt{(u_t)^2\left(f(r) - f^{-1}(r)v^2\right) - kf^2(r)}. \tag{20}$$

Allowed values of Ω are limited to

$$\Omega_- \le \Omega \le \Omega_+, \quad \Omega_\pm = \pm\frac{\sqrt{f(r)}}{r}. \tag{21}$$

corresponding to the photon motion.

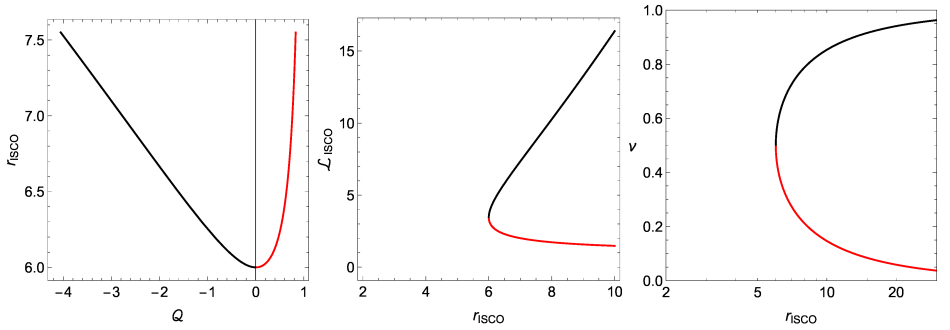

Figure 2. Left: The position of the ISCO of the charged particle in the dependence on the charge parameter Q. Middle: Angular momentum of the charged particle at ISCO against ISCO position. Right: velocity of the charged particle at ISCO. In all plots, the red lines correspond to the positive charge parameter $Q > 0$, while the black curves correspond to the negative charge parameter $Q < 0$.

2.4 Innermost stable circular orbit

An innermost stable circular orbit (ISCO) in the Schwarzschild spacetime is located at $r_{ISCO} = 6M$. In the case when the electric charge is included, it will be shifted outwards from $6M$. The local extremum of the function $\mathcal{L}_{\pm}$ determines the ISCO, namely, its radius, angular momentum and energy. ISCO can also be found from the condition of $\partial_r^2 V_{eff}(r, \mathcal{L}, Q) = 0$, which gives

$$\mathcal{L}^2 r^2 (J(r-2)+2) + r^4 (J(r-2) - r + 3) + \mathcal{L}^4 ((r-3)r + 3) = 0. \tag{22}$$

Solving this equation with respect to r gives us four solutions for the ISCO with only two of them being real and independent. One can also calculate the velocity v of the charged particle at the ISCO, which is given by the formula

$$v = \sqrt{\frac{1}{1 + \frac{r_{isco}^2}{\mathcal{L}_{isco}^2}}}. \tag{23}$$

Dependence of the ISCO position r_{isco} on the charge parameter Q and the change of the values of $\mathcal{L}_{isco}$ and v on the ISCO position are shown in Figure 2. ISCO is increasing for both positive and negative Q. Similar results have been also obtained recently by Hackstein and Hackmann (2020), where the ISCO in a similar setting is properly discussed.

3 THE ENERGY OF THE IONIZED PARTICLE

3.1 Conservation laws

Let us now consider the decay of a particle 1 into two fragments 2 and 3 close to the horizon of a weakly charged Schwarzschild black hole at the equatorial plane. One can write the

following conservation laws before and after decay

$$E_1 = E_2 + E_3, \quad L_1 = L_2 + L_3, \quad q_1 = q_2 + q_3, \tag{24}$$

$$m_1\dot{r}_1 = m_2\dot{r}_2 + m_3\dot{r}_3, \quad m_1 \geqslant m_2 + m_3, \tag{25}$$

where dot indicates derivatives with respect to the particle's proper time τ. Using the above conservation laws, one can find the equation

$$m_1 u_1^{\phi} = m_2 u_2^{\phi} + m_3 u_3^{\phi}. \tag{26}$$

Noticing that $u^{\phi} = \Omega u^t = \Omega e/f(r)$, where $e_i = (E_i + q_i A_t)/m_i$, with $i = 1, 2, 3$ indicating the particle's number, the equation (26) will take the following from

$$\Omega_1 m_1 e_1 = \Omega_2 m_2 e_2 + \Omega_3 m_3 e_3. \tag{27}$$

Solving the above equation with respect to the energy of one of the fragments, e.g. E_3 we find

$$E_3 = \frac{\Omega_1 - \Omega_2}{\Omega_3 - \Omega_2}(E_1 + q_1 A_t) - q_3 A_t, \tag{28}$$

where $\Omega_i = d\phi_i/dt$ is an angular velocity of an ith particle, given by (20), with restricted values (21).

3.2 The maximum energy of the ionized particle

To maximize the energy of the ionized particle we choose the particle 1 to be neutral, i.e. $q_1 = 0$. We are also free to choose the energy of the particle 1, which we set to its rest mass energy, i.e. $E_1 = m_1$ or $\mathcal{E}_1 = 1$. In this case, the angular velocity (20) for the particle 1 will take the following simple form

$$\Omega_1 = \frac{1}{r^2}\sqrt{2(r-2)}. \tag{29}$$

We choose the ionized particle to be the particle 3. The energy of the ionized particle is maximal, when the term $(\Omega_1 - \Omega_2)/(\Omega_3 - \Omega_2)$ is maximized. This occurs when we set the angular momentum of fragments to their limiting values. Then we find

$$\frac{\Omega_1 - \Omega_2}{\Omega_3 - \Omega_2}\Big|_{\max} = \frac{1}{\sqrt{2\, r_{\rm ion}}} + \frac{1}{2}. \tag{30}$$

We see that the ratio (30) is maximal, where the ionization point $r_{\rm ion}$ coincides with the horizon of the black hole. Thus, at $r_{\rm ion} = 2$, the ratio (30) is equal to unity. Finally, we write the expression for the energy of the ionized particle in the form

$$E_3 = \left(\frac{1}{\sqrt{2\, r_{\rm ion}}} + \frac{1}{2}\right) E_1 + \frac{q_3 Q}{r_{\rm ion}}. \tag{31}$$

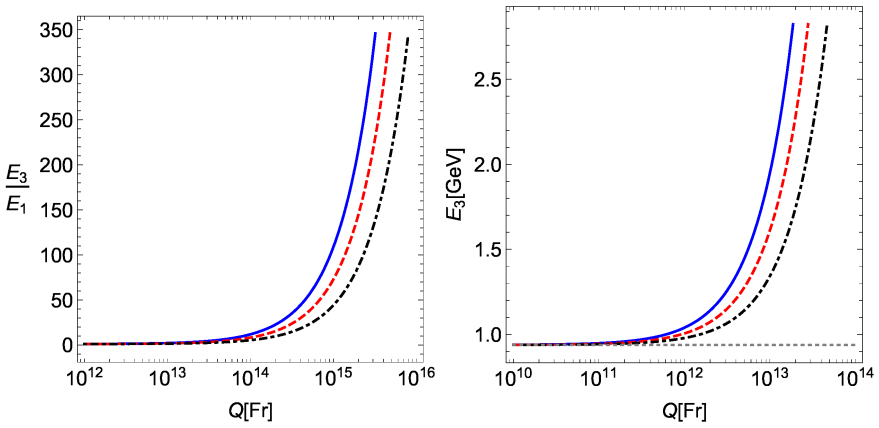

Figure 3. The ratio of energies of escaping proton and the neutral hydrogen and the energy of escaping proton in GeV (left) scaled by factor 100 (right) plotted against the black hole charge Q for the black hole mass $M = 10M_\odot$. The colors of curves denote different positions of the ionization point; blue: $r_{\rm ion} = 2GM/c^2$, red dashed: $r_{\rm ion} = 3GM/c^2$ and black dot-dashed: $r_{\rm ion} = 5GM/c^2$. The dotted grey line corresponds to the rest energy of the proton.

It is useful to define the ratio between the energies of ionized and neutral particles, which would represent the efficiency of the acceleration process. Writing the black hole mass and the speed of light explicitly, we find

$$\frac{E_3}{E_1} = \frac{1}{2} + \sqrt{\frac{M}{2\,r_{\rm ion}}} + \frac{q_3 Q}{m_1 c^2 r_{\rm ion}}. \tag{32}$$

One can see that the energy of the ionized particle is increasing only when q_3 and Q have the same sign, which is also expected.

In order to estimate the process quantitatively, let us consider the ionization of a neutral hydrogen atom consisting of a single proton and single electron in the vicinity of a stellar mass black hole of mass $10M_\odot$. When the electron is separated from the atom, the attained energy of the proton will depend on the charge of the black hole. The proton energy will be larger than the energy of the initially neutral atom, when the charge of the black hole is positive and decrease with increasing the distance between the ionization point and the black hole. We plot the energy of proton after ionization of neutral hydrogen atom in Fig.3, where we also give the ratio of energies of the proton and the neutral hydrogen. We clearly see that the energy of the proton can increase more than 100 times already for the black hole charge values above 10^{15}Fr, which is still more than 15 orders of magnitude smaller charge than the maximal Reissner-Nordström charge (2). Therefore, we conclude that a weakly charged Schwarzschild black hole can act as a high-energy particle accelerator.

4 CONCLUSIONS

We have studied the particle motion and ionization in the vicinity of a non-rotating Schwarzschild black hole carrying the small electric charge, whose gravitational effect on the spacetime metric is negligible. We started from the description of the motion of the charged particle and showed that the effective potential in the case of a weakly charged black hole increases (decreases) with increasing (decreasing) the electric interaction parameter Q. We found that the innermost stable circular orbit (ISCO) of the charged particle increases for both positive and negative values of the parameter Q. The results are in accord with previous similar studies by Pugliese et al. (2011); Zajacek and Tursunov (2019); Hackstein and Hackmann (2020).

We have found that the energy of fthe ionized particle can be much greater than the initial energy of the neutral particle if both charges of the ionized particle and the black hole have the same sign. Thus, the similar acceleration process occurring in the magnetized Kerr black hole spacetime and studied by Tursunov et al. (2020a) works also in the weakly charged non-rotating black hole case. We also estimated the energy of a proton after the ionization of the hydrogen atom in the vicinity of the stellar mass black hole. In this particular situation, we demonstrated that the energy of the proton can increase more than 100 times with respect to the energy of neutral hydrogen when the charge of the black hole is greater than 10^{15}Fr, which is still about 16 orders of magnitude smaller charge than the maximal Reissner-Nordström limit.

ACKNOWLEDGEMENTS

We would like to thank Martin Kološ and Zdeněk Stuchlík for useful comments and discussions. B.J. acknowledges the support from the internal student grant SU-STIP/21279/2020/32006/FPF-1 of the Silesian University in Opava. We also thank the organizers of RAGtime 2020 for providing a platform for a wonderful and stimulating online meeting.

REFERENCES

Bally, J. and Harrison, E. R. (1978), The electrically polarized universe., *The Astrophysical Journal*, **220**, p. 743.

Hackstein, J. P. and Hackmann, E. (2020), Influence of weak electromagnetic fields on charged particle ISCOs, *General Relativity and Gravitation*, **52**(2), 22, arXiv: 1911.07645.

Parthasarathy, S., Wagh, S. M., Dhurandhar, S. V. and Dadhich, N. (1986), High efficiency of the Penrose process of energy extraction from rotating black holes immersed in electromagnetic fields, *The Astrophysical Journal*, **307**, pp. 38–46.

Pugliese, D., Quevedo, H. and Ruffini, R. (2011), Motion of charged test particles in Reissner-Nordström spacetime, *Phys. Rev. D*, **83**(10), 104052, arXiv: 1103.1807.

Stuchlík, Z., Kološ, M., Kovář, J., Slaný, P. and Tursunov, A. (2020), Influence of Cosmic Repulsion and Magnetic Fields on Accretion Disks Rotating around Kerr Black Holes, *Universe*, **6**(2), p. 26.

Tursunov, A. and Dadhich, N. (2019), Fifty Years of Energy Extraction from Rotating Black Hole: Revisiting Magnetic Penrose Process, *Universe*, **5**(5), p. 125, arXiv: 1905.05321.

Tursunov, A., Stuchlík, Z., Kološ, M., Dadhich, N. and Ahmedov, B. (2020a), Supermassive Black Holes as Possible Sources of Ultrahigh-energy Cosmic Rays, *The Astrophysical Journal*, **895**(1), 14, arXiv: 2004.07907.

Tursunov, A., Zajaček, M., Eckart, A., Kološ, M., Britzen, S., Stuchlík, Z., Czerny, B. and Karas, V. (2020b), Effect of Electromagnetic Interaction on Galactic Center Flare Components, *The Astrophysical Journal*, **897**(1), 99, arXiv: 1912.08174.

Wagh, S. M., Dhurandhar, S. V. and Dadhich, N. (1985), Revival of the Penrose process for astrophysical applications, *The Astrophysical Journal*, **290**, pp. 12–14.

Wald, R. M. (1974), Black hole in a uniform magnetic field, *Phys. Rev. D*, **10**, pp. 1680–1685.

Weingartner, J. C., Draine, B. T. and Barr, D. K. (2006), Photoelectric Emission from Dust Grains Exposed to Extreme Ultraviolet and X-Ray Radiation, *The Astrophysical Journal*, **645**(2), pp. 1188–1197, arXiv: astro-ph/0601296.

Zajacek, M. and Tursunov, A. (2019), The Electric Charge of Black Holes: Is It Really Always Negligible, *The Observatory*, **139**, pp. 231–236, arXiv: 1904.04654.

Zajaček, M., Tursunov, A., Eckart, A. and Britzen, S. (2018), On the charge of the Galactic centre black hole, *Mon. Not. R. Astron Soc.*, **480**(4), pp. 4408–4423, arXiv: 1808.07327.

Proceedings of *RAGtime 20–22, 15–19 Oct., 16–20 Sept., 19–23 Oct., 2018/2019/2020, Opava, Czech Republic*
Z. Stuchlík, G. Török and V. Karas, editors, Silesian University in Opava, 2020, pp. 107–120

Magnetically ejected disks: Equatorial outflows near vertically magnetized black hole

Vladimír Karas,[1,a] Kostas Sapountzis[2]
and Agnieszka Janiuk[2]

[1]Astronomical Institute, Czech Academy of Sciences, Boční II 1401,
CZ-14100 Prague, Czech Republic
[2]Center for Theoretical Physics, Polish Academy of Sciences, Al. Lotnikow 32/46,
P-02-668 Warsaw, Poland
[a]vladimir.karas@cuni.cz

ABSTRACT
Black holes attract gaseous material from the surrounding environment. Cosmic plasma is largely ionized and magnetized because of electric currents flowing in the highly conductive environment near black holes; the process of accretion then carries the magnetic flux onto the event horizon, $r \simeq R_+$. On the other hand, magnetic pressure acts against accretion. It can not only arrest the inflow but it can even push the plasma away from the black hole if the magnetic repulsion prevails. The black hole does not hold the magnetic field by itself.

In this contribution we show an example of an equatorial outflow driven by a large scale magnetic field. We initiate our computations with a spherically symmetric distribution of gas, which flows onto the domain from a large distance, $r \gg R_+$. After the flow settles in a steady (Bondi) solution, we impose an axially symmetric configuration of a uniform (Wald) magnetic field aligned with the rotation axis of the black hole. Then we evolve the initial configuration numerically by employing the MHD code that approaches the force-free limit of a perfectly conducting fluid.

We observe how the magnetic lines of force start accreting with the plasma while an equatorial intermittent outflow develops and goes on ejecting some material away from the black hole.

Keywords: black hole physics – magnetic fields – accretion

1 INTRODUCTION

Accretion is ubiquitous process in the Universe. By gradual accretion, various components of highly diluted environment are gathered and brought onto cosmic bodies – planets, stars, even galaxies (see, e.g., Fox and Davé, 2017; Shakura, 2018). Accretion is driven primarily by action of gravitational and electromagnetic forces. Gravity of the central body acts at long range and it attracts gas and dust, whereas the electric and magnetic components can

978-80-7510-432-8

act in a complex, mutually interrelated manner; they can cause either attraction or repulsion of the plasma, depending on the conditions.

Astrophysical plasmas are characterized by their high conductivity which ensures that the force-free condition is typically an excellent approximation to describe the cosmic environment (Beskin, 2010). Moreover, in magnetospheres of compact objects like neutron stars and black holes there are regions where the energy density of the electromagnetic field greatly exceeds the inertial (kinetic, rest-mass, and thermal) energy of matter. Plasma motions follow the evolving magnetic field lines. Force-free electrodynamics describes magnetically dominated relativistic plasma as long as the inertial forces can be neglected; while this assumption is correct, in very diverse circumstances it becomes gradually violated in case of very low ionisation and low temperature, where the dissipation effects play a role, and for ultra-relativistic acceleration near the light cylinder, where the particle mass is important.

In the limit of vanishing magnetic field and sufficiently high density (short mean free path) the hydrodynamical approach is adequate. The best-known analytical framework then describes the stationary, spherically symmetric inflow, a.k.a. Bondi solution (Bondi, 1952), where the actual form of the flow is determined by the boundary conditions at infinity and at the black hole horizon. This has been generalized in several ways; in particular, Silich et al. (2008) include the effect of additional source of energy from stars of the Nuclear Star Cluster, which is relevant for many nuclei containing Nuclear Star Clusters, including the Galactic center source Sgr A* (Schödel et al., 2014). On the other hand, in the limiting case of zero density (electro-vacuum) the solution is described by the source-free coupled Einstein-Maxwell equations. These are tractable only under very constraining assumptions and symmetries, however, the problem can be simplified for electro-magnetic fields that are weak (albeit non-vanishing) in comparison with the gravitational field (the assumption valid in the vicinity of astrophysical black holes). Electro-magnetic test field solutions on the fixed background of Kerr metric then provide an adequate description of magnetic fields in interaction with the black hole gravity (Wald, 1974; King et al., 1975).

In this contribution we are interested in a gradually evolving structure of magnetic field, as the system goes over from the initial, homogeneous solution to the interaction with the force-free magnetosphere near an accreting Kerr black hole (Frank et al., 2002; Kato et al., 2008). We deliberately impose axial symmetry along the black hole rotation axis for the magnetic field and the inflowing medium (we employ a two-dimensional scheme). Although this constraint will have to be relaxed to describe astrophysically realistic systems, we want to reveal the transition from the initial state of magnetic lines running around the black hole, i.e., the magnetic flux being expelled out of the horizon (partially in the case of non-rotating or moderately rotating black hole, dimension-less spin parameter $|a| < 1$, and completely in the case of extreme rotation, $a = 1$; see Bičák and Dvořák, 1976). As the force-free plasma starts inflowing with spherical symmetry at the initial configuration, the Meissner expulsion is immediately diminished and, at later stages, the magnetic lines start to produce reconnection regions in the equatorial plane. Subsequently, localized blobs emerge and they are eventually ejected away from the black hole due to the magnetic pressure.

We build our study following a series of works that have been previously published by various authors. In particular, Komissarov and McKinney (2007) explored the magne-

tized, rotating black holes embedded in the plasma. By employing the general-relativistic magneto-hydrodynamics 2D HARM code (Gammie et al., 2003; McKinney, 2006; Sapountzis and Janiuk, 2019) they found that the Meissner expulsion indeed disappears due to the presence of accreting medium even in the case of (almost) maximally rotating black hole. Penna (2014) gave arguments to understand the essence of the Meissner–type magnetic field expulsion near black holes. Various authors (Pan and Yu, 2016; Gong et al., 2016; Camilloni et al., 2020) studied the analytical properties of force-free black-hole magnetospheres especially in the context of jets emerging from the vicinity of the ergosphere. Nathanail and Contopoulos (2014) and East and Yang (2018) noticed the formation of current sheets near a black hole immersed in a magnetized plasma. Some results suggest that the role of ergosphere is essential in producing the plasma structures and ejecting matter in the force-free medium (Blandford and Znajek, 1977).

2 THE MODEL SET-UP

2.1 Strong gravitational and weak magnetic fields

Gravitational field is described by Kerr metric, which can be written in the well-known Boyer-Lindquist coordinate system (t, r, θ, ϕ) (Misner et al., 2017; Chandrasekhar, 2002; Wald, 1984). This spacetime is asymptotically flat and it obeys the axial symmetry about the rotation axis and stationarity with respect to time; the singularity is hidden below the event horizon. The mass M of the black hole is concentrated in the origin of the coordinate system. The spin parameter a of the Kerr metric describes its rotation; the condition about the presence of the outer event horizon at a certain radius, $r = R_+$ (where the horizon encompasses the singularity) leads to the maximum value of the dimensionless spin rate: $|a \leq 1|$. The solution can be then written in the form of the metric element (Misner et al., 2017; Chandrasekhar, 2002)

$$\mathrm{d}s^2 = -\frac{\Delta\Sigma}{A}\,\mathrm{d}t^2 + \frac{\Sigma}{\Delta}\,\mathrm{d}r^2 + \Sigma\,\mathrm{d}\theta^2 + \frac{A\sin^2\theta}{\Sigma}\,(\mathrm{d}\phi - \omega\,\mathrm{d}t)^2\,, \tag{1}$$

where $\Delta(r) = r^2 - 2r + a^2$, $R_+ = 1 + \sqrt{1-a^2}$, $\Sigma(r,\theta) = r^2 + a^2\cos^2\theta$, $A(r,\theta) = (r^2+a^2)^2 - \Delta a^2 \sin^2\theta$, $\omega(r,\theta) = 2ar/A(r,\theta)$. Dimension-less geometrical units are assumed with the speed of light c and gravitational constant G set to unity. In physical units the gravitational radius is thus equal to $R_\mathrm{g} = c^{-2}GM \approx 4.8 \times 10^{-7} M_7$ pc; the corresponding light-crossing time-scale $t_\mathrm{g} = c^{-3}GM \approx 49\, M_7$ sec, where $M_7 \equiv M/(10^7 M_\odot)$.

Kerr metric is a solution of Einstein's equation for the gravitational field of a rotating black hole in vacuum. Even in the case of strongly magnetized gaseous environment around the black hole the contribution of an astrophysically realistic magnetic energy to the space/time curvature is negligible. We can thus neglect its effect on the metric terms and assume a weak-field limit on the background of Kerr black hole; the space-time metric is not evolved in our scheme. In order to initiate the numerical code we can employ an initially uniform magnetic field (Wald, 1974; Bičák et al., 2007), which is fully described

by two non-vanishing components of the four-potential,

$$A_t = Ba\left[r\Sigma^{-1}\left(1+\cos^2\theta\right)-1\right], \tag{2}$$
$$A_\phi = B\left[\tfrac{1}{2}\left(r^2+a^2\right)-a^2 r\Sigma^{-1}\left(1+\cos^2\theta\right)\right]\sin^2\theta, \tag{3}$$

in dimension-less Boyer-Lindquist coordinates and B is the magnetic intensity of the uniform field far from the event horizon. The magnetic field (and the associated electric component) are generated by currents flowing in the accreted medium far from the black hole, as the latter does not support its own magnetic field. The set of two non-vanishing four-potential vector components defines the structure of the electromagnetic tensor, $F_{\mu\nu} \equiv A_{[\mu,\nu]}$; by projecting onto a local observer frame one then obtains the electric and magnetic vectors $\boldsymbol{E}$ and $\boldsymbol{B}$.[1] However idealized the initial configuration may be, the numerical solution rapidly evolves in a complex entangled structure, with field lines turbulent within the accreting medium and more organized in the empty funnels that develop outside the fluid structure.

2.2 Two limiting cases for the initial distribution of plasma

The plasma forms an accretion disk or a torus residing in the equatorial plane, so that the axial symmetry is maintained. In a non-magnetized (purely hydrodynamical) limiting case one can find the classical solution for the density distribution $\rho \equiv \rho(r,z)$ and pressure $P \equiv P(r,z)$, and the geometrical shape $H \equiv H(r)$ of a non-gravitating barytropic torus $P = K\rho^k$. Introducing enthalpy of the medium, $W(P) \equiv \int dP/\rho$ and setting $P_{\rm in} = P_{\rm out} = 0$ at the inner and the outer edges of the density distribution (Abramowicz et al., 1978; Kozlowski et al., 1978)

$$W_{\rm out} - W_{\rm in} = \int_{R_{\rm in}}^{R_{\rm out}} \frac{l(R)^2 - l_{\rm kep}(R)^2}{R^3}\, dR = 0, \tag{4}$$

where $l_{\rm kep}(R)$ is the radial profile of the Keplerian angular momentum density in the equatorial plane. Several properties of this solution are worth mentioning (Abramowicz, 1971): (i) The level surfaces of functions P, ρ, and W coincide; (ii) If the torus boundary $P = 0$ forms a closed surface, the torus center is defined by where $dP/dR = 0$, the pressure is maximum; (iii) The shape of the torus can be found by integrating the vertical component of the Euler equation.

Above a certain critical value, $W > W_c$, the torus forms a stable configuration (see the shaded region), while for $W < W_c$ matter overflows onto the central object even if we neglect viscosity. This behaviour resembles the Roche lobe overflow in binary systems, however, here it is a consequence of the non-monotonic radial dependence of the Keplerian angular momentum in the relativistic regime near the black hole (Abramowicz et al., 1980;

[1] Let us note that typical cosmic plasmas are ionized and perfectly conducting, and so the approximation of force-free electromagnetic action is justified at high accuracy (e.g. Somov, 2012): $\boldsymbol{E} + \boldsymbol{v} \times \boldsymbol{B} = 0$, where $\boldsymbol{E}$ and $\boldsymbol{B}$ are electric and magnetic intensities, $\boldsymbol{v}$ is velocity of the plasma. Magnetic field is thus frozen in the plasma.

Penna et al., 2013). Whereas the material inflowing from atmosphere of a primary component of the binary system concentrates near the equatorial plane and naturally forms the torus, in the case of a single, isolated central black hole matching the inner (toroidal) structure to the outer reservoir of matter depends on many circumstances at the outer boundary region. This is also the case of super-masive black holes residing in nuclei of galaxies, which are fed by interstellar medium from a surrounding (spheroidal) nuclear star cluster and the galaxy bulge; flattening of the structure is a parameter that can vary from disk-type equatorial inflow up to perfectly spherical (Bondi-type) inflow/outflow solution (Silich et al., 2008; Różańska et al., 2017).

Unlike the above-discussed toroidal configuration, let us now assume that the angular momentum of accreted fluid is negligible and its velocity has a non-vanishing component only in the radial direction. At large radius, in our case suitable as a boundary condition, we are allowed to consider the problem within the framework of spherically symmetric Newtonian inflow with $v_r = v < 0$ (positive v would correspond to a symmetrical problem of an outflow or a wind). The equation of continuity gives $4\pi r^2 \rho(r) v(r) = -\dot{M}$, where the constant on the right-hand side has a meaning of mass accretion rate. In the Euler equation, density of the external force $\boldsymbol{f}$ has only the radial component, $GM\rho/r^2 = -f_r(r)$, and so we can write

$$v\,\frac{dv}{dr} + \frac{1}{\rho}\,\frac{dP}{dr} + \frac{GM}{r^2} = 0. \tag{5}$$

Introducing the sound speed by $dP = c_{\rm s}^2(r)\,d\rho$ the Euler equation can be manipulated into the well known form

$$\frac{1}{2}\left(1 - \frac{c_{\rm s}^2}{v^2}\right)\frac{d\,v^2}{dr} = -\frac{GM}{r^2}\left[1 - \frac{2c_{\rm s}^2 r}{GM}\right]. \tag{6}$$

The solutions can be classified according to their behaviour at the sonic point, where the medium flows at the speed of sound, $r_{\rm s} = GM/2c_{\rm s}^2(r_{\rm s})$. For the spherical adiabatic accretion one can find six qualitatively different solutions to the above equations in the (v, r)-plane. Inflows (accretion flows) and outflows (ejection or stellar wind) are both possible; which mode is realized in a particular situation depends on boundary conditions (in our case, only accretion is possible at the inner boundary).

Let us note that the assumptions about constancy of $l(r)$ and the vanishing magnetization, $\beta = \infty$, are astrophysically unrealistic but they are useful to simplify calculations and allow an analytical insight. The magnetization β parameter is taken here as ratio of total hydrodynamic pressure to the magnetic pressure within the magnetized fluid, i.e., $\beta \equiv U_{\rm tot}/U_{\rm mag}$. Realistic models must relax the extreme assumptions about the strict geometrical symmetry and stationarity to allow the system to evolve in time, which is a crucial aspect of the mutual interaction between different components.

As mentioned above, to overcome some of the limitations we adopt the numerical scheme by the HARM code (Gammie et al., 2003; McKinney, 2006).[2] This allows us to explore the

[2] In this paper we explore an axially symmetric configuration, which is obeyed by all components of the system: the gravitational field of the rotating black hole, the interacting electromagnetic field of external origin, and the

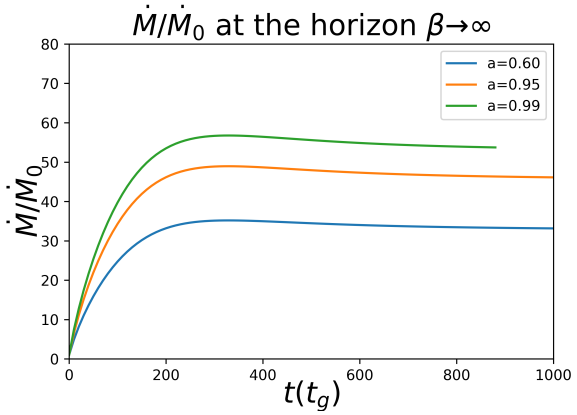

Figure 1. The accretion rate on the horizon of the black hole initially grows and then saturates as the steady state has been reached. The curves are normalized to an arbitrary value $\dot{M}_0$ and parameterized by three values of the dimension-less spin a. Time is in geometrical units and scaled with the black hole mass M.

parameter space of the system. A fraction of the material injected spherically at the outer boundary of the computational domain remains bound and it forms an accretion torus or an accretion disk associated with the central black hole. This occurs at a relatively small radius where relativistic effects play a crucial role and decide whether the gas falls onto the black hole or becomes redistributed and ejected (we do not include radiative cooling in the present work). The interplay between the frozen-in magnetic field and the infalling plasma that thermalizes the mechanical energy and generates additional overpressure, eventually determines the ratio between accretion and ejection.

3 RESULTS

3.1 Mass accretion rate

We set the outer boundary of the computational domain at the radius $10^3 R_{\rm g}$, where the inflow is purely radial at initial time. The inner boundary is set at $\simeq 0.65 R_{\rm g}$, i.e. a fraction of gravitational radius and also inside the horizon radius for the corresponding value of spin a. The grid domain has been resolved at 600×512 points in (r, θ) coordinates and the polytropic index set to $k = 4/3$. We use the magnetic intensity B of the Wald field to

fluid surrounding the black hole. We thus employ the two-dimensional version of the code. Imposing the axial symmetry allows us to examine the role of magnetic expulsion from the horizon of extreme Kerr black hole and to observe how this effect is reduced by the accreted plasma. At the same time we are not confused by non-axisymmetric effects, which are known to reduce the magnetic expulsion, too. It will be interesting to generalize our discussion to a non-axisymmetric configuration of an oblique (inclined with respect to the rotation axis) magnetic field.

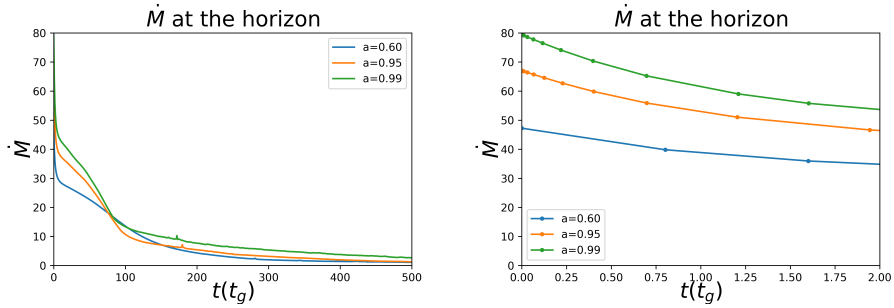

Figure 2. Gradually evolving accretion rate onto the magnetize black hole with the initial set-up of the Bondi inflow and the imposed Wald magnetic field for three values of spin a. The magnetization parameter $\beta \simeq 0.1$ (magnetically dominated medium) at $t = 0$. Long-term progress is shown in the left panel; a detail of the initial phase in the right panel.

determine the plasma parameter β (in our notation, β closer to zero corresponds to a more magnetized plasma).

In order to initialize the computation we employ the hydrodynamic (non-magnetized), purely spherical inflow. We set $\beta \to \infty$ and allow the inflow to build a steady-state Bondi accretion at a certain level of $\dot{M}$ (see Fig. 1). Once the inflow stabilizes to a quasi-steady state inflow, we impose the large-scale Wald magnetic field along the rotation axis, which is then evolved further. Because of the perfect conductivity and the force-free approximation (apart from the effective small-scale numerical dissipation), the magnetic field-lines remain attached to plasma. However, the evolution of the system can be strongly altered if the magnetic field is strong enough, so that its repulsive tendency halts accretion. This effect is governed by the magnetization β-parameter, which is not uniform across the computational domain and changes in time. While the accretion is not much influenced in the limit of negligible magnetization ($\beta \gg 1$), where the gravitational attraction of the black hole prevails, in the case of equipartition between the magnetic and hydrodynamic pressure ($\beta \approx 1$) near the horizon the inflow is partially diverted into an outflow and the accretion rate is diminished (see Fig. 2). Let us note that the mass and spin of the black hole are not updated during the simulation because the amount of accreted material is tiny compared to the black hole mass.

In the strongly magnetized case the accretion rate drops because an outflow develops in the equatorial plane, where the field lines expand radially and carry plasma with them. The field line expansion is not uniform across the integration domain, leading to the distortion of the field lines and eventually to the formation of the current sheet and the reconnection events happening in the equatorial plane (notice the associated spikes around $t = 180$). It is illustrative to plot the inverse accretion rate, where we can clearly identify four different phases of the system evolution (see Fig. 3). The section denoted A is where the initial Bondi accretion prevails; in part B we notice the formation of the current sheet followed by a rarefaction phase of the field lines in part C. Here, more matter is expelled from the

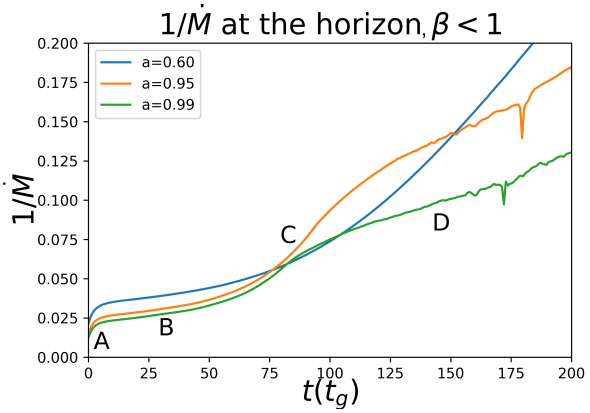

Figure 3. Graph of inverse accretion rate $1/\dot{M}$ exhibits four phases of the magnetized flow evolution. The initial configuration starts with the Bondi spherical inflow from the outer boundary of the integration domain. The central black hole rotates with the Kerr spin parameter a and it is magnetized by the Wald uniform magnetic field B. Spherical symmetry of the inflow is quickly lost by its interaction with the magnetic field but the axial symmetry is imposed in our 2D computations. In case of a rapidly rotating black hole, the magnetic flux vanishes initially (Meissner effect) but it starts growing with accretion of the plasma. Part of the inflowing material is diverted to an outflow along the equatorial plane and accelerated by reconnection events (they are caused by numerical resistivity); the resulting accretion rate thus gradually drops and it exhibits some random glitches at later stages of its temporal evolution (see the text for further details).

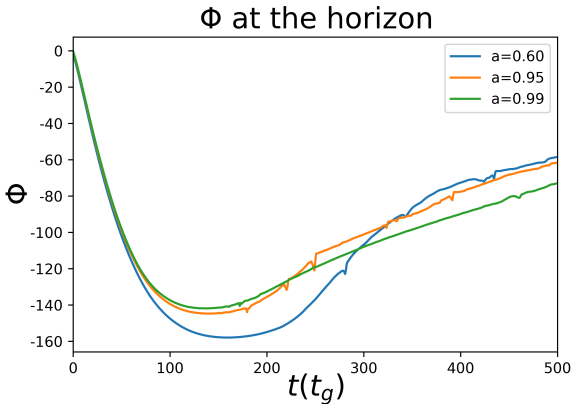

Figure 4. The magnetic flux $\Phi(t)$ (in arbitrary code units) across a hemisphere on the black hole horizon. The initially frozen-in magnetic flux grows (in absolute value) due to accretion of plasma. At later stages the flux starts decreasing as the magnetic intensity decreases and the field eventually escapes to radial infinity.

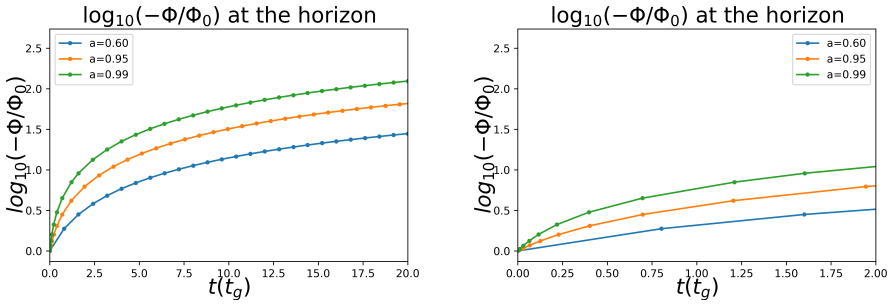

Figure 5. The initial phase of the flux evolution from the previous figure is shown in the semi-logarithmic scale and the dimensionless units (scaled by the typical values). At time zero the magnetic flux of the Wald configuration vanishes for Kerr black hole at extreme rotation ($a \to 1$) in agreement with the Meissner effect. The magnetic expulsion is eliminated as soon as some plasma gets accreted, even in the purely 2D configuration with the imposed axial symmetry.

black hole and it eventually ends up in a region of much lower density. In the D phase the reconnection events occur and the outflow accelerates near the equator.

3.2 Magnetic flux across a hemisphere

In order to reveal the changes of the magnetic field near the black hole, we study the evolution of the magnetic flux inflowing into the hemisphere located on the horizon. As mentioned above, the initial configuration is the vacuum solution of the uniform flux tube oriented in the direction parallel to the rotation axis, i.e. the Wald solution, but this configuration starts quickly changing once the inflowing plasma arrives in the domain.[3] As also mentioned above, the initial configuration for the plasma inflow is the Bondi solution. As soon as a field line enters the ergosphere, it has to terminate at the event horizon. Therefore, the magnetic field lines in a force-free magnetosphere are not expelled by even extreme rotation of the black hole. Figure 4 shows the magnetic flux as a function of time and Fig. 5 exhibits a more detailed view of the brief initial period. Finally we vary the value of the Wald magnetic intensity B parameter to obtain more initially magnetized case (lower plasma β). Notice that the code itself poses a limit $\beta > 10^{-4}$ under which it starts introducing artificial density floor in order to avoid numerical integration problems. Figures 6–7 show several snapshots of the magnetic field and plasma density at different resolution. An equatorial outflow forms at late stages of the system evolution and it drives plasmoids in the outward direction.

[3] Some more complicated configurations were explored by Kološ and Janiuk (2020). Interestingly, these authors found that a parabolic magnetic field also develops in the accretion torus funnel around the vertical axis, for any initial magnetic field configuration.

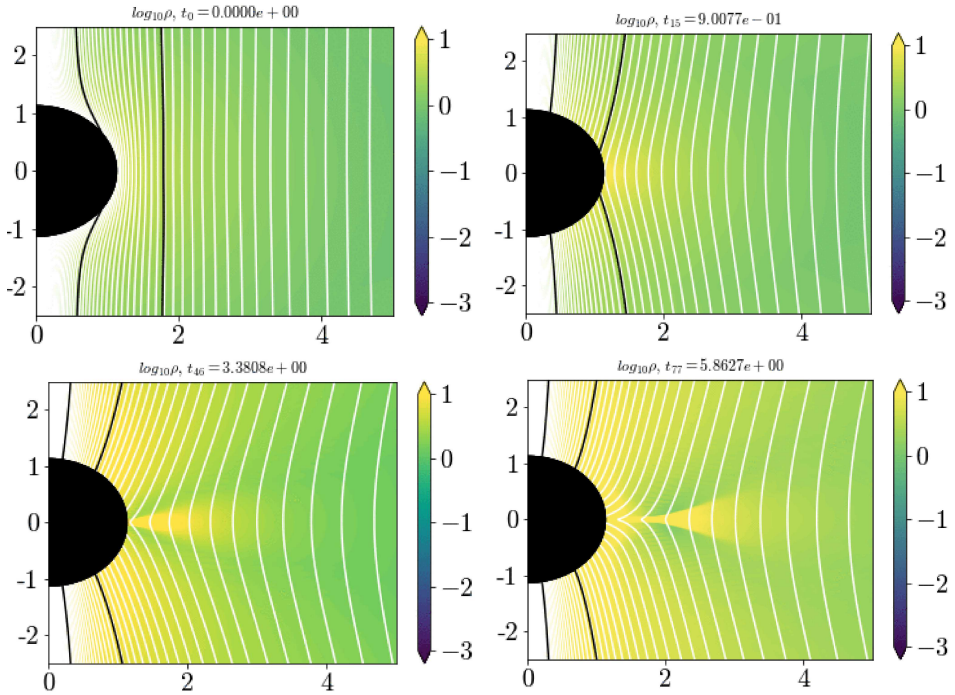

Figure 6. Four time steps (from top left to bottom right panels) with the magnetic field lines and colour-coded plasma density near a rapidly rotating ($a = 0.99$) black hole with $B = 8$. Magnetic field lines are expelled out of the horizon at $t = 0$ (before plasma starts to be accreted), but they start crossing the horizon and accreting with the plasma as time passes. We intentionally select the magnetically dominated system at the initial stage, $\beta(t = 0) \ll 1$, which is expected to support the Meissner expulsion. Still, once some plasma arrives at the event horizon, we observe rapid accretion of the magnetic flux which cannot inhibit the radial motion. At late stages the field lines adopt more radial configuration near horizon and they eventually induce the ejection of plasma in the equatorial plane. The logarithmic scale of density is shown on the colour bar in arbitrary units. Time (growing in the three snapshots from left to right) corresponds to the code units.

4 CONCLUSIONS

Astrophysical black holes can be detected and their parameters constrained by observations in the electromagnetic domain only if the accretion process takes place, lights up the system, and produces the characteristic spectral features and variability of the emerging radiation signal. However, the properties of the cosmic environment vary in very broad range: from magnetically dominated (almost) vacuum filaments of the organized field lines to the force-free field lines frozen in the accreting medium.

In the present contribution we were interested to explore the transition between two extreme states: from the initial configuration, where the Wald–type uniform field (aligned with the black hole rotation axis) comes to the contact with the Bondi–type radial inflow

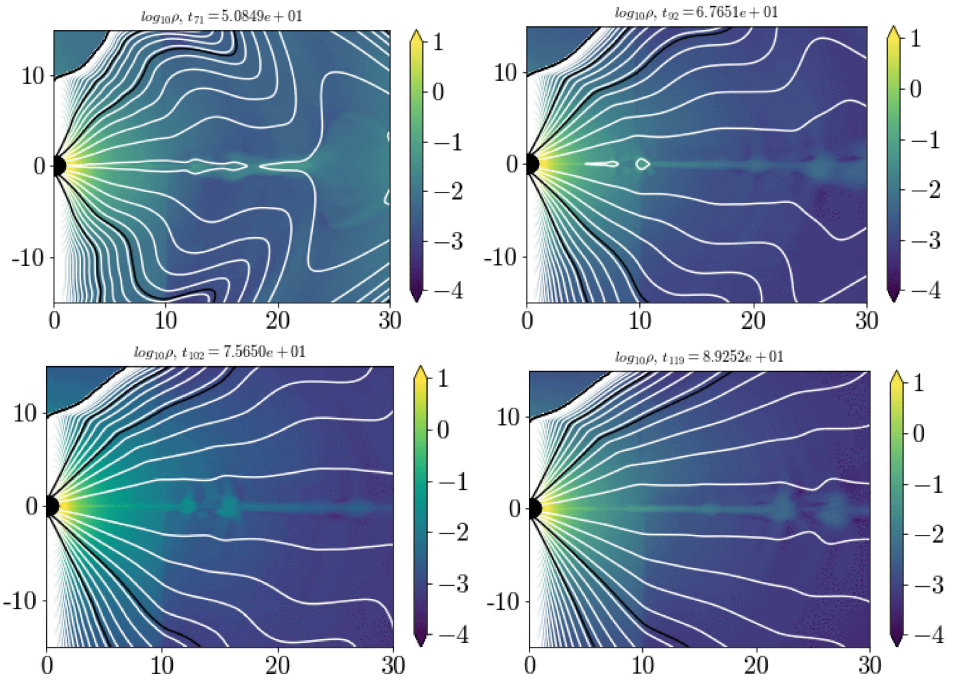

Figure 7. Similar as in the previous figure but plotted here over a larger integration domain and longer period of time. Ejection of equatorial material is observed in the form of plasmoids, which represent a disk or a ring of outflowing material in the adopted 2D approximation. In the vicinity of the rotating black hole ergosphere the frame-dragging effect acts on the plasma as well as the magnetic field lines. As a result of the frame-dragging mechanism, the outflowing material adopts a toroidal component of the orbital motion.

solution. The fluid drags the field lines onto the black hole, and simultaneously becomes influenced and partly expelled by the evolving magnetic field until the final state is reached after many dynamical periods. Let us note that the initial vacuum, ordered, homogeneous, parallel to the rotation axis magnetic field is an idealized situation. It has been frequently employed in order to define the starting configuration and we also use it as a test bed solution that can represent a rotating black hole embedded into a large-scale (exceeding the size of the horizon) magnetic filament, which allows us to model the rapid disappearance of the magnetic expulsion once the conducing medium starts to be accreted. An interesting development emerges as the magnetic lines are bent in the radial direction near the horizon and they start reconnecting in the equatorial plane, thus accelerating the outflow in the direction perpendicular to the rotation axis. In fact, the accretion of magnetic field lines onto the black hole starts the process of their bending from the initial Wald configuration to the split-monopole topology, which leads to the rapid disappearance of the Meissner expulsion in our system.

We can suggest that the resulting equatorial outflow is possible thanks to the fact that the Meissner effect does not operate in the magnetosphere filled with plasma.

Let us note that accretion disk backflows have been observed in various circumstances including the simulations of accreting black holes and stars (see Kluzniak and Kita, 2000; Mishra et al., 2020). In several aspects the system discussed in our present work is rather distinct: it does not include a magnetic star as a source of dipole-like magnetic field (we considered a black hole in the centre, which was magnetized by external currents), neither an equatorial accretion disk as the initial condition (Bondi spherical inflow was assumed as the condition at the outer boundary). Indeed, we suggest that the backflows are rather generic features that can occur in different accreting systems.

Abandoning the axial symmetry will be the next step towards a more realistic description. Also, once an oblique magnetic field (inclined with respect to the rotation axis) and a twisted (non-spherical as well as non-axisymetric) accretion flow are considered, we can expect the outflowing plasmoids to be scattered in a wide range of directions.

ACKNOWLEDGEMENTS

The authors thank the Czech Ministry of Education Youth and Sports Mobility project No. 8J20PL037 to support the Czech-Polish scientific cooperation, and the Czech Science Foundation – Deutsche Forschungsgemeinschaft collaboration project No. 19-01137J on processes around supermassive black holes. KS and AJ were supported by grants No. 2016/23/B/ST9/03114 and 2019/35/B/ST9/04000 from the Polish National Science Center. We acknowledge computational resources of the Warsaw ICM through the grant Gb79-9. The authors thank the referee for helpful comments and a number of suggestions to improve our text.

REFERENCES

Abramowicz, M., Jaroszynski, M. and Sikora, M. (1978), Relativistic, accreting disks., *Astron. Astrophys.*, **63**, pp. 221–224.

Abramowicz, M. A. (1971), The Relativistic von Zeipel's Theorem, *Acta Astronomica*, **21**, p. 81.

Abramowicz, M. A., Calvani, M. and Nobili, L. (1980), Thick accretion disks with super-Eddington luminosities, *The Astrophysical Journal*, **242**, pp. 772–788.

Beskin, V. S. (2010), *MHD Flows in Compact Astrophysical Objects: Accretion, Winds and Jets*, Astronomy and Astrophysics Library, Springer, Berlin, URL `https://cds.cern.ch/record/1338615`.

Bičák, J. and Dvořák, L. (1976), Stationary electromagnetic fields around black holes. II. General solutions and the fields of some special sources near a Kerr black hole., *General Relativity and Gravitation*, **7**(12), pp. 959–983.

Bičák, J., Karas, V. and Ledvinka, T. (2007), Black holes and magnetic fields, in V. Karas and G. Matt, editors, *Black Holes from Stars to Galaxies – Across the Range of Masses*, volume 238, pp. 139–144, arXiv: `astro-ph/0610841`.

Blandford, R. D. and Znajek, R. L. (1977), Electromagnetic extraction of energy from Kerr black holes., *Mon. Not. R. Astron Soc.*, **179**, pp. 433–456.

Bondi, H. (1952), On spherically symmetrical accretion, *Mon. Not. R. Astron Soc.*, **112**, p. 195.

Camilloni, F., Grignani, G., Harmark, T., Oliveri, R. and Orselli, M. (2020), Force-free magnetosphere attractors for near-horizon extreme and near-extreme limits of Kerr black hole, *arXiv e-prints*, arXiv:2007.15662, arXiv: 2007.15662.

Chandrasekhar, S. (2002), *The mathematical theory of black holes*, Oxford classic texts in the physical sciences, Oxford Univ. Press, Oxford, URL https://cds.cern.ch/record/579245.

East, W. E. and Yang, H. (2018), Magnetosphere of a spinning black hole and the role of the current sheet, *Phys. Rev. D*, **98**(2), 023008, arXiv: 1805.05952.

Fox, A. and Davé, R. (2017), *Gas accretion onto galaxies*, Astrophysics and space science library, Springer, Cham, URL https://cds.cern.ch/record/2258720.

Frank, J., King, A. and Raine, D. (2002), *Accretion Power in Astrophysics*, Cambridge University Press, 3 edition.

Gammie, C. F., McKinney, J. C. and Tóth, G. (2003), HARM: A Numerical Scheme for General Relativistic Magnetohydrodynamics, *The Astrophysical Journal*, **589**(1), pp. 444–457, arXiv: astro-ph/0301509.

Gong, X.-B., Liao, Y. and Xu, Z.-Y. (2016), A mathematical form of force-free magnetosphere equation around Kerr black holes and its application to Meissner effect, *Physics Letters B*, **760**, pp. 112–116, arXiv: 1603.08411.

Kato, S., Fukue, J. and Mineshige, S. (2008), *Black-Hole Accretion Disks: Towards a New Paradigm*, Kyoto University Press, ISBN 9784876987405, URL https://books.google.cz/books?id=mageNwAACAAJ.

King, A. R., Lasota, J. P. and Kundt, W. (1975), Black holes and magnetic fields, *Phys. Rev. D*, **12**(10), pp. 3037–3042.

Kluzniak, W. and Kita, D. (2000), Three-dimensional structure of an alpha accretion disk, *arXiv e-prints*, astro-ph/0006266, arXiv: astro-ph/0006266.

Kološ, M. and Janiuk, A. (2020), Simulations of black hole accretion torus in various magnetic field configurations, *arXiv e-prints*, arXiv:2004.07535, arXiv: 2004.07535.

Komissarov, S. S. and McKinney, J. C. (2007), The 'Meissner effect' and the Blandford-Znajek mechanism in conductive black hole magnetospheres, *Mon. Not. R. Astron Soc.*, **377**(1), pp. L49–L53, arXiv: astro-ph/0702269.

Kozlowski, M., Jaroszynski, M. and Abramowicz, M. A. (1978), The analytic theory of fluid disks orbiting the Kerr black hole., *Astron. Astrophys.*, **63**(1-2), pp. 209–220.

McKinney, J. C. (2006), General relativistic magnetohydrodynamic simulations of the jet formation and large-scale propagation from black hole accretion systems, *Mon. Not. R. Astron Soc.*, **368**(4), pp. 1561–1582, arXiv: astro-ph/0603045.

Mishra, R., Čemeljić, M. and Kluźniak, W. (2020), Backflow in Accretion Disk, in K. Małek, M. Polińska, A. Majczyna, G. Stachowski, R. Poleski, Ł. Wyrzykowski and A. óżańska, editors, *XXXIX Polish Astronomical Society Meeting*, volume 10, pp. 147–150, arXiv: 2006.01851.

Misner, C. W., Thorne, K. S. and Wheeler, J. A. (2017), *Gravitation*, Princeton University Press, Princeton, NJ, with a new foreword and a new preface, URL https://cds.cern.ch/record/2256533.

Nathanail, A. and Contopoulos, I. (2014), Black Hole Magnetospheres, *The Astrophysical Journal*, **788**(2), 186, arXiv: 1404.0549.

Pan, Z. and Yu, C. (2016), Analytic Properties of Force-free Jets in the Kerr Spacetime—II, *The Astrophysical Journal*, **816**(2), 77, arXiv: 1511.07925.

Penna, R. F. (2014), Black hole Meissner effect and Blandford-Znajek jets, *Phys. Rev. D*, **89**(10), 104057, arXiv: 1403.0938.

Penna, R. F., Kulkarni, A. and Narayan, R. (2013), A new equilibrium torus solution and GRMHD initial conditions, *Astron. Astrophys.*, **559**, A116, arXiv: 1309.3680.

Różańska, A., Kunneriath, D., Czerny, B., Adhikari, T. P. and Karas, V. (2017), Multiphase environment of compact galactic nuclei: the role of the nuclear star cluster, *Mon. Not. R. Astron Soc.*, **464**(2), pp. 2090–2102, arXiv: 1609.08834.

Sapountzis, K. and Janiuk, A. (2019), The MRI Imprint on the Short-GRB Jets, *The Astrophysical Journal*, **873**(1), 12, arXiv: 1802.02786.

Schödel, R., Feldmeier, A., Kunneriath, D., Stolovy, S., Neumayer, N., Amaro-Seoane, P. and Nishiyama, S. (2014), Surface brightness profile of the Milky Way's nuclear star cluster, *Astron. Astrophys.*, **566**, A47, arXiv: 1403.6657.

Shakura, N. (2018), *Accretion flows in astrophysics*, Astrophysics and space science library, Springer, Cham, URL https://cds.cern.ch/record/2646961.

Silich, S., Tenorio-Tagle, G. and Hueyotl-Zahuantitla, F. (2008), Spherically Symmetric Accretion onto a Black Hole at the Center of a Young Stellar Cluster, *The Astrophysical Journal*, **686**(1), pp. 172–180, arXiv: 0806.3054.

Somov, B. V. (2012), *Plasma Astrophysics; 2nd ed.*, Astrophysics and Space Science Library, Springer, New York, URL https://cds.cern.ch/record/1481601.

Wald, R. M. (1974), Black hole in a uniform magnetic field, *Phys. Rev. D*, **10**(6), pp. 1680–1685.

Wald, R. M. (1984), *General relativity*, Chicago Univ. Press, Chicago, IL, URL https://cds.cern.ch/record/106274.

Proceedings of *RAGtime 20–22, 15–19 Oct., 16–20 Sept., 19–23 Oct., 2018/2019/2020, Opava, Czech Republic*
Z. Stuchlík, G. Török and V. Karas, editors, Silesian University in Opava, 2020, pp. 121–132

The effect of magnetic field on the structure of strange quark star

Fatemeh Kayanikhoo[1,a] and Constança Providência[2]

[1]Nicolaus Copernicus Astronomical Center,
Bartycka 18, 00-716, Warszaw, Poland,
[2]CFisUC, Department of Physics, University of Coimbra, Coimbra, Portugal
[a]fatima@camk.edu.pl

ABSTRACT
The study of the strange quark stars is an interesting subject as they are a new possible type of compact object in extreme conditions. Theoretical studies suggest that the magnetic field inside the compact objects (neutron stars and SQS) may be of the order of $\sim 10^{18}$G. This strong magnetic field can affect the shape, mass, and radius of the compact objects. In the current work, we study the effect of the strong magnetic field on the equation of state and the structure of SQS. We show that the maximum gravitational mass of the SQS increases with increasing the magnetic field. Also, we find that our model corresponds to the 2 solar mass gravitational mass which is predicted for *PSR J1614-2230* and *PSR J0348+0432*. It is notable that the maximum gravitational mass in our model is $\sim 2.5 M_{\odot}$, that is comparable with the value that is predicted by detection of the gravitational wave by LIGO/Virgo collaboration. In addition, the results show that the star has an oblate shape under the effect of the strong magnetic field.

Keywords: Strange quark star – compact objects –magnetic field – quark matter – Landau effect

1 INTRODUCTION

Strange quark stars (SQS) are a possible type of compact object which remains after the end of the life of supermassive stars. After the first explosion of a massive star if the density of matter in the core of the star increases to the values above the nuclear saturation density ($\sim 10^{15}$) the quarks deconfine and a huge amount of energy ($\sim 10^{54}$ erg) released, there is a possibility that this energy leads to the second explosion which is super luminous and is called Quark-Nova (QN). The object which remains after the QN is a SQS (Ouyed et al., 2002; Ouyed and Staff, 2013; Nurmamat et al., 2019). Ouyed, Leahy, and Koning studied *CassiopeiaA* as an excellent candidate for the QN. They showed that the second explosion has happened some days after the supernova and leads to a transition from a neutron star to a quark star (Ouyed et al., 2015).

Compact object like hybrid stars and SQS contain strange quark matter (SQM) that can exist in extreme conditions (high density and temperature, and the strong magnetic fields), therefore the study of these objects has been undertaken by different groups in recent years. These objects are real laboratories to study fundamental physics in extreme conditions. In the current work, we study the effect of strong magnetic fields on the properties of the SQS. Like neutron stars and hybrid stars (the compact objects with a quark core), the SQS may have strong magnetic fields. If a massive star has a high magnetic field, during the core collapse of the supernova the magnetic flux is conserved and the compact object is created with a strong magnetic field. According to the theoretical studies the magnetic field in the core of compact objects reaches $\sim 10^{18}$ G (Lai and Shapiro, 1991; Haensel et al., 1986; Bocquet et al., 1995; Isayev, 2014).

It is notable that the properties of the star are affected by the strong magnetic field. There are several studies on the microscopic and macroscopic properties of compact objects in the presence of the magnetic field. Chatterjee, et al. studied the effect of a strong magnetic field on the EOS and the structure of a neutron star and they showed that the magnetic field breaks the spherical symmetry of neutron star(Chatterjee et al., 2015)

In the current paper, we study the effect of a strong magnetic field on the EOS and the structure of SQS. In the next section, we calculate the EOS of the system consisting of SQM (up, down, and strange quarks) in the presence of the strong magnetic field. In section 3 we study the anisotropic energy-momentum tensor of the system and the structure equations of SQS in a stationary, axisymmetric space-time. In section 4, we report the numerical results and discuss the magnetic field effects. In last section, we summarize and conclude our study.

2 THE EQUATION OF STATE OF STRANGE QUARK MATTER IN THE PRESENCE OF THE STRONG MAGNETIC FIELDS

The system we consider consists of SQM (up, down and strange quarks and an ignorable fraction of electrons $\sim 10^{-3}$). We calculate the EOS of this system by applying the MIT bag model. The Fermi relations by considering the effect of a strong magnetic field, regarding the Landau quantization effect (Mukhopadhyay et al., 2017; Landau and Lifshitz, 1977; Lopes and Menezes, 2015), are given by the following relations.

The single-particle energy density is defined as follows

$$\epsilon_{\rm i} = \left[p_{\rm i}^2 c^2 + m_{\rm i}^2 c^4 \left(1 + 2JB_{\rm D}\right)\right]^{1/2}, \tag{1}$$

where $p_{\rm i}$ and $m_{\rm i}$ are the momentum and the mass of quarks (i represents u, d, s), the Landau levels are denoted by J and the dimensionless magnetic field defined as $B_{\rm D} = B/B_{\rm C}$ ($B_{\rm C} = m_{\rm i}^2 c^3/q_{\rm i}\hbar$, with $q_{\rm i}$ the charge of quark i).

The number density of quarks is obtained as follows

$$\rho = \sum_{J=0}^{J_{\rm max}} \frac{2qB}{h^2 c} g(J) P_{\rm F}(J), \tag{2}$$

where $J_{\rm max}$ is the maximum Landau level ($J_{\rm max} = (\epsilon_{\rm Fmax}^2 - 1)/2m_i c B_D$), $g(J)$ and $P_{\rm F}(J)$ are the degenerecy and Fermi momentum of Jth Landau level. Therefore, the energy density

of SQM in the presence of the strong magnetic field is defined as

$$\varepsilon_{\rm tot} = \sum_{\rm i,j} \varepsilon_{\rm i}^{\rm (j)} + B_{\rm bag}. \tag{3}$$

The bag constant is denoted by $B_{\rm bag}$ and the kinetic energy density by $\varepsilon_{\rm i}$ ($j = +, -$ shows the spin up and apin down particles). The kinetic energy density is defined as follows

$$\varepsilon_{\rm i}^{\rm (j)} = \frac{2B_D}{(2\pi)^2\lambda^3} m_{\rm i}c^2 \sum_{J=0}^{J_{\rm max}} g_{\rm J}(1+2JB_{\rm D})\eta\left(\frac{X_{\rm F}^{\rm (j)}}{(1+2JB_{\rm D})^{1/2}}\right), \tag{4}$$

where

$$\eta(x) = \frac{1}{2}\left[x\sqrt{1+x^2} + \ln\left(x\sqrt{1+x^2}\right)\right] \tag{5}$$

and

$$x = \frac{X_{\rm F}^{\rm (j)}}{(1+2JB_{\rm D})^{1/2}} \tag{6}$$

and

$$X_{\rm F}^{\rm (j)} = (\epsilon_{\rm F}^{\rm (j)2} - 1 - 2JB_{\rm D})^{1/2}. \tag{7}$$

To calculate the energy density of SQM in a zero magnetic field, we calculate the value of number density and energy density when $J_{\rm max} \to \infty$.

The bag constant $B_{\rm bag}$ is defined with a Gaussian relation

$$B_{\rm bag}(\rho) = \bar{B}_\infty + \left(\bar{B}_0 - \bar{B}_\infty\right)\exp\left(-\beta\left(\frac{\rho}{\rho_0}\right)^2\right). \tag{8}$$

In above relation $\beta = \rho_0 = 0.17\,{\rm fm}^{-3}$, and $\bar{B}_0 = \bar{B}(\rho_0)$ is equal to $400\,{\rm MeV/fm}^3$. Also, $\bar{B}_\infty$ depends the parameter $\bar{B}_0$ and is obtained by the LOCV method (Heinz and Jacob, 2000).

The pressure of system is given by

$$P(\rho) = \rho\left(\frac{\partial\varepsilon_{\rm tot}}{\partial\rho}\right) - \varepsilon_{\rm tot}. \tag{9}$$

The EOS is plotted in Fig. 1 in the presence of magnetic fields 10^{17} G and 10^{18} G and absence of magnetic field ($B = 0$). We can see the effect of magnetic field on the EOS in comparison with $B = 0$. Also, the figure shows that the difference between the curves of different magnetic fields is not significant.

3 THE STRUCTURE EQUATIONS

In this section, we briefly present the Einstein field equations within 3+1 formalism in a stationary, axisymmetric space-time (Chatterjee et al., 2015).

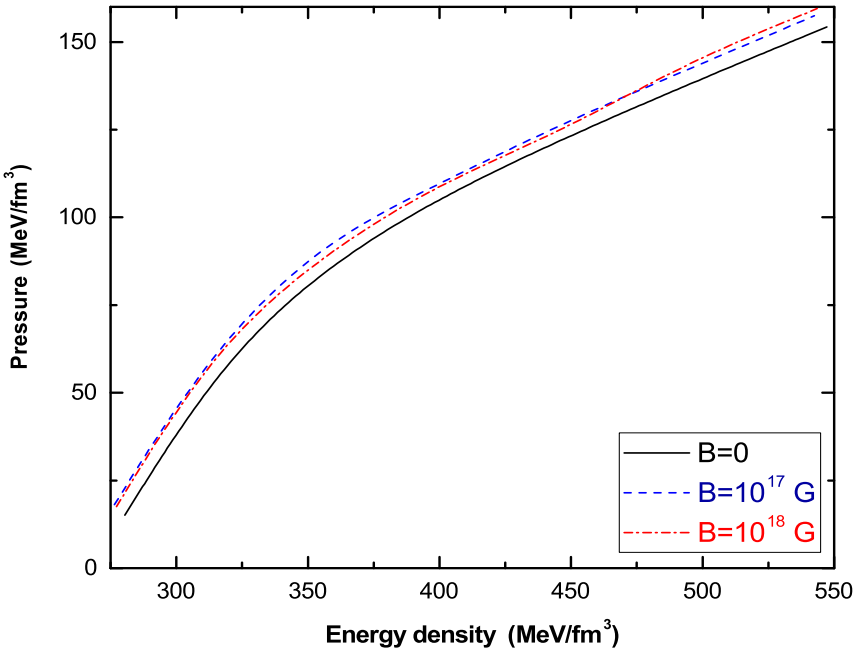

Figure 1. The pressure as a function of the energy density of SQM in the presence and absence of magnetic field.

The metric is given by

$$ds^2 = -N^2dt^2 + A^2(dr^2 + r^2d\theta^2) + \lambda^2 r^2 \sin^2(\theta)(d\phi - N^\phi dt)^2, \tag{10}$$

where N, A, λ, and N^ϕ are function of (r, θ). By applying 3+1 formalism we will have a set of four elliptic partial differential equations

$$\Delta_3 = 4\pi A^2(E^T + S_r^r + S_\theta^\theta + S_\phi^\phi) + \frac{\lambda^2 r^2 \sin^2(\theta)}{2N^2}\delta N^\phi \delta N^\phi - \delta\nu\delta(\nu + \beta), \tag{11}$$

$$\Delta_2[\alpha + \nu] = 8\pi A^2 S_\phi^\phi + \frac{3\lambda^2 r^2 \sin^2(\theta)}{4N^2}\delta N^\phi \delta N^\phi - \delta\nu\delta\nu, \tag{12}$$

$$\Delta_2[(N\lambda - 1)r\sin(\theta)] = 8\pi N A^2 \lambda r \sin(\theta)\left(S_r^r + S_\theta^\theta\right) \tag{13}$$

and

$$\left[\Delta_3 - \frac{1}{r^2\sin^2(\theta)}\right]\left(N^\phi r\sin(\theta)\right) = -16\pi\frac{NA^2}{\lambda^2}\frac{J^\phi}{r\sin(\theta)} + r\sin(\theta)\delta N^\phi\delta(\nu - 3\beta), \tag{14}$$

where $\nu = \ln N$, $\alpha = \ln A$, $\beta = \ln \lambda$, and J^{ϕ} is electromagnetic current. In the above equations, E^T, and S^i_j are total energy and stress, respectively. The notations Δ_2 and Δ_3 are introduced

$$\Delta_2 = \frac{\delta^2}{\delta r^2} + \frac{1}{r}\frac{\delta}{\delta r} + \frac{1}{r^2}\frac{\delta^2}{\delta \theta^2}, \tag{15}$$

$$\Delta_2 = \frac{\delta^2}{\delta r^2} + \frac{2}{r}\frac{\delta}{\delta r} + \frac{1}{r^2}\frac{\delta^2}{\delta \theta^2} + \frac{1}{r^2 \tan(\theta)}\frac{\delta}{\delta \theta}. \tag{16}$$

The the matter properties affects the structure of star through the energy-momentum tensor $T^{\mu\nu}$. In the presence of the magnetic field by considering the interaction of the electromagnetic field with the matter (magnetization), the energy-momentum tensor is given by

$$\begin{aligned} T^{\mu\nu} =& (\varepsilon + P)u^{\mu}u^{\nu} + Pg^{\mu\nu} + \frac{M}{B}\left[b^{\mu}b^{\nu} - (b.b)\left(u^{\mu}u^{\nu} + g^{\mu\nu}\right)\right] \\ &+ \frac{1}{\mu_0}\left[-b^{\mu}b^{\nu} + (b.b)\left(u^{\mu}u^{\nu} + \frac{1}{2}g^{\mu\nu}\right)\right], \end{aligned} \tag{17}$$

where the two first terms are the perfect fluid contribution, the third term is the magnetization contribution and the last term is the pure magnetic field contribution to the energy-momentum tensor. In the Eq. (17), ε is the energy density, P is the pressure of the perfect fluid, u^{μ} is the fluid 4-vector, $g^{\mu\nu}$ is the metric coefficient, B is the magnetic field, and b^{μ} is the magnetic field 4-vector. In the above relation, M is the scalar quantity which is defined as follows

$$M := \mu_0 \frac{m_{\mu}}{b_{\mu}}, \tag{18}$$

where m_{μ} is magnetization 4-vector. Here the magnetic field points in z-direction and we considered a non-rotating star. We can rewrite the energy-momentum tensor in the well-known form

$$T^{\mu}_{\nu} = \mathrm{diag}\left(\varepsilon + \frac{B^2}{2\mu_0}, P - MB + \frac{B^2}{2\mu_0}, P - MB + \frac{B^2}{2\mu_0}, P - \frac{B^2}{2\mu_0}\right). \tag{19}$$

The energy-momentum tensor Eq. (19) shows that the magnetization term reduces the total pressure of the star. It is also clear that the magnetic field reduces the parallel pressure but the perpendicular pressure is increasing by increasing the magnetic field. Consequently, the star will be deformed in the presence of a strong magnetic field.

In the next section we show the results of solving the equations by applying the LORENE (*Lorene/Codes/Mag _ eos _ star*) and using the defined EOS in the previous section (Gourgoulhon et al., 2016).

4 THE NUMERICAL RESULTS

In this section, we investigate the effect of the magnetic field on the structure of SQS by varying the current function k_0 defined through $j^{\phi} = \Omega j^{t} + (\varepsilon + P)k_0$, where Ω is the stellar angular velocity. We study the structure of SQS in two cases,

i) The magnetic field just affects the structure of SQS,

ii) The magnetic field affects the structure and the EOS of SQS.

We have found that in our model the current function can reach 30000. In other words, for $k_0 > 30000$ the SQS is not in a stable configuration.

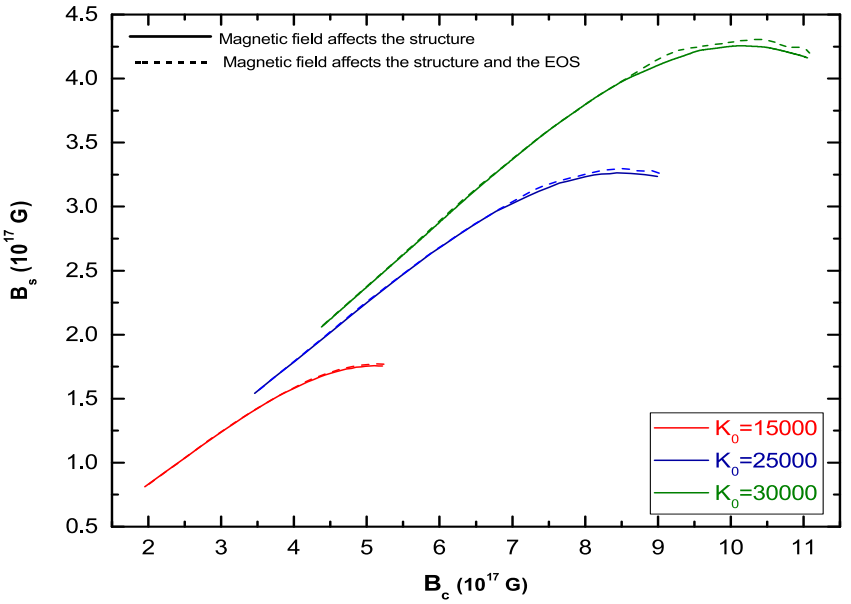

Figure 2. The surface magnetic field at the pole B_s as a function of the central magnetic field B_c.

In Fig. 2, we show the surface magnetic field of SQS in the pole B_s as a function of central magnetic field B_c. It is shown that B_s and B_c increase with increasing the current function. It is also shown that in the lowest value of k_0 the two considered cases cover each other and when $k_0 = 30000$, the difference between the two considered cases (dash lines and solid lines) is non negligible. The figure shows that the maximum central magnetic field is $B_c \sim 10^{18}$ G and that the maximum polar magnetic field at the surface $B_s \sim 4 \times 10^{17}$ G occurs at $k_0 = 30000$.

The gravitational mass $(M_g/M_{\odot})$ versus the central enthalpy H_c is plotted in the top panel of Fig. 3. The enthalpy can be translated to the baryonic density $n_B = (\varepsilon + P)e^{H}$. The figure shows that the gravitational mass increases as a function of central enthalpy in every considered case. The results show that the effect of the magnetic field on the EOS

has a negligible effect on the gravitational mass of SQS. It is shown that M_g increaces with increacing k_0. The maximum gravitational mass is 2.35 $M_\odot$ at $k_0 = 0$ ($k_0 = 0$ means that we are solving the TOV equations) and increaces to 2.48 $M_\odot$ at $k_0 = 30000$.

We have found that our model for the compact objects describes 2 $M_\odot$ stars as it is observed for the pulsars *PSR J1614-2230* ($M = 1.908 \pm 0.016\, M_\odot$) and *PSR J0348+0432* ($M = 2.01 \pm 0.04\, M_\odot$)(Demorest et al., 2010; Zhao, 2015), see Table 1. In addition, it is interesting to notice that the maximum gravitational mass corresponding to the maximum magnetic field in our calculations falls close to the predicted mass of the low mass compact object, with a mass 2.5 to 2.67 $M_\odot$ at 90% confidence, of the compact binary coalescence corresponding to the recent gravitational waves *GW190814* detected by the LIGO/Virgo collaboration. It is predicted at (Abbott et al., 2020).

In the bottom panel of Fig. 3, we show the mass-radius relation of SQS, and in Table1 we give the properties of the maximum mass configurations for different values of k_0, as well as the radius of 1.4 $M_\odot$ and 1.6 $M_\odot$ stars. It is clear that the radius increases with increasing the gravitational mass, when the gravitational mass reaches a certain value, the radius decreases and SQS collapses. In this figure, we show the central magnetic field corresponding to the maximum radius of SQS which increases from 4.60×10^{17} G to 9.15×10^{17} G. Forthermore, one can see the mass-radius relation clearly follows $R \propto M^\alpha$ where $\alpha \sim 3$ which is expected for SQS.

The radius of the maximum mass configuration increases from radius of SQS is 12.13 km for $k_0 = 0$ to 13.16 km at $k_0 = 30000$.

Table 1. The gravitational mass and radius of SQS in different current functions. Results for the maxmium mass configuration and for the $1.4M_\odot$ and $1.6M_\odot$ stars are shown.

k_0	$B_c(10^{17}\,\mathrm{G})$	$M_{g,max}(M_\odot)$	R_{max} (km)	$R_{1.4}$ (km)	$R_{1.6}$ (km)
$k_0 = 0$		2.35	12.13	10.74	11.10
$k_0 = 15000$	5.24	2.38	12.35	10.81	11.35
$k_0 = 25000$	9.02	2.43	12.80	11.13	11.59
$k_0 = 30000$	10.60	2.48	13.16	11.33	11.86

In Table 1 we show the values of the maximum gravitational mass and the corresponding radius in the third and fourth columns, respectively. We also give the radius of the stars with gravitation masses of 1.4 $M_\odot$ ($R_{1.4}$) and 1.6 $M_\odot$ ($R_{1.6}$). These results show that our model is compatible with the constraints imposed the *GW170817* analysis, in particular, the following constraints have been obtained $9.9 < R_{1.4} < 13.85$ km (Annala et al., 2018), $8.9 < R_{1.4} < 13.2$ km in (De et al., 2018) and $9.0 < R_{1.4} < 13.6$ km in Tews et al. (2018).

On the other hand, our $R_{1.4M_\odot}$ are within two sigma the predictions obtained from the *NICER* observation of the pulsar *PSR J0030+0451*. Miller and et al have estimated that the pulsar *PSR J0030+0451* has a radius $R_{1.4} = 13.02^{+1.24}_{-1.06}$ km for the gravitational mass $M = 1.44^{+0.15}_{-0.14}\, M_\odot$ within a 68% confidence interval (Miller et al., 2019). A different estimation

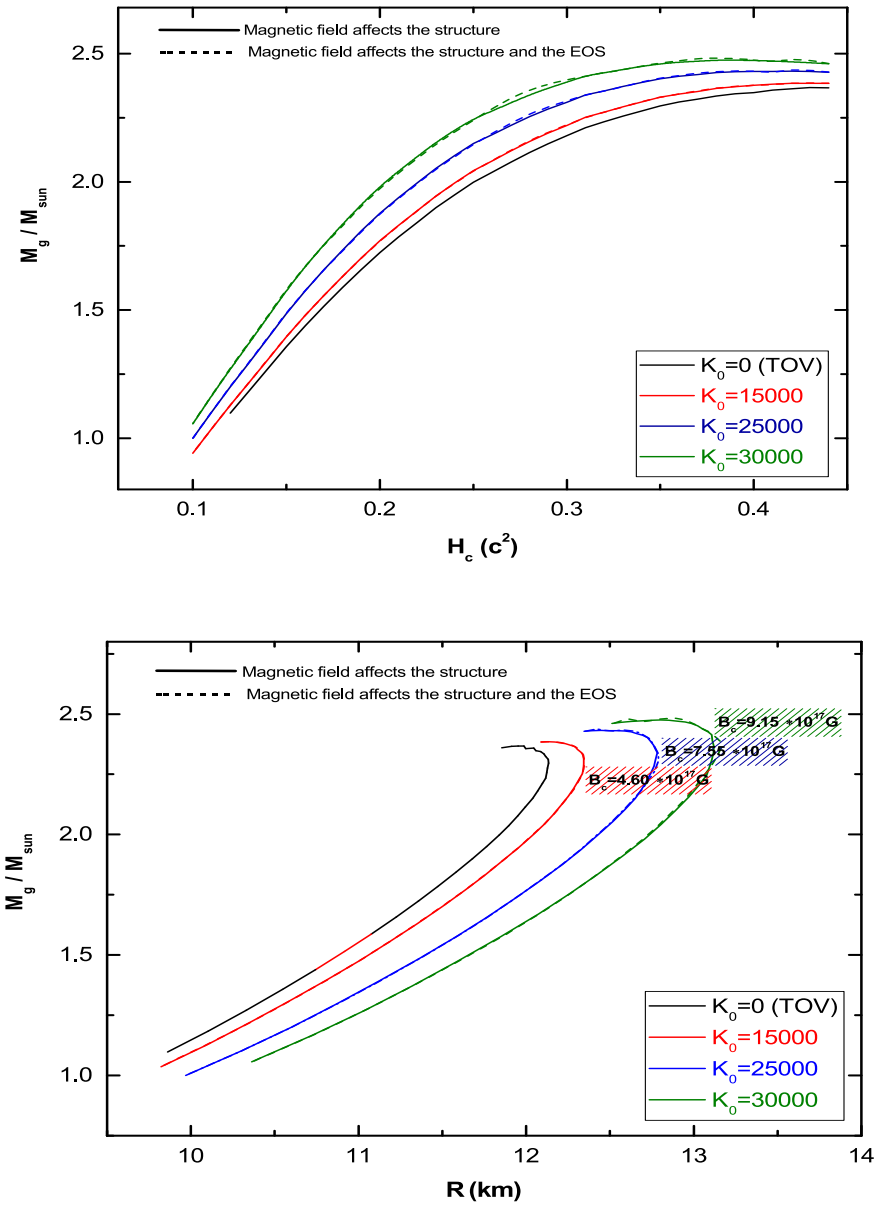

Figure 3. The gravitational mass as a function of central enthalpy (top) and the gravitational mass as a function of circumferential radius (bottom) for different values of the parameter k_0. In the bottom panel, we put the central magnetic field at the maximum radius (the critical point of the curve) in the same color given for each curve.

determined by Riley et al. (Riley et al., 2019) corresponds to a gravitational mass and a radius of $1.34^{+0.15}_{-0.16}\,M_\odot$ and $12.71^{+1.14}_{-1.19}$ km, respectively.

It has also been set a minimum radius of $R_{1.6} \geq 10.7$ for $1.6\,M_\odot$ star from the interpretation that the binary nS merger that gave rise to *GW170817* did not result from a prompt collapse to a black hole (Bauswein et al., 2017, 2019). In our study we have determined that $R_{1.6} > 10.7$ independently of the magnetic field considered. We conclude, therefore, that our model is also compatible with the constraint set on $R_{1.6}$.

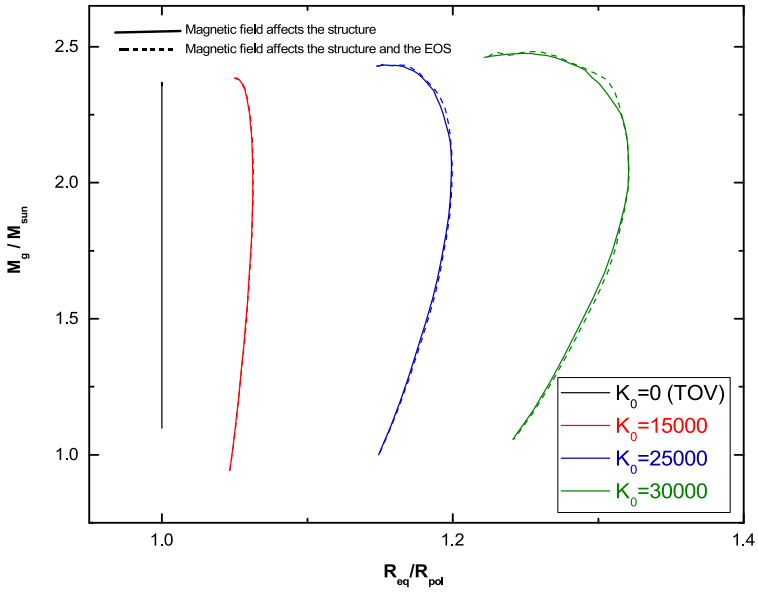

Figure 4. The gravitational mass versus the ratio of the equatorial and polar radius of SQS.

We mentioned in Sec. 3 that the magnetic field affects the shape of SQS as the parallel pressure is reduced and perpendicular pressure is increased according to the energy-momentum tensor Eq. (19). In Fig. 4, The gravitational mass is plotted as a function of $R_{\rm eq}/R_{\rm pol}$. We can see that by solving the TOV equations the SQS is completely in spherical symmetry, the ratio of equatorial and polar radius increases with increasing the current function, and at $k_0 = 30000$ this value reaches to 1.25. It is also clear that the effect of the magnetic field on the EOS does not affect the shape of SQS.

In Fig. 5, the magnetic field lines (top panel) and the enthalpy profile (bottom panel) are plotted in the plane (x, z). The profiles are plotted for the gravitational mass $2.48M_\odot$ and the polar surface magnetic field 4.25×10^{17} G. The bold line in both panels shows the surface of SQS. The magnetic field profile shows how the strong magnetic field can deviate

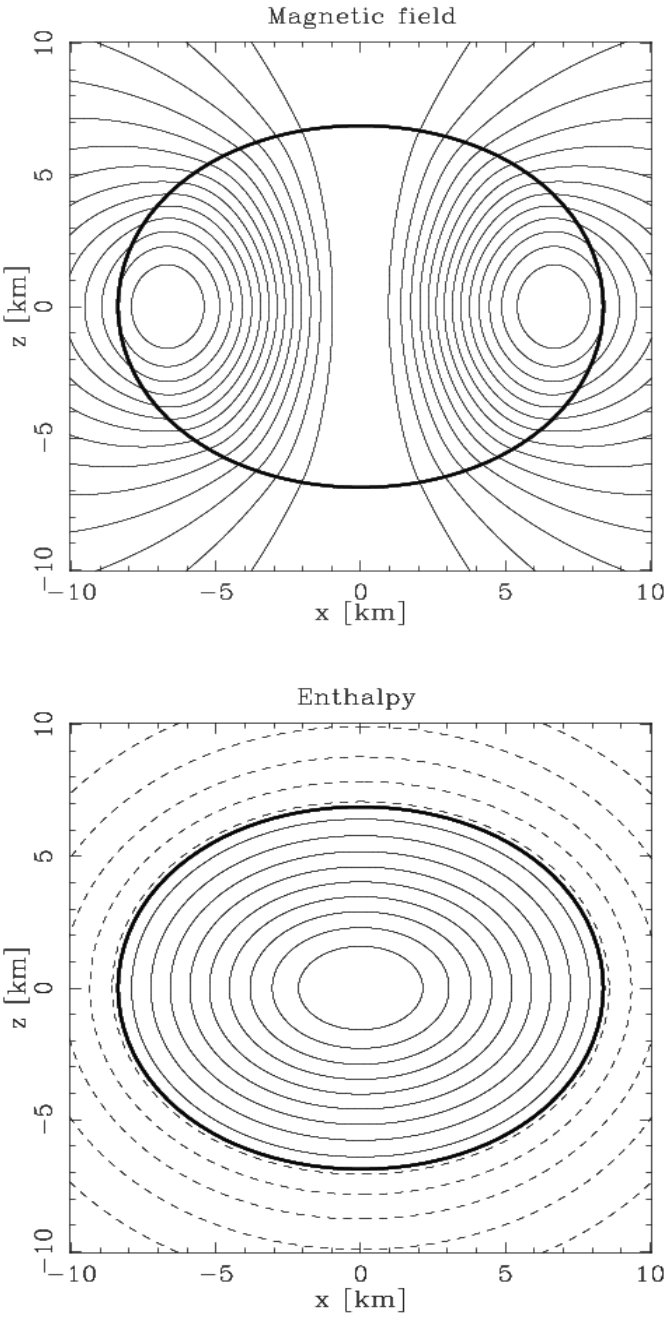

Figure 5. The profile of magnetic field lines (top) and the enthalpy profile (bottom) in meridional plane (x, z) for the maximum value of magnetic field $B_s = 4.25 \times 10^{17}$ G and gravitational mass $M_g = 2.5\, M_\odot$.

the shape of SQS from the spherical symmetry. In the enthalpy profile, the dash lines are negative enthalpy and the solid lines are positive enthalpy inside the SQS.

5 CONCLUSIONS

In this work, we studied the effect of a strong magnetic field on the microscopic and macroscopic properties of SQS. We calculated the EOS of SQM with the Landau quantization effect. To investigate the structure we assumed the stationary, axisymmetric space-time. The microscopic properties of matter affect the structure through the energy-momentum tensor. In the presence of the strong magnetic field, the energy-momentum tensor is in an anisotropic form. It is shown that the parallel and perpendicular pressures are reduced by the magnetization. The magnetic field reduces the parallel pressure and increases the perpendicular pressure.

We have found that the magnetic field in the core of SQS reaches to $\sim 10^{18}$ G where the maximum surface magnetic field at the pole is $\sim 4 \times 10^{17}$ G. The results show that the maximum gravitational mass and radius of SQS increase as the magnetic field becomes stronger and may reach the value $2.48\,M_{\odot}$ and the radius 13.16 km, respectively, taking the strongest field considered in the present study. This value of gravitational mass is comparable with the predicted, by the LIGO/Virgo collaboration, smallest value for the low mass object associated with the gravitational waves GW190814, in particular, at 90% confidence this compact object should have a mass between $2.5\,M_{\odot}$ and $2.67\,M_{\odot}$. This could indicate that this object is a strongly magnetized star. We have also shown that the radius predictions obtained from our model for magnetized and non-magnetized stars with a mass $1.4\,M_{\odot}$ and $1.6\,M_{\odot}$ is compatible with the values obtained from several different analysis of the *GW170817*.

It is also clear that the strong magnetic field affects the shape of the star. The strong magnetic field breaks down the spherical symmetry of the star. The ratio of equatorial and polar radius reaches 1.25 in the maximum value of the central magnetic field 10^{18} G.

ACKNOWLEDGEMENTS

This work has been done at the University of Coimbra. I would like to show my gratitude to Ivo Sengo and Dr. Helena Pais for technical assistance with LORENE. I would like to express my very great appreciation to Prof. Wlodek Kluzniak at Nicolaus Copernicus Astronomical Center. Publication supported in part by the Polish NCN grant No. 2019/33/B/ST9/01564.

REFERENCES

Abbott, R., Abbott, T. D., Abraham, S., Acernese, F., Ackley, K., Adams, C., Adhikari, R. X., Adya, V. B. and et al (2020), GW190814: Gravitational Waves from the Coalescence of a 23 Solar Mass Black Hole with a 2.6 Solar Mass Compact Object, *Astrophys. J.*, **896**(2), p. 44.

Annala, E., Gorda, T., Kurkela, A. and Vuorinen, A. (2018), Gravitational-wave constraints on the neutron-star-matter Equation of State, *Phys. Rev. Lett.*, **120**(17), p. 172703.

Bauswein, A., Friedrich, N. U. B., Blaschke, D., Chatziioannou, K. and et al (2019), Equation-of-state Constraints and the QCD Phase Transition in the Era of Gravitational-Wave Astronomy, *AIP Conf. Proc.*, **2127**(1), p. 020013.

Bauswein, A., Just, O., Janka, H. T. and Stergioulas, N. (2017), Neutron-star radius constraints from GW170817 and future detections, *Astrophys. J. Lett.*, **850**(2), p. 34.

Bocquet, M., Bonazzola, S., Gourgoulhon, E. and Novak, J. (1995), Rotating neutron star model with magnetic field, *Astron. Astrophys*, **301**, p. 757.

Chatterjee, D., Elghozi, T., Novak, J. and Oertel, M. (2015), Consistent neutron star models with magnetic-field-dependent equations of state, *Mon. Not. R. Astron. Soc*, **447**(4).

De, S., Finstad, D., Lattimer, J. M., Brown, D. A., Berger, E. and Biwer, C. M. (2018), Tidal Deformabilities and Radii of Neutron Stars from the Observation of GW170817, *Phys. Rev. Lett.*, **121**(9), p. 091102.

Demorest, P. B., Pennucci, T., Ransom, S. M., Roberts, M. S. E. and Hessels, J. W. T. (2010), A two-solar-mass neutron star measured using Shapiro delay, *Nature*, **467**, p. 1081.

Gourgoulhon, E., Grandclement, P., Marck, J. A., Novak, J. and Taniguchi, K. (2016), LORENE: Spectral methods differential equations solver.

Haensel, P., Zdunik, J. L. and Schaeffer, R. (1986), Strange quark stars, *Astron. Astrophys*, **160**(121).

Heinz, U. and Jacob, M. (2000), Evidence for a new state of matter: An assessment of the results from the CERN lead beam programme, *nucl-th/0002042*.

Isayev, A. A. (2014), Absolute stability window and upper bound on the magnetic field strength in a strongly magnetized strange quark star, *Int. J. Mod. Phys. A*, **29**(30).

Lai, D. and Shapiro, L. (1991), Cold equation of state in a strong magnetic field: Effect of inverse B-decay, *Astrophys. J.*, **383**, p. 745.

Landau, L. D. and Lifshitz, E. M. (1977), *Quantum Mechanics*, Pergamon Press, ISBN 978-0750635394.

Lopes, L. and Menezes, D. P. (2015), Stability window and mass-radius relation for magnetized strange quark stars, *J. Cosmol. Astropart. Phys.*, **8**(002).

Miller, M., Lamb, F., Dittmann, A., Bogdanov, S. and et al (2019), PSR J0030+0451 Mass and Radius from *NICER* Data and Implications for the Properties of Neutron Star Matter, *Astrophys. J. Lett.*, **887**(1), p. 24.

Mukhopadhyay, S., Atta, D. and Basu, D. N. (2017), Landau quantization and mass-radius relation of magnetized white dowarfsin general relativity, *Rom. Rep. Phys.*, **69**(101).

Nurmamat, N., Zhu, C., Lul, G., Wang, Z., Li, L. and Liu, H. (2019), Quark novae: An alternative chanel for the formation of isolated milisecond pulsars, *J. Astrophys. Astron*, **40**(32).

Ouyed, R., Dey, J. and Dey, M. (2002), Quark-Novae, *Astron. Astrophys*, **390**(3), p. 512.

Ouyed, R., Leahy, D. and Koning, N. (2015), Hints of a second explosion (a quark nova) in Cassiopeia A Supernova, *Res. Astron. Astrophys*, **15**(483).

Ouyed, R. and Staff, J. E. (2013), Quark-novae in neutron star - white dwarf binaries: a model for luminous (spin-down powered) sub-Chandrasekhar-mass Type Ia supernovae?, *Res. Astron. Astrophys*, **13**(4), p. 435.

Riley, T. E., Watts, A. L., Bogdanov, S. and et al (2019), A *NICER* View of PSR J0030+0451: Millisecond Pulsar Parameter Estimation, *Astrophys. J. Lett.*, **887**(1), p. 21.

Tews, I., Margueron, J. and Reddy, S. (2018), Critical examination of constraints on the equation of state of dense matter obtained from GW170817, *Phys. Rev. C*, **98**(4).

Zhao, X. F. (2015), The properties of the massive neutron star PSR J0348+0432, *Int. J. Mod. Phys. A*, **24**(08), p. 1550058.

Proceedings of *RAGtime 20–22, 15–19 Oct., 16–20 Sept., 19–23 Oct., 2018/2019/2020, Opava, Czech Republic*
Z. Stuchlík, G. Török and V. Karas, editors, Silesian University in Opava, 2020, pp. 133–143

Dynamical analysis approaches in spatially curved FRW spacetimes

Morteza Kerachian[1,a] Giovanni Acquaviva[1,b]
and Georgios Lukes-Gerakopoulos[2,c]

[1]Institute of Theoretical Physics, Faculty of Mathematics and Physics,
Charles University, CZ-180 00 Prague, Czech Republic
[2]Astronomical Institute of the Academy of Sciences of the Czech Republic,
Boční II 1401/1a, CZ-141 00 Prague, Czech Republic
[a]kerachian.morteza@gmail.com
[b]gioacqua@gmail.com
[c]gglukes@gmail.com

ABSTRACT
In this article, we summarize two agnostic approaches in the framework of spatially curved Friedmann-Robertson-Walker (FRW) cosmologies discussed in detail in (Kerachian et al., 2020, 2019). The first case concerns the dynamics of a fluid with an unspecified barotropic equation of state (EoS), for which the only assumption made is the non-negativity of the fluid's energy density. The second case concerns the dynamics of a non-minimally coupled real scalar field with unspecified positive potential. For each of these models, we define a new set of dimensionless variables and a new evolution parameter. In the framework of these agnostic setups, we are able to identify several general features, like symmetries, invariant subsets and critical points, and provide their cosmological interpretation.

Keywords: Gravitation – cosmology – dynamical systems

1 INTRODUCTION

The dynamical system analysis is a powerful tool that has broad applications in different fields of science. Dynamics itself was introduced by Newton through his laws of motion and gravitation. These laws enabled Newton to tackle the two-body problem of the Earth's motion around the Sun. Later on, when scientists tried to address the three-body problem of the Earth, the Moon and the Sun, they found it was too complicated to tackle it quantitatively. In the late 19th century, Henry Poincaré suggested that celestial mechanics could be studied by considering qualitative features of a system rather than quantitative founding in this way the branch of dynamical systems (Strogatz, 2018). In the context of cosmology dynamical systems analysis allows us to view the global evolution of a model, from its start near the initial singularity to its late-time evolution (Wainwright and Lim, 2005).

978-80-7510-432-8

The observations indicate that the universe is homogeneous and isotropic (Aghanim et al., 2018), which makes the Friedmann-Robertson-Walker (FRW) spacetime the relevant metric to model its evolution. Even if the universe appears to be spatially flat, considering a non-zero spatial curvature is still observationally viable and might help in alleviating some cosmological tensions (Ryan et al., 2019; Di Valentino et al., 2020). Therefore, in our work we used spatially curved FRW metrics.

According to Planck Collaboration et al. (2020), the total energy density of the universe consist of $\sim$ 68.5% dark energy, $\sim$ 26.5% cold dark matter, and $\sim$ 5% baryonic matter. There are three main approaches in order to understand the physics behind the dominant substance of the universe, i.e. the dark energy: the constant vacuum energy or cosmological constant, non-constant vacuum energy or scalar fields, and modified gravities. The cosmological constant scenario, expressed by the ΛCDM model, is considered as the standard model for describing dark energy, but since it suffers from several issues (Carroll, 2001; Bahamonde et al., 2018) there are plenty of models that compete with it. In this work, we explore the dynamics of two such models in a rather general framework.

The first type of models we analyse concerns the dynamics of barotropic fluids with $\epsilon \geq 0$ in spatially curved FRW without specifying the EoS (Kerachian et al., 2020). We allow the pressure P of the fluid to attain negative values in order to be able to describe cosmological models with accelerated expansion. In these models the speed of sound of the fluid is not necessarily less than the speed of light, which implies exotic EoS.

The second type of models we analyse concerns a curved FRW geometry non-minimally coupled to a scalar field with generic positive potential (Kerachian et al., 2019). A similar analysis has been performed by Hrycyna and Szydłowski (2010) in the presence of matter for flat FRW. Our formulation allows for several improvements in the aforementioned analysis by considering a generic spatially curved FRW model and a more general scalar field potential.

2 THE DYNAMICAL SYSTEM FOR BAROTROPIC FLUIDS

The Friedmann and the Raychaudhuri equations for a FRW cosmology with only one fluid component are given by

$$H^2 + \frac{k}{a^2} = \frac{\epsilon}{3}, \qquad 2\,\dot{H} + 3\,H^2 + \frac{k}{a^2} = -P, \tag{1}$$

respectively and the continuity equation for the energy density reads

$$\dot{\epsilon} + 3\,H(P + \epsilon) = 0\,. \tag{2}$$

In these equations, ϵ is the energy density, P is the pressure of the barotropic fluid, k is the spatial curvature, a is the scale factor, $H = \frac{\dot{a}}{a}$ is the Hubble expansion rate and $\dot{}$ denotes derivative with respect to the coordinate time.

By introducing the normalization $D^2 = H^2 + |k|/a^2$, we are able to present well-defined dimensionless variables, i.e. the variables which are valid for $k > 0$ and $k \leq 0$. These new dimensionless variables are

$$\Omega_\epsilon = \frac{\epsilon}{3\,D^2}, \quad \Omega_H = \frac{H}{D}, \quad \Omega_P = \frac{P}{D^2}, \quad \Omega_{\partial P} = \frac{\partial P}{\partial \epsilon}, \quad \Gamma = \frac{\partial^2 P}{\partial \epsilon^2}\epsilon. \tag{3}$$

In order to investigate the evolution of the dimensionless variables. we define a new evolution parameter τ as $d\tau = Ddt$. This new evolution parameter is well-defined during the whole cosmic evolution. Taking the derivative of the dimensionless variables with respect to τ provides the autonomous system

$$\Omega'_\epsilon = -\Omega_H \left[\Omega_p + \Omega_\epsilon \left(3 + 2\left(\frac{\dot{H}}{D^2} + \Omega_H^2 - 1\right)\right)\right], \tag{4}$$

$$\Omega'_H = \left(1 - \Omega_H^2\right)\left(\frac{\dot{H}}{D^2} + \Omega_H^2\right), \tag{5}$$

$$\Omega'_P = -\Omega_H \left[3\Omega_{\partial P}\left(\Omega_P + 3\Omega_\epsilon\right) + 2\Omega_P\left(\frac{\dot{H}}{D^2} + \Omega_H^2 - 1\right)\right], \tag{6}$$

$$\Omega'_{\partial P} = -\Omega_H \left(\frac{\Omega_P}{\Omega_\epsilon} + 3\right)\Gamma. \tag{7}$$

2.0.0.1 ***Positive curvature:*** For positive curvature $k > 0$, in terms of the new variables the Friedmann and Raychaudhuri equations (1) become respectively

$$\Omega_\epsilon = 1, \qquad \frac{\dot{H}}{D^2} = -\frac{1}{2}\left(\Omega_P + 1\right) - \Omega_H^2. \tag{8}$$

2.0.0.2 ***Non-positive curvature:*** For the non-positive spatial curvature $k \leq 0$, in terms of the new variables the Friedmann and Raychaudhuri equations (1) become respectively

$$\Omega_\epsilon = 2\,\Omega_H^2 - 1, \qquad \frac{\dot{H}}{D^2} = -\frac{1}{2}\left(\Omega_P + 1\right) + \left(1 - 2\Omega_H^2\right). \tag{9}$$

From the definition of Ω_H we have $\Omega_H^2 \leq 1$ and from the assumption $\epsilon \geq 0$, we get that $0 \leq \Omega_\epsilon \leq 1$ and $\frac{1}{2} \leq \Omega_H^2 \leq 1$.

2.1 Critical points and their interpretation

The next step is to investigate the critical points (i.e. those points for which $\mathbf{\Omega'} = 0$) of the autonomous system (4)- (7) and their stabilities. Once the critical points are determined, we can look for their cosmological interpretation. To do that a useful tool is the *deceleration parameter*

$$q = -1 - \frac{\dot{H}}{H^2} = -1 - \Omega_H^{-2}\,\frac{\dot{H}}{D^2}, \tag{10}$$

in which we used the definition of Ω_H.

2.1.0.1 ***Two de Sitter critical lines:*** There are two critical lines with a de Sitter behavior located at $\{\Omega_\epsilon, \Omega_H, \Omega_P, \Omega_{\partial P}\} = \{1, \pm 1, -3, \forall\}$. The critical line with $\Omega_H = 1$ (called A_+) has the typical cosmological constant behaviour ($q = -1$) and its eigenvalues are

$$\{\lambda_i^{A_+}\} = \{-2, 0, -3\left(1 + \Omega_{\partial P}\right)\}, \tag{11}$$

while the critical line with $\Omega_H = -1$ (called A_-) describes an exponentially shrinking universe ($q = -1$) and its eigenvalues are

$$\{\lambda_i^{A_-}\} = \{2, 0, 3\,(1 + \Omega_{\partial P})\}. \tag{12}$$

Eq. (11) and Eq. (12) imply that for $\Omega_{\partial P} < -1$ the critical points along the lines $A_\pm$ are saddle points. However, for $\Omega_{\partial P} \geq -1$ the stability of the points along $A_\pm$ can not be determined even by the center manifold theorem. To discuss their stability numerical examples for specific Γ have to be employed.

2.1.0.2 ***Static universe critical line:*** For positive spatial curvature, there is a critical line (called B) located at $\{\Omega_\epsilon, \Omega_H, \Omega_P, \Omega_{\partial P}\} = \{1, 0, -1, \forall\}$. This critical line describes a static universe, i.e $a = $ const. and its eigenvalues are

$$\{\lambda_i^{B}\} = \{0, -\sqrt{1 + 3\Omega_{\partial P}},\ \sqrt{1 + 3\Omega_{\partial P}}\}. \tag{13}$$

Eq. (13) implies that for $1 + 3\Omega_{\partial P} > 0$, the critical points along the line B are saddle; for $1 + 3\Omega_{\partial P} < 0$ these points are center; for $\Omega_{\partial P} = -1/3$ the corresponding points are degenerate and all eigenvalues are zero. Since the center manifold theory cannot be employed, we rely on a numerical inspection which shows that this point is marginally unstable.

For negative curvature, there is another critical line (called $\bar{B}$) corresponding to a static universe located at $\{\Omega_\epsilon, \Omega_H, \Omega_P, \Omega_{\partial P}\} = \{-1, 0, 1, \forall\}$, but as discussed in Sec. 2.0.0.2, $\Omega_\epsilon < 0$ cases are not part of our study.

2.2 General features of Γ: invariant subsets and critical points

In this section let us assume that the function Γ has roots $\tilde{\Omega}_{\partial P}$: this allows invariant subsets lying on $\{\Omega_H, \Omega_P\}$ planes. For each root of Γ, we get a pair of critical points $C_\pm$ located at $\{\Omega_H, \Omega_P\} = \{\pm 1, 3\,\tilde{\Omega}_{\partial P}\}$. Note that, for any new invariant subset $\{\Omega_H, \Omega_P\}$ there might be an intersection with the critical lines $A_\pm$ and B; for simplicity we denote these resulting critical points with the same name as the respective critical lines.

The scale factor for the critical point C_+ grows as $a \sim (t - t_0)^{\frac{2}{3(\tilde{\Omega}_{\partial P}+1)}}$, while for the critical point C_- it decreases as $a \sim (t_0 - t)^{\frac{2}{3(\tilde{\Omega}_{\partial P}+1)}}$. At these points the deceleration parameter reduces to $q = \frac{1}{2}(3\,\tilde{\Omega}_{\partial P} + 1)$. $C_\pm$ according to q represent an accelerated universe when $\tilde{\Omega}_{\partial P} < -\frac{1}{3}$ and a decelerated one when $\tilde{\Omega}_{\partial P} > -\frac{1}{3}$.

The points $C_\pm$ have eigenvalues

$$\{\lambda_i^{C_\pm}\} = \{\pm 3\,(1 + \tilde{\Omega}_{\partial P}), \pm(1 + 3\,\tilde{\Omega}_{\partial P})\}. \tag{14}$$

Based on these eigenvalues on the invariant subset $\{\Omega_H, \Omega_P\}$ and one can see that for $-\frac{1}{3} < \tilde{\Omega}_{\partial P}$ point C_+ (C_-) is a source (sink). For the case $-1 < \tilde{\Omega}_{\partial P} < -\frac{1}{3}$ instead $C_\pm$ are saddle. Finally, for $\tilde{\Omega}_{\partial P} < -1$ point C_+ (C_-) is a sink (source). These points can be seen in the examples shown in Figs. 1 and 2.

Since the stability of the critical points ($A_\pm$, B, and $C_\pm$) of the system depends on the value of $\tilde{\Omega}_{\partial P}$, we split our analysis into the following three ranges

$$-\frac{1}{3} < \tilde{\Omega}_{\partial P}, \qquad -1 < \tilde{\Omega}_{\partial P} < -\frac{1}{3}, \qquad \tilde{\Omega}_{\partial P} < -1. \tag{15}$$

and we are going to depict the invariant subset $\{\Omega_H, \Omega_P\}$ in these ranges. In Figs. 1, 2 we choose one representative value of $\tilde{\Omega}_{\partial P}$ for each range, since the topology of the trajectories is independent of the specific value inside each range. For simplicity we assume that the function Γ has only one root.

In order to be able to investigate the asymptotic behaviour of Ω_P, i.e. $\Omega_P = \pm\infty$, in Figs. 1 and 2 we used the transformation

$$X_P = \frac{\zeta \Omega_P}{\sqrt{1 + \zeta^2 \Omega_P^2}} \in [-1, 1], \tag{16}$$

where $\zeta > 0$ is just a constant rescaling parameter. The evolution equation for this variable for positive curvature becomes

$$X_P' = \frac{\Omega_H}{\zeta} \sqrt{1 - X_P^2} \left(X_P + 3\,\zeta \sqrt{1 - X_P^2}\right) \left(X_P - 3\,\zeta\,\Omega_{\partial P} \sqrt{1 - X_P^2}\right), \tag{17}$$

while for the non-positive curvature becomes

$$\begin{aligned} X_P' = & \frac{\Omega_H}{\zeta} \sqrt{1 - X_P^2} \left(9\,\zeta^2\,\Omega_{\partial P} \left(1 - 2\,\Omega_H^2\right) \left(1 - X_P^2\right) + \right. \\ & \left. + \zeta\, X_P \sqrt{1 - X_P^2} \left(1 - 3\,\Omega_{\partial P} + 2\,\Omega_H^2\right) + X_P^2\right), \end{aligned} \tag{18}$$

which along with the Eq. (5) define the compactified systems.

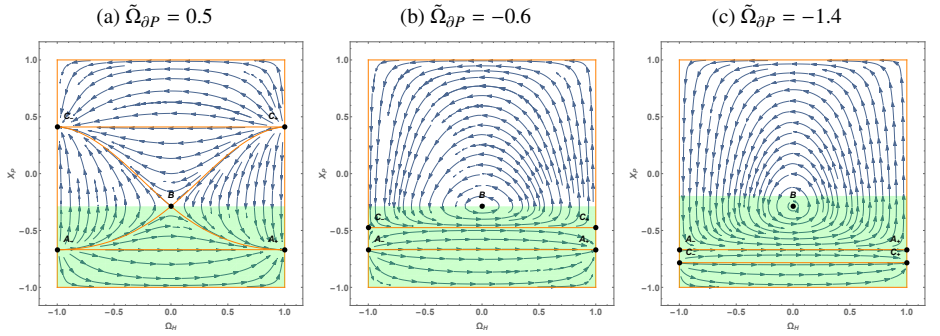

Figure 1. Invariant subsets for positive spatial curvature and $\zeta = 0.3$ plotted for three representative values of $\tilde{\Omega}_{\partial P}$ in the ranges given in Sec. 2.2.0.1. The orange thick lines are the separatrices of the system and the green shaded regions denote the part of the variable space where the universe is accelerating.

2.2.0.1 ***Positive curvature:*** Fig. 1 shows the invariant subsets $\{\Omega_H, X_P\}$ for the positive curvature, on which two additional invariant subsets are located at $\Omega_P = -3$ and $\Omega_P = 3\,\tilde{\Omega}_{\partial P}$.

2.2.0.2 ***Non-positive curvature*** For the non-positive curvature there are additional critical points once we consider the roots $\Gamma(\tilde{\Omega}_{\partial P}) = 0$. The locations of these critical points are $\{\Omega_H, \Omega_P\} = \{\pm\frac{1}{\sqrt{2}}, 0\}$ and they represent a Milne universe, since the deceleration parameter $q = 0$ and the scale factor evolves as $a = \pm \mid k \mid (t + c_1)$ for $\Omega_H = \pm\frac{1}{\sqrt{2}}$.

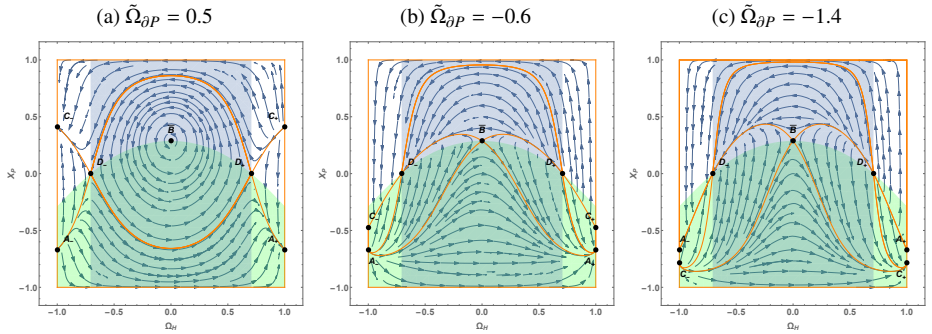

Figure 2. Invariant subsets for negative spatial curvature and $\zeta = 0.3$ plotted for three representative values of $\tilde{\Omega}_{\partial P}$ in the ranges given in Sec. 2.2.0.2. The orange thick lines are the separatrices. The blue shaded areas are the regions excluded by our assumption that $\Omega_\epsilon > 0$. The green shaded region are the part of the variable space where we have accelerating universe.

The critical point with $\Omega_H = \frac{1}{\sqrt{2}}$ denoted as D_+ has eigenvalues

$$\left\{\lambda_i^{D_+}\right\} = \left\{\sqrt{2}, -\frac{\sqrt{2}}{2}\left(1 + 3\,\tilde{\Omega}_{\partial P}\right)\right\}, \tag{19}$$

in the invariant subset $\{\Omega_H, \Omega_P\}$, whiles the critical point denoted as D_- has eigenvalues

$$\left\{\lambda_i^{D_-}\right\} = \left\{-\sqrt{2}, \frac{\sqrt{2}}{2}\left(1 + 3\,\tilde{\Omega}_{\partial P}\right)\right\}. \tag{20}$$

Eqs. (19) and (20) show that for $-\frac{1}{3} < \tilde{\Omega}_{\partial P}$ the critical points $D_\pm$ are saddles, while for $-\frac{1}{3} > \tilde{\Omega}_{\partial P}$, D_+ is a source and D_- is a sink.

3 THE DYNAMICAL SYSTEM FOR NON-MINIMALLY COUPLED SCALAR FIELD

The action of a scalar field non-minimally coupled to gravity reads

$$S = \int d^4x\,\sqrt{-g}\left(\frac{R}{2} + \mathcal{L}_\psi\right), \tag{21}$$

where $\mathcal{L}_\psi$ is the Lagrangian for the scalar field ψ:

$$\mathcal{L}_\psi = -\frac{1}{2}\left(g^{\mu\nu}\,\partial_\mu\psi\,\partial_\nu\psi + \xi R\psi^2\right) - V(\psi), \tag{22}$$

and $V(\psi)$ is a scalar field potential.

By variation of the action (21) with respect to $g_{\mu\nu}$, we arrive to the Einstein field equations

$$R_{\mu\nu} - \frac{1}{2} R\, g_{\mu\nu} = T^{\psi}_{\mu\nu}. \tag{23}$$

where the stress-energy tensor $T^{\psi}_{\mu\nu}$ for the non-minimally coupled scalar field reads

$$\begin{aligned} T^{\psi}_{\mu\nu} = {} & (1 - 2\,\xi)\, \nabla_\mu \psi\, \nabla_\nu \psi + \left(2\,\xi - \frac{1}{2}\right) g_{\mu\nu} \nabla^\alpha \psi\, \nabla_\alpha \psi - V(\psi)\, g_{\mu\nu} \\ & + \xi \left(R_{\mu\nu} - \frac{1}{2} g_{\mu\nu} R\right) \psi^2 + 2\,\xi \psi \left(g_{\mu\nu}\, \nabla^\alpha\, \nabla_\alpha - \nabla_\mu\, \nabla_\nu\right) \psi. \end{aligned} \tag{24}$$

By variation of the action with respect to the scalar field ψ we get the Klein-Gordon equation

$$\nabla_\mu\, \nabla^\mu\, \psi - \xi R \psi - \frac{\partial V(\psi)}{\partial \psi} = 0. \tag{25}$$

The Friedmann and the Raychaudhuri equations for the non-minimally coupled scalar field in the FRW background read

$$3 \left(H^2 + \frac{k}{a^2}\right) = \epsilon_\psi, \quad \left(2\,\dot{H} + 3\,H^2 + \frac{k}{a^2}\right) = -P_\psi, \tag{26}$$

respectively, while the Klein-Gordon equation reads

$$\ddot{\psi} + 3\,H\,\dot{\psi} + \partial_\psi V + 6\,\xi\,\psi \left(\dot{H} + 2\,H^2 + \frac{k}{a^2}\right) = 0. \tag{27}$$

Here the ϵ_ψ and P_ψ are defined as

$$\epsilon_\psi = \frac{1}{2}\,\dot{\psi}^2 + V(\psi) + 3\,\xi\,\psi \left(2\,H\,\dot{\psi} + \psi \left(H^2 + \frac{k}{a^2}\right)\right), \tag{28}$$

$$P_\psi = (1 - 4\,\xi)\,\frac{1}{2}\,\dot{\psi}^2 - V(\psi) - \xi \left(4\,H\,\psi\,\dot{\psi} + 2\,\psi\,\ddot{\psi} + \psi^2 \left(2\,\dot{H} + 3\,H^2 + \frac{k}{a^2}\right)\right). \tag{29}$$

We define a set of dimensionless variables which are well-defined for positive and non-positive curvatures:

$$\Omega = \frac{\psi}{\sqrt{1 + \xi\,\psi^2}}, \quad \Omega_H = \frac{H}{D}, \quad \Omega_\psi = \frac{\dot{\psi}}{\sqrt{6}\,D}, \tag{30}$$

$$\Omega_V = \frac{\sqrt{V}}{\sqrt{3}\,D}, \quad \Omega_{\partial V} = \frac{\partial_\psi V}{V}, \quad \Gamma = \frac{V \cdot \partial^2_\psi V}{(\partial_\psi V)^2} \tag{31}$$

where $D^2 = H^2 + \frac{|k|}{a^2}$. Similarly as for the dynamical system in Sec. 2, for these dimensionless variables the evolution parameter τ is defined as $d\tau = Ddt$. By taking derivatives of the dimensionless variables with respect to the evolution parameter we get

$$\Omega' = \sqrt{6}\,\Omega_\psi\,\left(1-\xi\,\Omega^2\right)^{3/2} \tag{32}$$

$$\Omega'_H = \left(1-\Omega_H^2\right)\left(\frac{\dot H}{D^2}+\Omega_H^2\right) \tag{33}$$

$$\Omega'_\psi = \frac{\ddot\psi}{\sqrt{6}\,D^2} - \Omega_\psi\,\Omega_H\left(\frac{\dot H}{D^2}+\Omega_H^2-1\right) \tag{34}$$

$$\Omega'_V = \Omega_V\left[\sqrt{\frac{3}{2}}\,\Omega_{\partial V}\,\Omega_\psi - \Omega_H\left(\frac{\dot H}{D^2}+\Omega_H^2-1\right)\right] \tag{35}$$

$$\Omega'_{\partial V} = \sqrt{6}\,\Omega_{\partial V}^2\,\Omega_\psi\,(\Gamma-1)\,, \tag{36}$$

where $\Gamma = V\cdot\partial_\psi^2 V/\left(\partial_\psi V\right)^2$ which is the so-called tracker parameter. This autonomous system of equations differs only in the $\frac{\ddot\psi}{\sqrt{6}\,D^2}$ and $\frac{\dot H}{D^2}$ terms for $k>0$ and $k\le 0$. Namely for positive curvature we get from Klein-Gordon and Raychaudhuri equations

$$\frac{\ddot\psi}{\sqrt{6}\,D^2} = -3\,\Omega_H\,\Omega_\psi - \sqrt{\frac{3}{2}}\,\Omega_{\partial V}\,\Omega_V^2 - \frac{\sqrt{6}\,\xi\,\Omega}{\sqrt{1-\xi\,\Omega^2}}\left(\frac{\dot H}{D^2}+\Omega_H^2+1\right),$$

$$\frac{\dot H}{D^2}+\Omega_H^2+1 = -\frac{1}{1-2\,\xi\,(1-3\,\xi)\,\Omega^2}\left\{-\frac{1}{2}\left(1-2\,\xi\,\Omega^2\right)\right.$$

$$\left.+\,\xi\,\Omega\,\sqrt{1-\xi\,\Omega^2}\left(\sqrt{6}\,\Omega_H\,\Omega_\psi+3\,\Omega_{\partial V}\,\Omega_V^2\right)+\frac{3}{2}\left(1-\xi\,\Omega^2\right)\left[(1-4\,\xi)\,\Omega_\psi^2-\Omega_V^2\right]\right\},$$

while for non-positive curvature these equations read

$$\frac{\ddot\psi}{\sqrt{6}\,D^2} = -3\,\Omega_H\,\Omega_\psi - \sqrt{\frac{3}{2}}\,\Omega_{\partial V}\,\Omega_V^2 + \frac{\sqrt{6}\,\xi\,\Omega}{\sqrt{1-\xi\,\Omega^2}}\left(1-\frac{\dot H}{D^2}-3\,\Omega_H^2\right),$$

$$\frac{\dot H}{D^2}+\Omega_H^2 = \frac{1}{2}-\Omega_H^2+\frac{1}{1-2\,\xi\,(1-3\,\xi)\,\Omega^2}\left\{3\,\xi^2\,\Omega^2\,\left(1-2\,\Omega_H^2\right)\right.$$

$$\left.-\,\xi\,\Omega\,\sqrt{1-\xi\,\Omega^2}\left(\sqrt{6}\,\Omega_H\,\Omega_\psi+3\,\Omega_{\partial V}\,\Omega_V^2\right)-\frac{3}{2}\left(1-\xi\,\Omega^2\right)\left[(1-4\,\xi)\,\Omega_\psi^2-\Omega_V^2\right]\right\}.$$

The respective Friedmann equations differ as well, i.e. for $k>0$

$$1 = 2\,\xi\,\Omega^2\left(1-\Omega_H^2\right)+3\,\xi\left(\sqrt{\frac{2}{3}}\,\Omega_H\,\Omega+\Omega_\psi\,\sqrt{1-\xi\,\Omega^2}\right)^2$$
$$+\,(1-3\,\xi)\,\Omega_\psi^2\left(1-\xi\,\Omega^2\right)+\Omega_V^2\left(1-\xi\,\Omega^2\right), \tag{37}$$

while for $k \leq 0$

$$1 = 2\left(1-\xi\,\Omega^2\right)\left(1-\Omega_H^2\right) + 3\,\xi\left(\sqrt{\frac{2}{3}}\,\Omega_H\,\Omega + \Omega_\psi\,\sqrt{1-\xi\,\Omega^2}\right)^2 + (1-3\,\xi)\,\Omega_\psi^2\left(1-\xi\,\Omega^2\right) + \Omega_V^2\left(1-\xi\,\Omega^2\right). \tag{38}$$

3.1 General features of the system

3.1.0.1 ***Symmetries.*** The dynamical system (32)-(36) remains invariant under the simultaneous transformation

$$\{\Omega, \Omega_H, \Omega_\psi, \Omega_V, \Omega_{\partial V}\} \to \{-\Omega, \Omega_H, -\Omega_\psi, \Omega_V, -\Omega_{\partial V}\}. \tag{39}$$

This symmetry, physically, is equivalent to the invariance under the transformation $\psi \to -\psi$. Since Ω_V is not affected by this transformation (39), then it must hold that $V(\psi) = V(-\psi) > 0$.

3.1.0.2 ***Singularities.*** In this system there are singular points arising from the decoupling of Raychaudhuri and Klein-Gordon equations, i.e. where the determinant of their Jacobian vanishes. These singular points, in terms of dimensionless variables, correspond to the vanishing of

$$\Omega = \pm\frac{1}{\sqrt{2\xi(1-3\xi)}}. \tag{40}$$

By substituting the former relation into the Friedmann constraints and solving for Ω_ψ one gets

$$\Omega_\psi = \frac{\sqrt{6\xi}\Omega_H + \sqrt{(\Omega_H^2 \mp \Omega_V^2 - 1)6\xi \pm \Omega_V^2}}{\sqrt{1-6\xi}}, \tag{41}$$

where the upper/lower sign corresponds to negative/positive curvature. In the range $\xi \in (0, 1/6)$, in both of these cases the coordinates $\left(\Omega, \Omega_\psi\right)$ of the singularity remain finite . For $\xi > 1/6$, Ω_ψ is complex. In the case of a flat spacetime $\Omega_H = \pm 1$ we call these singularities $\mathcal{S}_\pm$ respectively.

3.1.0.3 ***Invariant subsets.*** For the dynamical system. (32)-(36), one can identify some invariant subsets of the system. These invariant subsets are $\Omega_H = \pm 1$ (flat spacetime) and $\Omega_V = 0$ (free scalar field).

3.1.0.4 ***Critical points.*** Critical points and their physical interpretations of this system are summarized in the table 1.

Table 1. The critical elements of the system and their stability in the range $0 \leq \xi \leq 1/6$.

	Ω_ψ	Ω_H	Ω	Ω_V	$\Omega_{\partial V}$	Curvature	q	w_e	stability
$\mathcal{A}_+$	0	1	0	1	0	flat	-1	-1	sink
$\mathcal{A}_-$	0	−1	0	1	0	flat	-1	-1	source
$\mathcal{B}_+$	0	1	$0 < \Omega^2 < \frac{1}{2\xi}$	$\sqrt{\frac{1-2\xi\Omega^2}{1-\xi\Omega^2}}$	$-\frac{4\xi\Omega\sqrt{1-\xi\Omega^2}}{1-2\xi\Omega^2}$	flat	-1	-1	sink
$\mathcal{B}_-$	0	−1	$0 < \Omega^2 < \frac{1}{2\xi}$	$\sqrt{\frac{1-2\xi\Omega^2}{1-\xi\Omega^2}}$	$-\frac{4\xi\Omega\sqrt{1-\xi\Omega^2}}{1-2\xi\Omega^2}$	flat	-1	-1	source
$\mathcal{C}_\pm$	0	± 1	$\pm\frac{1}{\sqrt{2\xi}}$	0	$\forall$	flat	1	$\frac{1}{3}$	saddle
$\mathcal{D}_\pm$	0	$\pm\frac{1}{\sqrt{2}}$	$\forall$	0	$\forall$	negative	0	-	saddle

4 CONCLUSIONS

This work introduces general frameworks to analyze dynamical systems of:

- barotropic fluids with non-negative energy density and generic EoS,
- non-minimally coupled real scalar fields with generic potential in the absence of regular matter,

both cases are treated in spatially curved FRW spacetimes without cosmological constant. In both cases we have employed a general Γ function, which when specified reduces our general frameworks to specific models. We were able to identify critical elements and basic features of the systems for unknown Γ functions.

REFERENCES

Aghanim, N., Akrami, Y., Ashdown, M., Aumont, J., Baccigalupi, C., Ballardini, M., Banday, A., Barreiro, R., Bartolo, N., Basak, S. et al. (2018), Planck 2018 results. vi. cosmological parameters, *arXiv preprint arXiv:1807.06209*.

Bahamonde, S., Böhmer, C. G., Carloni, S., Copeland, E. J., Fang, W. and Tamanini, N. (2018), Dynamical systems applied to cosmology: dark energy and modified gravity, *Physics Reports*, **775**, pp. 1–122.

Carroll, S. M. (2001), The cosmological constant, *Living reviews in relativity*, **4**(1), p. 1.

Di Valentino, E., Melchiorri, A. and Silk, J. (2020), Planck evidence for a closed Universe and a possible crisis for cosmology, *Nature Astronomy*, **4**, pp. 196–203, arXiv: 1911.02087.

Hrycyna, O. and Szydłowski, M. (2010), Uniting cosmological epochs through the twister solution in cosmology with non-minimal coupling, *J. Cosmol. Astropart. Phys.*, **12**, 016, arXiv: 1008.1432.

Kerachian, M., Acquaviva, G. and Lukes-Gerakopoulos, G. (2019), Classes of nonminimally coupled scalar fields in spatially curved FRW spacetimes, *Physical Review D*, **99**(12), 123516, arXiv: 1905.08512.

Kerachian, M., Acquaviva, G. and Lukes-Gerakopoulos, G. (2020), Dynamics of classes of barotropic fluids in spatially curved FRW spacetimes, *Physical Review D*, **101**(4), 043535, arXiv: 2001.00825.

Planck Collaboration, Aghanim, N., Akrami, Y., Ashdown, M., Aumont, J., Baccigalupi, C., Ballardini, M. et al. (2020), Planck 2018 results - vi. cosmological parameters, *Astronomy & Astrophysics*, **641**, p. A6.

Ryan, J., Chen, Y. and Ratra, B. (2019), Baryon acoustic oscillation, hubble parameter, and angular size measurement constraints on the hubble constant, dark energy dynamics, and spatial curvature, *Monthly Notices of the Royal Astronomical Society*, **488**(3), pp. 3844–3856.

Strogatz, S. H. (2018), *Nonlinear dynamics and chaos with student solutions manual: With applications to physics, biology, chemistry, and engineering*, CRC press.

Wainwright, J. and Lim, W. (2005), Cosmological models from a dynamical systems perspective, *Journal of Hyperbolic Differential Equations*, **2**(02), pp. 437–469.

Proceedings of *RAGtime 20–22, 15–19 Oct., 16–20 Sept., 19–23 Oct., 2018/2019/2020, Opava, Czech Republic*
Z. Stuchlík, G. Török and V. Karas, editors, Silesian University in Opava, 2020, pp. 145–152

Charged particle motion around Schwarzschild black hole with split monopole magnetosphere

Martin Kološ[1,a] Dilshodbek Bardiev[2,b]
and Bakhtinur Juraev[2,c]

[1]Research Centre for Theoretical Physics and Astrophysics, Institute of Physics,
Silesian University in Opava, Bezručovo nám. 13, CZ-746 01 Opava, Czech Republic
[2]National University of Uzbekistan, Tashkent 100174, Uzbekistan
[a]martin.kolos@fpf.slu.cz
[b]bagandikovic@gmail.com
[c]bahti-bahti@mail.ru

ABSTRACT
Charged particle dynamics around Schwarzschild black hole with split monopole magnetic field has been examined. Using effective potential technique the position of stable circular orbits off- and in-equatorial plane has been found. Equations of motion for charged particle trajectories has been solved numerically and some particle trajectories has been given. Also frequencies for perturbed particle circular orbit has been calculated.

Keywords: charged particle – black holes – split magnetic monopole

1 INTRODUCTION

Weak test magnetic fields will have negligible effect on background spacetime or on the motion of neutral particles. However, for the motion of charged test particles, the influence of the magnetic field on particle dynamics can be really large. For charged test particle with charge q and mass m moving in vicinity of a black hole (BH) with mass M surrounded by magnetic field of the strength B, one can introduce a dimensionless quantity $qBGM/mc^4$ that can be identified as relative Lorenz force. This quantity can be quite large even for weak magnetic fields due to the large value of the specific charge q/m. In our approach the "charged particle" can represent matter ranging from electron to some charged inhomogeneity orbiting in the innermost region of the accretion disk. The charged particle specific charges q/m for any such structure will then range from the electron maximum to zero.

In this paper we will concentrate our attention on BH magnetosphere given by split monopole solution Blandford and Znajek (1977). The radial profile of the split monopole magnetic field configuration could be relevant for magnetic filed generated by thin accretion disk around BH Komissarov (2004) or also for magnetosphere generated by another BH accretion configurations but close to the BH horizon Komissarov (2005).

978-80-7510-432-8

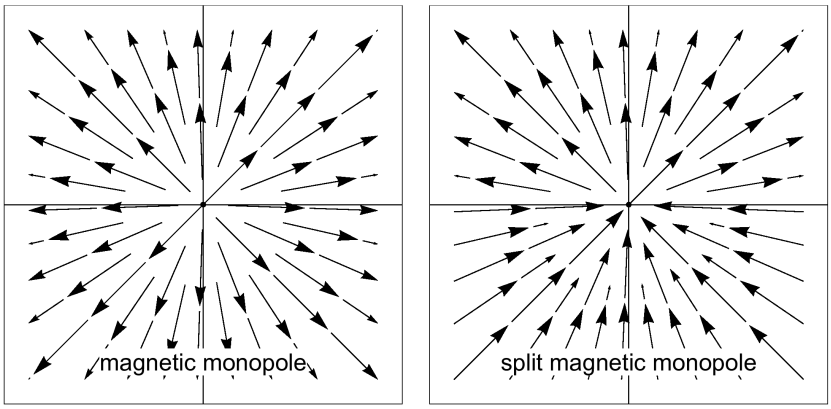

Figure 1. Magnetic field lines for monopole (left) and split monopole (right) solutions.

Throughout the present paper we use the spacelike signature $(-,+,+,+)$, and the system of geometric units in which $G = 1 = c$.

2 CHARGED PARTICLE DYNAMICS

We describe dynamics of charged particle with charge $q \neq 0$ in the vicinity of the Schwarzschild BH embedded in magnetic field, using Hamiltonian formalism Kološ et al. (2015).

The gravity will enter to the equations of motion through Schwarzschild black hole (with mass M) spacetime line element

$$\mathrm{d}s^2 = -\left(1-\frac{2M}{r}\right)\mathrm{d}t^2 + \left(1-\frac{2M}{r}\right)^{-1}\mathrm{d}r^2 + r^2\left(\mathrm{d}\theta^2 + \sin^2\theta\mathrm{d}\phi^2\right). \tag{1}$$

There are no magnetic monopoles in the classical theory of electromagnetism, and for magnetic field we have

$$\mathrm{div}\boldsymbol{B} = 0. \tag{2}$$

The source for magnetic monopole field, artificial magnetic monopole, will be located in coordinate system origin. Split monopole solution is monopole solution, where we change the orientation of magnetic filed lines below equatorial plane (III and IV quadrant) and hence the condition 2 will be satisfied, see Fig.1. The source for split monopole magnetic field configuration will be some electric current floating around the coordinate system origin in infinitesimally thin disk located in equatorial plane. In this work, we consider BH magnetosphere in the form of split monopole solution Blandford and Znajek (1977). The covariant component of the electromagnetic four-vector potential A^μ has only one non-zero component A_ϕ

$$A_\mu = (0,0,0,\epsilon\,|\cos\theta|), \tag{3}$$

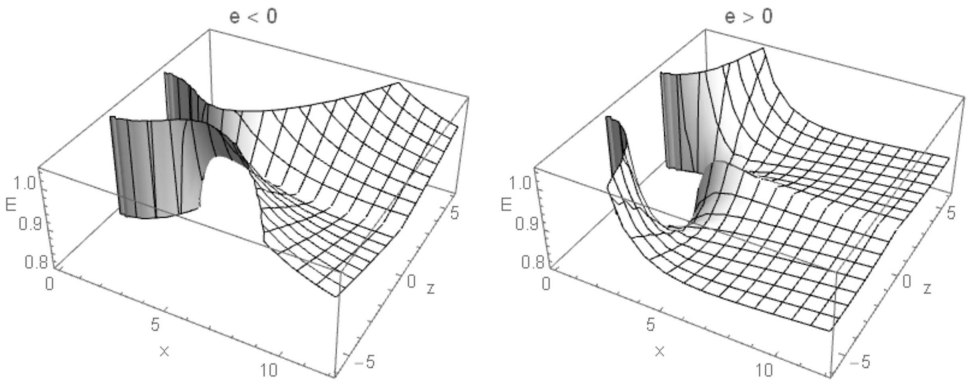

Figure 2. Effective potential $V_{\rm eff}(x, z)$ for charged particle motion around BH with split monopole magnetosphere.

Here the parameter ϵ specifies the magnetic field intensity. Split monopole magnetic field has same symmetries as the Schwarzschild BH background (1) - is static and spherically symmetric.

Hereafter, we put $M = 1$, i.e., we use dimensionless radial coordinate r (and time coordinate t). Cartesian coordinates can be found by the coordinate transformations

$$x = r\cos(\phi)\sin(\theta), \quad y = r\sin(\phi)\sin(\theta), \quad z = r\cos(\theta). \tag{4}$$

The equations of motion for charged particle can be obtained using Hamiltonian formalism

$$\frac{\mathrm{d}x^\mu}{\mathrm{d}\zeta} = \frac{\partial H}{\partial \pi_\mu}, \quad \frac{\mathrm{d}\pi_\mu}{\mathrm{d}\zeta} = -\frac{\partial H}{\partial x^\mu}, \qquad H = \frac{1}{2}g^{\alpha\beta}(\pi_\alpha - qA_\alpha)(\pi_\beta - qA_\beta) + \frac{m^2}{2} = 0, \tag{5}$$

where the kinematical four-momentum $p^\mu = mu^\mu = \mathrm{d}x^\mu/\mathrm{d}\zeta$ is related to the generalized (canonical) four-momentum π^μ by the relation $\pi^\mu = p^\mu + qA^\mu$. The affine parameter ζ of the particle is related to its proper time τ by the relation $\zeta = \tau/m$.

Due to the symmetries of the Schwarzschild spacetime (1) and the magnetic field (3), one can easily find the conserved quantities that are particle energy and axial angular momentum

$$\mathcal{E} = \frac{E}{m} = -\frac{\pi_t}{m} = -g_{tt}u^t, \quad \mathcal{L} = \frac{L}{m} = \frac{\pi_\phi}{m} = g_{\phi\phi}u^\phi + \frac{q}{m}A_\phi. \tag{6}$$

Using such symmetries one can rewrite the Hamiltonian (5) in the form

$$H = \frac{1}{2}g^{rr}p_r^2 + \frac{1}{2}g^{\theta\theta}p_\theta^2 + \frac{1}{2}g^{tt}E^2 + \frac{1}{2}g^{\phi\phi}(L - qA_\phi)^2 + \frac{1}{2}m^2 = H_{\rm D} + H_{\rm P}, \tag{7}$$

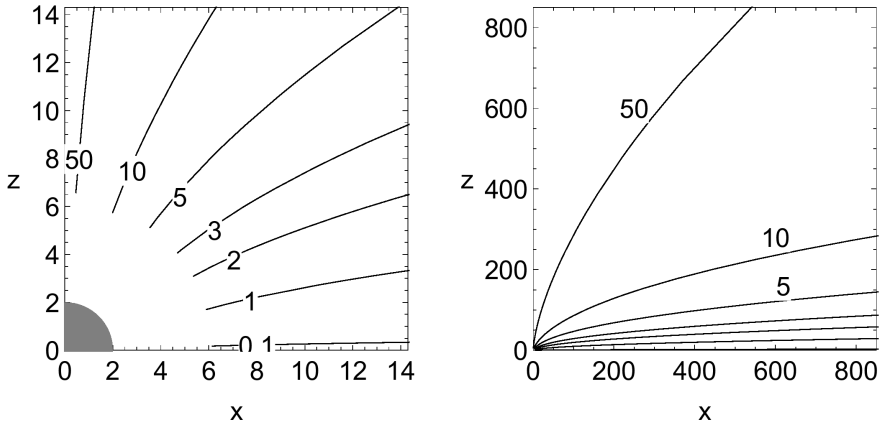

Figure 3. Positions of off equatorial stable circular orbits for various values of magnetic parameter e. The BH horizon is given by gray disk, while the points on each line denotes positions of stable circular orbits for different angular momenta L.

where we separated total Hamiltonian H into dynamical $H_{\rm D}$ (first two terms) and potential $H_{\rm P}$ (last two terms) parts.

For the description of charged particle motion we will use parameters: particle specific charge $\tilde{q}$, and magnetic field parameter e

$$\tilde{q} = q/m, \quad e = \epsilon\tilde{q}. \tag{8}$$

Energetic boundary for particle motion can be expressed from the equation (7)

$$\mathcal{E}^2 = V_{\rm eff}(r,\theta) \quad (\text{for } p_r = p_\theta = 0). \tag{9}$$

We introduced effective potential for charged particle $V_{\rm eff}(r,\theta)$ by the relation

$$V_{\rm eff}(r,\theta) \equiv -g_{tt}\left[g^{\phi\phi}\left(\mathcal{L} - \tilde{q}A_\phi\right)^2 + 1\right] = \left(1 - \frac{2}{r}\right)\left[\frac{(\mathcal{L} - e|\cos\theta|)^2}{r^2\cos^2\theta} + 1\right]. \tag{10}$$

The effective potential $V_{\rm eff}(r,\theta)$ combines the influence of gravitational potential (first term) with the influence of central force potential given by the specific angular momentum $\mathcal{L}$ and electromagnetic potential energy (terms in square brackets). The positive angular momentum of a particle $\mathcal{L} > 0$ means that the particle is revolved in the counter-clockwise motion around the black hole in x-y plane. Example of effective potential $V_{\rm eff}(r,\theta)$ behaviour can be found in Fig. 2. For charged particle we distinguish two following situations: *minus configuration* where $e < 0$ and *plus configuration* where $e > 0$.

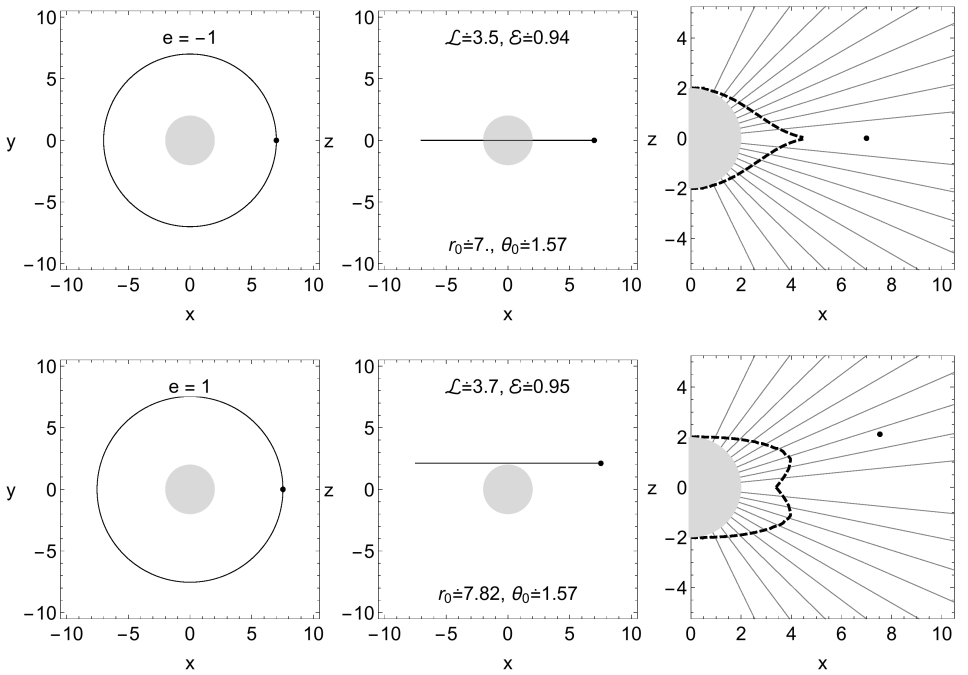

Figure 4. Example of stable circular equatorial and off-equatorial orbits around Schwarzschild BH (gray disk) with split monopole magnetosphere (gray lines). Particle trajectories are given by black curves, energetic boundary for the motion as dashed curves. Particle initially conditions are given in the figure, we also use $u^r_{(0)} = u^\theta_{(0)} = 0$.

3 TRAJECTORIES

Particles on circular orbits around compact object can form Keplerian accretion disk, with its inner edge given by innermost circular orbit (ISCO). The circular orbit parameters and ISCO position can be determined by examination of effective potential $V_{\rm eff}(r,\theta)$ function. The stationary points of the effective potential $V_{\rm eff}(r,\theta)$ function are given by

$$\partial_r V_{\rm eff}(r,\theta) = 0, \quad \partial_\theta V_{\rm eff}(r,\theta) = 0. \tag{11}$$

For minus configuration $e < 0$ the second equation in (11) has only one root at $\theta = \pi/2$. In another words, there is extrema of the $V_{\rm eff}(r,\theta)$ function located in the equatorial plane only.

For plus configuration $e > 0$ there are the second equation in the extrema condition (11) has more solutions - off-equatorial plane minima of effective potential $V_{\rm eff}$ can exist. The positions of the off-equatorial plane minima, where stable off-equatorial plane circular

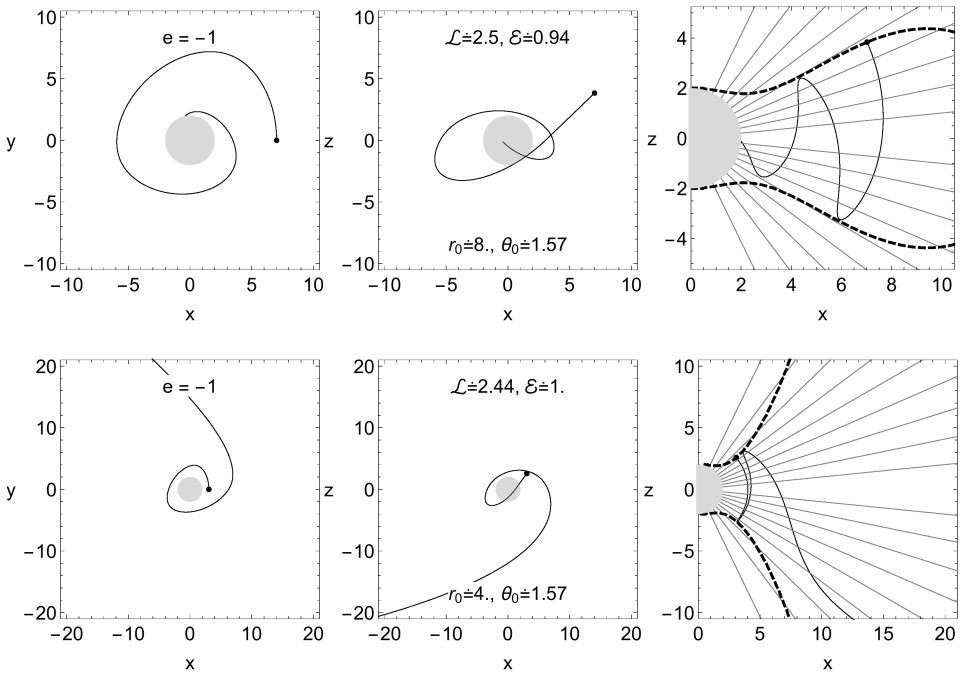

Figure 5. Charged particle capture and escape form Schwarzschild BH with split monopole magnetosphere, see Fig. 4 for description.

orbits are located, are given by

$$r_{\rm min} = \frac{1}{2}\left(\mathcal{L}^2 - e^2 + \sqrt{12e^2 + e^4 - 12\mathcal{L}^2 - 2e^2\mathcal{L}^2 + \mathcal{L}^4}\right), \tag{12}$$

$$\theta_{\rm min} = \arctan\left(\frac{\sqrt{\mathcal{L}^2 - e^2}}{e}\right). \tag{13}$$

The closest orbit to the BH horizon - the innermost off-equatorial plane stable circular orbit $r_{\rm off\,ISCO}$ is located at $r_{\rm off\,ISCO} = 6$M, see Fig.3.

Examples of charged particle circular orbits in and off-equatorial plane can be found in Fig. 4. We also give trajectories of escaping particle and particle captured by BH in Fig. 5. Magnetic monopole field has the same spherical symmetry as Schwarzschild BH metric background and hence there are no chaotic trajectories.

4 FREQUENCIES

If charged test particle is slightly displaced from the equilibrium position, which is located in a minimum of the effective potential $V_{\rm eff}(r,\theta)$ at r_0 and θ_0, the particle will start to

oscillate around the minimum realizing thus epicyclic motion governed by linear harmonic oscillations. For harmonic oscillations around the minima of the effective potential $V_{\rm eff}$, the evolution of the displacement coordinates $r = r_0 + \delta r, \theta = \theta_0 + \delta\theta$ is governed by the equations

$$\ddot{\delta r} + \omega_{\rm r}^2\,\delta r = 0, \quad \ddot{\delta\theta} + \omega_\theta^2\,\delta\theta = 0, \tag{14}$$

where dot denotes derivative with respect to the proper time τ of the particle ($\dot{x} = {\rm d}x/{\rm d}\tau$). Locally measured angular frequencies of the harmonic oscillatory motion are given by

$$\omega_{\rm r}^2 = \frac{1}{g_{rr}}\frac{\partial^2 H_{\rm P}}{\partial r^2}, \quad \omega_\theta^2 = \frac{1}{g_{\theta\theta}}\frac{\partial^2 H_{\rm P}}{\partial \theta^2}, \quad \omega_\phi = \frac{{\rm d}\phi}{{\rm d}\tau} = \mathcal{L}g^{\phi\phi} + e g_{tt}, \tag{15}$$

where we added also the Keplerian (axial) frequency ω_ϕ. Frequencies for perturbations of circular orbit in equatorial plane ($e < 0$) are

$$\omega_{\rm r}^2 = \frac{r-6}{r^4}, \quad \omega_\theta^2 = \frac{e^2(r-3)+r^2}{r^5}, \quad \omega_\phi^2 = \frac{1}{r^3}, \tag{16}$$

while for perturbations off-equatorial plane ($e > 0$) we have

$$\omega_{\rm r}^2 = \frac{r-6}{r^4}, \quad \omega_\theta^2 = \frac{e^2(r-3)+r^2}{r^5}, \quad \omega_\phi^2 = \frac{e^2(r-3)+r^2}{r^5}. \tag{17}$$

The locally measured angular frequencies $\omega_{\rm r}, \omega_\theta, \omega_\phi$, given by $\omega_\beta = {\rm d}\beta/{\rm d}\tau$ where $\beta \in \{{\rm r}, \theta, \phi\}$, are connected to the angular frequencies measured by the static distant observers (in the physical units) by the gravitational redshift transformation

$$\nu_\beta = \frac{1}{2\pi}\frac{c^3}{GM}\frac{{\rm d}\beta}{{\rm d}t} = \frac{1}{2\pi}\frac{c^3}{GM}\frac{\omega_\beta}{-g^{tt}\mathcal{E}(r)}. \tag{18}$$

Behavior of the frequencies $\nu_{\rm r}(r), \nu_\theta(r)$ and $\nu_\phi(r)$, as functions of the radial coordinate r, are demonstrated in Fig. 6 for both positive and negative magnetic parameters. The charged particle oscillations with frequencies $\nu_{\rm r}(r), \nu_\theta(r)$ and $\nu_\phi(r)$, could be used for fitting of still unsolved quasi-periodic oscillations (QPOs) observed in many Galactic Low Mass X-Ray Binaries (Kološ et al., 2015, 2017).

5 CONCLUSIONS

As general relativistic magnetohydrodynamics simulations are showing, the real magnetic field around BH can have quite complicated character Komissarov (2004, 2005). In this work we used split monopole magnetic field as simple model for large scale BH magnetosphere with radial character.

Split monopole magnetosphere around Schwarzschild BH will influence charged particle motion: for negative magnetic field parameter $e < 0$ we have standard stable circular orbits located in equatorial plane, while for positive magnetic field parameter $e > 0$ we have stable circular orbits located off-equatorial only. Innermost stable circular orbit is for both cases at radius $r_{\rm ISCO} = r_{\rm off\,ISCO} = 6$ M. Charged particle fundamental frequencies can be significantly influenced by presence of split monopole magnetic field.

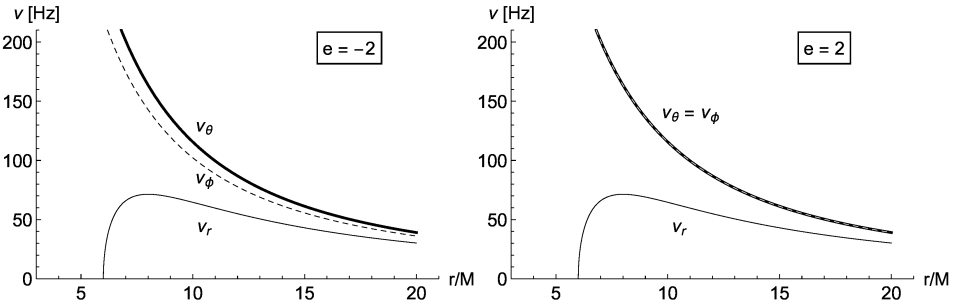

Figure 6. Frequencies for perturbation of in and off-equatorial plane circular orbits are ploted as function of radial position r. BH mass is take to be 10 solar masses.

ACKNOWLEDGEMENTS

The present work was created as a part of Erasmus+ mobility project and was supported by the GAČR 16-03564Y grant.

REFERENCES

Blandford, R. D. and Znajek, R. L. (1977), Electromagnetic extraction of energy from Kerr black holes, *Mon. Not. R. Astron Soc.*, **179**, pp. 433–456.

Kološ, M., Stuchlík, Z. and Tursunov, A. (2015), Quasi-harmonic oscillatory motion of charged particles around a Schwarzschild black hole immersed in a uniform magnetic field, *Classical and Quantum Gravity*, **32**(16), 165009, arXiv: 1506.06799.

Kološ, M., Tursunov, A. and Stuchlík, Z. (2017), Possible signature of the magnetic fields related to quasi-periodic oscillations observed in microquasars, *European Physical Journal C*, **77**, 860, arXiv: 1707.02224.

Komissarov, S. S. (2004), General relativistic magnetohydrodynamic simulations of monopole magnetospheres of black holes, *Mon. Not. R. Astron Soc.*, **350**, pp. 1431–1436, arXiv: astro-ph/0402430.

Komissarov, S. S. (2005), Observations of the Blandford-Znajek process and the magnetohydrodynamic Penrose process in computer simulations of black hole magnetospheres, *Mon. Not. R. Astron Soc.*, **359**, pp. 801–808, arXiv: astro-ph/0501599.

Proceedings of *RAGtime 20–22, 15–19 Oct., 16–20 Sept., 19–23 Oct., 2018/2019/2020, Opava, Czech Republic*
Z. Stuchlík, G. Török and V. Karas, editors, Silesian University in Opava, 2020, pp. 153–164

Simulations of black hole accretion torus in various magnetic field configurations

Martin Kološ[1,a] and Agnieszka Janiuk[2,b]

[1]Research Centre for Theoretical Physics and Astrophysics, Institute of Physics,
Silesian University in Opava, Bezručovo nám.13, CZ-74601 Opava, Czech Republic
[2]Center for Theoretical Physics, Polish Academy of Sciences,
Al. Lotnikow 32/46, 02-668 Warsaw, Poland
[a]martin.kolos@fpf.slu.cz
[b]agnes@cft.edu.pl

ABSTRACT
Using general relativistic magnetohydrodynamics simulations we study evolution of accretion torus around black hole endowed with five different initial magnetic field configurations: contour, loop, parabolic, monopole, uniform. Due to accretion of material onto black hole, parabolic magnetic field will develop in accretion torus funnel around vertical axis, while turbulent and chaotic magnetic field inside accretion torus will redistribute angular torus momentum inside torus and create corona around it.

Keywords: GRMHD simulation – accretion – black hole – magnetic field

1 INTRODUCTION

There are two long range forces in physics: gravity and electromagnetism (EM) and both of these forces are crucial for proper description of high energetic processes around black holes (BHs). In realistic astrophysical situations the EM field around a BH is not strong enough ($< 10^{18}$ Gs) to really contribute to spacetime curvature and rotating BH can be fully described by standard Kerr metric spacetime. Hence the EM field and matter orbiting around central BH can be considered just as test fields in axially symmetric Kerr spacetime background. While the distribution of matter around central BH can be well described by thin Keplerian accretion disk or thick accretion torus, the exact shape of EM field around BH, i.e. BH magnetosphere is more complicated. In the case of rotating neutron star (pulsar) inclined rotating dipole field is used - such magnetosphere is generated by currents flowing on the star surface. In the case of BHs one can assume the magnetosphere will be generated by currents flowing around BH inside accretion disk or torus.

Historically, the question of BH magnetosphere has been solved as vacuum solution of Maxwell equations in curved background. The solution of uniform magnetic field in Kerr metric has been found by Wald (Wald, 1974), and can serve as zero approximation to some more realistic BH magnetosphere. In elegant Wald uniform solution one can study

978-80-7510-432-8

combined effect of gravitational and Lorentz force acting on charged mass element. Unfortunately such electrovacuum stationary test field BH magnetosphere has limited astrophysical relevance - material orbiting around BH in the form of plasma should be included. Plasma effect on BH force-free magnetosphere has been included in the well-known work of Blandford & Znajek (Blandford and Znajek, 1977), where also the electromagnetic mechanism of BH rotational energy extraction has been introduced.

Several numerical techniques has been also employed, but the exact shape and intensity of BH magnetosphere, is still not yet properly resolved, although strong connection to the accretion processes is evident (Punsly, 2009; Meier, 2012). Simple and elegant solution of uniform magnetic field (Wald, 1974) could be used as first linear approximation to real BH magnetosphere model, but from GRMHD simulations of accretion processes one can expect the BH magnetosphere has more complicated structure and also changes in time (Tchekhovskoy, 2015; Janiuk et al., 2018). At small scales the turbulent magnetic field inside accretion disk is very important, since it enables the angular momentum transport inside the accretion disk due to the magnetorotational instability (MRI) (Balbus and Hawley, 1991; Sapountzis and Janiuk, 2019). At large scales one should use some analytic approximation to real turbulent large scale BH magnetosphere outside the accretion disk. The GRMHD simulations of magnetic field around BH (Nakamura et al., 2018; Porth et al., 2019; Lančová et al., 2019) can provide motivation for heuristic analytic solution for BH magnetosphere. Such analytic BH magnetosphere solution smooth out all small scale and fast time discrepancies and can represent real magnetic field around BH on long times and long scales. Inside this analytic BH magnetosphere one can then study fast physical processes like charged particle jet acceleration (Stuchlík and Kološ, 2016; Kopáček and Karas, 2018; Kopáček and Karas, 2020) which could be used as model for Ultra-High-Energy Cosmic Rays (UHECR) (Tursunov et al., 2020; Stuchlík et al., 2020).

2 NUMERICAL SIMULATION OF ACCRETION ONTO BH

In this technical section we will introduce equations for our model of accretion torus around BH. The equations will be given geometric units ($G = c = 1$) and as compared to the standard Gauss cgs system, the factor $1/\sqrt{4\pi}$ is absorbed in the definition of the magnetic field. Greek indices run through $[0, 1, 2, 3]$ while Roman indices span $[1, 2, 3]$.

2.1 Equations of ideal GRMHD in curved spacetime

In our simulations for this proceeding, black hole spin has been neglected, and Schwarzschild geometry has been used for description of central compact object. In the standard coordinates and in the geometric units Schwarzschild metrics takes form

$$\mathrm{d}s^2 = -f(r)\,\mathrm{d}t^2 + f(r)\,\mathrm{d}r^2 + r^2(\mathrm{d}\theta^2 + \sin^2\theta\,\mathrm{d}\phi^2), \qquad f(r) = 1 - \frac{2M}{r}, \tag{1}$$

where M gravitational mass of the central compact object. In the following, we put $M = 1$, i.e., we use dimensionless radial coordinate r and dimensionless time coordinate t. In the present paper we restrict our attention to the black hole spacetime region located above the outer event horizon at $r_\mathrm{h} = 2$.

The plasma orbiting around central Schwarzschild BH will be modeled using ideal GRMHD equations, where electric resistivity, self-gravitational, radiative and all non-equilibrium effects are neglected. The continuity, the four-momentum-energy conservation and induction equations within GRMHD framework are:

$$(\rho u^{\mu})_{;\mu} = 0, \qquad (T^{\mu}{}_{\nu})_{;\mu} = 0, \qquad (u^{\nu}b^{\mu} - u^{\nu}b^{\nu})_{;\mu} = 0, \tag{2}$$

The stress-energy tensor $T^{\mu\nu}$ is composed of gas and electromagnetic part

$$T^{\mu\nu}_{\rm gas} = (\rho + \tilde{u} + p)u^{\mu}u^{\nu} + pg^{\mu\nu}, \qquad T^{\mu\nu}_{\rm EM} = b^2u^{\mu}u^{\nu} + \frac{1}{2}b^2g^{\mu\nu} - b^{\mu}b^{\nu}, \tag{3}$$

$$T^{\mu\nu} = T^{\mu\nu}_{gas} + T^{\mu\nu}_{EM} = (\rho + \tilde{u} + p + b^2)u^{\mu}u^{\nu} + \left(p + b^2/2\right)g^{\mu\nu} - b^{\mu}b^{\nu}. \tag{4}$$

Variables in Eqs. (2-4) are: u^{μ} is gas four-velocity, $\tilde{u}$ is internal gas energy density, ρ is gas rest-mass density, p denotes gas pressure, and b^{μ} is the magnetic four-vector. Magnetic four-vector b^{μ} is related to magnetic field three-vector B^i

$$b^t = B^iu^{\mu}g_{i\mu}, \qquad b^i = (B^i + b^tu^i)/u^t. \tag{5}$$

Strength of the magnetic field in the fluid-frame is given by $b^2 = b^{\alpha}b_{\alpha}$, we can also define magnetization $\sigma = b^2/\rho$ and the plasma-β parameter $\beta = 2p/b^2$.

The equation of state (EOS) will be used in the form of ideal gas $p = (\hat{\gamma} - 1)\tilde{u}$, where $\hat{\gamma}$ is the adiabatic index (Gammie et al., 2003); for simulations with non-adiabatic EOS see (Janiuk, 2017).

2.2 Initial distribution of matter and EM field around central BH

Initial conditions in our simulation we will be toroidal perfect fluid configurations of neutral matter around central BH in the form of Polish donut model (Kozlowski et al., 1978; Abramowicz et al., 1978), while for magnetic field we will test various different configurations. The time evolution and relaxation of accretion torus magnetized matter and magnetic field into more realistic configuration will be studied using GRMHD simulation.

Due to stationarity and axial symmetry of our problem Eq. (1) we will assume $\partial_t X = 0$ and $\partial_{\varphi} X = 0$, with X being a generic spacetime tensor. In the equations for neutral matter distribution Eq. (2), the continuity equation is identically satisfied and the fluid dynamics is governed by the Euler equation only

$$(p + \varrho)u^{\alpha}\nabla_{\alpha}u^{\gamma} + h^{\beta\gamma}\nabla_{\beta}p = 0, \tag{6}$$

where $\nabla_{\alpha}g_{\beta\gamma} = 0$, $h_{\alpha\beta} = g_{\alpha\beta} + u_{\alpha}u_{\beta}$ is the projection tensor.

Polytropic equation of state is assumed in this work, and the matter is in orbital motion only $u^{\theta} = 0$ and $u^r = 0$. The Euler equation (6) can be written as an equation for the pressure $p(\varrho)$ as follows (Fishbone and Moncrief, 1976)

$$\frac{\partial_{\mu}p}{\varrho + p} = -\partial_{\mu}W + \frac{\Omega\partial_{\mu}l}{1 - \Omega\ell}, \qquad W \equiv -\ln\left(-g_{tt} - g_{\phi\phi}\Omega^2\right) + l_*\Omega, \tag{7}$$

where $l_* = l/(1 - \Omega l)$ is constant through the accretion torus and $\Omega = u^\phi/u^t$ is the fluid relativistic angular frequency related to distant observers. The fluid equilibrium is regulated by the balance of the gravitational and pressure terms versus centrifugal factors arising due to the fluid rotation and gravitational effects of the BH background.

Relativistic formulation of Maxwell's equations in curved spacetime is

$$\partial_\alpha F_{\mu\nu} + \partial_\nu F_{\alpha\mu} + \partial_\mu F_{\nu\alpha} = 0, \qquad \partial_\alpha F^{\alpha\beta} = \mu_0 J^\beta. \tag{8}$$

where J^β is electric current four-vector and electromagnetic tensor $F_{\mu\nu}$ is given by

$$F_{\mu\nu} = \partial_\mu A_\nu - \partial_\nu A_\mu, \tag{9}$$

where A^μ is electromagnetic four-vector. Assuming axial symmetry and absence of electric field, the only non-zero component of A^μ will be A^ϕ, and we can write $A^\mu = (0, 0, 0, A^\phi)$. The first of Maxwell's equations (8) is satisfied identically, while the second is giving the equation

$$r^2 \frac{\partial}{\partial r}\left[\left(1 - \frac{2}{r}\right)\frac{\partial}{\partial r} A_\phi\right] + \sin\theta \frac{\partial}{\partial \theta}\left(\frac{1}{\sin\theta}\frac{\partial}{\partial\theta} A_\phi\right) = -\mu_0 J^\phi r^4 \sin^2\theta. \tag{10}$$

This equation is Ampere's law, but it can be also wield as special case of Grad—Shafranov equation well known in MHD (Meier, 2012). Magnetic field three-vector $\mathbf{B} = (B^{\widehat{r}}, B^{\widehat{\theta}}, B^{\widehat{\phi}})$ can be related to four-vector component A_ϕ using

$$B^{\widehat{r}} = \frac{1}{\sqrt{-g}} A_{\phi,\theta} \quad B^{\widehat{\theta}} = -\left(1 - \frac{2}{r}\right)^{1/2} \frac{1}{r\sin\theta} A_{\phi,r}, \quad B^{\widehat{\phi}} = 0. \tag{11}$$

Magnetic field $\mathbf{B}$ is fully specified by electromagnetic four-potential A^μ, see Eq. (11). While the GRMHD HARM code is using magnetic field $\mathbf{B}$ in the simulations, it is sometimes more elegant to work with electromagnetic potential A^μ instead, for example visualization of magnetic field $\mathbf{B}$ can be easily plotted using contour lines of electromagnetic potential

$$A^\phi(r, \theta) = \text{const.} \tag{12}$$

2.3 HARM numerical code

HARM (High Accuracy Relativistic Magneto-hydrodynamics) is a conservative shock capturing scheme, for evolving the equations of GRMHD, developed by C. Gammie et al. (Gammie et al., 2003) and later improved and parallelized and released as HARM COOL code by A. Janiuk and her team at CFT PAS in Warsaw (Janiuk et al., 2018; Palit et al., 2019; Sapountzis and Janiuk, 2019).

Because stationary and spherically symmetric Schwarzschild BH metric (1) is not changing during whole GRMHD simulation, we can divide the whole space into fixed numerical grid. Moreover for our problem we restrict ourselves to two dimensional (r, θ) subspace. In this proceeding we use simulation domain $r \in [0.98\, r_\mathrm{h}, 100]$, $\theta \in [0, \pi]$ with resolutions 128×128 cells in nonlinear fixed grid.

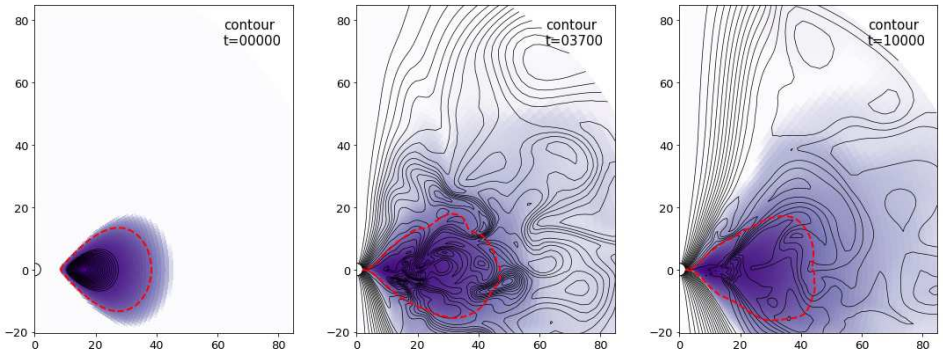

Figure 1. Stages of numerical GRMHD simulation of accretion torus in magnetic field following by matter density contours. Initial, middle and final stage of numerical GRMHD simulation of accretion torus in uniform magnetic field. Only 2D sections of full axially symmetric accretion torus are plotted, with x on horizontal axis and z (axis of BH rotation) on vertical axis. Black curves represent magnetic field lines, black circle at the origin of coordinates represent BH horizon. Different shades of blue color represents logarithmic density of matter from accretion torus - the region with 99% of maximal density (accretion torus itself) is bounded by thick red dashed curve, while the region with $10^{-6}\rho_{\rm max}$ (wind around accretion torus) is bounded by thick dashed curve. Time of the simulations in the unis of M is given in the right up corner.

3 RESULTS OF GRMHD SIMULATIONS

In this short contribution we will try to examine magnetic field structure around accreting BH using GRMHD simulations in HARM COOL code. As initial conditions for our simulations we will use accretion torus in hydrodynamic equilibrium which will be immersed into five different test magnetic field configurations.

Standard setting used in GRMHD simulations are: thick accretion torus around central rotating Kerr BH with dimensionless spin parameter $a = 0.9375$; torus inner radius at $r_{\rm in} = 6$ and the torus density maximum at $r_{\rm max} = 12$ (Gammie et al., 2003; Porth et al., 2019). Angular momentum distribution inside the torus is prescribed by Eq. (7) (Fishbone and Moncrief, 1976). In this proceeding we would like to simulate accretion torus around nonrotating Schwarzschild BH, but with similar central density as in Kerr BH case, hence for our simulation we use accretion torus with inner radius at $r_{\rm in} = 8$ and density maximum at $r_{\rm max} = 16$.

As seed for torus inhomogeneities, we perturb thermal pressure inside torus by $p^* = p\,(1 + X_p)$ function, where X_p is a uniformly distributed random variable between -0.02 and 0.02. We use ideal gas equation of state with an adiabatic index of $\hat{\gamma} = 4/3$. We will run the simulations till final time $t = 10^4$, which is around 30 orbits around black hole for matter from accretion torus. Since the accretion torus is in differential rotation we will relate torus orbital period to torus density maximum - one free test particle circular orbit around BH at $r = 16$ take $t \sim 363$ time in geometric units used in our simulation.

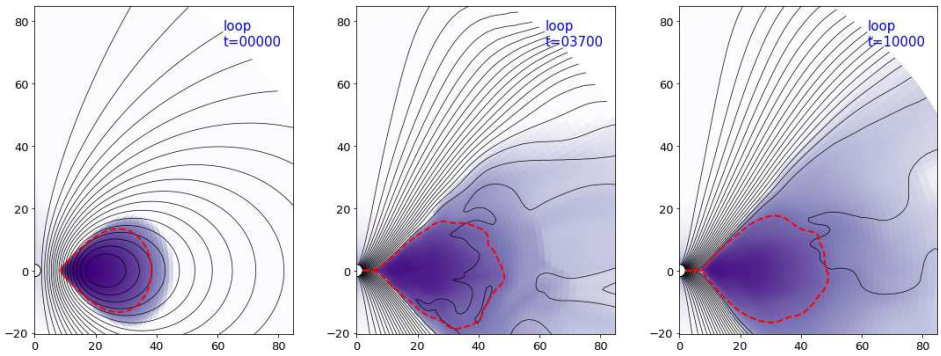

Figure 2. Stages of numerical GRMHD simulation of accretion torus in magnetic field given by current loop.

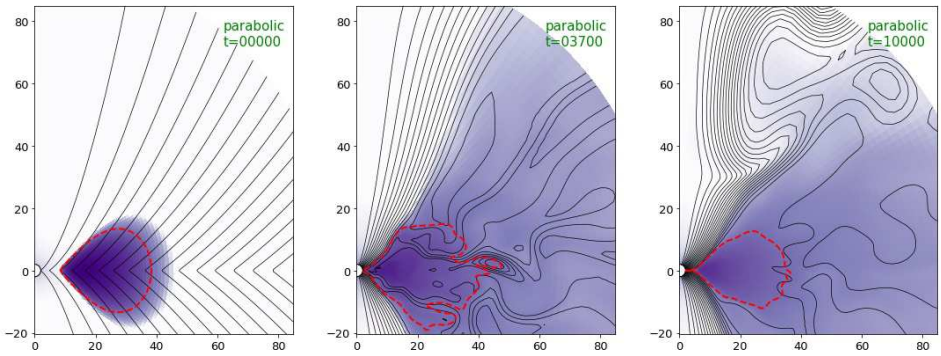

Figure 3. Stages of GRMHD simulation of accretion torus in split parabolic mag. field.

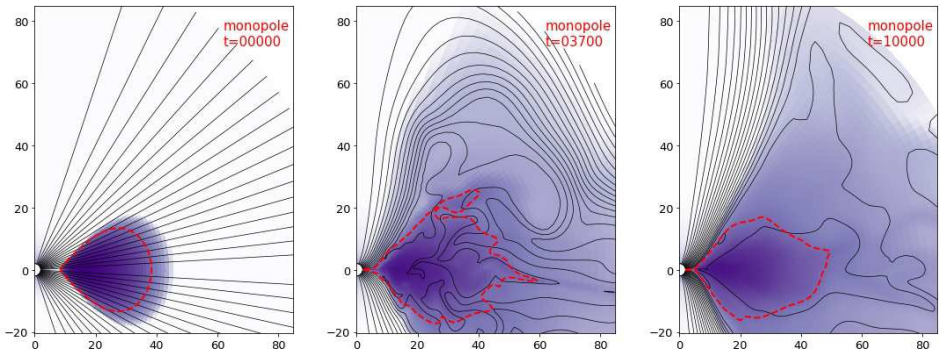

Figure 4. Stages of GRMHD simulation of accretion torus in split monopole mag. field.

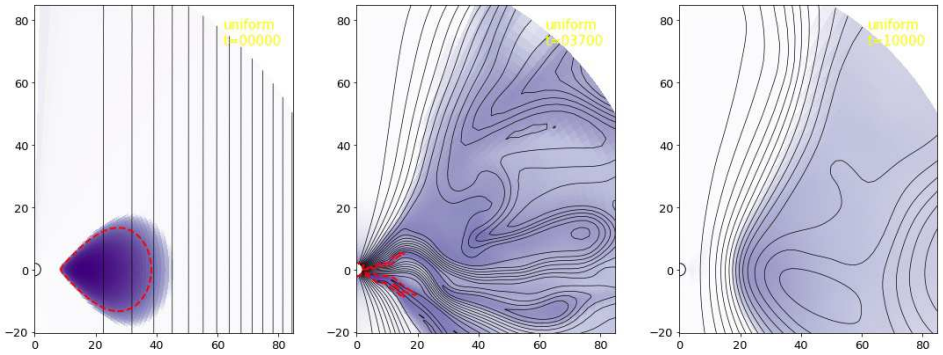

Figure 5. Stages of numerical GRMHD simulation of accretion torus in uniform magnetic field. Some problematic behavior is observed for uniform magnetic field configuration. Contrary to the previous four cases, the uniform magnetic field will disturb the accretion torus so much, that he will be quickly swallowed by BH. After ten orbits (middle subfigure) only strongly destroyed torus structure can be visible in the model.

Different magnetic field configurations will be tested as initial EM field in which the accretion torus will be immersed. Some of them are solution of vacuum Maxwell equation in curved spacetime Eq. (10), some of them are just heuristic approximation. We will start with standard initial setting for HARM torus simulation with poloidal magnetic field following the **contours** of matter (Gammie et al., 2003; Porth et al., 2019), given by

$$A_\phi = \frac{\rho(r,\theta)}{\rho_{\max}} - 0.2. \tag{13}$$

The magnetic field lines are closed curves focused around center at maximal torus density radius, see Fig. 1. Magnetic field strength has been set to $\beta = 2p_{\max}/b^2_{\max} = 100$, where $p_{\max}$ is gas pressure at torus density center ($r = 16, \theta = \pi/2$) and $b^2_{\max}$ is maximal magnetic field magnitude located at point $r \doteq 12, \theta \doteq 1.72$.

Another magnetic field configuration with closed magnetic field lines is magnetic field generated by current **loop** located in equatorial plane at given radii $r = R$ (Petterson, 1974), see Fig. 2. We will use simplified formula (1st leading term in expansion) for this Petterson current loop magnetic field (Kološ, 2017)

$$A_\phi = B\,\frac{R^3 r \sin\theta}{\left(R^2 + r^2\right)^{3/2}}, \tag{14}$$

where $B = 0.01726$ is constant specifying magnetic field magnitude and $R = 16$.

GRMHD simulations of accretion processes around central BH (Nakamura et al., 2018; Porth et al., 2019) are giving **parabolic** magnetic field as configuration inside the accretion torus funnel. Analytic formula for split parabolic magnetic field is given by

$$A_\phi = B\,r^k\,(1 - |\cos\theta|), \tag{15}$$

where we use coefficient $k = 0.75$ and constant $B = 0.14347$. Parabolic magnetic field with its open field-lines is plotted in Fig. 3.

Well know split **monopole** magnetic field, already studied using test particle dynamic approach in (Blandford and Znajek, 1977; Kološ et al., 2019), is given by

$$A_\phi = B(1 - |\cos\theta|), \tag{16}$$

where we use $B = 1.09014$. The magnetic field lines are straight radial lines pointing from the BH above equatorial plane, while to the BH below eq. plane, see Fig. 4. This magnetic configuration is solution of Maxwell equations (10), but current sheet in equatorial plane is needed.

Classical Wald **uniform** magnetic solution (Wald, 1974) is given by

$$A_\phi = B r^2 \sin^2\theta, \tag{17}$$

where $B = 0.00398$. The magnetic field lines are straight lines parallel with z-axis, see Fig. 5. This magnetic field configuration is solution of vacuum Maxwell equation (10), and has been extensively studied using test particle dynamic approach, see for example (Kološ et al., 2015) and reference there.

The initial matter configuration (accretion torus) is the same in all five studied magnetic field configurations and hence the plasma $\beta = 2p/b^2$ can be derived from magnetic strength b^2. Magnetic field strength in contour configuration, Eq. (13), has been normalized and plasma β-parameter has been set to $\beta = 100$. Maximal magnetic field strength $b^2_{\rm max} = 5.0272 \times 10^{-5}$ can be found at point $r \doteq 12, \theta \doteq 1.7$. Uniform, monopole, parabolic and loop magnetic fields Eqs. (14-17) have been normalized so they all will have magnetic field strength $b^2 = 5.0272 \times 10^{-5}$ at point $r \doteq 12, \theta \doteq 1.7$. From radial profiles of magnetic field strength b^2 plotted in Fig. 6 we can see that b^2 maximum for monopole, parabolic and loop magnetic fields is located at BH horizon. Uniform magnetic field strength b^2 is almost constant, having maximum at outer edge of simulation domain $r = 100$.

Magnetic field strength b^2 (magnetic field pressure) is closely related to magnetic field energy density. While the contour magnetic field has been defined in the accretion torus only, uniform/monopole/parabolic/loop magnetic fields exists through whole simulation domain. Monopole, parabolic and loop magnetic fields are strong close to the BH horizon, but they are decreasing in strength for larger r. On the another hand, the uniform magnetic field energy density is approximately constant. One can assume that there is much more energy located in uniform magnetic field configurations, then in another four studied cases.

As it could be seen from simulation results, presented in Figs. 1-5, from the beginning of the simulation till circa fifteen orbital periods ($t \sim 5000$) the accretion torus experience turbulent regime, when our tested magnetic field configurations are trying to reach some relaxed state. Contrary to the heuristic initial magnetic field configuration, the final relaxed state will be solution of full set of ideal MHD equations (2), and hence can represent proper realistic BH magnetosphere model. From twenty orbits ($t \sim 7500$) till the end of the simulation ($t = 10^4$) the accretion flow onto BH is stable and the accretion torus with magnetic field is not changing dramatically for contour/loop/parabolic/monopole magnetic field, see Fig. 7.

The evolution of uniform magnetic field configuration is different from another four studied cases and torus configuration gets destroyed by accretion and excretion. In Fig. 7

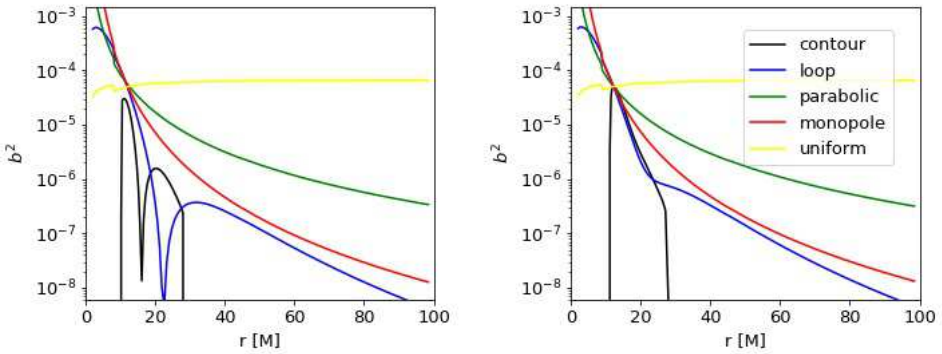

Figure 6. Radial profiles of magnetic field strength b^2 for all five magnetic field initial configurations. Left figure is section through whole (r, θ) simulation domain in equatorial plane ($\theta \doteq 1.57$), while right figure is section for $\theta \doteq 1.72$.

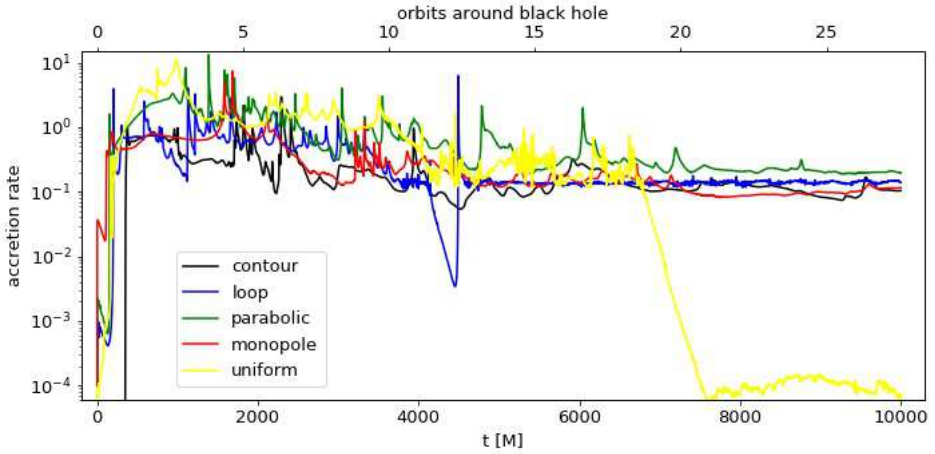

Figure 7. Mass accretion rate onto magnetized BH with different initial magnetic field configurations - see timeframes plotted at Figs. 1-5.

we can see slightly increased accretion rate at the beginning but only till $t \sim 7000$ after which the accretion process will stop and only little bit of torus mass remains in the simulation domain. Although the plasma β parameter is similar for all five studied magnetic field configuration, the amount of magnetic field energy hidden in uniform magnetic field is much bigger then in the another configurations.

The axially symmetric GRMHD simulations for our five different magnetic field configurations shows similar time evolution. After fifteen orbits they will all evolved into the more or less similar state with chaotic and turbulent magnetic field inside accretion

torus and regular parabolic magnetic field in accretion torus funnel. Only for uniform magnetic field initial configuration we can see different evolution. In this case the accretion torus structure is quickly destroyed and only some low density corona will remain around central BH.

In all tested cases the initial magnetic field configuration is quickly erased. After some time, one can distinguish in relaxed state solution new formed regions which can be classified according to the magnetic field shape and matter distribution.

Torus - Where the matter density in high $\rho \sim \rho_c$ and matter dominate over the magnetic field. Magnetic field inside torus is turbulent and chaotic and contributes to the accretion disk viscosity through magnetorotational instability.

Corona - Where the matter density is much lower $\rho \leq \rho_c$, but matter still dominate over the still turbulent magnetic field.

Jet funnel - Where the matter component is missing $\rho \leq 10^{-6}\rho_c$ and regular magnetic field with parabolic shape dominate the region.

Matter from corona low density region can be easily ionized at the jet funnel/corona boundary and description of collisionsless charged test particle dynamic in given magnetic field can be well applied in this jet funnel region. Funnel region with parabolic magnetic field will be important for charged particles acceleration to ultra-relativistic velocities (Stuchlík and Kološ, 2016; Kopáček and Karas, 2020).

4 CONCLUSIONS

In this short text we examined five different magnetic field configuration and tested their evolution during matter accretion process. Simple asymmetric torus orbiting around central BH has been penetrated by made up magnetic field configurations and using GRMHD numerical simulations we studied matter accretion onto BH and tested magnetic field evolution. Due to accretion of material onto BH, regular magnetic field with parabolic shape has develop in accretion torus funnel around vertical axis. Turbulent and chaotic magnetic field inside torus will redistribute angular momentum inside torus, create corona around the torus and will initiate BH accretion process.

In future work we would like to use GRMHD numerical simulations not only to calculate exact shape of BH magnetosphere but also to provide the distribution of different types of elementary particles and their velocities inside accretion torus (Janiuk et al., 2018). At the corona/jet funnel boundary, charged particles from the quasi-neutral accretion torus will no longer feel the pressure forces, and they can start to move under the combined influence of gravity and electromagnetic force. Hence charged particles can be accelerated and they can escape with ultrarelativistic velocities along magnetic field lines toward infinity (Tursunov et al., 2020; Stuchlík et al., 2020). Knowing the charged particles radiation losses over their full path to Earth atmosphere (Tursunov et al., 2018), one could be able to calculate the distribution of UHECR particles in the shower hitting Earth surface.

REFERENCES

Abramowicz, M., Jaroszynski, M. and Sikora, M. (1978), Relativistic, accreting disks, *Astron. Astrophys.*, **63**, pp. 221–224.

Balbus, S. A. and Hawley, J. F. (1991), A Powerful Local Shear Instability in Weakly Magnetized Disks. I. Linear Analysis, *The Astrophysical Journal*, **376**, p. 214.

Blandford, R. D. and Znajek, R. L. (1977), Electromagnetic extraction of energy from Kerr black holes, *Mon. Not. R. Astron Soc.*, **179**, pp. 433–456.

Fishbone, L. G. and Moncrief, V. (1976), Relativistic fluid disks in orbit around Kerr black holes, *The Astrophysical Journal*, **207**, pp. 962–976.

Gammie, C. F., McKinney, J. C. and Tóth, G. (2003), HARM: A Numerical Scheme for General Relativistic Magnetohydrodynamics, *The Astrophysical Journal*, **589**, pp. 444–457, arXiv: astro-ph/0301509.

Janiuk, A. (2017), Microphysics in the Gamma-Ray Burst Central Engine, *The Astrophysical Journal*, **837**(1), 39, arXiv: 1609.09361.

Janiuk, A., Sapountzis, K., Mortier, J. and Janiuk, I. (2018), Numerical simulations of black hole accretion flows, *arXiv e-prints*, arXiv:1805.11305, arXiv: 1805.11305.

Kološ, M., Stuchlík, Z. and Tursunov, A. (2015), Quasi-harmonic oscillatory motion of charged particles around a Schwarzschild black hole immersed in a uniform magnetic field, *Classical and Quantum Gravity*, **32**(16), 165009, arXiv: 1506.06799.

Kološ, M. (2017), Magnetic field generated by current loop in flat spacetime, in *Proceedings of RAGtime 17-19: Workshops on black holes and neutron stars*, pp. 91–98.

Kološ, M., Bardiev, D. and Juraev, B. (2019), Charged particle motion around Schwarzschild black hole with split monopole magnetosphere, in *Proceedings of RAGtime 20-21: Workshops on black holes and neutron stars*, pp. 00–00.

Kopáček, O. and Karas, V. (2018), Near-horizon Structure of Escape Zones of Electrically Charged Particles around Weakly Magnetized Rotating Black Hole, *The Astrophysical Journal*, **853**, 53, arXiv: 1801.01576.

Kopáček, O. and Karas, V. (2020), Near-horizon Structure of Escape Zones of Electrically Charged Particles around Weakly Magnetized Rotating Black Hole. II. Acceleration and Escape in the Oblique Magnetosphere, *The Astrophysical Journal*, **900**(2), 119, arXiv: 2008.04630.

Kozlowski, M., Jaroszynski, M. and Abramowicz, M. A. (1978), The analytic theory of fluid disks orbiting the Kerr black hole, *Astron. Astrophys.*, **63**, pp. 209–220.

Lančová, D., Abarca, D., Kluźniak, W., Wielgus, M., Sadowski, A. e., Narayan, R., Schee, J., Török, G. and Abramowicz, M. (2019), Puffy Accretion Disks: Sub-Eddington, Optically Thick, and Stable, *Astrophysical Journal Letters*, **884**(2), L37, arXiv: 1908.08396.

Meier, D. L. (2012), *Black Hole Astrophysics: The Engine Paradigm*.

Nakamura, M., Asada, K., Hada, K., Pu, H.-Y., Noble, S., Tseng, C., Toma, K., Kino, M., Nagai, H., Takahashi, K., Algaba, J.-C., Orienti, M., Akiyama, K., Doi, A., Giovannini, G., Giroletti, M., Honma, M., Koyama, S., Lico, R., Niinuma, K. and Tazaki, F. (2018), Parabolic Jets from the Spinning Black Hole in M87, *The Astrophysical Journal*, **868**(2), 146, arXiv: 1810.09963.

Palit, I., Janiuk, A. and Sukova, P. (2019), Effects of adiabatic index on the sonic surface and time variability of low angular momentum accretion flows, *Mon. Not. R. Astron Soc.*, **487**(1), pp. 755–768, arXiv: 1905.02289.

Petterson, J. A. (1974), Magnetic field of a current loop around a Schwarzschild black hole, *Phys. Rev. D*, **10**, pp. 3166–3170.

Porth, O., Chatterjee, K., Narayan, R., Gammie, C. F., Mizuno, Y., Anninos, P., Baker, J. G.,

Bugli, M., Chan, C.-k. and Davelaar, J. (2019), The Event Horizon General Relativistic Magnetohydrodynamic Code Comparison Project, *arXiv e-prints*, arXiv:1904.04923, arXiv: 1904.04923.

Punsly, B. (2009), *Black Hole Gravitohydromagnetics*, Springer-Verlag Berlin Heidelberg.

Sapountzis, K. and Janiuk, A. (2019), The MRI Imprint on the Short-GRB Jets, *The Astrophysical Journal*, **873**(1), 12, arXiv: 1802.02786.

Stuchlík, Z. and Kološ, M. (2016), Acceleration of the charged particles due to chaotic scattering in the combined black hole gravitational field and asymptotically uniform magnetic field, *European Physical Journal C*, **76**, 32, arXiv: 1511.02936.

Stuchlík, Z., Kološ, M., Kovář, J., Slaný, P. and Tursunov, A. (2020), Influence of Cosmic Repulsion and Magnetic Fields on Accretion Disks Rotating around Kerr Black Holes, *Universe*, **6**(2), p. 26.

Tchekhovskoy, A. (2015), Launching of Active Galactic Nuclei Jets, in I. Contopoulos, D. Gabuzda and N. Kylafis, editors, *The Formation and Disruption of Black Hole Jets*, volume 414 of *Astrophysics and Space Science Library*, p. 45.

Tursunov, A., Kološ, M., Stuchlík, Z. and Galtsov, D. V. (2018), Radiation Reaction of Charged Particles Orbiting a Magnetized Schwarzschild Black Hole, *The Astrophysical Journal*, **861**, 2, arXiv: 1803.09682.

Tursunov, A., Stuchlík, Z., Kološ, M., Dadhich, N. and Ahmedov, B. (2020), Supermassive Black Holes as Possible Sources of Ultrahigh-energy Cosmic Rays, *The Astrophysical Journal*, **895**(1), 14, arXiv: 2004.07907.

Wald, R. M. (1974), Black hole in a uniform magnetic field, *Phys. Rev. D*, **10**, pp. 1680–1685.

Proceedings of *RAGtime 20–22, 15–19 Oct., 16–20 Sept., 19–23 Oct., 2018/2019/2020, Opava, Czech Republic*
Z. Stuchlík, G. Török and V. Karas, editors, Silesian University in Opava, 2020, pp. 165–174

Emergence of magnetic null points in electro-vacuum magnetospheres of compact objects: The case of a plunging neutron star

Ondřej Kopáček[1,a] Tayebeh Tahamtan[2]
and Vladimír Karas[1]

[1]Astronomical Institute, Czech Academy of Sciences,
Boční II 1401, Prague, CZ-141 31, Czech Republic
[2]Institute of Theoretical Physics, Faculty of Mathematics and Physics, Charles University,
V Holešovičkách 2, Prague, CZ-180 00, Czech Republic
[a]kopacek@ig.cas.cz

ABSTRACT
Relativistic effects of compact objects onto electromagnetic fields in their vicinity are investigated using the test-field approximation. In particular, we study the possible emergence of magnetic null points which are astrophysically relevant for the processes of magnetic reconnection. While the magnetic reconnection occurs in the presence of plasma and may lead to violent mass ejection, we show here that strong gravitation of the supermassive black hole may actively support the process by suitably entangling the field lines even in the electro-vacuum description. In this contribution we further discuss the case of a dipole-type magnetic field of the neutron star on the plunging trajectory to the supermassive black hole. While we have previously shown that given model in principle admits the formation of magnetic null points, here we explore whether and where the null points appear for the astrophysically relevant values of the parameters.

Keywords: Black hole – neutron star – plunging trajectory – magnetosphere – magnetic reconnection

1 INTRODUCTION

Strong gravity may significantly influence the structure of the electromagnetic fields. On the other hand, the electromagnetic field contributes to the stress energy tensor $T_{\mu\nu}$, which constitutes the source term in the Einstein field equations, and thus affects the geometry of the spacetime. In general, we need to solve coupled Einstein-Maxwell equations to determine the geometry given by the metric $g_{\mu\nu}$ and the electromagnetic field described by the tensor $F_{\mu\nu}$. Nevertheless, the field intensities encountered in the astrophysical context (including extreme magnetic fields of magnetars; Beskin et al. (2016)) allow to employ

978-80-7510-432-8

the test-field approximation which neglects its effect on the geometry of the spacetime and Maxwell equations are solved independently to determine the electromagnetic field.

Curved spacetimes of compact objects (black holes or neutron stars) may substantially deform the electromagnetic field in its neighborhood and several purely relativistic effects arise. In particular, in the case of extremal rotating black hole any external axisymmetric magnetic field is expelled from the event horizon. Expulsion of the field lines is known as black hole Meissner effect and it was originally discussed for particular test-field solutions and later also for several exact solutions describing magnetized black holes (Bičák and Ledvinka, 2000; Karas and Vokrouhlický, 1991; Bičák and Janiš, 1985; Wald, 1974), and recently it has been further generalized using the formalism of weakly isolated horizons (Gürlebeck and Scholtz, 2018, 2017).

While the axisymmetry is crucial for the Meissner effect to operate, other types of relativistic effects may appear if we consider non-axisymmetric systems of magnetized compact objects. In particular, it has been shown that rotating Kerr black hole set in uniform motion in external asymptotically homogeneous magnetic field misaligned with the spin axis creates extremely complicated structure of field lines leading to the close contact of the lines of anti-parallel orientation and even to the formation of X-type null points (Karas and Kopáček, 2009). Magnetic null points are typically associated with the process of magnetic reconnection occurring in plasma and presence of charged matter and electric currents is essential for their emergence in classical magnetohydrodynamics. However, it appears that relevant structure of magnetic field may be formed due to relativistic effects of frame-dragging and spacetime curvature even in the electro-vacuum magnetospheres (Karas et al., 2014, 2013, 2012).

More recently, the vacuum magnetosphere of a neutron star in the vicinity of a supermassive black hole was considered in this context. In particular, it has been shown that magnetic null points may form even in the Rindler approximation of this system (Kopáček et al., 2018). Rindler limit neglects the spacetime curvature, which is justified in the very vicinity of the black hole horizon, and gravitation of the static black hole is represented solely by the acceleration (MacDonald and Suen, 1985). Rindler approximation is consistent with the final stages of the plunging trajectory until the neutron star reaches the horizon of the central massive black hole. While the formation of the magnetic nulls within the magnetosphere could support the release of energy leading to the acceleration of charged matter and high-power electromagnetic emission, the scenario in which a stellar mass compact object is inspiralling and finally plunges into supermassive black hole (i.e., extreme mass ratio inspiral; EMRI) also represents a promising source of gravitational waves for the future space-based observatories like LISA (Babak et al., 2017).

In the previous paper (Kopáček et al., 2018), we employed the Rindler approximation to find the solution of Maxwell equations for the plunging neutron star idealized as a rotating conducting spherical source of dipolar magnetic field arbitrarily inclined with respect to the axis of rotation. We discussed the solution in near zone (without the radiative terms) and, in particular, we found that magnetic null points may emerge within such magnetosphere. Nevertheless, the system was treated in geometrized units scaled by the mass of the central black hole and the consistency with the parameters of realistic astrophysical systems has not been verified. In this contribution we discuss physical values of parameters

and check whether the formation of magnetic null points in the magnetosphere is indeed astrophysically relevant.

2 PLUNGING NEUTRON STAR

We consider a neutron star at the final stage of its inspiral close to the horizon of the supermassive Schwarzschild black hole. Near-horizon region of the Schwarzschild spacetime may be approximated by the flat Rindler spacetime (D'Orazio and Levin, 2013; MacDonald and Suen, 1985; Rindler, 1966) with metric given in Rindler coordinates (t, x, y, z) as follows:

$$\mathrm{d}s^2 = -\alpha^2 \mathrm{d}t^2 + \mathrm{d}x^2 + \mathrm{d}y^2 + \mathrm{d}z^2, \tag{1}$$

where the lapse function α is given as $\alpha = g_H z$ and g_H denotes the horizon surface gravity. We use dimensionless geometrized units where the speed of light $c = 1$.

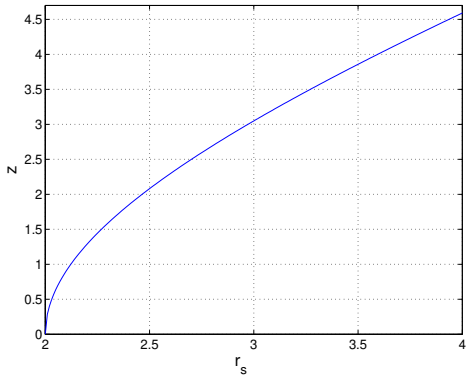

Figure 1. Rindler coordinate z, measuring the proper distance from the event horizon of the black hole, as a function of the Schwarzschild radial coordinate r_s.

Relation between Rindler coordinates and Minkowski coordinates (T, X, Y, Z) is given by the transformation:

$$T = z \sinh(g_H t), \quad X = x, \quad Y = y, \quad Z = z \cosh(g_H t). \tag{2}$$

Rindler coordinate z measures the proper distance from the horizon:

$$z = \int_2^{r_s} \frac{\mathrm{d}r}{\sqrt{1 - 2/r}} = \log\left(\frac{\sqrt{1 - 2/r_s} + 1}{|\sqrt{1 - 2/r_s} - 1|}\right) + r_s \sqrt{1 - 2/r_s}, \tag{3}$$

where r_s is the Schwarzschild radial coordinate scaled by the rest mass of the black hole M (i.e., $M = 1$ is set in all equations). Rindler horizon at $z = 0$ corresponds to the

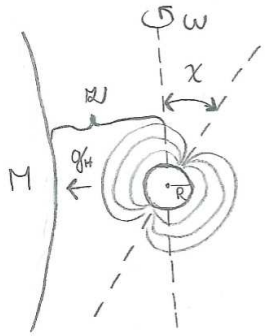

Figure 2. Sketch of the investigated model (not to scale). Neutron star of the radius R is rotating with the angular frequency ω and its dipole-type magnetic field is inclined by angle χ with respect to the rotation axis. The neutron star is plunging into the nearby horizon of the supermassive black hole with mass M and the proper distance from the horizon is given by the Rindler coordinate z. In the adopted near-horizon approximation, the gravitational effects of the black hole are fully characterized by the acceleration g_H.

Schwarzschild event horizon at $r_s = 2$ and Rindler approximation of the Schwarzschild spacetime thus remains appropriate for sufficiently small z (e.g., to keep $r_s \lessapprox 2.5$ demands $z \lessapprox 2$). The relation (3) between z and r_s is plotted in Fig. 1.

We consider a vacuum magnetosphere of a superconducting neutron star of radius R and rotation frequency ω as a source of dipolar magnetic field with the inclination angle χ with respect to the rotation axis. The neutron star is free-falling from its initial position at $(0, 0, Z_s)$ towards the horizon. The plunge is parametrized by the Rindler coordinate time t and the star's position in Rindler coordinates evolves as $(0, 0, Z_s/\cosh g_H t)$. Sketch of the model is presented in Fig. 2. Spatial distance from the dipole is expressed in Rindler coordinates as follows:

$$r = \sqrt{x^2 + y^2 + (z\,\cosh(g_H t) - Zs)^2}, \tag{4}$$

and retarded time τ is given as:

$$\tau = T - r = z\,\sinh(g_H t) - \sqrt{x^2 + y^2 + (z\,\cosh(g_H t) - Zs)^2}\,. \tag{5}$$

Resulting electromagnetic field for the freely falling rotating magnetic dipole was derived in Kopáček et al. (2018) while the similar setup was previously considered by D'Orazio and Levin (2013). In the near zone (dropping all radiative terms) we obtain following components of the magnetic field vector expressed in Rindler coordinates for the observer co-moving with the Rindler frame:

$$B_x = \frac{m}{r^5}\left\{\cosh(g_H t)\left[\sin(\chi)\left\{3\,x\,[x\,\cos(\omega\tau) + y\,\sin(\omega\tau)] - r^2\,\cos(\omega\tau)\right\} + 3\,(z\,\cosh(g_H t) - Z_s)\,x\,\cos(\chi)\right]\right.$$
$$- \omega\sinh(g_H t)\left[(z\,\cosh(g_H t) - Z_s)\sin(\chi)\left\{\frac{5\,R^2\,y}{r^2}\,(x\,\cos(\omega\tau) + y\,\sin(\omega\tau)) + (r^2 - R^2)\,\sin(\omega\tau)\right\}\right.$$
$$\left.\left. + R^2\,y\,\cos(\chi)\left(\frac{5\,(z\,\cosh(g_H t) - Z_s)^2}{r^2} - 1\right)\right]\right\}, \tag{6}$$

$$B_y = \frac{m}{r^5}\left\{\cosh(g_H t)\left[\sin(\chi)\left\{3\,y\,[x\,\cos(\omega\tau) + y\,\sin(\omega\tau)] - r^2\,\sin(\omega\tau)\right\} + 3\,(z\,\cosh(g_H t) - Z_s)\,y\,\cos(\chi)\right]\right.$$
$$+ \omega\sinh(g_H t)\left[(z\,\cosh(g_H t) - Z_s)\sin(\chi)\left\{\frac{5\,x\,R^2}{r^2}\,(x\,\cos(\omega\tau) + y\,\sin(\omega\tau)) + (r^2 - R^2)\,\cos(\omega\tau)\right\}\right.$$
$$\left.\left. + R^2\,x\,\cos(\chi)\left(\frac{5\,(z\,\cosh(g_H t) - Z_s)^2}{r^2} - 1\right)\right]\right\}, \tag{7}$$

$$B_z = \frac{m}{r^5}\left[3\,(z\,\cosh(g_H t) - Z_s)\,\sin(\chi)\,[x\,\cos(\omega\tau) + y\,\sin(\omega\tau)] + \cos(\chi)\left(3\,(z\,\cosh(g_H t) - Z_s)^2 - r^2\right)\right], \tag{8}$$

where m is the magnitude of the dipole moment.

3 MAGNETIC NULL POINTS

Magnetic null points (NPs) are locations within the magnetosphere where the components of the magnetic field (6)-(8) simultaneously vanish, i.e., $(B_x, B_y, B_z) = (0, 0, 0)$. We have numerically confirmed that NPs may develop in the employed model of the magnetosphere and identified following necessary conditions for their existence in given setup: (i) non-zero acceleration ($g_H > 0$); (ii) inclination of the dipole $\chi \neq 0, \pi/2$; and (iii) rotation of the dipole $\omega > 0$ (Kopáček et al., 2018). Moreover, we discussed how the emergence and the position of the NP depends on the Rindler time t and radius of the neutron star R for several values of inclination χ. Regarding the former, we were able to numerically locate the NP only for some period of coordinate time t which slightly differed for each χ. For fixed t we investigated the effect of radius R. We found that presence of conducting sphere is not crucial for the formation of NPs, which were located also for $R = 0$. With increasing value of R, the location of NP changes and may approach the surface of the star, however, it always remains outside ($r > R$).

In the previous analysis we discussed the formation of NPs and their locations with respect to the parameters in geometrized dimensionless units scaled by the rest mass of the central black hole M. In this contribution we intend to verify the consistency of observed effects with realistic astrophysical system of neutron star plunging into supermassive black hole.

Rotation of the neutron stars is detected directly in pulsars with observed periods in the range $P_{\rm SI} \approx 10^{-3} - 10$ s (Hessels et al., 2006; Tan et al., 2018) and angular frequency in SI units $\omega_{\rm SI} = 2\pi/P_{\rm SI}$ is related to its dimensionless value ω as follows:

$$\omega = \frac{\omega_{\rm SI}\ (1472\ \text{m})}{c}\left(\frac{M}{M_\odot}\right), \tag{9}$$

where the factor 1472 m is the value of solar mass $M_\odot$ in geometrized units.

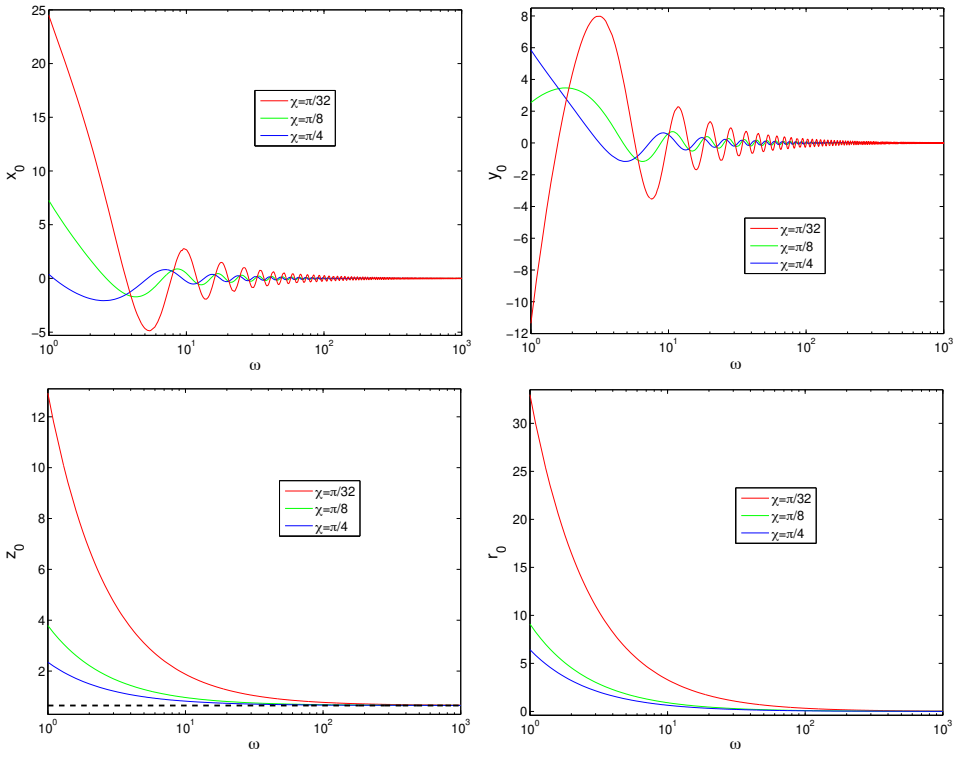

Figure 3. Rindler coordinates x_0, y_0, z_0 and the distance from the dipole r_0 of the magnetic null point as a function of the rotation frequency ω for several values of the inclination angle χ. Dashed line in the bottom left panel indicates the current location of the plunging neutron star at $z = 0.648$. Remaining parameters of the model are fixed as: $Z_s = 1$, $g_H t = 1$ and $R = 10^{-5}$.

Radius of the neutron star is $R_{\rm SI} \approx 10\,$km and its value R in dimensionless units is given as :

$$R = \frac{R_{\rm SI}}{(1472\ {\rm m})}\left(\frac{M_\odot}{M}\right). \tag{10}$$

For the central black hole we consider a mass range of $M \approx 10^6 - 10^9 M_\odot$. The lower mass limit yields the dimensionless frequency in the range $\omega \approx 3 - 3\times 10^4$ while the upper limit leads to $\omega \approx 3\times 10^3 - 3\times 10^7$. In the previous analysis (Kopáček et al., 2018) we fixed the frequency as $\omega = 1$ which is, however, below the relevant astrophysical range, and discussed the role of remaining parameters. Here we complete the discussion and study the effect of increasing ω on the formation and location of the NP in the magnetosphere.

Iterative root-finding routine is applied to numerically locate NPs of the field (6)-(8) with sufficient precision. In Fig. 3 we present Rindler coordinates x_0, y_0, z_0 and the distance r_0 of the NP as a function of ω for several values of inclination χ. It shows that the NP gradually

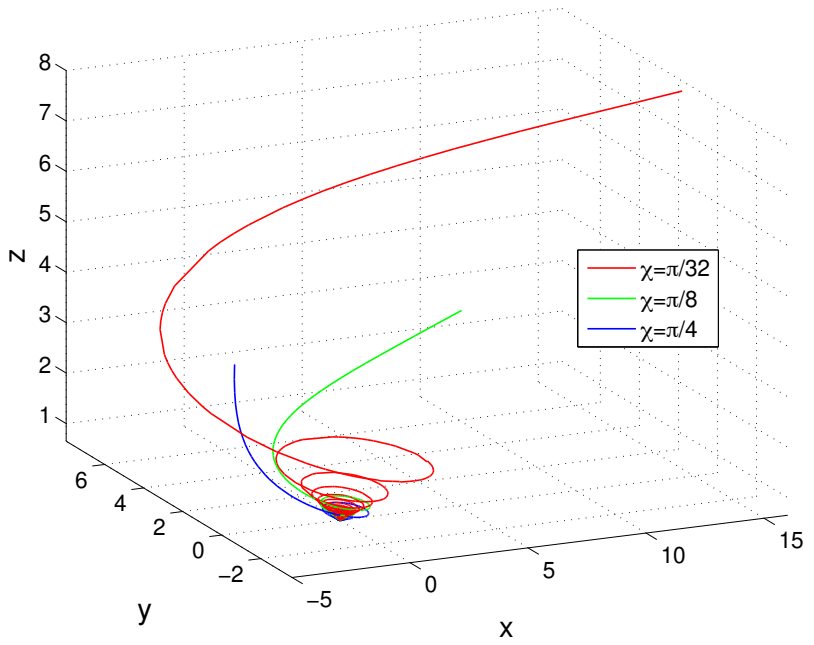

Figure 4. Locations of the magnetic null points with varying frequency ω for several values of the inclination angle χ. Magnetic null points gradually approach the neutron star located at $(x, y, z) = (0, 0, 0.648)$ as ω increases. Same data sets as in Fig. 3 are presented here.

approaches the neutron star as ω increases and that for each ω the NP is always closer for higher inclinations. Locations of the same set of NPs are presented in 3D plot in Fig. 4 which shows the gradual *inspiral* of the NP to the vicinity of the neutron star as the rotation frequency rises.

The values of remaining parameters of the model were fixed as: $Z_s = 1$, $g_H t = 1$ and $R = 10^{-5}$. Given value of R corresponds to the mass $M \approx 10^6\ M_\odot$ set in Eq. (10). In agreement with previous results we observe that NPs approach the neutron star but always remain above its surface. The value of the initial location of the star $Z_s = 1$ corresponds to the Schwarzschild radial coordinate $r_s \approx 2.1$ which is consistent with the Rindler approximation. The choice of $g_H t = 1$ does not put any astrophysical constraint as the Rindler coordinate time t is a free parameter which parametrizes the plunge.

The behavior of the magnetic field close to the NP with $\omega = 100$ and $\chi = \pi/32$ is shown in Fig. 5. Structure of the field lines in this region becomes very complicated and the field intensity changes rapidly on the small spatial scale. With higher ω the variability of the field in the close vicinity of the neutron star further increases and makes the structure of the field lines too complex for the visual inspection.

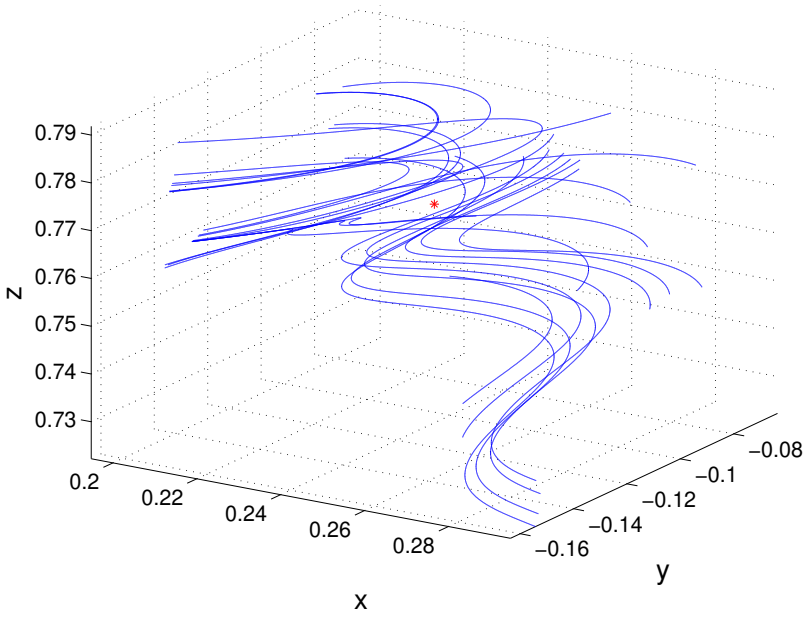

Figure 5. Magnetic field lines in the vicinity of the null point (red mark) located at $x_0 = 0.245$, $y_0 = -0.114$ and $z_0 = 0.771$. The following values of parameters are set: $Z_s = 1$, $g_H t = 1$, $\omega = 100$, $\chi = \pi/32$ and $R = 10^{-5}$.

For the same reason, the numerical method used to locate NPs encounters increasing difficulties for $\omega \gtrsim 1000$. However, the behavior for $\omega \leq 1000$ observed in Figs. 3 and 4 suggests that NPs would further approach the surface of the neutron star. With high spin frequencies, $\omega > 1000$, we expect to find the NPs in the immediate neighborhood of the neutron star[1], which is located near the horizon of the central black hole and Rindler approximation may thus be applied to describe this region of the magnetosphere.

4 SUMMARY

Locations of magnetic null points which emerge in the electro-vacuum magnetosphere of the neutron star near the supermassive black hole were discussed. We verified the astrophysical relevance of the investigated scenario and completed our previous analysis. In particular, we studied the role of spin frequency ω and found that realistic values of ω generally allow the formation of the NP close to the neutron star, which guarantees the consistency with employed Rindler approximation of the Schwarzschild spacetime.

[1] The formation of the NP within the superconducting interior of the star is not possible as demonstrated in previous paper (Kopáček et al., 2018).

The results suggest that during the final stages of the inspiral, the strong gravity effects of central black hole support the release of electromagnetic energy in the process of magnetic reconnection leading to the acceleration of charged particles and powerful emission of electromagnetic radiation from the magnetosphere of the infalling neutron star.

ACKNOWLEDGEMENTS

This work was supported from the following grants of the Grant agency of the Czech republic: No. 17-06962Y (O. K.), No. 17-13525S (T. T.) and No. 19-01137J (V. K.). We acknowledge the Inter-Excellence COST project LTC 18058 of the Czech Ministry of Education, Youth and Sports.

REFERENCES

Babak, S., Gair, J., Sesana, A., Barausse, E., Sopuerta, C. F., Berry, C. P. L., Berti, E., Amaro-Seoane, P., Petiteau, A. and Klein, A. (2017), Science with the space-based interferometer LISA. V. Extreme mass-ratio inspirals, *Physical Reiew D*, **95**(10), 103012, arXiv: 1703.09722.

Beskin, V. S., Balogh, A., Falanga, M., Lyutikov, M., Mereghetti, S., Piran, T. and Treumann, R. A. (2016), *The Strongest Magnetic Fields in the Universe*.

Bičák, J. and Janiš, V. (1985), Magnetic fluxes across black holes, *Monthly Notices of the Royal Astronomical Society*, **212**, pp. 899–915.

Bičák, J. and Ledvinka, T. (2000), Electromagnetic fields around black holes and Meissner effect, *Nuovo Cimento B Serie*, **115**, p. 739, arXiv: gr-qc/0012006.

D'Orazio, D. J. and Levin, J. (2013), Big black hole, little neutron star: Magnetic dipole fields in the Rindler spacetime, *Physical Reiew D*, **88**(6), 064059, arXiv: 1302.3885.

Gürlebeck, N. and Scholtz, M. (2017), Meissner effect for weakly isolated horizons, *Physical Reiew D*, **95**(6), 064010, arXiv: 1702.06155.

Gürlebeck, N. and Scholtz, M. (2018), Meissner effect for axially symmetric charged black holes, *Physical Reiew D*, **97**(8), 084042, arXiv: 1802.05423.

Hessels, J. W. T., Ransom, S. M., Stairs, I. H., Freire, P. C. C., Kaspi, V. M. and Camilo, F. (2006), A Radio Pulsar Spinning at 716 Hz, *Science*, **311**, pp. 1901–1904, arXiv: astro-ph/0601337.

Karas, V., Kopacek, O., Kunneriath, D. and Hamersky, J. (2014), Oblique Magnetic Fields and the Role of Frame Dragging near Rotating Black Hole, *Acta Polytechnica*, **54**, pp. 398–413, arXiv: 1408.2452.

Karas, V. and Kopáček, O. (2009), Magnetic layers and neutral points near a rotating black hole, *Classical and Quantum Gravity*, **26**(2), 025004, arXiv: 0811.1772.

Karas, V., Kopáček, O. and Kunneriath, D. (2012), Influence of frame-dragging on magnetic null points near rotating black holes, *Classical and Quantum Gravity*, **29**(3), 035010, arXiv: 1201.0009.

Karas, V., Kopáček, O. and Kunneriath, D. (2013), Magnetic Neutral Points and Electric Lines of Force in Strong Gravity of a Rotating Black Hole, *International Journal of Astronomy and Astrophysics*, **3**, pp. 18–24, arXiv: 1303.7251.

Karas, V. and Vokrouhlický, D. (1991), On interpretation of the magnetized Kerr-Newman black hole., *Journal of Mathematical Physics*, **32**, pp. 714–716.

Kopáček, O., Tahamtan, T. and Karas, V. (2018), Null points in the magnetosphere of a plunging neutron star, *Physical Reiew D*, **98**(8), 084055, arXiv: 1810.04220.

MacDonald, D. A. and Suen, W.-M. (1985), Membrane viewpoint on black holes: Dynamical electromagnetic fields near the horizon, *Physical Reiew D*, **32**, pp. 848–871.

Rindler, W. (1966), Kruskal Space and the Uniformly Accelerated Frame, *American Journal of Physics*, **34**, pp. 1174–1178.

Tan, C. M., Bassa, C. G., Cooper, S., Dijkema, T. J., Esposito, P., Hessels, J. W. T., Kondratiev, V. I., Kramer, M., Michilli, D., Sanidas, S., Shimwell, T. W., Stappers, B. W., van Leeuwen, J., Cognard, I., Grießmeier, J.-M., Karastergiou, A., Keane, E. F., Sobey, C. and Weltevrede, P. (2018), LOFAR Discovery of a 23.5 s Radio Pulsar, *The Astrophysical Journal*, **866**, 54, arXiv: 1809.00965.

Wald, R. M. (1974), Black hole in a uniform magnetic field, *Phys. Rev. D*, **10**, pp. 1680–1685.

Proceedings of *RAGtime 20–22, 15–19 Oct., 16–20 Sept., 19–23 Oct., 2018/2019/2020, Opava, Czech Republic*
Z. Stuchlík, G. Török and V. Karas, editors, Silesian University in Opava, 2020, pp. 175–184

Probing dark energy through perfect fluid thermodynamics

Georgios Lukes-Gerakopoulos[1,a] Giovanni Acquaviva[2,b] and Charalampos Markakis[3,4,5,c]

[1]Astronomical Institute of the Academy of Sciences of the Czech Republic, Boční II 1401/1a, CZ-141 31 Prague, Czech Republic
[2]Institute of Theoretical Physics, Faculty of Mathematics and Physics, Charles University, CZ-180 00 Prague, Czech Republic
[3]DAMTP, University of Cambridge, Wilberforce Rd, Cambridge CB3 0WA, UK
[4]NCSA, University of Illinois at Urbana-Champaign, 1205 West Clark St, MC-257, Urbana, IL 61801, USA
[5]School of Mathematical Sciences, Queen Mary University of London, Mile End Road, London E1 4NS, UK
[a]gglukes@gmail.com
[b]gioacqua@gmail.com
[c]c.markakis@damtp.cam.ac.uk

ABSTRACT
We demonstrate that the thermodynamics of a perfect fluid describing baryonic matter can, in certain limits, lead to an equation of state similar to that of dark energy. We keep the cosmic fluid equation of state quite general by just demanding that the speed of sound is positive and less than the speed of light. In this framework, we discuss some propositions by looking at the asymptotic behaviour of the cosmic fluid.

Keywords: Dark energy – perfect fluid thermodynamics

1 INTRODUCTION

In this work we attempt to tackle the issue of dark energy (see, e.g., Peebles and Ratra, 2003) by considering just usual baryonic matter in an ever-expanding Universe. We try to keep the investigation's assumptions as general as possible. Thus, we do not specify the equation of state (EOS) and we avoid to limit the study to a specific spacetime. In this framework the baryonic matter is described by an irrotational relativistic perfect fluid. For our analysis we follow a perfect fluid formalism introduced by Lichnerowicz (1967) and Carter (1979), which in recent works was employed mainly for neutron stars (see, e.g., Gourgoulhon, 2006; Markakis et al., 2017).

In particular, we consider a perfect fluid in an equilibrium configuration with proper energy density ϵ. The state of the fluid depends on two parameters, which can be taken

978-80-7510-432-8

to be the rest-mass density ρ and specific entropy (entropy per unit rest-mass) s. Then the EOS of the fluid is given by a function

$$\epsilon = \epsilon(\rho, s) \ . \tag{1}$$

From Eq. (1) one can derive the first law of thermodynamics:

$$d\epsilon = \mu \frac{d\rho}{m_b} + T d(s\rho) \, , \tag{2}$$

where m_b denotes the rest mass of a baryon and μ is the baryon chemical potential. The pressure p and specific enthalpy h are functions of ρ and s entirely determined by Eq. (1):

$$p = -\epsilon + \rho T \, s + \frac{\mu}{m_\mathrm{b}} \rho \, , \tag{3}$$

$$h := \frac{\epsilon + p}{\rho} = \frac{\mu}{m_\mathrm{b}} + T s \ . \tag{4}$$

Note that Eq. (3) can be obtained by the extensivity property of the energy density, while the second equality of Eq. (4) comes from Eq. (3). Now Eqs. (2) and (4) yield the thermodynamic relations

$$\mathrm{d}\epsilon = h \, \mathrm{d}\rho + \rho T \, \mathrm{d}s \, , \tag{5}$$

$$\mathrm{d}p = \rho \, \mathrm{d}h - \rho T \, \mathrm{d}s \, . \tag{6}$$

Moreover, writing $h = h(\rho, s)$ and differentiating yields

$$\mathrm{d}h = \frac{h c_\mathrm{s}^2}{\rho} \mathrm{d}\rho + \left. \frac{\partial h}{\partial s} \right|_\rho \mathrm{d}s \, , \tag{7}$$

where

$$c_\mathrm{s}^2 = \left. \frac{\partial p}{\partial \epsilon} \right|_s = \frac{\rho}{h} \left. \frac{\partial h}{\partial \rho} \right|_s \tag{8}$$

is the speed of sound. In order to ensure causal evolution, given the upper bound for signal propagation set by the speed of light, physically admissible fluids should have

$$0 \lesssim s_m^2 \leq c_s^2 \leq 1, \tag{9}$$

where s_m^2 is an arbitrarily close to zero cut-off value for the speed of sound.

A simple perfect fluid is characterized by the energy-momentum tensor

$$T_\alpha{}^\beta = h \rho \, u_\alpha u^\beta + p \, g_\alpha{}^\beta = (\epsilon + p) \, u_\alpha u^\beta + p \, g_\alpha{}^\beta \, , \tag{10}$$

where $g_{\alpha\beta}$ is the spacetime metric and u^μ is the timelike vector tangent to the fluid's flow, satisfying the normalization condition $u^\alpha u_\alpha = -1$. Such energy-momentum tensor is the

source in Einstein's field equations (EFE) $G_\alpha{}^\beta = T_\alpha{}^\beta$, which are assumed to hold throughout this work. By taking the covariant divergence of EFE, the doubly contracted Bianchi identities $\nabla_\beta G_\alpha{}^\beta \equiv 0$ assure the covariant conservation of energy-momentum

$$\nabla_\beta T_\alpha{}^\beta = 0\,, \tag{11}$$

which is the relativistic version of Euler equation. Using Eq. (6) with variation evaluated along the flow lines ($d \to u^\alpha \nabla_\alpha$) and thanks to the normalization of the timelike vector u^α, eq.(11) takes the form

$$\nabla_\alpha T^\alpha{}_\beta = p_\beta \nabla_\alpha (\rho u^\alpha) + \rho \left[u^\alpha \Omega_{\alpha\beta} - T \nabla_\beta s \right] = 0\,, \tag{12}$$

where $p_\alpha = h u_\alpha$ is the *canonical momentum* of a fluid element, and its exterior derivative $\Omega_{\alpha\beta} := \nabla_\alpha p_\beta - \nabla_\beta p_\alpha$ is the *canonical vorticity 2-form*. If we assume the rest-mass (or baryon) conservation

$$\nabla_\alpha (\rho u^\alpha) = 0\,, \tag{13}$$

Eq. (12) yields the relativistic Euler equation in the canonical form:

$$u^\alpha \Omega_{\alpha\beta} = T \nabla_\beta s\,. \tag{14}$$

Contraction of eq. (14) with the four-velocity u^β makes the left-hand side vanish identically.[1] Hence the specific entropy is constant along the flow lines:

$$u^\alpha \nabla_\alpha s = 0\,. \tag{15}$$

This reflects the fact that the Euler equation describes *adiabatic flows*, *i.e.* there are no heat fluxes in the fluid nor particle production. The adiabatic character of the fluid as expressed by Eq. (15) is a consequence of assuming rest-mass conservation Eq. (13).

2 THERMODYNAMICAL RELATIONS FOR AN IRROTATIONAL FLUID

The condition for irrotational fluid flow is $\Omega_{\alpha\beta} = 0$, and implies through Eq. (14) that the specific entropy is constant, *i.e.* $\mathrm{d}s = 0$. The fundamental relations Eqs. (5)-(7) reduce to

$$\mathrm{d}h = \frac{h\, c_\mathrm{s}^2}{\rho}\, \mathrm{d}\rho\,, \tag{16}$$

$$\mathrm{d}\epsilon = h\, \mathrm{d}\rho\,, \tag{17}$$

$$\mathrm{d}p = \rho\, \mathrm{d}h\,. \tag{18}$$

[1] This is because the left-hand side, after contraction with u^β, ends up being a product of the symmetric term $u^\alpha u^\beta$ with the antisymmetric 2-form $\Omega_{\alpha\beta}$.

Using the limits set by Eq. (9) and making the reasonable assumption that the rest-mass density is a positive quantity, since we consider fluid composed only of baryonic matter, we arrive through Eq. (16) to

$$\int_{\rho_1}^{\rho} \frac{s_m^2 \mathrm{d}\rho'}{\rho'} \leq \int_{\rho_1}^{\rho} \frac{c_s^2 \mathrm{d}\rho'}{\rho'} \leq \int_{\rho_1}^{\rho} \frac{\mathrm{d}\rho'}{\rho'} \quad \Rightarrow \quad \left(\frac{\rho}{\rho_1}\right)^{s_m^2} \leq \frac{h}{h_1} \leq \frac{\rho}{\rho_1}\,, \tag{19}$$

where index "1" refers to the integration constants of the specific fluid with equation of state described by the speed of sound c_s^2, not by the lower bound and upper bounds of Eq. (9). Note that we have assumed that $d\rho > 0$. Eq. (19) implies $\left(\frac{\rho}{\rho_1}\right)^{s_m^2-1} \leq 1$, which gives that $\rho_1 \leq \rho$, since $s_m^2 < 1$, i.e. the integration constant ρ_1 corresponds to the minimum of the allowed values for the rest-mass density of the fluid. Moreover, inequality (19) implies that $h/h_1 > 0$. At this point we do not make any assumption about the sign of the specific enthalpy.

Because of Eq. (17), Eq. (19) results in

$$\begin{aligned} &\frac{1}{\rho_1^{s_m^2}} \int_{\rho_1}^{\rho} \rho'^{s_m^2} \mathrm{d}\rho' \leq \frac{1}{h_1} \int_{\rho_1}^{\rho} h \mathrm{d}\rho' \leq \frac{1}{\rho_1} \int_{\rho_1}^{\rho} \rho' \mathrm{d}\rho' \\ \Rightarrow &\frac{\rho_1}{1+s_m^2} \left[\left(\frac{\rho}{\rho_1}\right)^{s_m^2+1} - 1\right] \leq \frac{\epsilon - \epsilon_1}{h_1} \leq \frac{\rho_1}{2} \left[\left(\frac{\rho}{\rho_1}\right)^{2} - 1\right], \end{aligned} \tag{20}$$

where $\int_{\rho_1}^{\rho} h \mathrm{d}\rho' = \int_{\epsilon_1}^{\epsilon} \mathrm{d}\epsilon'$ was employed.

From Eqs. (16) and (18) we get

$$\mathrm{d}p = c_s^2 h \mathrm{d}\rho\,. \tag{21}$$

Taking into account Eq. (21), from Eq. (19) and Eq. (9) we have

$$\begin{aligned} &\frac{s_m^2}{\rho_1^{s_m^2}} \int_{\rho_1}^{\rho} \rho'^{s_m^2} \mathrm{d}\rho' \leq \frac{1}{h_1} \int_{\rho_1}^{\rho} c_s^2 h \mathrm{d}\rho' \leq \frac{1}{\rho_1} \int_{\rho_1}^{\rho} \rho' \mathrm{d}\rho' \\ \Rightarrow &\frac{s_m^2 \rho_1}{1+s_m^2} \left[\left(\frac{\rho}{\rho_1}\right)^{s_m^2+1} - 1\right] \leq \frac{p - p_1}{h_1} \leq \frac{\rho_1}{2} \left[\left(\frac{\rho}{\rho_1}\right)^{2} - 1\right], \end{aligned} \tag{22}$$

where $\int_{\rho_1}^{\rho} c_s^2 h \mathrm{d}\rho' = \int_{p_1}^{p} \mathrm{d}p'$ was employed. Since $\rho \geq \rho_1$, inequality (22) gives that $(p-p_1)/h_1 \geq 0$, while inequality (20) gives that $(\epsilon-\epsilon_1)/h_1 \geq 0$. For $\rho = \rho_1$, Eqs. (19), (20), (22) reduce to $h = h_1$, $\epsilon = \epsilon_1$, $p = p_1$ respectively, which is trivial but self-consistent.

2.0.1 Assuming constant speed of sound

Assuming c_s^2 is independent of specific enthalpy, i.e. constant, then by following similar steps as for arriving to the inequalities (19), (20), (22), we get

$$\epsilon - \epsilon_1 = \frac{1}{1+c_s^2}\,\rho_1\, h_1 \left[\left(\frac{\rho}{\rho_1}\right)^{1+c_s^2} - 1\right], \tag{23}$$

$$p - p_1 = \frac{c_s^2}{1+c_s^2}\,\rho_1\, h_1 \left[\left(\frac{\rho}{\rho_1}\right)^{1+c_s^2} - 1\right], \tag{24}$$

which leads to

$$p = c_s^2\,(\epsilon - \epsilon_1) \; + p_1\,. \tag{25}$$

Note that if one changes the equation of the state of the fluid, i.e. c_s^2, the integration constants denoted with "1" change as well.

3 ASYMPTOTIC BEHAVIORS

3.1 Rest-mass density

The rest mass conservation (13) can be rewritten as:

$$\dot{\rho} + \rho\,\theta = 0\,, \tag{26}$$

where $\theta = \nabla_\alpha u^\alpha$ is the expansion scalar of the congruence u^α, $\dot{} = u^\alpha \nabla_\alpha$ denotes the derivative with respect to a relevant time parameter t along the congruence u^α. Integrating Eq. (26) along the time parameter t leads to

$$\rho = \rho_0\, e^{-\int_{t_0}^{t} \theta(t')\,\mathrm{d}t'}\,, \tag{27}$$

with initial condition $\rho(t_0) = \rho_0$.

Proposition 1. *For a perfect fluid moving along an expanding congruence with conserved positive rest-mass, the rest-mass density vanishes asymptotically, $\rho \to 0^+$, in the limit $t \to \infty$.*

Proof. Since we have an expanding congruence, there exists a $k > 0$, such that $\theta \geq k$. Eq. (27) then leads to

$$\rho = \rho_0\, e^{-\int_{t_0}^{t} \theta(t')\,\mathrm{d}t'} \leq \rho_0\, e^{-\int_{t_0}^{t} k\,\mathrm{d}t'} = \rho_0\, e^{-k(t-t_0)} \to 0 \quad \text{for} \quad t \to \infty\,. \tag{28}$$

Since $\rho > 0$, one has $\rho \to 0^+$ for $t \to \infty$, i.e. the rest mass density asymptotically vanishes. □

Proposition 1 and the fact that $\rho_1 \leq \rho$ suggests that ρ_1 must be an infinitesimally small positive quantity, i.e. $\rho_1 \equiv 0^+$. Moreover, Proposition 1 implies that for $t \to \infty$ Eqs. (23), (24) derived for a fluid with constant non-zero speed of sound lead to

$$\epsilon - \epsilon_1 \simeq -\frac{1}{1+c_s^2}\,\rho_1\, h_1\,, \tag{29}$$

$$p - p_1 \simeq -\frac{c_s^2}{1+c_s^2}\,\rho_1\, h_1\ . \tag{30}$$

To show an interesting implication of these relations, let us fix the constants of integration by considering the vanishing pressure limit, $p_1 = 0$. In this limit, one typically imposes that the specific enthalpy is equal to unity. Then, the relation $\epsilon + p = \rho h$, for $p = p_1 = 0$ and $h = h_1 = 1$, implies

$$\epsilon_1 = \rho_1\,. \tag{31}$$

With these constraints on the constants, we obtain the following expressions for Eqs. (29), (30):

$$p \simeq -\frac{\epsilon_1\, c_s^2}{1+c_s^2}\,, \tag{32}$$

$$\epsilon \simeq \frac{\epsilon_1\, c_s^2}{1+c_s^2}\,. \tag{33}$$

It is immediately evident that Eq. (33) represents a constant positive contribution to the energy density for any $c_s^2 > 0$, if $\epsilon_1 = \rho_1 > 0$. In a cosmological context such term behaves like a *cosmological constant*, since $p = -\epsilon$. This has been already noticed for the case of the stiff fluid ($c_s = 1$) by Christodoulou (1995).

Applying proposition 1 on the inequalities (20), (22) and using the (31) choice for fixing the constants, we arrive at:

$$-\frac{\epsilon_1\, s_m^2}{1+s_m^2} \lesssim p \lesssim -\frac{\epsilon_1}{2}\,, \tag{34}$$

$$\frac{\epsilon_1\, s_m^2}{1+s_m^2} \lesssim \epsilon \lesssim \frac{\epsilon_1}{2}\,. \tag{35}$$

Eq. (35) still implies a constant positive contribution to the energy density for $t \to \infty$, but Eq. (34) is only possible if $\epsilon_1 = 0$, since $s_m^2 \ll 1$. Thus, we are led to $\epsilon_1 = 0$, which means that Eqs. (34), (35) respectively lead to $p \simeq \epsilon \simeq 0$. Moreover, since the above inequalities include the constant speed case as a subcase, then $\epsilon_1 = 0$ for Eqs. (32), (33), so they do not imply the existence of a cosmological constant. On the other hand, this result might be suggesting that the choice (31) we have made to fix the constants is not the proper one.

In fact if we do not fix the constants, according to Proposition 1 the inequalities (19), (20), (22) reduce to

$$\frac{h}{h_1} \simeq 0, \tag{36}$$

$$-\frac{\rho_1}{1+s_m^2} \lesssim \frac{\epsilon-\epsilon_1}{h_1} \lesssim -\frac{\rho_1}{2}\,, \tag{37}$$

$$-\frac{s_m^2\rho_1}{1+s_m^2} \lesssim \frac{p-p_1}{h_1} \lesssim -\frac{\rho_1}{2}\,. \tag{38}$$

Again because of $s_m^2 \ll 1$, Eq. (38) can hold only if ρ_1 is exactly zero. Note that even if s_m^2 was equal to zero ρ_1 had to be zero as well. By not allowing the rest mass energy density to acquire the zero value, we have arrived to a contradiction. If one would allow it, then it would not be possible to derive the inequalities in Sec. 2. To resolve this contradiction, one might claim that the relations derived in Sec. 2 hold only for finite time intervals, i.e. they do not hold for $t \to \infty$. To discuss the asymptotic behaviors, we need propositions like Proposition 1.

3.2 Enthalpy

Evaluating the thermodynamic relation Eq. (7) along the flow lines, and implementing Eq. (15), yields the relation

$$u^\alpha \nabla_\alpha h = \frac{hc_s^2}{\rho} u^\alpha \nabla_\alpha \rho\,, \tag{39}$$

which can be used to rewrite the rest-mass conservation equation (13) as

$$0 = \nabla_\alpha (\rho u^\alpha) \tag{40}$$

$$= \frac{\rho}{hc_s^2}\left(u^\alpha \nabla_\alpha h + hc_s^2 \nabla_\alpha u^\alpha\right). \tag{41}$$

The continuity equation for the rest-mass density as expressed by Eq. (41) is

$$\dot{h} = -c_s^2\,\theta\, h\,, \tag{42}$$

For generic time-dependent speed of sound and expansion scalar, one then has

$$h = h_0\, e^{-\int_{t_0}^{t} c_s^2(t')\,\theta(t')\,\mathrm{d}t'}\,, \tag{43}$$

with initial condition $h(t_0) = h_0$.

3.2.1 Strong Energy Condition

Proposition 2. *Consider a perfect fluid moving along an expanding and isotropic congruence, with conserved rest-mass and satisfying the Strong Energy Condition (SEC); then if the speed of sound is a function of time defined in the interval* $(0, 1]$*, in the limit* $t \to \infty$ *one necessarily has* $\epsilon \to 0$ *and* $p \to 0$*.*

Proof. The equation of rest-mass conservation can be rewritten in the form Eq. (42), whose general solution is given by eq.(43). We would like to evaluate the behavior of h in the limit when $t \to \infty$ by obtaining an upper and a lower bound.

Lower bound. First of all $c_s^2(t) \in (0, 1]$, so we can write

$$h = h_0 \, e^{-\int_{t_0}^{t} c_s^2(t')\,\theta(t')\,\mathrm{d}t'} \;\geq\; h_0 \, e^{-\int_{t_0}^{t} \theta(t')\,\mathrm{d}t'} \,. \tag{44}$$

Secondly, the Raychaudhuri equation for an isotropic timelike congruence u^α reads

$$\dot{\theta} = -\left(\frac{1}{3}\theta^2 + R_{\alpha\beta}u^\alpha u^\beta\right). \tag{45}$$

Because of the SEC, the last term is positive. Hence we get the inequality

$$\dot{\theta} \leq -\frac{1}{3}\theta^2 \,. \tag{46}$$

Integration of such inequality gives

$$\theta \leq \frac{3\,\theta_0}{3 + \theta_0\, t}\,, \tag{47}$$

with $\theta_0 = \theta(t_0)$. Applying such bound to the rightmost term of Eq. (44) gives

$$\begin{aligned} h \geq h_0 \, e^{-\int_{t_0}^{t} \theta(t')\,\mathrm{d}t'} &\geq h_0 \, e^{-\int_{t_0}^{t} \frac{3\,\theta_0}{3+\theta_0\, t'}\,\mathrm{d}t'} \\ &= h_0 \left(\frac{3 + \theta_0 t_0}{3 + \theta_0 t}\right)^3 \to 0 \quad \text{for} \quad t \to \infty \,. \end{aligned} \tag{48}$$

Hence $h \geq 0$ for $t \to \infty$.

Upper bound. By assumption, the product $c_s^2(t)\theta(t)$ is strictly positive: hence there exists a constant $k > 0$ such that $c_s^2(t)\theta(t) \geq k > 0$ for any finite time. The function h can then be bounded from above in the following way:

$$\begin{aligned} h = h_0 \, e^{-\int_{t_0}^{t} c_s^2(t')\,\theta(t')\,\mathrm{d}t'} &\leq h_0 \, e^{-\int_{t_0}^{t} k\,\mathrm{d}t'} \\ &= h_0 \, e^{-k(t-t_0)} \to 0 \quad \text{for} \quad t \to \infty \,. \end{aligned} \tag{49}$$

Hence $h \leq 0$ for $t \to \infty$.

Putting together the results of both bounds, we find that $h = 0$ in the limit $t \to \infty$. At the same time $\rho \to 0$ in the same limit, because of Proposition 1. Thus, one has that $h \equiv \frac{\epsilon + p}{\rho} \to 0$ implies that $p + \epsilon \to 0$.

Lastly, the SEC requires $p + \frac{1}{3}\epsilon \geq 0$: the only case in which the condition $p + \epsilon \to 0$ is consistent with this bound is when both $\epsilon \to 0$ and $p \to 0$ (left panel of Fig. 1). □

Note that Proposition 1 by itself could not lead to $p + \epsilon \to 0$, since the asymptotic bounded value of the specific enthalpy was not guaranteed.

Proposition 2 is a general statement about the impossibility for a "well defined" isotropic perfect fluid satisfying the SEC to have a non-trivial pressure asymptotically. Hence, in the following propositions we drop SEC and specialize to a spatially flat Friedmann-Robertson-Walker (FRW) spacetime.

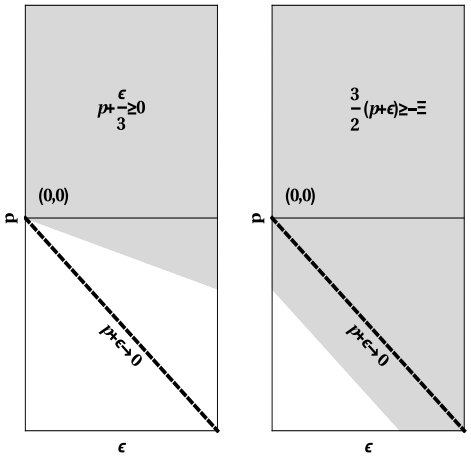

Figure 1. Left panel: The plane of allowed EoS assuming SEC, Proposition 2. Right Panel: The plane of allowed EoS assuming bounded rate of congruence expansion, Proposition 3. In both panels we assume that the energy density is $\epsilon \geq 0$.

3.2.2 Bounded Rate of Expansion

Proposition 3. *Consider a perfect fluid moving along an expanding congruence in a flat FRW spacetime, with conserved rest-mass and a rate of expansion bounded by* Ξ*; then if the speed of sound is a function of time defined in the interval* $(0, 1]$*, in the limit* $t \to \infty$ *one has* $\epsilon + p \to 0$*, without necessarily* $\epsilon \to 0$ *and* $p \to 0$*, and* $0 \lesssim \Xi$*.*

Proof. The *upper bound* stays the same as in Proposition 2, so $h \leq 0$ for $t \to \infty$. *Lower bound.* A positive, but bounded rate of congruence expansion means that $\dot{\theta} \leq \Xi$, thus $\theta(t) \leq \Xi(t - t_0) + \theta_0$. Then, Eq. (44) gives

$$h \geq h_0\, e^{-\int_{t_0}^{t} \theta(t')\,\mathrm{d}t'} \geq h_0\, e^{-\int_{t_0}^{t} \Xi(t-t_0)+\theta_0 \mathrm{d}t'} = h_0\, e^{-(\Xi(t-t_0)^2/2+\theta_0(t-t_0))} \to 0 \quad \text{for} \quad t \to \infty\,. \tag{50}$$

Putting together the results of both bounds, we find that $h = 0$ in the limit $t \to \infty$. Thus, again one has that $p + \epsilon \to 0$.

However, from the isotropic Raychaudhuri Eq. (45) we have:

$$-\left(\frac{1}{3}\theta^2 + R_{\alpha\beta}u^\alpha u^\beta\right) \leq \Xi \Rightarrow -\frac{3}{2}(\epsilon + p) \leq \Xi\,, \tag{51}$$

where we used Friedmann equation $\theta^2 = 3\epsilon$. Thus, in this case the solution $\epsilon \to 0$, $p \to 0$ is not the only allowed to have $\epsilon + p \to 0$ (right panel of Fig. 1). Actually, $p \to -\epsilon$ implies that $0 \lesssim \Xi$. □

Note that proposition 3 allows an exponential growth for FRW

$$3\frac{\dot{a}}{a} = \theta = \Xi(t - t_0) + \theta_0 \Rightarrow a \leq a_0 e^{(\Xi(t-t_0)^2/2 + \theta_0(t-t_0))/3}$$

even if $\Xi = 0$. Thus, to have exponential growth the minimal requirement is that $\dot{\theta} \leq 0$.

4 SUMMARY

Starting from a general thermodynamical treatment of usual matter, in the form of an irrotational perfect fluid, our investigation indicates that a constant speed of sound for usual matter is not a viable way to provide a cosmological constant. We have given a formal proof that if the strong energy condition holds, usual matter cannot provide negative pressure. Moreover, we have provided a formal proof that for a flat FRW spacetime containing only usual matter, for which the strong energy condition is violated, negative pressure is possible .

ACKNOWLEDGEMENTS

G.L-G is supported by Grant No. GAČR-17-06962Y of the Czech Science Foundation. G.A. is supported by Grant No. GAČR-17-16260Y of the Czech Science Foundation. C.M. is supported by the European Union's Horizon 2020 research and innovation programme under the Marie Skłodowska-Curie grant agreement No 753115.

REFERENCES

Carter, B. (1979), Perfect fluid and magnetic field conservation laws in the theory of black hole accretion rings, in C. Hazard and S. Mitton, editors, *Active Galactic Nuclei*, pp. 273–300.

Christodoulou, D. (1995), Self-gravitating relativistic fluids: A two-phase model, *Archive for Rational Mechanics and Analysis*, **130**, pp. 343–400.

Gourgoulhon, E. (2006), An introduction to relativistic hydrodynamics, in M. Rieutord and B. Dubrulle, editors, *EAS Publications Series*, volume 21 of *EAS Publications Series*, pp. 43–79.

Lichnerowicz, A. (1967), *Relativistic Hydrodynamics and Magnetohydrodynamics*, New York: Benjamin.

Markakis, C., Uryū, K., Gourgoulhon, E., Nicolas, J.-P., Andersson, N., Pouri, A. and Witzany, V. (2017), Conservation laws and evolution schemes in geodesic, hydrodynamic, and magnetohydrodynamic flows, *Phys. Rev. D*, **96**(6), p. 064019.

Peebles, P. J. E. and Ratra, B. (2003), The cosmological constant and dark energy, *Rev. Mod. Phys.*, **75**, pp. 559–606.

Proceedings of *RAGtime 20–22, 15–19 Oct., 16–20 Sept., 19–23 Oct., 2018/2019/2020, Opava, Czech Republic*
Z. Stuchlík, G. Török and V. Karas, editors, Silesian University in Opava, 2020, pp. 185–201

Oscillations of non-slender tori in the external Hartle-Thorne geometry

Monika Matuszková,[1,a] Kateřina Klimovičová,[1,b]
Gabriela Urbancová,[1,c] Debora Lančová,[1,d]
Eva Šrámková[1] and Gabriel Török[1]

[1]Research Centre for Computational Physics and Data Processing,
Institute of Physics, Silesian University in Opava, Bezručovo nám. 13,
CZ-746 01 Opava, Czech Republic
[a]monika.matuszkova@physics.slu.cz
[b]katerina.klimovicova@physics.slu.cz
[c]gabriela.urbancova@physics.slu.cz
[d]debora.lancova@physics.slu.cz

ABSTRACT
We examine the influence of the quadrupole moment of a slowly rotating neutron star on the oscillations of non-slender accretion tori. We apply previously developed methods to perform analytical calculations of frequencies of the radial epicyclic mode of a torus in the specific case of the Hartle-Thorne geometry. We present here our preliminary results and provide a brief comparison between the calculated frequencies and the frequencies previously obtained assuming both standard and linearized Kerr geometry. Finally, we shortly discuss the consequences for models of high-frequency quasi-periodic oscillations observed in low-mass X-ray binaries.

Keywords: neutron star – thick accretion disc – Hartle-Thorne metric

1 INTRODUCTION

Numerous interesting features have been discovered during the long history of X-ray observations of low-mass X-ray binaries (LMXBs). One of them is the fact that variability of the X-ray radiation coming from these sources occurs at frequencies in the order of up to hundreds of Hertz with the highest values reaching above 1.2 kHz. Even though the discovery of this rapid variability was made almost 30 years ago, to this day, there is no convincing explanation of its origin. The phenomenon is called the high-frequency quasi-periodic oscillations (HF QPOs) and many models have been proposed in the attempt to explain its nature (see, e.g., Török et al., 2016a; Kotrlová et al., 2020 and references therein).

It has been noticed that the HF QPOs frequencies are in the same order as those corresponding to orbital motion in the very close vicinity of a compact object, such as neutron

978-80-7510-432-8

star (NS) or black hole (BH). This suggests that there is a relation between the QPO phenomenon and the physics behind the motion of matter close to the accreting object. Since positions of specific orbits in the accretion disk (such as its inner edge) and the associated orbital frequencies depend on the properties of the central object, there is a believe that it is possible to infer the compact object properties from the QPOs data.[1]

In the above context, several studies have focused on a possible relation between the QPOs and an oscillatory motion of an accretion torus formed in the innermost accretion region (Kluzniak and Abramowicz, 2001; Kluźniak et al., 2004; Abramowicz et al., 2003a,b; Rezzolla et al., 2003; Bursa, 2005; Török et al., 2005; Dönmez et al., 2011; Török et al., 2016a; de Avellar et al., 2018).

Straub and Šrámková (2009) and Fragile et al. (2016) have performed calculations of frequencies of the epicyclic oscillations of fluid tori assuming Kerr geometry, which describes rotating BHs. Here we follow their approach and consider slowly rotating NSs and their spacetimes described by the Hartle-Thorne geometry (Hartle, 1967; Hartle and Thorne, 1968). We present the first, preliminary results of our calculations of the radial epicyclic oscillation frequencies and provide a brief comparison of these to the frequencies obtained previously for the Kerr and linearized Kerr geometries. Finally, we discuss some consequences for models of NS QPOs.

2 OSCILLATIONS OF TORI IN AXIALLY SYMMETRIC SPACETIMES

We consider an axially symmetric geometry. The spacetime element may be expressed in the general form as

$$\mathrm{d}s^2 = g_{tt}\mathrm{d}t^2 + 2g_{t\varphi}\mathrm{d}t\mathrm{d}\varphi + g_{rr}\mathrm{d}r^2 + g_{\theta\theta}\mathrm{d}\theta^2 + g_{\varphi\varphi}\mathrm{d}\varphi^2. \tag{1}$$

We use the units in which $c = G = 1$ with c being the speed of light and G the gravitational constant.

2.1 Equilibrium configuration

We assume a perfect fluid torus in the state of pure rotation with constant specific angular momentum l as described in Abramowicz et al. (2006); Blaes et al. (2006).

In this case, the fluid forming the torus has a four-velocity u^μ with only two non-zero components,

$$u^\mu = A(1, 0, 0, \Omega), \tag{2}$$

where A is the time component u^t and Ω is the orbital velocity. One may write

$$A = u^t = (-g_{tt} - 2\Omega g_{t\varphi} - \Omega^2 g_{\varphi\varphi})^{-1/2}, \tag{3}$$

$$\Omega = \frac{u^\varphi}{u^t} = \frac{g^{t\varphi} - l g^{\varphi\varphi}}{g^{tt} - l g^{t\varphi}}. \tag{4}$$

[1] We often use the shorter term "QPOs" instead of "HF QPOs" throughout the paper.

The perfect fluid with density ρ, pressure p and the energy density e is characterised by the stress-energy tensor

$$T^{\mu\nu} = (p + e)u^{\mu}u^{\nu} + pg^{\mu\nu}. \tag{5}$$

For a polytropic fluid, we may write:

$$p = K\rho^{\frac{n+1}{n}}, \tag{6}$$

$$e = np + \rho, \tag{7}$$

where K and n denote the polytropic constant and the polytropic index, respectively. In this work, we use $n = 3$, which describes a radiation-pressure-dominated torus.

The Euler formula is obtained from the energy–momentum conservation law, $\nabla_{\mu}T^{\mu}{}_{\nu} = 0$, using the assumption of $l = const$. (Abramowicz et al., 1978, 2006)

$$\nabla_{\mu}(\ln \mathcal{E}) = -\frac{\nabla_{\mu}p}{p + e}, \tag{8}$$

with $\mathcal{E}$ being the specific energy

$$\mathcal{E} = -u_t = \left(-g^{tt} + 2lg^{t\varphi} - l^2 g^{\varphi\varphi}\right)^{-1/2}. \tag{9}$$

By integrating (8) we obtain the Bernoulli equation (Fragile et al., 2016; Horák et al., 2017)

$$H\mathcal{E} = const., \tag{10}$$

where $H = \frac{p+e}{\rho}$ denotes the enthalpy in the form presented by Fragile et al. (2016) and Horák et al. (2017). From relation (10), we can derive the equations describing the structure and shape of the torus:

$$\frac{p}{\rho} = \frac{p_0}{\rho_0} f(r, \theta), \tag{11}$$

$$f(r, \theta) = \frac{1}{nc_{\mathrm{s},0}^2}\left[\left(1 + nc_{\mathrm{s},0}^2\right)\frac{\mathcal{E}_0}{\mathcal{E}} - 1\right], \tag{12}$$

$$\tag{13}$$

where c_{s} is the sound speed in the fluid defined as (Abramowicz et al., 2006)[2]

$$c_{\mathrm{s}}^2 = \frac{\partial p}{\partial \rho} = \frac{n + 1}{n}\frac{p}{\rho}, \tag{14}$$

and the subscript 0 denotes the quantities evaluated at the torus centre. From equations (6) and (11), one can obtain the following formulae for pressure and density of the fluid:

$$p = p_0 \left[f\,(r, \theta)\right]^{n+1}, \tag{15}$$

$$\rho = \rho_0 \left[f\,(r, \theta)\right]^{n}. \tag{16}$$

[2] The definition is fully valid for $c_{\mathrm{s}} << 1$, but this has no significant effect on our results.

It is useful to introduce new coordinates $\overline{x}$ and $\overline{y}$ by relations

$$\overline{x} = \frac{\sqrt{g_{rr,0}}}{\beta}\left(\frac{r - r_0}{r_0}\right), \tag{17}$$

$$\overline{y} = \frac{\sqrt{g_{\theta\theta,0}}}{\beta}\left(\frac{\frac{\pi}{2} - \theta}{r_0}\right). \tag{18}$$

In these coordinates, we have $\overline{x} = 0$ and $\overline{y} = 0$ at the torus centre. We furthermore introduce a β parameter determining the torus thickness, which is connected to the sound speed at the torus centre in the following manner (Abramowicz et al., 2006; Blaes et al., 2006):

$$\beta^2 = \frac{2nc_{\mathrm{S},0}^2}{r_0^2\Omega_0^2A_0^2}. \tag{19}$$

The surface of the torus, which coincides with the surface of zero pressure, is given by the condition $f(r, \theta) = 0$. An example of the torus cross-section is shown in Figure 1 illustrating the character of the equipressure surfaces for different values of β. An equilibrium torus is formed when the perfect fluid fills up a closed equipressure surface. The largest possible torus arises by filling up the equipressure surface that has a crossing point – the so-called cusp. We call this structure, for which we have $\beta = \beta_{\mathrm{cusp}}$, the "cusp torus". Notice that, for $\beta > \beta_{\mathrm{cusp}}$, the equipressure surfaces are no longer closed and no torus therefore can be formed.

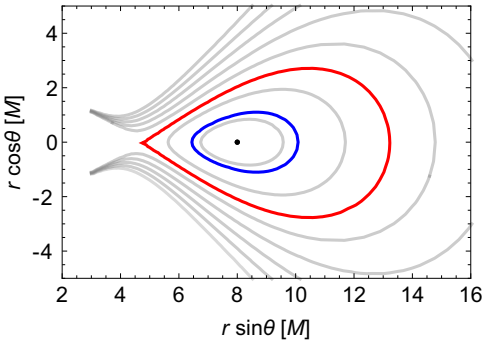

Figure 1. Meridional cross-section illustrating the shape of the equipressure surfaces in the Schwarzschild geometry. The red line marks a cusp torus with $\beta = \beta_{\mathrm{cusp}}$, the blue line corresponds to an equilibrium torus with $\beta < \beta_{\mathrm{cusp}}$, and the black dot denotes the centre of the torus (as well as the infinitely slender torus with $\beta \to 0$).

2.2 The oscillating configuration

We assume the effective potential $\mathcal{U}$ (e.g. Abramowicz et al., 2006) in the form

$$\mathcal{U} = g^{tt} - 2l_0g^{t\varphi} + l_0^2g^{\varphi\varphi}. \tag{20}$$

An infinitesimally slender torus with $\beta \to 0$ at r_0 with specific angular momentum l_0 undergoing a small axially symmetric perturbation in the radial direction will oscillate with the frequency equal to the radial epicyclic frequency of a free test particle given by (Abramowicz and Kluźniak, 2005; Aliev and Galtsov, 1981)

$$\nu_r^2 = \frac{1}{4\pi^2} \frac{\mathcal{E}_0^2}{2A_0^2 g_{rr,0}} \left. \frac{\partial^2 \mathcal{U}}{\partial r^2} \right|_0 . \tag{21}$$

Now let us investigate how the frequency changes when the torus becomes thicker and/or when the perturbation is not axially symmetric. Assume small perturbations of all quantities around the equilibrium state in the form (Abramowicz et al., 2006; Blaes et al., 2006)

$$\delta X(t, r, \theta, \varphi) = \delta X(r, \theta) \mathrm{e}^{i(m\varphi - \omega t)}, \tag{22}$$

where m is the azimuthal number and ω is the angular frequency of the oscillations. In this work, we focus on two modes of oscillations: the axially symmetric ($m = 0$) and the first non-axisymmetric ($m = -1$) radial epicyclic modes.

From the continuity equation $\nabla_\mu (\rho u^\mu) = 0$, one can get the relativistic version of the Papaloizou-Pringle equation (Abramowicz et al., 2006; Fragile et al., 2016), [3]

$$\frac{1}{\sqrt{-g}} \partial_\mu \frac{\sqrt{-g} g^{\mu\nu} f^n \partial_\nu W}{n c_{\mathrm{s},0}^2 f + 1} + (l_0 \omega - m)^2 \frac{\Omega g^{t\phi} - g^{\phi\phi}}{1 - \Omega l_0} \frac{f^n}{n c_{\mathrm{s},0}^2 f + 1} W = \\ = - \frac{2n\mathcal{A}^2 \left(\overline{\omega} - m\overline{\Omega} \right)^2}{\beta^2 r_0^2} f^{n-1} W, \tag{23}$$

where $\{\mu, \nu\} \in \{r, \theta\}$, $\mathcal{A} \equiv A/A_0$, $\overline{\Omega} \equiv \Omega/\Omega_0$, $\overline{\omega} \equiv \omega/\Omega_0$, g is the determinant of the metric tensor and W equals to (Abramowicz et al., 2006)

$$W = - \frac{\delta p}{A\rho \left(\omega - m\Omega \right)}. \tag{24}$$

Equation (23) has no analytical solution except for the limit case of an infinitely slender torus ($\beta \to 0$). In the case of non-slender tori ($\beta > 0$), the equation can be solved using a perturbation method (see, e.g., Straub and Šrámková (2009)).

2.2.1 Solving the Papaloizou-Pringle equation

When the exact solution for a simplified case is known (as for $\beta \to 0$), we can use perturbation theory to find the solution for more complicated cases ($\beta > 0$). [4]

By expanding the quantities $\overline{\omega}$, W, $\mathcal{A}$, $\overline{\Omega}$, f in β (Straub and Šrámková, 2009)

$$Q = Q^{(0)} + \beta Q^{(1)} + \beta^2 Q^{(2)} + \cdots , \qquad Q \in \left\{ \overline{\omega}, W, \mathcal{A}, \overline{\Omega}, f \right\}, \tag{25}$$

[3] For the sake of simplicity, from now on, we will use $f = f(r, \theta)$.

[4] Note the perturbation method gives reasonable results only for small values of β and our results are therefore valid only for slightly non-slender tori.

substituting that into equation (23), and comparing the coefficients of appropriate order in β, we obtain the corresponding corrections to W and ω. Note that the zero order corresponds to the slender torus case ($\beta \to 0$), in which we have $\omega = 2\pi\nu_r$.

Using this procedure, Straub and Šrámková (2009) have derived the expression for the radial epicyclic mode frequency with the second order accuracy, which may be written as

$$\omega_{r,\mathrm{m}} = 2\pi\,\nu_r + m\,\Omega_0 + P_\mathrm{m}\beta^2 + \mathcal{O}\left(\beta^3\right), \tag{26}$$

where P_m denotes the second order correction term for which the explicit form can be found in their paper.

3 THE HARTLE-THORNE GEOMETRY

The exterior solution of the Hartle-Thorne metric is characterized by three parameters: the gravitational mass M, angular momentum J and the quadrupole moment Q of the star. We use this metric assuming dimensionless forms of the angular momentum and the quadrupole moment, $j = J/M^2$ and $q = Q/M^3$, which can be in the Schwarzschild coordinates written as (Abramowicz et al., 2003)[5]:

$$g_{tt} = -\left(1 - \frac{2M}{r}\right)\left[1 + j^2F_1(r) + qF_2(r)\right], \tag{27}$$

$$g_{rr} = \left(1 - \frac{2M}{r}\right)^{-1}\left[1 + j^2G_1(r) - qF_2(r)\right], \tag{28}$$

$$g_{\theta\theta} = r^2\left[1 + j^2H_1(r) + qH_2(r)\right], \tag{29}$$

$$g_{\varphi\varphi} = r^2\sin^2\theta\left[1 + j^2H_1(r) + qH_2(r)\right], \tag{30}$$

$$g_{t\varphi} = -\frac{2M^2}{r}j\sin^2\theta, \tag{31}$$

where (using the $u = \cos\theta$ substitution)

$$\begin{aligned} F_1(r) = &-\left[8Mr^4(r-2M)\right]^{-1} \\ &\left[u^2\left(48M^6 - 8M^5r - 24M^4r^2 - 30M^3r^3 - 60M^2r^4 + 135Mr^5 - 45r^6\right)\right. \\ &\left. + (r-M)\left(16M^5 + 8M^4r - 10M^2r^3 - 30Mr^4 + 15r^5\right)\right] + A_1(r), \end{aligned} \tag{32}$$

[5] Note misprints in the original paper.

$$F_2(r) = [8Mr(r-2M)]^{-1}\left[5\left(3u^2-1\right)(r-M)\left(2M^2+6Mr-3r^2\right)\right] - A_1(r), \tag{33}$$

$$G_1(r) = [8Mr(r-2M)]^{-1}\left[\left(L(r)-72M^5r\right) - 3u^2\left(L(r)-56M^5r\right)\right] - A_1(r), \tag{34}$$

$$L(r) = 80M^6 + 8M^4r^2 + 10M^3r^3 + 20M^2r^4 - 45Mr^5 + 15r^6, \tag{35}$$

$$A_1(r) = \frac{15\left(r^2-2M\right)\left(1-3u^2\right)}{16M^2}\ln\left(\frac{r}{r-2M}\right), \tag{36}$$

$$H_1(r) = \left(8Mr^4\right)^{-1}\left(1-3u^2\right)\left(16M^5+8M^4r-10M^2r^3+15Mr^4+15r^5\right) + A_2(r), \tag{37}$$

$$H_2(r) = (8Mr)^{-1}\,5\left(1-3u^2\right)\left(2M^2-3Mr-3r^2\right) - A_2(r), \tag{38}$$

$$A_2(r) = \frac{15\left(r^2-2M\right)\left(3u^2-1\right)}{16M^2}\ln\left(\frac{r}{r-2M}\right). \tag{39}$$

While for $j = 0$ and $q = 0$ the Hartle-Thorne metric coincides with the Schwarzschild metric, by setting $j = a/M$ and $q = j^2$ and performing a coordinate transformation into the Boyer-Lindquist coordinates (Abramowicz et al., 2003),

$$r_{\rm BL} = r - \frac{a^2}{2r^3}\left[(r+2M)(r-2M) + u^2(r-2M)(r+3M)\right], \tag{40}$$

$$\theta_{\rm BL} = \theta - \frac{a^2}{2r^3}(r+2M)\cos\theta\sin\theta, \tag{41}$$

we obtain Kerr geometry expanded upon the second order in the dimensionless angular momentum.

4 OSCILLATIONS OF TORI IN THE VICINITY OF ROTATING NEUTRON STARS

Let us now study the changes that arise in the torus structure and for the frequencies of its oscillations when the Hartle-Thorne geometry is assumed to describe the spacetime geometry.[6] The main motivation behind this analysis is related to models of NS QPOs. While the Kerr geometry is (likely) proper to be used in the context of BH QPOs (e.g., Kotrlová et al., 2020), its validity in the case of NS QPOs is limited to very compact NSs only.

4.1 The Hartle-Thorne geometry parameters range relevant to rotating NSs

A thorough discussion of the relevance of the Hartle-Thorne geometry for the calculations of the geodesic orbital motion and QPO models frequencies is presented in Urbancová et al. (2019). Here we just briefly summarize the appropriate ranges of the individual parameters that are implied by the present NS equations of state. The maximum value of the specific

[6] Following Straub and Šrámková (2009) and Fragile et al. (2016), we use a Wolfram Mathematica code, which has been extended to the Hartle-Thorne geometry.

angular momentum of a NS is about $j_{\max} \sim 0.7$, the specific quadrupole moment takes values from $q/j^2 \sim 1.5$ for a very massive (compact) NS up to $q/j^2 \sim 10$ for a low-mass NS (Urbancová et al., 2019). The conservative expectations of the NS mass values are about $1.4 - 2.5\, M_\odot$.

4.2 The quadrupole moment influence on the non-oscillating torus shape and size

In Figures 2 and 3, we present meridional cross-sections of tori carried out in different geometries, namely the Schwarzschild, Kerr, linearized Kerr, and the Hatle-Thorne geometry. The figures also show plots of the Keplerian angular momentum and the angular momentum of the fluid (which is constant across the torus), and the radial extentions of the tori. For both figures, the top panels correspond to $j = 0$ (a non-rotating NS, i.e., the Schwarzschild geometry), and the bottom panels to $j = 0.2$ (Figure 2) and $j = 0.4$ (Figure 3). The radial coordinate r_0 is chosen such that the radial epicyclic frequency of a free test particle defined at this coordinate reaches its maximum.

In Table 1, we provide a quantitative comparison of the radial extensions of tori from Figures 2 and 3. It is given in terms of the proper radial distance, $r_{\rm prop}$, measured between the minimal, $r_{\min}$, and the maximal, $r_{\max}$, radial coordinate of the torus surface,

$$\Delta r_{\rm prop} = \int_{r_{\min}}^{r_{\max}} \sqrt{g_{rr}}\, {\rm d}r. \tag{42}$$

Table 1. The percentual differences in the proper radial extension $\Delta r_{\rm prop}$ of tori in the Hartle-Thorne geometry and in the Schwarzschild, Kerr, and linearized Kerr geometries. The displayed values correspond to the situations illustrated in Figures 2 and 3.

Geometry	Schwarzschild		Kerr		Lin. Kerr	
Spin j	0.2	0.4	0.2	0.4	0.2	0.4
HT ($q = j^2$)	− 5 %	− 11 %	+ 2 %	− 5 %	− 1 %	− 13 %
HT ($q = 10j^2$)	− 7 %	− 12 %	− 1 %	− 6 %	− 4 %	− 14 %

4.3 The quadrupole moment influence on the radial epicyclic oscillations of non-slender tori

We use equation (26) to derive the radial epicyclic mode frequency as a function of the radius of the torus centre r_0. In Figure 4, we plot the frequencies of both the $m = 0$ (left panel) and $m = -1$ (middle panel) radial epicyclic modes. These are compared for the four different geometries assuming $j = 0.2$. The right panel of this figure illustrates the behaviour of tori cross-sections corresponding to maxima of the $m = 0$ radial epicyclic mode frequency. Figure 5 then provides the same illustration but for $j = 0.4$.

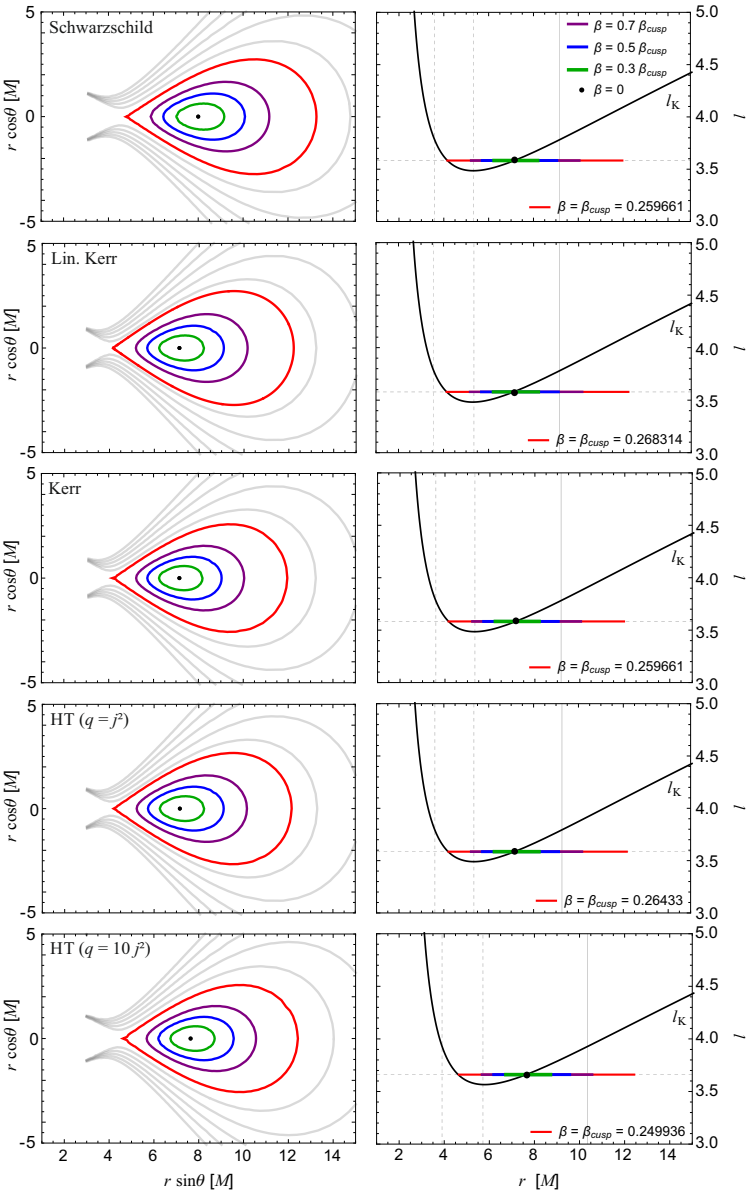

Figure 2. Illustration of some characteristics of tori carried out in different geometries. The tori are centered at the radial coordinate at which the radial epicyclic frequency of a free test particle reaches its maximum. Left panels: Meridional cross-sections of the equipressure surfaces determining the shape of the tori. From top to bottom, the results correspond to calculations carried out in the Schwarzschild, linearized Kerr ($j = 0.2$), Kerr ($j = 0.2$), and the Hartle-Thorne ($j = 0.2, q = j^2$ and $j = 0.2, q = 10j^2$) geometry. Right panels: Plots of the specific angular momentum of the fluid (which is constant across the torus) along with the Keplerian angular momentum. The intersection points of the two functions marked by the spots correspond to the centre of the tori. The coloured segments indicate the corresponding radial extentions of the tori.

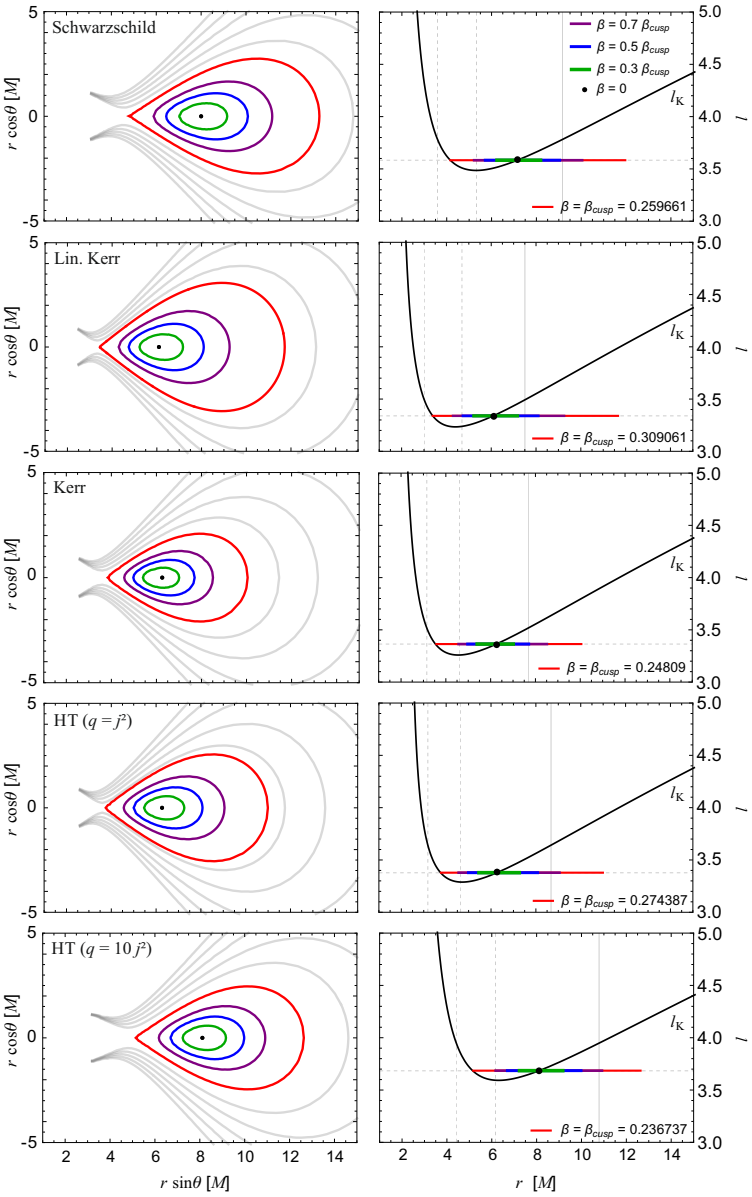

Figure 3. The same as in Figure 2 but for $j = 0.4$.

In Table 2, we provide a quantitative comparison of the maximal frequencies of the $m = 0$ radial epicyclic mode for tori of maximal thicknesses (i.e., the frequencies denoted by the red dots in the left panels of Figures 4 and 5) for the Hartle-Thorne and the other three geometries. In Table 3, we then present the same but for the $m = -1$ radial epicyclic mode (i.e., the frequencies denoted by the red dots in the middle panels of Figures 4 and 5). The proper radial extension of tori related to Tables 2 and 3 (i.e., those shown in the right panels of Figures 4 and 5) are compared in Table 4.

Table 2. The percentual differences in the maximal values of frequencies of the $m = 0$ radial epicyclic mode of the cusp tori in the Hartle-Thorne geometry and in the Schwarzschild, Kerr, and linearized Kerr geometries. The displayed values correspond to the situations illustrated in Figures 4 and 5.

Geometry	Schwarzschild		Kerr		Lin. Kerr	
Spin j	0.2	0.4	0.2	0.4	0.2	0.4
HT ($q = j^2$)	+ 15 %	+ 35 %	0 %	0 %	− 1 %	− 4 %
HT ($q = 10j^2$)	+ 8 %	+ 4 %	− 6 %	− 23 %	− 7 %	− 26 %

Table 3. The percentual differences in the frequency of the $m = -1$ radial epicyclic mode of the cusp tori in the Hartle-Thorne geometry and in the Schwarzschild, Kerr, and linearized Kerr geometries. The frequency is evaluated at the radius at which the $m = 0$ radial epicyclic mode frequency has its maximum. The displayed values correspond to the situations illustrated in Figures 4 and 5.

Geometry	Schwarzschild		Kerr		Lin. Kerr	
Spin j	0.2	0.4	0.2	0.4	0.2	0.4
HT ($q = j^2$)	+ 20 %	+ 49 %	0 %	− 1 %	− 1 %	− 8 %
HT ($q = 10j^2$)	+ 5 %	− 10 %	− 23 %	− 40 %	− 14 %	− 44 %

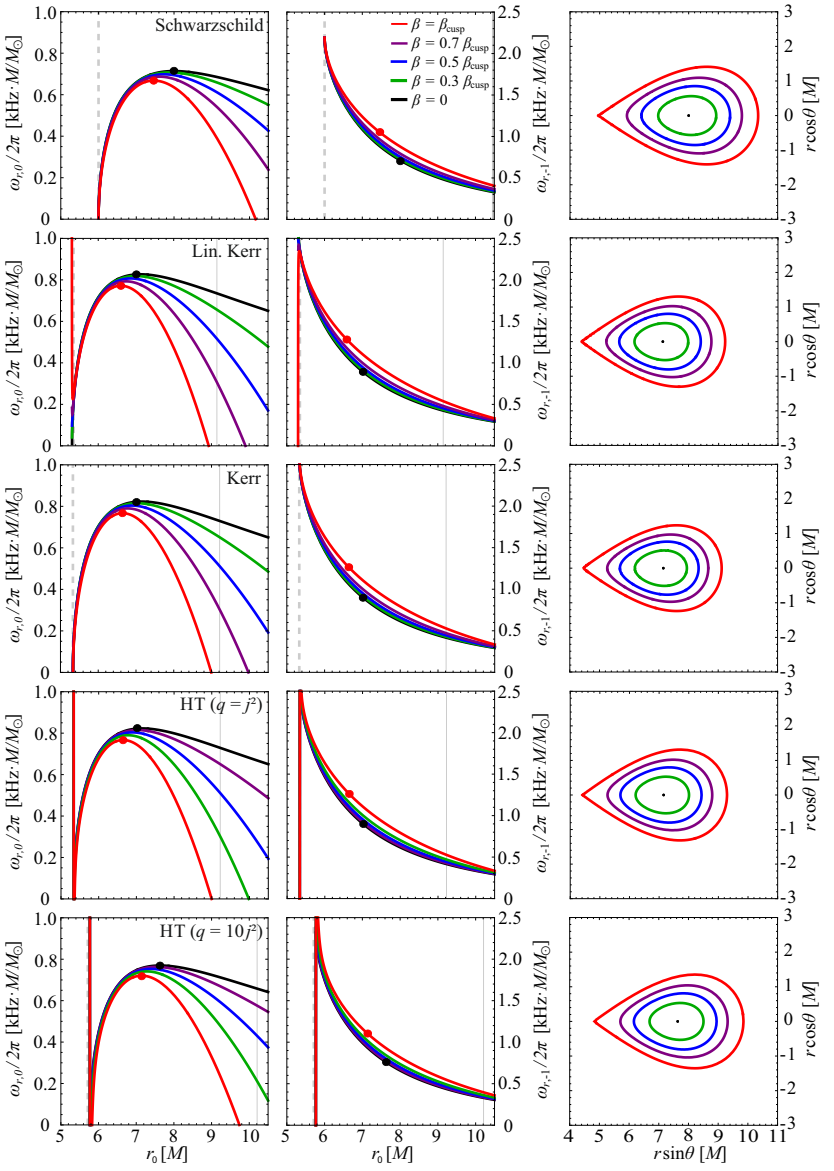

Figure 4. Frequencies of the radial epicyclic mode.
Left panels: The $m = 0$ case. From top to bottom: the Schwarzschild, linearized Kerr, Kerr, and the Hartle-Thorne ($q = j^2$ and $q = 10j^2$) geometry. For rotating stars, we assume $j = 0.2$. The maximal frequencies allowed for the slender torus and for the cusp torus are denoted by the black and red spots, respectively.
Middle panels: The same but for the $m = -1$ case. The coloured spots denote the frequency value corresponding to the radius at which the $m = 0$ radial mode frequency has its maximum.
Right panels: Tori that would oscillate with the maximal value of the $m = 0$ radial epicyclic mode frequency for a given torus thickness.

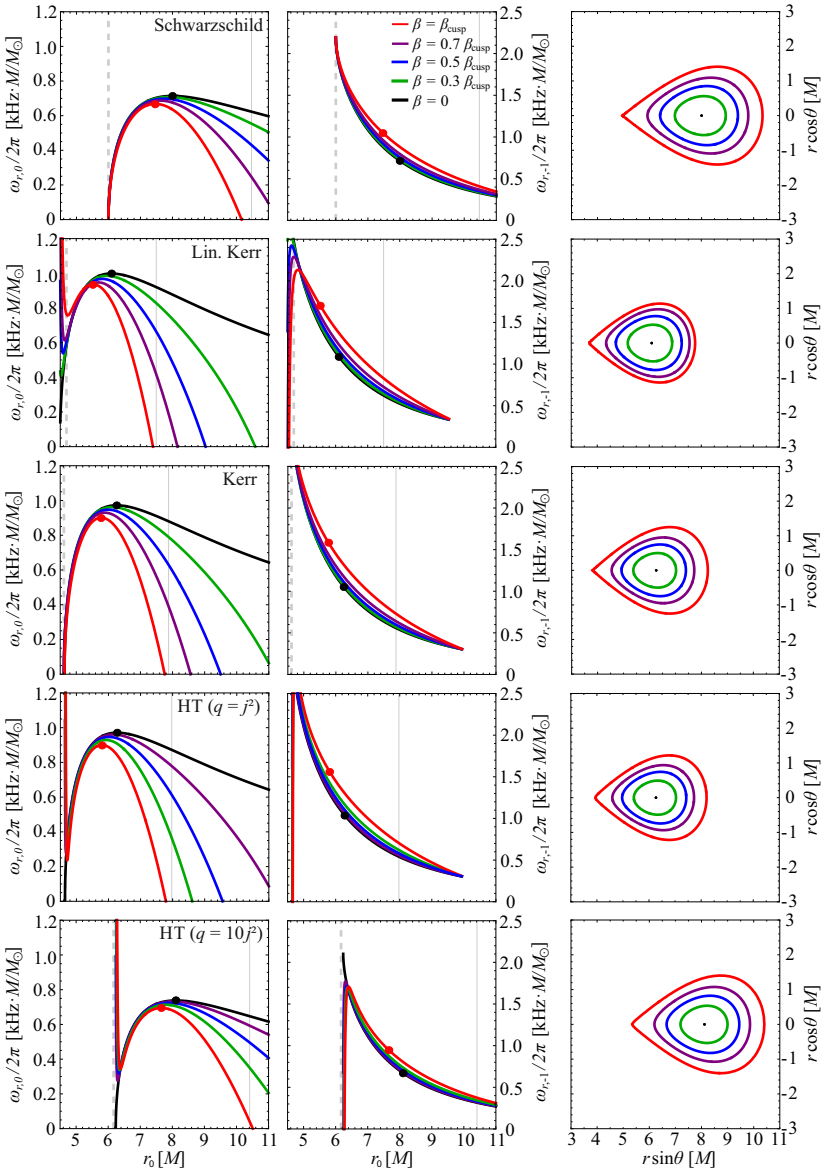

Figure 5. The same as in Figure 4 but for $a = 0.4$.

Table 4. The percentual differences in the proper radial extension $\Delta r_{\rm prop}$ of the cusp tori relevant to Tables 2 and 3 and shown in the right panels of Figures 4 and 5.

Geometry	Schwarzschild		Kerr		Lin. Kerr	
Spin j	0.2	0.4	0.2	0.4	0.2	0.4
HT ($q = j^2$)	− 7 %	− 17 %	0 %	− 4 %	0 %	+ 1 %
HT ($q = 10j^2$)	− 6 %	− 7 %	− 4 %	+ 7 %	+ 2 %	+ 13 %

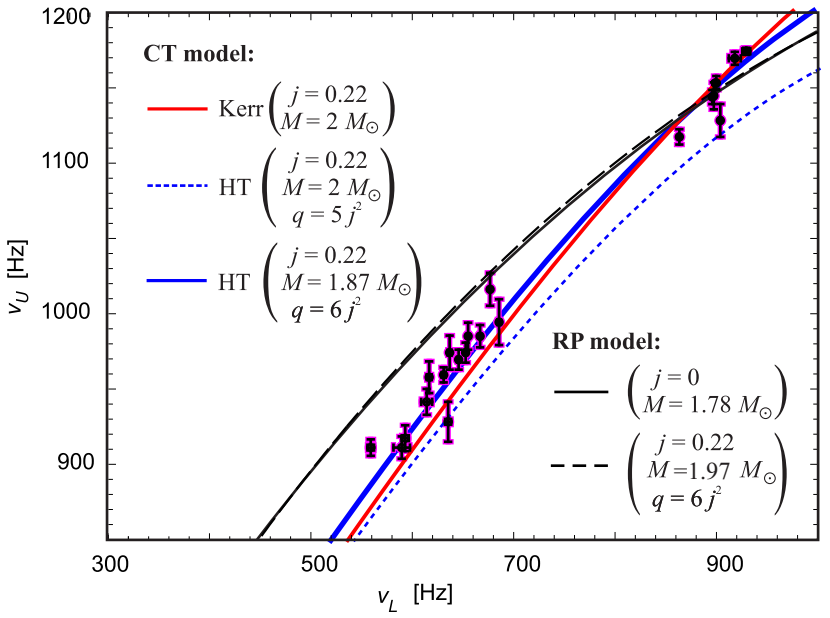

Figure 6. Frequency correlations predicted by the CT model vs. data of the 4U 1636-53 atoll source. The fit for $j = 0.22$ obtained under the consideration of the Kerr geometry (the curve marked as Kerr) is compared here to two examples of predictions obtained under the consideration of the Hartle-Thorne geometry (the curves marked as HT). Examples of the best fits predicted by the relativistic precession model for a given j and q are shown as well (the curves marked as RP model).

5 DISCUSSION AND CONCLUSIONS

Our results indicate that, while the shape of the non-oscillating tori is not much sensitive to the NS quadrupole moment, the frequencies of the radial epicyclic modes of tori oscillations are affected significantly. Clearly, the difference of the frequencies of oscillations

of tori around BHs and NSs can reach tens of percents. Although a more detailed analysis is certainly needed (including the completion of the radial epicyclic mode investigation as well as the investigation of the vertical epicyclic mode behaviour), we may already conclude that the consideration of the quadrupole moment induced by the NS rotation likely should have an impact on the modeling of the high-frequency quasi-periodic oscillations.

Our conclusion is demonstrated in Figure 6. There we consider a recently proposed QPO model (CT model; Török et al., 2016a) and compare the frequencies predicted by the model for several combinations of M, j, q with the frequencies observed in the 4U 1636-53 atoll source (the data are taken from Barret et al., 2006; Török, 2009). We include in the figure examples of correlations predicted by the relativistic precession model (Stella and Vietri, 1999). This model provides less promising fits of the data than the CT model while the effects associated to the NS rotation do not imply a significant improvement (see Török et al., 2012; Török et al., 2016b,a). It is clear from the figure that even when we restrict ourselves to values of the Hartle-Thorne spacetime parameters that are consistent with up-to-date models of neutron stars, no conceivable smooth curve can reproduce the data in a significantly better way compared to the CT model.

ACKNOWLEDGEMENTS

We acknowledge two internal grants of the Silesian University, SGS/12, 13/2019. We wish to thank the INTER-EXCELLENCE project No. LTI17018. KK thanks to the INTER-EXCELLENCE project No. LTT17003. DL thanks the Student Grant Foundation of the Silesian University in Opava, Grant No. SGF/1/2020, which has been carried out within the EU OPSRE project entitled "Improving the quality of the internal grant scheme of the Silesian University in Opava", reg. number: CZ.02.2.69/0.0/0.0/19_073/0016951. The autors were also supported by the ESF projects No. CZ.02.2.69/0.0/0.0/18_054/0014696.

REFERENCES

Abramowicz, M., Jaroszynski, M. and Sikora, M. (1978), Relativistic, accreting disks, *Astronomy and Astrophysics*, **63**, pp. 221–224.

Abramowicz, M. A., Almergren, G. J. E., Kluzniak, W. and Thampan, A. V. (2003), The hartle-thorne circular geodesics, arXiv: gr-qc/0312070v1.

Abramowicz, M. A., Blaes, O. M., Horák, J., Kluzniak, W. and Rebusco, P. (2006), Epicyclic oscillations of fluid bodies: II. Strong gravity, *Classical and Quantum Gravity*, **23**, pp. 1689–1696, arXiv: astro-ph/0511375.

Abramowicz, M. A., Bulik, T., Bursa, M. and Kluźniak, W. (2003a), Evidence for a 2:3 resonance in Sco X-1 kHz QPOs, *A&A*, **404**, pp. L21–L24, arXiv: astro-ph/0206490.

Abramowicz, M. A., Karas, V., Kluzniak, W., Lee, W. H. and Rebusco, P. (2003b), Non-Linear Resonance in Nearly Geodesic Motion in Low-Mass X-Ray Binaries, *PAS*, **55**, pp. 467–466, arXiv: astro-ph/0302183.

Abramowicz, M. A. and Kluźniak, W. (2005), Epicyclic Frequencies Derived From The Effective Potential: Simple And Practical Formulae, *Astrophysics and Space Science*, **300**, pp. 127–136, arXiv: astro-ph/0411709.

Aliev, A. N. and Galtsov, D. V. (1981), Radiation from relativistic particles in nongeodesic motion in a strong gravitational field, *General Relativity and Gravitation*, **13**, pp. 899–912.

Barret, D., Olive, J.-F. and Miller, M. C. (2006), The coherence of kilohertz quasi-periodic oscillations in the X-rays from accreting neutron stars, *MNRAS*, **370**, pp. 1140–1146, arXiv: astro-ph/0605486.

Blaes, O. M., Arras, P. and Fragile, P. C. (2006), Oscillation modes of relativistic slender tori, *Monthly Notices of the Royal Astronomical Society*, **369**, pp. 1235–1252, arXiv: astro-ph/0601379.

Bursa, M. (2005), Global oscillations of a fluid torus as a modulation mechanism for black-hole high-frequency QPOs, *Astronomische Nachrichten*, **326**(9), pp. 849–855, arXiv: astro-ph/0510460.

de Avellar, M. G. B., Porth, O., Younsi, Z. and Rezzolla, L. (2018), Kilohertz QPOs in low-mass X-ray binaries as oscillation modes of tori around neutron stars - I, *MNRAS*, **474**, pp. 3967–3975.

Dönmez, O., Zanotti, O. and Rezzolla, L. (2011), On the development of quasi-periodic oscillations in Bondi-Hoyle accretion flows, *MNRAS*, **412**(3), pp. 1659–1668, arXiv: 1010.1739.

Fragile, P. C., Straub, O. and Blaes, O. (2016), High-frequency and type-c QPOs from oscillating, precessing hot, thick flow, *Monthly Notices of the Royal Astronomical Society*, **461**(2), pp. 1356–1362.

Hartle, J. B. (1967), Slowly Rotating Relativistic Stars. I. Equations of Structure, *APJL*, **150**, p. 1005.

Hartle, J. B. and Thorne, K. S. (1968), Slowly Rotating Relativistic Stars. II. Models for Neutron Stars and Supermassive Stars, *APJ*, **153**, p. 807.

Horák, J., Straub, O., Šrámková, E., Goluchová, K. and Török, G. (2017), Epicyclic oscillations of thick relativistic disks, in *RAGtime 17-19: Workshops on Black Holes and Neutron Stars*, pp. 47–59, URL https://ui.adsabs.harvard.edu/abs/2017bhns.work...47H.

Kluzniak, W. and Abramowicz, M. A. (2001), The physics of kHz QPOs—strong gravity's coupled anharmonic oscillators, *arXiv e-prints*, astro-ph/0105057, arXiv: astro-ph/0105057.

Kluźniak, W., Abramowicz, M. A., Kato, S., Lee, W. H. and Stergioulas, N. (2004), Nonlinear Resonance in the Accretion Disk of a Millisecond Pulsar, *APJL*, **603**(2), pp. L89–L92, arXiv: astro-ph/0308035.

Kotrlová, A., Šrámková, E., Török, G., Goluchová, K., Horák, J., Straub, O., Lančová, D., Stuchlík, Z. and Abramowicz, M. A. (2020), Models of high-frequency quasi-periodic oscillations and black hole spin estimates in Galactic microquasars, *A&A*, **643**, A31, arXiv: 2008.12963.

Rezzolla, L., Yoshida, S. and Zanotti, O. (2003), Oscillations of vertically integrated relativistic tori - I. Axisymmetric modes in a Schwarzschild space-time, *MNRAS*, **344**, pp. 978–992, arXiv: astro-ph/0307488.

Stella, L. and Vietri, M. (1999), kHz Quasiperiodic Oscillations in Low-Mass X-Ray Binaries as Probes of General Relativity in the Strong-Field Regime, *PRL*, **82**(1), pp. 17–20, arXiv: astro-ph/9812124.

Straub, O. and Šrámková, E. (2009), Epicyclic oscillations of non-slender fluid tori around Kerr black holes, *Classical and Quantum Gravity*, **26**(5), 055011, arXiv: 0901.1635.

Török, G. (2009), Reversal of the amplitude difference of kHz QPOs in six atoll sources, *A&A*, **497**, pp. 661–665, arXiv: 0812.4751.

Török, G., Abramowicz, M. A., Kluźniak, W. and Stuchlík, Z. (2005), The orbital resonance model for twin peak kHz quasi periodic oscillations in microquasars, *A&A*, **436**, pp. 1–8.

Török, G., Bakala, P., Šrámková, E., Stuchlík, Z., Urbanec, M. and Goluchová, K. (2012), Mass-angular-momentum relations implied by models of twin peak quasi-periodic oscillations, arXiv: 1408.4220v1.

Török, G., Goluchová, K., Horák, J., Šrámková, E., Urbanec, M., Pecháček, T. and Bakala, P. (2016a), Twin peak quasi-periodic oscillations as signature of oscillating cusp torus, *MNRAS*, **457**, pp. L19–

L23, arXiv: 1512.03841.

Török, G., Goluchová, K., Urbanec, M., Šrámková, E., Adámek, K., Urbancová, G., Pecháček, T., Bakala, P., Stuchlík, Z., Horák, J. and Juryšek, J. (2016b), Constraining Models of Twin-Peak Quasi-periodic Oscillations with Realistic Neutron Star Equations of State, *The Astrophysical Journal*, **833**, 273, arXiv: 1611.06087.

Urbancová, G., Urbanec, M., Török, G., Stuchlík, Z., Blaschke, M. and Miller, J. C. (2019), Epicyclic Oscillations in the Hartle-Thorne External Geometry, *The Astrophysical Journal*, **877**(2), 66, arXiv: 1905.00730.

Proceedings of *RAGtime 20–22, 15–19 Oct., 16–20 Sept., 19–23 Oct., 2018/2019/2020, Opava, Czech Republic*
Z. Stuchlík, G. Török and V. Karas, editors, Silesian University in Opava, 2020, pp. 203–208

Backflow in simulated MHD accretion disks

Ruchi Mishra,[1,a] Miljenko Čemeljić[1,2]
and Włodek Kluźniak[1]

[1]Nicolaus Copernicus Astronomical Center, Polish academy of Sciences,
Bartycka 18, 00-716 Warsaw, Poland
[2]Academia Sinica, Institute of Astronomy and Astrophysics, P.O. Box 23-141,
Taipei 106, Taiwan
[a]rmishra@camk.edu.pl

ABSTRACT
We perform resistive MHD simulations of accretion disk with alpha-viscosity, accreting onto a rotating star endowed with a magnetic dipole. We find backflow in the presence of strong magnetic field and large resistivity, and probe for the dependence on Prandtl number. We find that in the magnetic case the distance from the star at which backflow begins, the stagnation radius, is different than in the hydrodynamic case, and the backflow shows non-stationary behavior. We compare the results with hydrodynamics simulations.

Keywords: stars: magnetic fields – accretion, accretion disks – methods: numerical magnetohydrodynamics (MHD)

1 INTRODUCTION

When matter falls onto a massive object, it often takes the form of a rotating gaseous disk, known as an accretion disk. The process of accretion is understood by a mechanism where the angular momentum from gas is transported outwards which allows the matter to slowly fall into the central object. Accretion plays important role in formation of most astronomical objects such as galaxies, stars and planets. Hence it is important to understand the accretion process.

We are particularly interested in a special class of objects consisting of magnetized stellar type objects, such as T-Tauri stars and white dwarfs or neutron stars in close binary systems. They are mostly surrounded by accretion disk, and have a well defined magnetosphere. In order to understand how accretion takes place in presence of magnetic field we perform non-ideal magneto-hydrodynamic (MHD) numerical simulations.

While spanning the parameter space, we find that in some cases the accretion flow is directed away from the central star. We explore conditions for such behaviour. After the Introduction, In §2 we briefly present our numerical setup, and in §3 present results of our simulations. In §4 we present a comparison with the purely hydrodynamical (HD) case.

978-80-7510-432-8

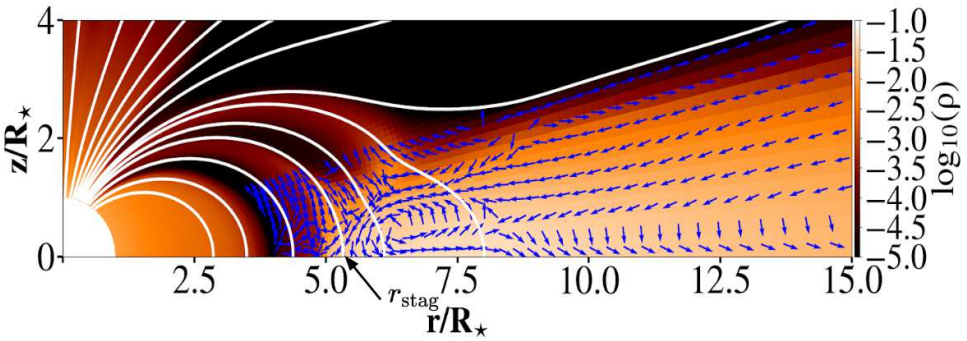

Figure 1. Density in a logarithmic colour grading in MHD simulation with $\alpha_{\rm v} = 1$, $\alpha_{\rm m} = 0.4$, with the initially dipolar magnetic field of 1000 G, for a slowly rotating star. The stagnation radius $r_{\rm stag} = 5.5$ stellar radii. The blue arrows indicate the direction of flow.

2 NUMERICAL SETUP

We perform two-dimensional axisymmetric, viscous and resistive magnetohydrodynamic star-disk simulations. Details of our setup are presented in Čemeljić (2019). We use the publicly available PLUTO code (v.4.1) Mignone et al. (2007, 2012), with a logarithmically stretched grid in radial direction in spherical coordinates, and uniformly spaced co-latitudinal grid. Resolution is $R \times \theta = [217 \times 100]$ grid cells, stretching the domain to 30 stellar radii, in a quadrant of the meridional plane. The solved equations are, in CGS units:

$$\frac{\partial \rho}{\partial t} + \nabla \cdot (\rho \boldsymbol{v}) = 0 \tag{1}$$

$$\frac{\partial (\rho \boldsymbol{v})}{\partial t} + \nabla \cdot \left[\rho \boldsymbol{v}\boldsymbol{v} + \left(P + \frac{B^2}{8\pi} \right) \widetilde{I} - \frac{\boldsymbol{B}\boldsymbol{B}}{8\pi} - \widetilde{\tau} \right] = \rho g \tag{2}$$

$$\frac{\partial E}{\partial t} + \nabla \cdot \left[\left(E + P + \frac{B^2}{8\pi} \right) \boldsymbol{v} - \frac{(\boldsymbol{v} \cdot \boldsymbol{B})\boldsymbol{B}}{4\pi} \right] = \rho \boldsymbol{g} \cdot \boldsymbol{v} \tag{3}$$

$$\frac{\partial \boldsymbol{B}}{\partial t} + \nabla \times (\boldsymbol{B} \times \boldsymbol{v} + \eta_m \boldsymbol{J}) = 0 \tag{4}$$

The above equations are continuity equation, momentum equation, energy equation and induction equation respectively. The symbols have their usual meaning: ρ and v are the matter density and velocity, P is the pressure, B is the magnetic field and $\eta_{\rm m}$ and $\widetilde{\tau}$ represent the resistivity and the viscous stress tensor, respectively.

We perform a parameter study by changing the magnetic field strength, resistivity and alpha viscosity for star rotating at 10% of the equatorial mass-shedding limit $\Omega = 0.1\ \Omega_{\rm br}$. In our setup the viscosity parameter $\alpha_{\rm v}$, which describes the strength of the viscous torque, allowing the disk to accrete, is varied from 0 to 1. The resistivity parameter $\alpha_{\rm m}$, which defines coupling of the stellar magnetic field with the disk material, is also varied from 0 to 1. The effect of changes in those two parameters is described by the magnetic Prandtl

$\alpha_{\rm v}$	$\alpha_{\rm m}$	$P_{\rm m} = \frac{2}{3}\frac{\alpha_{\rm v}}{\alpha_{\rm m}}$	$B_\star$(G)	$\Omega_\star/\tilde{\Omega}$	Backflow	$R_{\rm stag}$	Type
0.1	0.1	0.60	1000	0.1	No	–	–
0.4	0.1	2.60	1000	0.1	No	–	–
1.0	0.1	6.60	1000	0.1	No	–	–
0.1	0.4	0.16	1000	0.1	No	–	–
0.4	0.4	0.60	1000	0.1	No	–	–
1.0	0.4	1.60	1000	0.1	No	–	–
0.1	1.0	0.06	1000	0.1	Yes	6 ± 1	steady
0.2	1.0	0.13	1000	0.1	Yes	7.5 ± 1.5	steady
0.3	1.0	0.20	1000	0.1	Yes	6 ± 1	steady
0.4	1.0	0.26	1000	0.1	Yes	6 ± 2	steady
0.5	1.0	0.30	1000	0.1	Yes	6 ± 1	steady
0.6	1 0	0.40	1000	0.1	Yes	6 ± 1	steady
0.7	1.0	0.46	1000	0.1	Yes	8 ± 0.5	intermittent
0.8	1.0	0.53	1000	0.1	Yes	8 ± 0.5	intermittent
1.0	1.0	0.60	1000	0.1	No	–	–

Table 1. List of parameters and results : presence of backflow, stagnation radius and type of backflow for strongly magnetized, slowly rotating stars

number:

$$P_{\rm m} = \frac{2}{3}\frac{\alpha_{\rm v}}{\alpha_{\rm m}} \tag{5}$$

Each simulation in our parameter study is run until a quasi-stationary state is reached.

3 BACKFLOW IN MHD DISK

A snapshot in a quasi-stationary state in our simulation is shown in Fig. 1. The accretion disk is truncated at a few stellar radii due to magnetic pressure. The accretion flow is channelled into a funnel flow where the flow follows the magnetic field lines. In the outer region of the disk the accretion flow is towards the central star. In the inner region of the disk, along the midplane of the disk, the flow is away from the star–this flow is termed as backflow in the accretion disk. Such equatorial outflow was first reported in the analytical work by Urpin (1984). Global solution for three dimensional viscous alpha accretion disk was obtained in Kita (1995) and Kluzniak and Kita (2000). Equatorial backflow is not uncommon. It was obtained in numerical simulations in Kley and Lin (1992), Igumenshchev

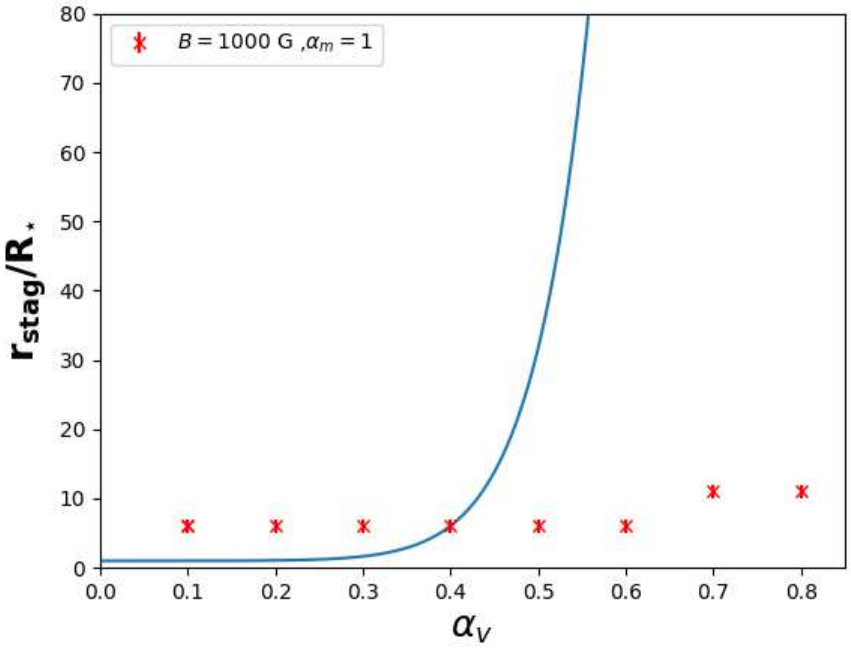

Figure 2. Position of the stagnation radius in simulations with different viscosity coefficients $\alpha_{\rm v}$ for magnetic resistive coefficient $\alpha_{\rm m} = 1$. The blue solid curve is from the Kluzniak and Kita (2000) purely HD analytical solution.

et al. (1996), Rozyczka et al. (1994), and also recently in MRI simulations by Mishra et al. (2019) and in GRMHD simulation of RIAF (Radioactively inefficient accretion flow) in White et al. (2020)

Backflow appears in the disk for particular combinations of $\alpha_{\rm v}$ and $\alpha_{\rm m}$ parameters. In the Table 1 we present different parameters, and we check whether there is backflow in the disk. Lower values of resistive parameter $\alpha_{\rm m}$ restrict backflow in the disk. For higher values of resisitive parameter, a backflow is obtained. We obtain two kinds of backflows: a steady, or an intermittent flow. Intermittent backflow is found as we approach higher values of viscosity parameter. We also show the presence of backflow in dependence on magnetic Prandtl number $P_{\rm m}$. Above a critical value of magnetic Prandtl number, which is about $P_{\rm m} \sim 0.6$, there is no backflow in the disk.

4 COMPARISON WITH BACKFLOW IN HD DISK

Initializing with the Kluzniak and Kita (2000) solutions, we performed numerical simulations in purely hydrodynamical cases in Mishra et al. (2020). Backflow is obtained in the mid-plane of the disk for alpha viscosity coefficient $\alpha_{\rm v} < 0.6$. The starting point of backflow, stagnation radius, is found to be a function of alpha viscosity. In our MHD simulations we obtain backflow for even higher values of $\alpha_{\rm v}$. The stagnation radius, in the case of slowly rotating stars, shows to be independent of alpha viscosity – see Fig. 2.

5 CONCLUSIONS

We find backflow in the simulated MHD disk in a part of the parameter space. In the presence of strong magnetic field and high resisitivity, we obtain backflow for higher values of viscous parameter than critical $\alpha_{\rm v}$ in purely HD case. We find a dependence of backflow on magnetic Prandtl number, $P_{\rm m}$, where for values $P_{\rm m} < 0.6$ there is a backflow. As we approach the critical $P_{\rm m}$, there is intermittent backflow in the disk. We do not find the same relationship of stagnation radius and viscosity parameter as the one obtained in purely HD cases.

ACKNOWLEDGEMENTS

Work at the Copernicus Center was funded by the Polish NCN grant No. 2019/33/B/ST9/01564. MČ developed the setup for star-disc simulations while in CEA, Saclay, under the ANR Toupies grant, and partly worked on it while in Shanghai Astronomical Observatory, supported by CAS President's International Fellowship for Visiting Scientists (grant No. 2020VMC0002). We thank ASIAA/TIARA (PL and XL clusters) in Taipei, Taiwan and NCAC (CHUCK cluster) in Warsaw, Poland, for access to Linux computer clusters used for high-performance computations. We thank the PLUTO team for the possibility to use the code.

REFERENCES

Igumenshchev, I. V., Chen, X. and Abramowicz, M. A. (1996), Accretion discs around black holes: two-dimensional, advection-cooled flows, *Mon. Not. R. Astron. Soc*, **278**(1), pp. 236–250, arXiv: astro-ph/9509070.

Kita, D. B. (1995), *A Study of the Vertical and Radial Structure of Polytropic Accretion Disks*, Ph.D. thesis, The University of Wisconsin - Madison.

Kley, W. and Lin, D. N. C. (1992), Two-dimensional Viscous Accretion Disk Models. I. On Meridional Circulations in Radiative Regions, *Astrophys. J.*, **397**, p. 600.

Kluzniak, W. and Kita, D. (2000), Three-dimensional structure of an alpha accretion disk, *arXiv Astrophysics e-prints*, arXiv: astro-ph/0006266.

Mignone, A., Bodo, G., Massaglia, S., Matsakos, T., Tesileanu, O., Zanni, C. and Ferrari, A. (2007), PLUTO: A Numerical Code for Computational Astrophysics, *Astrophys. J.*, **170**(1), pp. 228–242, arXiv: astro-ph/0701854.

Mignone, A., Zanni, C., Tzeferacos, P., van Straalen, B., Colella, P. and Bodo, G. (2012), The PLUTO Code for Adaptive Mesh Computations in Astrophysical Fluid Dynamics, *Astrophys. J.*, **198**(1), 7, arXiv: 1110.0740.

Mishra, B., Begelman, M. C., Armitage, P. J. and Simon, J. B. (2019), Strongly magnetized accretion discs: structure and accretion from global magnetohydrodynamic simulations, *Monthly Notices of the Royal Astronomical Society*, **492**(2), pp. 1855–1868, ISSN 0035-8711, arXiv: https://academic.oup.com/mnras/article-pdf/492/2/1855/31838331/stz3572.pdf, URL https://doi.org/10.1093/mnras/stz3572.

Mishra, R., Čemeljić, M. and Kluźniak, W. (2020), Backflow in Accretion Disk, *arXiv e-prints*, arXiv:2006.01851, arXiv: 2006.01851.

Rozyczka, M., Bodenheimer, P. and Bell, K. R. (1994), A Numerical Study of Viscous Flows in Axisymmetric alpha -Accretion Disks, *Astrophys. J.*, **423**, p. 736.

Urpin, V. A. (1984), Hydrodynamic flows in accretion disks., *sovast*, **28**, pp. 50–53.

Čemeljić, M. (2019), "Atlas" of numerical solutions for star-disk magnetospheric interaction, *Astrophys. J.*, **624**, A31, arXiv: 1811.02808.

White, C. J., Quataert, E. and Gammie, C. F. (2020), The Structure of Radiatively Inefficient Black Hole Accretion Flows, *Astrophys. J.*, **891**(1), 63, arXiv: 2001.10634.

Proceedings of *RAGtime 20–22, 15–19 Oct., 16–20 Sept., 19–23 Oct., 2018/2019/2020, Opava, Czech Republic*
Z. Stuchlík, G. Török and V. Karas, editors, Silesian University in Opava, 2020, pp. 209–219

Can conformal gravity mimic the rotation of Kerr black hole in terms of particle dynamics?

Bakhtiyor Narzilloev[1,2,a] and Javlon Rayimbaev[2,3,4,b]

[1]Center for Field Theory and Particle Physics and Department of Physics, Fudan University, 200438 Shanghai, China,
[2]Ulugh Beg Astronomical Institute, Astronomicheskaya 33, Tashkent 100052, Uzbekistan,
[3]National University of Uzbekistan, Tashkent 100174, Uzbekistan
[4]Institute of Nuclear Physics, Ulughbek, Tashkent 100214, Uzbekistan
[a]nbakhtiyor18@fudan.edu.cn
[b]javlon@astrin.uz

ABSTRACT
Testing different theories of gravity through test particle motion around black holes can help deeply understand the nature of the gravity. In this paper we investigated harmonic oscillations of charged particle around a black hole with conformal parameters assuming that a black hole is immersed in the uniform external magnetic field and showed that the increase of the conformal parameters increases the radial frequency ν_r and decreases the other two, ν_ϕ and ν_θ. Then, we considered test particle to be neutral and studied the possibility of mimicking the rotation parameter of Kerr black hole with parameters of black hole in conformal gravity using the results on radius of innermost stable circular orbits (ISCO). We have shown that the conformal parameter L can mimic the spin parameter of Kerr black hole up to $a = 0.45M$ in the case of the parameter $N = 3$ and this value goes down for the smaller values of the parameter N.

Keywords: Conformal gravity – Harmonic oscillations –Kerr black hole – test particle – ISCO.

1 INTRODUCTION

One of the fundamental problems of general theory of relativity is the presence of singularity in almost all known exact analytical solutions of the field equations. For the black hole solutions the central physical singularity with the infinite curvature is unavoidable. There are several attempts to avoid the singularity: coupling with nonlinear electrodynamics (Bardeen, 1968; Hayward, 2006; Ayón-Beato and García, 1998), conformal transformations (Englert et al., 1976; Narlikar and Kembhavi, 1977; Mannheim, 2012; Bars et al., 2014; Bambi et al., 2017, 2016) etc.

One of the possible ways of excluding the physical singularity in the black hole solutions is using the conformal gravity where metric tensor is transformed as

$$g_{\mu\nu} \to g^*_{\mu\nu} = \Omega^2 g_{\mu\nu}\,, \tag{1}$$

with $\Omega = \Omega(x)$ being a conformal factor of transformation.

Using the modification of Einstein's gravity by the auxiliary scalar field ϕ (dilaton) one may obtain the following Lagrangian for gravity

$$\mathcal{L}_1 = \phi^2 R + 6\, g^{\mu\nu}(\partial_\mu\phi)(\partial_\nu\phi)\,. \tag{2}$$

Other efficient way of introducing conformal gravity without introducing dilaton can be performed via following Lagrangian

$$\mathcal{L}_2 = a\, C^{\mu\nu\rho\sigma} C_{\mu\nu\rho\sigma} + b\, {}_*R^{\mu\nu\rho\sigma} R_{\mu\nu\rho\sigma}\,. \tag{3}$$

where $C^{\mu\nu\rho\sigma}$ is the Weyl tensor, $R^{\mu\nu\rho\sigma}$ is the Riemann tensor, ${}_*R^{\mu\nu\rho\sigma}$ is the dual of the Riemann tensor, a and b are constants.

In Einstein's theory of gravity the singularity can be resolved by suitable conformal transformation if a spacetime metric $g_{\mu\nu}$ is singular in a gauge. Singularity-free black hole solutions in conformal gravity have been proposed in Refs. (Bambi et al., 2017, 2016). It was shown that these spacetimes are geodetically complete because no massless or massive particles can reach the center of the black hole in a finite amount of time or for a finite value of the affine parameter (Bambi et al., 2017, 2016). Within this theory the curvature invariants do not diverge at the center $r = 0$.

The space-time metric of the spherically symmetric static black hole in Schwarzschild coordinates (t, r, θ, ϕ) in conformal gravity can be described as (Bambi et al., 2017, 2016)

$$\mathrm{d}s^2 = S(r)\left[-f(r)\mathrm{d}t^2 + \frac{\mathrm{d}r^2}{f(r)} + r^2\left(\mathrm{d}\theta^2 + \sin^2\mathrm{d}\phi^2\right)\right]\,, \tag{4}$$

where $f(r) = f = 1 - 2M/r$ is the lapse function and the scaling factor $S(r)$ has the following form

$$S(r) = S = \left(1 + \frac{L^2}{r^2}\right)^{2N}\,, \tag{5}$$

with N being a quantity describing conformal gravity assumed to be an integer, L is a new conformal parameter of the black hole coming from the theory.

The electromagnetic fields of slowly rotating neutron stars in conformal gravity have been studied in Ref. Turimov et al. (2018). The authors of Ref. (Zhou et al., 2018) have tested the conformal gravity with the SMBH observation. The energy conditions for conformal gravity are studied in (Toshmatov et al., 2017a) while scalar perturbations of nonsingular nonrotating black holes in conformal gravity have been studied in (Toshmatov et al., 2017b). Charged and magnetized particle motion around rotating non-singular black hole immersed in the external uniform magnetic field in conformal gravity has been studied in

(Narzilloev et al., 2020a; Haydarov et al., 2020) as well as in the spacetime of the quasi-Kerr compact object (Narzilloev et al., 2019). Particle dynamics around the deformed NUT spacetime has been investigated in (Narzilloev et al., 2020).

In most astrophysical observations and measurements of energetic and optical processes around supermassive black hole (SMBH) such as QPOs, ISCO radius measurements (Stuchlík et al. (2020); Kolos, Martin et al. (2020)) and the black hole shadow central gravitating objects are considered as rotating Kerr ones. However, parameters of some alternative and extended theories of gravity may provide similar effects on the processes around the black holes as the spin parameter of the Kerr model. It is one of the problems in relativistic astrophysics where difficulty of distinguishing the central static black hole with the parameters of alternative theories from rotating Kerr black hole takes a place. In our previous papers we have investigated how black hole charge (Rayimbaev et al. (2020); Vrba et al. (2020); Turimov et al. (2020); Narzilloev et al. (2020b)) and different parameters of alternative theories of gravity (Haydarov et al. (2020); Haydarov et al. (2020); Abdujabbarov et al. (2020); Rayimbaev et al. (2020)) can mimic the spin of rotating Kerr black holes proving the same values of ISCO radius for magnetized particles.

No-hair theorem states that black hole can not have its own magnetic moment. However, it is possible to consider a black hole in an external magnetic field generated by external sources. The first approach to get solution of Maxwell equation for the components of the external asypmtotically uniform magnetic field in curved spacetime is Wald's method (Wald (1974)) and during the past years the method has been developed by several authors (Aliev et al. (1986); Aliev and Gal'tsov (1989); Aliev and Özdemir (2002); Stuchlík et al. (2014); Stuchlík and Kološ (2016)).

This work is devoted to the study of test particle motion around non rotating compact object in conformal gravity and organized as follows: The Sect. 2 is devoted to the study of charged particle motion where we mostly focus on the QPOs of charged particles. In Sect. 3 neutral particles motion around black hole in conformal gravity have been investigated where we discuss possible ways of mimicking the rotation parameter of Kerr black hole with confomal parameters. We summarize our results in Sect. 5.

Throughout this work we use signature $(-,+,+,+)$ for the spacetime and geometrized unit system $G = c = 1$ (However, for an astrophysical application we have written the speed of light and Newtonian constant explicitly in our expressions). Latin indices run from 1 to 3 and Greek ones from 0 to 3.

2 CHARGED PARTICLE MOTION

In this section we study charged particle motion around a black hole in conformal gravity in the presence of the external uniform magnetic field. The Hamilton-Jacobi equation for test particle with mass m and the charge e can be expressed as (Narzilloev et al., 2020b)

$$g^{\mu\nu}\left(\frac{\partial \mathcal{S}}{\partial x^{\mu}} + eA_{\mu}\right)\left(\frac{\partial \mathcal{S}}{\partial x^{\nu}} + eA_{\nu}\right) = -m^2 \,, \tag{6}$$

where $A^\alpha = (0, 0, 0, B/2)$ is a four vector potential of the external magnetic field B. The solution of equation (6) can be sought in the following form

$$\mathcal{S} = -\mathcal{E}t + \mathcal{L}\phi + \mathcal{S}_r(r) + \mathcal{S}_\theta(\theta)\,, \tag{7}$$

where $\mathcal{E}$ and $\mathcal{L}$ are the energy and the angular momentum of the test particle respectively.

It is convenient to consider particle motion on a constant plane $\dot{\theta} = 0$ ($p_\theta = 0$) and one can write the radial part as

$$\dot{r}^2 + V_{\rm eff}(r;\theta) = \mathcal{E}^2\,, \tag{8}$$

where the effective potential has a form

$$V_{\rm eff}(r;\theta) = f(r)\left[S(r) + \left(\frac{\mathcal{L}}{r\sin\theta} + \omega_{\rm B} r S(r)\sin\theta\right)^2\right], \tag{9}$$

with magnetic coupling parameter $\omega_{\rm B} = eB/(2mc)$ or so-called cyclotron frequency which characterizes the interaction between charged particle and the external magnetic field.

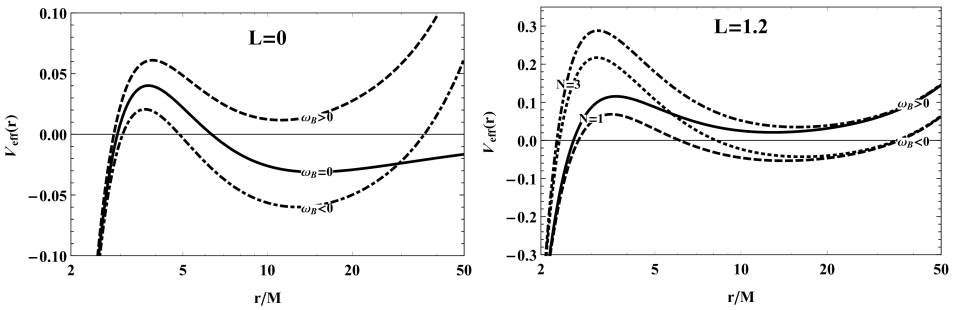

Figure 1. The radial dependence of effective potential of charged particle for the different values of the conformal, scale, and magnetic coupling parameters.

Fig. 1 shows the radial dependence of the effective potential of the charged particle. One can see from the figure that when $\omega_{\rm B} > 0$ effective potential is bigger than the case of $\omega_{\rm B} < 0$ and it increases with the increase of the values of parameters L and N. It is worth to note that at large distances the effect of magnetic field plays an important role rather than the effect of conformal gravity.

2.1 Harmonic oscillations

If a charged test particle is slightly displaced from the equilibrium position, at r_0 and $\theta_0 = \pi/2$, being stable circular orbit, which corresponds to the minimum of the effective potential $V_{\rm eff}(r,\theta)$ the particle will start oscillating around the minimum realizing thus epicyclic motion governed by linear harmonic oscillations. For harmonic oscillations around the minimum of the effective potential $V_{\rm eff}(r)$, the evolution of the displacement of

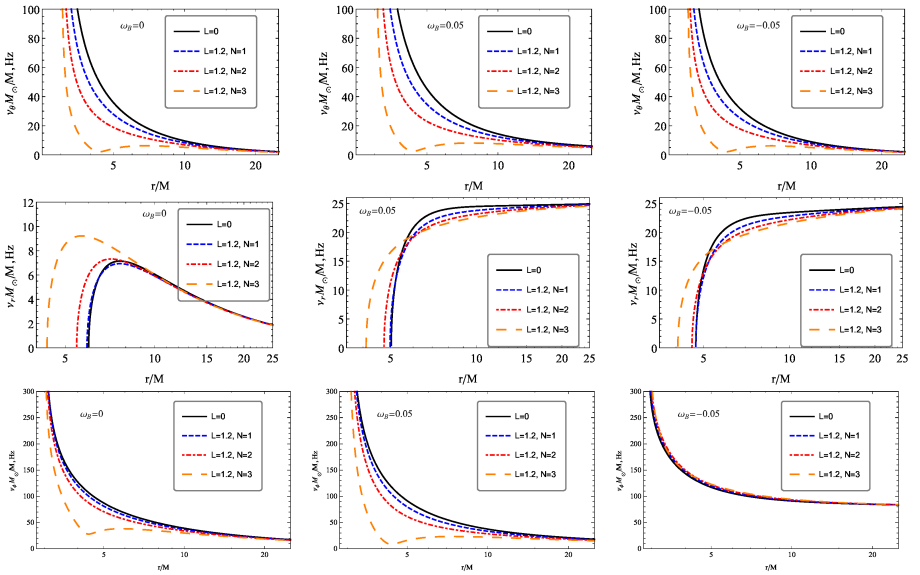

Figure 2. Radial profiles of fundamental frequencies of charged particles around Schwarzschild black hole in conformal gravity, measured by an observer at infinity, for different values of magnetic coupling $\omega_{\rm B}$ and conformal parameters L and N .

coordinates reads $r = r_0 + \delta r$, $\theta = \theta_0 + \delta\theta$. Locally measured angular frequencies of the harmonic oscillators can be expressed as

$$\omega_r^2 = \frac{1}{g_{rr}}\frac{\partial^2 V_{\rm eff}}{\partial r^2} \,, \tag{10}$$

$$\omega_\theta^2 = \frac{1}{g_{\theta\theta}}\frac{\partial^2 V_{\rm eff}}{\partial \theta^2} \,, \tag{11}$$

$$\omega_\phi = \mathcal{L} - g_{\phi\phi}\omega_{\rm B} \,. \tag{12}$$

Frequencies themselves can be written using the following expression in the unit of Hz

$$\nu_i = \frac{1}{2\pi}\frac{c^3}{GM}\Omega_i \,, \tag{13}$$

where $i = r, \theta, \phi$ and

$$\Omega_i = \frac{1}{\sqrt{-g_{tt}}}\omega_i \,. \tag{14}$$

The radial dependence of fundamental frequencies of particles is presented in Fig. 2. One can see from the figures that values of radial oscillations increase with the increase of L,N while others decrease with the increase of latter.

3 TEST PARTICLE MOTION AROUND BLACK HOLE IN CONFORMAL GRAVITY

In this part we restrict our calculations considering the test particle to be electrically neutral and investigate its motion around static black hole in conformal gravity. The Hamilton-Jacobi equation of motion of test particles (6) reduces to

$$g^{\mu\nu}\frac{\partial \mathcal{S}}{\partial x^{\mu}}\frac{\partial \mathcal{S}}{\partial x^{\nu}} = -m^2 \,. \tag{15}$$

On the equatorial plane ($\theta = \pi/2$) the equations of motion can be expressed using conservative quantities, specific energy $\mathcal{E}$ and angular momentum l as

$$\dot{t} = \frac{\mathcal{E}}{f\,\mathrm{S}} \,, \tag{16}$$

$$\dot{r}^2 = \mathcal{E}^2 - f\mathrm{S}\left(1 + \frac{l^2}{r^2}\right) \,, \tag{17}$$

$$\dot{\phi} = \frac{l}{\mathrm{S}r^2} \,. \tag{18}$$

One can define the effective potential of radial motion of magnetized particles on equatorial plane as

$$\dot{r}^2 = \mathcal{E}^2 - 1 - 2V_{\mathrm{eff}} \,, \tag{19}$$

where the effective potential has the following form

$$V_{\mathrm{eff}} = \frac{1}{2}\left[f\,\mathrm{S}\left(1 + \frac{l^2}{r^2}\right) - 1\right] \,, \tag{20}$$

Now we will consider orbits of test particles to be circular, or more specifically the innermost stable ones. Using the following standard conditions

$$V_{\mathrm{eff}}(r) = \mathcal{E}^2 \,, \qquad V'_{\mathrm{eff}}(r) = 0 \,, \qquad V''_{\mathrm{eff}}(r) = 0 \,, \tag{21}$$

one can easily find the values of ISCO radius. Angular momentum for circular orbits can also be found from the equations above that reads

$$\mathcal{L} = \frac{r^2\left[L^2(4MN + M - 2Nr) + Mr^2\right]}{L^2[r(2N+1) - M(4N+3)] + r^2(r-3M)} \,. \tag{22}$$

The energy of the charged particle at circular orbits will have the following form

$$\mathcal{E} = \frac{\left(L^2 + r^2\right)(r-2M)^2\left(1 + \frac{L^2}{r^2}\right)^{2N}}{r\left\{L^2[r(2N+1) - M(4N+3)] + r^2(r-3M)\right\}} \,. \tag{23}$$

Fig. 3 illustrates the radial profiles of the angular momentum and energy of the test particle at circular orbits on equatorial plane. One can see that the angular momentum and

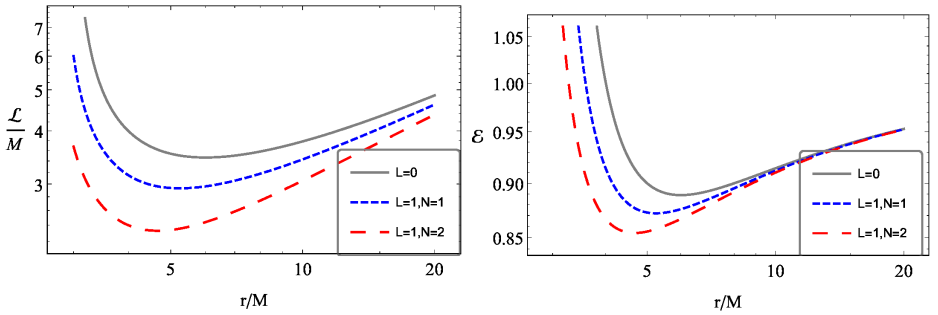

Figure 3. Redial dependence of specific angular momentum ($\mathcal{L}$ at the left panel) and energy ($\mathcal{E}$ at the right panel) of the particles for circular stable orbits

the energy of the particle decrease in the presence of conformal parameters. It can be also seen that the plots are shifted to the left which corresponds to the decrease of the ISCO.

Using the condition for the stability of circular orbits ($\partial_r^2 V_{\text{eff}} \geq 0$) one can write

$$L^4\left[M(8N(4N+3)+1)r - 2M^2(4N+1)(4N+3) - 4N(2N+1)r^2\right] + 2L^2Mr^2[r(2N+1) - M(4N+3)] + Mr^4(r-6M) \geq 0\,. \tag{24}$$

One can see from Eq. (24) that in the absence of conformal part $L = 0$ we get $r_{\text{isco}} = 6M$ being the value of ISCO in Schwarzschild case. The analytical form of the solution of Eq. (24) is quite complicated and it would be difficult to see the effects of conformal parameters L and N on ISCO radius of the test particle from such expression. Thus, it is better to show detailed analysis in plot form which we will do here.

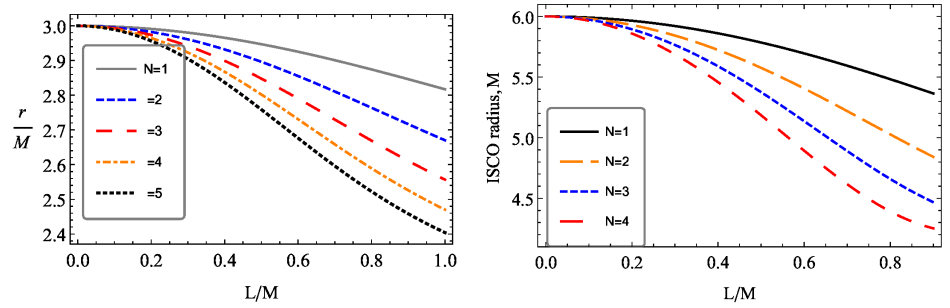

Figure 4. Dependence of the minimal distance of circular orbits (left panel) and ISCO radius (right panel) of test particles around black hole in conformal gravity on the conformal parameter L for the fixed values of the parameter N.

From the condition above one can get the relation between the ISCO radius and conformal parameters. The Fig. 4 shows the profiles of ISCO radius depending on conformal parameters. One can see that the increase of both conformal parameters causes to decrease

the ISCO radius and the minimal radius of circular orbits. One can also mention that both plots have similar shapes for the given ranges of conformal parameter L.

3.1 Can conformal gravity parameters mimic the rotation parameter of Kerr BH?

As an astrophysical application of the studies of the ISCO of neutral particles orbiting around the non-rotating black hole in conformal gravity, we consider here the possibility of mimicking the spin parameter a of Kerr black hole with the parameters L and N of black hole in conformal gravity using the results for ISCO.

The ISCO radius of the test particles for co-rotating orbits around Kerr BH is given by the relation (Bardeen et al., 1972)

$$r_{\rm ISCO} = 3 + \mathrm{Z}_2 - \sqrt{(3-\mathrm{Z}_1)(3+\mathrm{Z}_1+2\mathrm{Z}_2)}\,, \tag{25}$$

where

$$\mathrm{Z}_1 = 1 + \left(\sqrt[3]{1-a} + \sqrt[3]{1+a}\right)\sqrt[3]{1-a^2}\,, \qquad \mathrm{Z}_2 = \sqrt{3a^2+\mathrm{Z}_1^2}\,.$$

But, since in the given form the value of ISCO radius depends on the choice of coordinate system we need to deal with invariant quantity that defines the ISCO radius to compare the results in two different spacetime metrics. As for such invariant quantity we use the line element which takes the following form on equatorial plane where we set all the coordinates to constants except the coordinate ϕ

$$\mathrm{d}s_\phi = \sqrt{g_{\phi\phi}}\mathrm{d}\phi\,, \tag{26}$$

and after integrating the length of such circular orbit becomes

$$l_{ISCO} = 2\pi\sqrt{g_{\phi\phi}}|_{r=r_{ISCO}}\,. \tag{27}$$

The invariant ISCO radius then can be defined as

$$R_{ISCO} = \frac{l_{ISCO}}{2\pi}\,, \tag{28}$$

and one can get the degeneracy between the spin of the Kerr metric and conformal parameters for the matching value of such radius obtained for these two spacetime metrics.

Now we may investigate how well the conformal parameters can mimic the rotation parameter of Kerr one through the matching invariant ISCO radius, R_{ISCO}. In Fig. 5 we show the degeneracy between rotation parameter of Kerr black hole and static black hole with conformal parameters. One may see that the conformal parameter L can mimic the spin parameter of Kerr black hole providing the same value for ISCO radius of test particles up to the value of $a/M \simeq 0.45$ when $N = 3$ and such mimicking value becomes smaller with the decrease of the parameter N and it takes the value $a/M \simeq 0.3$ for $N = 1$.

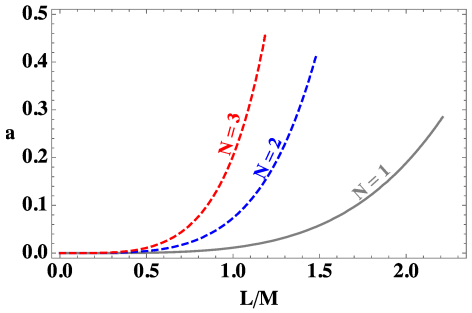

Figure 5. Relation that shows how the spin parameter a of Kerr black hole and corresponding conformal parameter L provide the same ISCO radius for test particles for the different values of the parameter N.

4 CONCLUSION

In this work, we have studied charged particle motion around a static black hole with conformal paramters immersed in the external uniform magnetic field. Investigation of the QPO for the charged particle showed that the frequency of the radial oscillation becomes higher for bigger conformal parameters while the other fundamental frequencies have opposite behaviour. We have also studied circular motion of neutral test particles around Schwarzschild black hole in conformal gravity. Analysis of the studies of specific energy and angular momentum for circular stable orbits show that the increase of both conformal parameters cause to decrease of the energy and angular momentum. It is obtained that the value of ISCO radius decreases with the increase of both conformal parameters. Comparisons of the ISCO of the test particle around a black hole in conformal gravity with the Kerr black hole show that the conformal parameter L can mimic the spin of Kerr black hole up to $a = 0.45$ in the case of the parameter $N = 3$ and this value decreases with the decrease of the parameter N.

ACKNOWLEDGEMENTS

This research is supported by Grants No. VA-FA-F-2-008, No.MRB-AN-2019-29 of the Uzbekistan Ministry for Innovative Development. BN acknowledges support from the China Scholarship Council (CSC), Grant No. 2018DFH009013.

REFERENCES

Abdujabbarov, A., Rayimbaev, J., Turimov, B. and Atamurotov, F. (2020), Dynamics of magnetized particles around 4-D Einstein Gauss-Bonnet black hole, *Physics of the Dark Universe*, **30**, 100715.

Aliev, A. N. and Gal'tsov, D. V. (1989), REVIEWS OF TOPICAL PROBLEMS: "Magnetized" black holes, *Soviet Physics Uspekhi*, **32**, pp. 75–92.

Aliev, A. N., Galtsov, D. V. and Petukhov, V. I. (1986), Negative absorption near a magnetized black hole - Black hole masers, *Astrophys. Space Sci.*, **124**, pp. 137–157.

Aliev, A. N. and Özdemir, N. (2002), Motion of charged particles around a rotating black hole in a magnetic field, *Mon. Not. R. Astron. Soc.*, **336**, pp. 241–248, arXiv: gr-qc/0208025.

Ayón-Beato, E. and García, A. (1998), Regular Black Hole in General Relativity Coupled to Nonlinear Electrodynamics, *Physical Review Letters*, **80**, pp. 5056–5059, arXiv: gr-qc/9911046.

Bambi, C., Malafarina, D. and Modesto, L. (2016), Black supernovae and black holes in non-local gravity, *Journal of High Energy Physics*, **2016**(4), 147, arXiv: 1603.09592.

Bambi, C., Modesto, L. and Rachwał, L. (2017), Spacetime completeness of non-singular black holes in conformal gravity, *JCAP*, **5**, 003, arXiv: 1611.00865.

Bardeen, J. (1968), in C. DeWitt and B. DeWitt, editors, *Proceedings of GR5*, p. 174, Tbilisi, USSR, Gordon and Breach.

Bardeen, J. M., Press, W. H. and Teukolsky, S. A. (1972), Rotating Black Holes: Locally Nonrotating Frames, Energy Extraction, and Scalar Synchrotron Radiation, *Astrophys. J.*, **178**, pp. 347–370.

Bars, I., Steinhardt, P. and Turok, N. (2014), Local conformal symmetry in physics and cosmology, *Phys. Rev. D*, **89**(4), 043515, arXiv: 1307.1848.

Englert, F., Truffin, C. and Gastmans, R. (1976), Conformal invariance in quantum gravity, *Nuclear Physics B*, **117**(2), pp. 407–432.

Haydarov, K., Abdujabbarov, A., Rayimbaev, J. and Ahmedov, B. (2020), Magnetized particle motion around black holes in conformal gravity: Can magnetic interaction mimic spin of black holes?, *Universe*, **6**(3), ISSN 2218-1997, URL https://www.mdpi.com/2218-1997/6/3/44.

Haydarov, K., Rayimbaev, J., Abdujabbarov, A., Palvanov, S. and Begmatova, D. (2020), Magnetized particle motion around magnetized Schwarzschild-MOG black hole, *European Physical Journal C*, **80**(5), 399, arXiv: 2004.14868.

Hayward, S. A. (2006), Formation and Evaporation of Nonsingular Black Holes, *Physical Review Letters*, **96**(3), 031103, arXiv: gr-qc/0506126.

Kolos, Martin, Shahzadi, Misbah and Stuchlík, Zdenek (2020), Quasi-periodic oscillations around kerr-mog black holes, *Eur. Phys. J. C*, **80**(2), p. 133, URL https://doi.org/10.1140/epjc/s10052-020-7692-5.

Mannheim, P. D. (2012), Making the Case for Conformal Gravity, *Foundations of Physics*, **42**(3), pp. 388–420, arXiv: 1101.2186.

Narlikar, J. V. and Kembhavi, A. K. (1977), Space-time singularities and conformal gravity., *Nuovo Cimento Lettere*, **19**, pp. 517–520.

Narzilloev, B., Abdujabbarov, A., Bambi, C. and Ahmedov, B. (2019), Charged particle motion around a quasi-Kerr compact object immersed in an external magnetic field, *Phys. Rev. D*, **99**(10), 104009, arXiv: 1902.03414.

Narzilloev, B., Malafarina, D., Abdujabbarov, A. and Bambi, C. (2020), On the properties of a deformed extension of the NUT space-time, *Eur. Phys. J. C*, **80**(8), p. 784, arXiv: 2003.11828.

Narzilloev, B., Rayimbaev, J., Abdujabbarov, A. and Bambi, C. (2020a), Charged particle motion around non-singular black holes in conformal gravity in the presence of external magnetic field, *arXiv e-prints*, arXiv:2005.04752, arXiv: 2005.04752.

Narzilloev, B., Rayimbaev, J., Shaymatov, S., Abdujabbarov, A., Ahmedov, B. and Bambi, C. (2020b), Can the dynamics of test particles around charged stringy black holes mimic the spin of Kerr black holes?, *Physical Review D*, **102**(4), 044013, arXiv: 2007.12462.

Rayimbaev, J., Abdujabbarov, A., Jamil, M., Ahmedov, B. and Han, W.-B. (2020), Dynamics of test particles around renormalization group improved schwarzschild black holes, *Phys. Rev. D*, **102**, p. 084016, URL https://link.aps.org/doi/10.1103/PhysRevD.102.084016.

Rayimbaev, J., Figueroa, M., Stuchlík, Z. and Juraev, B. (2020), Test particle orbits around regular black holes in general relativity combined with nonlinear electrodynamics, *Phys. Rev. D*, **101**(10), 104045.

Stuchlík, Z. and Kološ, M. (2016), Acceleration of the charged particles due to chaotic scattering in the combined black hole gravitational field and asymptotically uniform magnetic field, *European Physical Journal C*, **76**, 32, arXiv: 1511.02936.

Stuchlík, Z., Kološ, M., Kovář, J., Slaný, P. and Tursunov, A. (2020), Influence of Cosmic Repulsion and Magnetic Fields on Accretion Disks Rotating around Kerr Black Holes, *Universe*, **6**(2), p. 26.

Stuchlík, Z., Schee, J. and Abdujabbarov, A. (2014), Ultra-high-energy collisions of particles in the field of near-extreme Kehagias-Sfetsos naked singularities and their appearance to distant observers, *Phys. Rev. D*, **89**(10), 104048.

Toshmatov, B., Bambi, C., Ahmedov, B., Abdujabbarov, A. and Stuchlík, Z. (2017a), Energy conditions of non-singular black hole spacetimes in conformal gravity, *European Physical Journal C*, **77**, 542, arXiv: 1702.06855.

Toshmatov, B., Bambi, C., Ahmedov, B., Stuchlík, Z. and Schee, J. (2017b), Scalar perturbations of nonsingular nonrotating black holes in conformal gravity, *Phys. Rev. D*, **96**(6), 064028, arXiv: 1705.03654.

Turimov, B., Ahmedov, B., Abdujabbarov, A. and Bambi, C. (2018), Electromagnetic fields of slowly rotating magnetized compact stars in conformal gravity, *Phys. Rev. D*, **97**(12), 124005, arXiv: 1805.00005.

Turimov, B., Rayimbaev, J., Abdujabbarov, A., Ahmedov, B. and Stuchlík, Z. c. v. (2020), Test particle motion around a black hole in einstein-maxwell-scalar theory, *Phys. Rev. D*, **102**, p. 064052, URL https://link.aps.org/doi/10.1103/PhysRevD.102.064052.

Vrba, J., Abdujabbarov, A., Kološ, M., Ahmedov, B., Stuchlík, Z. and Rayimbaev, J. (2020), Charged and magnetized particles motion in the field of generic singular black holes governed by general relativity coupled to nonlinear electrodynamics, *Phys.Rev.D*, **101**(12), 124039.

Wald, R. M. (1974), Black hole in a uniform magnetic field, *Phys. Rev. D.*, **10**, pp. 1680–1685.

Zhou, M., Cao, Z., Abdikamalov, A., Ayzenberg, D., Bambi, C., Modesto, L. and Nampalliwar, S. (2018), Testing conformal gravity with the supermassive black hole in 1H0707-495, *Phys. Rev. D*, **98**(2), 024007, arXiv: 1803.07849.

Proceedings of *RAGtime 20–22, 15–19 Oct., 16–20 Sept., 19–23 Oct., 2018/2019/2020, Opava, Czech Republic*
Z. Stuchlík, G. Török and V. Karas, editors, Silesian University in Opava, 2020, pp. 221–231

Detection of chaotic behavior in time series

Radim Pánis,[1,a] Martin Kološ[1,b] and Zdeněk Stuchlík[1,c]

[1]Research Centre for Theoretical Physics and Astrophysics, Institute of Physics,
Silesian University in Opava, Bezručovo nám. 13, CZ-746 01 Opava, Czech Republic
[a]pan0010@slu.cz
[b]martin.kolos@physics.slu.cz
[c]zdenek.stuchlik@physics.slu.cz

ABSTRACT

Deterministic chaos is phenomenon from nonlinear dynamics and it belongs to greatest advances of twentieth-century science. Chaotic behavior appears apart of mathematical equations also in wide range in observable nature, so as in there originating time series. Chaos in time series resembles stochastic behavior, but apart of randomness it is totally deterministic and therefore chaotic data can provide us useful information. Therefore it is essential to have methods, which are able to detect chaos in time series, moreover to distinguish chaotic data from stochastic one. Here we present and discuss the performance of standard and machine learning methods for chaos detection and its implementation on two well known simple chaotic discrete dynamical systems - Logistic map and Tent map, which fit to the most of the definitions of chaos.

Keywords:
chaos – fractal dimension – recurrence quantification analysis – machine learning – logistic map – time series – tent map

1 INTRODUCTION

As already mentioned chaotic behavior is natural phenomena and the first touch with chaos one assigns the study of the three-body problem by Henri Poincaré (1880). Mathematically, deterministic chaos is the phenomenon which can arise in dynamical systems. In discrete dynamical systems, chaos can appear even for one dimensional systems, while in continuous dynamical systems, deterministic chaos can only arise in three or more dimensions. Finite-dimensional linear systems cannot produce chaos, for a dynamical system to produce chaotic behavior, it must be either infinite-dimensional or nonlinear. The main properties of chaotic systems are e.g. the most known sensitivity to initial conditions or more "mainstream" term - butterfly effect, which means that, even the arbitrarily close initial points can evolve into significantly different trajectories. Other property one should mention are strange attractors. While most of the types of nice regular systems provide very simple attractors, such as points or circular curves called limiting cycles, chaotic motion leads to

978-80-7510-432-8

something what is known as the strange attractor, which is attractor with magnificent details and great complexity.

With chaos it is not easy, so we have some dynamical systems, which are chaotic everywhere, but there are also cases, where chaotic behavior appears only in a subset of the phase space, then a large set of initial conditions leads to orbits that converge to this chaotic region. Chaotic behavior is for some systems as for example for logistic and tent map easy controllable and it depends on one parameter. Generally, bifurcation occurs when small smooth change of "chaotic parameter" (the bifurcation parameter) makes abrupt or topological change in behavior of the system. This dependency (or period-doubling transition from some N-point to an 2N-point attractor) on the chaotic parameter is nicely shown on the bifurcation diagram. For the purpose of presenting of the nonlinear methods of chaos detection we use superposition of graphics, where we display on the bifurcation diagram the estimates of chaotic behavior by later mentioned methods. We applied these methods on time series belonging to given "chaotic parameter" and we plot this estimation of chaoticity on the bifurcation diagram.

Strange attractors are special and they even have a fractal structure, and therefore one can calculate fractal dimension of them, which can provide useful information about the system even when the equations of the dynamical system are unknown and we can observe only one of its coordinates. For estimation of fractal dimension we present two methods, namely, Box-counting and Correlation dimension, classical approach of studying dynamical systems is the calculation of Lyapunov exponent, for this, one needs to know the rules of evolution for given dynamical system (equations), we however try to work only with one dimensional input, so we also use a numerical approach and compare both results. Another approach we use is recurrence quantification analysis (RQA), roughly speaking, it is numerical description of recurrence graph - graphical tool for investigating properties of dynamical systems. The last approach is lately again very popular Machine learning (ML), which has many advantages when dealing with nonlinear data and has proved its abilities in many useful applications. We use for our purpose all seven possible ML implementations build in Mathematica software, which is also used for all the calculations.

These methods are also used in (Pánis et al., 2019), where the information about the matter dynamics and electromagnetic field structure around compact object (black hole or neutron star) are provided, while the chaotic charged test particles dynamics around a Schwarzschild black hole immersed in an external uniform magnetic field is examined.

2 METHODS OF DETECTION OF CHAOTIC BEHAVIOR IN TIME SERIES

2.1 Box-counting method

Box-counting (D_0) or box dimension is one of the most widely used estimations of fractal dimension. The calculation and empirical estimation of this method is quiet simple compared to another ones. We present the general idea behind the algorithm, for more detailed description one can look at (Schroeder, 1991). For a set S in a Euclidean space $\mathbb{R}^n$ we

define Box-counting as

$$D_0 = \lim_{\epsilon \to 0} \frac{\ln N(\epsilon)}{\ln \frac{1}{\epsilon}}, \tag{1}$$

where $N(\epsilon)$ is the number of boxes of side length ϵ required to cover the set. Dimension of S is estimated by seeing how the logarithmic rate of $N(\epsilon)$ increase as $\epsilon \to 0$, or in words as we make the grid finer.

2.2 Correlation dimension

Very popular tool for detecting chaos in experimental data is calculation of the Correlation dimension (D_2). The general idea behind computing correlation dimension is to find out for some small ϵ the number of points $C(\epsilon)$ (correlation sum), which Euclidean distance is smaller than ϵ.

$$D_2 = \lim_{\epsilon \to 0} \frac{\ln C(\epsilon)}{\ln \epsilon}, \tag{2}$$

one computes this for various number of ϵ and D_2 can be then approximated again by fitting of the logarithmic values.

It is worth mentioning that D_2 and D_0 is part of D_q family of fractal dimensions (Schroeder, 1991) defined as

$$D_q = \lim_{\epsilon \to 0} \frac{1}{q-1} \frac{\ln \sum_k p_k^q}{\ln \epsilon} \quad -\infty \leq q \leq \infty, \tag{3}$$

where, p_k denotes relative frequency with which fractal's points are falling inside the k-th cell.

For $q = 0$ we obtain already mentioned Box-counting dimension, for $q \to 1$ we obtain information dimension, which numerator is denoted as the Shannon's entropy and for $q = 2$ we obtain correlation dimension.

There is several algorithm approaches of calculation correlation dimension, lets just mention the approximation of $C(\epsilon)$ published in (Grassberger and Procaccia, 1983):

$$\hat{C}(\epsilon) = \lim_{N \to \infty} \frac{2}{N(N-1)} \sum_{i<j} H(\epsilon - |x_i - x_j|), \tag{4}$$

where H is Heaviside step function.

When using the nonlinear methods one should not omit importance of embedding dimension and then also closely connection to Takens's theorem about reconstruction of state space from sequence of observations (Takens, 1981). Embedding dimension creates from series of length $N+m-1$ for some given m series of N vectors, where i-th component looks like:

$$x_i = (x_{i-m+1}, x_{i-m+2}, ..., x_i) \in \mathbb{R}^m. \tag{5}$$

One of the purposes of embedding dimension, in context of Correlation dimension is to distinguish between chaotic and random time series. Where by chaotic series for increasing $m \in \mathbb{N}$ fractal dimension estimation stabilizes at some value $D < m$, while for random series, dimension goes along with m to infinity.

2.3 Lyapunov exponent

Lyapunov exponents apart of previous methods are originally used for investigation of dynamical systems, or rather said not any fractals. In short, it is a number that describe the amount of separation of trajectories which are infinitesimally close. Near trajectories in chaotic systems diverge exponentially, what leads to positive Lyapunov exponents. The amount of separation can differ for various directions of initial separation vector. Because of this fact, there is a spectrum of Lyapunov exponents, which corresponds to the phase space dimension.

For example if we consider logistic map $f(x) = rx(1-x), r \in [0,4]$ as an typical example of simple chaotic system, which is more precisely one-dimensional nonlinear difference equation. The Lyapunov exponent can be calculated directly from the expression of the f function from the formula

$$\lambda(r) = \lim_{N\to\infty} \frac{1}{N} \sum_{n=0}^{N-1} \ln\left[\left|f'\left(f^n(x_0)\right)\right|\right]. \tag{6}$$

However we try to work only with time series inputs which is not allowing us to use such a formula. We assumed in future to apply our methods on observational data from the telescope. This approach leads us to use method, which is determining Lyapunov exponents from time series. The maximal Lyapunov exponent characterizes the spectra and therefore denotes amount of predictability for some dynamical system. It can be calculated without knowledge of a model which produces the time series. We use the method based on the statistical properties of the divergence of neighboring trajectories approach introduced by Kantz, (Kantz, 1994). Our algorithm applied to logistic map is very similar to formula 6 which could be found for example also in (Enns, 2001).

2.4 Recurrence quantification analysis

The recurrence quantification analysis is quiet widely used tool for investigating the state space trajectories. Simply said it determines the number and duration of recurrences of a dynamical system. RQA is developed since 1992 (Zbilut and Webber, 1992; Marwan, 2008), where the novel approach based on averaging along with the way of setting the correct input parameters, which provide more accurate RQA measures is presented in (Bhatta et al., 2020). Recurrence plot provides a graphical tool for observing periodicity of phase space trajectories and was introduced in (Eckmann et al., 1987). This observing is possible through visualization of a symmetrical square matrix, in which the elements correspond to times at which a state of a dynamical system recurs.

One can define RP which measures recurrences of a trajectory $x_i \in R^d$ in phase space

$$R_{i,j} = H\left(\epsilon - \|x_i - x_j\|\right) \quad i,j = 1,...,N, \tag{7}$$

where N is the number of measured points x_i, ϵ is a threshold distance and $\|\cdot\|$ is a norm. From this equation we obtain the already mentioned symmetrical square matrix of zeroes and ones. When we will represent this two repeating elements with different colors in a plot we obtain the discussed RP. Threshold value parameter determinate density of RP plot.

RQA tools with well established short forms, which we use for investigating of chaotic trajectories are:

(1) RR - The recurrence rate is simplest tool, which measures density of recurrence points in the recurrence plot, or in another words, it counts the number of ones in RP and divides them by number of all elements in the matrix. RR reflects the chance that some state of the system will recur

$$RR = \frac{1}{N^2} \sum_{i,j=1}^{N} R_{i,j}. \tag{8}$$

(2) DET - Determinism is rate of recurrence points which build diagonal lines. DET determines how predictable the system is

$$DET = \frac{\sum_{l=l_{min}}^{N} lP(l)}{\sum_{i,j=1}^{N} R_{i,j}}, \tag{9}$$

where $P(l)$ denotes the frequency distribution of lengths l of the diagonal lines.

(3) LL - Is average diagonal line length, which is in relation with the time of predictability of the system. It reflects the average time for which any two parts of trajectory are close, this time can be denoted as mean prediction time

$$LL = \frac{\sum_{l=l_{min}}^{N} lP(l)}{\sum_{l=l_{min}}^{N} P(l)}. \tag{10}$$

(4) ENTR - Entropy or the Shannon entropy of the probability distribution of the diagonal line lengths p(l), which are reflecting complexity of the system's deterministic structure

$$ENTR = -\sum_{l=l_{min}}^{N} p(l) \ln p(l)), \tag{11}$$

where $p(l)$ is probability that a diagonal line is exactly of the length l can be estimated from the frequency distribution $P(l)$ with $p(l) = \frac{P(l)}{\sum_{l=l_{min}}^{N} P(l)}$.

2.5 Machine learning

Machine learning is very powerful tool, which founds application in many fields, lets just mention language translating algorithms, computer vision, beating best Go player in the world (Silver et al., 2017b), or chess programs of different architecture (Silver et al., 2017a) in an incredible fashion. In this work only basic principles of machine learning are presented. Roughly speaking machine learning is field of computer science, strongly connected to another fields as optimization, statistics, linear algebra, etc.

Its beginning goes to 1950's and as many inventions in computer science or better said in science in general. Machine learning was not invented by single person, let's only mention

Table 1. Comparison of time in seconds required for different nonlinear methods applied on time series generated by logistic map. For parameter r varying from 2 to 4 with the step of 0.01 leads to 200 time series, with initial value $x_0 = 0.1$ we did set up the iterations to length 100, 1000 and 10000 and compared the time needed for the calculation for given methods.

Method / Length	100	1000	10000
Box-count	0.354	0.416	3.519
Correlation dim.	4.155	26.54	2353
Lyapunov exp.	3.294	119.5	12574
RQA- RR	0.164	6.332	507.8
RQA-DET	0.209	6.069	916.9
RQA-ENTR	0.197	7.247	1128
RQA-LAM	0.197	7.248	1128
ML-Rand. For.	0.677	1.212	7.479

A. Samuel, who used first the term "Machine learning". Machine learning is using algorithms on data samples to discover known or unknown patterns in data, this dividing of patterns leads to basic divisions of machine learning and namely supervised, semi-supervised and unsupervised learning. The wide range of applications announces the good ability of handling nonlinear data. Our intention of using machine learning is to decide whether a trajectory of a particle is chaotic or not. For this purpose we use supervised machine learning, where we train various ML algorithms with samples calculated by classical methods already described, namely, (Box-counting, Correlation dimension, Lyapunov exponent, RQA - RR, DET, LL, ENTR) with effort to use all the different properties of them and the training set consists overall of 100 examples.

3 CONCLUSION

Deterministic chaos is hardly predictable and apparently random behavior which can appear in dynamical systems. Classical example of such nonlinear dynamical system is logistic map, denoted by quadratic recurrence equation

$$x_{n+1} = r x_n (1 - x_n) . \tag{12}$$

Given the initial value $x_0 \in (0, 1)$, the logistic map (12) will generate sequence of real numbers $x_n \in (0, 1)$. The behavior of such sequence x_n strongly depends on logistic map parameter $r \in [2, 4]$. Roughly speaking is the behavior on the interval $r \in (2, r_0)$ regular (rather predictable) and on the interval $r \in [r_0, 4]$ is chaotic (hardly predictable or rather unpredictable) with some occasional "islands of regularity". The transition between regular and chaotic behaviors happens for parameter $r = r_0 \approx 3.56995$. Bifurcation diagram for logistic map, with asymptotically approached values of the sequence, is shown in Fig. 1 depicted by gray background points.

For chaos detection and chaotic behavior description in sequences of numbers following methods have been tested: Box-counting method (section 2.1), Correlation dimension (2.2),

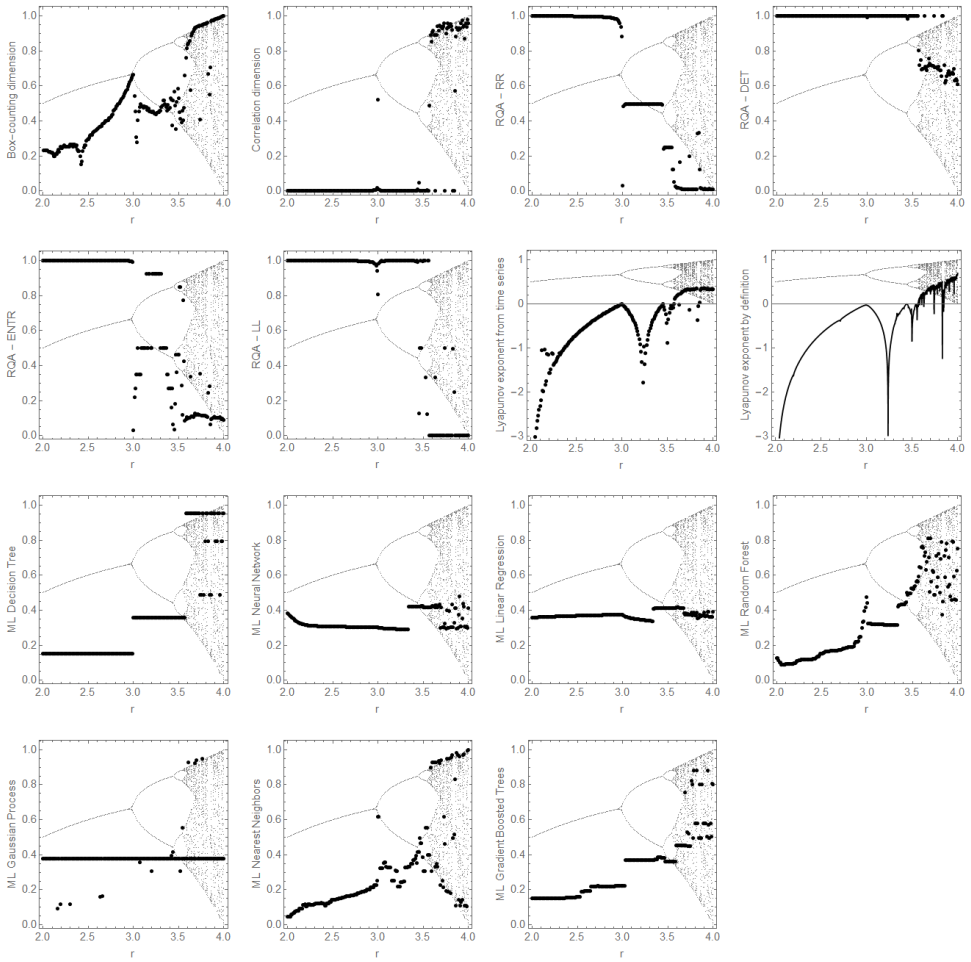

Figure 1. Comparison of different nonlinear methods for time series generated by logistic map $x_{n+1} = rx_n(1 - x_n)$. For different parameter $r \in [2, 4]$ we generate 10000 points series with initial value $x_0 = 0.1$. All the methods detect more chaoticity when we enter the chaotic region for value $r > r_0 \approx 3.56995$. RQA tools however, are working in reverse fashion as one can see, they denote more chaotic regions with lower numbers and vice versa, the data (chaoticity estimations) for RQA-LL and RQA-ENTR have been transformed into interval $[0, 1]$.

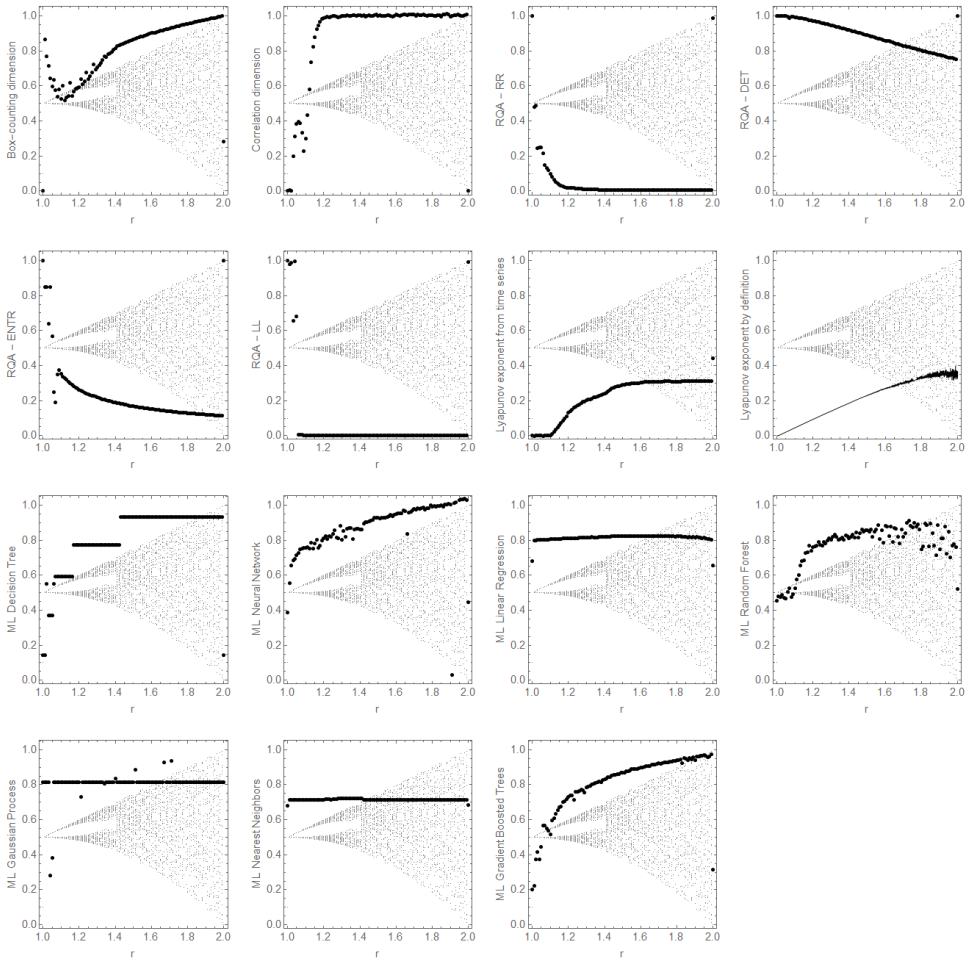

Figure 2. Comparison of different nonlinear methods for time series generated by tent map defined as $x_{n+1} = f_r(x_n) = \begin{cases} rx_n & \text{for } x_n < \frac{1}{2} \\ r(1-x_n) & \text{for } x_n \geq \frac{1}{2} \end{cases}$. For different parameter $r \in [1,2]$ we generate 10000 points series with initial value $x_0 = 0.1$.

Lyapunov exponent (2.3), RQA (2.4) and diferent machine learning algorithms (2.5). All of the algorithms we use in this article are capable to use one dimensional sequence of real numbers (time series) as input. From the point of observation is important to distinguish between chaotic sequences ruled by some (unknown) laws and random sequences obeying for example some stochastic distribution, which can contribute to the noise part in the detected signal. The theoretical boundary of distinguishing between chaos and random sequences is sequence length (Ott, 1993). If the nonlinear dynamical system has many degrees of freedom, then for short sequences is impossible to tell.

To clear up how the nonlinear methods works is shown on four representative sequences $x_n^{(1)}, x_n^{(2)}, x_n^{(3)}, x_n^{(4)}$ of length 10^4, where $x_n^{(1)}$ is regular sequence, $x_n^{(2)}$ is weakly chaotic sequence generated by logistic map with $r = 3.6$, $x_n^{(3)}$ is strongly chaotic sequence generated by logistic map with $r = 4$, and $x_n^{(4)}$ is sequence of pseudo-random numbers. The results are presented in Tab. 2.

In detail we have tested the nonlinear methods on sequences of numbers generated by logistic and tent map for various values of parameter r, see Fig. 1 and 2, the application/testing of the methods on a specific task can be found in (Pánis et al., 2019). The important common sign of all these methods is that, they are able to detect more chaoticity when divergence of trajectories in bifurcation diagram occurs, in other words, when there is more than one fixed point. This fact we can observe for example when $r = 3$ for logistic map in Fig. 1 and for r little above value 1 for tent map in Fig. 2. However, this is not undeniable true for all the cases, what leads to different estimations of chaoticity for different methods. Box-counting and Lyapunov exponent method show approximately linear behavior when moving to point, where the divergence of the trajectories begins, while when moving to such a point chaoticity is increasing and decreasing by leaving it. Correlation dimension shows little bit different behavior, when nonchaotic region is denoted by values close to zero and the level of chaos starts rapidly grow only from small distance from the region of divergence of trajectories in bifurcation diagram, this behavior is also observable by RQA tools, however in reversed fashion. Satisfying is the detection of chaoticity for logistic map for the $r \geq 3.56995$, when all these methods are showing the highest values of chaoticity, in this region are also "islands of regularity" though, what means not all the estimations of chaos in this region should be high. By tent map is the behavior of the methods also satisfying, we should not omit the fact the divergence of trajectories starts from very small values above $r = 1$ and grows with r moving to value $r = 2$, where from our definition of tent map and initial condition value $x_0 = 0.1$ the behavior gets suddenly quiet regular again.

As expected different machine learning algorithms produce different results. Random Forest algorithm seems to produce quiet reliable result - our estimation of chaoticity is getting higher most of the time as the r parameter grows, the exceptions could be explained by the fact there are also "islands of regularity" in the chaotic region.

The time spent for calculation of the individual graphics in Fig. 1 is presented in Tab. 1, where we in addition present also the times consumed in the cases for shorter time series in order to catch the nonlinear growth of time consumption with larger input. From here we can see that the Box-counting method is the fastest, but when looking on the results the other methods seem to be more precise. The time spent also strongly depends on the sequence length - such dependence is nonlinear in the case of almost all the methods. For

Table 2. Comparison of values of different nonlinear methods applied on regular, chaotic and pseudo-random generated series of the length 10 000.

Met./ Type	Regular	Weak ch.	Strong ch.	P.-rand.
Box-count	0.0969	0.8343	1	1
Corr. dim.	$5 * 10^{-15}$	0.8943	0.8735	0.9978
Lyap. exp.	$-7 * 10^{-16}$	0.1889	0.3289	0.0842
RQA-RR	0.4999	0.0183	0.0116	0.0057
RQA-DET	1	0.6959	0.6114	0.0113
RQA-ENTR	8.5152	0.8951	0.8202	0.0296
RQA-LAM	5001	5.6299	2.8507	2.0006
ML-Rand. For.	0.5915	0.6917	0.7869	0.3788

most of the methods we have programmed and tested several variants for each of them according to algorithm architecture and settings of adjustable parameters. The goal was to obtain good and also computing time acceptable results, the code in Mathematica is available on the GitHub repositary at (Pánis, 2019).

In previous texts and presented Figures 1, 2, and tables 2 and 1 we provide brief overview about the common and novel methods used in nonlinear time series analysis, which can provide useful hints for potential users in the sense of finding suitable method when studying the nonlinear phenomena. Proclaim any here discussed method as the best would be misleading, and this ambiguity expresses aptly the saying, that every complicated question has a simple answer which is wrong. When choosing a method for particular purpose, one should have a good idea about the data structure as well as have in mind the definitions of the methods when discussing the results in the context of the underlying physics. Considering the main properties of data, when choosing a method, one should definitely have in mind the available hardware capabilities along with the dimensions of the data.

For very large data sets definitely the Box-counting and ML methods should be suitable, however when considering ML, the available data for training set constriction have to be mentioned. Lyapunov exponents are popular in physics from the point of interpretation and connection to the direct physical properties of the systems. RQA in the trade-off with longer computational time needed provide more numerical descriptions of the data, the connection to the physical properties in terms of Blazars can be found in (Bhatta et al., 2020) and the enhancing of the computational time needed could be the point of future research in a context of GPU usage.

ACKNOWLEDGMENTS

This work was supported by the Student Grant Foundation of the Silesian University in Opava, Grant No. SGF/4/2020, which has been carried out within the EU OPSRE project entitled “Improving the quality of the internal grant scheme of the Silesian University in Opava”, reg. number: CZ.02.2.69/0.0/0.0/19_073/0016951. ZS thanks for the support of the Institute of Physics and Research Centre of Theoretical Physics and Astrophysics,

at the Silesian University in Opava. RP acknowledge the institutional support of Silesian University in Opava and the grant SGS/12/2019. We are very thankful to the anonymous referee for his/her thorough and careful reading of the paper and very useful comments and suggestions which helped improve the presentation of the paper significantly.

REFERENCES

Bhatta, G., Pánis, R. and Stuchlík, Z. (2020), Deterministic Aspect of the γ-ray Variability in Blazars, *arXiv e-prints*, arXiv:2010.15085, arXiv: 2010.15085.

Eckmann, J.-P., Oliffson Kamphorst, S. and Ruelle, D. (1987), Recurrence plots of dynamical systems, *EPL (Europhysics Letters)*, **4**, p. 973.

Enns, R. (2001), *Nonlinear physics with Mathematica for scientists and engineers*, Birkhauser, Boston, ISBN 978-0-8176-4223-5.

Grassberger, P. and Procaccia, I. (1983), Characterization of strange attractors, *Physical Review Letters*, **50**, pp. 346–349.

Kantz, H. (1994), A robust method to estimate the maximal Lyapunov exponent of a time series, *Physics Letters A*, **185**, pp. 77–87.

Marwan, N. (2008), A historical review of recurrence plots, *European Physical Journal Special Topics*, **164**, pp. 3–12, arXiv: 1709.09971.

Ott, E. (1993), *Chaos in dynamical systems*, Cambridge University Press.

Pánis, R., Kološ, M. and Stuchlík, Z. (2019), Determination of chaotic behaviour in time series generated by charged particle motion around magnetized Schwarzschild black holes, *European Physical Journal C*, **79**(6), 479, arXiv: 1905.01186.

Pánis, R. (2019), Chaos detection, https://github.com/radim525/Chaos-detection.

Schroeder, M. (1991), *Fractals, chaos, power laws. Minutes from an infinte paradise*.

Silver, D., Hubert, T., Schrittwieser, J., Antonoglou, I., Lai, M., Guez, A., Lanctot, M., Sifre, L., Kumaran, D., Graepel, T., Lillicrap, T., Simonyan, K. and Hassabis, D. (2017a), Mastering Chess and Shogi by Self-Play with a General Reinforcement Learning Algorithm, *ArXiv e-prints*, arXiv: 1712.01815.

Silver, D., Schrittwieser, J., Simonyan, K., Antonoglou, I., Huang, A., Guez, A., Hubert, T., Baker, L., Lai, M., Bolton, A., Chen, Y., Lillicrap, T., Hui, F., Sifre, L., van den Driessche, G., Graepel, T. and Hassabis, D. (2017b), Mastering the game of Go without human knowledge, *Nature*, **550**, pp. 354–359.

Takens, F. (1981), *Detecting strange attractors in turbulence*, volume 898, p. 366.

Zbilut, J. P. and Webber, C. L. (1992), Embeddings and delays as derived from quantification of recurrence plots, *Physics Letters A*, **171**, pp. 199–203.

Proceedings of *RAGtime 20–22, 15–19 Oct., 16–20 Sept., 19–23 Oct., 2018/2019/2020, Opava, Czech Republic*
Z. Stuchlík, G. Török and V. Karas, editors, Silesian University in Opava, 2020, pp. 233–243

On the metric bundles of axially symmetric spacetimes

Daniela Pugliese[1,a] and Hernando Quevedo[2]

[1]Institute of Physics and Research Centre of Theoretical Physics and Astrophysics, Faculty of Philosophy & Science, Silesian University in Opava, Bezručovo náměstí 13, CZ-74601 Opava, Czech Republic
[2]Dipartimento di Fisica, Università di Roma "La Sapienza", I-00185 Roma, Italy Instituto de Ciencias Nucleares, Universidad Nacional Autónoma de México, AP 70543, México, DF 04510, Mexico
[a]d.pugliese.physics@gmail.com

ABSTRACT
We present the definition of metric bundles (**MBs**) in axially symmetric geometries and give explicit examples for solutions of Einstein equations. These structures have been introduced in Pugliese and Quevedo (2019) to explain some properties of black holes (**BHs**) and naked singularities (**NSs**), investigated through the analysis of the limiting frequencies of stationary observers, which are at the base of a Killing horizon definition for these black hole spacetimes. In Pugliese and Quevedo (2019), we introduced the concept of **NS** Killing throats and bottlenecks associated to, and explained by, the **MBs**. In particular, we proved that the horizon frequency can point out a connection between **BHs** and **NSs**. We detail this definition in general and review some essential **MBs** properties as seen in different frames and exact solutions.

Keywords: black holes – naked singularities – Killing horizons – metric bundles

1 INTRODUCTION

The aim of this work is to discuss the main properties of the metric bundles (**MBs**) for axially symmetric spacetimes, concentrating on some exact solutions. In this particular case, **MB** is a family of spacetimes defined by one characteristic photon (circular) orbital frequency ω and characterized by a particular relation between the metric parameters. This concept is used to establish a relation between black holes (**BHs**) and naked singularities (**NSs**) spacetimes. In Pugliese and Quevedo (2019), we performed an analysis of the **MBs** corresponding to the equatorial plane of the Kerr, Reissner-Nordström and Kerr-Newman geometries. The off-equatorial case of the Kerr spacetime is considered in detail in Pugliese and Quevedo (2019a).

A **MB** is represented by a curve on the so-called extended plane (Pugliese and Quevedo, 2019), which is the entire collection of a parameterized family of solutions. For concreteness, we now consider the family of Kerr spacetimes. All the **MBs** are tangent to the

horizon curve as represented on the extended plane. Then, the horizon curve emerges as the envelope surface of the set of **MBs**. It turns out that **WNSs** (weak naked singularities), for which the spin-mass ratio is close to the value of the extreme **BH**, are related to a portion of the inner horizon, whereas strong naked singularities (**SNSs**) with $a > 2M$ are related to the outer horizon. In addition, **WNSs** are characterized by the presence of Killing bottlenecks, which are defined as "restrictions" of the Killing throats that appear in **WNSs**. Killing throats or tunnels, in turn, emerge through the analysis of the radii $r_s^{\pm}(\omega, a)$ of light surfaces, which depend on the frequency of the stationary observers ω and the spin parameter a (Pugliese and Quevedo, 2018, 2019). In the case of **NS** geometries, a Killing throat is a connected region in the $r - \omega$ plane, which is bounded by the radii $r_s^{\pm}(\omega, a)$ and contains all the stationary observers allowed within the limiting frequencies $[\omega_-, \omega_+]$. In the case of **BHs**, a Killing throat is either a disconnected region in the Kerr spacetime or a region bounded by non-regular surfaces in the extreme Kerr **BH** spacetime. The limiting case of a Killing bottleneck occurs in the extreme Kerr spacetime, as seen in the Boyer-Lindquist frame, where the narrowing actually closes on the **BH** horizons. Killing throats and bottlenecks were grouped in Tanatarov and Zaslavskii (2017) in structures named "whale diagrams" of the Kerr and Kerr-Newman spacetimes–see also Mukherjee and Nayak (2018); Zaslavskii (2018). Moreover, Killing bottlenecks, interpreted in Pugliese and Quevedo (2019) as "horizons remnants" and related to **MBs** in Pugliese and Quevedo (2019); Pugliese and Quevedo (2019a), appear also connected with the concept of pre-horizon regime introduced in de Felice (1991); de Felice and Usseglio-Tomasset (1991). The pre-horizon was analyzed in de Felice and Usseglio-Tomasset (1991). It was concluded that a gyroscope would conserve a memory of the static or stationary initial state, leading to the gravitational collapse of a mass distribution (de Felice and Usseglio-Tomasset, 1992; de Felice and Yunqiang, 1993; de Felice and Sigalotti, 1992; Chakraborty et al., 2017).

More in general, **MBs** have interesting properties that allow us to explore in an alternative way some aspects of the geometries that define the bundle, providing an alternative interpretation of Killing horizons (in terms of a set of solutions–the extended plane) and establishing a connection between **NSs** and **BHs**, based on the fact that each bundle is tangent to the horizon curve. Moreover, as we shall see below, metric bundles highlight some properties of the horizons that could influence the exterior properties of **BH** geometries by means of characteristic frequencies. The **MBs** concept can have significant repercussions in the study of **BH** physics, in the interpretation of **NSs** solutions and in the horizons and **BH** thermodynamics.

In this work, we present the **MBs** definition and discuss their properties in the context of **BH** thermodynamics. We analyze the Kerr, Kerr-Newman and Reissner-Nordström metric bundles. The explicit expressions for metric bundles in the Kerr-de Sitter spacetime are also given. Finally, we present some concluding remarks.

2 METRIC BUNDLES

We start by considering the case of the Kerr spacetime. The Kerr metric, in Boyer-Lindquist (BL) coordinates, can be expressed as

$$\mathrm{d}s^2 = -\frac{\Delta - a^2\sin^2\theta}{\rho^2}\mathrm{d}t^2 + \frac{\rho^2}{\Delta}\mathrm{d}r^2 + \rho^2\mathrm{d}\theta^2 + \frac{\sin^2\theta\left(\left(a^2+r^2\right)^2 - a^2\Delta\sin^2\theta\right)}{\rho^2}\mathrm{d}\phi^2 - 2\frac{aM\sin^2(\theta)\left(a^2-\Delta+r^2\right)}{\rho^2}\mathrm{d}\phi\mathrm{d}t\,, \tag{1}$$

$$\Delta \equiv r^2 - 2Mr + a^2, \quad \text{and} \quad \rho^2 \equiv r^2 + a^2\cos^2\theta\,. \tag{2}$$

It describes an axisymmetric, stationary, asymptotically flat spacetime. The parameter $M \geq 0$ is interpreted as the mass of the gravitational source, while the rotation parameter $a \equiv J/M$ (spin) is the specific angular momentum, and J is the total angular momentum of the source. This is a stationary and axisymmetric geometry with Killing fields $\xi_t = \partial_t$ and $\xi_\phi = \partial_\phi$, respectively.

In this work, we will consider also the Kerr-Newman (KN) geometry which corresponds to an electrovacuum axisymmetric solution with a net electric charge Q, described by metric (1) with $\Delta_{KN} \equiv r^2 + a^2 + Q^2 - 2Mr$. The solution $a = 0$ and $Q \neq 0$ constitutes the static case of the spherically symmetric and charged Reissner-Nordström spacetime. The horizons and the outer and inner static limits for the **KN** geometry are, respectively,

$$r_\mp = M \mp \sqrt{M^2 - (a^2+Q^2)}, \quad r_\epsilon^\mp = M \mp \sqrt{M^2 - a^2\cos^2\theta - Q^2}\,, \tag{3}$$

which for $a = 0$, $Q = 0$, and $a = Q = 0$ leads to $(r_\pm, r_\epsilon^\pm)$ in the Reissner-Nordström, Kerr and Schwarzschild geometries, respectively. Note that the **KN** horizons $r_\pm$ can be re-parameterized for the total charge $\mathcal{Q}_T$ and its variation with respect to the parameter $\mathcal{Q}_T$ is exactly the same as for the corresponding radii $r_\pm$ in the **RN** or Kerr solution. This aspect will be significant in the study of the **MBs** dependence from the two charges (a, Q).

On the BHs horizons

For the analysis of some properties of the horizons, we focus for simplicity on the case $Q = 0$. Then, for the Kerr **BH** geometry the horizons and ergospheres radii are given by $r_\pm = M \pm \sqrt{M^2 - a^2}$ and $r_\epsilon^\pm = M \pm \sqrt{M^2 - a^2\cos^2\theta}$, respectively.

Metric bundles are defined as the set of metrics that satisfy the condition $\mathcal{L}_\mathcal{N} \equiv \mathcal{L}\cdot\mathcal{L} = 0$, where $\mathcal{L}$ is the Killing vector $\mathcal{L} \equiv \partial_t + \omega\partial_\phi$. Solutions could be either **BHs** or **NSs**. The quantity ω will be called the frequency or the **MBs** angular velocity. In **BH** spacetimes, this Killing vector defines also the thermodynamic variables and the Killing horizons.

On the Killing vector $\mathcal{L}$ and the condition $\mathcal{L}_\mathcal{N} = 0$

The event horizons of a spinning **BH** are Killing horizons with respect to the Killing field $\mathcal{L}_H \equiv \partial_t + \omega_H\partial_\phi$, where ω_H is the angular velocity of the horizons, representing the **BH** rigid rotation (the event horizon of a stationary asymptotically flat solution with matter satisfying suitable hyperbolic equations is a Killing horizon). The Kerr horizons are, therefore, null surfaces, $\mathcal{S}_0$, whose null generators coincide with the orbits of an one-parameter group of

isometries, i.e., in general, there exists a Killing field $\mathcal{L}$, which is normal to $\mathcal{S}_0$. In general, a Killing horizon is a lightlike hypersurface (generated by the flow of a Killing vector), where the norm of a Killing vector is null. In the limiting case of the static Schwarzschild spacetime ($a = 0$, $Q = 0$) or the Reissner Nordström spacetime ($a = 0$, $Q \neq 0$), the event horizons are Killing horizons with respect to the Killing vector ∂_t. More precisely, for static (and spherically symmetric) **BH** spacetimes, the event, apparent, and Killing horizons with respect to the Killing field ξ_t coincide.

The **BH** event horizon of stationary solutions have constant surface gravity (which is the content of the zeroth **BH** law-area theorem– the surface gravity is constant on the horizon of stationary black holes (Chrusciel et al., 2012; Wald, 1999)). The **BH** surface area is non-decreasing (second **BH** law establishing the impossibility to achieve by a physical process a **BH** state with zero surface gravity.) Moreover, the **BH** surface gravity, which is a conformal invariant of the metric, may be defined as the rate at which the norm $\mathcal{L}_\mathcal{N}$ of the Killing vector $\mathcal{L}$ vanishes from outside ($r > r_+$). (For a Kerr spacetime, this is $\mathcal{SG}_{Kerr} = (r_+ - r_-)/2(r_+^2 + a^2)$ and, however, the surface gravity re-scales with the conformal Killing vector, i.e. it is not the same on all generators but, because of the symmetries, it is constant along one specific generator). In the extreme case, where $r_\pm = M$, the surface gravity is zero and, consequently, the temperature is $T_H = 0$, but its entropy (and therefore the **BH** area) is not null (Chrusciel et al., 2012; Wald, 1999, 2001). This fact has consequences also with respect to the stability against Hawking radiation (a non-extremal **BH** cannot reach an extremal case in a finite number of steps–third **BH** law). The variation of the **BH** mass, horizon area and angular momentum, including the surface gravity and angular velocity on the horizon, are related by the first law of **BH** thermodynamics: $\delta M = (1/8\pi)\kappa\delta A + \omega_H \delta J$. In here, the term dependent on the **BH** angular velocity represents the "work term" of the first law, while the fact that the surface gravity is constant on the **BH** horizon, together with other considerations, allows us to associate it with the concept of temperature. More precisely, we can formalize this relation by writing explicitly the Hawking temperature as $T_H = \hbar c\kappa/2\pi k_B$, where k_B, is the Boltzmann constant and κ is the surface gravity. Temperature $T = \kappa/(2\pi)$; entropy $S = A/(4\hbar G)$, where A is the area of the horizon $A = 8\pi m r_+$; pressure $p = -\omega_h$; volume $V = GJ/c^2$ ($J = amc^3/G$); internal energy U= GM ($M = c^2 m/G$= mass), where m is the mass.

Here we study **MBs** which are defined by the condition $\mathcal{L}_\mathcal{N} = 0$; therefore, it is convenient to re-express some of the concepts of **BH** thermodynamics mentioned before in terms of $\mathcal{L}_\mathcal{N}$. Firstly, the norm $\mathcal{L}_\mathcal{N} \equiv \mathcal{L}^\alpha \mathcal{L}_\alpha$ is constant on the **BH** horizon. Secondly, the constant $\kappa : \nabla^\alpha \mathcal{L}_\mathcal{N} = -2\kappa\mathcal{L}^\alpha$, evaluated on the *outer* horizon r_+, defines the **BH** surface gravity, i.e., κ =constant on the orbits of $\mathcal{L}$ (equivalently, it is valid that $\mathcal{L}^\beta \nabla_\alpha \mathcal{L}_\beta = -\kappa\mathcal{L}_\alpha$ and $L_\mathcal{L}\kappa = 0$, where $L_\mathcal{L}$ is the Lie derivative–a non affine geodesic equation).

Stationary observers and causal structure

The condition $\mathcal{L}_\mathcal{N} = 0$ is also related to the definition of stationary observers. Stationary observers are characterized by a four-velocity of the form $u^\alpha = \gamma\mathcal{L}^\alpha$ ($\mathcal{L}^\alpha \equiv \xi_t^\alpha + \omega\xi_\phi^\alpha$); thus, $\gamma^{-2} \equiv -\bar{\kappa}\mathcal{L}_\mathcal{N}$, where γ is a normalization factor. The spacetime causal structure of the Kerr geometry can be then studied by considering also stationary observers (Malament, 1977): *timelike* stationary particles have limiting orbital frequencies, which are the photon orbital

frequencies $\omega_\pm$, i.e., solutions to the condition $\mathcal{L}_\mathcal{N} = 0$:

$$\omega_\pm \equiv \omega_Z \pm \sqrt{\omega_Z^2 - \omega_*^2}, \quad \omega_*^2 \equiv \frac{g_{tt}}{g_{\phi\phi}} = \frac{g^{tt}}{g^{\phi\phi}}, \quad \omega_Z \equiv -\frac{g_{\phi t}}{g_{\phi\phi}}. \tag{4}$$

Therefore, timelike stationary observers have orbital frequencies (from now on simply called frequencies) in the interval $\omega \in [\omega_-, \omega_+]$. Thus, frequencies $\omega_\pm$ evaluated on $r_\pm$ provide the frequencies $\omega_H^\pm$ of the Killing horizons.

For completeness, we also derive the frequencies ω_H of the horizons in the Kerr-Newman case,

$$\omega_H^- = \frac{aM\left(2M\sqrt{M^2 - (a^2 + Q^2)} - Q^2 + 2M^2\right)}{4M^2a^2 + Q^4}, \tag{5}$$

$$\omega_H^+ = \frac{aM}{2M\sqrt{M^2 - (a^2 + Q^2)} - Q^2 + 2M^2}. \tag{6}$$

The limiting Reissner-Nordström and Kerr cases can be obtained by imposing the conditions $a = 0$ and $Q = 0$, respectively.

Metric bundles: definition, structure and characteristic frequencies

Metric bundles are a set of metric tensors that can include only **BHs** *or* **BHs** *and* **NSs**, such that each geometry of the set has, at a certain radius r, equal limiting photon frequency $\omega_b \in \{\omega_+, \omega_-\}$, which is called *characteristic bundle frequency*. Therefore, **MBs** are solution of the zero-norm condition $\mathcal{L}_\mathcal{N}(\omega_b) = 0$.

It can be proved that *all* the **MBs** are tangent to the horizon curve in the extended plane[1] – see Fig. (1). Then, the horizon curve emerges as the envelope surface of the set of **MBs**. As a consequence, in Pugliese and Quevedo (2019) we introduced the concept of weak naked singularities (**WNSs**) as those metrics related to a portion of the inner horizon, whereas strong naked singularities (**SNSs**) are related to the outer horizon in the extended plane.

It can be proved that all the frequencies $\omega_\pm$, in any point of a **BH** or **NS** geometry, are horizon frequencies in the extended plane or, in other words, since the **MBs** are tangent to the horizon curve, each characteristic frequency of the bundle ω_b is a horizon frequency $\omega_b = \omega_H^x$, where $\omega_H^x \in \{\omega_H^-, \omega_H^+\}$.

For seek of clarity, first we formalize this definition for the Kerr case as a one-parameter family of solutions parameterized with the spin a (or a/M). The generalization to the case of several parameters is straightforward as, for example, in **KN** and **RN** geometries. These cases will be also addressed explicitly below. Particularly, the frequency ω_b of the bundle is the inner or outer horizon frequencies of the spacetime, which is tangent to the horizon at a radius r_g and a spin a_g (*bundle tangent spin*). In addition, the bundle is characterized by the frequency ω_0 of the *bundle origin*, i.e., the point $r = 0$ and $a = a_0$ in the extended plane. Thus, the **MBs** are all characterized by a frequency $\omega_b = \omega_H^x(a_g)$, where a_g is the

[1] An *extended plane* π^+ is the set of points $(a/M, \mathcal{Q})$, where $\mathcal{Q}$ is any quantity that characterizes the spacetime and depends on a. In general, the extended plane is an $(n + 1)$-dimensional surface, where n is the number of independent parameters that enter $\mathcal{Q}$ (Pugliese and Quevedo, 2019).

bundle tangent spin, and the frequency ω_0 at $r = 0$, where $a = a_0$. The relation between a_0, a_g, r_g, and ω_b, significant for the bundle characterization, is particularly simple in the case of a spherically symmetric geometry or on the equatorial plane of an axisymmetric geometry. However, in general, the relation, involving also the **MB** origin a_0, depends on the plane $\sigma \equiv \sin^2\theta$ (Pugliese and Quevedo, 2019a).

MBs can be closed on the horizon. In Pugliese and Quevedo (2019), this property has been shown to be due to the rotation of the singularity: the curves, which define the **BH** horizons for the static **RN** case, can be are open; the analysis of the **KN** case represented in Pugliese and Quevedo (2019) shows the influence of the spin in the bending and separation into two families of curves on the equatorial plane. On the other hand, in Pugliese and Quevedo (2019a) we proved that, on planes with $\sigma < 1$, there can be open Kerr bundles. Then, **MBs** of axisymmetric spacetimes have a non-trivial extension corresponding to negative bundle frequencies $\omega_b < 0$. These **MBs** extensions, associated to characteristic frequencies $\omega_b = -\omega_H^{\pm}$ equal in magnitude to the horizon frequencies, clearly are not tangent to the horizon curve in the negative frequencies extension of the extended plane. However, these **MBs** branches are tangent to the horizon curve in the plane with positive frequencies $-\omega_b > 0$.

Horizon relations for Kerr geometries on the equatorial plane $\sigma = 1$

Horizons relations I:
origin frequencies: $\omega_0^{-1} \equiv a_0^{\pm}/M = \frac{2r_{\pm}(a_g)}{a_g} \equiv \omega_H^{-1}(a_g)$;
horizons frequencies: $\omega_H^{+}(r_g, a_g) = \omega_0 = Ma_0^{-1}$, $\omega_H^{-}(r'_g, a_g) = \omega'_0 = M/a'_0$, where $r'_g \in r_-$ $(r_+ = r_g, r_- = r'_g)$.
Horizons relations II:
There is $\omega'_0 = \frac{1}{4\omega_0}$, $\omega_H^{+}\omega_H^{-} = \frac{1}{4}$ and $(a_0^{+}(a_g)a_0^{-}(a_g) = 4M^2)$, $a_0^{\pm}/M = \frac{2r_{\pm}(a_g)}{a_g}$–see Pugliese and Quevedo (2019).

In the Kerr **MBs**, the Killing vector $\mathcal{L}_{\mathcal{N}}$ is a function of r, a and $\sigma \equiv \sin^2\theta$. The equatorial plane is a notable case, showing in many aspects similarities with the case of static limiting geometries, where $\mathcal{L}_{\mathcal{N}}$ is a function of r and a, only.

Explicit form of the metric bundles
Here, we present explicit expressions for the KN **MBs** and their limits:
Kerr geometries-equatorial plane $\sigma = 1$**:**

$$a_{\omega}^{\pm}(r, \omega; M) \equiv \frac{2M^2\omega \pm \sqrt{r^2\omega^2\left[M^2 - r(r+2M)\omega^2\right]}}{(r+2M)\omega^2}, \tag{7}$$

KN geometries-equatorial plane $\sigma = 1$**:**

$$a_{\omega}^{\mp} = \frac{\mp\sqrt{r^4\omega^2\left\{\omega^2\left[Q^2 - r(r+2M)\right] + M^2\right\}} + \omega M(Q^2 - 2rM)}{\omega^2\left[Q^2 - r(r+2M)\right]}, \tag{8}$$

$$\text{or} \quad (Q_{\omega}^{\pm})^2 \equiv \frac{r\left\{\omega^2\left[a^2(r+2M) + r^3\right] - 4aM^2\omega - rM^2 + 2M^3\right\}}{(a\omega - M)^2}, \tag{9}$$

RN geometries:

$$(Q_{\omega}^{\pm})^2 = r\left(\frac{r^3}{M^2}\omega^2 - r + 2M\right). \tag{10}$$

In the **RN** geometries, the limiting frequencies are $\omega_{\pm} = \pm\frac{M\sqrt{Q^2+(r-2M)r}}{r^2}$. The **KN** frequencies $\omega_{\pm}$ do not depend explicitly on Q_T; this means that the electric and rotational parameters of the geometry play a different role in the solutions $\omega_{\pm}$=constant.

Explicitly, if we consider a surface $a_g(a_0; Q)$ of the tangent **MBs** spins in the case $a_0 \neq 0$, where Q is a parameter, we obtain

KN bundle origin spin-equatorial plane:

$$a_0 = \frac{2M^2 - Q^2 \mp 2M\sqrt{M^2 - (a^2 + Q^2)}}{a} \quad (r_{\mp}), \tag{11}$$

KN bundle tangent spin:

$$a_g^{\mp}(a_0) = \frac{a_0\left(2M^2 - Q^2\right) \mp 2M\sqrt{a_0^2\,(M^2 - Q^2) - Q^4}}{a_0^2 + 4M^2} \tag{12}$$

$$\text{where} \quad a_0 > a_L(Q) \equiv \sqrt{-\frac{Q^4}{Q^2 - M^2}} \quad \text{with} \quad Q^2 \in [0, M^2].$$

These functions are very important to derive a relation between **BHs** (with tangent spins a_g) and **NSs** (with origin spins a_0), as discussed in Pugliese and Quevedo (2019), and also the transformation laws for **BHs** in the extended plane, as explicitly shown in Pugliese and Quevedo (2019a).

The relation between **BHs** and **NSs** can be formalized by analyzing the function of the tangent spin $a_g(a_0)$ in terms of the **MB** origin a_0 as follows

Kerr geometry $\sigma = 1$**:**

$$\forall\, a_0 > 0, \quad a_g \equiv \frac{4a_0M^2}{a_0^2 + 4M^2} \quad \text{where} \quad a_g \in [0, M] \quad \text{and} \quad \lim_{a_0\to 0} a_g = \lim_{a_0\to\infty} a_g = 0,$$

$a_g(a_0 = 2M) = M$. Alternatively, we can explicitly write the relation between the tangent spin and the radius as follows:

$$a_{tangent}(r) \equiv \frac{r(M - r_g) + Mr_g}{\sqrt{-(r_g - 2M)r_g}} \tag{13}$$

$$\text{where} \quad r_g \in [0, 2M], \quad a_g = a_{\pm}: \quad \frac{r_g}{M} \equiv \frac{2a_0^2}{a_0^2 + 4M^2}.$$

Some general results from the study of metric bundles in the extended plane

We now summarize some general results obtained in Pugliese and Quevedo (2019); Pugliese and Quevedo (2019a). For simplicity, we focus on the equatorial plane of the Kerr geometry so that a **MB** can be represented as a curve on the plane (a, r).

Vertical lines r =constant in the extended plane

Vertical lines r =constant in the extended plane intersect specific **MBs**. First, on a point r, there is always a maximum of two intersections (limiting cases are on the horizon curve or on the origin $r = 0$ and $a_0 = 0$ or $r = 2M$ and $a_0 = 0$), which provide the two limit frequencies $\omega_{\pm} \equiv \{\omega_b, \omega_b^{'}\}$, corresponding to the two characteristic frequencies of the two **MBs**. These are also horizon frequencies $\omega_{\pm} \equiv \{\omega_b, \omega_b^{'}\} \equiv \{\omega_H^x(a_g), \omega_H^y(a_g^{'})\}$, respectively, where $(x, y) = \pm$ and a_g and $a_g^{'}$. They are the tangent spins of the two **MBs** with frequency ω_b and $\omega_b^{'}$, respectively. We clarify in Pugliese and Quevedo (2019a) the precise correspondence between $\{x, y, \pm\}$. In fact, these quantities are related to the notion of **BH** inner horizon confinement, discussed firstly in Pugliese and Quevedo (2019), and to the horizon replicas introduced in Pugliese and Quevedo (2019a). The **BH** inner horizon confinement is related to the notion of bottleneck as well. It is based on the fact that it is not possible to find a bundle outside the outer event horizon ($r > r_+$) in the plane (and for any geometry a) with a characteristic frequency equal to that of the inner horizon. This implies that outside the horizon of a given spacetime, it is not possible to find a photon limiting frequency equal to the inner horizon frequency. Nevertheless, it is possible to find such orbits for the frequencies of the outer horizon. However, it is possible to find frequencies of the inner horizon in the Kerr case for σ sufficiently small (sufficiently close to the rotation axis); therefore, it is possible to "extract" this inner horizon frequency on an "orbit" $r > r_+ : \mathcal{L} \cdot \mathcal{L} = 0$.

This notion led to the definition in Pugliese and Quevedo (2019a) of the horizon replicas. These structures occur when there is a point r of the bundle such that the characteristic bundle frequencies $\omega_b(a) \in \{\omega_H^+(a_p), \omega_H^-(a_p)\}$ are located exactly at $r_{\pm}(a_p) > r_+(a)$, that is, on the horizon with frequency $\omega_b(a)$. Such orbits are, therefore, called horizons replicas (these are clearly related to the vertical lines of the extended plane crossing the horizon curve on the tangent point to the bundle).

Horizontal lines a =constant on the extended plane

Horizontal lines a =constant on the extended plane determine a particular geometry and are related to the orbits with frequencies equal to that of the Killing horizons in the extended plane and, therefore, to the concept of horizon replicas.

The Kerr-de-Sitter metric bundle

To complete this overview of the **MBs** of axisymmetric spacetimes, we present here the explicit expressions for the Kerr-de Sitter geometry, which has an interesting and complex horizon structure. Further details on these specific solutions can be found in Pugliese and Stuchlík (2019b).

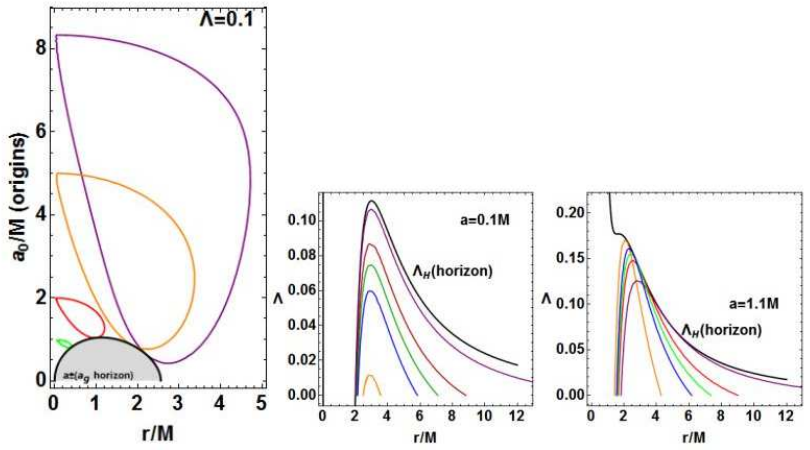

Figure 1. Kerr-de-Sitter geometry: Equatorial plane ($\sigma = 1$). Left panel: Metric bundles of the Kerr-de-Sitter geometries in the plane $(a/M, r/M)$ for fixed cosmological constant $\Lambda > 0$. The black thick curve is the horizon curve in the extended plane. Metric bundles are tangent to the horizon curve. The origin spins a_0 are also shown. The tangent spin a_g is on the horizon curve. Each bundle (curve) has a specific frequency (the lower bundle corresponds to greater frequencies due to the fact that the inner horizon frequency is always greater then the outer horizon frequency, a part in the extreme **BH** case), which is the horizon frequency of the point (a, r) of the bundle, particularly, at the origin $(a = a_0, r = 0)$ and tangent point $(a = a_g, r = r_g)$. Center and right panel: Bundles in the $(\Lambda, r/M)$ plane for different spins and frequencies. Black curves represent the horizon. Each curve is for a different fixed frequency ω (the lower the curve, the greater the frequency).

Kerr-de-Sitter metric bundle, general form in Λ:

$$\Lambda_\omega \equiv \frac{-6\sin^2(\theta)\left[\omega^2\left(a^2+r^2\right)^2 + a^2 - 4aMr\omega\right]}{\left[a^2\cos(2\theta)+a^2+2r^2\right]\left[a\sin^2(\theta)\left[a\omega^2\left(a^2+r^2\right)-2\omega\left(a^2+r^2\right)+a\right]+r^2\right]} + \frac{6\left[a^2\omega^2\sin^4(\theta)\left[a^2+r(r-2M)\right]+a^2+r(r-2M)\right]}{\left[a^2\cos(2\theta)+a^2+2r^2\right]\left[a\sin^2(\theta)\left[a\omega^2\left(a^2+r^2\right)-2\omega\left(a^2+r^2\right)+a\right]+r^2\right]}. \quad (14)$$

This expression gives the form of the **MBs** in the Kerr-de-Sitter spacetime in terms of the cosmological constant $\Lambda > 0$ for any plane $\sigma \equiv \sigma^2\theta$. Similar solutions can easily be found in terms of a_ω. The extended plane is represented, however, a 3D space. In Figs. (1), we show different representations of this case.

3 CONCLUDING REMARKS

We discussed the concept of metric bundles of axially symmetric spacetimes. In Eqs. (7), (8) and (9) explicit expression of these bundles are given on the equatorial plane of the

Kerr geometries, Kerr-Newman spacetimes and for the spherically symmetric Reissner-Nordström spacetime. In Eq. (14), we present the expression for the Kerr-de-Sitter geometry. Figs (1) illustrate these **MBs** and their main features such as the origins a_0 and the tangent points a_g on the horizon curve in the extended plane, where the **MBs** are represented as curves. At the end of Sec. (2), we discussed some results concerning the general properties of the geometries defined by the bundles, as extracted from the analysis of these structures, such as the **BH** horizon confinement and horizon replicas. The issues discussed in this article refer to the study of Pugliese and Quevedo (2019), where the concept of metric bundle was first introduced and the definition of Killing throat and bottleneck for the Kerr, Kerr-Newman and Reissner-Nordström spacetimes were considered. In Pugliese and Quevedo (2019a), we present the general definition on an arbitrary plane of the Kerr geometry and give definition of horizon replicas. In a future work, we intend to generalize this study to other spacetimes (Pugliese and Stuchlík, 2019b) and investigate in detail the consequences for the **BH** thermodynamical properties as described in Sec. (2). Kerr-de Sitter **MBs** eventually face the problem of finding a convenient **MBs** parametrization and definition in spherically symmetric spacetimes. The **MBs** tangency with the horizons curves, characteristic of the axially symmetric spacetimes, reduces to an approximation for the static geometries, while an adaptation of the (conformal invariant) **MBs** definitions to the static case is possible. **MBs** utility lies in enlightening spacetime properties emerging in the extended plane, related to the local causal structure and **BH** thermodynamics such as the surface gravity, temperature and luminosity. The extended plane and metric bundles connect different points of one geometry and different geometries, providing a new frame of interpretation of these metrics families. Some spacetime properties can be detected by stationary observers and the light-like orbits in the region outside the **BH** horizon. In this sense, we mention the horizons confinement and the replicas. There is a replica when certain properties of a **BH** horizon are replicated in other points of the same or different spacetimes. There is also the vice versa effect called confinement, as we proved for a portion of the Kerr inner horizon curve. Significant for the transformations from one solution to another, **MBs** represent a global frame for the **BHs** analysis. Of direct astrophysical interest, **MBs**, read in terms of the light surfaces, relate many aspects of **BHs** physics, such as "**BH**" images, and several processes, which constrain energy extraction, such as the **BHs** jet emission and jet collimation, or regulate the Blandford-Znajek process. They also constraint accretion disks or the Grad-Shafranov equation for the force free magnetosphere around **BHs**.

ACKNOWLEDGEMENTS

D.P. acknowledges partial support from the Junior GAČR grant of the Czech Science Foundation No:16-03564Y.

REFERENCES

Chakraborty, C., Kocherlakota, P., Patil, M., Bhattacharyya, S., Joshi, P. S. and Królak, A. (2017), Distinguishing kerr naked singularities and black holes using the spin precession of a test gyro in

strong gravitational fields, *Phys. Rev. D*, **95**, p. 084024.

Chrusciel, P. T., Lopes Costa, J. and Heusler, M. (2012), Stationary Black Holes: Uniqueness and Beyond, *Living Rev. Rel.*, **15**, p. 7, arXiv: 1205.6112.

de Felice, F. (1991), Rotating frames and measurements of forces in general relativity, *Mon. Not. R. Astron Soc.*, **252**, pp. 197–202.

de Felice, F. and Sigalotti, L. D. G. (1992), Rotating stars - The angular momentum constraints, *The Astrophysical Journal*, **389**, pp. 386–391.

de Felice, F. and Usseglio-Tomasset, S. (1991), On the pre-horizon regime in the kerr metric, *Classical and Quantum Gravity*, **8**(10), pp. 1871–1880.

de Felice, F. and Usseglio-Tomasset, S. (1992), Circular orbits and relative strains in schwarzschild space-time, *General Relativity and Gravitation*, **24**(10), pp. 1091–1100, ISSN 1572-9532.

de Felice, F. and Yunqiang, Y. (1993), A finite incompressible mass shell as a source of schwarzschild spacetime, *Classical and Quantum Gravity*, **10**(10), pp. 2059–2066.

Malament, D. B. (1977), The class of continuous timelike curves determines the topology of spacetime, *Journal of Mathematical Physics*, **18**(7), pp. 1399–1404.

Mukherjee, S. and Nayak, R. K. (2018), Collisional penrose process and jets in kerr naked singularity, *Astrophysics and Space Science*, **363**(8), p. 163, ISSN 1572-946X.

Pugliese, D. and Quevedo, H. (2018), Observers in Kerr spacetimes: the ergoregion on the equatorial plane, *Eur. Phys. J.*, **C78**(1), p. 69, arXiv: 1801.06149.

Pugliese, D. and Quevedo, H. (2019), Disclosing connections between black holes and naked singularities: Horizon remnants, Killing throats and bottlenecks, *Eur. Phys. J.*, **C79**(3), p. 209.

Pugliese, D. and Quevedo, H. (2019a), Metric bundles of the Kerr geometry: the general case. Killing horizons confinement, Naked singularities and characteristic frequencies, *to be submitted*.

Pugliese, D. and Stuchlík, Z. (2019b), in preparation, .

Tanatarov, I. V. and Zaslavskii, O. B. (2017), Collisional super-penrose process and wald inequalities, *General Relativity and Gravitation*, **49**(9), p. 119, ISSN 1572-9532.

Wald, R. M. (1999), Gravitation, thermodynamics, and quantum theory, *Class. Quant. Grav.*, **16**, pp. A177–A190, arXiv: gr-qc/9901033.

Wald, R. M. (2001), The thermodynamics of black holes, *Living Reviews in Relativity*, **4**(1), p. 6.

Zaslavskii, O. B. (2018), Super-Penrose process and rotating wormholes, *Phys. Rev.*, **D98**(10), p. 104030.

Proceedings of *RAGtime 20–22, 15–19 Oct., 16–20 Sept., 19–23 Oct., 2018/2019/2020, Opava, Czech Republic*
Z. Stuchlík, G. Török and V. Karas, editors, Silesian University in Opava, 2020, pp. 245–255

Effects of polytropic equations of state and toroidal magnetic fields on the accreting tori sequences in ringed accretion disks

Daniela Pugliese[1,a] and Zdeněk Stuchlík[1,b]

[1]Institute of Physics and Research Centre of Theoretical Physics and Astrophysics, Silesian University in Opava, Bezručovo náměstí 13, CZ-74601 Opava, Czech Republic
[a]d.pugliese.physics@gmail.com
[b]zdenek.stuchlik@physics.cz

ABSTRACT
We consider ringed accretion disks (**RADs**), representing models of aggregates of corotating and counterrotating toroids orbiting a central Kerr super-massive black hole (**SMBH**). We comment on the system of two-tori governed by the polytropic equation of state and including a toroidal magnetic field. We found the **RADs** leading function describing the **RAD** inner structure and governing the distribution of orbiting toroidal structures and the emergence of the (hydro-mechanical) instabilities in the disk. We perform this analysis first in pure hydrodynamical models by considering one-specie perfect fluid toroids and then by considering the contribution of the toroidal magnetic field.

Keywords: Accretion – Accretion disks – Black holes – Active Galactic Nucleai (AGN)

1 INTRODUCTION

Active Galactic Nucleai (**AGNs**) provide a rich scenario to observe **SMBHs** interacting with their environments. Chaotical, discontinuous accretion episodes may leave traces in the form of matter remnants orbiting the central attractor producing sequences of orbiting toroidal structures with strongly different features as different rotation orientations with respect to the Kerr **BH** where corotating and counterrotating accretion stages can be mixed.

Motivated by these facts, ringed accretion disks (**RADs**) model structured toroidal disks which may be formed during several accretion regimes occurred in the lifetime of non-isolated Kerr **BHs**. **RAD** features a system made up by several axi-symmetric matter configurations orbiting in the equatorial plane of a single central Kerr **SMBH**. Both corotating and counterrotating tori are possible constituents of the **RADs**. This model was first introduced in Pugliese and Montani (2015) and then detailed in Pugliese and Stuchlík (2015, 2016, 2017, 2018c,b,a, 2019); Pugliese and Montani (2018).

The model strongly binds the fluid and **BH** characteristics providing indications on the situations where to search for **RADs** observational evidences. The number of the instability points is generally limited to n=2 and depends on the dimensionless spin of the rotating central attractor. The phenomenology associated with these toroidal complex structures may be indeed very wide, providing a different interpretative framework. Obscuring and screening tori, possibly evident as traces (screening) in x-ray spectrum emission, are also strongly constrained. More generally, observational evidence is expected by the spectral features of **AGNs** X-ray emission shape, due to X-ray obscuration and absorption by one of the tori, providing a **RAD** fingerprint as a radially stratified emission profile.

In Sec. (2) we introduce the model and the main definitions used throughout this article. In Sec. (2.1) we focus on **RAD** with polytropic tori. In Sec. (3) we analyze the effects of a toroidal magnetic field in the formation of several magnetized accretion tori. Concluding remarks are in Sec. (4). Appendix (A) summarizes the main constraints on the **RAD** structure.

2 RINGED ACCRETION DISKS

Ringed accretion disk (**RAD**) is a fully general relativistic model of axially symmetric but "knobby" accretion disk orbiting on the equatorial plane of a Kerr **SMBH**. It constitutes an aggregate of corotating and counter-rotating perfect fluid, one particle species, tori orbiting on the equatorial plane on one central **BH** attractor. Because of the symmetries of the system (stationarity and axial-symmetry), it is regulated by the Euler equation only with a barotropic equation of state (**EoS**) $p = p(\varrho)$:

$$T_{\mu\nu} = (p+\varrho)U_\mu U_\nu - p g_{\mu\nu}, \quad \frac{\nabla_\mu p}{p+\varrho} = -\nabla_\mu \ln(U_t) + \frac{\Omega \nabla_\mu \ell}{1-\Omega\ell} \tag{1}$$

$$\Omega = \frac{U^\phi}{U^t} = -\frac{g_{tt}}{g_{\phi\phi}}\ell_0 = \frac{f(r)}{r^2\sin^2\theta}\ell_0, \quad \ell = -\frac{U_\phi}{U_t}.$$

$$V_{eff}(\ell) \equiv u_t \quad W \equiv \ln V_{eff}(\ell),$$

((t, r, ϕ, θ) are Boyer-Lindquist coordinates), $V_{eff}(\ell)$ is the effective torus potential, Ω is the fluid relativistic angular frequency, ℓ specific angular momenta, assumed constant and conserved for each **RAD** component but variable in the **RAD** distribution U^a is the fluid four velocity, and $T_{\mu\nu}$ is the fluid energy momentum tensor.

We introduce the following definitions: we use the notation () to indicate a configuration as a function which can be closed, C, or open O. Specifically, toroidal surfaces correspond to the equipotential surfaces, critical points of $V_{eff}(\ell)$ as function of r.

Consequently tori are determined as solutions of W : $\ln(V_{eff}) = \mathrm{c} = \text{constant}$ (or equivalently $V_{eff} = K$ =constant). We indicate the possible solutions as **C**, for the cross–sections of the closed surfaces (equilibrium quiescent torus); $\mathrm{C}_\times$, for the cross–sections of the closed cusped surfaces (accreting torus) and $\mathbf{O}_\times$, for the cross sections of the open cusped surfaces, which are generally associated to proto-jet configurationsPugliese and Stuchlík (2018a, 2016).

Sign $Q_{\pm}$ for a general quantity refers to counterrotating (Q_{+}) and corotating (Q_{-}) tori respectively. We introduce the concept of $\ell_{corotating}$ disks, defined by the condition $\ell_{(i)}\ell_{(o)} > 0$, and $\ell_{counterrotating}$ disks defined by the relations $\ell_{(i)}\ell_{(o)} < 0$. The two $\ell_{corotating}$ tori can be both corotating, $\ell a > 0$, or counterrotating, $\ell a < 0$, with respect to the central attractor spin $a > 0$. We use short notation $()_i < ()_o$ and $()_o > ()_i$ for the inner and outer configurations of a **RAD** couple.

An essential part of the **RAD** analysis is the characterization of the boundary conditions on each torus in the agglomerate and the **RAD** disk inner structure. The model is constructed investigating the function representing the angular momentum distribution inside the disk which is not constant. This sets the toroids location (and equilibrium) in the agglomerate and it coincides, in the hydrodynamical **RAD** model of perfect fluids, with the distribution of specific angular momentum of the fluid in each agglomerate toroid. This function can be written as

Leading (HD) RAD function:

$$\ell^{\mp} = \left.\frac{a^3 + ar(3r - 4M) \mp \sqrt{r^3\Delta^2/M}}{a^2M - (r - 2M)^2 r}\right|_{r^*}, \tag{2}$$
$$\Delta \equiv r^2 - 2Mr + a^2,$$

(M is the central **BH** mass). Each point $r > r_{mso}$ (marginally stable orbit) on curve $\ell^{\mp}$ fixes the center (points of maximum density inside the torus) of the toroidal **RAD** component and $r < r_{mso}$ sets possible instabilities points of the toroids, more details can be found in Pugliese and Stuchlík (2015, 2017). Because of the importance of this function in defining the inner structure of the **RAD**, this is called Leading **RAD** function.

We shall see in Sec. (3) that changing the energy-momentum tensor by including a toroidal magnetic field will make it convenient to change the leading function $\ell^{\pm}$ adopted in the Hydrodynamical (HD) case to a different one. This new function obtained from the study of the magnetic field in the **RAD** can represent and regulate the tori distribution. In Sec. (A), we include a summary of the main constraints on the **RAD** inner structure–Pugliese and Stuchlík (2015, 2017)

2.1 Polytropic tori

We conclude this section considering **RAD** tori with polytropic fluids: $p = \kappa\varrho^{1+1/n}$. We develop some general considerations on the **EoS** and the polytropic **RAD** tori governed by the **EoS**: $p = \kappa\varrho^{\gamma}$, where $\kappa > 0$ is a constant and $\gamma = (1 + 1/n)$ is the polytropic index, in Pugliese et al. (2013). Details of this analysis can be found in Pugliese and Stuchlík (2019). We also refer to this analysis for commenting on the tori energetics of various **RAD** configurations, and significance in the case of polytropic tori. It has been shown in Pugliese et al. (2013); Pugliese and Stuchlík (2019) that for the Schwarzschild geometry ($a = 0$) there is a specific classification of eligible geometric polytropics, and a specific class of polytropics is characterized by a discrete range of values for the index γ. Therefore, we can propose a general classification for the tori ($C, C_{\times}$), as for proto-jets $O_{\times}$, assuming a particular representation of the density function. We can write the density ϱ as a function

of γ. However, we concentrate our attention on the **RAD** components C and $C_\times$ for which $K < 1$ and there is :

$$\varrho_\gamma \equiv \kappa^{1/(\gamma-1)}\bar{\varrho}_\gamma \quad \text{and} \quad \bar{\varrho}_\gamma \equiv \left[\frac{1}{\kappa}\left(V_{eff}^{-\frac{\gamma-1}{\gamma}} - 1\right)\right]^{\frac{1}{(\gamma-1)}} \quad \text{for} \tag{3}$$
$$\gamma \neq 1 \quad \text{with} \quad \varrho_\gamma \equiv \mathbb{C}^{1/(-1+\gamma)}, \quad \mathbb{C} \equiv (V_{eff}^{-2})^{\frac{\gamma-1}{2\gamma}} - 1.$$

(note $\mathbb{C}$ is actually a function of $K \in]K_{\min}, K_{\max}]$, while $K_{\max} < 1$, regulates whether the torus is quiescent or in accretion). The pressure p, associated to the solution in Eq. (3), depends on $k^{\frac{1}{1-\gamma}}$. It decreases with κ more slowly then ϱ.

We consider the case $K < 1$ with the condition $\varrho > 0$, verified, according to Eq. (3), for $\gamma > 1$. Integration of the ϱ density function in the polytropic case where $\gamma = 4/3$ is shown in Figs (1). The situation for different indices, and particularly $\gamma = 5/3$, is also shown, integration of density profiles have been specified particularly for the couple $C_\times^- < C_\times^+$. Note that we can then directly impose several constraints for the density function. Some simple example, including special (composite) density profiles in the case $\varrho^-_{[+]} = \varrho^i_\gamma - \varrho^o_\gamma = \varrho_\Phi$ =constant, have

$$[K_i = \left(\left[\varrho_\Phi - \epsilon\left(K_o^{-\frac{\gamma-1}{\gamma}} - 1\right)^{\frac{1}{\gamma-1}}\right]^{\gamma-1} + 1\right)^{-\frac{\gamma}{\gamma-1}}. \tag{4}$$

In Figs (1) we show the profiles ϱ_Φ for $\epsilon = -1$. Important to note that these relations are generally seen as constraints on *independent* solutions for each **RAD** components. Toroidal configurations emerging from these constraints ($\varrho^-_{[+]}$) as in Fig (1) are by no means directly matched with solutions for two different **RAD** components coupled through the background. The **RADs** effective potential (a potential describing the entire macrostructure as introduced in Pugliese and Stuchlík (2015)) can be derived from composite energy-momentum tensors made by collections of the fluid tensors, decomposed in each fluid adapted frame. This holds for not colliding tori. They will be naturally coupled through the unique background metric tensor $g_{\mu\nu}$ and proper boundary conditions imposed on the fluid density and pressure. The boundary conditions by the step-functions cuts $H(\theta)$ defining the **RAD** in the two forms of potential functions included in the energy momentum tensor. Nevertheless, the projection after 3 + 1 decomposition, defining the 3D hyperplane $h^{(i)}_{ij}$, has to be done according to the orthogonality condition for fluids field velocity vectors $\mathbf{u}^{(i)}$, respectively, for the $(i)-$torus. These solutions can create special tori surfaces from the condition on the constant pressure. Moreover, these constraints can found application in the collision analysis within the limits considered before to infer the final states (es. final merger tori). (Other notable cases can be founded using the constraints $\varrho_{[\times]} = \varrho^i_\gamma\varrho^o_\gamma$ =constant, $\varrho_{\{\times\}} = \varrho_\gamma(K^iK^o)$ =constant or $\varrho^\pm_{\{+\}} = \varrho_\gamma(K^i \pm K^o)$ =constant.). It is possible to show that not all these profiles are related to quiescent of accreting toroids.

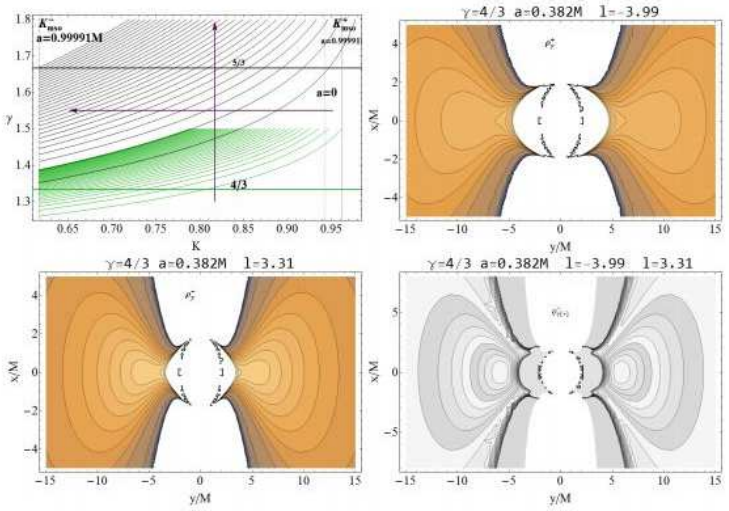

Figure 1. *Left panel:* Profiles of constant rationalized density function ϱ_k in Eq. (3) in the plane $\gamma - K$, $\gamma > 1$ is the polytropic index, $K \in [K^{\pm}_{mso}, 1]$ is the K-parameter attached to any tori at constant ℓ. The values $K^{\pm}_{mso}$ for the two **SMBHs** with spin $a = 0$ and $a = 0.99991M$ are also plotted. Corotating (**[-]**) and counterrotating fluids ([+]) are considered. Indices $\gamma = 4/3$ considered also in the analysis of Pugliese and Stuchlík (2019) and $\gamma = 5/3$ are shown. Arrows follow the increasing values of ϱ_γ. The region in the range $\gamma \in [4/3, 5/3]$ has been partially thicken with highlighted (green-colored) K-constant curves. Density profiles $\varrho^{\pm}_{\gamma}$ for corotating (*bottom left panel*) and counterrotating tori (*upper right panel*) are shown orbiting around a **SMBH** with spin $a = 0.382M$, and the specific angular momentum of the fluids is $\ell = -3.99$ and $\ell = 3.31$ and the polytropic index $\gamma = 4/3$. (x, y) are Cartesian coordinates. Bottom right panel shows the profiles of constant composite density function $\varrho^{-}_{\gamma[+]}$ defined in Sec. (2.1).

3 INFLUENCE OF TOROIDAL MAGNETIC FIELD IN MULTI-ACCRETING TORI

In this section, we consider **RAD** with toroidal sub-structures regulated by the presence in the force balance equation of a toroidal magnetic field component. We refer to the analysis of Pugliese and Montani (2018), the toroidal magnetic field form used here is the well known Komissarov-solution Komissarov (2006), used in the approach Pugliese and Montani (2013, 2018), see also Adámek and Stuchlík (2013); Hamersky and Karas (2013); Karas et al. (2014); Zanotti and Pugliese (2015); Stuchlik et al. (2020). In this section, we use mainly dimensionless units.

3.1 Ideal GR-MHD

Before considering the model of magnetized **RAD**, it is convenient to review some basic notions of ideal GR-MHD. The fluids energy-momentum tensor can be written as the

composition of the two components

$$
\begin{aligned}
T^{\rm f}_{ab} =&(\varrho + p)U_aU_b - \epsilon\, p g_{ab} \qquad (5)\\
T^{\rm em}_{ab} =&-\epsilon\left(F_{ac}F_b{}^c - \frac{1}{4}F_{cd}F^{cd}g_{ab}\right) = \frac{g_{ab}}{2}(E^2+B^2) - (E_aE_b + B_aB_b)\\
&- 2\epsilon\breve{\mathcal{G}}_{(a}U_{b)} - \epsilon U_aU_b(E^2+B^2),\\
\nabla_{[a}F_{bc]} =&0, \quad \nabla^aF_{ab} = \epsilon J_b, \quad J^a = \varrho_c U^a + j^a,
\end{aligned}
$$

(quantities are measured by an observers moving with the fluid). $\breve{\mathcal{G}}_a$ denotes the Pointing vector, $U^aU_a = \epsilon$, (ϵ in this section is clearly a signature sign) and $h_{ab} \equiv g_{ab} - \epsilon U_aU_b$, is the projection tensor, where $\nabla_\alpha g_{\beta\gamma} = 0$. Considering the charge density and conduction current with the Ohm's law, there is $j^a = \sigma^{ab}E_b, \quad J^a = \varrho_c U^a + \sigma E^a$. We consider isotropic fluids for which $\sigma^{ab} = \sigma g^{ab}$, σ is the electrical conductivity coefficient. For ideal conductive plasma there is $\sigma \to \infty$ ($E_a = F_{ab}U^b = 0$): the electromagnetic field does not have a direct effect on the conservation equation along the flow lines, or

$$U_a\nabla^a\varrho + (p+\varrho)\nabla^aU_a - U^bF_b{}^c(\nabla^aF_{ac}) = 0, \qquad (6)$$

In the ideal MHD

$$(p+\varrho)U^a\nabla_aU^c - \epsilon h^{bc}\nabla_b p - \epsilon(\nabla^aF_{ad})F^{cd} = 0, \qquad (7)$$

and

$$U^a\nabla_a s = \frac{1}{nT}U^bF_b{}^c\nabla^aF_{ac}. \qquad (8)$$

(T is the temperature and n is the particle number density). In infinitely conducting plasma there is $U^a\nabla_a s = 0$ and the entropy per particle is conserved along the flow lines of each toroids. a particular case of interest is when s is a constant of both space and time implying $p = p(\varrho)$. Pugliese and Valiente Kroon (2016); Pugliese and Kroon (2012).

3.2 Magnetized tori

We consider an infinitely conductive plasma in the magnetized case where $F_{ab}U^a = 0$, F_{ab}, $U^aB_a = 0$, $\partial_\phi B^a = 0$ and $B^r = B^\theta = 0$. The toroidal magnetic field contribution in each **RAD** component can be written by considering,

$$B^\phi = \sqrt{\frac{2p_B}{g_{\phi\phi} + 2\ell g_{t\phi} + \ell^2 g_{tt}}} \qquad (9)$$

or alternatively

$$B^\phi = \sqrt{2\mathcal{M}\omega^q}\left(g_{t\phi}g_{t\phi} - g_{tt}g_{\phi\phi}\right)^{(q-2)/2}V_{eff}(\ell)$$

with $p_B = \mathcal{M}\left(g_{t\phi}g_{t\phi} - g_{tt}g_{\phi\phi}\right)^{q-1}\omega^q$ the magnetic pressure, ω is the fluid enthalpy, q and $\mathcal{M}$ (magnitude) are constant; V_{eff} is a function of the metric and the angular momentum

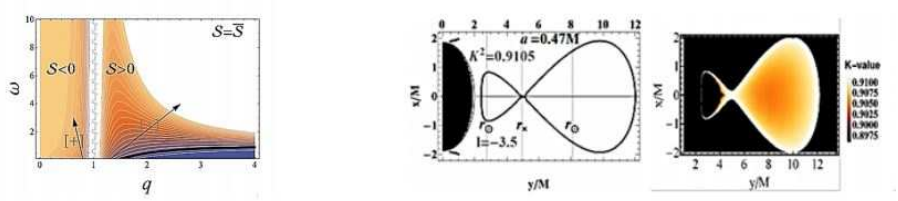

Figure 2. Left panel: Profiles of $\mathcal{S}$ =constant in the panel ω-q, where ω is the fluid enthalpy and q is a magnetic field family parameter. Arrow directions indicate the increasing values of $\mathcal{S}$ $q = 1$ is a singular value for $\mathcal{S}$. At $q < 1$ ($\mathcal{S} < 0$) excretion tori (density profiles in the right panel) appear. From Pugliese and Montani (2018).

ℓ–Komissarov (2006); Zanotti and Pugliese (2015); Pugliese and Montani (2013); Adámek and Stuchlík (2013); Hamersky and Karas (2013); Karas et al. (2014). The Euler equation for the HD case is modified by the term:

$$\partial_\mu \tilde{W} = \partial_\mu \left[\ln V_{eff} + \mathcal{G}\right], \tag{10}$$

where

$$(a \neq 0) : \mathcal{G}(r,\theta) = \mathcal{S}\left(\mathcal{A}V_{eff}^2\right)^{q-1}; \tag{11}$$

and

$$\mathcal{A} \equiv \ell^2 g_{tt} + 2\ell g_{t\phi} + g_{\phi\phi},\ \mathcal{S} \equiv \frac{q\mathcal{M}\omega^{q-1}}{q-1},$$

We here concentrate on $q > 1$ as, the magnetic parameter $\mathcal{S}$ is negative for $q < 1$, where excretion tori are possible Stuchlík (2005); Stuchlík et al. (2009); Slaný and Stuchlík (2005); Stuchlík and Schee (2010). $q = 1$, gives singular value for $\mathcal{S}$, see Figs (2). In this new frame, the analysis of **RAD** structure is performed by considering the new equation $\tilde{W} \equiv \mathcal{G}(r,\theta) + \ln(V_{eff}) = K$. The deformed potential function $\widetilde{V}_{eff}^2$,

$$\widetilde{V}_{eff}^2 \equiv V_{eff}^2 e^{2\mathcal{S}\left(\mathcal{A}V_{eff}^2\right)^{q-1}} = \tag{12}$$
$$= \frac{\left(g_{t\phi}g_{t\phi} - g_{tt}g_{\phi\phi}\right)\exp\left(2S\left(g_{t\phi}g_{t\phi} - g_{tt}g_{\phi\phi}\right)^{q-1}\right)}{\ell^2 g_{tt} + 2\ell g_{t\phi} + g_{\phi\phi}} = K^2.$$

For $\mathcal{S} = 0$ (or $\mathcal{M} = 0$), this reduces to the effective potential V_{eff}^2 for the HD case: V_{eff}^2: $\widetilde{V}_{eff}^2 = V_{eff}^2 + \frac{2\mathcal{S}\left(\mathcal{A}V_{eff}^2\right)^q}{\mathcal{A}} + \mathrm{O}\left(\mathcal{S}^2\right)$.

$$\mathcal{S}_n = \frac{\mathcal{M}\ln^n(\omega)(n + \ln(\omega) + 1)}{\Gamma(n+2)} \text{ for } n \geq 0 \text{ and } q \gtrsim 1, \tag{13}$$

where $\Gamma(x)$ is the Euler gamma function. As for the HD case in Eq. (2), we could find the **RAD** angular momentum distribution:

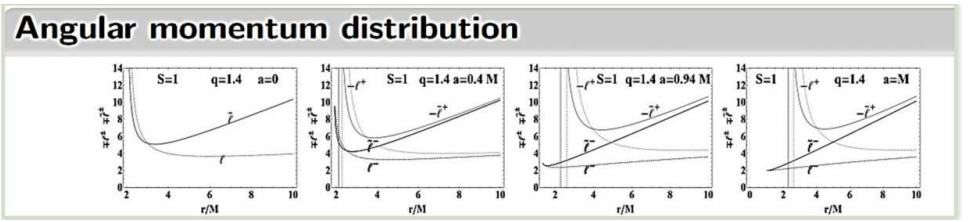

Figure 3. Magnetized **RAD**: angular momentum profiles $\tilde{\ell}$ in comparison with the HD case ℓ, for different values of the magnetic parameters $\mathcal{S}$, q and the **BH** dimensionless spin a/M, varying from the Schwarzschild case $a = 0$ to the extreme Kerr **BH** $a = M$ for corotating (-) and counterrotating (+) fluids. From Pugliese and Montani (2018).

$$\widetilde{\ell^{\mp}} \equiv \frac{\Delta\left(a^3 + ar\left[4Q(r-M)\mathcal{S}\Delta^Q + 3r - 4\right] \mp \sqrt{r^3\left[\Delta^2 + 4Q^2(r-1)^2 r\mathcal{S}^2\Delta^{2Q+1} + 2Q(r-1)^2 r\mathcal{S}\Delta^{Q+1}\right]}\right)}{a^4 - a^2(r-3)(r-2)r - (r-2)r\left[2Q(r-1)\mathcal{S}\Delta^{Q+1} + (r-2)^2 r\right]} \tag{14}$$

(dimensionless units), where there is

$$\lim_{\mathcal{S}\to 0} \widetilde{\ell^{\mp}} = \lim_{q\to 1} \widetilde{\ell^{\mp}} = \ell^{\pm}, \quad Q \equiv q - 1$$

see Figs (3). However the introduction of a toroidal magnetic field B, makes the study of the momentum distribution within the disk rather complicated. In Pugliese and Montani (2018), it was adopted as a function derived from the $\mathcal{S}$ parameter:

Leading RAD function:

$$\mathcal{S}_{crit} \equiv -\frac{\Delta^{-Q}}{Q}\frac{a^2(a-\ell)^2 + 2r^2(a-\ell)(a-2\ell) - 4r(a-\ell)^2 - \ell^2 r^3 + r^4}{2r(r-1)\left[r(a^2-\ell^2) + 2(a-\ell)^2 + r^3\right]}. \tag{15}$$

This function represents the new leading function for the distribution of tori in the **RAD** instead of Eq. (14) with a toroidal magnetic field component. (Each torus is on a line $\mathcal{S}$ =constant). This is able to determine **(1)** the limits on the value of the magnetic parameter for the tori formation, **(2)** the emergence of HD instability associated with the cusped configurations $C_\times$ and $()_\times$, **(3)** the emergence of collision between two tori of a **RAD** couple. It highlights the difference between magnetized corotating and counter-rotating tori with respect to the central black hole. (This difference is also evident from the dependence in Eq. (15) from the quantities $(a \pm \ell)$.) As demonstrated in Pugliese and Montani (2018), such magnetized tori can be formed in the **RAD** macro configurations for sufficiently small $(q\mathcal{S})$ and the constraints described in Sec. (A) are essentially confirmed for the magnetized case.

4 CONCLUDING REMARKS

The **RAD** dynamics is strongly affected by the the dimensionless spin of the central **BH** and the fluids relative rotation, especially in the magnetized case considered in Sec. (3).

In general, there is evidence of a strict correlation between **SMBH** spin, fluid rotation and magnetic fields in **RADs** formation and evolution. The analysis presented here poses constraints on tori formation and emergence of **RADs** instabilities in the phases of accretion onto the central attractor and tori collision emergence Pugliese and Stuchlík (2017, 2019). Eventually the **RAD** frame investigation constraints specific classes of tori that could be observed around some specific **SMBHs** identified by their dimensionless spin. As a sideline result, we provided a full characterization of the counter rotating tori in the multi-accreting systems. This model is designed for an extension to a dynamic GRMHD setup. From observational viewpoint, **AGN** Xray variability suggests connection between X-rays and the innermost regions of accretion disk. In Sochora et al. (2011); Karas and Sochora (2010); Schee and Stuchlík (2009, 2013) such relatively indistinct excesses of the relativistically broadened emission-line components are predicted to be arising in a well-confined radial distance in the accretion structure originating from a series of episodic accretion events.

Another significant aspect is the possibility to relate the **RAD** oscillations and their components with **QPOs**. The radially oscillating tori of the couple could be related to the high-frequency quasi-periodic oscillations (**QPOs**). Finally, for a discussion on the relation among Papaloizou-Pringle (**PP**) global incompressible modes in the tori, the Papaloizou-Pringle Instability (**PPI**), a global-hydrodynamic-non-axisymmetric instability, and the Magneto-Rotational Instability (MRI) modes, see Pugliese and Montani (2018); Bugli et al. (2018).

As an extension of this model to a more general situation, multi-orbiting configurations, considering tilted warped disks are also studied in Pugliese and Stuchlík (2020a,b). This possibility, rather probable as a scenario in the initial phases of tori formation, could be investigated as perturbation or deformation of the axis-symmetric equatorial model considered here.

ACKNOWLEDGEMENTS

D.P. acknowledges partial support from the Junior GAČR grant of the Czech Science Foundation No:16-03564Y. Z. S. acknowledges the Albert Einstein Centre for Gravitation and Astrophysics supported by grant No. 14-37086G. We are grateful to the anonymous referee for her/his suggestions which have improved of manuscript.

APPENDIX A: BASIC HD-RAD CONSTRAINTS

In this section we show some main constraints of the **RAD** models by schematically summarizing the analysis of Pugliese and Stuchlík (2017, 2019).

In general, two quiescent tori (not cusped tori) can exist in all Kerr spacetimes if their specific angular momenta are properly related. Whereas there are only following four double tori with a critical (cusped) topology: **i)** $C^{\pm}_{\times} < C^{\pm}$ **ii)**, $C^{+}_{\times} < C^{\pm}$,**iii)** $C^{-}_{\times} < C^{\pm}$ and **iv)** $C^{-}_{\times} < C^{+}_{\times}$–

Moreover: • for $\ell_{corotating}$ tori or in the background of a static (Schwarzschild) attractor only the inner torus can be accreting (with a cusp). • In the $\ell_{counterrotating}$ couple, an cusped corotating torus has to be the inner one of the couple whereas the outer counterrotating

torus can be in quiescent or with a cusp. If there is $C_{\times}^{-}$ (or for a static attractor), then $C_{\times}^{-}$ is part of $C_{\times}^{-} < C^{-}$ or $C_{\times}^{-} < ()^{+}$, doubled system.

Therefore, summarizing the situation for corotating and counterrotating **RAD** components, in particular there is: • a corotating torus can be the outer of a couple with an inner counterrotating cusped surface. The outer torus of this couple may be corotating (quiescent), or counterrotating cusped or in quiescence. Both the inner corotating and the outer counterrotating torus of the couple can have a cusp. • A counterrotating torus can reach the (HD) instability as the inner configuration of an $\ell_{corotating}$ or $\ell_{counterrotating}$ couple or, viceversa, the outer torus of an $\ell_{counterrotating}$ couple. If the cusped torus is $C_{\times}^{+}$, it follows that there is no inner counterrotating torus, but there can be $C_{\times}^{+} < C^{\pm}$ or $()^{-} < C_{\times}^{+}$.

REFERENCES

Adámek, K. and Stuchlík, Z. (2013), Magnetized tori in the field of kerr superspinars, *Classical and Quantum Gravity*, **30**(20), p. 205007.

Bugli, M., Guilet, J., Muller, E., Del Zanna, L., Bucciantini, N. and Montero, P. J. (2018), Papaloizou-Pringle instability suppression by the magnetorotational instability in relativistic accretion discs, *Mon. Not. Roy. Astron. Soc.*, **475**, p. 108, arXiv: 1707.01860.

Hamersky, J. and Karas, V. (2013), Effect of the toroidal magnetic field on the runaway instability of relativistic tori, *Astron. Astrophys.*, **555**, p. A32, arXiv: 1305.6515.

Karas, V., Kopáček, O., Kunneriath, D. and Hamerský, J. (2014), Oblique magnetic fields and the role of frame dragging near rotating black hole, *Acta Polytech.*, **54**(6), pp. 398–413, arXiv: 1408.2452.

Karas, V. and Sochora, V. (2010), Extremal Energy Shifts of Radiation from a Ring Near a Rotating Black Hole, *The Astrophysical Journal*, **725**, pp. 1507–1515, arXiv: 1010.5785.

Komissarov, S. S. (2006), Magnetized tori around Kerr black holes: analytic solutions with a toroidal magnetic field, *Mon. Not. R. Astron Soc.*, **368**, pp. 993–1000, arXiv: astro-ph/0601678.

Pugliese, D. and Kroon, J. A. V. (2012), On the evolution equations for ideal magnetohydrodynamics in curved spacetime, *Gen. Rel. Grav.*, **44**, pp. 2785–2810, arXiv: 1112.1525.

Pugliese, D. and Montani, G. (2013), Squeezing of toroidal accretion disks, *EPL*, **101**(1), p. 19001, arXiv: 1301.1557.

Pugliese, D. and Montani, G. (2015), Relativistic thick accretion disks: morphology and evolutionary parameters, *Phys. Rev.*, **D91**(8), p. 083011, arXiv: 1412.2100.

Pugliese, D. and Montani, G. (2018), Influence of toroidal magnetic field in multiaccreting tori, *Mon. Not. Roy. Astron. Soc.*, **476**(4), pp. 4346–4361, arXiv: 1802.07505.

Pugliese, D., Montani, G. and Bernardini, M. G. (2013), On the Polish doughnut accretion disk via the effective potential approach, *Mon. Not. Roy. Astron. Soc.*, **428**(2), pp. 952–982, arXiv: 1206.4009.

Pugliese, D. and Stuchlík, Z. (2015), Ringed accretion disks: equilibrium configurations, *Astrophys. J. Suppl.*, **221**, p. 25, arXiv: 1510.03669.

Pugliese, D. and Stuchlík, Z. (2016), Ringed accretion disks: instabilities, *Astrophys. J. Suppl.*, **223**(2), p. 27, arXiv: 1603.00732.

Pugliese, D. and Stuchlík, Z. (2017), Ringed accretion disks: evolution of double toroidal configurations, *Astrophys. J. Suppl.*, **229**(2), p. 40, arXiv: 1704.04063.

Pugliese, D. and Stuchlík, Z. (2018a), Proto-jet configurations in RADs orbiting a Kerr SMBH: symmetries and limiting surfaces, *Class. Quant. Grav.*, **35**(10), p. 105005, arXiv: 1803.09958.

Pugliese, D. and Stuchlík, Z. (2018b), Relating Kerr SMBHs in active galactic nuclei to RADs configurations, *Class. Quant. Grav.*, **35**(18).

Pugliese, D. and Stuchlík, Z. (2018c), Tori sequences as remnants of multiple accreting periods of Kerr SMBHs, *JHEAp*, **17**, pp. 1–37, arXiv: 1711.04530.

Pugliese, D. and Stuchlík, Z. (2019), RADs energetics and constraints on emerging tori collisions around super-massive Kerr Black Holes, arXiv: 1903.05970.

Pugliese, D. and Stuchlík, Z. (2020a), Embedded BHs and multipole globules: clustered misaligned thick accretion disks around static SMBHs, *Classical and Quantum Gravity*, **37**(19), 195025, arXiv: 2006.03282.

Pugliese, D. and Stuchlík, Z. (2020b), Limiting effects in clusters of misaligned toroids orbiting static SMBHs, *Mon. Not. R. Astron Soc.*, **493**(3), pp. 4229–4255, arXiv: 2003.05700.

Pugliese, D. and Valiente Kroon, J. A. (2016), On the locally rotationally symmetric Einstein Maxwell perfect fluid, *Gen. Rel. Grav.*, **48**(6), p. 74, arXiv: 1410.1335.

Schee, J. and Stuchlík, Z. (2009), Profiles of emission lines generated by rings orbiting braneworld Kerr black holes, *Gen. Rel. Grav.*, **41**, pp. 1795–1818, arXiv: 0812.3017.

Schee, J. and Stuchlík, Z. (2013), Profiled spectral lines generated in the field of Kerr superspinars, *Journal of Cosmology and Astroparticle Physics*, **2013**(04), pp. 005–005, arXiv: 0812.3017.

Slaný, P. and Stuchlík, Z. (2005), Relativistic thick discs in the kerr–de sitter backgrounds, *Classical and Quantum Gravity*, **22**(17), pp. 3623–3651.

Sochora, V., Karas, V., Svoboda, J. and Dovčiak, M. (2011), Black hole accretion rings revealed by future X-ray spectroscopy, *Mon. Not. R. Astron Soc.*, **418**, pp. 276–283, arXiv: 1108.0545.

Stuchlík, Z. (2005), Influence of the relict cosmological constant on accretion discs, *Mod. Phys. Lett.*, **A20**, p. 561, arXiv: 0804.2266.

Stuchlik, Z., Kološ, M., Kovář, J., Slaný, P. and Tursunov, A. (2020), Influence of Cosmic Repulsion and Magnetic Fields on Accretion Disks Rotating around Kerr Black Holes, *Univ.*, **6**(26).

Stuchlík, Z. and Schee, J. (2010), Appearance of Keplerian discs orbiting Kerr superspinars, *Class. Quant. Grav.*, **27**, p. 215017, arXiv: 1101.3569.

Stuchlík, Z., Slany, P. and Kovar, J. (2009), Pseudo-Newtonian and general relativistic barotropic tori in Schwarzschild-de Sitter spacetimes, *Class. Quant. Grav.*, **26**, p. 215013, arXiv: 0910.3184.

Zanotti, O. and Pugliese, D. (2015), Von Zeipels theorem for a magnetized circular flow around a compact object, *Gen. Rel. Grav.*, **47**(4), p. 44, arXiv: 1412.6447.

Proceedings of *RAGtime 20–22, 15–19 Oct., 16–20 Sept., 19–23 Oct., 2018/2019/2020, Opava, Czech Republic*
Z. Stuchlík, G. Török and V. Karas, editors, Silesian University in Opava, 2020, pp. 257–262

On maximum energy cutoff in the hotspot of radiogalaxies 3C 105 and 3C 445

Yelyzaveta Pulnova[1,2,a] and Anabella Araudo[2,3,b]

[1]Institute of Theoretical Physics, Faculty of Mathematics & Physics, Charles University, V Holešovičkách 2/747, Prague, Czech Republic
[2]ELI Beamlines, Institute of Physics, Czech Academy of Sciences, 25241 Dolní Břežany, Czech Republic
[3]Astronomical Institute, Czech Academy of Sciences, Boční II 1401, CZ-141 00 Prague, Czech Republic
[a]Yelyzaveta.Pulnova@eli-beams.eu
[b]Anabella.Araudo@eli-beams.eu

ABSTRACT
The origin of Ultra-High-Energy Cosmic Rays is still unknown, and Active Galactic Nuclei have been proposed as candidates to accelerate these particles. Using the well-resolved radio emission from radiogalaxies 3C 105 and 3C 445 we investigate the standard assumption that the distribution of non-thermal electrons has a maximum energy cutoff due to the synchrotron cooling. We show that as a consequence this would lead to an unphysically large number density in the hotspot. This result has important implications for the origin of Ultra-High-Energy Cosmic Rays.

Keywords: Ultra-high-energy cosmic rays – diffusive shock acceleration –synchrotron cooling

1 INTRODUCTION

Ultra-high-energy cosmic rays (UHECR) are charged particles detected on Earth with energy higher than 10^{18} eV. The origin of these particles is still unknown. The very upper limit to the maximum achievable energy was estimated by Hillas (1984) by assuming that the maximum displacement of a charged particle by an electric field is the size of the system L. The Hillas energy, or the maximum energy achievable by a particle with charge Zq, is

$$E_{\rm Hillas} \sim 10^{18} \left(\frac{v}{c}\right)\left(\frac{L}{\rm kpc}\right)\left(\frac{B}{100\mu{\rm G}}\right) \ {\rm eV}, \tag{1}$$

where B is the magnetic field and v the velocity of the plasma. We see that for compact objects a strong magnetic field is required, while for a weak field the source should be extended enough. White dwarfs, active galactic nuclei, galaxy clusters, and radio galaxies are candidates to accelerate UHECRs. In this work, we study the hotspots in the termination region of radiogalaxy jets.

978-80-7510-432-8

Table 1. From left to right, we list the name of the source, the redshift (z), the scale (in kpc arcsec^{-1}), the distance (in Gpc), the radio spectral index α, the steepness of the relativistic electrons energy distribution $s = 2\alpha + 1$, and the proton to electron energy density ratio a.

Source	z	scale	d	α	s	a
3C 105	0.089	1.642	0.4017	0.8	2.6	4.51
3C 445	0.0562	1.077	0.2479	0.75	2.5	6.58

Araudo et al. (2016) [A16] showed that the maximum energy of particles accelerated in the hotspots of FR II radiogalaxies is $\sim$ 10 TeV, and therefore much smaller than the energy of UHECRs. Based on theoretical and observational constraints, and for a sample of sources (3C 105, 3C 195, 3C 227, 3C 403, and 3C 445), [A16] demonstrated that at least the plasma density is unreasonably large, hotspots cannot accelerate UHECRs. In the present contribution, we analyze the southern hotspots in 3C 105 and 3C 445 but considering the substructures in the hotspots.

2 THE CASES STUDY 3C 105 S AND 3C 445 S

We select the southern hotspots in radiogalaxies 3C 105 and 3C 445 from where high-resolution radio data taken by the Very Large Array (VLA) are available in the literature. Parameters used for the analysis are listed in Table 1.

3C 105 South

Radiogalaxy 3C 105 is located at redshift $z = 0.089$. At radio frequencies (8.4 GHz), three knots denoted in Fig. 1 as S1, S2, and S3 are resolved in the southern hotspot (Migliori et al., 2020).

3C 445 South

Radiogalaxy 3C 445 is located at redshift $z = 0.05623$. The southern hotspot 3C 445 South has two components at 22 GHz denoted as SE and SW for Eastern and Western knots, respectively (Orienti et al., 2020). SE is well-resolved and sufficiently larger and brighter than the SW knot. The latter has a compact radio-loud part and is surrounded by the large cloud of the radio fainter emitting matter, which is neglected in our analysis.

3 EQUIPARTITION MAGNETIC FIELD

We estimate the intensity of the magnetic field separately for every knot of the hotspot. By assuming equipartition between the non-thermal electron and magnetic energy densities,

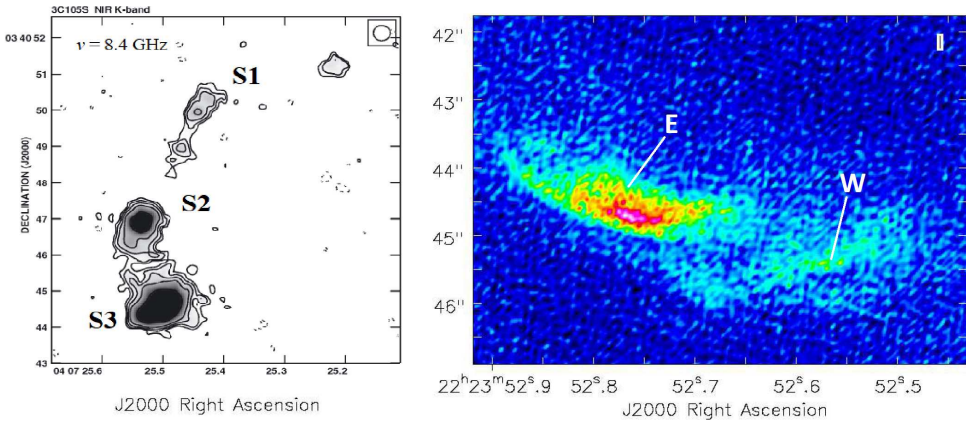

Figure 1. *Left:* Southern hotspot of radiogalaxy 3C 105 at 8.4 GHz. The three knots are denoted as S1, S2 and S3. Credit: Mack et al. (2009). *Right:* The hotspot complex 3C 445 South at 22 GHz. Eastern and Western components are denoted as E, W, respectively. Credit: Orienti et al. (2020)

which means $U_{e,\mathrm{NT}} = U_{\mathrm{mag}}$, we obtain

$$\frac{B_{e,\mathrm{eq}}^2}{8\pi} = U_{e,\mathrm{NT}} = \int_{E_{e,\mathrm{min}}}^{E_{\mathrm{e,max}}} E N_e(E_e)\mathrm{d}E_e \propto B_{e,\mathrm{eq}}^{-\frac{s+1}{2}}, \tag{2}$$

where $N_e = K_e(s)E_e^{-s}$ is the power-law energy distribution of the non-thermal electrons and $E_{e,\mathrm{min}}$ and $E_{e,\mathrm{max}}$ are the minimum and maximum energies of the electron distribution. Note that $s > 2$ in all the sources in our sample, and therefore most of the energy is contained in the low-energy part of N_e. We assume $E_{e,\mathrm{min}} = 50 m_e c^2$.

To include protons in our calculations we consider that the energy density in non-thermal protons is $U_{p,NT} = aU_{e,NT}$, where $a = (m_p/m_e)^{(3-s)/2}$, m_e and m_p are the electron and proton mass, respectively. Then the total equipartition magnetic field can be determined from $B_{\mathrm{eq}} = \sqrt{1+a}B_{\mathrm{eq,e}}$, given

$$B_{\mathrm{eq}} = \xi(s)\left(\frac{\epsilon_{\mathrm{syn},\nu}}{10^{-34}\ \mathrm{erg\ s^{-1}\ cm^{-3}\ Hz^{-1}}}\right)^{\frac{2}{s+5}}\left(\frac{\nu}{\mathrm{GHz}}\right)^{\frac{s-1}{s+5}}\mu\mathrm{G} \tag{3}$$

where $\epsilon_{\mathrm{syn},\nu} = 4\pi d^2 S_\nu V^{-1}$ is synchrotron emissivity per unit frequency, ν is the observed frequency. Constant $\xi(s)$ in the case of 3C 105 corresponds to value 96, and 106 otherwise. To calculate the volume V of the emitting regions at the given observed frequency, from Fig. 1 we estimate the minor axes l_{min} and areas of each knot of the hotspots. In Table 2 we list the values of l_{min}, V, and B_{eq} for all the sources in our sample.

4 SYNCHROTRON COOLING AND THE PLASMA NUMBER DENSITY

Hotspots in the termination shocks in radiogalaxy jets show a cutoff of the synchrotron spectrum, in the optical-IR band, i.e. at $\nu_{\mathrm{c}} \sim 10^{13} - 10^{15}$ Hz. From the cutoff of the

Table 2. Observed and derived parameters of the hotspots. From left to right, we list the name of the source and the non-thermal component in the hotspot, the observed frequency ν and measured flux density S_ν, the projected size S and the minor axis $l_{\rm min}$, the volume V, the equipartition magnetic field $B_{\rm eq}$ and $n_{\rm min}$ (see Eq. 7).

Source	Comp.	ν [GHz]	S_ν [mJy]	S [″×″]	$l_{\rm min}$ [kpc]	V [kpc^3]	$B_{\rm eq}$ [μG]	$n_{\rm min}$ [cm^{-3}]
3C 105	S1	8.4	18.4	1.30×0.59	0.97	1.052	198	0.61
	S2	8.4	372	1.68×0.94	1.54	3.422	267	450
	S3	8.4	260	2.20×1.20	1.98	7.387	198	184
3C 445	SE	22	14.24	2.63×0.91	0.51	0.201	229	0.44
	SW	22	2.92	1.02×0.15	0.08	0.002	512	0.83

synchrotron spectrum, we estimate the maximum energy of accelerated electrons (Lang (2013))

$$E_{e,\rm max} = m_e c^2 \sqrt{\frac{4\pi m_e c}{3q}} \sqrt{\frac{\nu_c}{B}} \sim 0.3 \left(\frac{\nu_{\rm c}}{10^{14}\,{\rm Hz}}\right)^{0.5} \left(\frac{B}{100\,\mu{\rm G}}\right)^{-0.5} {\rm TeV}. \quad (4)$$

It is commonly assumed in the literature that $E_{e,\rm max}$ is determined by synchrotron cooling (Prieto et al., 2002), with a timescale $t_{\rm synchr} \sim 450/(E_{e,\rm max}B^2)$. By equating $t_{\rm acc} = t_{\rm synchr}$, where $t_{\rm acc} = 20D/v_{\rm sh}^2$ is the acceleration time via diffusive shock acceleration, we obtain that the diffusion coefficient is

$$D_{s,c} = 30.7 \frac{v_{\rm sh}^2}{E_{e,\rm max}B^2} = 6.8\times10^{30} \left(\frac{v_{\rm sh}}{c}\right)^2 \left(\frac{\nu_{\rm c}}{10^{14}\,{\rm Hz}}\right)^{-0.5} \left(\frac{B}{100\,\mu{\rm G}}\right)^{-1.5} {\rm cm^2\,s^{-1}}. \quad (5)$$

We assume the shock velocity $v_{\rm sh} = c/3$ in our calculations.

The diffusion coefficient is defined as $D = \lambda c/3$, where $\lambda = r_g^2/s$ is the mean-free path in the small scale diffusion regime, $r_{\rm g}$ is the mean-free path, and s is the scale-length of the magnetic turbulence. The minimum value of s is the ion skin depth $c/\omega_{\rm pi}$. Therefore, by considering $s = c/\omega_{\rm pi}$ we obtain that the maximum value of the diffusion coefficient is

$$D_{\rm max} = \frac{1}{3} r_g^2 \omega_{\rm pi} = 3\times10^{28} \left(\frac{\nu_{\rm c}}{10^{14}\,{\rm Hz}}\right)\left(\frac{n}{\rm cm^{-3}}\right)^{0.5} \left(\frac{B}{100\,\mu{\rm G}}\right)^{-3} {\rm cm^2\,s^{-1}}. \quad (6)$$

If $E_{e,\rm max}$ is determined by synchrotron cooling, then the condition $D_{s,c} < D_{\rm max}$ needs to be satisfied. By following the procedure described in [A16], we determine the minimum plasma density in the hotspot to satisfy the condition $D_{s,c} = D_{\rm max}$ giving

$$n_{\rm min} = 5.3\times10^4 \left(\frac{v_{\rm sh}}{c}\right)^4 \left(\frac{\nu_{\rm c}}{10^{14}\,{\rm Hz}}\right)^{-3} \left(\frac{B}{100\,\mu{\rm G}}\right)^{3} {\rm cm^{-3}}. \quad (7)$$

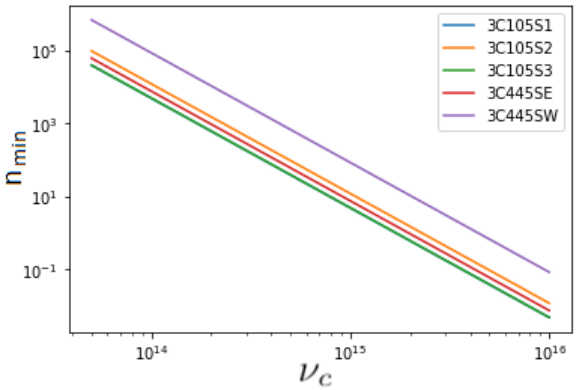

Figure 2. The log-log plot of a lower limit of the number density $n_{\rm min}$ for the cutoff frequencies ν_c in the vicinity of typical values. We use $B = B_{\rm eq}$. Curves from sources 3C 105 S1 and 3C 105 S3 are overlapping.

In Fig. 2 we plot $n_{\rm min}$ as a function of the cutoff frequency ν_c. We chose the vicinity of the typical cutoff frequencies $\nu_c \sim 10^{14} - 10^{15}$ Hz (Orienti et al., 2012)). The values we obtained are far above the typical range of values for the hotspots number density.

5 CONCLUSIONS

Our calculations indicate that electron's maximum energy might not be determined by synchrotron cooling because this assumption leads to unreasonably large values of the lower limit for the plasma number density $n_{\rm min}$ (see Tab. 2). For comparison the upper limit for plasma number density in Cyg A and 3C 475 is $n \sim 10^{-4}{\rm cm}^{-3}$ (Dreher et al., 1987).

Araudo et al. (2016) and Araudo et al. (2018) proposed that electrons maximum energy cutoff in the hotspots of radiogalaxies is due to escape downstream of a quasi-perpendicular shock. In this case, the maximum energy of protons is $E_{p,\rm max} = E_{e,\rm max}$. In this context, the maximum achievable energy of protons in the hotspot of the radiogalaxies 3C 105 S and 3C 445 S is $E_{p,\rm max} \sim$ TeV and therefore these hotspots can not accelerate UHECR. In a more general context, Bell et al. (2018) showed that relativistic shocks are unable to accelerate UHECRs.

ACKNOWLEDGEMENTS

Y.P. thanks ELI Beamlines for the financial support under the project LM2018141. A.T.A. thanks the Czech Science Foundation under the grant GAČR 20-19854S titled "Particle Acceleration Studies in Astrophysical Jets".

REFERENCES

Araudo, A. T., Bell, A. R., Blundell, K. M. and Matthews, J. H. (2018), On the maximum energy of non-thermal particles in the primary hotspot of cygnus a, *Monthly Notices of the Royal Astronomical Society*, **473**(3), pp. 3500–3506.

Araudo, A. T., Bell, A. R., Crilly, A. and Blundell, K. M. (2016), Evidence that the maximum electron energy in hotspots of FR II galaxies is not determined by synchrotron cooling, *Monthly Notices of the Royal Astronomical Society*, **460**(4), pp. 3554–3562.

Bell, A. R., Araudo, A. T., Matthews, J. H. and Blundell, K. M. (2018), Cosmic-ray acceleration by relativistic shocks: Limits and estimates, *Monthly Notices of the Royal Astronomical Society*, **473**(2), pp. 2364–2371, ISSN 13652966.

Dreher, J., Carilli, C. and Perley, R. (1987), The faraday rotation of cygnus a-magnetic fields in cluster gas, *The Astrophysical Journal*, **316**, pp. 611–625.

Hillas, A. M. (1984), The origin of ultra-high-energy cosmic rays, *Annual review of astronomy and astrophysics*, **22**, pp. 425–444.

Lang, K. R. (2013), *Astrophysical Formulae: Space, time, matter and cosmology*, Springer.

Mack, K.-H., Prieto, M., Brunetti, G. and Orienti, M. (2009), Near-infrared/optical counterparts of hotspots in radio galaxies, *Monthly Notices of the Royal Astronomical Society*, **392**(2), pp. 705–717.

Migliori, G., Orienti, M., Coccato, L., Brunetti, G., D'Ammando, F., Mack, K. H. and Prieto, M. A. (2020), Particle acceleration in low-power hotspots: modelling the broad-band spectral energy distribution, *Monthly Notices of the Royal Astronomical Society*, **495**(2), pp. 1593–1607.

Orienti, M., Migliori, G., Brunetti, G., Nagai, H., D'Ammando, F., Mack, K.-H. and Prieto, M. A. (2020), Jansky VLA observations of synchrotron emitting optical hotspots of 3C 227 and 3C 445 radio galaxies, *Monthly Notices of the Royal Astronomical Society*, **494**(2), pp. 2244–2253, ISSN 0035-8711.

Orienti, M., Prieto, M. A., Brunetti, G., Mack, K.-H., Massaro, F. and Harris, D. E. (2012), Complex particle acceleration processes in the hotspots of 3C 105 and 3C 445, *Monthly Notices of the Royal Astronomical Society*, **419**(3), pp. 2338–2348.

Prieto, M. A., Brunetti, G. and Mack, K.-H. (2002), Particle accelerators in the hot spots of radio galaxy 3c 445, imaged with the vlt, *Science*, **298**(5591), pp. 193–195.

Proceedings of *RAGtime 20–22, 15–19 Oct., 16–20 Sept., 19–23 Oct., 2018/2019/2020, Opava, Czech Republic*
Z. Stuchlík, G. Török and V. Karas, editors, Silesian University in Opava, 2020, pp. 263–276

Dynamics of magnetized particles around Reissner-Nordström black holes

Javlon Rayimbaev[1,2,3,a] and Nozima Juraeva[1,b]

[1] Ulugh Beg Astronomical Institute, Astronomicheskaya 33, Tashkent 100052, Uzbekistan,
[2] National University of Uzbekistan, Tashkent 100174, Uzbekistan
[3] Institute of Nuclear Physics, Ulughbek, Tashkent 100214, Uzbekistan
[a] javlon@astrin.uz
[b] nozima@astrin.uz

ABSTRACT
This paper is devoted to studying the dynamics of magnetized particles around electrically charged Reissner-Nordström (RN) black hole immersed in an external asymptotically uniform magnetic field. Here, we have focused on the effects of the external magnetic field and the electric charge of the RN black hole on the range of stable circular orbits for magnetized particles. We have shown that the dimensionless magnetic interaction parameter between magnetic dipole moment of a magnetized particle orbiting the black hole and the external magnetic field must be less than 1 in absolute value in order to allow stable circular orbits and with increasing of the electric charge of the black hole the range where circular orbits are allowed decreases while the increase of external magnetic field causes to increase it.

Keywords: Magnetized particles –charged black hole –external magnetic field

1 INTRODUCTION

Particle motion around a compact gravitational object is the special subject of highly motivated interest, since it may be used to develop new tests and probe the theories describing the gravitational interaction in the strong field regime. Particularly, black hole as gravitational compact object is useful astrophysical object to study the particle dynamics around the latter. Being simple object astrophysical black holes can be described with a few parameters, namely black hole total mass M, rotation parameter a, and electric charge Q. Static spherically-symmetric electrically charged black hole is described by the Reissner-Nordström (RN) solution Reissner (1916); Nordström (1918).

The electromagnetic field surrounding black hole or neutron star plays an important role in astronomical observation of compact objects through electromagnetic radiation or its influence to astrophysical processes around it. Even in the case of test electromagnetic field, when electromagnetic potential does not change the spacetime structure, the influence of the electromagnetic field to the energetic and dynamical processes around gravitational compact objects is essential. Despite no hair theorem, according to which the black

978-80-7510-432-8

hole cannot have its own intrinsic magnetic field Misner et al. (1973) one may explore the external magnetic field surrounding the black hole. Particularly the electromagnetic field structure around rotating black hole embedded in an external asymptotically uniform magnetic field has been studied in the pioneering paper Wald (1974). In past years, different properties of the electromagnetic fields in the vicinity of black holes immersed in external asymptotically uniform magnetic fields and proper magnetic field of rotating magnetized neutron stars with dipolar structure were widely studied by several authors in different models of gravity Aliev et al. (1986); Aliev and Gal'tsov (1989); Aliev and Özdemir (2002); Benavides-Gallego et al. (2019); Stuchlík et al. (2014); Stuchlík and Kološ (2016); Rayimbaev and Tadjimuratov (2020); Rayimbaev et al. (2015, 2019b,a, 2020). This electromagnetic field will change the dynamics of charged particle in close black hole environment Chen et al. (2016); Hashimoto and Tanahashi (2017); Dalui et al. (2019); Han (2008); de Moura and Letelier (2000); Morozova et al. (2014); Narzilloev et al. (2020). Together with charged particles one may study the influence of electromagnetic field near the black hole to magnetized particle motion. The dynamics of particles with intrinsic nonzero dipolar magnetic field around non-rotating and rotating black holes immersed in external magnetic field have been studied in de Felice and Sorge (2003); de Felice et al. (2004). Our recent works have been devoted to study the magnetized particle motion around black hole in magnetic field in different gravity models and theories Rayimbaev (2016); Rayimbaev et al. (2020); Toshmatov et al. (2015); Abdujabbarov et al. (2014); Rahimov et al. (2011); Rahimov (2011); Haydarov et al. (2020); Haydarov et al. (2020); Abdujabbarov et al. (2020); Vrba et al. (2020).

The paper is organized as follows: In Sect. 2 we study dynamics of magnetized particles around electrically RN black hole immersed in an external asymptotically uniform magnetic field in comoving observer frame. Finally, we summarize our results in Sect. 3.

We use the space-time signature $(-,+,+,+)$ and geometrized units system $G_{\rm N} = c = 1$. The Latin indices are expected to run from 1 to 3 and the Greek ones from 0 to 3.

2 MAGNETIZED PARTICLE MOTION AROUND ELECTRICALLY CHARGED RN BLACK HOLE IN MAGNETIC FIELD

The spacetime exterior to electrically charged RN black hole with total mass M and electric charge Q can be described by the metric:

$$\mathrm{d}s^2 = -f(r)\mathrm{d}t^2 + \frac{1}{f(r)}\mathrm{d}r^2 + r^2\mathrm{d}\theta^2 + r^2\sin^2\theta\mathrm{d}\phi^2 \,, \tag{1}$$

where the radial metric function is

$$f(r) = 1 - \frac{2M}{r} + \frac{Q^2}{r^2} \,. \tag{2}$$

Since there is no interaction between magnetized particles and electric charged RN black hole we assume that the black hole immersed in an external asymptotically uniform magnetic field and finally, the electromagnetic four-potentials can be expressed using the Wald

method Wald (1974) in the following form

$$A_\phi = \frac{1}{2} B_0 r^2 \sin^2\theta \,, \tag{3}$$

$$A_t = -\frac{Q}{r} \,, \tag{4}$$

where B_0 is asymptotic value of the external uniform magnetic field. One may immediately find the non-zero components of the electromagnetic tensor using the definition $F_{\mu\nu} = A_{\nu,\mu} - A_{\mu,\nu}$ in the following form

$$F_{r\phi} = B_0 r \sin^2\theta \,, \tag{5}$$

$$F_{\theta\phi} = B_0 r^2 \sin\theta\cos\theta \,, \tag{6}$$

$$F_{rt} = \frac{Q}{r^2} \tag{7}$$

The orthonormal components of the magnetic field around electrically charged RN black hole measured by proper observer

$$B^\alpha = \frac{1}{2}\eta^{\alpha\beta\sigma\mu} F_{\beta\sigma} w_\mu \,, \tag{8}$$

where w_μ is four-velocity of the proper observer, $\eta_{\alpha\beta\sigma\gamma}$ is the pseudo-tensorial form of the Levi-Civita symbol $\epsilon_{\alpha\beta\sigma\gamma}$ with the relations

$$\eta_{\alpha\beta\sigma\gamma} = \sqrt{-g}\epsilon_{\alpha\beta\sigma\gamma} \qquad \eta^{\alpha\beta\sigma\gamma} = -\frac{1}{\sqrt{-g}}\epsilon^{\alpha\beta\sigma\gamma} \,, \tag{9}$$

and $g = \det|g_{\mu\nu}| = -r^4 \sin^2\theta$ for spacetime metric (1) are

$$B^{\hat{r}} = B_0 \cos\theta, \qquad B^{\hat{\theta}} = \sqrt{f(r)} B_0 \sin\theta \,. \tag{10}$$

According to de Felice and Sorge (2003) the equation of motion of magnetized particles in the spacetime of a black hole immersed in the external magnetic field can be described by the following Hamilton-Jacobi equation

$$g^{\mu\nu}\frac{\partial \mathcal{S}}{\partial x^\mu}\frac{\partial \mathcal{S}}{\partial x^\nu} = -\left(m - \frac{1}{2} D^{\mu\nu} F_{\mu\nu}\right)^2 \,, \tag{11}$$

where m is mass of the particle, $\mathcal{S}$ is the action for magnetized particles in the spacetime of the black hole, the scalar term came from the product of polarization and electromagnetic field tensors $D^{\mu\nu}F_{\mu\nu}$ being responsible for the interaction between the external magnetic field and dipole moment of magnetized particles. The polarization tensor $D^{\mu\nu}$ corresponding to the magnetic dipole moment of magnetized particles is describes by the relation de Felice and Sorge (2003):

$$D^{\alpha\beta} = \eta^{\alpha\beta\sigma\nu} u_\sigma \mu_\nu, \qquad D^{\alpha\beta} u_\beta = 0 \,, \tag{12}$$

where μ^ν and u^ν are the four-vector of magnetic dipole moment and four-velocity of magnetized particles by the fiducial comoving observer. The electromagnetic field tensor can be decomposed through $F_{\alpha\beta}$ by electric E_α and magnetic B^α field components as

$$F_{\alpha\beta} = u_{[\alpha}E_{\beta]} - \eta_{\alpha\beta\sigma\gamma}u^\sigma B^\gamma. \tag{13}$$

One can find the product of polarization and electromagnetic tensors taking account the condition given in Eq. (12) in the following form

$$D^{\mu\nu}F_{\mu\nu} = 2\mu^{\hat{\alpha}}B_{\hat{\alpha}} = 2\mu B_0\mathcal{L}[\lambda_{\hat{\alpha}}]\,, \tag{14}$$

where $\mu = \sqrt{|\mu_{\hat{i}}\mu^{\hat{i}}|}$ is the norm of the dipole magnetic moment of magnetized particles and $L[\lambda_{\hat{\alpha}}]$ is the tetrad $\lambda_{\hat{\alpha}}$ attached to the comoving fiducial observer being the function of the radial coordinate and the black hole parameters.

Here we investigate dynamics of magnetized particles in circular orbits around electrically charged RN black hole in the weak magnetic interaction approximation due to weakness of the external magnetic field or/and the particle is less magnetized

$$\left(D^{\mu\nu}F_{\mu\nu}\right)^2 \to 0.$$

This approximation is astrophysical relevant since the external magnetic fieldin black hole environment is comparatively weak (Piotrovich et al. (2011)). The action for magnetized particles at the equatorial plane (where $\theta = \pi/2$ and $\dot{\theta} = 0$) can be described by the following form

$$\mathcal{S} = -Et + L\phi + \mathcal{S}_r\,, \tag{15}$$

which allows to separate the variables in Hamilton-Jacobi equation. The equation of radial motion of magnetized particles can be found as

$$\dot{r}^2 = \mathcal{E}^2 - V_{\rm eff}(r, Q, l, b)\,, \tag{16}$$

where the effective potential of radial motion of magnetized particles has the following form:

$$V_{\rm eff}(r, Q, l, b) = f\left(1 + \frac{l^2}{r^2} - b\mathcal{L}[\lambda_{\hat{\alpha}}]\right)\,, \tag{17}$$

where $b = 2\mu B_0/m$ is magnetic interaction parameter responsible to the interaction between dipole moment of magnetized particles and external magnetic field and $l = L/m$ is specific angular momentum of magnetized particles.

In real astrophysical scenarios one may treat a neutron star with the magnetic dipole moment $\mu = (1/2)B_{\rm NS}R_{\rm NS}^3$, like a magnetized particle, orbiting a supermassive black hole (SMBH) immersed in an external magnetic field with different configurations. In such a case the magnetic coupling parameter b can easily be estimated through the observational parameters of the neutron star and the approximate value of the external magnetic field around the SMBH in the following form:

$$b = \frac{B_{\rm NS}R_{\rm NS}^3B_{\rm ext}}{m_{\rm NS}} \simeq \frac{\pi}{10^3}\left(\frac{B_{\rm NS}}{10^{12}{\rm G}}\right)\left(\frac{B_{\rm ext}}{10{\rm G}}\right)\left(\frac{R_{\rm NS}}{10^6{\rm cm}}\right)^3\left(\frac{m_{\rm NS}}{1.4M_\odot}\right)^{-1}. \tag{18}$$

One may apply the calculation to estimate the value of the magnetic coupling parameter for a realistic case of the magnetar SGR (PSR) J1745–2900 orbiting around Sagittarius A* (Sgr A*). In the estimation of the coupling parameter we have considered magnetic field around SgrA* is in the order of 10 G, the magnetic dipole moment of the magnetar $\mu \approx 1.6 \times 10^{32}\mathrm{G}\cdot\mathrm{cm}^3$ and its mass $m \approx 1.4 M_\odot$ (Mori et al. (2013)) as

$$b_{\mathrm{PSRJ1745-2900}} \simeq 0.716 \left(\frac{B_{\mathrm{ext}}}{10\mathrm{G}}\right) . \tag{19}$$

Generally, the circular motion of test particles around axially symmetric black holes describes by the following standard condition

$$\dot{r} = 0, \qquad \frac{\partial V_{\mathrm{eff}}(r; Q, l, b)}{\partial r} = 0 . \tag{20}$$

The explicit expressions for the orthonormal tetrad carried the fiducial observer $\mathcal{L}[\lambda_{\hat{\alpha}}]$ can be formulated for circular motion at the equatorial plane around spherical symmetric black hole in the following form

$$\lambda_{\hat{t}} = e^{\Psi}\left(\partial_t + \Omega\partial_\phi\right) , \tag{21}$$

$$\begin{aligned}\lambda_{\hat{r}} =& e^{\Psi}\left[-\frac{\Omega r}{\sqrt{f(r)}}\partial_t - \frac{\sqrt{f(r)}}{r}\partial_\phi\right]\sin(\Omega_{FW}t) \\ &+ \sqrt{f(r)}\cos(\Omega_{FW}t)\partial_r ,\end{aligned} \tag{22}$$

$$\lambda_{\hat{\theta}} = \frac{1}{r}\partial_\theta , \tag{23}$$

$$\begin{aligned}\lambda_{\hat{\phi}} =& e^{\Psi}\left[\frac{\Omega r}{\sqrt{f(r)}}\partial_t + \frac{\sqrt{f(r)}}{r}\partial_\phi\right]\cos(\Omega_{FW}t) \\ &+ \sqrt{f(r)}\sin(\Omega_{FW}t)\partial_r ,\end{aligned} \tag{24}$$

where Ω_{FW} is Fermi-Walker angular velocity de Felice and Sorge (2003) and

$$e^{-\Psi} = \sqrt{f(r) - \Omega^2 r^2} , \tag{25}$$

with Ω is the angular velocity of the particles measured by a distant observer defined as

$$\Omega = \frac{\mathrm{d}\phi}{\mathrm{d}t} = \frac{\mathrm{d}\phi/\mathrm{d}\tau}{\mathrm{d}t/\mathrm{d}\tau} = \frac{f(r)}{r^2}\frac{l}{\mathcal{E}} . \tag{26}$$

We will study the motion of a magnetized particle orbiting at the equatorial plane assuming the magnetic dipole moment of the magnetized particle is always perpendicular to the equatorial plane and parallel to the external magnetic field. The orthonormal components of the external magnetic field measured by the observer comoving with the magnetized particle take the following form

$$B_{\hat{r}} = B_{\hat{\phi}} = 0 , \qquad B_{\hat{\theta}} = B_0 f(r)\, e^{\Psi} . \tag{27}$$

The induced electric field measured by the comoving observer can be written as

$$E_{\hat{r}} = B_0 \Omega r \cos(\Omega_{FW} t) \sqrt{f(r)} e^{\Psi} , \tag{28}$$

$$E_{\hat{\theta}} = 0 , \tag{29}$$

$$E_{\hat{\phi}} = B_0 \Omega r \sin(\Omega_{FW} t) \sqrt{f(r)} e^{\Psi} . \tag{30}$$

In case when the Fermi-Walker and the particles angular velocities measured by proper observer are zero ($\Omega_{FW} = \Omega = 0$), the above tetrad turns to tetrad of the proper observe (see Rezzolla and Zanotti (2001) in the case $a = 0$) and the magnetic field components in Eq.(27) equals to the components in Eq.(10) and the induced electric field vanishes.

One may find the possible values of the magnetic coupling parameter β for circular orbits from the first condition in Eq, (20)

$$b(r; l, \mathcal{E}, Q) = \frac{1}{\mathcal{L}[\lambda_{\hat{\sigma}}]} \left(1 + \frac{l^2}{r^2} - \frac{\mathcal{E}^2}{f(r)} \right) . \tag{31}$$

Inserting Eq.(27) into (14) we can find the interaction part of the Eq. (11)

$$D \cdot F = 2\mu B_0 f(r)\, e^{\Psi} , \tag{32}$$

One can find the analytic form of the term $\mathcal{L}[\lambda_{\hat{\sigma}}]$ by the comparison of Eq.(32) with Eq.(14) in the following form

$$\mathcal{L}[\lambda_{\hat{\sigma}}] = e^{\Psi} f(r) . \tag{33}$$

Finally, the magnetic interaction parameter $b(r; l, \mathcal{E}, Q)$ for stable circular orbits has the following form

$$b(r; l, \mathcal{E}, Q) = \left(\frac{1}{f(r)} - \frac{l^2}{\mathcal{E}^2 r^2} \right)^{1/2} \left(1 + \frac{l^2}{r^2} - \frac{\mathcal{E}^2}{f(r)} \right) . \tag{34}$$

Eq. (34) implies that a magnetized particle with magnetic coupling parameter b corresponds to circular stable orbit r with the energy $\mathcal{E}$ and angular momentum l.

Fig. 1 shows the radial dependence of the magnetic coupling parameter b for the different values of electric charge of RN black hole for the fixed values of the specific energy and angular momentum. One can see from the top panel of Fig. 1 that the maximal (minimal) values of the magnetic interaction parameter for the fixed values of the specific energy $\mathcal{E} = 0.9$ and angular momentum $l/M = 4$ ($l/M = 2\sqrt{5}$) increases (decreases) with the increase of electric charge of RN black hole.

Now we analyze the values of the magnetic interaction parameter corresponding to stable orbits for magnetized particles. It can be found using following set of equations de Felice and Sorge (2003); Rayimbaev (2016):

$$b = b(r; l, \mathcal{E}, Q), \qquad \frac{\partial b(r; l, \mathcal{E}, Q)}{\partial r} = 0 . \tag{35}$$

One can see from Eq. (35) contains two system of equations including five free parameters: four of them related to the magnetized particle $(b, r, l, \mathcal{E})$ and one to the spacetime (Q),

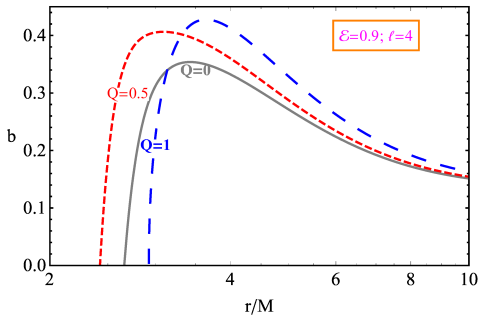

Figure 1. The radial dependence of magnetic coupling parameter for the different values of electric charge of RN black hole. In plots we used the values for the specific energy $\mathcal{E} = 0.9$ and for angular momentum $l = 4M$ (top panel) and $l = 2\sqrt{5}M$ (bottom panel). The black hole charge and specific angular momentum read as $Q \to Q/M$ and $l \to l/M$, respectively.

so its solution can be found in terms of any two of the five parameters as independent variables. To solve the system of equations, we prefer to use the magnetic interaction parameter b and radius of the circular orbits r as free parameters. The specific energy $\mathcal{E}$ and the angular momentum l of the magnetized particle are considered as a functions of the radial coordinate and electric charge of RN black hole Q:

$$\mathcal{E}_{\rm min}(r; l, Q) = \frac{l\left[r(r-2M)+Q^2\right]}{r^2\sqrt{Mr-Q^2}}\,. \tag{36}$$

The expression (36) corresponds to the possible values of the specific energy of the magnetized particle at stable circular orbits.

Fig. 2 demonstrates radial dependence of the specific energy of magnetized particles corresponding to circular motion for the different values of electric charge of RN black hole at the fixed value of the specific angular momentum $l = 4M$. One can see from the figure that the energy increases with the increase of the black hole charge due to increase of gravitational potential of the spacetime around RN black hole and inner circular orbit's position shifts towards to the central black hole.

Substituting (36) into (34) one to calculate the minimum value of the magnetic interaction parameter of the magnetic particle for the fixed value of the specific energy as

$$b_{\rm min}(r; l, Q) = \frac{\sqrt{r(r-3M)+2Q^2}}{r\,(Mr-Q^2)\left[r(r-2M)+Q^2\right]} \times\left\{l^2\left(3Mr-2Q^2-r^2\right)+Mr^3-Q^2r^2\right\}. \tag{37}$$

Figure 3 illustrates the radial dependence of the minimal values of magnetic interaction parameter of magnetized particles corresponding to circular orbits at the value of the specific angular momentum $l = 2\sqrt{5}M$ for different values of electric charge of RN black hole.

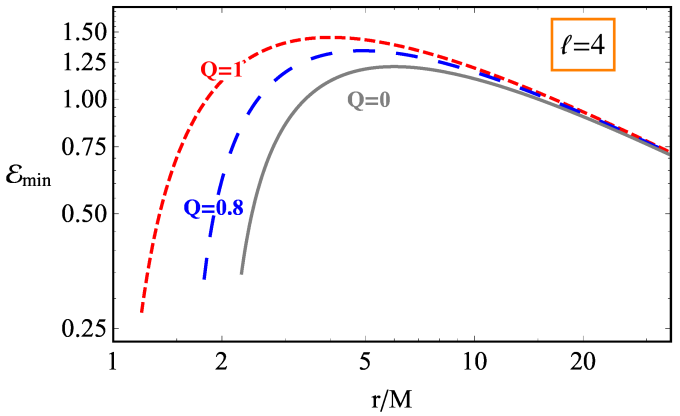

Figure 2. Radial profile of minimal energy of the magnetized particle for the different values of electric charge of RN black hole. Read the specific angular momentum and electric charge of RN black hole as $l \to l/M$ and $Q \to Q/M$, respectively.

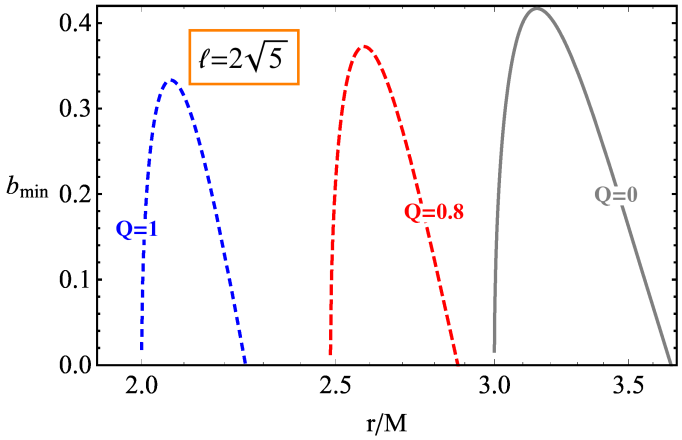

Figure 3. Radial profile of minimal value of magnetic interaction parameter b of magnetized particles with the specific angular momentum $l/M = 2\sqrt{5}$ for the different values of electric charge of RN black black hole. Units of the black hole charge and specific angular momentum are given in the unit of mass M

One can see that the maximal values of minimum interaction parameter decreases with the increase of electric charge of the black hole and the circular orbits corresponding to the fixed specific angular momentum shifts towards the black hole at the center of the orbits.

Let us consider the maximum value for the angular momentum that the particle can be in stable circular orbits which can be found using condition $\partial b_{\min}/\partial r = 0$ as:

$$l_{\min}(r;Q) = \frac{r\left(Q^2 - Mr\right)}{\sqrt{\left[r(r-3M)+2Q^2\right]\left[r(2r-3M)+Q^2\right]}}. \tag{38}$$

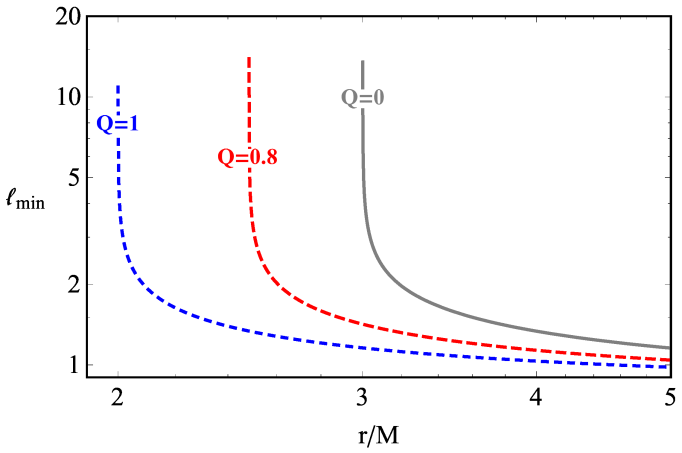

Figure 4. Radial profiles of minimum specific angular momentum of magnetized particles corresponding to stable circular orbits around charged RN black hole for the different values of electric charge of the black hole. Here the unit of the specific angular momentum and the black hole charge are given the unit of mass M.

Figure 4 shows radial dependence of minimum specific angular momentum for stable circular orbits of magnetized particles around RN black hole for the different values of the electric charge of the black hole. One can see that the value of minimum specific angular momentum is increased with increasing electric charge of RN black hole and the position where the angular momentum is maximum also shifts towards central black hole.

The extreme value of the magnetic interaction parameter b can be found by inserting equation (38) into the equation (37) in the following form

$$b_{\text{extr}}(r;Q) = \frac{2r\sqrt{r(r-3M)+2Q^2}}{r(2r-3M)+Q^2}\,. \tag{39}$$

Figure 5 demonstrates radial dependence of minimum magnetic interaction parameter for freely falling magnetized particles and extreme values of the interaction parameter corresponding to stable circular orbits of magnetized particles around RN black hole for the different values of electric charge of RN black hole. The colored area shows possible value of magnetic interaction parameter corresponding to the area where stable circular orbits are allowed. Dashed lines correspond to the minimum values of the b parameter at $l = 0$ and solid ones correspond to the extreme value of the parameter b. Gray, light-blue and

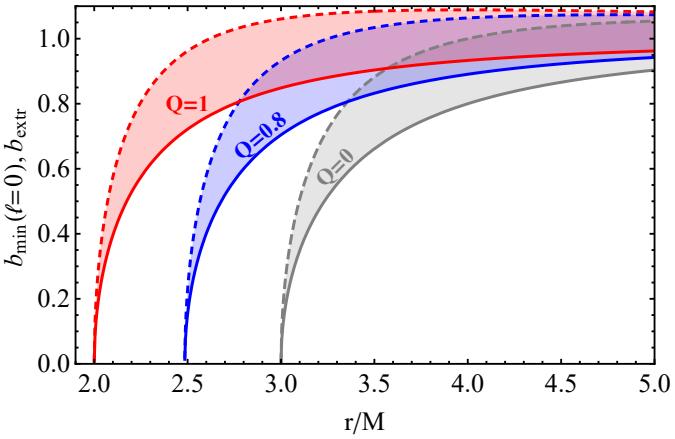

Figure 5. The radial profiles of minimal value of magnetic interaction parameter of free falling magnetized particles and extreme values of the interaction parameter are shown for the different values of electric charge of RN black hole. Unit of the electric charge is given in mass M.

light-red colored areas correspond to the values of electric charge of the black hole $Q = 0$, $Q/M = 0.8$ and $Q/M = 1$, respectively. One can see from the Fig. 5 that the inner position of circular orbits shifts to the center of black hole.

Thus, the extreme value of the parameter b corresponds to maximum value of the critical stable circular orbits $r_{\rm max}$ and it can be found through the solution of the following equation with respect to r

$$b_{\rm ext}(r; Q) = b \, . \tag{40}$$

The minimum value for the circular stable orbits can be found solving the following equation with respect to r,

$$b_{\rm min}(r; Q)|_{l=0} = b \, . \tag{41}$$

The distance between maximum and minimum radius of circular stable orbits $\Delta r = r_{\rm max} - r_{\rm min}$ give us the allowed area of the stable orbits for a magnetized particle. That means the circular stable orbits of a magnetized particle with the given interaction parameter b are confined in the range $r_{\rm max}(b; Q) > r > r_{\rm min}(b; Q)$. However, one can see from the equations (37) and (39) it is quite complicated to obtain the analytic solutions of equations (40) and (41). We solve the equation numerically and present the results in a table form.

The area of stable circular orbits of magnetized particles for the different values of electric charge of RN black hole is presented in Table 1 corresponding to the angular moment from 0 to $l_{\rm min}$. One can see from the table that the area is more dependent from interaction parameter than from electric charge of RN black hole.

One may express the dependence of minimum values of the specific angular momentum on magnetic coupling parameter β solving by the equation $b = b_{\rm min}$ with respect to the

Q/M	$b = 0.1$	$b = 0.5$	$b = 0.8$	$b = 0.95$	$b = 1$
0.1	0.004195	0.1346	0.6517	8.18971	–
0.3	0.004119	0.1322	0.640777	8.0494	–
0.5	0.003961	0.1273	0.61802	7.7598	–
0.8	0.003536	0.1139	0.5575	6.9981	–
1	0.003155	0.1023	0.50436	6.2388	–

Table 1. $\Delta r = r_{\max} - r_{\min}$ as function of the magnetic interaction parameter b and electric charge of RN black hole. The values of the range Δr are given in the units of $1.5(M/M_{\odot})$ km.

specific angular momentum l

$$l^2_{\min}(r; b, Q) = \frac{r\left(Q^2 - Mr\right)}{\left[r(r-3M) + 2Q^2\right]^{3/2}} \times \left\{b\left(r(r-2M) + Q^2\right) - r\sqrt{r(r-3M) + 2Q^2}\right\}. \tag{42}$$

Now one can easily get the dependence of the minimum value of specific energy inserting Eq. (42) into Eq. (36):

$$\mathcal{E}^2_{\min}(r; b, Q) = \frac{\sqrt{Mr - Q^2}\left[r(r-2M) + Q^2\right]}{r\left[r(r-3M) + 2Q^2\right]^{3/2}} \times \left\{r\sqrt{r(r-3M) + 2Q^2} - b\left[r(r-2M) + Q^2\right]\right\}. \tag{43}$$

3 CONCLUSION

In this paper, we have explored the dynamics of magnetized particles in the vicinity of an electrically charged RN black hole immersed in an external asymptotically uniform magnetic field using the Hamilton-Jacobi equation.

In the case of an electrically charged RN black hole due to the absence of interaction between the electric charge of the black hole and dipole moment of magnetized particles, we have assumed that the black hole is immersed in an external asymptotically uniform magnetic field. We have shown that the value of the magnetic coupling parameter for circular orbits and the energy which the magnetic coupling parameter minimum increase as the increase of the charge of RN black hole, while the minimum value of the parameter b decreases.

The range, where stable orbits are allowed, for the magnetized particle with the value $b_{extr} < 1$, narrows for the bigger values of the black hole charge and it becomes wider for the particle with the larger magnetic coupling parameter. When the magnetic coupling parameter of the particle is bigger than 1, the stable orbits do not exist around a black hole in the external magnetic field. The result of the study may be helpful for the estimations of the upper limits of the external magnetic field value around the black hole in the considerations of pulsars (neutron stars) as (dipolar) magnetized particles orbiting around the central supermassive black hole.

ACKNOWLEDGEMENTS

This research is supported by Grants No. VA-FA-F-2-008, No.MRB-AN-2019-29 of the Uzbekistan Ministry for Innovative Development.

REFERENCES

Abdujabbarov, A., Ahmedov, B., Rahimov, O. and Salikhbaev, U. (2014), Magnetized particle motion and acceleration around a Schwarzschild black hole in a magnetic field, *Physica Scripta*, **89**(8), 084008.

Abdujabbarov, A., Rayimbaev, J., Turimov, B. and Atamurotov, F. (2020), Dynamics of magnetized particles around 4-D Einstein Gauss-Bonnet black hole, *Physics of the Dark Universe*, **30**, 100715.

Aliev, A. N. and Gal'tsov, D. V. (1989), REVIEWS OF TOPICAL PROBLEMS: "Magnetized" black holes, *Soviet Physics Uspekhi*, **32**, pp. 75–92.

Aliev, A. N., Galtsov, D. V. and Petukhov, V. I. (1986), Negative absorption near a magnetized black hole - Black hole masers, *Astrophys. Space Sci.*, **124**, pp. 137–157.

Aliev, A. N. and Özdemir, N. (2002), Motion of charged particles around a rotating black hole in a magnetic field, *Mon. Not. R. Astron. Soc.*, **336**, pp. 241–248, arXiv: gr-qc/0208025.

Benavides-Gallego, C. A., Abdujabbarov, A., Malafarina, D., Ahmedov, B. and Bambi, C. (2019), Charged particle motion and electromagnetic field in γ spacetime, *Phys. Rev. D*, **99**, p. 044012, arXiv: 1812.04846.

Chen, S., Wang, M. and Jing, J. (2016), Chaotic motion of particles in the accelerating and rotating black holes spacetime, *Journal of High Energy Physics*, **2016**(9), 82, arXiv: 1604.02785.

Dalui, S., Majhi, B. R. and Mishra, P. (2019), Presence of horizon makes particle motion chaotic, *Physics Letters B*, **788**, pp. 486–493, arXiv: 1803.06527.

de Felice, F. and Sorge, F. (2003), Magnetized orbits around a Schwarzschild black hole, *Classical and Quantum Gravity*, **20**, pp. 469–481.

de Felice, F., Sorge, F. and Zilio, S. (2004), Magnetized orbits around a Kerr black hole, *Classical and Quantum Gravity*, **21**, pp. 961–973.

de Moura, A. P. S. and Letelier, P. S. (2000), Chaos and fractals in geodesic motions around a nonrotating black hole with halos, *Phys. Rev. E*, **61**(6), pp. 6506–6516, arXiv: chao-dyn/9910035.

Han, W. (2008), Chaos and dynamics of spinning particles in Kerr spacetime, *General Relativity and Gravitation*, **40**(9), pp. 1831–1847, arXiv: 1006.2229.

Hashimoto, K. and Tanahashi, N. (2017), Universality in chaos of particle motion near black hole horizon, *Phys. rev. D*, **95**(2), 024007, arXiv: 1610.06070.

Haydarov, K., Abdujabbarov, A., Rayimbaev, J. and Ahmedov, B. (2020), Magnetized particle motion around black holes in conformal gravity: Can magnetic interaction mimic spin of black holes?, *Universe*, **6**(3), ISSN 2218-1997, URL https://www.mdpi.com/2218-1997/6/3/44.

Haydarov, K., Rayimbaev, J., Abdujabbarov, A., Palvanov, S. and Begmatova, D. (2020), Magnetized particle motion around magnetized Schwarzschild-MOG black hole, *European Physical Journal C*, **80**(5), 399, arXiv: 2004.14868.

Misner, C. W., Thorne, K. S. and Wheeler, J. A. (1973), *Gravitation*, W. H. Freeman, San Francisco.

Mori, K., Gotthelf, E. V., Zhang, S., An, H., Baganoff, F. K., Barrière, N. M., Beloborodov, A. M., Boggs, S. E., Christensen, F. E., Craig, W. W., Dufour, F., Grefenstette, B. W., Hailey, C. J., Harrison, F. A., Hong, J., Kaspi, V. M., Kennea, J. A., Madsen, K. K., Markwardt, C. B., Nynka, M., Stern, D., Tomsick, J. A. and Zhang, W. W. (2013), NuSTAR Discovery of a 3.76 s Transient Magnetar Near Sagittarius A*, *The Astronomical Journal Letters*, **770**(2), L23, arXiv: 1305.1945.

Morozova, V. S., Rezzolla, L. and Ahmedov, B. J. (2014), Nonsingular electrodynamics of a rotating black hole moving in an asymptotically uniform magnetic test field, *Phys. Rev. D*, **89**(10), 104030, arXiv: 1310.3575.

Narzilloev, B., Rayimbaev, J., Abdujabbarov, A. and Bambi, C. (2020), Charged particle motion around non-singular black holes in conformal gravity in the presence of external magnetic field, *arXiv e-prints*, arXiv:2005.04752, arXiv: 2005.04752.

Nordström, G. (1918), On the Energy of the Gravitation field in Einstein's Theory, *Koninklijke Nederlandse Akademie van Wetenschappen Proceedings Series B Physical Sciences*, **20**, pp. 1238–1245.

Piotrovich, M. Y., Silant'ev, N. A., Gnedin, Y. N. and Natsvlishvili, T. M. (2011), Magnetic fields and quasi-periodic oscillations of black hole radiation, *Astrophysical Bulletin*, **66**, pp. 320–324.

Rahimov, O. G. (2011), Magnetized Particle Motion around Black Hole in Braneworld, *Modern Physics Letters A*, **26**, pp. 399–408, arXiv: 1012.1481.

Rahimov, O. G., Abdujabbarov, A. A. and Ahmedov, B. J. (2011), Magnetized particle capture cross section for braneworld black hole, *Astrophysics and Space Science*, **335**(2), pp. 499–504, arXiv: 1105.4543.

Rayimbaev, J., Abdujabbarov, A., Jamil, M., Ahmedov, B. and Han, W.-B. (2020), Dynamics of test particles around renormalization group improved schwarzschild black holes, *Phys. Rev. D*, **102**, p. 084016, URL https://link.aps.org/doi/10.1103/PhysRevD.102.084016.

Rayimbaev, J. and Tadjimuratov, P. (2020), Can modified gravity silence radio-loud pulsars?, *Physical Review D*, **102**(2), 024019.

Rayimbaev, J., Turimov, B. and Ahmedov, B. (2019a), Braneworld effects in plasma magnetosphere of a slowly rotating magnetized neutron star, *International Journal of Modern Physics D*, **28**(10), 1950128-209.

Rayimbaev, J., Turimov, B., Marcos, F., Palvanov, S. and Rakhmatov, A. (2020), Particle acceleration and electromagnetic field of deformed neutron stars, *Modern Physics Letters A*, **35**(9), 2050056.

Rayimbaev, J., Turimov, B. and Palvanov, S. (2019b), Plasma magnetosphere of slowly rotating magnetized neutron star in branewold, in *International Journal of Modern Physics Conference Series*, volume 49 of *International Journal of Modern Physics Conference Series*, pp. 1960019–209.

Rayimbaev, J. R. (2016), Magnetized particle motion around non-Schwarzschild black hole immersed in an external uniform magnetic field, *Astrophys Space Sc*, **361**, 288.

Rayimbaev, J. R., Ahmedov, B. J., Juraeva, N. B. and Rakhmatov, A. S. (2015), Plasma magnetosphere of deformed magnetized neutron star, *Astrophys Space Sc*, **356**, pp. 301–308.

Reissner, H. (1916), Über die Eigengravitation des elektrischen Feldes nach der Einsteinschen Theorie, *Annalen der Physik*, **355**(9), pp. 106–120.

Rezzolla, L. and Zanotti, O. (2001), An improved exact riemann solver for relativistic hydrodynamics, *Journ. of Fluid Mech.*, **449**, p. 395.

Stuchlík, Z. and Kološ, M. (2016), Acceleration of the charged particles due to chaotic scattering in the combined black hole gravitational field and asymptotically uniform magnetic field, *European Physical Journal C*, **76**, 32, arXiv: 1511.02936.

Stuchlík, Z., Schee, J. and Abdujabbarov, A. (2014), Ultra-high-energy collisions of particles in the field of near-extreme Kehagias-Sfetsos naked singularities and their appearance to distant observers, *Phys. Rev. D*, **89**(10), 104048.

Toshmatov, B., Abdujabbarov, A., Ahmedov, B. and Stuchlík, Z. (2015), Motion and high energy collision of magnetized particles around a Hořava-Lifshitz black hole, *Astrophys Space Sci*, **360**, 19.

Vrba, J., Abdujabbarov, A., Kološ, M., Ahmedov, B., Stuchlík, Z. and Rayimbaev, J. (2020), Charged and magnetized particles motion in the field of generic singular black holes governed by general relativity coupled to nonlinear electrodynamics, *Phys.Rev.D*, **101**(12), 124039.

Wald, R. M. (1974), Black hole in a uniform magnetic field, *Phys. Rev. D.*, **10**, pp. 1680–1685.

Proceedings of *RAGtime 20–22, 15–19 Oct., 16–20 Sept., 19–23 Oct., 2018/2019/2020, Opava, Czech Republic*
Z. Stuchlík, G. Török and V. Karas, editors, Silesian University in Opava, 2020, pp. 277–286

Exact solutions of Einstein field equations

Sanjar Shaymatov,[1,2,3,4,a] Bobomurat Ahmedov,[1,2,3,b]
Ashfaque Bokhari[5,c] and Yuri Vyblyi[6,d]

[1]Ulugh Beg Astronomical Institute, Astronomy St. 33, Tashkent 100052, Uzbekistan,
[2]National University of Uzbekistan, Tashkent 100174, Uzbekistan
[3]Tashkent Institute of Irrigation and Agricultural Mechanization Engineers,
Kori Niyozi 39, Tashkent 100000, Uzbekistan
[4]Institute for Theoretical Physics and Cosmology, Zheijiang University of Technology,
Hangzhou 310023, China
[5]Department of Mathematics and Statistics, King Fahd University of Petroleum
and Minerals, Dhahran 31261, Saudi Arabia
[6]B. I. Stepanov Institute of Physics, National Academy of Sciences of Belarus, Minsk, Belarus
[a]sanjar@astrin.uz
[b]ahmedov@astrin.uz
[c]abokhari@kfupm.edu.sa
[d]vyblyi@gmail.com

ABSTRACT
We study the general form of spacetime metric representing gravitating axially symmetric compact objects. The properties, such as energy momentum tensor and interior and exterior geometry, of such objects are discussed. Due to the complex nature of gravitational field equations, especially interior of axial symmetric objects, we consider exact solutions of the special case of spherical symmetry object.

Keywords: Einstein field equations – exact solutions

1 INTRODUCTION

Recently discovered dark matter and dark energy in the universe has lead to construction of various modified theories of gravity as being alternate to the Einstein general theory of Relativity. These extended theories of gravity are likely to provide new exact solutions for (GR) the gravitational objects and from this point of view it is becoming extremely important to parametrize solutions of gravitational field equations. Most popular among them is Johannsen and Psaltis parametrization (Johannsen and Psaltis, 2011) and in recent years there were several attempts in this direction (see for example (Rezzolla and Zhidenko, 2014; Konoplya et al., 2016)). Following the parameterization of Rezzolla and Zhidenko (Rezzolla and Zhidenko, 2014), recently, the general parametrization for spherically symmetric and asymptotically flat black-hole spacetimes has been developed in an arbitrary metric theory of gravity (Konoplya et al., 2020). The exact axisymmetric and static solution of the Einstein equations coupled to the axisymmetric and static gravitating scalar field

978-80-7510-432-8

has also been investigated recently (Turimov et al., 2018). Later on, an anisotropic version of the well-known Tolman VII solution has been presented as stated by the gravitational decoupling by the minimal geometric deformation approach and this leads to determine an exact and physically acceptable interior two-fluid solution representing behavior of compact objects (Hensh and Stuchlík, 2019). There is also investigation that presents an exact solution describing the Schwarzschild-like black hole surrounded by the dust cosmological background for spherically symmetric dust distribution (Jaluvkova et al., 2017).

In this context, our interest in this paper is to write and discuss general expression for the axial spactime metric which could be valid for different theories of gravity. We study the general of the spactime metric of axially symmetric gravitational compact objects and test whether it is possible to have interior solution leading to the formation of naked singularity.

The first major work on study of singularities in GR dates back to 1965 when Penrose presented his seminal work on singularity theorems (Penrose, 1965). This theorem, which was later called the Penrose-Hawking singularity theorem, implies that the occurrence of singularities in GR is inevitable as long as matter obeys certain energy conditions. The super-dense regions of matter arising from gravitational collapse could be hidden from the outside observer giving rise to a black hole or it could be visible leading to a naked singularity (Hawking and Ellis, 1973). Penrose-Hawking theorem investigated the conditions that give rise to the emergence of singularities in GR (Hawking and Penrose, 1970). The presence of these singularities represent a breakdown of Einstein's theory as they give rise to the notion of geodesic incompleteness. Although the Penrose-Hawking theorem proved the existence of singularities, it did not shed light on the nature of the singularities arising in General Relativity as the theory allows both types of singularity to form in a scenario of gravitational collapse depending on the initial data from which the collapse develops. In fact, the occurrence of naked singularities in nature has been so far considered the limit of Einstein's theory and poses serious theoretical challenges as it indicates the breakdown of predictability in physics. This in turn led to the formulation of the cosmic censorship hypothesis proposed by Penrose (Penrose, 1969) in 1969 for validity of the Einstein gravity, preventing the singularity from being seen for observers outside. Irrespective of the fact that the cosmic censorship conjecture has not been proven yet, there have been, however, a large amount of work done in this context (see, e.g. Jacobson and Sotiriou, 2010; Saa and Santarelli, 2011; Li and Bambi, 2013; Düztaş et al., 2020; Barausse et al., 2010; Rocha and Cardoso, 2011; Shaymatov et al., 2015; Sorce and Wald, 2017; Shaymatov et al., 2019, 2020b; Gwak, 2018; Shaymatov et al., 2020a; Jiang and Zhang, 2020; Yang et al., 2020).

2 AXIALLY SYMMETRIC GRAVITATIONAL COMPACT OBJECTS

The axial symmetry, e.g., rotation of the central gravitational object, makes the gravitational field equations very complicated to obtain their exact solutions. In fact, the well-known Kerr (Kerr, 1963), Carter (Carter, 1968) and the Kerr-de Sitter (Carter, 1973) spacetime metrics have been known as external vacuum solutions, and they refer to partial solutions and correspond to a special kind of gravitational source. These solutions are associated with the gravitational field of a rotating uncharged or charged black hole, respectively (Carter, 1971). However, the exact interior solutions of gravitational field equations that can serve

as the basis for any significant physical model of a rotating body have not yet been obtained. Hence, possible non-trivial results related to the interior solution being established even before solving the Einstein equations on the basis of only the equations of motion represent a definite value.

The established nature of pure rotation of the source having only single axis means that the quadratic form has axial symmetry and does not depend on time. Therefore, there is a frame of reference in which coordinates x^0, r, θ, and φ can be entered, thereby reflecting the time and axial symmetry of the metric in an explicit form. Having assumed precisely this nature of the coordinates and the frame of reference, in the general case, both in the inner and outer regions, the quadratic form for line element can be given as follows (Arifov, 1983):

$$\mathrm{d}s^2 = -(\mathrm{d}x^0)^2 + D(\mathrm{d}x^0 + E\sin^2\theta\mathrm{d}\phi)^2 + F\mathrm{d}r^2 + G\mathrm{d}\theta^2 + H\sin^2\theta\mathrm{d}\phi^2, \tag{1}$$

where D, E, F, G, and H are unknown functions depending only from r and θ coordinates.

The rotating black hole metric in Boyer-Lindquist coordinates, in particular, can be reduced to the following form

$$\mathrm{d}s^2 = -(\mathrm{d}x^0)^2 + \frac{\chi r}{r^2 + a^2\cos^2\theta}\left(\mathrm{d}x^0 + a\sin^2\theta\mathrm{d}\phi\right)^2 + \frac{r^2 + a^2\cos^2\theta}{r^2 - \chi r + a^2}\mathrm{d}r^2 + \left(r^2 + a^2\cos^2\theta\right)\mathrm{d}\theta^2 + \left(r^2 + a^2\right)\sin^2\theta\mathrm{d}\phi^2\,, \tag{2}$$

with χ being a constant having same meaning as in the Schwarzschild solution, with constant a is related to the total angular momentum of the rotating massive body.

At this stage we write the non-zero components of the metric tensor corresponding to the form (1) as

$$g_{00} = -(1 - D)\,,\ g_{03} = DE\sin^2\theta\,,\ g_{11} = F\,,\ g_{22} = G\,,$$
$$g_{33} = \left(DE^2\sin^2\theta + H\right)\sin^2\theta\,, \tag{3}$$

and non-zero inverse components are

$$g^{00} = -\frac{1}{N}\left(DE^2\sin^2\theta + H\right)\,,\ g^{03} = \frac{1}{N}DE\,,\ g^{11} = \frac{1}{F}\,,\ g^{22} = \frac{1}{G}\,,$$
$$g^{33} = \frac{1}{N\sin^2\theta}(1 - D)\sin^{\theta}\,,\ g = -NGF\sin^2\theta\,, \tag{4}$$

with $N = DE^2\sin^2\theta + H(1 - D)$.

It is worth noting that the axial symmetry of the spacetime metric (1) allows its simplification. Using two arbitrary coordinate transformation functions

$$r \to r' = r'(r,\theta)\,,\quad \text{and}\quad \theta \to \theta' = \theta'(r,\theta)\,, \tag{5}$$

one of the functions D, E, F, G and H, or any combination of them can be reduced to a predetermined function, while maintaining the orthogonality of the transformed r' and θ'

axes, namely the equality of the component g'^{12}. Further simplification is no longer possible. In the general case, the symmetry of the problem requires finding four independent functions included in the metric (1) and depending on two arguments.

If we introduce the notation for the derivatives

$$X' = \frac{\partial X}{dr} \quad \text{and} \quad \dot{X} = \frac{\partial X}{d\theta}\,, \tag{6}$$

the non-zero components of the Christoffel symbols take the form:

$$\begin{aligned}
&\Gamma^0_{01} = \frac{1}{2N}\left(D^2EE'\sin^2\theta - HD'\right), \Gamma^1_{00} = -\frac{D'}{2F}\,,\\
&\Gamma^0_{02} = \frac{1}{2N}\left[\left(\dot{E}\sin\theta + 2E\cos\theta\right)D^2E\sin\theta - H\dot{D}\right], \Gamma^2_{00} = -\frac{\dot{D}}{2G}\,,\\
&\Gamma^0_{13} = \frac{\sin^2\theta}{2N}\left[D^2E^2D'\sin^{\theta} + DEH' - H\,(DE)'\right],\\
&\Gamma^0_{23} = \frac{\sin^2\theta}{2N}\left[\left(\dot{E}\sin^{\theta} + 2E\cos\theta\right)D^2E^2\sin\theta + DE\dot{H} - H\left(\dot{DE}\right)\right],\\
&\Gamma^1_{03} = -\frac{\sin^2\theta}{2F}\,(DE)', \Gamma^2_{03} = -\frac{\sin\theta}{2G}\left[\left(\dot{DE}\right)\sin\theta + 2DE\cos\theta\right],\\
&\Gamma^3_{01} = -\frac{1}{2N}\left[(DE)' - D^2E'\right], \Gamma^1_{11} = \frac{F'}{2F}\,, \Gamma^1_{12} = \frac{\dot{F}}{2F}\,,\\
&\Gamma^3_{02} = \frac{1}{2N}\left[\left(\dot{DE}\right) - D^2\dot{E} + 2\,(1-D)\,DE\cot\theta\right], \Gamma^1_{22} = -\frac{G'}{2F}\,,\\
&\Gamma^1_{33} = -\frac{\sin^2\theta}{2F}\left[\left(DE^2\right)'\sin^2\theta + H'\right], \Gamma^2_{11} = -\frac{\dot{F}}{2G}\,, \Gamma^2_{22} = \frac{\dot{G}}{2G}\,, \Gamma^2_{12} = \frac{G'}{2G}\,.
\end{aligned} \tag{7}$$

A frame of reference, in which the quadratic form for a rotating body can be reduced to the one in (1), is characterized by a complex motion of its components. Their absolute acceleration, $w_\mu = u_{\mu;\nu}u^\nu$ (where u^μ is the 4-velocity), is given by

$$w_0 = w_3 = 0\,,\ w_1 = -\frac{D'}{2\,(1-D)} \quad \text{and } w_2 = -\frac{\dot{D}}{2\,(1-D)}\,, \tag{8}$$

which are everywhere orthogonal to the family of hypersurfaces $D = const$. The non-zero components of the rotation tensor, $\mathbf{A} = \frac{1}{2}\left(u_{\mu,\nu} - u_{\nu,\mu} + u_\mu w_\nu - u_\nu w_{mu}\right)$, take the forms:

$$\begin{aligned}
&\mathbf{A}_{oi} = \mathbf{A}_{12} = 0\,,\ \mathbf{A}_{13} = \frac{1}{2}\frac{(DE)' - D^2E'}{(1-D)^{3/2}}\sin^2\theta\,,\\
&\mathbf{A}_{23} = \frac{1}{2}\frac{\left(\dot{DE}\right) - D^2\dot{E}}{(1-D)^{3/2}}\sin^2\theta + \frac{DE}{\sqrt{1-D}}\sin\theta\cos\theta\,.
\end{aligned} \tag{9}$$

The family of hypersurfaces being everywhere orthogonal to the direction of rotation components of the reference frame satisfies the following equation:

$$\frac{dr}{d\theta} = \frac{\mathbf{A}_{13}G}{\mathbf{A}_{23}F}\,. \tag{10}$$

For Kerr metric, in particular, the solutions of this equation belongs to the family

$$r^2 + a\cos\theta\,(a\cos\theta - const) = 0\,,\ \theta \neq \frac{\pi}{2}\,, \tag{11}$$

with equatorial hypersurface $\theta = \pi/2$.

Let the internal state of the source be described by the energy-momentum tensor $T^{\mu\nu} = (\rho + p)\,u^\mu u^\nu + pg^{\mu\nu}$ of an ideal fluid, the pressure and energy density. In the coordinates given in (1), we have the 4-velocity components u^1 and u^2 of the source being equal to zero, and if we introduce the following notation

$$\frac{\mathrm{d}\phi}{\mathrm{d}x^0} = \omega(r,\theta)\,, \tag{12}$$

then non-zero component becomes

$$u^3 = \frac{\mathrm{d}\phi}{\mathrm{d}\sigma} = \omega u^0\,, \tag{13}$$

where σ refers to the source's proper time.
From the above 4-velocity components $u^\mu\{u^0, 0, 0, \omega u^0\}$ and $u_\mu\{u_0, 0, 0, u_3\}$ respectively read

$$u^0 = \sqrt{1 - D\left(1 + \omega E\sin^2\theta\right)^2 - \omega^2 H\sin^2\theta}\,, \tag{14}$$

and

$$\begin{aligned} u_0 &= -\frac{1 - D\left(1 + \omega E\sin^2\theta\right)}{\sqrt{1 - D\left(1 + \omega E\sin^2\theta\right)^2 - \omega^2 H\sin^2\theta}}\,,\\ u_3 &= -\frac{DE\sin^2\theta\left(1 + \omega E\sin^2\theta\right) + \omega H\sin^2\theta}{\sqrt{1 - D\left(1 + \omega E\sin^2\theta\right)^2 - \omega^2 H\sin^2\theta}}\,. \end{aligned} \tag{15}$$

The internal state of the source is determined by three functions ρ, p and ω as a function of r and θ, and two of them are independent, i.e. ρ (or p) and ω. From all type of axial rotation bodies, solid-body rotation must be distinguished in the case in which $a = const$. In this case and in its own reference frame, both conditions imposed on the quadratic form, namely, stationarity and axial symmetry, can be expressed explicitly. Indeed, the transition $\phi \to \phi + \omega x^0$ to its own reference frame, in which $u^3 = 0$, does not change the quadratic forms (1). This is due to the fact that the relative distances between elements of a source rotating as a solid body remain unchanged. If the rotation of the gravitating object maintaining axial symmetry does not obey the solid angle law, then in its own frame of reference the metric can preserve axial symmetry in an explicit form, but can lose the explicit expression of the stationarity property. The metric already depends on time in its own frame of reference. The change in the relative distances between the elements of the source at constant coordinates assumes the metric tensor in its own reference frame. Equations (14) and

(15) retain their form for solid body rotation and in own reference frame if one formally sets $\omega = 0$.

At this stage we find out what restrictions are imposed by the equations of motion, $T^{\mu\nu}{}_{;\nu} = 0$, on the internal functions ρ, p and ω of the rotating body. Two of the four equations of motion corresponding to the coordinates x^0 and φ are satisfied identically. The other two equations are given by:

$$p' = \frac{1}{2}(\rho + p)\frac{D' + 2\omega(DE)'\sin^2\theta + \omega^2\left(DE^2\sin^2\theta + H\right)'\sin^2\theta}{1 - D\left(1 + \omega E\sin^2\theta\right)^2 - \omega^2 H\sin^2\theta}, \tag{16}$$

$$\dot{p} = \frac{1}{2}(\rho + p)\frac{\dot{D} + 2\omega\left(DE\dot{\sin}^2\theta\right) + \omega^2\left[\left(DE^2\sin^2\dot{\theta} + H\right)\sin^2\theta\right]}{1 - D\left(1 + \omega E\sin^2\theta\right)^2 - \omega^2 H\sin^2\theta}. \tag{17}$$

The above equations can be rewritten as follows:

$$\frac{\mathrm{d}p}{\rho + p} = \mathrm{d}Log\left[1 - D\left(1 + \omega E\sin^2\theta\right)^2 - \omega^2 H\sin^{\theta}\right]^{-1/2} - \frac{DE\sin^2\theta\left(1 + \omega E\sin^2\theta\right) + \omega H\sin^2\theta}{1 - D\left(1 + \omega E\sin^2\theta\right)^2 - \omega^2 H\sin^2\theta}d\omega. \tag{18}$$

From above the left side is, according to the thermodynamic equation of state, the total differential function

$$\int\frac{\mathrm{d}p}{\rho + p}, \tag{19}$$

which is solved further for an incompressible ideal fluid and since the first term on the right is also a total differential, the second term on the right can then only be a total differential of some function r and θ in the case of $\omega(r,\theta) \neq const$. This would be possible if and only if the factor in front of $d\omega$ depends on ω and does not explicitly depend on r and θ, i.e.,

$$\frac{DE\sin^2\theta\left(1 + \omega E\sin^2\theta\right) + \omega H\sin^2\theta}{1 - D\left(1 + \omega E\sin^2\theta\right)^2 - \omega^2 H\sin^2\theta} = b(\omega), \tag{20}$$

where $b(\omega)$ is an arbitrary function. The above equation (20) establishes an algebraic relationship between four functions of coordinates r and θ, i.e, ω, $(1 - D)$, $DE\sin^2\theta$ and $\left(DE\sin^2\theta + H\right)\sin^2\theta$. However, in the case of rotation of the gravitating body, there appears no such dependence. The equations of motion are thus given by,

$$\exp\left[\int\frac{\mathrm{d}p}{\rho + p} + \int b(\omega)\mathrm{d}\omega\right] = \frac{const}{\sqrt{1 - D\left(1 + \omega E\sin^2\theta\right)^2 - \omega^2 H\sin^2\theta}}, \tag{21}$$

if $\omega(r,\theta) \neq const$ while

$$\exp\left[\int \frac{\mathrm{d}p}{\rho + p}\right] = \frac{const}{\sqrt{1 - D\left(1 + \omega E \sin^2\theta\right)^2 - \omega^2 H \sin^2\theta}}, \tag{22}$$

if $\omega = const$.

For an incompressible ideal fluid $\rho = const$, for example, the equations of motion are completely integrated by

$$\rho + p = \frac{const}{\sqrt{1 - D\left(1 + \omega E \sin^2\theta\right)^2 - \omega^2 H \sin^2\theta}}. \tag{23}$$

The hypersurface, on which the pressure is constant, is called equipotential. The section of the equipotential hypersurface of the coordinate hyperpsurface $x^0 = const$ obviously refers to the closed surface. Equipotential hypersurfaces form, according to (21-22), a one-parameter family.

Theorem 1

The boundary of an axially rotating body is an equipotential hypersurface, on which the pressure is zero. The shape of the border is determined by

$$\left[1 - D\left(1 + \omega E \sin^2\theta\right)^2 - \omega^2 H \sin^2\theta\right] \exp\left\{-2\int b(\omega) d\omega\right\} = const, \tag{24}$$

if $\omega(r,\theta) \neq const$ while

$$D\left(1 + \omega E \sin^2\theta\right)^2 + \omega^2 H \sin^2\theta = const, \tag{25}$$

in the case of solid body rotation.

A certain correspondence can be established between the distribution functions of pressure and mass density of rotating and non-rotating bodies.

Theorem 2

For each given equation of state of matter of an axially rotating body and given distribution of the angular velocity ω in the quadratic frame of reference (1) there exists such a coordinate grid that the distribution functions of pressure, density of the number of particles, and density of mass-energy coincide with the corresponding functions of a non-rotating body in a quadratic reference frame, and the boundaries of the body are coordinate hypersurfaces $r = const$.

3 CONCLUSIONS

In this work, we have discussed general form of axial symmetric spacetime which could be applied to the possible solutions of field equations in various extended theories of gravity.

We have seen in the above that the general solution of Einstein's equations for a stationary axially symmetric source, the equation of state and the distribution of the angular velocity of rotation of the substance given, and the boundaries being free correspond to two types of the structure of the source. The first type of sources represents only one external solution having free boundary for which pressure and density of mass and number of particles take a maximum value in the center and fall monotonically towards the boundary. Another type of sources has two, internal and external, boundaries at which the pressure is equal to zero; a cavity free from matter and thermal radiation from the source, with a singular time-like world line in the center and the pressure and density of the mass and number of particles take maximum values at the critical hypersurface and fall monotonically towards both boundaries. As a consequence of the analysis we showed that it is possible to have only an external solution associated with rotation parameter and realized that it is however impossible to obtain interior solution in the case of rotation.

ACKNOWLEDGEMENTS

S.S. and B.A. acknowledge the support of Uzbekistan Ministry for Innovative Development Grants No. VA-FA-F-2-008 and No. MRB-AN-2019-29. Y.V. acknowledges the support of State Committee of Science and Technology of the Republic of Belarus, Grant F19UZBG-014. Bobomurat Ahmedov and Ashfaque H. Bokhari at KFUPM would like to acknowledge the support received from KFUPM under University Funded Grant No. SB191039.

REFERENCES

Arifov, L. Y. (1983), *General theory of relativity and gravitation.*

Barausse, E., Cardoso, V. and Khanna, G. (2010), Test Bodies and Naked Singularities: Is the Self-Force the Cosmic Censor?, *Phys. Rev. Lett.*, **105**(26), 261102, arXiv: 1008.5159.

Carter, B. (1968), Global Structure of the Kerr Family of Gravitational Fields, *Physical Review*, **174**(5), pp. 1559–1571.

Carter, B. (1971), Axisymmetric Black Hole Has Only Two Degrees of Freedom, *Physical Review Letters*, **26**(6), pp. 331–333.

Carter, B. (1973), Black hole equilibrium states., in *Black Holes (Les Astres Occlus)*, pp. 57–214.

Düztaş, K., Jamil, M., Shaymatov, S. and Ahmedov, B. (2020), Testing Cosmic Censorship Conjecture for Extremal and Near-extremal (2+1)-dimensional MTZ Black Holes, *Class. Quantum Grav.*, **37**(17), p. 175005, arXiv: 1808.04711.

Gwak, B. (2018), Weak cosmic censorship conjecture in Kerr-(anti-)de Sitter black hole with scalar field, *J. High Energy Phys.*, **09**, 81, arXiv: 1807.10630.

Hawking, S. W. and Ellis, G. F. R. (1973), *The large-scale structure of space-time.*

Hawking, S. W. and Penrose, R. (1970), The Singularities of Gravitational Collapse and Cosmology, *Proc R. Soc. Lond. A*, **314**, pp. 529–548.

Hensh, S. and Stuchlík, Z. (2019), Anisotropic Tolman VII solution by gravitational decoupling, *European Physical Journal C*, **79**(10), 834, arXiv: 1906.08368.

Jacobson, T. and Sotiriou, T. P. (2010), Spinning Black Holes as Particle Accelerators, *Phys. Rev. Lett.*, **104**(2), 021101, arXiv: 0911.3363.

Jaluvkova, P., Kopteva, E. and Stuchlik, Z. (2017), The model of the black hole enclosed in dust: the flat space case, *General Relativity and Gravitation*, **49**(6), 80, arXiv: 1602.01266.

Jiang, J. and Zhang, M. (2020), Weak cosmic censorship conjecture in Einstein-Maxwell gravity with scalar hair, *Eur. Phys. J. C*, **80**(3), 196.

Johannsen, T. and Psaltis, D. (2011), Metric for rapidly spinning black holes suitable for strong-field tests of the no-hair theorem, *Phys. Rev. D*, **83**(12), 124015, arXiv: 1105.3191.

Kerr, R. P. (1963), Gravitational Field of a Spinning Mass as an Example of Algebraically Special Metrics, *Physical Review Letters*, **11**(5), pp. 237–238.

Konoplya, R., Rezzolla, L. and Zhidenko, A. (2016), General parametrization of axisymmetric black holes in metric theories of gravity, *Phys. Rev. D*, **93**(6), 064015, arXiv: 1602.02378.

Konoplya, R. A., Pappas, T. D. and Stuchlík, Z. (2020), General parametrization of higher-dimensional black holes and its application to Einstein-Lovelock theory, *Phys. Rev. D*, **102**(8), 084043, arXiv: 2007.14860.

Li, Z. and Bambi, C. (2013), Destroying the event horizon of regular black holes, *Phys. Rev. D*, **87**(12), 124022, arXiv: 1304.6592.

Penrose, R. (1965), Gravitational Collapse and Space-Time Singularities, *Physical Review Letters*, **14**(3), pp. 57–59.

Penrose, R. (1969), Gravitational Collapse: the Role of General Relativity, *Riv. Nuovo Cimento*, **1**, 252.

Rezzolla, L. and Zhidenko, A. (2014), New parametrization for spherically symmetric black holes in metric theories of gravity, *Phys. Rev. D*, **90**(8), 084009, arXiv: 1407.3086.

Rocha, J. V. and Cardoso, V. (2011), Gravitational perturbation of the BTZ black hole induced by test particles and weak cosmic censorship in AdS spacetime, *Phys. Rev. D*, **83**(10), 104037, arXiv: 1102.4352.

Saa, A. and Santarelli, R. (2011), Destroying a near-extremal Kerr-Newman black hole, *Phys. Rev.*

D, **84**(2), 027501, arXiv: 1105.3950.

Shaymatov, S., Dadhich, N. and Ahmedov, B. (2019), The higher dimensional Myers-Perry black hole with single rotation always obeys the Cosmic Censorship Conjecture, *Eur. Phys. J. C*, **79**(7), p. 585, arXiv: 1809.10457, URL https://doi.org/10.1140/epjc/s10052-019-7088-6.

Shaymatov, S., Dadhich, N. and Ahmedov, B. (2020a), Six-dimensional Myers-Perry rotating black hole cannot be overspun, *Phys. Rev. D*, **101**(4), 044028, arXiv: 1908.07799.

Shaymatov, S., Dadhich, N., Ahmedov, B. and Jamil, M. (2020b), Five-dimensional charged rotating minimally gauged supergravity black hole cannot be over-spun and/or over-charged in non-linear accretion, *Eur. Phys. J. C*, **80**(5), 481, arXiv: 1908.01195.

Shaymatov, S., Patil, M., Ahmedov, B. and Joshi, P. S. (2015), Destroying a near-extremal Kerr black hole with a charged particle: Can a test magnetic field serve as a cosmic censor?, *Phys. Rev. D*, **91**(6), 064025, arXiv: 1409.3018.

Sorce, J. and Wald, R. M. (2017), Gedanken experiments to destroy a black hole. II. Kerr-Newman black holes cannot be overcharged or overspun, *Phys. Rev. D*, **96**(10), 104014, arXiv: 1707.05862.

Turimov, B., Ahmedov, B., Kološ, M. and Stuchlík, Z. (2018), Axially symmetric and static solutions of Einstein equations with self-gravitating scalar field, *Phys. Rev. D*, **98**(8), 084039, arXiv: 1810.01460.

Yang, S.-J., Chen, J., Wan, J.-J., Wei, S.-W. and Liu, Y.-X. (2020), Weak cosmic censorship conjecture for a Kerr-Taub-NUT black hole with a test scalar field and particle, *Phys. Rev. D*, **101**(6), 064048, arXiv: 2001.03106.

Proceedings of *RAGtime 20–22, 15–19 Oct., 16–20 Sept., 19–23 Oct., 2018/2019/2020, Opava, Czech Republic*
Z. Stuchlík, G. Török and V. Karas, editors, Silesian University in Opava, 2020, pp. 287–297

From gappy to ringed: signatures of an accretion disk radial structure in profiles of the reflection line

Marcel Štolc,[1a] Michal Zajaček[2] and Vladimír Karas[1]

[1]Astronomical Institute of the Czech Academy of Sciences,
Boční II 1401, CZ-14100 Prague, Czech Republic
[2]Center for Theoretical Physics, Polish Academy of Sciences,
Al. Lotników 32/46, 02-668 Warsaw, Poland
[a]stolcml@gmail.com

ABSTRACT
The standard scenario of a geometrically thin, planar accretion disk can be violated by a number of effects that must operate in astrophysically more realistic schemes. Even within a highly simplified framework of an axially symmetric (2D), steady, Keplerian accretion, the radial structure can be different from the predictions of the classical Shakura-Sunyaev theory. In this contribution, we consider stars and stellar-mass black holes that can be embedded within the accretion disk, where they can induce the formation of gaps in the radial density profile. We focus on the theoretical profiles of a spectral line produced by reflection of the surface of both gappy accretion disk and a ring-like structure near a black hole. We describe the relativistic effects in an approximative manner. While a smooth accretion disk leads to a typical, double-horn shape with unequal wings due to Doppler boosting and an additional peak due to the lensing amplification at high inclination angle, the gaps and rings give rise to a more complex dependence which reflects the location and the radial extent of the inhomogeneities in the accretion flow.

Keywords: black holes – accretion disks – radiation

1 INTRODUCTION

Vigorous accretion of matter onto a supermassive black hole is the most essential characteristic of Active Galactic Nuclei (AGN; Peterson, 2009). While astrophysical black holes are described by only two parameters, mass M and angular momentum J (Misner et al., 1973), parameters of the gaseous flow are countless. They can span a very wide range of values depending on the AGN type, which is determined mainly by the surrounding cosmic environment. Especially the accretion rate, $\dot{M}$, and its efficiency, η, are crucial. However, also the geometry of the accretion flow plays an important role. We start our discussion by assuming hydrodynamical accretion structure, where the flow maintains a standard-type, planar, geometrically thin accretion disk (cf. Shakura and Sunyaev, 1973;

978-80-7510-432-8

Page and Thorne, 1974), or a more luminous slim accretion disk (Abramowicz et al., 1988; Narayan and Yi, 1994)) with higher luminosity and non-negligible thickness in the vertical direction. Properties of the system are further defined by the central black hole: the Kerr metric with the outer radius of the event horizon and the spin parameter $a \equiv J/Mc^2$. Also the presence of an outflow or a magnetized jet emanating along the rotation axis will needs to be taken into account in radio loud AGN (see Boettcher et al., 2012 for a review).

We start our discussion by assuming the standard, stationary and axially symmetric accretion flow orbiting at Keplerian velocity in the equatorial plane. The continued accretion maintains a certain level of activity of the system. We neglect the effects of self-gravity of the accretion flow, which might lead to the development of density enhancements ("planets") in some locations, however, we consider the presence of a body which orbits at a certain radius in the plane and represents an embedded star, which had formed within the disk or whose trajectory became inclined into the accretion disk by the preceding orbital evolution (Collin and Zahn, 1999; Karas and Šubr, 2001). Depending on the system parameters, the star may or may not induce a radial gap in the accretion disk.

We assume that the star orbital evolution starts at a larger distance (at the grinding radius, Syer et al., 1991) which is the distance where the orbit is dragged into the disk plane. Then it proceeds gradually down to smaller radii. The time-scale of the process depends on the accretion disk parameters (esp. the accretion rate, $\dot{M}$), parameters of the star (radius $R_\star$, mass $M_\star$), and those of the central black hole. Depending on these parameters the orbital evolution is dominated by losses of orbital energy and orbital angular momentum of the star via density waves, gap formation, or gravitational waves (relevant just very close to BH; see e.g. Ward, 1986; Artymowicz, 1994; Karas and Šubr, 2001; Narayan, 2000) .

Indeed, gaps in gaseous disks are often explained by the presence of embedded bodies - stars and planets. They form due to the action of Lindblad and viscous torques (e.g. Lin and Papaloizou, 1986, and subsequent citations) and they can deepen by consuming the gas (Lubow and D'Angelo, 2006; Rosenthal et al., 2020). Vice versa, as an embedded star proceeds closer to the critical radius, it can act as a source of material for the accretion disk in the moment of its tidal disruption or partial tidal disruption (Hills, 1975; Rees, 1988).

Recent observations hint that the gap formation might be revealed via the sudden transformation of the X-ray properties of AGN (Ricci et al., 2020). These events offer a way to peer into change of the nature of radiative processes such as tidal disruption. Furthermore, Gültekin and Miller (2012) show that the theoretical study of the spectral energy distribution (SED) offers a way of accretion disk structure diagnosis, such as gaps in the inner disk in case of the black hole merger.

A gappy structure of accretion disks may actually be universal during the system evolution. This is, on one hand, related to the structure formation in the Universe, when frequent merger events during the peak of the quasar activity, led to the formation of supermassive black hole binary and triple systems. Before the black hole merger, a formation of a gap or at least a crescent in the disk is natural (Gültekin and Miller, 2012). A second scenario does not even depend on the presence of other bodies around the primary black hole. It is generally believed that accretion flows undergo transitions in basic magneto-hydrodynamic properties – the thin cold disk is located towards the outer parts of the accretion flow, while in the inner parts, hot diluted advection dominated accretion flows (ADAFs) are present (Yuan and Narayan, 2014). The ADAF part can be expanding or contracting, which leads

to the shift of the source position in the X-ray hardness–luminosity diagram ("q-shaped" or "turtle-head" diagram, Fender et al., 2004; Svoboda et al., 2017). The truncation radius where the thin disk transforms into the hot diluted flow shrinks with the increasing accretion rate $\dot{M}$ (Esin et al., 1997; Narayan and McClintock, 2008; Yuan and Narayan, 2014). Given that ADAFs have significantly lower densities than thin cold disks, they could be perceived as evolving "gaps" in the disk.

2 MODEL

Stars can get on bound orbits close to the central supermassive black hole by two dynamical channels (Mapelli and Gualandris, 2016):

(1) *in-situ* formation, where stars form locally in a non-standard way from a denser gas,
(2) *migration* scenario, in which stars form at larger distances and migrate inwards via a fast dynamical process.

Both processes likely contributed to the build-up of the nuclear star cluster at the center of the Milky Way, which is one of the densest stellar clusters in the Galaxy and an ideal testbed for studying stellar dynamical processes close to the supermassive black hole (Schödel et al., 2014; Alexander, 2017). In the first *in situ* scenario, stars can either form in the outer parts of an accretion disk or in the infalling molecular cloud that undergoes a disruption. In the second *migration* scenario, stars are brought to the black hole in the infalling stellar cluster. In addition, the disruption of a binary on an eccentric orbit, so-called Hills mechanism, is a special case of the migration mechanism. In the following, we use the second *migration* scenario to illustrate how a group of stars can get aligned with the accretion disk plane and subsequently perturb its structure.

The stochastic perturbations of the trajectory of a stellar cluster can cause it to wander into the Galactic centre where it becomes gravitationally bound to the supermassive black hole at its centre. The star cluster then orbits the supermassive black hole with its constituents (stars) crossing the accretion disk during each passage (e.g. Šubr and Karas, 1999; MacLeod and Lin, 2020). The repetitive intersections of stars and the accretion disk together with the drag of the accretion disk induce that the stars with non-zero inclination converge onto the orbital plane of the accretion disk. In addition, once in the orbital plane, the high-eccentric trajectories get circularized. That leads to the power-law change of the star cluster distribution (Karas and Šubr, 2001).

In the following, let us define the effective radius of a star, $R_{\mathrm{inf}\star}$. This is a length-scale where the stellar gravitational or the magneto-hydrodynamic influence prevails over that of the black hole gravitational influence or the accretion disk total pressure (ram+thermal+magnetic pressure), respectively. The ratio of the sphere of the influence of the star and the accretion disk scale-height $\frac{R_{\mathrm{inf}\star}}{H}$ predisposes the ability of the star to form a gap or not with the basic condition $\frac{R_{\mathrm{inf}\star}}{H} \gtrsim 1$ and $\frac{R_{\mathrm{inf}\star}}{H} < 1$, respectively. In the latter case, the stars get engulfed by the accretion disk gas while co-rotating with it and will eventually give rise to density waves propagating through the disk. The stellar influence radius also depends on the sense of the orbital motion. For wind-blowing stars, it is larger for stars co-rotating with the disk and smaller for stars counter-rotating. For the counter-rotating wind-blowing stars,

the stagnation radius gets smaller because of the larger relative velocity. The ratio of the stagnation radii between the co-rotating and the counter-rotating orbits can be expressed as $R^{\mathrm{c}}_{\mathrm{stag}}/R^{\mathrm{cc}}_{\mathrm{stag}} \sim \sqrt{4\zeta^2+1} > 1$, where $\zeta = v_{\mathrm{K}}/c_{\mathrm{s}}$ is the ratio of the local Keplerian velocity to the local sound speed. On the other hand, for the objects without any type of the outflow (e.g. stellar black holes), the counter-rotating orbits with respect to the accretion disk are expected to have a larger tidal Hill radius by a factor of as much as $R^{\mathrm{cc}}_{\mathrm{H}}/R^{\mathrm{c}}_{\mathrm{H}} \sim 3^{2/3} \sim 2.08$ (for circular orbits) in comparison with perturber orbits co-rotating with the disk material (Innanen, 1979; Zajaček et al., 2014). These estimates of tidal radii are based on the simple particle approximation and will be investigated in detail in our future studies.

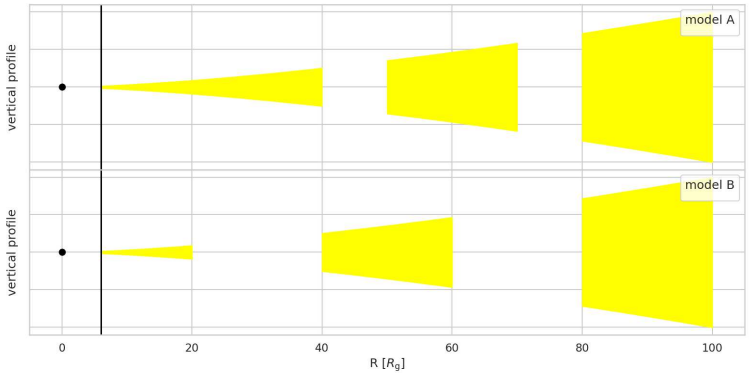

Figure 1. Two examples illustrate how we describe gaps in the model of a gappy accretion disk spectral line: model A (narrow gaps within the disk; see the top panel) in comparison with a ring-like structure in B (wide intervals separate rather narrow accretion rings; see the bottom panel). The black point marks the position of a supermassive black hole; the black vertical line is the ISCO radius.

We build upon the earlier results of Štolc et al. (2020) (in prep.), where we simulated the spectral line profiles with an accretion disk having only one gap. In our current toy model, we we allow the concurrent existence of multiple gaps. Thus, we divide our study into two scenarios – a gappy accretion disk (model A) and ring-like accretion disk (model B) based on the size of the gaps (see Figure 1). In other words, the extreme case of A would be the smooth disk, where the gaps disappear, whereas the extreme B case just corresponds to several narrow rings separated from each other (Sochora et al., 2011).

3 METHODOLOGY AND RESULTS

In our model, we assume the supermassive black hole to be of Schwarzschild type, which corresponds to the case of a vacuum metric solution outside of an object with the electric charge and the angular momentum equal to zero. We further consider the whole system to be immersed in high-energetic medium – corona. The intrinsic profile of radiation reflected on an accretion disk depends on the ratio of size of the accretion disk and the corona $\frac{R}{R_c}$

(Fabian et al., 1989). Fabian et al. (1989) show that the dependence of the intrinsic profile of the reflected radiation is $\propto \frac{1}{R^2}$ for the ratio $\frac{R}{R_c} \approx 1$ and $\propto \frac{1}{R^3}$ for the ratio $\frac{R}{R_c} > 1$.

Calculation of the monochromatic flux of radiation reflected on an accretion disk follows from the general definition (e.g. Hubený and Mihalas, 2014),

$$F_\nu^i = \int I_\nu(n_x, n_y, n_z) n^i \mathrm{d}\Omega,\ i = 1, 2, 3 \tag{1}$$

integrating over all solid angles. The matter distribution in our model corresponds to the standard Shakura-Sunyaev thin disk scheme (cf. Shakura and Sunyaev, 1973; Page and Thorne, 1974). Adopting the axial symmetry of the system ($\partial_\varphi = 0$) the eq. (1) reads as

$$F_\nu \approx \int I_\nu \,\mathrm{d}S,\ \mathrm{d}S = R\,\mathrm{d}R\,\mathrm{d}d\varphi. \tag{2}$$

To get observed values of the monochromatic flux of radiation we have to use the Liouville's theorem that is referencing the special relativistic relation between *observed* and *emitted* intensity and frequency as

$$\frac{I_{\mathrm{observed}}}{I_{\mathrm{emitted}}} = \frac{\nu^3_{\mathrm{observed}}}{\nu^3_{\mathrm{emitted}}}. \tag{3}$$

The ratio of *observed* and *emitted* frequency defines the gravitational redshift

$$g = \frac{\nu_{\mathrm{observed}}}{\nu_{\mathrm{emitted}}}. \tag{4}$$

Combining the eq. (2), (3) and (4) we get the expression for the observed monochromatic flux of radiation as

$$F_{\mathrm{observed}} \approx \int \frac{\nu^3_{\mathrm{observed}}}{\nu^3_{\mathrm{emitted}}} I_{\mathrm{emitted}} \mathrm{d}S = \int g^3 I_{\mathrm{emitted}}\,\mathrm{d}S,\ \mathrm{d}S = R\,\mathrm{d}R\,\mathrm{d}\varphi. \tag{5}$$

Assuming the supermassive black hole in our simulations to be a Schwarzschild black hole we use the redshift factor accounting not only for the special relativistic effect but for the gravitational light-bending as well. The redshift factor then reads as (Pecháček et al., 2005)

$$g(R, \varphi, I) = \frac{\sqrt{R(R-3)}}{R + \sin(\varphi)\sin(I)\sqrt{R - 2 + 4(1 + \cos(\varphi)\sin(I))^{-1}}} \tag{6}$$

with R, φ and I as radial co-ordinate, azimuthal co-ordinate and inclination respectively. In order to observe both special and general relativistic effects of the simulated spectral line profiles more clearly we limit our calculations in sense of radial extent of the accretion disk, i.e. the range of radial co-ordinate is ($6R_{\mathrm{g}}$, $100\ R_{\mathrm{g}}$).

The following plots examine the background-subtracted spectral features, so the underlying continuum is neglected. Figures 2–7 show the comparison of the spectral line profile for both models A and B (with gaps) with the intrinsic profile of reflected radiation as $\propto \frac{1}{R^2}$ and $\propto \frac{1}{R^3}$ from the entire disk (without gaps, i.e., unperturbed). Red dashed vertical line marks the intrinsic frequency.

The spectral line profiles are quite narrow which is caused due to the lower value of inclination as 35 deg (see Figures 2–3). We observe the decrease of the radiation flux of the spectral line in the model B compared to the model A. We can also notice that the number of peaks in the spectral line of the perturbed accretion disk is three times more that of the case involving the unperturbed accretion disc.

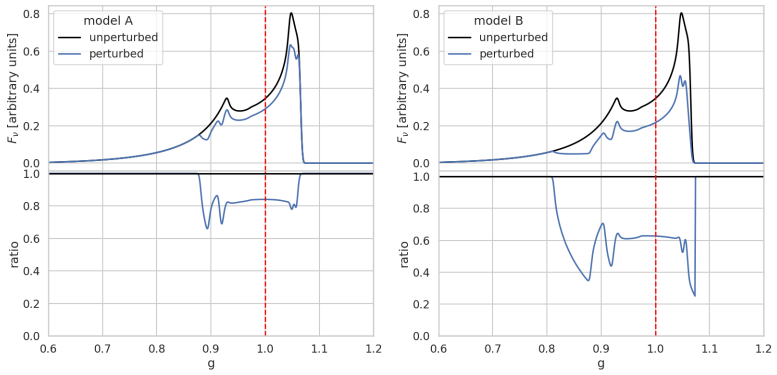

Figure 2. Comparison of spectral line profiles for model A (left panel) and model B (right panel) with intrinsic intensity $I_\nu \propto \frac{1}{R^2}$. The view angle is 35 deg.

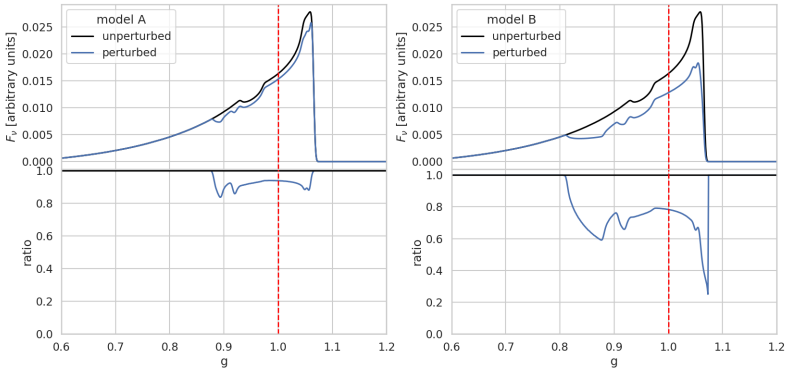

Figure 3. The same as in the previous figure but for $I_\nu \propto \frac{1}{R^3}$.

Changing the value of the inclination to 60 deg and 85 deg (see Figures 4–5 and Figures 6–7, respectively) the spectral line profiles get more stretched. Hence we observe the decrease of the of the radiation flux in the spectral line of model B compared to model A more

clearly as it spans across bigger region of *observed* frequencies. The number and positions of the spectral line peaks are more distinguishable as well.

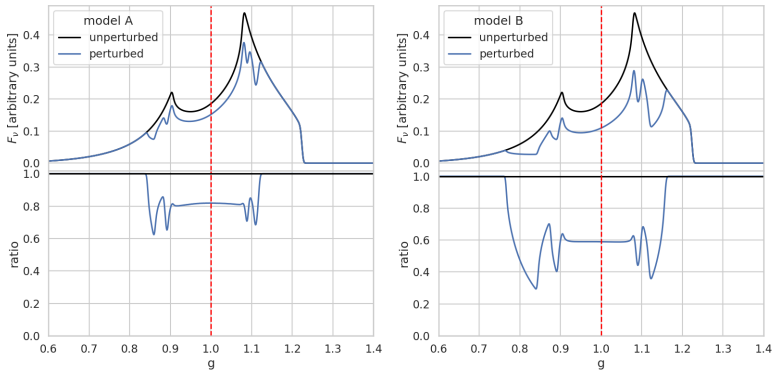

Figure 4. Comparison of spectral line profiles for model A (left panel) and model B (right panel) with intrinsic intensity $I_\nu \propto \frac{1}{R^2}$. The view angle is 60 deg.

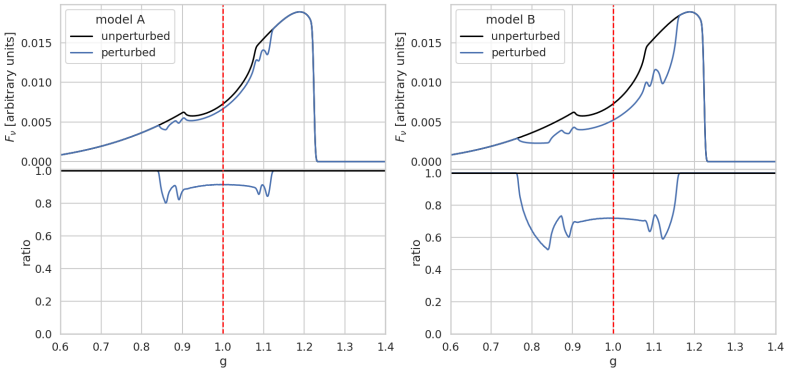

Figure 5. The same as in the previous figure but for $I_\nu \propto \frac{1}{R^3}$.

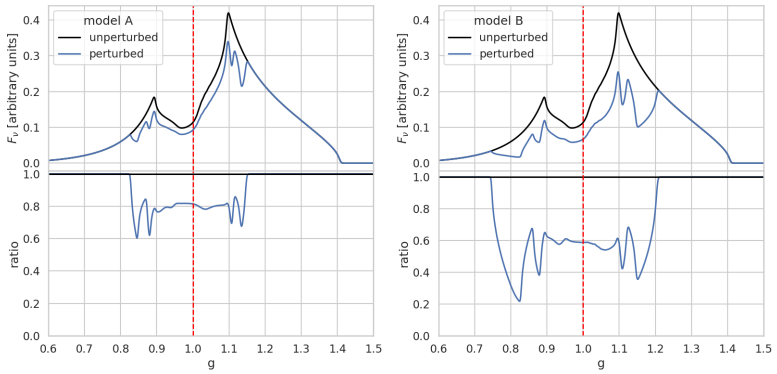

Figure 6. Comparison of spectral line profiles for model A (left panel) and model B (right panel) with intrinsic intensity $I_\nu \propto \frac{1}{R^2}$. The view angle is 85 deg.

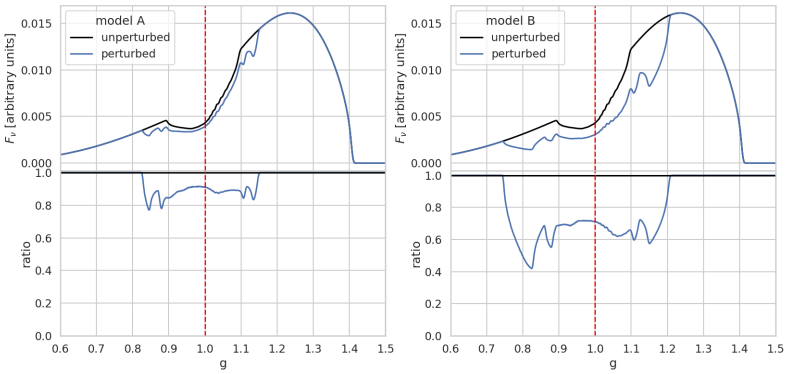

Figure 7. The same as in the previous figure but for $I_\nu \propto \frac{1}{R^3}$.

The spectral line profiles for the model B show overall less radiation flux than the spectral line profiles for the model A, independent on the intrinsic radiation intensity of the reflected radiation. That is to be expected as the area of reflection medium in model B is smaller than the area of reflection medium in model A. The number of peaks in both model A and model B equals to 6. That is a direct result of superposition of 3 spectral line profiles coming from the 3 individual "sub-disks" of the former unperturbed accretion disk structure.

4 DISCUSSION AND CONCLUSIONS

Our plots of the model reflection line show how the growing number of gaps in the accretion disk, their radial position and width lead to a growing complexity of the spectral profile, namely, the number of peaks compared to an unperturbed case. The latter exhibits just two peaks of the classical double-horn shape depending on the observer's view angle (Karas et al., 1992). To be more specific in our examples, we expect that number N of gaps, will result in spectral line profile with $(2N + 2)$ peaks (in the above given example, e.g., $N = 2$ translates to 6 peaks). Changing from the model A to B we clearly observe this developing spectral feature together with the decrease in the radiation flux.

The model A could correspond to a binary star being trapped by the supermassive black hole potential. After the component separation of the binary system they both subsequently induce gaps, given the condition $\frac{R_{\mathrm{inf}\star}}{H} \gtrsim 1$ holds for each one. The accretion disks on the verge of collapse due thermal or viscous perturbations tend to form rings and dissolve (e.g. Frank et al., 2002). This rather short stage transition would be in agreement with the model B that we propose.

We defer the study of astrophysically realistic interpretation of gap sizes together with respective timescales (e.g. Takeuchi et al., 1996) which will require taking into account the gravitational sphere of influence of a smaller body in face of perturbations from a more massive one, as governed by the Hill or Bondi-Hoyle-Lyttleton radii, respectively. Further analysis will have to consider the interaction of both the stellar wind and the magnetosphere with the accretion disk's gas (e.g., Zajaček et al., 2015, 2016), so the radius of sphere of influence of a star should then lead to the formation of relatively wide gaps.

ACKNOWLEDGEMENTS

We acknowledge the collaboration grant of the Czech Science Foundation and Deutsche Forschungsgemeinschaft (No. 19-01137J). MZ acknowledges the financial support by the National Science Center in Poland, grant No. 2017/26/A/ST9/00756 (Maestro 9). In addition, MZ also acknowledges the NAWA financial support under the agreement PPN/WYM/2019/1/00064 to perform a three-month exchange stay at the Astronomical Institute of the Czech Academy of Sciences in Prague.

REFERENCES

Abramowicz, M. A., Czerny, B., Lasota, J. P. and Szuszkiewicz, E. (1988), Slim Accretion Disks, *ApJ*, **332**, p. 646.

Alexander, T. (2017), Stellar Dynamics and Stellar Phenomena Near a Massive Black Hole, *ARA&A*, **55**(1), pp. 17–57, arXiv: 1701.04762.

Artymowicz, P. (1994), Orbital Evolution of Bodies Crossing Disks Due to Density and Bending Wave Excitation, *ApJ*, **423**, p. 581.

Boettcher, M., Harris, D. E. and Krawczynski, H. (2012), *Relativistic Jets from Active Galactic Nuclei*.

Collin, S. and Zahn, J.-P. (1999), Star formation and evolution in accretion disks around massive black holes., *A&A*, **344**, pp. 433–449.

Esin, A. A., McClintock, J. E. and Narayan, R. (1997), Advection-Dominated Accretion and the Spectral States of Black Hole X-Ray Binaries: Application to Nova Muscae 1991, *ApJ*, **489**(2), pp. 865–889, arXiv: astro-ph/9705237.

Fabian, A. C., Rees, M. J., Stella, L. and White, N. E. (1989), X-ray fluorescence from the inner disc in Cygnus X-1., *MNRAS*, **238**, pp. 729–736.

Fender, R. P., Belloni, T. M. and Gallo, E. (2004), Towards a unified model for black hole X-ray binary jets, *MNRAS*, **355**(4), pp. 1105–1118, arXiv: astro-ph/0409360.

Frank, J., King, A. and Raine, D. (2002), Accretion Power in Astrophysics, *Cambridge University Press; 3 edition*, pp. 80–84.

Gültekin, K. and Miller, J. M. (2012), Observable Consequences of Merger-driven Gaps and Holes in Black Hole Accretion Disks, *ApJ*, **761**(2), 90, arXiv: 1207.0296.

Hills, J. G. (1975), Possible power source of Seyfert galaxies and QSOs, *Nature*, **254**, pp. 295–298.

Hubený, I. and Mihalas, D. (2014), *Theory of Stellar Atmospheres*, ISBN ISBN9781400852734.

Innanen, K. A. (1979), The limiting radii of direct and retrograde satellite orbits, with applications to the solar system and to stellar systems., *AJ*, **84**, pp. 960–963.

Karas, V., Vokrouhlický, D. and Polnarev, A. G. (1992), In the vicinity of a rotating black hole: a fast numerical code for computing observational effects., *MNRAS*, **259**, pp. 569–575.

Karas, V. and Šubr, L. (2001), Orbital decay of satellites crossing an accretion disc, *A&A*, **376**, pp. 686–696, arXiv: astro-ph/0107232.

Lin, D. N. C. and Papaloizou, J. (1986), On the Tidal Interaction between Protoplanets and the Protoplanetary Disk. III. Orbital Migration of Protoplanets, *ApJ*, **309**, p. 846.

Lubow, S. H. and D'Angelo, G. (2006), Gas Flow across Gaps in Protoplanetary Disks, *ApJ*, **641**(1), pp. 526–533, arXiv: astro-ph/0512292.

MacLeod, M. and Lin, D. N. C. (2020), The Effect of Star-Disk Interactions on Highly Eccentric Stellar Orbits in Active Galactic Nuclei: A Disk Loss Cone and Implications for Stellar Tidal Disruption Events, *ApJ*, **889**(2), 94, arXiv: 1909.09645.

Mapelli, M. and Gualandris, A. (2016), *Star Formation and Dynamics in the Galactic Centre*, volume 905, p. 205.

Misner, C. W., Thorne, K. S. and Wheeler, J. A. (1973), *Gravitation (San Francisco: W.H. Freeman and Co)*.

Narayan, R. (2000), Hydrodynamic Drag on a Compact Star Orbiting a Supermassive Black Hole, *ApJ*, **536**(2), pp. 663–667, arXiv: astro-ph/9907328.

Narayan, R. and McClintock, J. E. (2008), Advection-dominated accretion and the black hole event horizon, *NewAR*, **51**(10-12), pp. 733–751, arXiv: 0803.0322.

Narayan, R. and Yi, I. (1994), Advection-dominated Accretion: A Self-similar Solution, *ApJL*, **428**, p. L13, arXiv: astro-ph/9403052.

Page, D. N. and Thorne, K. S. (1974), Disk-Accretion onto a Black Hole. Time-Averaged Structure of Accretion Disk, *ApJ*, **191**, pp. 499–506.

Pecháček, T., Dovčiak, M. and Karas, V. (2005), The relativistic shift of spectral lines from black-hole accretion discs, pp. 137–141.

Peterson, B. M. (2009), *Active galactic nuclei (Cambridge Univ. Press: Cambridge)*, p. 138.

Rees, M. J. (1988), Tidal disruption of stars by black holes of 10^6-10^8 solar masses in nearby galaxies, *Nature*, **333**(6173), pp. 523–528.

Ricci, C., Kara, E., Loewenstein, M., Trakhtenbrot, B., Arcavi, I., Remillard, R., Fabian, A. C., Gendreau, K. C., Arzoumanian, Z., Li, R., Ho, L. C., MacLeod, C. L., Cackett, E., Altamirano, D., Gand hi, P., Kosec, P., Pasham, D., Steiner, J. and Chan, C. H. (2020), The Destruction and

Recreation of the X-Ray Corona in a Changing-look Active Galactic Nucleus, *ApJL*, **898**(1), p. L1.

Rosenthal, M. M., Chiang, E. I., Ginzburg, S. and Murray-Clay, R. A. (2020), How consumption and repulsion set planetary gap depths and the final masses of gas giants, *MNRAS*, **498**(2), pp. 2054–2067, arXiv: 2004.13720.

Schödel, R., Feldmeier, A., Neumayer, N., Meyer, L. and Yelda, S. (2014), The nuclear cluster of the Milky Way: our primary testbed for the interaction of a dense star cluster with a massive black hole, *Classical and Quantum Gravity*, **31**(24), 244007, arXiv: 1411.4504.

Shakura, N. I. and Sunyaev, R. A. (1973), Reprint of 1973A&A....24..337S. Black holes in binary systems. Observational appearance., *A&A*, **500**, pp. 33–51.

Sochora, V., Karas, V., Svoboda, J. and Dovčiak, M. (2011), Black hole accretion rings revealed by future X-ray spectroscopy, *MNRAS*, **418**(1), pp. 276–283, arXiv: 1108.0545.

Svoboda, J., Guainazzi, M. and Merloni, A. (2017), AGN spectral states from simultaneous UV and X-ray observations by XMM-Newton, *A&A*, **603**, A127, arXiv: 1704.07268.

Syer, D., Clarke, C. J. and Rees, M. J. (1991), Star-disc interactions near a massive black hole, *MNRAS*, **250**, pp. 505–512.

Takeuchi, T., Miyama, S. M. and Lin, D. N. C. (1996), Gap Formation in Protoplanetary Disks, *ApJ*, **460**, p. 832.

Šubr, L. and Karas, V. (1999), An orbiter crossing an accretion disc, *A&A*, **352**, pp. 452–458, arXiv: astro-ph/9910401.

Ward, W. R. (1986), Density waves in the solar nebula: Diffential Lindblad torque, *Icar*, **67**(1), pp. 164–180.

Yuan, F. and Narayan, R. (2014), Hot Accretion Flows Around Black Holes, *ARA&A*, **52**, pp. 529–588, arXiv: 1401.0586.

Zajaček, M., Eckart, A., Karas, V., Kunneriath, D., Shahzamanian, B., Sabha, N., Mužić, K. and Valencia-S., M. (2016), Effect of an isotropic outflow from the Galactic Centre on the bow-shock evolution along the orbit, *MNRAS*, **455**(2), pp. 1257–1274, arXiv: 1510.02285.

Zajaček, M., Karas, V. and Eckart, A. (2014), Dust-enshrouded star near supermassive black hole: predictions for high-eccentricity passages near low-luminosity galactic nuclei, *A&A*, **565**, A17, arXiv: 1403.5792.

Zajaček, M., Karas, V. and Kunneriath, D. (2015), Galactic Center Minispiral: Interaction Modes of Neutron Stars, *Acta Polytechnica*, **55**(3), pp. 203–214, arXiv: 1507.00706.

Proceedings of *RAGtime 20–22, 15–19 Oct., 16–20 Sept., 19–23 Oct., 2018/2019/2020, Opava, Czech Republic*
Z. Stuchlík, G. Török and V. Karas, editors, Silesian University in Opava, 2020, pp. 299–315

Perturbing the accretion flow onto a supermassive black hole by a passing star

Petra Suková[1,a] Michal Zajaček[2] Vojtěch Witzany[3] and Vladimír Karas[1]

[1]Astronomical Institute of the Czech Academy of Sciences,
Boční II 1401, 141 00, Prague, Czech Republic
[2]Center for Theoretical Physics, Polish Academy of Sciences,
Al. Lotnikow 32/46, 02-668 Warsaw, Poland
[3]School of Mathematics and Statistics, University College Dublin,
Belfield, Dublin 4, D04 V1W8, Ireland
[a]petra.sukova@asu.cas.cz

ABSTRACT
The close neighbourhood of a supermassive black hole contains not only accreting gas and dust, but also stellar-sized objects like stars, stellar-mass black holes, neutron stars, and dust-enshrouded objects that altogether form a dense nuclear star-cluster. These objects interact with the accreting medium and they perturb the otherwise quasi-stationary configuration of the accretion flow. We investigate how the passages of a star can influence the black hole gaseous environment with GRMHD 2D and 3D simulations. We focus on the changes in the accretion rate and the associated emergence of outflowing blobs of plasma.

Keywords: black holes – accretion, accretion disks – active galactic nuclei

1 INTRODUCTION

In the supermassive black hole environment we can expect and in the case of our Galactic center even observationally resolve the presence of stars that form a dense nuclear star-cluster (Peißker et al., 2020 and references theirein). We can only deduce the number of neutron stars, stellar-mass black holes and other stellar-sized objects originating as an inevitable outcome of the stellar evolution and the feedback processes (Neumayer et al., 2020). If they are indeed embedded in the accretion flow, the mutual interaction between those objects and gas can lead to observable effects, in particular the changes in accretion rate, ejection of plasma blobs and the redistribution of accreting gas. This should then lead to temporal changes of the outgoing radiation.

In the present work we assume that the averaged accretion flow is centered on the plane perpendicular to the rotation axis of the central black hole (the equatorial plane). The field of the black hole is described by the Kerr metric (Misner et al., 1973). While the

978-80-7510-432-8

gravitational field of the black hole obeys the conditions of axial symmetry and stationarity, the accretion flow can be highly turbulent and non-stationary (Kato et al., 2008).

The motion of stars and the resulting impact on the accretion flow can reveal signatures of the orbital period at the corresponding radius (Karas and Vokrouhlický, 1994; Pihajoki, 2016). Therefore, we explore in our contribution the impact of the passages of stars through the accreting medium. We want to understand the effects that this may have on the accretion rate, and we explore whether a fraction of the material can be set on escaping trajectories.

2 SET-UP OF THE NUMERICAL PROCEDURE

We perform global general-relativistic magneto-hydrodynamical (GRMHD) simulation within the assumed fixed spacetime metric. We compare the results obtained in 2D and 3D simulations of the flow using the publicly available code `HARMPI` (Ressler et al., 2015; Tchekhovskoy et al., 2007). The adopted numerical tool is based on the original HARM code (Gammie et al., 2003; Noble et al., 2006), which we have modified in order to explore the effects of mutual interactions between the gaseous medium and the transiting body of a star. The code uses a conservative, shock-capturing scheme with a staggered magnetic field representation and adaptive time step Δt.

We follow the evolution of gas under the assumption of vanishing resistivity and the polytropic equation of state $p = K\rho^{\gamma}$ with the adiabatic index $\gamma = 13/9$. The background spacetime is described by the Kerr metric with the spin parameter $a = 0.5$ (for definiteness of the example), using the modified Kerr-Schild coordinates penetrating below the horizon (Misner et al., 1973). We defined the grid with logarithmic spacing in the r-direction in such a way that there are always at least 5 cells below the horizon. In the θ direction, the grid is concentrated along the equatorial plane (Tchekhovskoy et al., 2011). Thanks to the non-uniform spacing of the grid, we have higher resolution in the region of interest and we do not need to employ the mesh refinement. The outer boundary of the grid is set at $R_{\rm out} = 2 \cdot 10^4\,\mathrm{M}$. For more details of the numerical setup, see the forthcoming paper (Suková et al., 2021, work in progress).

3 RESULTS

We present preliminary results from several computational runs that complement a more detailed discussion in (Suková et al., 2021, work in progress). In the latter paper we explore the role of the shape and orientation of the stellar orbits, while here we focus more on the effects of the resolution of the computational grid and the exact realisation of the body moving through the gaseous medium. Hence, we will be able to better constrain the possible uncertainties in our results.

3.1 Effects of the grid resolution

The resolution of the grid influences our simulations in two ways. First, the resolution is crucial to capture the MRI in the flow, thus the accretion rate and the complexity of the flow are affected. Second, the exact description of the star, its shape and minimal possible

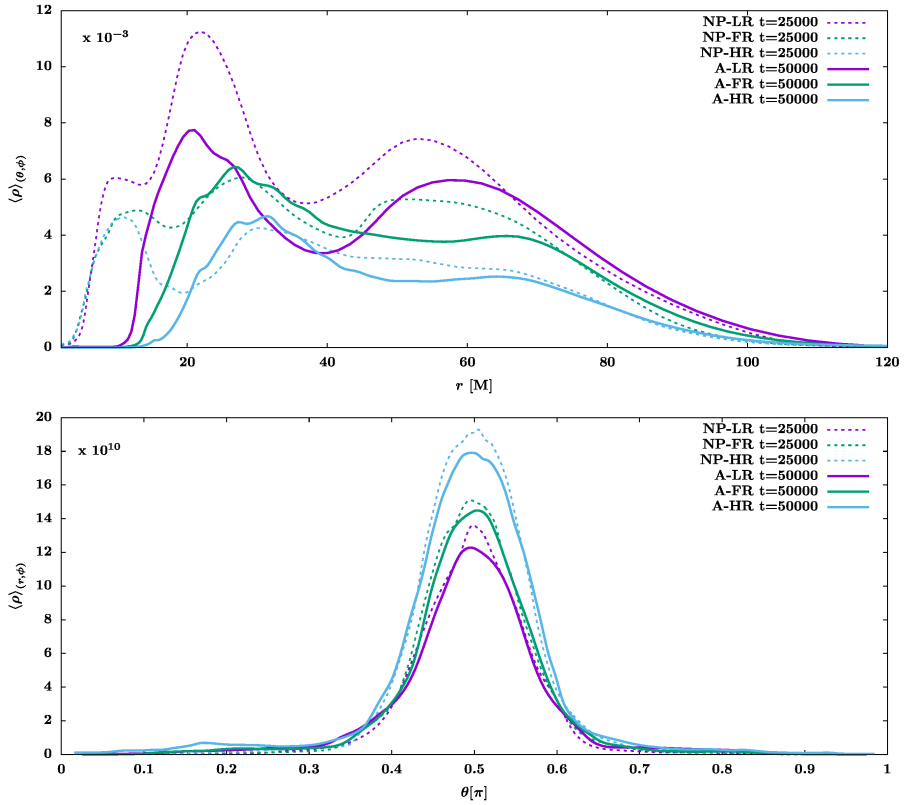

Figure 1. The radial (top) and angular (bottom) profiles of averaged density $\langle\rho\rangle_{(\theta,\phi)}(r)$ and $\langle\rho\rangle_{(r,\phi)}(\theta)$. The dashed lines show the profile at $t_{\rm in} = 25000\,\mathrm{M}$ for LR (purple), FR (green) and HR (blue) runs; the solid lines are computed at $t_{\rm f} = 50000\,\mathrm{M}$.

diameter are constrained by the resolution. Because we let the torus evolve before turning on the perturbation, the state of the flow at the moment when the star starts to orbit the black hole is not the same as the initial conditions. Therefore we first explore the effect of the resolution on the non-perturbed evolution, and we turn to the study of how the action of the star depends on the resolution afterwards.

3.1.1 Non-perturbed evolution of the accretion flow

Additionally to the 2D runs presented in (Suková et al., 2021, work in progress), which were computed with the fiducial resolution (FR) of $n_r = 252, n_\theta = 192$, we present here also the results of runs in the low resolution (LR) of $n_r = 192, n_\theta = 144$, and the high resolution (HR) set-up of $n_r = 384, n_\theta = 288$. We initialized the computation with the same parameters for each resolution, which is the torus from the family of solutions introduced by

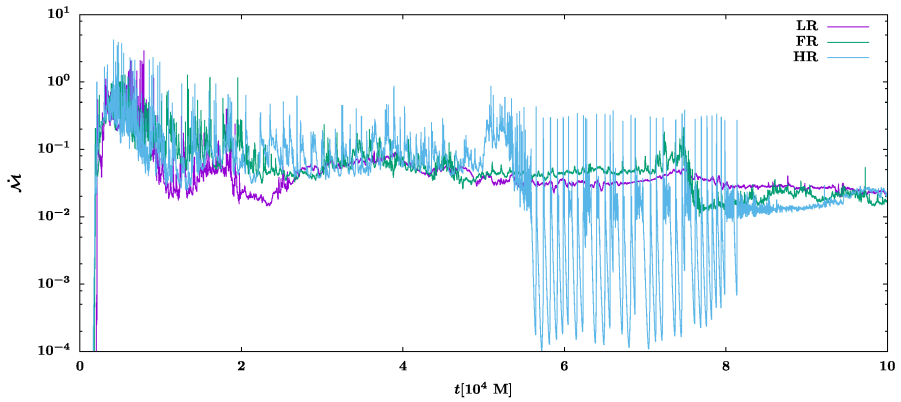

Figure 2. Time dependence of accretion rate $\dot{\mathcal{M}}$ is plotted for the non-perturbed runs with LR (purple), FR (green) and HR (blue). Frequent, intermittent fluctuations are characteristic.

Witzany and Jefremov (2018) with $\kappa = 7.61, l_0 = 8.46098\,\mathrm{M}$ stretching from $r_{\mathrm{min}} = 20\,\mathrm{M}$ to $r_{\mathrm{max}} = 90\,\mathrm{M}$. The torus is threaded by a poloidal magnetic field with field lines that follow the isocontours of density; the gas to magnetic pressure ratio equals to $\beta = p_g/p_m = 100$. The star is described as a gradual perturbation (GP) contained within the full star volume (see Section 3.2.2 for further details).

We check the ability to describe the MRI in our computations in the following way. At the radius of the density maximum in the initial state we find how many cells N_θ in θ direction are used to cover the density scale height H, which is defined as the height at which the density decreases to ρ_{max}/e. This number turns out to be $N_\theta = 20$ for LR, $N_\theta = 28$ for FR and $N_\theta = 42$ for HR. Then, according to Hawley et al. (2011) the quality Q_z of the resolution of the unstable MRI modes is estimated as

$$Q_z \approx 0.6\, N_\theta \left(\frac{100}{\beta}\right)^{1/2} \left(\frac{\langle v_{\mathrm{A}z}^2 \rangle}{\langle v_{\mathrm{A}}^2 \rangle}\right)^{1/2}, \tag{1}$$

where $v_{\mathrm{A}} \propto B/\sqrt{\rho}$ is the Alfvén speed and $v_{\mathrm{A}z}$ its z-component. It is generally required that $Q_z \gtrsim 10$ for a satisfactory resolution of the vertical MRI modes. In our geometry we have $B_r \sim B_\theta$ and $B_\phi = 0$ and thus $v_{\mathrm{A}z} \sim v_{\mathrm{A}}$. Therefore, with our choice $\beta = 100$, the value of Q_z ranges between ∼10 and ∼20 for our three resolutions, so all of them should yield satisfactory MRI evolution.

After the code initialization we let the torus evolve at given resolution. The state of the torus at $t_{\mathrm{in}} = 25\,000\,\mathrm{M}$ is then taken as the initial state for the run with the moving star. Hence, the shape of the torus and the accretion rate profile just before perturbation also depend on the resolution. We compare the distribution of matter in the accretion disk by

means of the averaged densities defined as

$$\langle\rho\rangle_{(\theta,\phi)}(r) = \frac{\int_0^{2\pi}\int_0^{\pi}\rho\sqrt{-g}\,\mathrm{d}\theta\mathrm{d}\phi}{\int_0^{2\pi}\int_0^{\pi}\sqrt{-g}\,\mathrm{d}\theta\mathrm{d}\phi}, \tag{2}$$

$$\langle\rho\rangle_{(r,\phi)}(\theta) = \frac{\int_0^{2\pi}\int_0^{R_{\rm out}}\rho\sqrt{-g}\,\mathrm{d}r\mathrm{d}\phi}{\int_0^{2\pi}\int_0^{R_{\rm out}}\sqrt{-g}\,\mathrm{d}r\mathrm{d}\phi}. \tag{3}$$

The profiles of these quantities at time $t_{\rm in} = 25000\,\mathrm{M}$ are plotted in Fig. 1 by dashed lines. While the angular shape of the torus is not affected by the resolution very much (except of the slightly different normalization), the radial shape of the flow exhibits various differences. The inner and outer edges of the tori approximately coincide but between them we observe differently located peaks and dips, which is also linked to slightly different accretion rates (see Fig. 2). The onset of accretion and the initial rise of accretion rate is similar for each resolution, the same holds true for the character of the relaxation to a quasi-stationary level; however, higher resolution shows more variability.

Most interestingly, the run NP-HR exhibits, for a certain time interval, a quasi-periodic flaring activity. This is due to the fact that during the evolution a dip in density in the torus forms when the inner part of the torus empties faster than new matter from the outer part of the torus comes inside. At a certain point, the density in the innermost region decreases until the flow is completely squeezed out of the equatorial plane and the magnetic field is reorganized. The reorganization happens at a radius of about $\sim 10\,\mathrm{M}$, where the magnetic field lines transition into an ordered vertical field that stretches along the symmetry axis from the bottom to the top of the simulation domain while not intersecting the black hole (see the first and second row in Fig. 3). At that point a small blob of matter is separated from the main body of the torus by the reconnected magnetic field lines and then it becomes quickly accreted into the black hole. The gas pressure at the inner edge of the torus is too low for the gas to be able to go through the strong magnetic field, hence the torus is detached from the black hole until new matter piles up and pushes the magnetic field lines back into the black hole. This repeats several times until the inner part of the torus fills again with enough gas to sustain stable accretion. Similar behaviour was seen also in some of the perturbed runs, where the inhibition of the matter inflow is caused by the motion of the star.

Run	u_t	u_ϕ	$t_{\rm end}$[M]	r[M]	$\mathcal{R}$[M]	resolution
A	-0.9557	0.479	$5\cdot10^4$	10	1	LR, FR, HR
B	-0.9761	3.295	$5\cdot10^4$	15 – 25	1	LR, FR, HR
G	-0.9557	0.479	$5\cdot10^4$	10	0.1	FR, HR

Table 1. Summary of the star's orbital parameters in perturbed runs used to study the grid resolutions effects. u_t and u_ϕ are the geodesic constants of motion in Kerr spacetime, $t_{\rm end}$ is the final time of the simulation, r shows the radial range of the orbit, $\mathcal{R}$ is the radius of the star and in the last column we show with which resolution the case was computed.

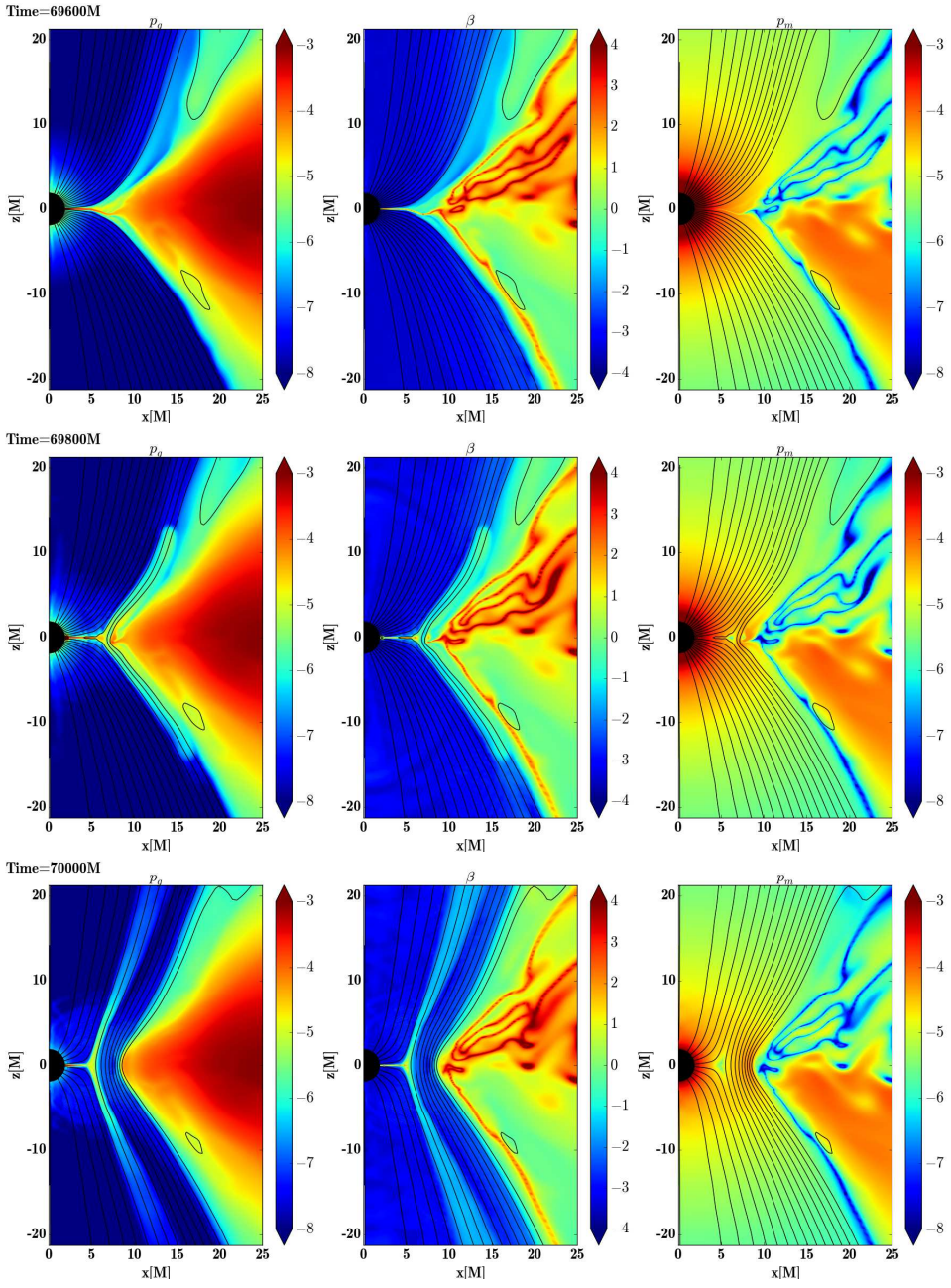

Figure 3. Slices from run NP-HR at three time instances $t = 69600$ M, $t = 69600$ M and $t = 70000$ M. In the first column we show the gas pressure p_g, in the middle column the gas to magnetic pressure ratio β, and in the right column magnetic pressure p_m.

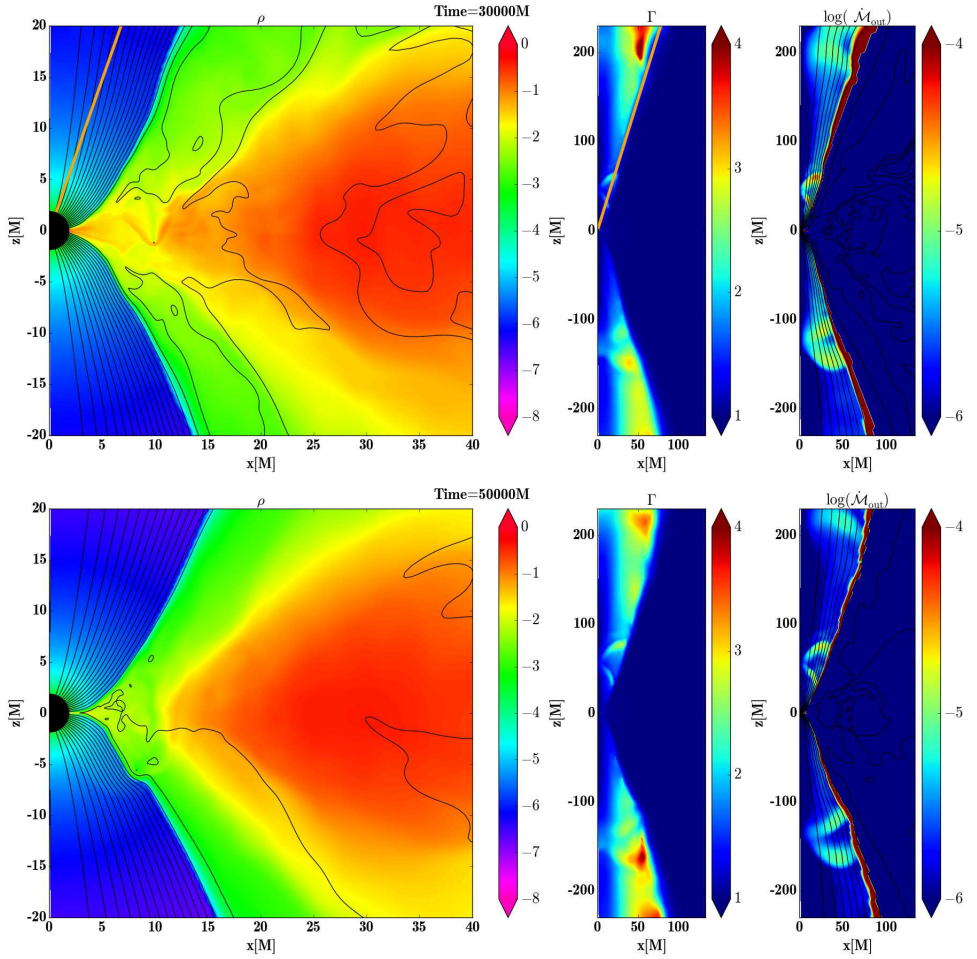

Figure 4. Slices from the simulation G-HR at time $t = 30000\,\mathrm{M}$ (top) and $t = 50000\,\mathrm{M}$ (bottom). The radius of the star $\mathcal{R} = 0.1\,\mathrm{M}$ is on the lower limit constrained by the used resolution. In the top panel the opening angle (20°) of the funnel on the larger scale is denoted by orange straight line. The bow shock caused by the moving star can be seen expanding into the black hole and also outwards into the torus. The star expels gaseous blobs into the funnel. In the bottom panel the reduction of density of accreting gas below the star orbit is visible. The blobs are still outflowing in a quasi-periodic manner.

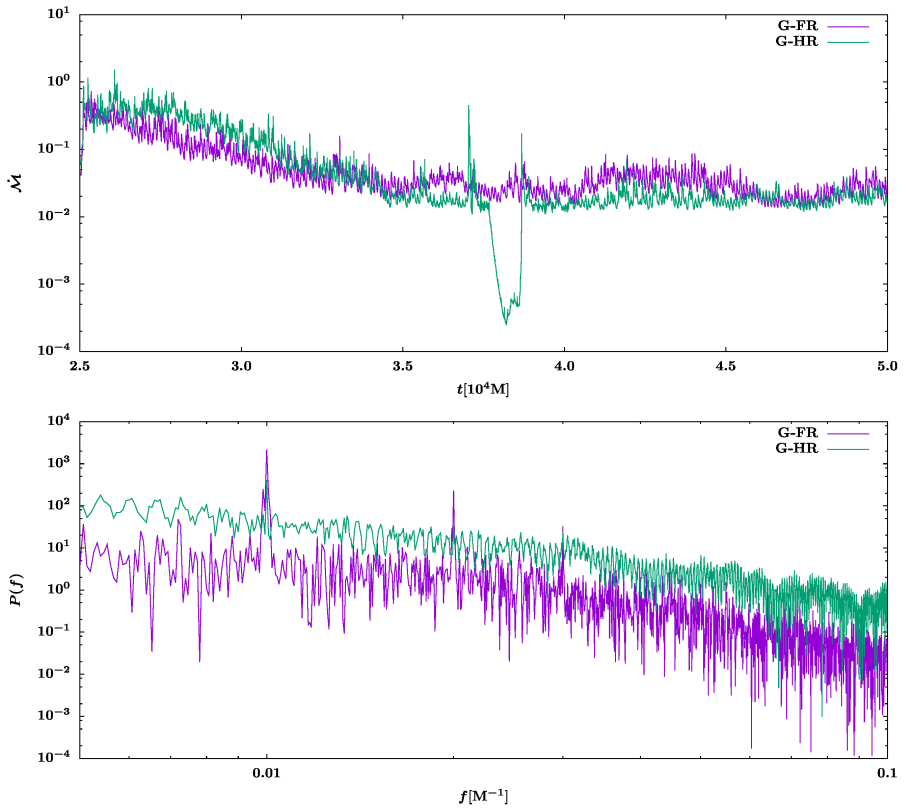

Figure 5. Time dependence of the accretion rate $\dot{\mathcal{M}}$ for runs G-FR and G-HR. The corresponding PSD computed from the settled state $t \in (3.5, 5) \cdot 10^4$ M (bottom).

3.1.2 Interaction of the star with the flow

We chose three different cases of the perturbing star and ran the simulations with LR, FR and HR. These runs are denoted as A,B and G (in accordance with (Suková et al., 2021, work in progress)) and the orbital parameters of the star motion for each run are summarised in Table 1. Orbit A corresponds to a nearly circular orbit going close to the black hole rotational axis, orbit B is then embedded in the accretion torus. The radius of the perturbing star is $\mathcal{R} = 1\,\mathrm{M}$. Orbit G is the same as orbit A, but the radius of the star is smaller, $\mathcal{R} = 0.1\,\mathrm{M}$. All the choices of star orbits induced pronounced effects on the structure of the accreting torus as well as on the time dependence of the accretion rate.

We present slices from the simulation runs which contain three plots. On the first plot on the left the density ρ in (arbitrary) code units in logarithmic scale is shown, in the middle plot we show the Lorentz factor Γ of the gas and in the third plot the "outflowing accretion

rate" is given, as computed according to

$$\dot{\mathcal{M}}_{\rm out} = \rho \frac{u^r}{u^t} \sqrt{-g}\, {\rm d}\theta\, {\rm d}\phi \qquad \text{for}\, \Gamma > 1.155, \tag{4}$$

$$\dot{\mathcal{M}}_{\rm out} = 0 \qquad \text{for}\, \Gamma \leq 1.155\,. \tag{5}$$

Such definition ensures that we follow only the rapidly outflowing gas in the funnel region and not the slowly moving gas in the torus. The second and third plots display a larger portion of the computational grid, however this is still zoom into the inner part of the grid, which spans up to $r_{\rm out} = 2 \cdot 10^4\,{\rm M}$. The example is given in Fig. 4, where the HR version of run G at time $t = 30000\,{\rm M}$ and at the end of the run $t_f = 50000\,{\rm M}$ is shown.

The HR simulation of run G exhibits qualitatively similar results as the FR run, including the choking of the torus in the innermost part, the consequent decrease of accretion rate by approximately one order of magnitude, and the existence of blobs of matter outflowing mainly along the boundary between the funnel and the torus in a quasi-period manner. The accretion rate and the power spectrum density (PSD) obtained by the Fourier transform of the accretion rate are plotted in the top and the bottom panels of Fig. 5, respectively. Even though the FR resolution is barely capturing the star in the grid, the mean value of the accretion rate decreases in a similar manner in the FR and HR runs. The HR run, however, exhibits a few larger peaks and one significant drop of accretion rate, while in the FR run such substantial variability is not seen. In both cases, the PSD shows a pronounced peak at $f = 10^{-2}\,{\rm M}^{-1}$, which corresponds to half of the orbital period of the star. We could not repeat this run with LR, since it has a grid too sparse to capture such a small star.

For runs with star A the accretion rate profile for all the three resolutions is given in Fig 6. The initial decrease of the accretion rate is similar for each case, however, the LR run exhibits fewer periodic peaks with a higher amplitude and it settles at a larger accretion rate than the FR and HR runs. The two runs with higher resolution coincide very well except of a transient flaring period and a slightly lower mean accretion rate value in the HR case. The radial and angular distributions of the gas at the end of the run is shown in Fig. 1 with solid lines. While the LR run shows higher peaks and a dip in the center, the shapes of FR and HR profiles coincide quite well. The quasi-periodic features in the accretion rates are observable for runs with all resolutions and the power spectra of runs A-FR and A-HR coincide very well, while in A-LR case the corresponding peaks are weaker.

The FR resolution of run B was found in a substantially flaring state with variations in the accretion rate spanning more than three orders of magnitude. The computation with LR shows a similar decrease of the accretion rate as FR, however, only three episodes of big dips and peaks occurred in this case. The amplitude of the oscillation is almost the same, while the time duration of the dips is a little shorter than in FR. Interestingly, in the HR case it also takes a longer time to develop the flaring state and the dips are longer, whereas the peaks have a similar duration.

3.2 Effect of the used approximation to the star motion

The effect of a solid star equipped with a magnetic field and a stellar wind moving in the accretion flow is very complicated. We have to simplify the picture to be able to describe

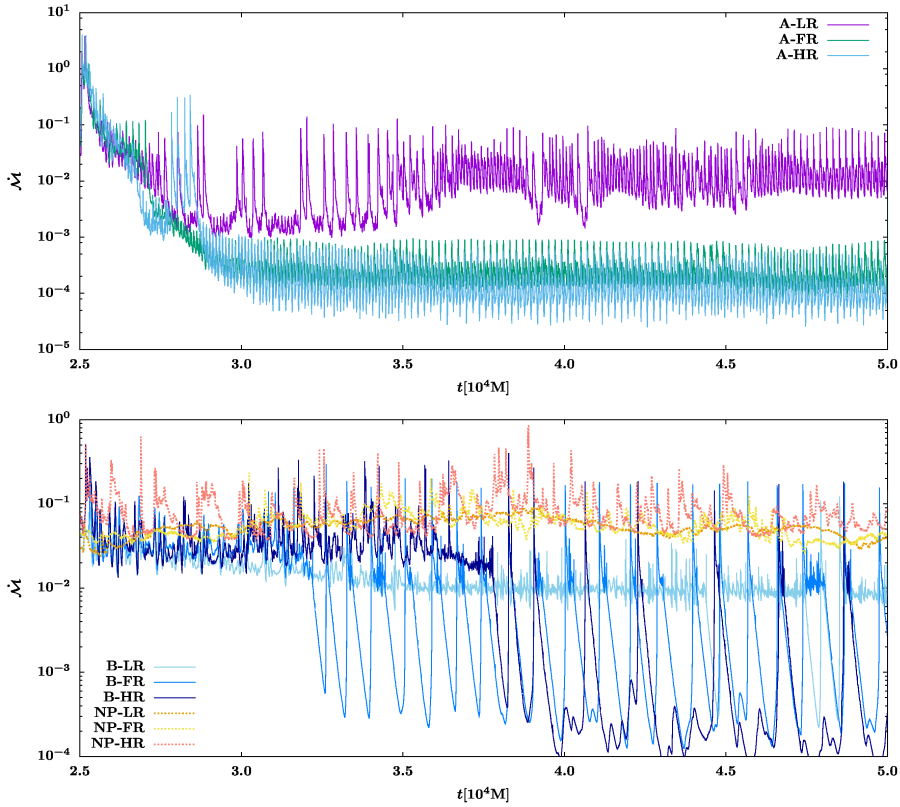

Figure 6. Time dependence of the accretion rate $\dot{\mathcal{M}}$ for the runs perturbed by star A with LR (purple), FR (green) and HR (blue) in the top panel. Bottom panel shows the same for runs with star B (solid lines) and non-perturbed runs (dotted lines).

such a process in our simulations. We focus on the dynamical effect of the star on the accreting gas, and we thus neglect the possible feedback of the gas on the star motion or structure. Therefore, the star can be treated as a test body moving along a geodesic trajectory. We also neglect the possible accretion of the gas on the star (even if the star was to be understood as a stellar-mass black hole) or strong wind outflow from the star that could enrich the accretion flow. Therefore, we consider the star to be only a solid body, which is pushing the gas along its trajectory. However, still several different simple approximations of this scenario can be used. Here we compare results from the so-called impulse approximation and a gradual perturbation of the gas by the moving star. We use the fiducial resolution $n_r = 252, n_\theta = 192$.

3.2.1 Impulse approximation

The most simplistic approach is the so-called impulse approximation (IA), where the transit of the star is simulated such that the gas in the tube corresponding to the volume through which the star moves gets the impulse by the star at the moment when the star passes through the equatorial plane (Syer et al., 1991; Vokrouhlický and Karas, 1993). This is a particularly well substantiated description for supersonic transits. We consider a star moving on a circular orbit, compute its orbital frequency and with this frequency we periodically set the velocity of the gas as equal to the orbital velocity of the star. The perturbed region is thus described by the following relations,

$$|(r - r_{\rm star})| < \mathcal{R}, \tag{6}$$

$$|(\theta - \theta_{\rm star})| < \Delta\theta, \tag{7}$$

$$t_{\rm perturb} = nT_{\rm orb}. \tag{8}$$

The free parameter of this approximation is the angular width of the perturbed region, which we set to two different values: $\Delta\theta = \pi/4$ in run IA-pi/4 and $\Delta\theta = \pi/64$ in run IA-pi/64. In this way we either perturb almost all gas of the torus along the path of the star in the former case or only a relatively small region close to the equatorial plane in the latter case.

3.2.2 Gradual perturbation

The second approach considers a sequential action of the moving star on the gas - we called it gradual perturbation (GP). We solve the geodesic equation for the star motion along with the GRMHD evolution of the plasma. Then in each time step we change the velocity of the gas as equal to the velocity of the star within a region ascribed to the star. In this way we simulate the fact that the solid body of the star moves in the grid at a given velocity.

Run	IA-pi/64	IA-pi/4	A-front face	A	A-one way
$\bar{\mathcal{M}}$	$3.2 \cdot 10^{-2}$	$7.8 \cdot 10^{-2}$	$2.9 \cdot 10^{-4}$	$2.8 \cdot 10^{-4}$	$1.3 \cdot 10^{-4}$
$\mathcal{A}$	22.5	6.57	2.78	3.17	5.37
$f_1[\,\mathrm{M}^{-1}]$	0.0049	0.0049	0.010	0.010	0.005
$f_2[\,\mathrm{M}^{-1}]$	0.0148	0.0099	0.005	0.005	0.010
$f_3[\,\mathrm{M}^{-1}]$	0.0099	0.0149	0.020	0.020	0.015

Table 2. The mean accretion rate $\bar{\mathcal{M}}$ and the amplitude of oscillations $\mathcal{A}$ during the settled state $t \in (35000, 50000)\,\mathrm{M}$ of the runs with different star realisations, for which $t_{\rm end} = 5 \cdot 10^4\,\mathrm{M}$, $r = 1\mathrm{M}$, $\mathcal{R} = 1\,\mathrm{M}$ with resolution FR. We have 2 runs with the impulse approximation, IA-pi/64 perturbs cells in an annulus sector with the angular width $\Delta\theta = \pi/64$ and radial width $\mathcal{R}$, while in IA-pi/4 the annular sector of the perturbed region is much larger ($\Delta\theta = \pi/4$). In Run A-front face we perturb cells in the disc shaped region with $\Delta\theta = \pi/4$ moving along the geodesics, in run A the star is described as a sphere with radius $\mathcal{R}$. Run A-one way differs from run A in the way that the perturbation is turned on only when the star moves "downwards", that is $v^\theta = \frac{\mathrm{d}x^\theta}{\mathrm{d}t} > 0$. The frequencies of the first three highest peaks in the power spectrum f_1, f_2, f_3 is in the last three rows.

To study also the effect of the exact shape of the moving body, we set the region corresponding to the star in two different ways:

(1) We consider a disc-shaped region with the radius equal to the star radius, which is only several zones wide in the θ-direction. Hence, the perturbation is done in the domain consisting of cells satisfying

$$|(r - r_{\rm star})| < \mathcal{R}, \tag{9}$$

$$|(\theta - \theta_{\rm star})| < \Delta\theta \qquad \Delta\theta = 4\pi/n_\theta = \pi/48, \tag{10}$$

where r, θ are BL coordinates of the grid cell center. This corresponds to a "front face" of the star moving in the flow and is used in run A-front face.

(2) All grid cells with cell centers located at (r, θ) in BL coordinates occupying the full volume of the star described in 2D simulations by

$$(\Delta x)^t = 0, \tag{11}$$

$$(\Delta x)^r = r - r_{\rm star}, \tag{12}$$

$$(\Delta x)^\theta = \theta - \theta_{\rm star}, \tag{13}$$

$$(\Delta x)^\phi = 0, \tag{14}$$

$$d = \sqrt{g^{\rm BL}_{\alpha\beta}\Delta x^\alpha \Delta x^\beta}, \tag{15}$$

$$d < \mathcal{R} \tag{16}$$

are perturbed. This approach, which we consider as the best available description of the star, will be used in Suková et al. (2021, work in progress) for all simulations.

The comparison of the aforementioned approaches is done on the example of (nearly) circular orbit passing perpendicularly through the equatorial plane with $r_{\rm star} = 10\,{\rm M}$, which was with the last realization of the star already shown as run A-FR in Sec. 3.1. All the runs are initiated with the evolved torus at $t_{\rm in} = 25000\,{\rm M}$ similarly as our other computations and the fiducial resolution is used. The accretion rates for all types of star realizations are compared in the top panel of Fig. 7, while the PSD is shown on the bottom panel.

We compare the accretion rate profile, its mean value $\bar{\mathcal{M}}$ and the amplitude of the peaks computed according to

$$\mathcal{A} = {\rm abs}\left(\frac{\max(\mathcal{M}) - \min(\mathcal{M})}{\bar{\mathcal{M}}}\right), \tag{17}$$

where the average, maximal and minimal values are taken from the settled time period $t \in (35000, 50000)\,{\rm M}$. The results are summarised in table 2.

The most prominent difference between the two approaches is seen in the case of IA used in runs IA-pi/4 and IA-pi/64: the accretion rate decreases only by about one order of magnitude, while in the case of GP, the accretion rate drops by more than three orders of magnitude. The temporal profile of the accretion rate shows quasi-periodical structures. While in all runs, we can clearly see the presence of the orbital frequency of the star, which

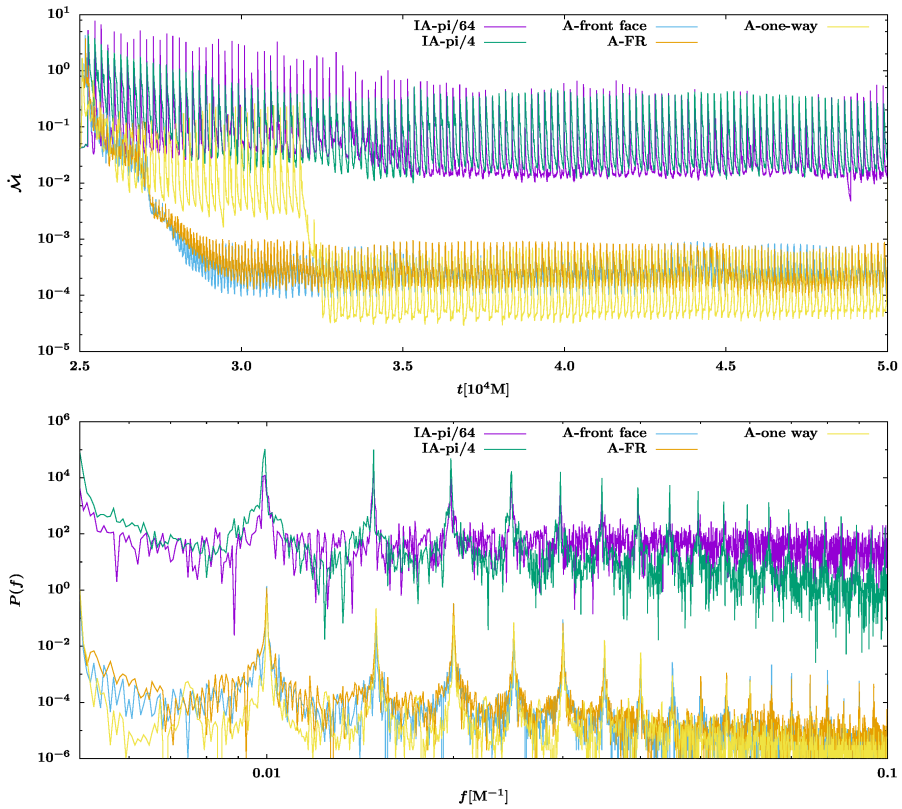

Figure 7. Time dependence of the accretion rate $\dot{\mathcal{M}}$ for runs with different star realizations (top). The corresponding power spectrum is computed from the settled state $t \in (35000, 50000)\,\mathrm{M}$ (bottom).

is $f_{\mathrm{orb}} = 4.955 \cdot 10^{-3}\,\mathrm{M}^{-1}$, and its multiples, the peaks of the accretion rate are larger in case of impulse approximation.

In contrast to the used approximation, the exact realization of the perturbed region does not affect the results significantly. The accretion rate mean values as well as the frequency and amplitudes of the oscillations coincide very well for the pairs of runs IA-pi/64 and IA-pi/4 and A-front face and A. Therefore, the evolution of the gas depends only weakly on the exact shape of the star, as long as the radius of star remains the same.

3.2.3 One-way transit of the star

Two-dimensional simulations are simplified and incomplete due to the imposed "squeezing" ϕ (azimuthal) direction into a single 2D slice. This averaging can lead to some artificial effects in the gas evolution because in reality the star transits through the disc in one direction at one half of the disc and in the other direction in the opposite half of the disc,

while in our simulations the star passes through the disc in both directions at similar place. Therefore, we have repeated run A with the complete (3D) geodesic motion, so that the perturbation is turned on only when $v^\theta = \frac{\mathrm{d}x^\theta}{\mathrm{d}t} > 0$ (that is when the star moves "downwards" in our slice), which reflects more accurately the local evolution of the gas (run A – one way).

The corresponding accretion rate and its power spectrum are shown in Fig. 7. We can see that the transient time at the beginning of the simulation lasts longer with quite high peaks and higher values of the accretion rate, however after $\sim 8000M$ the accretion rate drops to even slightly smaller values than in run A. The power spectrum shows that in case of run A – one way, the most prominent peak with $f = 5 \cdot 10^{-3}\,\mathrm{M}^{-1}$ corresponds to the star orbital frequency, while in case of run A and A – front face the peak at its double value $f = 10^{-2}\,\mathrm{M}^{-1}$ gets more power, which is in accordance with our expectations.

The evolution of the gas shows one interesting feature distinct from the run A, which is the formation of blobs wrapped in magnetic field-line loops that develop and depart toward the opposite direction than the motion of the star (i.e. "upwards" – see top panel of Fig. 8). Later, when the accretion rate decreases, the outflowing blobs of matter proceed asymmetrically with respect to the equatorial plane. There are larger blobs going downwards along the funnel boundary, but there are also fainter blobs moving upwards – see the bottom panel of Fig. 8. Because in reality the star moves in the opposite direction through the other half of the disc, there will be an asymmetric outflow of matter also with respect to the rotational axis and the position of stronger and fainter outflow will rotate around the axis with the precession frequency of the star orbit. The possible helical trajectory of the expelled gas has to be studied in 3D simulations.

4 DISCUSSIONS AND CONCLUSIONS

In the present paper we examined the effect of repetitive transits of a model star across the accretion slab. We focused on the role of the numerical set-up of the adopted scheme, the effects of grid resolution and the approximation used for the passages of the star. Even the current simplified approach indicates an interesting possibility of influencing the accretion rate by the repetitive transits and ejecting plasmoids from the inner disk with quasi-periodic signatures of the stellar orbit.

The comparison of LR, FR and HR runs has shown that the FR and HR yield very similar results, both qualitatively and quantitatively, while the LR runs, which probably render the MRI poorly, differ more significantly. However, the flaring state of the torus is still quite sensitive to the resolution of the grid. We can attribute this to the fact that, in the flaring state, the inner part of the torus is squeezed to a very thin layer, hence the description of the exact process of the blob separation and the following accretion needs a very high resolution along the equatorial plane, both in the r and θ directions. It is then left for a future study with a better resolution of the inner region to capture the shape, amplitude and frequency of the peaks in the flaring state more accurately.

The runs with different orbits showed that the presence of the star has a substantial effect on the accretion flow for various configurations. We observed that the accretion can be effectively inhibited, in particular when the star moves close to the black hole (on the radii $\sim 10\,\mathrm{M}$), where a drop of the accretion rate by three orders of magnitude was

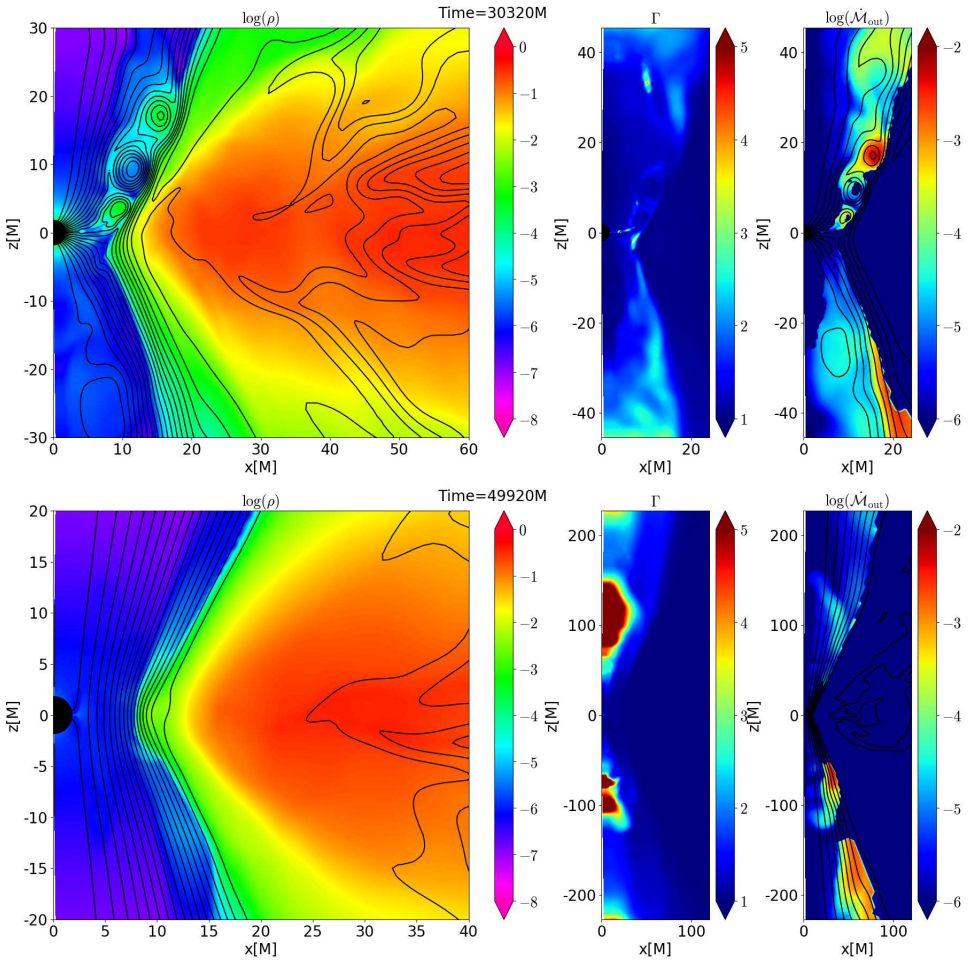

Figure 8. Slices from the run A-one way. The top panel shows the time $t = 30320\,\mathrm{M}$ before the accretion rate drops down. The blobs encircled by magnetic field lines outgoing upwards along the boundary between the funnel and the torus can be seen. On the bottom panel the situation at $t = 49920\,\mathrm{M}$ illustrates the detaching of the torus from the black hole, the existence of long vertical magnetic field lines, which do not end in the black hole, and large blobs of gas outflowing downwards, while small blobs are outflowing upwards.

found. We also observed blobs of matter expelled from the torus into the empty magnetised funnel region. The blobs are then magnetically accelerated outwards with mildly relativistic speeds along the boundary between the funnel and the torus, which has an opening angle of about 20° with respect to the rotation axis. These results will be studied in a separate study (Suková et al., 2021, work in progress).

We expect that the main features found in our simulations, such as the decrease of accretion rate, presence of quasi-periodic features stimulated by the orbital frequency of the star and outflowing blobs, are described sufficiently well by our FR and HR resolution, so these results should persist in more detailed computations. The simulation with one-way transit of the star has shown that in the full 3D case we can expect a non-axisymmetrical ejection of plasmoids in the funnel region. They can represent a spot rotating around the axis with the precession frequency of the star orbit.

Let us note that our computations were performed while assuming negligible radiative cooling of the flow. Hence our results are applicable mainly in the low-luminous galactic nuclei, such as Sgr A* in the center of our galaxy (Yuan and Narayan, 2014). Even though the simulations with radiative cooling have shown that even in case of Sgr A* for some observationally allowed values of accretion rate the inclusion of cooling has an effect on the accretion torus (Yoon et al., 2020), the overall structure of the accretion flow remains similar as in the non-cooled state. If the accretion rate becomes higher, reaching about three to one order bellow the Eddington accretion rate, the cooling becomes substantial and the flow transforms into a cold Keplerian accretion disc. The issue of stellar transits in active galactic nuclei with high accretion rates will, therefore, require the inclusion of cooling into the scheme.

ACKNOWLEDGEMENTS

The authors acknowledge the Czech Science Foundation - Deutsche Forschungsgemeinschaft collaboration project (GAČR 19-01137J), and the Czech-Polish mobility program (MŠMT 8J20PL037). MZ acknowledges the financial support by the National Science Center, Poland, grant No. 2017/26/A/ST9/00756 (Maestro 9) as well as the NAWA financial support under the agreement PPN/WYM/2019/1/00064 to perform a three-month exchange stay at the Charles University and the Astronomical Institute of the Czech Academy of Sciences in Prague. VW was supported by European Union's Horizon 2020 research and innovation programme under grant agreement No 894881.

REFERENCES

Gammie, C. F., McKinney, J. C. and Tóth, G. (2003), Harm: A numerical scheme for general relativistic magnetohydrodynamics, *ApJ*, **589**(1), p. 444.

Hawley, J. F., Guan, X. and Krolik, J. H. (2011), Assessing quantitative results in accretion simulations: From local to global, *The Astrophysical Journal*, **738**(1), p. 84.

Karas, V. and Vokrouhlický, D. (1994), Relativistic Precession of the Orbit of a Star near a Supermassive Black Hole, *The Astrophysical Journal*, **422**, p. 208.

Kato, S., Fukue, J. and Mineshige, S. (2008), *Black-Hole Accretion Disks – Towards a New Paradigm (Kyoto University Press: Kyoto)*.

Misner, C. W., Thorne, K. S. and Wheeler, J. A. (1973), *Gravitation (San Francisco: W.H. Freeman and Co.)*.

Neumayer, N., Seth, A. and Böker, T. (2020), Nuclear star clusters, *The Astronomy and Astrophysics Review*, **28**(1), 4, arXiv: 2001.03626.

Noble, S. C., Gammie, C. F., McKinney, J. C. and Del Zanna, L. (2006), Primitive Variable Solvers for Conservative General Relativistic Magnetohydrodynamics, *The Astrophysical Journal*, **641**(1), pp. 626–637, arXiv: astro-ph/0512420.

Peißker, F., Eckart, A., Zajaček, M., Ali, B. and Parsa, M. (2020), S62 and S4711: Indications of a Population of Faint Fast-moving Stars inside the S2 Orbit—S4711 on a 7.6 yr Orbit around Sgr A*, *The Astrophysical Journal*, **899**(1), 50, arXiv: 2008.04764.

Pihajoki, P. (2016), Black hole accretion disc impacts, *Mon. Not. R. Astron Soc.*, **457**(2), pp. 1145–1161, arXiv: 1510.07642.

Ressler, S. M., Tchekhovskoy, A., Quataert, E., Chandra, M. and Gammie, C. F. (2015), Electron thermodynamics in GRMHD simulations of low-luminosity black hole accretion, *Mon. Not. R. Astron Soc.*, **454**, pp. 1848–1870, arXiv: 1509.04717.

Syer, D., Clarke, C. J. and Rees, M. J. (1991), Star-disc interactions near a massive black hole, *Mon. Not. R. Astron Soc.*, **250**, pp. 505–512.

Tchekhovskoy, A., McKinney, J. C. and Narayan, R. (2007), WHAM: a WENO-based general relativistic numerical scheme - I. Hydrodynamics, *Mon. Not. R. Astron Soc.*, **379**, pp. 469–497, arXiv: 0704.2608.

Tchekhovskoy, A., Narayan, R. and McKinney, J. C. (2011), Efficient generation of jets from magnetically arrested accretion on a rapidly spinning black hole, *Monthly Notices of the Royal Astronomical Society: Letters*, **418**(1), pp. L79–L83, arXiv: https://onlinelibrary.wiley.com/doi/pdf/10.1111/j.1745-3933.2011.01147.x, URL https://onlinelibrary.wiley.com/doi/abs/10.1111/j.1745-3933.2011.01147.x.

Vokrouhlický, D. and Karas, V. (1993), A star orbiting around a supermassive rotating black hole : free motion and corrections due to star-disc collisions., *Mon. Not. R. Astron Soc.*, **265**, pp. 365–378.

Witzany, V. and Jefremov, P. (2018), New closed analytical solutions for geometrically thick fluid tori around black holes - numerical evolution and the onset of the magneto-rotational instability, *A&A*, **614**, p. A75, URL https://doi.org/10.1051/0004-6361/201732361.

Yoon, D., Chatterjee, K., Markoff, S. B., van Eijnatten, D., Younsi, Z., Liska, M. and Tchekhovskoy, A. (2020), Spectral and imaging properties of Sgr A* from high-resolution 3D GRMHD simulations with radiative cooling, *Monthly Notices of the Royal Astronomical Society*, **499**(3), pp. 3178–3192, ISSN 0035-8711.

Yuan, F. and Narayan, R. (2014), Hot Accretion Flows Around Black Holes, *ARA&A*, **52**, pp. 529–588, arXiv: 1401.0586.

Proceedings of *RAGtime 20–22, 15–19 Oct., 16–20 Sept., 19–23 Oct., 2018/2019/2020, Opava, Czech Republic*
Z. Stuchlík, G. Török and V. Karas, editors, Silesian University in Opava, 2020, pp. 317–326

Einstein–scalar field–square root nonlinear electrodynamics solution

Tayebeh Tahamtan[1,2,a]

[1]Institute of Theoretical Physics, Faculty of Mathematics and Physics,
Charles University, V Holešovičkách 2, 180 00 Prague 8, Czech Republic
[2]Institute of Physics, Faculty of Philosophy & Science, Silesian University in Opava,
Bezručovo nám. 13, CZ-746 01 Opava, Czech Republic
[a]tahamtan@utf.mff.cuni.cz

ABSTRACT
We study the influence of scalar fields on a specific model of nonlinear electrodynamics (the square root Lagrangian) spacetime. We show that the singular horizon created by scalar field in spherically symmetric static scalar-vacuum spacetimes is still present when nonlinear electrodynamics is added. For the obtained solution, we investigate the timelike geodesic motions of a test particle by studying the effective potential.

Keywords: Exact solution – black hole – scalar field – nonlinear electrodynamics – geodesic equation

1 INTRODUCTION

Studying scalar field when coupled to gravity whether minimally or nonminimally is an old subject in general relativity. The first exact spacetime solution with scalar field minimally coupled to gravity in this context was found by Fisher in 1948 (Fisher, 1948) and later was rediscovered several times (Wyman, 1981; Buchdahl, 1959; Bergmann and Leipnik, 1957; Janis et al., 1968). This scalar-vacuum static spherically symmetric solution was generalized to Einstein Maxwell scalar field solution (Penney, 1969; Janis et al., 1969; Uhlíř and Dittrich, 1973; Teixeira et al., 1974, 1976; Eriş and Gürses, 1977; Banerjee and Choudhury, 1977). The most famous and frequently used form of Fisher solution is the one described in (Janis et al., 1968), where they showed that such spacetime contains a singular pointlike event horizon. This solution is referred to as Janis–Newuman–Winicour (JNW) spacetime.

Presence of naked singularities or irregular horizons was shown to be typical for scalar field spacetimes by J. E. Chase in 1970 in what is now known as the "Chase theorem" (Chase, 1970). According to it, roughly any static spherically symmetric vacuum solution minimally coupled to massless scalar field can not have a regular horizon, any potential horizon is necessarily the locus of a curvature singularity (see (Tafel, 2014) for generalization including potential for the scalar field). These results are connected to scalar no-hair

978-80-7510-432-8

theorem nicely reviewed in (Herdeiro and Radu, 2015) where they study four dimensional asymptotically flat black holes with scalar hair in various types of scalar field models coupled to gravity.

Our motivation is to confirm whether the Chase theorem still holds when, additionally to massless scalar field, other sources are present, such as Nonlinear Electrodynamics (NE). Nonlinear electrodynamics is a nonlinear theory of electromagnetic field and various models exist with different Lagrangians. The most famous and successful model is Born–Infeld (Born and Infeld, 1934) which in the weak field limit goes to the linear Maxwell theory and in the strong field limit its Lagrangian tends to $\sim \sqrt{F_{\mu\nu}F^{\mu\nu}}$ (square root model), with $F_{\mu\nu}$ being electromagnetic tensor.

Since we were not able to find an exact solution for Born–Infeld model when scalar field minimally coupled to gravity is present, we chose the "square root" model as its approximation in the strong field regime. We believe one can extend any results related to an event horizon in the square root model to Born–Infeld model since horizons appear in strong field regime. Apart from this reason, square root Lagrangians were studied because of their interesting properties long time ago (Nielsen and Olesen, 1973; Gaete and Guendelman, 2006; Vasihoun and Guendelman, 2014) even before the rise in popularity of NE where it gained attention recently.

Previously, we studied square root model NE in Kundt class of geometries which contain exact gravitational waves (Tahamtan and Svitek, 2017).

In (Svítek et al., 2020; Tahamtan and Svitek, 2014), it is shown that the spacetime singularity sourced by static spherically symmetric scalar field is resolved at the quantum level. In (Svitek and Tahamtan, 2016), we show that scalar-field sources in static, highly symmetric geometries (JNW) tend to vanish in the ultraboost limit instead of being converted into waves.

Scalar field solutions can be generalized beyond spherical symmetry to truly dynamical situation (Tahamtan and Svitek, 2015, 2016) using Robinson–Trautman class of geometries. The results confirm no-hair theorem in the asymptotic stationary limit. This class of geometries can be coupled to NE as well (Tahamtan and Svitek, 2016).

2 SCALAR FIELD AND SQUARE ROOT LAGRANGIAN

We consider the following action, describing a scalar field and an electromagnetic field in the form of nonlinear electrodynamics minimally coupled to gravity,

$$S = \frac{1}{2}\int \mathrm{d}^4x\,\sqrt{-g}\left[\mathcal{R} + \nabla_\mu\varphi\nabla^\mu\varphi + \mathcal{L}(F)\right], \tag{1}$$

where $\mathcal{R}$ is the Ricci scalar for the metric $g_{\mu\nu}$ (we use units convention $c = \hbar = 8\pi G = 1$). The massless scalar field φ is considered real and the NE Lagrangian $\mathcal{L}(F)$ is assumed to be an arbitrary function of the electromagnetic field invariant $F = F_{\mu\nu}F^{\mu\nu}$ constructed from a closed Maxwell 2-form $F_{\mu\nu}$.

We consider the static spherically symmetric metric

$$\mathrm{d}s^2 = -f(r)\,\mathrm{d}t^2 + \frac{\mathrm{d}r^2}{f(r)} + R(r)^2\mathrm{d}\Omega^2\,, \tag{2}$$

where $\mathrm{d}\Omega^2 = \mathrm{d}\theta^2 + \sin\theta^2\mathrm{d}\phi^2$. We assume t, r, θ, ϕ coordinate ordering.

By applying the variation with respect to the metric using the action (1), we obtain Einstein equations

$$G^{\mu}{}_{\nu} = T^{\mu}{}_{\nu} = {}^{\mathrm{SF}}T^{\mu}{}_{\nu} + {}^{\mathrm{EM}}T^{\mu}{}_{\nu}. \tag{3}$$

where the superscript SF indicates scalar field and EM electromagnetic contribution to energy momentum tensor. For finding an exact solution for our metric functions corresponding to the scalar field and nonlinear electrodynamics sources, we first express the energy momentum tensors for these sources explicitly.

The energy momentum tensor generated by the scalar field is given by

$${}^{\mathrm{SF}}T_{\mu\nu} = \nabla_{\mu}\varphi\,\nabla_{\nu}\varphi - \frac{1}{2}g_{\mu\nu}\,g^{\alpha\beta}\nabla_{\alpha}\varphi\nabla_{\beta}\varphi \tag{4}$$

which for a radial scalar field and our metric anzats (2) reduces to

$${}^{\mathrm{SF}}T^{\mu}{}_{\nu} = \frac{f\,\varphi_{,r}^2}{2}diag\left\{-1, 1, -1, -1\right\}. \tag{5}$$

The wave equation of a massless scalar field ($\Box\varphi = 0$, where $\Box$ is a standard d'Alembert operator) with respect to our metric (2) leads to

$$f\,\varphi_{,r}\,R^2 = const. \tag{6}$$

And the electromagnetic energy momentum tensor contribution is defined as following

$${}^{\mathrm{EM}}T^{\mu}{}_{\nu} = \frac{1}{2}\left\{\delta^{\mu}{}_{\nu}\mathcal{L} - (F_{\nu\lambda}F^{\mu\lambda})\mathcal{L}_F\right\}, \tag{7}$$

in which $\mathcal{L}_F = \frac{d\mathcal{L}(F)}{dF}$. Obviously for the Maxwell case $\mathcal{L} = -F$ and $\mathcal{L}_F = -1$.

For our particular choice of nonlinear electrodynamics model, square root Lagrangian $\mathcal{L} = -\sqrt{F}$, the energy momentum tensor simplifies considerably

$${}^{\mathrm{NE}}T^{\mu}{}_{\nu} = diag\left\{-\frac{\sqrt{F}}{2}, -\frac{\sqrt{F}}{2}, 0, 0\right\}. \tag{8}$$

Since our spacetime is static and spherically symmetric, we assume this to hold for electromagnetic field as well and consider the following electromagnetic field two-form for purely magnetic field

$$\mathbf{F} = F_{\theta\phi}\,\mathrm{d}\theta \wedge \mathrm{d}\phi\,, \tag{9}$$

where $F_{\theta\phi} = q_m \sin\theta$ and q_m can be considered as a magnetic charge. All the modified Maxwell equations (the source–free nonlinear Maxwell equations are $\mathrm{d}\boldsymbol{F} = 0, \mathrm{d}(\mathcal{L}_F\,{}^*\boldsymbol{F}) = 0$, where ${}^*\boldsymbol{F}$ is a dual of electromagnetic two-form $\boldsymbol{F}$) are satisfied trivially. The electromagnetic invariant $F = F_{\mu\nu}F^{\mu\nu}$ becomes

$$F = \frac{2\,q_m^2}{R^4}\,. \tag{10}$$

We start to solve the coupled system by considering tt and rr components of Einstein equations (3), namely $G^t{}_t - G^r{}_r = T^t{}_t - T^r{}_r$ and we immediately obtain

$$\varphi_{,r}^2 = -\frac{2\,R_{,rr}}{R}. \tag{11}$$

From the above equation and (6) we are able to find f in terms of R

$$f = \sqrt{-\frac{C_0^2}{2\,R^3\,R_{,rr}}}\,. \tag{12}$$

The rest of Einstein equations will constrain the form of R. From $G^t{}_t - T^t{}_t = 0$, we get

$$f\left(\frac{R_{,r}}{R}\right)^2 + \frac{R_{,r}}{R}\,f_{,r} - \frac{1}{R^2} + f\,\frac{R_{,rr}}{R} + \frac{q_m}{\sqrt{2}}\frac{1}{R^2} = 0\,, \tag{13}$$

which together with (12) gives the following expressions for R, f and from (11) for the scalar field φ

$$R(r) = \sqrt{\beta^2\left(r+\tilde{C}_1\right)\left(r-\tilde{C}_2\right) - C_0^2} \times \exp\left(-\Omega(r)\right)\,, \tag{14}$$

$$f(r) = -\,\frac{e^{2\Omega(r)}}{\beta\,\sqrt{2}}\,, \tag{15}$$

$$\varphi(r) = \frac{2\,\sqrt{2}C_0}{\beta\left(\tilde{C}_1+\tilde{C}_2\right)}\,\Omega(r)\,, \tag{16}$$

where $\tilde{C}_1$ and $\tilde{C}_2$ are integration constants and we introduced parameters β, ρ and a function $\Omega(r)$ in the following way

$$\beta = \left(q_m - \sqrt{2}\right), \tag{17}$$

$$\rho = \sqrt{\beta^2\left(\tilde{C}_1+\tilde{C}_2\right)^2 + 4C_0^2}, \tag{18}$$

$$\Omega(r) = \frac{\beta\left(\tilde{C}_1+\tilde{C}_2\right)}{2\,\rho}\,\ln\left(\frac{r-r_0}{r-\tilde{r}_0}\right) \tag{19}$$

where $r_0 = \frac{1}{2}\left(\tilde{C}_2 - \tilde{C}_1 - \rho/\beta\right)$, $\tilde{r}_0 = r_0 + \rho/\beta$ and β should be negative for preserving the metric signature. After some simplifications, the equations (14) and (15) become

$$R(r) = \sqrt{\beta^2\,(r-r_0)\,(r-\tilde{r}_0)}\left[\frac{r-\tilde{r}_0}{r-r_0}\right]^{\frac{\nu}{2}}\,, \tag{20}$$

$$f(r) = -\,\frac{1}{\beta\,\sqrt{2}}\left[\frac{r-r_0}{r-\tilde{r}_0}\right]^{\nu}\,, \tag{21}$$

where $\nu = \frac{|\beta(\tilde{C}_1+\tilde{C}_2)|}{\rho} \geq 0$.

It is clear that f is vanishing at $r = r_0$ indicating horizon. Behavior of R is driven by the power of $(r - r_0)$, which is $\frac{\nu-1}{2}$. Depending on whether $\nu \lessgtr 1$, R would be zero, finite or diverge. Considering the definition for ρ from (18), it is clear that $\nu < 1$ if we have $C_0 \neq 0$ (nontrivial scalar field). Thus at $r = r_0$ the function R is vanishing and this location corresponds to a point instead of a sphere.

Note that since β is negative, $r_0 > \tilde{r}_0$. So at r_0 there is an outermost horizon and it is a candidate for the outer event horizon of a black hole but we need to see the behavior of Ricci scalar at $r = r_0$ to determine its regularity.

Ricci scalar with respect to our metric anzats (2) is

$$Ricci = -f_{,rr} - \frac{4}{R}\left(f R_{,r}\right)_{,r} - 2f\left(\frac{R_{,r}}{R}\right)^2 + \frac{2}{R^2} \tag{22}$$

and using (22), we obtain the following expression

$$Ricci \sim (r - r_0)^{\nu-2}\,.$$

Since $\nu < 1$ the Ricci scalar at $r = r_0$ is clearly diverging.

It is clear from (20) and (21) that it is difficult to obtain the metric function f in terms of R, for this reason we use a parametric plot for f in terms of R to see the behavior in terms of the areal radius which has better physical interpretation (see Fig. 1). The behavior is clearly monotonous and the curves for different β approach the location of curvature singularity at $R = 0$ smoothly.

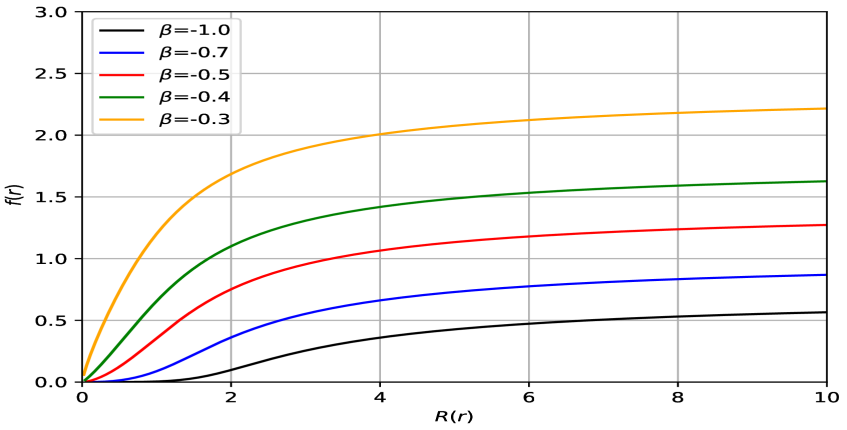

Figure 1. The metric function $f(r)$ in terms of $R(r)$ with different values of β.

So in our solution, the event horizon is also a true singularity which confirms the role of scalar field in spoiling horizon regularity even in this NE model. Since this is the stationary

state of geometry it shows that the no-hair theorem is valid in this case as well since we have not found black hole spacetime with both nongravitational fields being nontrivial.

The scalar field (16) becomes

$$\varphi(r) = \frac{\sqrt{2}C_0}{\rho} \ln\left[\frac{r - r_0}{r - \tilde{r}_0}\right] \tag{23}$$

and it is clear that at $r = r_0$, it diverges as well and the same applies to electromagnetic invariant (10) and therefore to NE energy momentum tensor (8).

The obtained solution, (20) and (21), is a NE generalization of Janis, Newmann and Winicour solution (Janis et al., 1968) and the original solution is recovered for $q_m = 0$ while as well setting $\tilde{C}_1 = \tilde{C}_2$.

If we consider a special case when the scalar field vanishes, $C_0 = 0$, then necessarily $\nu = 1$ and the solution in (20) and (21) will be equivalent to (Tahamtan, 2020) upon trivial changes in coordinates and constants.

If we assume that both $\tilde{C}_1$ and $\tilde{C}_2$ vanish then the form of the metric functions simplifies

$$R(r) = \sqrt{\beta^2 r^2 - C_0^2}\,, \tag{24}$$

$$f(r) = -\frac{1}{\beta\sqrt{2}}\,, \tag{25}$$

leading to spacetime containing timelike naked singularity. When q_m in β vanishes then the solution becomes equivalent to (Tahamtan and Svitek, 2016) with some trivial redefinition of coordinate r.

All the above mentioned solutions with nontrivial scalar field do not possess regular horizon. Although Maxwell theory and square root NE are significantly different since both their weak field limit and strong field behavior disagree, when coupled to scalar field they both produce singular horizon or naked singularity. This indicates dominant negative role of the scalar field in horizon formation. Note that there is crucial difference already for solutions without scalar field because square root model geometry (Tahamtan, 2020) only possesses single horizon compared to Reissner–Nordström solution which can have two and global asymptotics disagree as well. Nevertheless, the scalar field produces solutions with similar characteristic — singular horizons — in both cases.

3 GEODESIC MOTION

We study particle motion in order to understand the physical properties of the spacetime under consideration. We will use the variational principle and the Euler—Lagrange equations for timelike geodesics. The Lagrangian reduces to kinetic part only and has the following form

$$2L = -f\dot{t}^2 + \frac{\dot{r}^2}{f} + R^2\left(\dot{\theta}^2 + \sin\theta^2\,\dot{\phi}^2\right) \tag{26}$$

in which dot denotes the derivative with respect to the proper time τ. Because of spherical symmetry we study the particle motion in equatorial plane, so $\theta = \frac{\pi}{2}$. By using Euler–Lagrange equations we find two conserved quantities, E (energy) and l (orbital angular momentum), as expected for static and spherically symmetric spacetime which admits two Killing vectors $(\partial_t, \partial_\phi)$. The energy and angular momentum are given by

$$E = f\,\dot{t} \tag{27}$$

$$l = R^2\,\dot{\phi} \tag{28}$$

Substituting the above expressions into (26), we obtain equation for radial component of fourvelocity corresponding to timelike geodesic motion

$$\dot{r}^2 + V_{\text{eff}} = E^2 \tag{29}$$

where V_{eff} is the effective potential given by

$$V_{\text{eff}} = f\left(\frac{l^2}{R^2} + 1\right). \tag{30}$$

For plotting the effective potential, we consider the following values of constants: $C_0 = 1, \tilde{C}_1 = -3, \tilde{C}_2 = 1$. The only remaining constant parameter is β and we plot our graphs for its different values. Since the domain for β is $(-\infty, 0)$ the domain of $\nu = \frac{|\beta|}{\sqrt{\beta^2+1}}$ is $(0, 1)$. Because $\nu = 1$ is attained asymptotically for $\beta \to \infty$ more interesting changes in behavior happen for smaller β.

First, we plot the effective potential for zero angular momentum, $l = 0$, in this case the potential and the metric function f would be the same (30), see Fig. 2. When the absolute value of β is increasing the effective potential (metric function f) is decreasing. The zeros are the spacetime singularity points which appear at different r for different β but all correspond to $R(r) = 0$. This plot shows that the radially falling particle approaches singularity with velocity depending on the value of β.

Next, we plot the effective potential for $l = 1$ and different values of β (same as those used for $l = 0$ case), see Fig. 3. Here, similar to case when $l = 0$ the potential values are decreasing with increasing absolute value of β. As it is shown in the plot, for some values of β the effective potential character changes and one global minimum appears indicating stable circular orbits.

4 CONCLUSION AND FINAL REMARKS

We showed that static scalar field spacetime coupled to $\sim -\sqrt{F}$ Lagrangian which captures the strong field regime of many NE models (e.g., Born–Infeld) admits generalized solution of Janis–Newman–Winicour. Similar to all minimally coupled scalar field solutions, the spacetime has an irregular horizon which is in agreement with the Chase theorem. Our result and the previous ones show that the effect of scalar field on the spacetime geometry is dominant. Note that in the absence of scalar field, square root model Lagrangian solution represents a black hole solution with regular horizon.

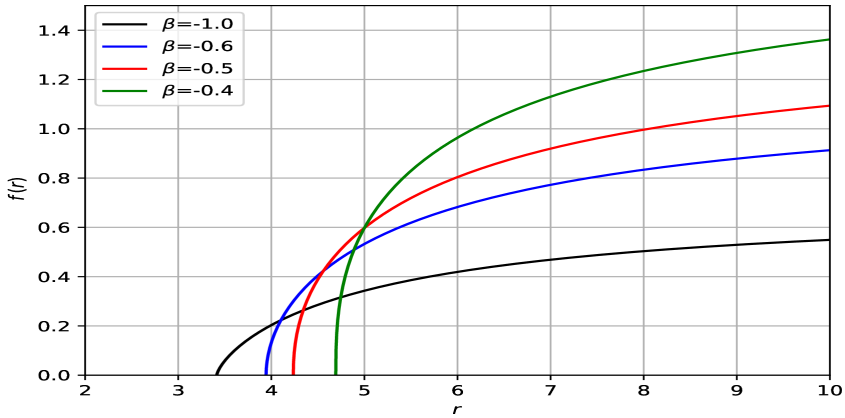

Figure 2. Effective potential V_{eff} for $l = 0$ and different values of β.

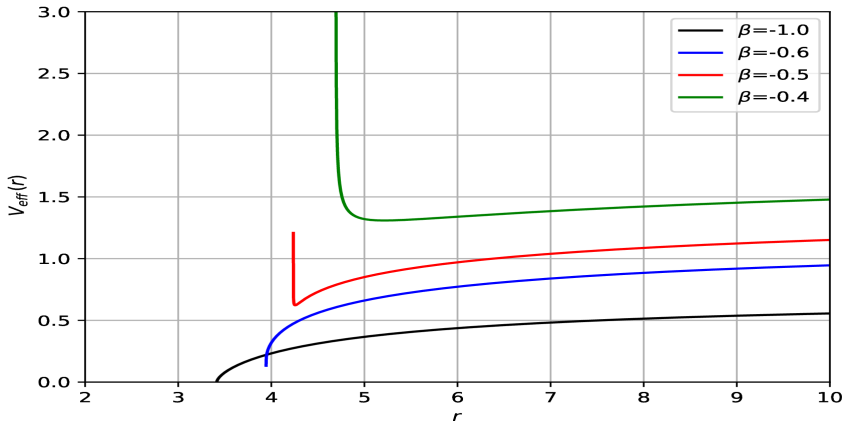

Figure 3. Effective potential V_{eff} for $l = 1$ and different values of β.

Furthermore, we studied timelike geodesic motion of a test particle. The obtained effective potential shows that for nonzero angular momentum and certain values of parameter β it is possible to have stable circular orbits. These stable circular orbits around singularity could give rise to disc configurations around the singularity and further study can give clear observational signatures such objects might exhibit.

In future, we will generalize this solution to massive scalar field with potentials.

ACKNOWLEDGEMENTS

This work was supported by the research grant GAČR 17-13525S.

REFERENCES

Banerjee, A. and Choudhury, S. B. D. (1977), Stationary axially symmetric coupled einstein-maxwell-scalar fields, *Phys. Rev. D*, **15**, pp. 3062–3064, URL https://link.aps.org/doi/10.1103/PhysRevD.15.3062.

Bergmann, O. and Leipnik, R. (1957), Space-time structure of a static spherically symmetric scalar field, *Phys. Rev.*, **107**, pp. 1157–1161, URL https://link.aps.org/doi/10.1103/PhysRev.107.1157.

Born, M. and Infeld, L. (1934), Foundations of the new field theory, *Proceedings of the Royal Society of London. Series A, Containing Papers of a Mathematical and Physical Character*, **144**, pp. 425–451.

Buchdahl, H. A. (1959), Reciprocal static metrics and scalar fields in the general theory of relativity, *Phys. Rev.*, **115**, pp. 1325–1328, URL https://link.aps.org/doi/10.1103/PhysRev.115.1325.

Chase, J. E. (1970), Event horizons in static scalar-vacuum space-times, *Communications in Mathematical Physics*, **19**(4), pp. 276–288, ISSN 1432-0916, URL https://doi.org/10.1007/BF01646635.

Eriş, A. and Gürses, M. (1977), Stationary axially-symmetric solutions of einstein–maxwell-massless scalar field equations, *Journal of Mathematical Physics*, **18**(7), pp. 1303–1304, arXiv: https://doi.org/10.1063/1.523419, URL https://doi.org/10.1063/1.523419.

Fisher, I. Z. (1948), Scalar mesostatic field with regard for gravitational effects, *Zh. Eksp. Teor. Fiz.*, **18**, pp. 636–640, arXiv: gr-qc/9911008.

Gaete, P. and Guendelman, E. (2006), Confinement from spontaneous breaking of scale symmetry, *Physics Letters B*, **640**(4), pp. 201 – 204, ISSN 0370-2693, URL http://www.sciencedirect.com/science/article/pii/S0370269306009671.

Herdeiro, C. A. R. and Radu, E. (2015), Asymptotically flat black holes with scalar hair: A review, *International Journal of Modern Physics D*, **24**(09), p. 1542014, arXiv: https://doi.org/10.1142/S0218271815420146, URL https://doi.org/10.1142/S0218271815420146.

Janis, A. I., Newman, E. T. and Winicour, J. (1968), Reality of the Schwarzschild Singularity, *Phys. Rev. Lett.*, **20**, pp. 878–880.

Janis, A. I., Robinson, D. C. and Winicour, J. (1969), Comments on einstein scalar solutions, *Phys. Rev.*, **186**, pp. 1729–1731.

Nielsen, H. and Olesen, P. (1973), Local field theory of the dual string, *Nuclear Physics B*, **57**(2), pp. 367 – 380, ISSN 0550-3213, URL http://www.sciencedirect.com/science/article/pii/0550321373901077.

Penney, R. (1969), Generalization of the reissner-nordström solution to the einstein field equations, *Phys. Rev.*, **182**, pp. 1383–1384, URL https://link.aps.org/doi/10.1103/PhysRev.182.1383.

Svitek, O. and Tahamtan, T. (2016), Ultrarelativistic boost with scalar field, *Gen. Rel. Grav.*, **48**(2), p. 22, arXiv: 1406.6334.

Svítek, O., Tahamtan, T. and Zampeli, A. (2020), Quantum fate of timelike naked singularity with scalar hair, *Annals Phys.*, **418**, p. 168195, arXiv: 1606.05635.

Tafel, J. (2014), Static spherically symmetric black holes with scalar field, *Gen. Rel. Grav.*, **46**, p. 1645, [Gen. Rel. Grav.46,1645(2014)], arXiv: 1112.2687.

Tahamtan, T. (2020), Scalar Hairy Black Holes in the presence of Nonlinear Electrodynamics, *Phys. Rev. D*, **101**(12), p. 124023, arXiv: 2006.02810.

Tahamtan, T. and Svitek, O. (2014), Resolution of curvature singularities from quantum mechanical and loop perspective, *Eur. Phys. J.*, **C74**(8), p. 2987, arXiv: 1312.7806.

Tahamtan, T. and Svitek, O. (2015), Robinson-Trautman solution with scalar hair, *Phys. Rev.*, **D91**(10), p. 104032, arXiv: 1503.09080.

Tahamtan, T. and Svitek, O. (2016), Properties of Robinson–Trautman solution with scalar hair, *Phys. Rev.*, **D94**(6), p. 064031, arXiv: 1603.07281.

Tahamtan, T. and Svitek, O. (2016), Robinson–Trautman solution with nonlinear electrodynamics, *Eur. Phys. J.*, **C76**(6), p. 335, arXiv: 1510.01183.

Tahamtan, T. and Svitek, O. (2017), Kundt spacetimes minimally coupled to scalar field, *Eur. Phys. J.*, **C77**(6), p. 384, arXiv: 1505.01791.

Teixeira, A. F. d. F., Wolk, I. and Som, M. M. (1974), Generalized static electromagnetic fields in relativity, *Journal of Mathematical Physics*, **15**(10), pp. 1756–1759, arXiv: https://doi.org/10.1063/1.1666538, URL https://doi.org/10.1063/1.1666538.

Teixeira, A. F. F., Wolk, I. and Som, M. M. (1976), On static electrovacs with scalar fields, *Journal of Physics A: Mathematical and General*, **9**(1), pp. 53–58.

Uhlíř, M. and Dittrich, J. (1973), Zero-mass scalar and electrostatic fields with the central symmetry in the general relativity, *Czechoslovak Journal of Physics B*, **23**, pp. 1–9, URL https://doi.org/10.1007/BF01596871.

Vasihoun, M. and Guendelman, E. (2014), Gravitational and topological effects on $\sqrt{-F^2}$ confinement dynamics, *International Journal of Modern Physics A*, **29**(23), p. 1430042.

Wyman, M. (1981), Static Spherically Symmetric Scalar Fields in General Relativity, *Phys. Rev.*, **D24**, pp. 839–841.

Proceedings of *RAGtime 20–22, 15–19 Oct., 16–20 Sept., 19–23 Oct., 2018/2019/2020, Opava, Czech Republic*
Z. Stuchlík, G. Török and V. Karas, editors, Silesian University in Opava, 2020, pp. 327–336

Construction of Taub-NUT black hole solutions in general relativity coupled to nonlinear electrodynamics

Bobir Toshmatov,[1,2,3,a] Sardor Tojiev[1]
and Jakhongir Xomidjonov[4]

[1]Ulugh Beg Astronomical Institute, Astronomy str. 33,
Tashkent 100052, Uzbekistan,
[2]Tashkent Institute of Irrigation and Agricultural Mechanization
Engineers, Kori Niyoziy 39, Tashkent 100000, Uzbekistan
[3]Webster University in Tashkent, Alisher Navoiy 13, Tashkent 100011, Uzbekistan
[4]Physics Department, Ferghana Polytechnical Institute, Ferghana str. 86,
Ferghana 150107, Uzbekistan
[a]toshmatov@astrin.uz

ABSTRACT
We present a formalism of construction of the Taub-NUT black hole (BH) solutions in general relativity (GR) coupled to the nonlinear electrodynamics (NED). We have shown that the constructed spacetimes can be electrically, magnetically or dyonically charged.

Keywords: Nonlinear electrodynamics – black holes – Taub-NUT spacetime

1 INTRODUCTION

It has been shown that the most general axially symmetric vacuum solution with separable equation of motion is the Kerr-NUT solution (Dadhich and Turakulov, 2002). Further it also turns out that the metric is invariant under the transformation $M \leftrightarrow il, r \leftrightarrow ia\lambda$, where λ is an angle coordinate. Under this duality transformation, it can interestingly be shown that Kerr solution is dual to massless Kerr-NUT solution (Nouri-Zonoz et al., 1999; Turakulov and Dadhich, 2001). The charged version of the general Kerr-NUT solution is the general Kerr-Newman-NUT solution, and this charge can only be electric and not magnetic. There is quite an extensive literature on NUT geometry in an attempt to understand its physical nature and properties. We would like to refer to an excellent review (Lynden-Bell and Nouri-Zonoz, 1998) critiquing all the earlier works as well as it makes a strong case for NUT parameter to be looked upon as gravomagnetic charge – a dual to gravoelectric charge mass. Of course it has a number of undesirable features such as it is not asymptotically flat and admits closed timelike curves. NUT parameter could by and large be considered as gravomagnetic charge (Mukherjee et al., 2019; Dadhich and Patel, 2002).

978-80-7510-432-8

In the present paper we aim to develop formalism for construction of black hole solutions in the GR coupled to the NED in the Taub-NUT framework. The first of all, we seek for the possibility if the dyonically charged, i.e., electrically and magnetically charged at the same time, solutions can be constructed in this framework. If there is no such possibility, we solve the field equations for the electrically and magnetically charged spacetimes separately. This paper is organised as follows: in section 2 we present the main equations of motion of the system GR coupled to the NED. In section 3 the construction of the black hole solutions in GR coupled to the linear electrodynamics is presented in the Taub-NUT framework, while section 4 is devoted to the construction of the static, axially symmetric electrically and magnetically charged black hole solution in GR coupled to the NED is presented. Finally, in section 5 we summarize the results obtained in the paper. Throughout the paper, we adopt the following signature convention $(-,+,+,+)$ for the space-time metric and make use of natural units, thus setting $c = \hbar = G = 1$.

2 BH SOLUTIONS COUPLED IN NED WITH NUT SYMMETRY

The action of Einstein's gravity coupled to the NED is given as

$$S = \frac{1}{16\pi}\int \mathrm{d}^4x\,\sqrt{-g}\,(R - L)\ , \tag{1}$$

where g is the determinant of the metric tensor $g_{\mu\nu}$, R is the scalar curvature, and L represents the Lagrangian density of the NED field that is function of the EM field strength, $L = L(F)$, with $F = F_{\mu\nu}F^{\mu\nu}$, where $F_{\mu\nu}$ is the EM field tensor that can be written in terms of a gauge potential A_μ as $F_{\mu\nu} = \partial_\mu A_\nu - \partial_\nu A_\mu$. Definition of the EM field tensor shows that $F_{\mu\nu}$ is anti-symmetric and it has only six independent components.

By neglecting the EM sources, one can write the covariant equations of motion in the form

$$G_{\mu\nu} = T_{\mu\nu}\ , \tag{2}$$

$$\nabla_\nu\,(L_F F^{\mu\nu}) = 0\ , \tag{3}$$

where the Einstein tensor $G_{\mu\nu} = R_{\mu\nu} - Rg_{\mu\nu}/2$ and $T_{\mu\nu}$ is the energy-momentum tensor of the EM field determined by the relation

$$T_{\mu\nu} = 2\left(L_F F^{\alpha}_{\mu}F_{\nu\alpha} - \frac{1}{4}g_{\mu\nu}L\right)\ , \tag{4}$$

where $L_F = \partial_F L$.

The line element of the static, axially symmetric Taub-NUT BH reads

$$\mathrm{d}s^2 = -\frac{\Delta}{\Sigma}\,(\mathrm{d}t - \chi\mathrm{d}\phi)^2 + \Sigma\left(\frac{\mathrm{d}r^2}{\Delta} + \mathrm{d}\theta^2\right) + \Sigma\sin^2\theta\mathrm{d}\phi^2\ , \tag{5}$$

where

$$\Delta = r^2 - 2m(r)r - l^2, \quad \Sigma = r^2 + l^2, \quad \chi = -2l\cos\theta,$$

The Carter tetrad of 1-forms for the spacetime matric (5) is written as (Znajek, 1977)

$$\begin{aligned}
&\omega^t = \sqrt{\frac{\Delta}{\Sigma}}(\mathrm{d}t - \chi \mathrm{d}\phi)\,, \quad \omega^r = \sqrt{\frac{\Sigma}{\Delta}}\mathrm{d}r\,, \\
&\omega^\theta = \sqrt{\Sigma}\mathrm{d}\theta\,, \quad \omega^\phi = \sqrt{\Sigma}\sin\theta \mathrm{d}\phi\,.
\end{aligned} \tag{6}$$

The non-zero components of the Einstein tensor are given by

$$\begin{aligned}
&G_{tt} = \frac{2r^2\Delta m'}{\Sigma^3}, \qquad G_{t\phi} = -\frac{2\chi r^2 \Delta m'}{\Sigma^3}, \\
&G_{rr} = -\frac{2r^2 m'}{\Sigma\Delta}, \qquad G_{\theta\theta} = -\frac{2l^2 m'}{\Sigma} - rm'', \\
&G_{\phi\phi} = \frac{2r^2\Delta m'}{\Sigma^3}\chi^2 - \left(\frac{2l^2 m'}{\Sigma} + rm''\right)\sin^2\theta.
\end{aligned} \tag{7}$$

Here we have the following relation among components of the Einstein tensor:

$$G_{\phi\phi} = G_{\theta\theta}\sin^2\theta + G_{tt}\chi^2\,. \tag{8}$$

One can easily notice that if the mass is constant, $m(r) = M$, then, the all the components vanish and we end up with the Schwarzschild Taub-NUT solution. Now we are going to obtain some solutions by coupling general relativity in Taub-NUT framework with NED which can be electrically or magnetically charged.

3 IN LINEAR ELECTRODYNAMICS

The linear electrodynamics is defined by the Maxwell theory which is characterized by the lagrangian density

$$L = F\,, \tag{9}$$

namely, $L_F = 1$. If the spacetime has electric charge Q_e and magnetic charge Q_m, in the linear electrodynamics the 4- potential of the EM field can be expressed by the 1-form of Carter tetrad (6) (Znajek, 1977) as

$$A = -\frac{Q_e r}{\sqrt{\Sigma\Delta}}\omega^t - \frac{Q_m\cot\theta}{\sqrt{\Sigma}}\omega^\phi, \tag{10}$$

i.e.,

$$A = -\frac{Q_e r}{\Sigma}(\mathrm{d}t - \chi\mathrm{d}\phi) - Q_m\cos\theta\mathrm{d}\phi. \tag{11}$$

3.1 Electrically charged spacetime

If we consider the spacetime is electrically charged, then the vector potential (11) takes the form:

$$A_\mu = -\frac{Q_e r}{\Sigma}\delta^t_\mu - \frac{2Q_e rl\cos\theta}{\Sigma}\delta^\phi_\mu, \tag{12}$$

Then, we have the following non-zero covariant components of the EM field tensor:

$$F_{tr} = \frac{Q_e\left(l^2-r^2\right)}{\Sigma^2}, \quad F_{r\phi} = \frac{2lQ_e\cos\theta\left(r^2-l^2\right)}{\Sigma^2},$$
$$F_{\theta\phi} = \frac{2lQ_e r\sin\theta}{\Sigma}\,. \tag{13}$$

The non-zero contravariant components of the EM field tensor are found by the relation $F^{\mu\nu} = g^{\alpha\mu}g^{\beta\nu}F_{\alpha\beta}$ and are given by:

$$F^{tr} = \frac{Q_e\left(r^2-l^2\right)}{\Sigma^2}, \quad F^{t\theta} = \frac{4l^2Q_e r\cot\theta}{\Sigma^3},$$
$$F^{\theta\phi} = \frac{2lQ_e r\csc\theta}{\Sigma^3}\,. \tag{14}$$

By combining covariant (13) and contravariant (14) Maxwell tensor, we obtain F as

$$F = -\frac{2Q_e^2\left(r^4-6l^2r^2+l^4\right)}{\Sigma^4}\,. \tag{15}$$

The nonvanoshing components of energy-momentum tensor are found from (4) as

$$T_{tt} = \frac{Q_e^2\Delta}{\Sigma^3}, \quad T_{t\phi} = -\frac{Q_e^2\chi\Delta}{\Sigma^3},$$
$$T_{rr} = -\frac{Q_e^2}{\Sigma\Delta}, \quad T_{\theta\theta} = \frac{Q_e^2}{\Sigma},$$
$$T_{\phi\phi} = \frac{Q_e^2}{\Sigma}\sin^2\theta + \frac{Q_e^2\Delta}{\Sigma^3}\chi^2\,, \tag{16}$$

Here we have an interesting relation

$$T_{\phi\phi} = T_{\theta\theta}\sin^2\theta + T_{tt}\chi^2\,. \tag{17}$$

that is symmetric counterpart of the relations in components of the Einstein tensor (8). Because of these symmetry, number of independent equations of the Einstein equations is decreased by one. Now by solving the Einstein equations (2) by using the non-zero componnets of Einstein tensor (7) and energy-momentum tensor of the electrically charged spacetime in linear electrodynamics (16), we obtain two differential equations $m' - Q_e^2/2r = 0$ and $m'' + Q_e^2/r^3 = 0$ which give the following general mass function:

$$m = M - \frac{Q_e^2}{2r}\,, \tag{18}$$

If we insert mass function (18) to the spacetime metric (5), it reduces to the electrically charged Reissner-Nordström-Taub-NUT solution.

3.2 Magnetically charged spacetime

If we consider the Taub-NUT spacetime (5) is magnetically charged in linear electrodynamics then, the 4-potential of the EM field is given as $A_\phi = -Q_m \cos\theta$. Then, only non-zero independent component of the EM tensor is $F_{\theta\phi} = Q_m \sin\theta$. And contravariant non-zero components of it are given as

$$F^{t\theta} = -\frac{Q\chi \csc\theta}{\Sigma^2} , \quad F^{\theta\phi} = \frac{Q \csc\theta}{\Sigma^2} . \tag{19}$$

The EM field strength or lagrangian density of Maxwell electrodynamics is

$$F = \frac{2Q_m^2}{\Sigma^2} , \tag{20}$$

The nonvanishing components of energy-momentum tensor are found from (4) and they are the same with the ones of the electrically charged case (16). Therefore, we will not repeat the calculations, instead we will give the final result which the mass function of the magnetically charged Taub-NUT solution in linear electrodynamics is given as

$$m = M - \frac{Q_m^2}{2r} , \tag{21}$$

and it represents the magnetically charged Reissner-Nordström-Taub-NUT solution in linear electrodynamics.

4 IN NONLINEAR ELECTRODYNAMICS

In this section we consider more general case which is construction of electrically and magnetically charged solution of general relativity coupled to the NED in Taub-NUT framework. The nonlinear electrodynamics is defined by the lagrangian density which is nonlinear function of EM field strength F, i.e.,

$$L_F \equiv \frac{\partial L}{\partial F} \neq \text{Constant.} \tag{22}$$

Construction of the electrically and magnetically charged, spherically symmetric, asymptotically flat solutions of general relativity coupled to the NED have been presented by several authors (Ayón-Beato and García, 1998; Bronnikov, 2000; Burinskii and Hildebrandt, 2002; Fan and Wang, 2016; Bronnikov, 2017; Toshmatov et al., 2018a,b,c). Here, for the first time we present the construction electrically and magnetically charged, axially symmetric, asymptotically non-flat (Taub-NUT) solution in general relativity coupled to the NED.

4.1 Electrically charged solution

In this subsection we present the construction of electrically charged, axially symmetric non-flat Taub-NUT solution in the NED. Let us generalize the vector potential (11) as

$$A = \psi(r)\frac{r^2}{\Sigma}(\mathrm{d}t - \chi \mathrm{d}\phi) . \tag{23}$$

Covariant components of the EM tensor

$$F_{tr} = -\frac{r^2\psi'}{\Sigma} - \frac{2l^2 r\psi}{\Sigma^2}\,, \quad F_{r\theta} = -\frac{r^2\psi'\chi}{\Sigma} - \frac{2l^2 r\psi\chi}{\Sigma^2},$$
$$F_{\theta\phi} = -\frac{2lr^2\psi\sin\theta}{\Sigma}, \tag{24}$$

Contravariant components of the EM tensor

$$F^{tr} = \frac{r^2\psi'}{\Sigma} + \frac{2l^2 r\psi}{\Sigma^2}, \quad F^{t\theta} = \frac{2lr^2\psi\chi\csc\theta}{\Sigma^3},$$
$$F^{\theta\phi} = -\frac{2lr^2\psi\csc\theta}{\Sigma^3}\,, \tag{25}$$

The EM field strength of the electrically charged spacetime of the NED in the Taub-NUT geometry is given by

$$F = -\frac{2r^2}{\Sigma^2}\left[r^2\psi'^2 + \frac{4l^2 r\psi\psi'}{\Sigma} + \frac{4l^2(l^2-r^2)\psi^2}{\Sigma^2}\right]. \tag{26}$$

From (4) one finds the non-zero components the energy-momentum tensor of the NED as

$$T_{tt} = \Delta\left[\frac{2r^2 L_F\left(2l^2\psi + r\Sigma\psi'\right)^2}{\Sigma^5} + \frac{L}{2\Sigma}\right],$$
$$T_{t\phi} = -\Delta\chi\left[\frac{2r^2 L_F\left(2l^2\psi + r\Sigma\psi'\right)^2}{\Sigma^5} + \frac{L}{2\Sigma}\right],$$
$$T_{rr} = -\frac{\Sigma^2}{\Delta}\left[\frac{2r^2 L_F\left(2l^2\psi + r\Sigma\psi'\right)^2}{\Sigma^5} + \frac{L}{2\Sigma}\right], \tag{27}$$
$$T_{\theta\theta} = \frac{8l^2 r^4 L_F\psi^2}{\Sigma^3} - \frac{1}{2}\Sigma L,$$
$$T_{\phi\phi} = \left[\frac{8l^2 r^4 L_F\psi^2}{\Sigma^3} - \frac{1}{2}\Sigma L\right]\sin^2\theta + \Delta\left[\frac{2r^2 L_F\left(2l^2\psi + r\Sigma\psi'\right)^2}{\Sigma^5} + \frac{L}{2\Sigma}\right]\chi^2,$$

Here again the relation (17) is satisfied. By substituting the Einstein (7) and energy-momentum (27) tensors into the Einstein equations (2), we obtain the following two independent equations:

$$\frac{2r^2 L_F\left(2l^2\psi + r\Sigma\psi'\right)^2}{\Sigma^3} - \frac{2r^2 m'}{\Sigma} + \frac{1}{2}\Sigma L = 0\,,$$
$$\frac{8l^2 r^4 L_F\psi^2}{\Sigma^3} + \frac{2l^2 m'}{\Sigma} - \frac{1}{2}\Sigma L + rm'' = 0\,, \tag{28}$$

By solving equations (28) with respect to L and L_F, simultaneously, we arrive at the expressions

$$L = \frac{2rm''\left(2l^2\psi + r\Sigma\psi'\right)^2}{\Sigma\left[4l^2r^2\psi^2 + (2l^2\psi + r\Sigma\psi')^2\right]} + \frac{4l^2m'\left[\left(2l^2\psi + r\Sigma\psi'\right)^2 + 4r^4\psi^2\right]}{\Sigma^2\left[4l^2r^2\psi^2 + (2l^2\psi + r\Sigma\psi')^2\right]}\,, \tag{29}$$

$$L_F = \frac{\Sigma^2\left[2\left(r^2 - l^2\right)m' - r\Sigma m''\right]}{2r^2\left[4l^2r^2\psi^2 + (2l^2\psi + r\Sigma\psi')^2\right]}\,, \tag{30}$$

Moreover, from the conservation of charge that is defined by $\mu = t$ in equation (3), one obtains the following relation:

$$\left[rL_F\left(\frac{2l^2\psi}{\Sigma} + r\psi'\right)\right]' + \frac{4l^2r^2L_F\psi}{\Sigma^2} = 0\,, \tag{31}$$

If $l = 0$ is considered, then we arrive at the conservation of charge in the spherically symmetric spacetimes in GR coupled to the NED (Toshmatov et al., 2018c)

$$\left(r^2L_F\psi'\right)' = 0\,. \tag{32}$$

4.2 Magnetically charged solution

In this subsection we consider construction of magnetically charged Taub-NUT solution in the NED. Nonzero components of the EM field tensor of the magnetically charged NED are $F_{\theta\phi} = Q_m \sin\theta = -F_{\phi\theta}$. The EM field strength is

$$F = \frac{2Q_m^2}{(r^2 + l^2)^2}\,, \tag{33}$$

From (4) one finds the non-zero components the energy-momentum tensor of the NED as

$$\begin{aligned} T_{tt} &= \frac{L\Delta}{2\Sigma}, \qquad T_{t\phi} = -\frac{L\Delta\chi}{2\Sigma}, \\ T_{rr} &= -\frac{L\Sigma}{2\Delta}, \qquad T_{\theta\theta} = \frac{2Q^2L_F}{\Sigma} - \frac{1}{2}L\Sigma, \\ T_{\phi\phi} &= \left(\frac{2Q^2L_F}{\Sigma} - \frac{1}{2}L\Sigma\right)\sin^2\theta + \frac{L\Delta\chi^2}{2\Sigma}. \end{aligned} \tag{34}$$

Here again we have the interesting relation (17). By substituting the Einstein (7) and energy-momentum (34) tensors into the Einstein equations (2), we obtain two independent equations

$$\frac{1}{2}\Sigma L - \frac{2r^2 m'}{\Sigma} = 0,$$
$$\frac{2Q_m^2 L_F}{\Sigma} - \frac{1}{2}\Sigma L + \frac{2l^2 m'}{\Sigma} + rm'' = 0, \tag{35}$$

By solving equations (35), we obtain

$$L = \frac{4r^2 m'}{\Sigma^2}, \tag{36}$$
$$L_F = \frac{2(r^2 - l^2)m' - r\Sigma m''}{2Q_m^2}, \tag{37}$$

If we assume that the EM field is linear, i.e., the Maxwell field, $L = F$ and $L_F = 1$, and NUT charge parameter is equal to zero, $l = 0$, then, by solving the above equations we arrive at the mass function $m = M - Q_m^2/2r$ that represents again the Reissner-Nordström solution which is the solution of the Einstein-Maxwell equations. If $l \neq 0$, it represents the Reissner-Nordström-Taub-NUT spacetimes.

4.3 Dyonically charged solution

As in the previous subsections we have shown that the electrically and magnetically charged solutions can be obtained in GR coupled to the NED in the static spacetime with NUT symmetry, in the current subsection we consider if it is possible to construct the spacetime admitting both charges at the same time. To do so, we must solve the field equations (2) and (3) for the line element of the spacetime (5) with the 4-electromagnetic potential (11). Due to the cumbersome forms of equations, we do not report them here, but instead, we only present the results. Thus, solving the Einstein field equations, we obtain that to have the dyonically charged spacetime in GR coupled to the NED with NUT symmetry, the Lagrangian density of the NED must be related to the mass function of the spacetime via the following expressions:

$$L = \frac{2r^2 (Am' + Bm'')}{\Sigma^3 \left[\Sigma \left(Q_m^2 + r^4\psi'^2\right) + 4l^2 r^2 \psi^2 + 4lr^2\psi \left(lr\psi' - Q_m\right)\right]}, \tag{38}$$
$$L_F = \frac{2\left(r^4 - l^4\right)m' - r\Sigma^2 m''}{2\left[\Sigma \left(Q_m^2 + r^4\psi'^2\right) + 4l^2 r^2 \psi^2 + 4lr^2\psi \left(lr\psi' - Q_m\right)\right]} \tag{39}$$

where

$$A = 2\left[\Sigma^2\left(l^2 r^2 \psi'^2 + Q_m^2\right) + 4l^2\left(l^4 + r^4\right)\psi^2 + 4lr\Sigma\psi\left(l^3\psi' - Q_m r\right)\right],$$
$$B = r\Sigma\left(r\Sigma\psi' + 2l^2\psi\right)^2,$$

Moreover, from the conservation of charge that is defined by $\mu = t$ in equation (3), one obtains the following relation:

$$\left[rL_F\left(\frac{2l^2\psi}{\Sigma} + r\psi'\right)\right]' - \frac{2l\left(Q_m\Sigma - 2lr^2\psi\right)}{\Sigma^3} = 0\,, \tag{40}$$

If $l = 0$ is considered, then we again arrive at the conservation of charge in the spherically symmetric spacetimes in GR coupled to the NED (32) and it confirms the pioneering results in (Demianski et al., 1986; Mazharimousavi and Halilsoy, 2012). In the linear electrodynamics ($L_F = \text{const}$), that would give us the well-known Coulomb's potential $\psi = Q_e/r$.

5 CONCLUSION

In the present paper we demonstrated the formalism for construction of axially symmetric, static, asymptotically non-flat black hole solutions in GR coupled to the NED in the Taub-NUT framework. The presented formalism is easy to handle as by switching off the NUT parameter of the spacetime, one can smoothly turn to the spherically symmetric, asymptotically flat counterparts of the spacetimes, or by turning off the charge parameter, one can recover the well-known solutions of the GR coupled to the NED or linear electrodynamics. The formalism has shown that in the Taub-NUT framework the electrically, magnetically and dyonically charged spacetime can be constructed.

ACKNOWLEDGEMENTS

The present work was supported by Uzbekistan Ministry for Innovation Development Grants No. VA-FA-F-2-008 and No. MRB-AN2019-29.

REFERENCES

Ayón-Beato, E. and García, A. (1998), Regular Black Hole in General Relativity Coupled to Nonlinear Electrodynamics, *Phys. Rev. Lett.*, **80**, pp. 5056–5059, arXiv: gr-qc/9911046.

Bronnikov, K. A. (2000), Comment on "Regular Black Hole in General Relativity Coupled to Nonlinear Electrodynamics", *Phys. Rev. Lett.*, **85**, p. 4641.

Bronnikov, K. A. (2017), Comment on "Construction of regular black holes in general relativity", *Phys. Rev. D*, **96**(12), 128501, arXiv: 1712.04342.

Burinskii, A. and Hildebrandt, S. R. (2002), New type of regular black holes and particlelike solutions from nonlinear electrodynamics, *Phys. Rev. D*, **65**(10), 104017, arXiv: hep-th/0202066.

Dadhich, N. and Patel, L. K. (2002), A curious electrovac spacetime as $G = 0$ limit of the NUT space, *arXiv e-prints*, gr-qc/0208064, arXiv: gr-qc/0208064.

Dadhich, N. and Turakulov, Z. Y. (2002), The most general axially symmetric electrovac spacetime admitting separable equations of motion, *Classical and Quantum Gravity*, **19**(11), pp. 2765–2775, arXiv: gr-qc/0112031.

Demianski, M., Rasband, S. N. and Corben, H. C. (1986), Book review, *Foundations of Physics*, **16**(8), pp. 839–845.

Fan, Z.-Y. and Wang, X. (2016), Construction of regular black holes in general relativity, *Phys. Rev. D*, **94**(12), 124027, arXiv: 1610.02636.

Lynden-Bell, D. and Nouri-Zonoz, M. (1998), Classical monopoles: Newton, NUT space, gravomagnetic lensing, and atomic spectra, *Rev. Mod. Phys.*, **70**(2), pp. 427–445, arXiv: gr-qc/9612049.

Mazharimousavi, S. H. and Halilsoy, M. (2012), 'Square root' of the Maxwell Lagrangian versus confinement in general relativity, *Phys. Lett. B*, **710**(3), pp. 489–492, arXiv: 1201.2321.

Mukherjee, S., Chakraborty, S. and Dadhich, N. (2019), On some novel features of the Kerr-Newman-NUT spacetime, *Eur. Phys. J. C*, **79**(2), 161, arXiv: 1807.02216.

Nouri-Zonoz, M., Dadhich, N. and Lynden-Bell, D. (1999), A spacetime dual to the NUT spacetime, *Classical and Quantum Gravity*, **16**(3), pp. 1021–1026, arXiv: gr-qc/9812042.

Toshmatov, B., Stuchlík, Z. and Ahmedov, B. (2018a), Comment on "Construction of regular black holes in general relativity", *Phys. Rev. D*, **98**(2), 028501, arXiv: 1807.09502.

Toshmatov, B., Stuchlík, Z. and Ahmedov, B. (2018b), Electromagnetic perturbations of black holes in general relativity coupled to nonlinear electrodynamics: Polar perturbations, *Phys. Rev. D*, **98**(8), 085021, arXiv: 1810.06383.

Toshmatov, B., Stuchlík, Z., Schee, J. and Ahmedov, B. (2018c), Electromagnetic perturbations of black holes in general relativity coupled to nonlinear electrodynamics, *Phys. Rev. D*, **97**(8), 084058, arXiv: 1805.00240.

Turakulov, Z. Y. and Dadhich, N. (2001), A Stationary Vacuum Solution Dual to the Kerr Solution, *Mod. Phys. Lett. A*, **16**(30), pp. 1959–1962, arXiv: gr-qc/0106042.

Znajek, R. L. (1977), Black hole electrodynamics and the Carter tetrad., *Mon. Not. R. Astron. Soc.*, **179**, pp. 457–472.

Proceedings of *RAGtime 20–22, 15–19 Oct., 16–20 Sept., 19–23 Oct., 2018/2019/2020, Opava, Czech Republic*
Z. Stuchlík, G. Török and V. Karas, editors, Silesian University in Opava, 2020, pp. 337–342

On magnetized orbits around Schwarzschild black hole

Bobur Turimov,[1,2,a] Bobir Toshmatov[2,3,4] and Zdeněk Stuchlík[1]

[1]Research Centre for Theoretical Physics and Astrophysics, Institute of Physics, Silesian University in Opava, Bezručovo nám. 13, CZ-74601 Opava, Czech Republic
[2]Ulugh Beg Astronomical Institute, Astronomy str. 33, Tashkent 100052, Uzbekistan
[3]Webster University in Tashkent, Alisher Navoiy 13, Tashkent 100011, Uzbekistan
[4]Tashkent Institute of Irrigation and Agricultural Mechanization Engineers, Kori Niyoziy 39, Tashkent 100000, Uzbekistan
[a]F180340@fpf.slu.cz

ABSTRACT
We study circular orbits of magnetized particle around Schwarzschild black hole immersed in the uniform magnetic field. Despite the topic overlaps with the one of [Classical and Quantum Gravity **20**, 469 (2003)], our calculations complement it by correcting effective potential of the magnetized particle presented in it. As a rule, the effective potential is independent of the energy of test particle. We briefly demonstrate the formalism and present qualitative picture on the effect of the magnetic coupling parameter on innermost stable circular orbits.

Keywords: Schwarzschild spacetime – magnetized particle – innermost stable circular orbit

In the paper (de Felice and Sorge, 2003), the circular orbits of a particle with mass m possessing magnetic dipole momentum $\boldsymbol{\mu}$ around Schwarzschild black hole with mass M immersed in the asymptotically uniform magnetic field $\boldsymbol{B}$ that is perpendicular to the orbital plane was studied. In this paper we refine the results presented in that paper by addressing the problem associated with that effective potential of the magnetized particle. For the reader's sake, prior to attracting one's attention to the problem, we aim to address, we here briefly highlight the main equations presented in the paper (de Felice and Sorge, 2003), till we reach the problem. As a starting point, let us choose the Hamilton-Jacobi equation for the uncharged and spinless particle, but still possessing the magnetic dipole moment in the following form (de Felice and Sorge, 2003):

$$g^{\mu\nu}p_\mu p_\nu - mD^{\mu\nu}F_{\mu\nu} + m^2 = 0\,, \tag{1}$$

where p_μ is the four-momentum and m is mass of the test particle. The explicit form of the product of polarization tensor $D_{\mu\nu}$ and the electromagnetic field tensor $F_{\mu\nu}$ has shown as

$$D^{\mu\nu}F_{\mu\nu} = 2\mu_\alpha B^\alpha = 2\mu_{\hat{\alpha}}B^{\hat{\alpha}} = -\mathcal{U} \ll m\,. \tag{2}$$

After introducing the new definitions for the radial coordinate r, energy E, angular momentum L, and magnetic parameter:

$$\rho = \frac{r}{2M}\,, \quad \lambda = \frac{L}{2mM}\,, \quad \gamma = \frac{E}{m}\,, \quad \beta = \frac{2\mu B_0}{m}\,, \tag{3}$$

the authors derived the equation for the radial motion in the form (de Felice and Sorge, 2003)

$$4M^2\left(\frac{\mathrm{d}\rho}{\mathrm{d}\tau}\right)^2 = \gamma^2 - V(\rho;\lambda,\gamma,\beta)\,, \tag{4}$$

where τ is the proper time along particle trajectory and the effective potential $V(\rho;\lambda,\gamma,\beta)$ is defined as (de Felice and Sorge, 2003)

$$V(\rho;\lambda,\gamma,\beta) = \left(1-\frac{1}{\rho}\right)\left[1+\frac{\lambda^2}{\rho^2} - \frac{\beta\left(1-\frac{1}{\rho}\right)}{\sqrt{1-\frac{1}{\rho}-4M^2\Omega^2\rho^2}}\right]. \tag{5}$$

where Ω is the angular velocity, measured by a distant observer often called Keplerian frequency, defined as

$$\Omega = \frac{d\phi}{dt} = \frac{u^\phi}{u^t} = \frac{\lambda}{2M\gamma}\frac{\rho-1}{\rho^3}\,. \tag{6}$$

Finally, we arrived at the point where we think the problem is. Indeed, eq. (5) reproduces the effective potential for the neutral particle in the field of the Schwarzschild black hole, if the magnetic coupling is neglected ($\beta = 0$). In the Ref. (de Felice and Sorge, 2003), the authors aimed to discover the effect of the magnetic interaction parameter, β, on the circular motion of the particle. To do so, finding the correct form of the effective potential is crucial, as it is a problem of motion in the central field. As a rule, the effective potential in equation (4) should not depend on the specific energy of the particle. However, if one applies expression of the angular velocity of the particle (6) into the effective potential (5), the effective potential will depend on the specific energy of the particle, as in the case of the paper (de Felice and Sorge, 2003), that contradicts the rule. As proof of that, analogously it is enough to show that the Keplerian frequency (6) is independent of the specific energy (actually, in general, it is independent of both the specific energy and specific angular momentum of the test particle). Therefore, in order to escape from this contradiction, we propose the following procedure:

- In the circular orbit, the particle's four-velocity is given as $u^\mu = (u^t, 0, 0, u^\phi)$ and from the normalization condition of the four-velocity $u_\mu u^\mu = -1$ we obtain

$$u^t = \frac{1}{\sqrt{-g_{tt} - \Omega^2 g_{\phi\phi}}} = \frac{1}{\sqrt{1-\frac{1}{\rho}-4M^2\Omega^2\rho^2}}\,. \tag{7}$$

- On the other hand, since motion of the particle with magnetic momentum in the external magnetic field does not follow the geodesics, by using the (radial) non-geodesic equation for magnetized particle proposed in (Preti, 2004)

$$\frac{D}{D\tau}\left[(m+\mathcal{U})u^{\alpha}\right] = -\mathcal{U}^{,\alpha}\,, \tag{8}$$

we find the following relation:

$$\frac{g_{tt,r}+\Omega^2 g_{\phi\phi,r}}{g_{tt}+\Omega^2 g_{\phi\phi}} = -\frac{2\mathcal{U}_{,r}}{m+\mathcal{U}}\,, \tag{9}$$

where sub-index $_{,\alpha}$ indicates the derivative with respect to coordinate x^{α}. Note that in the derivation of equation (9), u^t is eliminated by using equation (7). Hereafter, applying simple algebraic operations, one can obtain the explicit expression of the angular velocity of the magnetized particle in the circular orbit in the following form:

$$\Omega = \sqrt{-\frac{g_{tt,r}+2g_{tt}\ln(m+\mathcal{U})_{,r}}{g_{\phi\phi,r}+2g_{\phi\phi}\ln(m+\mathcal{U})_{,r}}}\,. \tag{10}$$

One can see from expression (10) that the Keplerian frequency depends only on the space-time metric and interaction potential, $\mathcal{U}$. In the absence of the interaction term, $\mathcal{U}=0$ or $\mu=0$, the angular velocity of the magnetized particle in the circular orbit, (10), reduces to the well-known Keplerian frequency of the neutral test particle in the Schwarzschild spacetime, $\Omega_0 = \sqrt{-g_{tt,r}/g_{\phi\phi,r}} = \sqrt{M/r^3}$.

On the other hand, one has to keep in mind that the interaction potential $\mathcal{U}$ is a function of Ω (See, for example: (de Felice and Sorge, 2003)):

$$\mathcal{U} = \beta\frac{mg_{tt}}{\sqrt{-g_{tt}-\Omega^2 g_{\phi\phi}}} = \beta U(\rho,\beta)\,, \tag{11}$$

and Ω is itself function of magnetic parameter from equation (10).

Before go on further let us introduce the normalized interaction potential $\mathcal{U}\to\mathcal{U}/m$. Now we first find Ω from equation (11) then substitute it into equation (9), and taking into account $\mathcal{U}\ll m$, one can have the following differential equation:

$$2\mathcal{U}_{,r} = -\frac{g_{\phi\phi,r}}{g_{\phi\phi}} - \frac{\mathcal{U}^2}{\beta^2 g_{tt}}\left(\frac{g_{\phi\phi,r}}{g_{\phi\phi}} - \frac{g_{tt,r}}{g_{tt}}\right)\,, \tag{12}$$

or using equations (11) and (3), one can have

$$\beta U_{,\rho} = -\frac{1}{\rho} + \frac{(2\rho-3)}{2(\rho-1)^2}U^2\,. \tag{13}$$

Unfortunately, it is difficult to get an analytical solution for equation (13), however, one can use perturbation in order to obtain a semi-analytical solution for U at least in linear

order approximation. Then new interaction potential U can be expanded in the power of β parameter as

$$U(\rho,\beta) = U_0(\rho) + \beta U_1(\rho) + ... \tag{14}$$

Substituting it into equation (13), hereafter performing simple algebra one can obtain $U_i(\rho)$ in the form:

$$U_0(\rho) = \left(1-\frac{1}{\rho}\right)\left(1-\frac{3}{2\rho}\right)^{-1/2}, \tag{15}$$

$$U_1(\rho) = \frac{(\rho-1)^2}{(2\rho-3)}\frac{U_0'(\rho)}{U_0(\rho)} = \frac{(\rho-3)(\rho-1)}{2(3-2\rho)^2\rho}. \tag{16}$$

Finally, in linear approximation of β parameter, the effective potential for magnetized particle can be written as

$$V(\rho) = \left(1-\frac{1}{\rho}\right)\left[1+\frac{\lambda^2}{\rho^2}+\beta\left(1-\frac{1}{\rho}\right)\left(1-\frac{3}{2\rho}\right)^{-1/2}\right]. \tag{17}$$

As it is seen, the effective potential for the magnetized particle moving in the field of the Schwarzschild black hole immersed in the uniform magnetic field significantly different from the one presented in (de Felice and Sorge, 2003). Even from this point, one can say that the characteristic circular orbits, such as marginally (i.e., innermost or outermost) stable circular orbits evaluated from the effective potential (17) are different from the ones presented in (de Felice and Sorge, 2003). To estimate these differences quantitatively, let us study one of the most important characteristic circular orbits, such as innermost stable circular orbits. The stability of the circular orbits is guaranteed by the non-negativity of the second derivative of the effective potential with respect to the radial coordinate. If the equality holds then, the solutions of this equation give the innermost stable circular orbits. As this equation has cumbersome form in our case and the solutions cannot be written analytically, we decided to present it in the following form:

$$\beta = -\frac{4\sqrt{2}(\rho-3)\sqrt{\rho}(2\rho-3)^{3/2}}{\rho[5\rho(4\rho-21)+174]-81}, \tag{18}$$

One can easily notice from eq. (18) that in the absence of the magnetic coupling of parameter ($\beta = 0$), one recovers the radius of ISCO of the neutral particle around Schwarzschild black hole ($\rho = 3$). Moreover, in Fig. 1 we demonstrate the dependence of the ISCO radius from the magnetic coupling parameter. One can see from Fig. 1 that for negative values of the magnetic coupling parameter, the stable circular orbits of the magnetized particle are located very far from the black hole, i.e., negative values of the magnetic coupling parameter increases the radius of ISCO. As figure shows, the radius of the ISCO diverges for β tends to -0.8 from right side, $\beta \to -0.8_+$. Thus, from this property we determine that for the existence of the ISCO, the minimum value of the magnetic coupling parameter

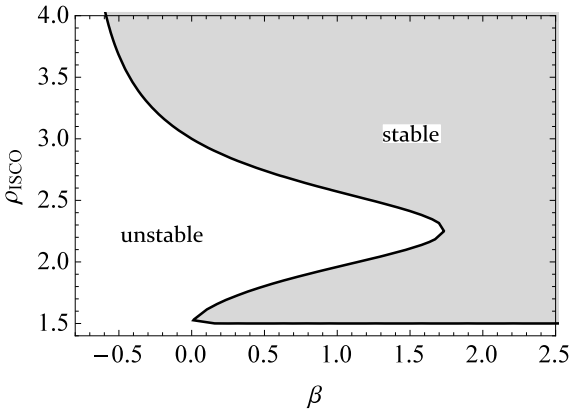

Figure 1. Dependence of the ISCO radius from the magnetic coupling parameter. Where shaded and white regions represent the ones that the stable and unstable circular orbits occupy, respectively.

is $\beta_{min} = -0.8$. On the other hand, for the existence of the ISCO, positive values of β is also restricted. This maximum value is $\beta_{max} = 1.7329$ at which the ISCO is located at $\rho_{\rm ISCO} = 2.2587$. If the value $\beta > \beta_{max}$, the stable circular orbits can exist anywhere of the spacetime outside photonspehere ($\rho > 1.5$).

In this paper, we have presented guidelines on how to derive the effective potential for the magnetized particle orbiting around the Schwarzschild black hole in the presence of the external uniform magnetic field. One has to emphasize that in Ref. (de Felice et al., 2004) the same problem but in the Kerr, spacetime was solved by using the same approach. Later, in Refs. (Preti and de Felice, 2005, 2006) the same approach was applied for the magnetized particle motion around the Schwarzschild and Kerr black holes in the presence of the dipole magnetic field. Now we think that it makes sense if scenarios considered in the papers (de Felice et al., 2004; Preti and de Felice, 2005, 2006) can be recalculated by the method we presented and make comparison with the results shown in them. We keep that calculations for our near future projects.

ACKNOWLEDGEMENTS

This research is supported by the internal student grant SGS/12/2019 of Silesian University in Opava.

REFERENCES

de Felice, F. and Sorge, F. (2003), Magnetized orbits around a Schwarzschild black hole, *Classical and Quantum Gravity*, **20**(3), pp. 469–481.

de Felice, F., Sorge, F. and Zilio, S. (2004), Magnetized orbits around a Kerr black hole, *Classical and Quantum Gravity*, **21**(4), pp. 961–973.

Preti, G. (2004), General relativistic dynamics of polarized particles in electromagnetic fields, *Phys. Rev. D*, **70**(2), 024012.

Preti, G. and de Felice, F. (2005), Magnetically induced confinement nearby a Schwarzschild black hole, *Phys. Rev. D*, **71**(2), 024009.

Preti, G. and de Felice, F. (2006), Magnetically induced confinement near a Kerr black hole, *Classical and Quantum Gravity*, **23**(3), pp. 955–970.

Proceedings of *RAGtime 20–22, 15–19 Oct., 16–20 Sept., 19–23 Oct., 2018/2019/2020, Opava, Czech Republic*
Z. Stuchlík, G. Török and V. Karas, editors, Silesian University in Opava, 2020, pp. 343–350

Neutron stars with quark cores

Martin Urbanec[1a] and Martin Fuzik[1]

[1]Research Centre for Computational Physics and Data Processing,
Institute of Physics, Silesian University in Opava,
Bezručovo nám. 13, CZ-746 01 Opava, Czech Republic
[a]martin.urbanec@physics.slu.cz

ABSTRACT
We investigate physical conditions under which nuclear matter may cross to quark matter using several equations of state for both phases. We calculate the combined equation of state using the nuclear matter equation of state for low-density region and the quark matter equation of state for the high-density region using Maxwell construction. Then we use it to calculate properties of non-rotating compact stars with quark cores and hadronic surface. We focus primarily on the maximum mass of a non-rotating star and on the moment of inertia of quark core for different combinations of selected equations of state. This work is the starting point for future investigation of rotating neutron stars with quark cores.

Keywords: Neutron stars – phase transitions – hybrid stars

1 INTRODUCTION

Neutron stars are the densest objects with internal structure currently known to exist in the Universe. Their structure is governed by general relativity and nuclear physics of very dense matter (densities in the cores of neutron stars can reach values several times higher than standard nuclear matter density). The matter in the cores of neutron stars is in the standard picture composed of neutrons, protons, and electrons in β-equilibrium, however, at sufficiently high densities the matter can undergo the phase transition to deconfined quarks.

Phase transitions in neutron stars are of huge interest since they can affect the global properties of neutron stars like the neutron star mass M, radius R moment of inertia I or the Love numbers Λ. For the current status of phase transition in compact stars see the recent overview by Blaschke and Chamel (2018).

Since phase transition to quark matter corresponds to the transition to a form of matter that is energetically preferable at high densities, it leads to the softening of the equation of state in that region. Equation of state with phase transition describing hybrid stars should therefore allow for the maximum mass that is smaller than the maximum mass allowed by the hadronic equation of state without phase transition. Therefore observations of massive neutron stars constrain the hadronic equation of state even if it does not describe the whole interior of the observed star. Currently, the most massive neutron stars known are $M = 2.01 \pm 0.04 M_\odot$ by Antoniadis et al. (2013) and $M = 1.97 \pm 0.04$ by Demorest et al.

978-80-7510-432-8

(2010) that are both in a binary system with a white dwarf, and massive enough to put serious constraints on the equation of state of neutron star matter. Other observational constraints on equations of state with phase transition have been discussed also by Kurkela et al. (2014) who shown that constraints from neutron star observations on the equation of state of neutron star matter are insensitive to the size of quark matter core. The maximum mass of neutron stars with quark cores was also discussed by other authors - see e.g. Zdunik and Haensel (2013).

In this short presentation, we focus on simple calculations using several equations of state of hadronic matter and for each, we calculate the physical conditions of Maxwell phase transition to simple MIT Bag model with various values of bag constant. We calculate non-rotating models of compact stars with quark core and focus on mass-radius relation, on maximum mass, and on the moment of inertia of quark core.

2 MODEL

2.1 Equations of state

Hadronic EoS: In our presentation we use selection of representative hadronic equations of state namely APR (Akmal et al., 1998), FPS (Lorenz et al., 1993), Gandolfi (Gandolfi et al., 2010), KDE (Agrawal et al., 2005), NRAPR (Steiner et al., 2005), SLy4 Rikovska Stone et al. (2003), and UBS (Urbanec et al., 2010). Each of these equations of state is composed of an equation of state describing nuclear matter composed of neutrons, protons, electrons, and muons in β-equilibrium based on various theoretical models of nucleon-nucleon interaction and are matched to a standard set of equations of state describing the low-density region, where the matter is composed of stable atomic nuclei or free neutrons in equilibrium with nuclei (Baym et al., 1971).

Quark EoS: We assume the quark core to consist of mass-less u and d quarks. To describe quark matter we use MIT Bag model (Chodos et al., 1974; Farhi and Jaffe, 1984; Haensel et al., 1986) where pressure P is related to energy density ρ by

$$P = \frac{1}{3}(\rho - 4B), \tag{1}$$

where B is Bag constant that gives energy density corresponding to zero pressure $\rho_0 = 4B$. The factor $1/3$ can be related to sound speed of quark matter $v_\mathrm{s} = c\sqrt{\mathrm{d}P/\mathrm{d}\rho} = c/\sqrt{3}$. The baryon number density is given as

$$n_\mathrm{B} = \left[\frac{4(1-2\alpha_\mathrm{c}/\pi)^{1/3}}{9\pi^{2/3}\hbar}(\rho - B)\right]^{3/4}, \tag{2}$$

where α_c is strong interaction coupling constant. Chemical potential per baryon is given by

$$\mu_\mathrm{B} = \frac{\rho + P}{n_\mathrm{B}}. \tag{3}$$

In our calculations we take $\alpha_\mathrm{c} = 0$ and for bag constant we choose six different values $B = \{2; 2.5; 3; 3.5; 4; 4.5\} \times 10^{14}\mathrm{g.cm}^{-3}$.

Phase transition For all possible combinations of hadronic EoS and quark EoS, we calculate pressure and baryonic chemical potential of the phase transition using Maxwell construction, i.e. the resulting EoS has continuous chemical potential as a function of pressure $\mu_{\rm B} = \mu_{\rm B}(P)$. Phase transition takes place at pressure $P_{\rm pt}$ and baryonic chemical potential $\mu_{\rm pt}$ that is calculated for each combination of the hadronic equation of state and quark equation of state from our selection. The same approach to model the phase transition was used e.g. by Benić et al. (2015) or by Alvarez-Castillo et al. (2019) where they used more advanced quark EoS based on QCD and used relativistic mean-field model EoS of hadronic matter.

Compact star models Global properties of non-rotating compact stars are given by differential equations of hydrostatic equilibrium - TOV equation (Tolman, 1939; Oppenheimer and Volkoff, 1939)

$$\frac{{\rm d}P}{{\rm d}r} = -\frac{(\rho + P)\left[m(r) + 4\pi r^3 P\right]}{r\left[r - 2m\left(r\right)\right]}, \tag{4}$$

where $m(r)$ is mass inside a sphere of radius r and is given by

$$\frac{{\rm d}m(r)}{{\rm d}r} = 4\pi\rho r^2. \tag{5}$$

The set of differential equation is solved for given value of central pressure. Equations are integrated while the pressure remains positive and the radius r where pressure vanishes is giving the surface of compact star, i.e. $P(R) = 0$ with R being the radius of the compact star. Mass is given by $M = m(R)$. We also calculate moment of inertia of the star $I_{\rm tot}$ given by (Hartle, 1967)

$$I_{\rm tot} = -\frac{2}{3}\int_0^R r^3 \left(\frac{{\rm d}j}{{\rm d}r}\right)\left(\frac{\tilde{\omega}}{\Omega}\right){\rm d}r, \tag{6}$$

where Ω is angular velocity of the star and j is given by $j = 1/\sqrt{-g_{rr}g_{tt}}$. The function $\tilde{\omega}$ is found by solving equation

$$\frac{1}{r^4}\frac{\rm d}{{\rm d}r}\left(r^4 j\frac{{\rm d}\tilde{\omega}}{{\rm d}r}\right) + \frac{4}{r}\frac{{\rm d}j}{{\rm d}r}\tilde{\omega} = 0. \tag{7}$$

One can find a moment of inertia of the quark core $I_{\rm core}$ by performing the integral in eq. (6) to $r_{\rm pt} = r(P = P_{\rm pt})$ instead performing the integral to the surface where $r = R$.

3 RESULTS AND DISCUSSION.

We solved the structure equations described in the previous section to obtain mass, radius, a moment of inertia of the whole star, and the moment of inertia of the quark core as a function of central pressure. At first, we solved the problem for purely hadronic equations of state and we present the mass-radius relation on the left panel of Fig. 1. The results when we assumed only quark matter described by the MIT Bag model is presented on the right

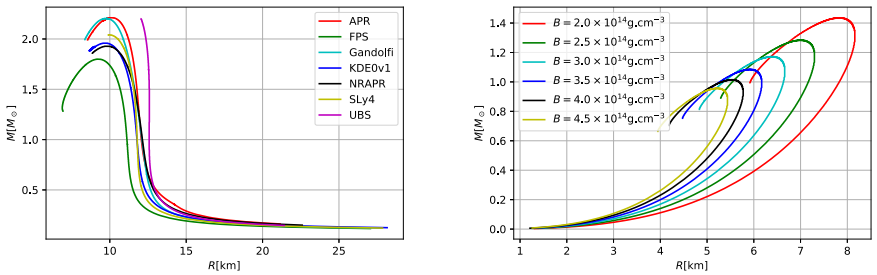

Figure 1. Mass vs radius of neutron stars with hadronic equations of state (left) and quark stars with MIT Bag model (right).

panel of Fig. 1. The maximum mass of quark stars is given purely by bag constant in a simple model we assumed here and was discussed by Haensel et al. (1986). They found a maximum mass and corresponding radius, a moment of inertia, and central density as a function of Bag constant (see eq. (28) in Haensel et al. (1986) and related discussion for details)[1].

Mass-radius relations of hybrid stars (neutron stars with quark cores) are discussed on Fig. 2 where each panel correspond to a particular value of bag constant and bag constant is increasing from the top left to bottom right. The lines at each panel starting on the right where mass is smallest and radius largest are corresponding to lower central pressures. As central pressure increases the radius is becoming smaller and mass is increasing. On the left panel of the top row, where $B = 2.0 \times 10^{14}\mathrm{g.cm}^{-3}$(left) the mass reaches maximum values (different for each hadronic equation of state but well bellow $1M_{\odot}$). After that, the mass is decreasing and starts to increase again. The stellar models when mass is decreasing with central pressure increasing are unstable against radial perturbations. After reaching minima the mass starts to increase, stellar models are stable again and the mass reaches new maxima. This second maximum is primarily given by the value of bag constant and is almost the same for all considered hadronic equations of state. We can see that for a small interval of masses the stable configuration may have two different radii. These objects are usually called twin stars - see Benić et al. (2015) for a more interesting case of high mass twin stars. In the case of our selection of equations of state, none of the hybrid star models meets the highest observed mass of $2.01 \pm 0.04M_{\odot}$. The only equation of state that meets the requirement is the UBS with $B = 4.5 \times 10^{14}\mathrm{g.cm}^{-3}$ but the mass is reached before the quark core starts to be present (see bottom right panel of Fig. 3 demonstrating there is no quark core before maximum mass is reached).

We calculated the moment of inertia of quark core I_{core} and we present its size relative to the total moment of inertia I_{tot} versus gravitational mass on Fig. 3. One can see that

[1] Haensel et al. (1986) were motivated by the investigation of strange stars, objects that are composed by a mixture of u,d and s quarks and the quark phase is energetically preferable up to zero pressure. In our case quark matter becomes energetically favorable if $P > P_{\mathrm{pt}}$.

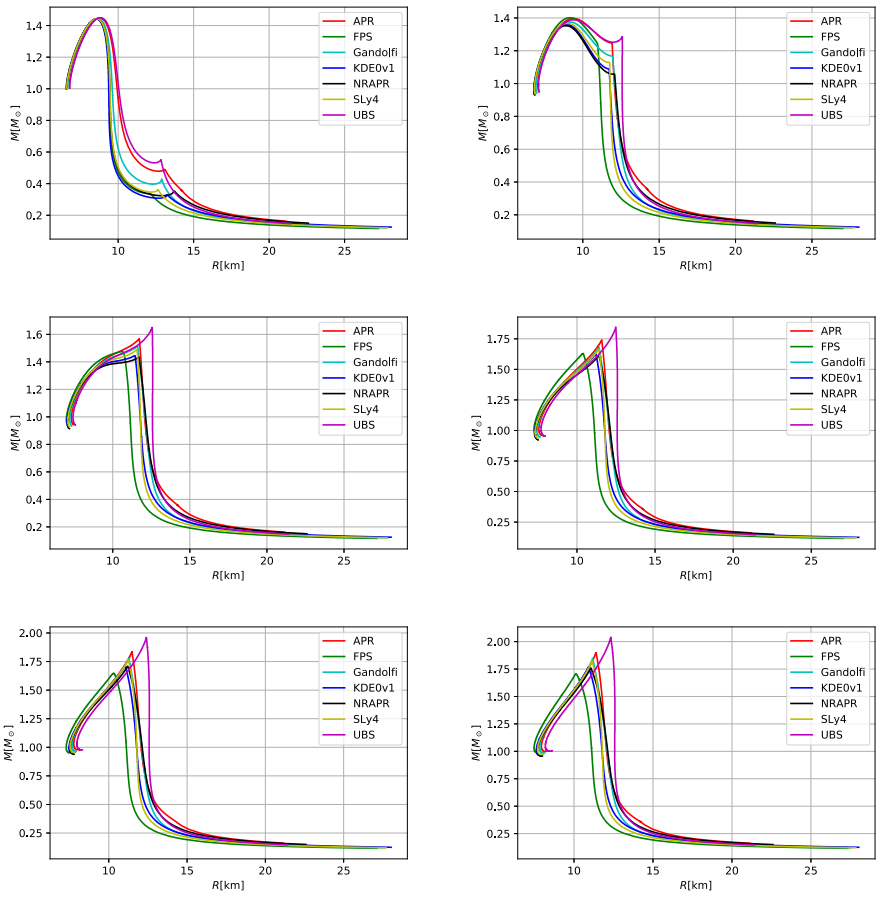

Figure 2. Mass vs radius of neutron stars with quark matter cores. Each panel represents stars having the same quark EoS but different hadronic equations of state. The values of Bag constants are (top left to bottom right) $B = \{2; 2.5; 3; 3.5; 4; 4.5\} \times 10^{14}\text{g.cm}^{-3}$ and all phase transitions are calculated using Maxwell construction. We can see that for a very small value of bag constant $B = 2 \times 10^{14}\text{g.cm}^{-3}$the maximum mass is dominated by the equation of state of quark matter, while in the case of higher values bag constant the hadronic equation of state plays an important role. Quark matter core is present in most of maximum mass configurations apart from the one with UBS EoS (see Fig 3).

the maximum size of quark core in stable compact stars corresponds to the lowest value of bag constant and that $I_{\text{core}}/I_{\text{tot}}$ is decreasing with increasing bag constant. Even for the highest values of B the quark core is present before reaching maximum mass except for UBS equation of state.

In this short proceeding, we presented a simple analysis of phase transition using several hadronic equations of state and combined each of them with the simplest form of MIT bag

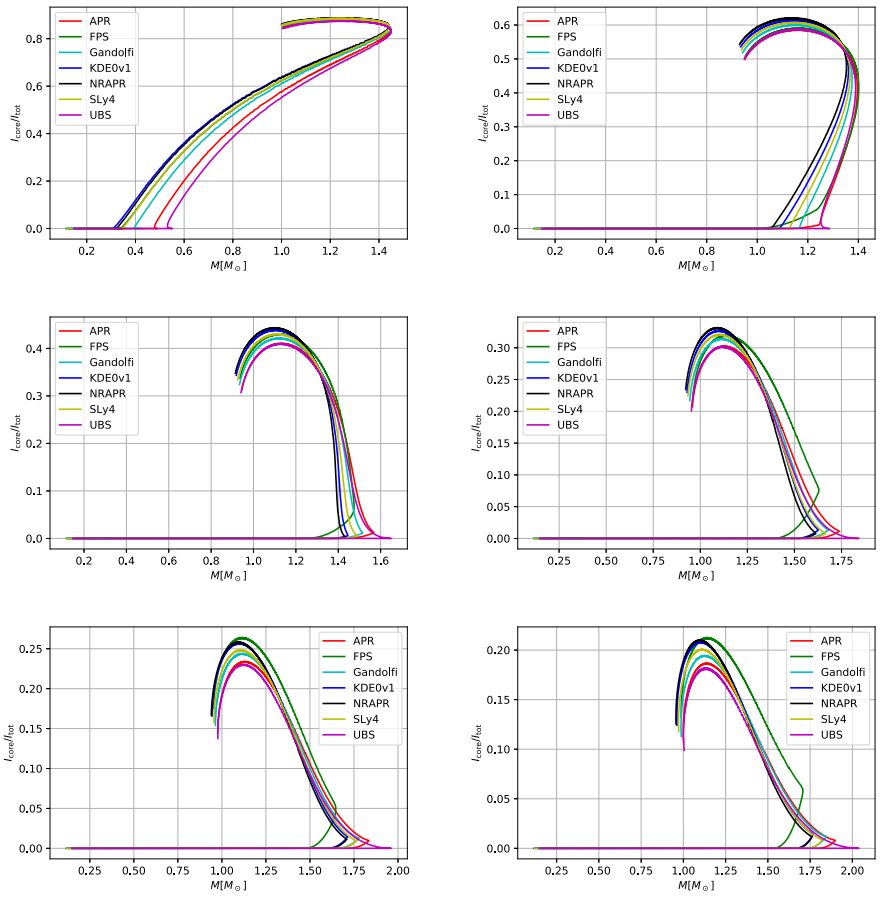

Figure 3. Moment of inertia of the quark core relative to the moment of inertia of the whole star. Each panel represents stars having the same quark EoS but different hadronic equations of state. The values of Bag constants are (top left to bottom right) $B = \{2; 2.5; 3; 3.5; 4; 4.5\} \times 10^{14}\text{g.cm}^{-3}$ and all phase transitions are calculated using Maxwell construction. One can see that quark matter core starts to be present before maximum mass is reached in most of the cases, however, in the case of UBS the stable configurations can have quark core only in the two of investigated cases (top row).

model calculated for various values of bag constant. We showed that for low values of bag constant the maximum mass is determined by the value of bag constant while the hadronic equation of state plays an important role for higher values of bag constant. That is the starting point for our future investigation where we plan to use a more advanced equation of state of quark matter and investigate also rotating objects.

ACKNOWLEDGEMENTS

The present work was supported by the Czech Grant LTT17003.

REFERENCES

Agrawal, B. K., Shlomo, S. and Au, V. K. (2005), Determination of the parameters of a Skyrme type effective interaction using the simulated annealing approach, *Phys Rev C*, **72**(1), 014310, arXiv: nucl-th/0505071.

Akmal, A., Pandharipande, V. R. and Ravenhall, D. G. (1998), Equation of state of nucleon matter and neutron star structure, *Phys. Rev C*, **58**(3), pp. 1804–1828, arXiv: nucl-th/9804027.

Alvarez-Castillo, D. E., Blaschke, D. B., Grunfeld, A. G. and Pagura, V. P. (2019), Third family of compact stars within a nonlocal chiral quark model equation of state, *Phys Rev D*, **99**(6), 063010, arXiv: 1805.04105.

Antoniadis, J., Freire, P. C. C., Wex, N., Tauris, T. M., Lynch, R. S., van Kerkwijk, M. H., Kramer, M., Bassa, C., Dhillon, V. S., Driebe, T., Hessels, J. W. T., Kaspi, V. M., Kondratiev, V. I., Langer, N., Marsh, T. R., McLaughlin, M. A., Pennucci, T. T., Ransom, S. M., Stairs, I. H., van Leeuwen, J., Verbiest, J. P. W. and Whelan, D. G. (2013), A Massive Pulsar in a Compact Relativistic Binary, *Science*, **340**(6131), p. 448, arXiv: 1304.6875.

Baym, G., Pethick, C. and Sutherland, P. (1971), The Ground State of Matter at High Densities: Equation of State and Stellar Models, *ApJ*, **170**, p. 299.

Benić, S., Blaschke, D., Alvarez-Castillo, D. E., Fischer, T. and Typel, S. (2015), A new quark-hadron hybrid equation of state for astrophysics. I. High-mass twin compact stars, *A&A*, **577**, A40, arXiv: 1411.2856.

Blaschke, D. and Chamel, N. (2018), *Phases of Dense Matter in Compact Stars*, volume 457, p. 337.

Chodos, A., Jaffe, R. L., Johnson, K. and Thorn, C. B. (1974), Baryon structure in the bag theory, *Phys Rev D*, **10**(8), pp. 2599–2604.

Demorest, P. B., Pennucci, T., Ransom, S. M., Roberts, M. S. E. and Hessels, J. W. T. (2010), A two-solar-mass neutron star measured using Shapiro delay, *Nature*, **467**(7319), pp. 1081–1083, arXiv: 1010.5788.

Farhi, E. and Jaffe, R. L. (1984), Strange matter, *Phys Rev D*, **30**(11), pp. 2379–2390.

Gandolfi, S., Illarionov, A. Y., Fantoni, S., Miller, J. C., Pederiva, F. and Schmidt, K. E. (2010), Microscopic calculation of the equation of state of nuclear matter and neutron star structure, *MNRAS*, **404**(1), pp. L35–L39, arXiv: 0909.3487.

Haensel, P., Zdunik, J. L. and Schaefer, R. (1986), Strange quark stars, *A&A*, **160**(1), pp. 121–128.

Hartle, J. B. (1967), Slowly Rotating Relativistic Stars. I. Equations of Structure, *ApJ*, **150**, p. 1005.

Kurkela, A., Fraga, E. S., Schaffner-Bielich, J. and Vuorinen, A. (2014), Constraining Neutron Star Matter with Quantum Chromodynamics, *ApJ*, **789**(2), 127, arXiv: 1402.6618.

Lorenz, C. P., Ravenhall, D. G. and Pethick, C. J. (1993), Neutron star crusts, *Phys Rev Lett*, **70**(4), pp. 379–382.

Oppenheimer, J. R. and Volkoff, G. M. (1939), On Massive Neutron Cores, *Physical Review*, **55**(4), pp. 374–381.

Rikovska Stone, J., Miller, J. C., Koncewicz, R., Stevenson, P. D. and Strayer, M. R. (2003), Nuclear matter and neutron-star properties calculated with the Skyrme interaction, *Phys Rev C*, **68**(3), 034324.

Steiner, A. W., Prakash, M., Lattimer, J. M. and Ellis, P. J. (2005), Isospin asymmetry in nuclei and neutron stars [review article], *Phys Rep*, **411**(6), pp. 325–375, arXiv: nucl-th/0410066.

Tolman, R. C. (1939), Static Solutions of Einstein's Field Equations for Spheres of Fluid, *Physical Review*, **55**(4), pp. 364–373.

Urbanec, M., Beták, E. and Stuchlík, Z. (2010), Observational Tests of Neutron Star Relativistic Mean Field Equations of State, *Acta Astronomica*, **60**(2), pp. 149–163, arXiv: 1007.3446.

Zdunik, J. L. and Haensel, P. (2013), Maximum mass of neutron stars and strange neutron-star cores, *A&A*, **551**, A61, arXiv: 1211.1231.

Proceedings of *RAGtime 20–22, 15–19 Oct., 16–20 Sept., 19–23 Oct., 2018/2019/2020, Opava, Czech Republic*
Z. Stuchlík, G. Török and V. Karas, editors, Silesian University in Opava, 2020, pp. 351–355

Levitating atmospheres around naked singularities

Ronaldo S. S. Vieira[1,a] and Włodek Kluźniak[2,b]

[1]Centro de Ciências Naturais e Humanas, Universidade Federal do ABC, 09210-580 Santo André, SP, Brazil
[2]Copernicus Astronomical Center, ul. Bartycka 18, PL-00-716, Warszawa, Poland
[a]ronaldo.vieira@ufabc.edu.br
[b]wlodek@camk.edu.pl

ABSTRACT
For a wide class of spherically symmetric naked singularities there is a sphere within which gravity is effectively repulsive. In such spacetimes accreting matter cannot reach the singularity and will instead form a levitating atmosphere, which is kept suspended by gravity alone. The density of the atmosphere has a maximum at a definite radius. In its qualitative properties the atmosphere is analogous to the recently discussed atmospheres that are supported by radiation pressure above luminous neutron stars, however for the levitating atmospheres around a naked singularity no radiation needs to be present.

Keywords: Naked singularities – levitating atmospheres – hydrostatic equilibrium

1 INTRODUCTION

Stellar atmospheres are widely studied in the Newtonian gravity context, a general qualitative property being that their density and pressure profiles always decrease with radius. Recently, it was discovered that near-Eddington luminous neutron stars may have atmospheres detached from their surfaces if general relativistic effects are taken into account, either in the optically thin or in the optically thick case (Wielgus et al., 2015, 2016). These equilibrium configurations were called "levitating atmospheres" (Wielgus et al., 2015), since they lie at a finite distance from the stellar surface and have definite inner and outer radii. The oscillation modes of these atmospheres were studied in Abarca and Kluźniak (2016); Bollimpalli and Kluźniak (2017); Bollimpalli et al. (2019).

Here we investigate whether similar structures can appear in the absence of radiation. We find that indeed they can, if we consider spherically symmetric spacetimes generated by a central naked singularity. These naked-singularity spacetimes appear not only in general relativity, but also in solutions to modified theories of gravity. They generally present a zero-gravity radius, a stable equilibrium point for radial particle motion. Below, we present equilibrium atmospheric solutions which "levitate" around these singularities, being supported solely by gravity – the central repulsive-gravity region.

978-80-7510-432-8

2 REPULSIVE GRAVITY IN NAKED-SINGULARITY SPACETIMES

Let us consider a spherically symmetric spacetime metric of the form[1]

$$\mathrm{d}s^2 = -e^{2\Phi}\,\mathrm{d}t^2 + e^{2\Lambda}\,\mathrm{d}r^2 + r^2\,(\mathrm{d}\theta^2 + \sin^2\theta\,\mathrm{d}\varphi^2)\,. \tag{1}$$

The four-acceleration of a static observer is given by $a_\mu = \partial_\mu\Phi$ (Semerák et al., 1999). For metric (1) we have only a radial component, $a_r = \Phi'(r)$. Therefore, if there is a radius r_o such that $\Phi'(r_o) = 0$, particles at rest in the sphere labelled by r_o will remain at rest. We will have then an equilibrium radius for test-particle motion. If $\Phi''(r_o) > 0$ this equilibrium is stable; moreover, for $r < r_o$ we will have a region where gravity behaves as a "repulsive force". We call the equilibrium sphere of radius r_o the "zero-gravity sphere". Many spherically symmetric naked-singularity spacetimes behave this way, having an equilibrium radius for particle motion at a finite distance from the singularity (e.g., Pugliese et al. (2011); Stuchlík and Schee (2014); Vieira et al. (2014); Goluchová et al. (2015); Boshkayev et al. (2016)). We will see that, whenever this is the case, a spherical shell of matter will inevitably form around this radius, whose thickness becomes larger as its peak density grows.

3 LEVITATING ATMOSPHERES

If $\Phi''(r_o) > 0$ at the zero-gravity sphere, then we expect that accreting matter onto the singularity starts accumulating around that radius, giving rise to a dense structure with a peak at r_o. We call it a levitating atmosphere, in analogy with the recently found levitating atmospheres around luminous neutron stars in general relativity (Wielgus et al., 2015).

Consider a test-fluid atmosphere around the singularity. It is described by a perfect-fluid energy-momentum tensor

$$T^{\mu\nu} = (\varepsilon + p)\,u^\mu u^\nu + p\,g^{\mu\nu}, \tag{2}$$

where ε is the fluid's energy density and p its pressure. Let us assume that the naked-singularity spacetime is a solution of a theory of gravity where the usual conservation laws are valid for matter. The equation of hydrostatic equilibrium is then obtained from $T^{\mu\nu}{}_{;\nu} = 0$ and, neglecting relativistic contributions to internal energy ($\varepsilon = \rho$, the mass density) and assuming $p \ll \rho$, reads (Schutz, 2009)

$$\frac{1}{\rho}\frac{\mathrm{d}p}{\mathrm{d}r} = -\frac{\mathrm{d}\Phi}{\mathrm{d}r}. \tag{3}$$

This equation has the same form of the Newtonian equation of hydrostatic equilibrium, where Φ is the gravitational potential.

[1] We work in geometrized units $c = G = 1$.

3.1 Geometrically thin approximation

By the preceding discussion, the atmospheres should have a peak of density and pressure at the zero-gravity radius r_o. If the atmospheres are geometrically thin, we can Taylor expand the function Φ to second order in $(r - r_o)$ as

$$\Phi(r) - \Phi(r_o) \approx \frac{1}{2}\Phi''(r_o)\,(r - r_o)^2 \tag{4}$$

and then solve the hydrostatic equilibrium equation (3) given the atmosphere's equation of state.

3.1.1 Isothermal solution

For an isothermal atmosphere with an ideal gas equation of state

$$p = [k_B T/(\mu\, m_p)]\,\rho\,, \tag{5}$$

where k_B is Boltzmann's constant, m_p is the proton mass, and $\mu = 1$ is the mean molecular weight for Hydrogen (since the gas is not ionized), we obtain a Gaussian profile for its pressure, peaked at $r = r_o$,

$$p(r) = p_o \exp\left[-\frac{\mu\, m_p}{2k_B T}\,\Phi''(r_o)\,(r - r_o)^2\right], \tag{6}$$

with the corresponding density profile being given by the ideal gas law.

3.1.2 Polytropic solutions

For a polytropic equation of state of the form

$$p = K\rho^\gamma \tag{7}$$

we have

$$p(r) = p_o\left\{1 - \frac{1 - 1/\gamma}{2K^{1/\gamma}\,(p_o)^{1-1/\gamma}}\,\Phi''(r_o)\,(r - r_o)^2\right\}^{\gamma/(\gamma-1)}, \tag{8}$$

with $p_o = p(r_o)$, and a corresponding density profile

$$\rho(r) = \rho_o\left\{1 - \frac{1 - 1/\gamma}{2K\,\rho_o^{(\gamma-1)}}\,\Phi''(r_o)\,(r - r_o)^2\right\}^{1/(\gamma-1)}. \tag{9}$$

The temperature profile is given by

$$T = T_o\left\{1 - \left(\frac{1 - 1/\gamma}{k_B T_o/(\mu\, m_p)}\right)\cdot\frac{1}{2}\,\Phi''(r_o)\,(r - r_o)^2\right\}^{\gamma}, \tag{10}$$

assuming an ideal gas law. We remark that the isothermal solution falls exponentially with coordinate distance from r_o in this approximation. However, we do not expect the

atmosphere to be isothermal near the singularity, so there should be a cutoff radius at a finite value of r. On the other hand, all the polytropic solutions have (positive) inner and outer edges given by the condition $p(r) = 0$.

Therefore, in the geometrically thin approximation all the profiles depend on the spacetime metric only via two numbers: the zero-gravity radius r_o and the (positive) value of $\Phi''(r_o)$. In particular, the atmospheres will have the same shape regardless of the peculiarities of each spacetime; for a given equation of state, the difference will appear in the position of its peak and in the width of the profiles.

4 CONCLUSIONS

If accreting matter gradually falls onto the singularity, for instance via an accretion disc, then it will lose energy while falling the potential well of Φ. It is a property of thin accretion discs in the presence of central repulsive gravity that their inner rim is precisely at the zero-gravity radius (e.g., Stuchlík and Schee (2014); Vieira et al. (2014)). When matter flows through this inner edge of the disk, it will spread in the polar directions over a spherical shell of the same radius. If it starts falling onto the singularity, it will have to climb the potential well generated by the central repulsive gravity region. Since the energy of the flowing matter will not be sufficient to do so, it will be driven back to larger radii and oscillate around r_o. Eventually, due to viscous forces in the fluid, it will settle down at r_o and form the levitating atmosphere.

In this way, matter will never reach the singularity. If enough matter is deposited in the atmosphere, so that the geometrically thin approximation is not valid anymore, exact solutions may give us the optical depth of denser atmospheres and therefore define whether these may be optically thick. In that case, for external observers, the singularity may appear not so different from a gas planet. Therefore a natural astrophysical process, namely accretion, may "cloak" the singularity with a dense spherical layer of optically thick gas. The question of whether this "levitating cloak" also occurs in nonspherical configurations, such as rotating singularities, deserves further investigation.

ACKNOWLEDGEMENTS

The authors thank Maciek Wielgus for interesting discussions. WK acknowledges the hospitality at Federal University of ABC, Brazil, where part of this work was developed. This study was financed in part by the Coordenação de Aperfeiçoamento de Pessoal de Nível Superior - Brasil (CAPES) - Finance Code 001, via the Brazilian CAPES - PrInt internationalization program, and by the Polish NCN grant No. 2019/33/B/ST9/01564.

REFERENCES

Abarca, D. and Kluźniak, W. (2016), Radial oscillations of a radiation-supported levitating shell in Eddington luminosity neutron stars, *Mon. Not. R. Astron. Soc.*, **461**(3), pp. 3233–3238, arXiv: 1604.04485, URL https://ui.adsabs.harvard.edu/abs/2016MNRAS.461.3233A.

Bollimpalli, D. A. and Kluźniak, W. (2017), Radial modes of levitating atmospheres around Eddington luminosity neutron stars, *Mon. Not. R. Astron. Soc.*, **472**(3), pp. 3298–3303, arXiv: 1703.04224, URL https://ui.adsabs.harvard.edu/abs/2017MNRAS.472.3298B.

Bollimpalli, D. A., Wielgus, M., Abarca, D. and Kluźniak, W. (2019), Atmospheric oscillations provide simultaneous measurement of neutron star mass and radius, *Mon. Not. R. Astron. Soc.*, **487**(4), pp. 5129–5142, arXiv: 1812.01299, URL https://ui.adsabs.harvard.edu/abs/2019MNRAS.487.5129B.

Boshkayev, K., Gasperín, E., Gutiérrez-Piñeres, A. C., Quevedo, H. and Toktarbay, S. (2016), Motion of test particles in the field of a naked singularity, *Phys. Rev. D*, **93**(2), 024024, arXiv: 1509.03827, URL http://adsabs.harvard.edu/abs/2016PhRvD..93b4024B.

Goluchová, K., Kulczycki, K., Vieira, R. S. S., Stuchlík, Z., Kluźniak, W. and Abramowicz, M. (2015), Hořava's quantum gravity illustrated by embedding diagrams of the Kehagias-Sfetsos spacetimes, *General Relativity and Gravitation*, **47**, 132, arXiv: 1511.01345, URL http://adsabs.harvard.edu/abs/2015GReGr..47..132G.

Pugliese, D., Quevedo, H. and Ruffini, R. (2011), Circular motion of neutral test particles in Reissner-Nordström spacetime, *Phys. Rev. D*, **83**(2), 024021, arXiv: 1012.5411, URL http://adsabs.harvard.edu/abs/2011PhRvD..83b4021P.

Schutz, B. (2009), *A first course in general relativity*, Cambridge University Press, UK.

Semerák, O., Zellerin, T. and Žáček, M. (1999), The structure of superposed Weyl fields, *Mon. Not. R. Astron. Soc.*, **308**, pp. 691–704, URL http://adsabs.harvard.edu/abs/1999MNRAS.308..691S.

Stuchlík, Z. and Schee, J. (2014), Optical effects related to Keplerian discs orbiting Kehagias&Sfetsos naked singularities, *Classical and Quantum Gravity*, **31**(19), 195013, arXiv: 1402.2891, URL http://adsabs.harvard.edu/abs/2014CQGra..31s5013S.

Vieira, R. S. S., Schee, J., Kluźniak, W., Stuchlík, Z. and Abramowicz, M. (2014), Circular geodesics of naked singularities in the Kehagias-Sfetsos metric of Hořava's gravity, *Phys. Rev. D*, **90**(2), 024035, arXiv: 1311.5820, URL http://adsabs.harvard.edu/abs/2014PhRvD..90b4035V.

Wielgus, M., Kluźniak, W., Sądowski, A., Narayan, R. and Abramowicz, M. (2015), Stable, levitating, optically thin atmospheres of Eddington-luminosity neutron stars, *Mon. Not. R. Astron. Soc.*, **454**(4), pp. 3766–3770, arXiv: 1505.06099, URL https://ui.adsabs.harvard.edu/abs/2015MNRAS.454.3766W.

Wielgus, M., Sądowski, A., Kluźniak, W., Abramowicz, M. and Narayan, R. (2016), Levitating atmospheres of Eddington-luminosity neutron stars, *Mon. Not. R. Astron. Soc.*, **458**(4), pp. 3420–3428, arXiv: 1512.00094, URL https://ui.adsabs.harvard.edu/abs/2016MNRAS.458.3420W.

Proceedings of *RAGtime 20–22, 15–19 Oct., 16–20 Sept., 19–23 Oct., 2018/2019/2020, Opava, Czech Republic*
Z. Stuchlík, G. Török and V. Karas, editors, Silesian University in Opava, 2020, pp. 357–374

Missing bright red giants in the Galactic center: A fingerprint of its once active state?

Michal Zajaček[1a] Anabella Araudo[2,3] Vladimír Karas[3]
Bożena Czerny[1] Andreas Eckart[4,5] Petra Suková[3]
Marcel Štolc[3] and Vojtěch Witzany[6]

[1]Center for Theoretical Physics, Polish Academy of Sciences,
Al. Lotników 32/46, 02-668 Warsaw, Poland
[2]ELI Beamlines, Institute of Physics, Czech Academy of Sciences,
CZ-25241 Dolní Břežany, Czech Republic
[3]Astronomical Institute of the Czech Academy of Sciences,
Boční II 1401, CZ-14100 Prague, Czech Republic
[4]I. Physikalisches Institut der Universität zu Köln,
Zülpicher Strasse 77, D-50937 Köln, Germany
[5]Max-Planck-Institut für Radioastronomie (MPIfR),
Auf dem Hügel 69, D-53121 Bonn, Germany
[6]School of Mathematics and Statistics, University College Dublin,
Belfield, Dublin 4, D04 V1W8, Ireland
[a]zajacek@cft.edu.pl

ABSTRACT
In the Galactic center nuclear star cluster, bright late-type stars exhibit a flat or even a decreasing surface density profile, while fainter late-type stars maintain a cusp-like profile. Historically, the lack of red giants in the Galactic center was discovered via the drop in the strength of the CO absorption bandhead by Kris Sellgren et al. (1990), later followed by the stellar number counts based on the high angular resolution near-infrared observations. Several mechanisms were put forward that could have led to the preferential depletion of bright red giants: star-star collisions, tidal stripping, star-accretion disc collisions, or an infall of a massive cluster or a secondary black hole. Here we propose a novel scenario for the bright red-giant depletion based on the collisions between red giants and the nuclear jet, which was likely active in the Galactic center a few million years ago and could have led to the formation of the large-scale γ-ray Fermi bubbles. The process of the jet-induced ablation of red giants appears to be most efficient within ~ 0.04 pc (S-cluster), while at larger distances it was complemented by star–accretion disc collisions and at smaller scales, tidal stripping operated. These three mechanisms likely operated simultaneously and created an apparent core of late-type stars within ~ 0.5 pc.

Keywords: Galaxy: center — stars: supergiants — galaxies: jets — stars: kinematics and dynamics

978-80-7510-432-8

1 INTRODUCTION

The analysis of the intergrated diffuse starlight at $2.3\,\mu$m of the Galactic center region within $\sim$ 1.2 pc revealed a drop in the CO absorption bandhead strength inside $\sim$ 0.6 pc (Sellgren et al., 1990). Since CO molecules are present in the extended atmospheres of late-type stars, this discovery indicated the missing red-giant problem. Later on, with the development of the adaptive optics technology, individual sources were detected, initially up to magnitude 16 in the K_s-band, now even up to magnitude 19. This allowed to construct surface-density distributions of late-type and early-type stars. Buchholz et al. (2009) found that late-type stars have a flat surface-density distribution, while young OB stars have a cusp-like distribution in the same region. Recently, Gallego-Cano et al. (2018) studied the surface density distribution of late-type stars up to the observed magnitudes of $K_s = 18$ mag. They recovered the previous findings of the core-like distribution for giant late-type stars in the range $12.5 - 16$ mag, while the faint stars with $K_s \approx 18$ mag exhibit a single power-law 3D distribution with the slope of $\gamma \simeq 1.4$ (the surface density slope is $\Gamma \approx \gamma - 1 = 0.4$). Gallego-Cano et al. (2018) estimate that $\sim$ 100 bright giants could be missing within the projected distance of $\sim$ 0.3 pc. An independent analysis by Habibi et al. (2019) confirms these findings. They can also recover a single power-law surface-density distribution ("cusp") of faint giants ($K_s < 17$ mag) with the projected power-law index of $\Gamma \simeq 0.34$, while they estimate that about 4-5 bright giants appear to be missing within the S-cluster region ($\sim$ 0.04 pc). In addition, they constrain the least and the most extended atmospheres of late-type stars in the range between 4 and $30\,R_\odot$ located within $\sim$ 0.02 pc.

By constructing the K-band luminosity function (KLF) of late-type stars and by fitting theoretical luminosity functions to it, Schödel et al. (2020) inferred that $\sim$ 80% of the stellar mass of the Nuclear Star Cluster (NSC) formed 10 Gyr or earlier. This episode was followed by a quiescent phase, and another $\sim$ 15% formed 5 Gyr ago. The remaining few percent could have formed within the last 100 Myr. This implies that the star-formation in the NSC is rather episodic (Pfuhl et al., 2011) and most of the stellar mass is old.

In the Galactic center, the two-body relaxation time is of the order of 1 Gyr,

$$\tau_{\rm relax} = \frac{0.34\sigma_\star^3}{G^2 m_\star \rho_\star \log\Lambda} \sim$$
$$\sim 1.8\times10^9 \left(\frac{\sigma_\star}{10^2\,{\rm km\,s^{-1}}}\right)^3 \left(\frac{m_\star}{1\,M_\odot}\right)^{-1} \left(\frac{\rho_\star}{10^6\,M_\odot\,{\rm pc^{-3}}}\right)^{-1} {\rm yr}\,, \quad (1)$$

where we considered the Coulomb logarithm of the order of 10 and the stellar mass density estimate of $\sim 10^6\,M_\odot\,{\rm pc^{-3}}$ is based on the enclosed mass as determined by Schödel et al. (2009). The relaxation time could further be shortened by a factor of at least 10 due to the presence of massive perturbers (Perets et al., 2007). Given that $\tau_{\rm relax}$ is comparable or even shorter than the formation time of most of late-type stars, the late-type NSC is expected to be relaxed and its 3D number density should follow a single power-law profile similar to the theoretical Bahcall-Wolf cusp ($n_{\rm BW} \propto r^{-3/2}$ for unequal stellar masses according to Bahcall and Wolf, 1977 and $n_\bullet \propto r^{-2}$ for stellar black holes; see also Alexander, 2005, 2017 for reviews). Schödel et al. (2020) confirm in their analysis that late-type stars in all magnitude bins follow a single power-law surface-density profile, except for the brightest

stars with the observed K-band magnitude in the range of 15 – 13 mag, which exhibit a flat to a decreasing surface-density profile that can be described by a broken power law.

To explain this apparent paradox of missing bright red giants, several mechanisms have been proposed based on their preferential effect on bigger stars with more extended, loosely-bound envelopes. Below we list the main proposed mechanisms:

- tidal disruption of red giants and tidal stripping of their envelopes by the supermassive black hole (SMBH; Hills, 1975; Rees, 1988; Bogdanović et al., 2014; King, 2020),
- red giant–accretion disc (clump) collisions (Armitage et al., 1996; Amaro-Seoane and Chen, 2014; Amaro-Seoane et al., 2020; Kieffer and Bogdanović, 2016),
- collisions of red giants with field stars and compact remnants (Phinney, 1989; Sellgren et al., 1990; Morris, 1993; Genzel et al., 1996; Dale et al., 2009)
- mass segregation effects: the infall of a secondary massive black hole (Baumgardt et al., 2006; Merritt and Szell, 2006) or the infall of a massive cluster (Kim and Morris, 2003; Ernst et al., 2009; Antonini et al., 2012) or the dynamical segregation of stellar black holes (Morris, 1993),
- central luminosity source as a source of ionizing radiation (Sellgren et al., 1990).

In the following, we present a novel scenario reminiscent of the last scenario that includes a central luminosity source that photoionizes molecular content in the large envelopes of red giants, including the CO molecule (Sellgren et al., 1990). However, instead of photoionization, we focus on the possibility of the mechanical ablation of large red-giant atmospheres by a nuclear jet, which could have been significantly more active in the Galactic center a few million years ago. The observed γ-ray Fermi (Su et al., 2010) and radio bubbles (Heywood et al., 2019) as well as the X-ray chimneys (Ponti et al., 2019) and optical ionization cones (Bland-Hawthorn et al., 2019) could be its fingerprints. We describe the model and analyze its consequences in detail in Zajaček et al. (2020). In this contribution, we summarize the main concepts and subsequently, we compare different scenarios of the red giant depletion and how they can complement each other on different spatial scales from Sgr A*.

2 MODEL DESCRIPTION

The basic assumption in our model is the active jet phase of Sgr A*. Recently, multiwavelength evidence has been accumulated for the presence of bipolar cones – these include γ-ray Fermi bubbles (Su et al., 2010), radio bubbles (Heywood et al., 2019), X-ray chimneys (Ponti et al., 2019), and optical large-scale ionization cones (Bland-Hawthorn et al., 2019). Their overall energy content appears to be consistent with the active jet and/or the nuclear disc outflows with the kinetic luminosity of $L_{\rm j} = 2.3^{+5.1}_{-0.9} \times 10^{42}\,{\rm erg\,s^{-1}}$ (Miller and Bregman, 2016). On the other hand, a nuclear starburst appears to be inconsistent with the bubble energetics by about a factor of 100 (Bland-Hawthorn and Cohen, 2003; Bland-Hawthorn et al., 2019). Guo and Mathews (2012) simulated the formation of the Fermi bubbles by an active jet and the basic energetics and properties could be explained by the jet duration of $t_{\rm jet} \sim 0.1-0.5\,{\rm Myr}$. Taking into account the total energy content of ionization cones of $E_{\rm cone} \sim 10^{56} - 10^{57}\,{\rm erg}$ (Bland-Hawthorn et al., 2019), the jet kinetic luminosity

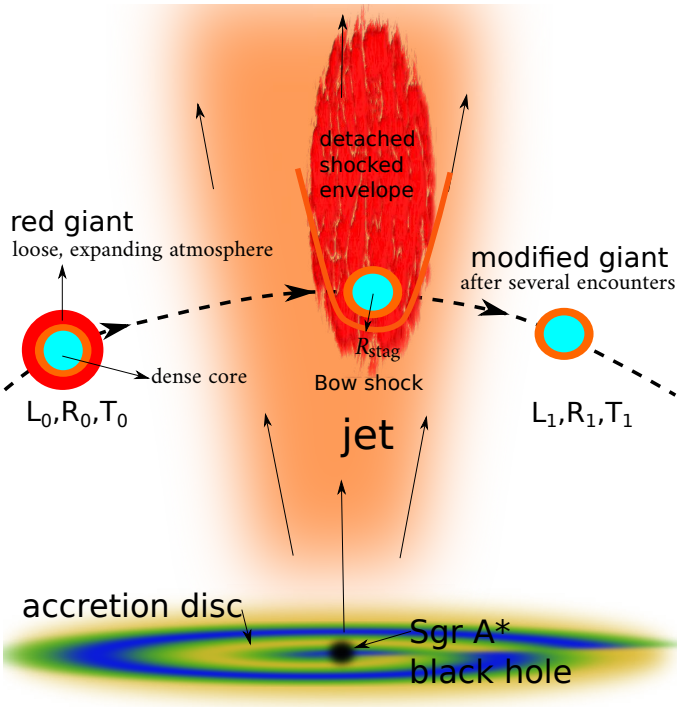

Figure 1. Illustration of the red giant as it crosses the jet during the active phase of Sgr A* a few million years ago. a red giant consists of a dense core surrounded by a loose and expanding atmosphere. While crossing the jet, its outer layers get ablated, which results in a modified appearance – higher effective temperature and a drop in near-infrared luminosity after repetitive encounters. For further details, see Zajaček et al. (2020).

can be estimated as $L_{\rm j} \sim E_{\rm cone}/t_{\rm jet} \sim 6.3\times10^{42} - 3.2\times10^{44}\,{\rm erg\,s^{-1}}$. This is in agreement with the upper limit given by the Eddington luminosity of Sgr A*,

$$L_{\rm Edd} = 5\times10^{44}\left(\frac{M_\bullet}{4\times10^6\,M_\odot}\right)\,{\rm erg\,s^{-1}}\,. \tag{2}$$

The active jet during the Galactic center Seyfert phase was dominated by the kinetic pressure (Guo and Mathews, 2012). The kinetic luminosity can be estimated using the conversion efficiency $\eta_{\rm j}$ as $L_{\rm j} = \eta_{\rm j} L_{\rm acc} \lesssim \eta_{\rm j} L_{\rm Edd}$, where $L_{\rm acc}$ is the bolometric accretion luminosity. Since $\eta_{\rm j} < 0.7$ for most radio galaxies (Ito et al., 2008), this yields the upper limit of $L_{\rm j} < 3.5\times10^{44}\,{\rm erg\,s^{-1}}$. In the following, we explore the jet-star interaction for $L_{\rm j} = 10^{41} - 10^{44}\,{\rm erg\,s^{-1}}$, where the lower limit was estimated for the current quiescent phase of Sgr A* (Yusef-Zadeh et al., 2012).

During the Seyfert phase of Sgr A* that occurred 3.5 ± 1 Myr ago (Bland-Hawthorn et al., 2019), most of the NSC late-type stars were certainly present since 80% of the stellar mass formed at least 10 Gyr ago (Schödel et al., 2020). Given this setup, it is straightforward

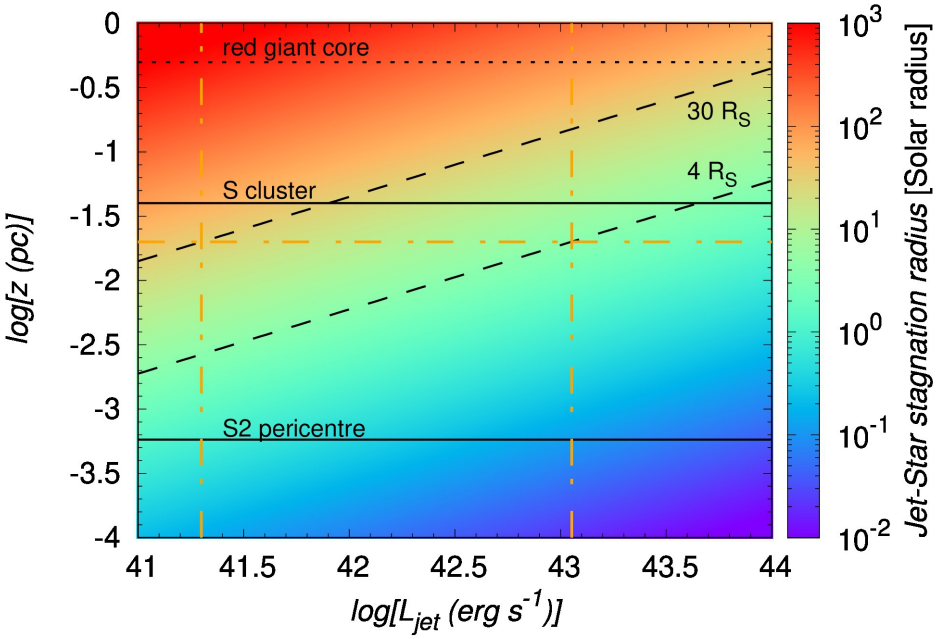

Figure 2. Stagnation radius $R_{\rm stag}/R_\odot$ as a function of the jet luminosity (in erg s^{-1}) and of the distance from Sgr A* (in parsecs). Two horizontal black lines mark the extent of the S cluster – from the S2 pericenter up to 0.04 pc (or 1"). Two dashed black lines depict $R_{\rm stag}$ equal to 30 (top) and 4 Solar radii (bottom), respectively. To instruct the reader, we also plot the vertical dot-dashed lines that mark the jet kinetic luminosities, which would result in the atmosphere ablation at 30 $R_\odot$ (left) and 4 $R_\odot$ (right) at the distance of $z = 0.02$ pc. The horizontal dotted black line depicts the approximate length-scale of the red-giant core at 0.5 pc (see e.g. Sellgren et al., 1990).

to invoke a scenario where red giants, supergiants, and asymptotic giant-branch stars cross the jet. This scenario was studied extensively in relation to the non-thermal emission of jetted active galactic nuclei (AGN; see e.g. Barkov et al., 2010, 2012; Araudo et al., 2013; Perucho et al., 2017). Here we focus instead on the expected impact of the repetitive jet-star interactions on the visual appearance of red giants, mainly in the near-infrared domain, see Fig. 1 for illustration. Even in the current quiescent state of Sgr A*, there is evidence for the interaction of wind-blowing stellar objects with the ambient wind or even a low surface-brightness jet (Yusef-Zadeh et al., 2020). Clear examples are comet-shaped sources X3, X7 (Mužić et al., 2010), and the bow-shock source X8 (Peißker et al., 2019) located in the so-called mini-cavity.

The basic length-scale that determines where the red-giant envelope is truncated is given by the stagnation radius $R_{\rm stag}$, where the stellar-wind pressure $P_{\rm sw}$ is comparable to the jet

kinetic pressure $P_{\rm j}$, which leads to

$$R_{\rm stag} = z\tan\theta\sqrt{\frac{\dot{m}_{\rm w}v_{\rm w}c}{4L_{\rm j}}} = \\ = 27\left(\frac{z}{0.04\,{\rm pc}}\right)\left(\frac{\dot{m}_{\rm w}}{10^{-8}\,M_{\odot}{\rm yr}^{-1}}\right)^{\frac{1}{2}}\left(\frac{v_{\rm w}}{10\,{\rm km\,s}^{-1}}\right)^{\frac{1}{2}}\left(\frac{L_{\rm j}}{10^{42}\,{\rm erg\,s}^{-1}}\right)^{-\frac{1}{2}} R_{\odot}, \quad (3)$$

where z is the distance of the star from Sgr A*, $\dot{m}_{\rm w}$ is the stellar mass-loss rate, $v_{\rm w}$ is the terminal stellar-wind velocity. The half-opening angle θ is set to 12.5° (see Li et al., 2013 for the opening angle estimate for Sgr A*). The stellar parameters – $\dot{m}_{\rm w}$ and $v_{\rm w}$ – are scaled to the typical values for red giants (Reimers, 1987). According to Eq. (3), the typical stagnation radius in the S cluster region (~ 0.04 pc) is comparable to the largest atmosphere radius of $30\,R_{\odot}$ inferred by Habibi et al. (2019). In Fig. 2, we plot the stagnation radius in Solar radii with respect to the expected jet luminosity and the distance from Sgr A* (in parsecs). Within the S cluster, the stagnation radius can reach $30\,R_{\odot}$ up to a few Solar radii only, depending on the exact location and the jet luminosity. These values of $R_{\rm stag}$ generally reach below the atmosphere of larger red giants.

The number of encounters between the jet and the red giant is expected to be at least of the order of 1000 since the orbital timescale $P_{\rm orb}$ is much smaller than $t_{\rm jet}$. Once a red giant enters the jet, it will continue to cross it during subsequent orbits during the jet lifetime. In principle, the vector resonant relaxation and/or the jet precession could cause that the interaction halts. For the following estimates, we assume that these processes take place on longer timescales than the jet lifetime (see also Zajaček et al., 2020 for a detailed discussion of these effects). The number of red giant–jet encounters is then approximately,

$$n_{\rm cross} = 2\frac{t_{\rm jet}}{P_{\rm orb}} \sim 2\times10^{4}\left(\frac{t_{\rm jet}}{0.5\,{\rm Myr}}\right)\left(\frac{M_{\bullet}}{4\times10^{6}\,M_{\odot}}\right)^{\frac{1}{2}}\left(\frac{z}{0.01\,{\rm pc}}\right)^{-\frac{3}{2}}. \quad (4)$$

Within the S cluster, the number of encounters reaches $n_{\rm cross} \simeq 1.4\times10^{6}$ at the S2 pericentre ($r_{\rm p} \sim 0.58$ mpc) and goes down to $n_{\rm cross} \simeq 2500$ at 0.04 pc. These estimates represent upper limits since during the jet existence the vector resonant relaxation operates that changes the orbital inclination and the star may leave the collisional orbit before the jet ceases its activity. In addition, the same can occur due to the potential jet precession (caused by a secondary black hole or the Lense-Thirring effect) that can change the jet direction on the timescales of tens of years for some sources, such as OJ287 (Britzen et al., 2018).

During one encounter, the mass removal from the red giant of radius $R_{\star}$ can be estimated from the balance of jet kinetic force and the gravitational force acting on the shell to be removed, $P_{\rm j}\pi R_{\star}^{2} \simeq Gm_{\star}\Delta M_{1}/R_{\star}^{2}$, from which follows,

$$\frac{\Delta M_{1}}{M_{\odot}} \approx 4\times10^{-10}\left(\frac{L_{\rm j}}{10^{42}\,{\rm erg\,s}^{-1}}\right)\left(\frac{R_{\star}}{100\,R_{\odot}}\right)^{4}\left(\frac{z}{0.04\,{\rm pc}}\right)^{-2}\left(\frac{\theta}{0.22}\right)^{-2}\left(\frac{m_{\star}}{M_{\odot}}\right)^{-1}. \quad (5)$$

The mass removed during $n_{\rm cross}$ encounters can be estimated simply as $\Delta M_{\rm cross} \simeq n_{\rm cross}\Delta M_1$, which yields,

$$\Delta M_{\rm cross} \sim n_{\rm cross}\Delta M_1 \approx$$
$$\approx 10^{-4}\left(\frac{L_{\rm j}}{10^{42}\,{\rm erg\,s^{-1}}}\right)\left(\frac{R_\star}{100\,R_\odot}\right)^4\left(\frac{z}{0.01\,{\rm pc}}\right)^{-\frac{7}{2}}\times$$
$$\left(\frac{\theta}{0.22}\right)^{-2}\left(\frac{m_\star}{M_\odot}\right)^{-1}\left(\frac{t_{\rm jet}}{0.5\,{\rm Myr}}\right)\left(\frac{M_\bullet}{4\times10^6\,M_\odot}\right)^{\frac{1}{2}}\,M_\odot\,. \quad (6)$$

Since 80% of the stellar mass formed 10 Gyrs or more ago, red giants in the NSC are expected to have gone through several AGN-like phases. Typical AGN phases are short, of the order of 10^5 years, while the total growth time of the SMBHs is between 10^7 and 10^9 years (Schawinski et al., 2015). This implies at least $n_{\rm AGN} \sim 10^2$ AGN-like events during the Galaxy lifetime. The total removed mass during all active phases then is, $\Delta M_{\rm AGN} \sim n_{\rm AGN}n_{\rm cross}\Delta M_1$, which makes the numerical estimate in Eq. (6) larger by at least two orders of magnitude.

The mass removal from red giants estimated by Eqs. (5)-(6) and the associated impulse can also effect the orbit of late-type stars. The effect of one encounter is typically negligible, but the cumulative effect of several thousand crossings through the jet can noticeably change the dynamics of the largest red giants. This is, however, beyond the scope of the current contribution and the effect will be studied in detail in our future studies.

We plot the distance profiles of the removed mass from red giants for different jet luminosities ($L_{\rm j} = 10^{42}\,{\rm erg\,s^{-1}}$ and $L_{\rm j} = 10^{44}\,{\rm erg\,s^{-1}}$) and atmosphere radii ($R_\star = 50\,R_\odot$ and $R_\star = 100\,R_\odot$) in Fig. 3. In addition, we also include the profile for the longer duration of the jet activity (1 Myr; solid green line) as well as the cumulative mass removal for red giants going through 100 AGN phases (dash-dotted blue line). For comparison, we also show the cumulative mass removal during star–disc interactions according to Kieffer and Bogdanović (2016) (dashed and dotted horizontal orange lines) assuming that the star-disc mass removal is constant throughout the studied distance range. However, star-disc interactions are expected to remove the mass more efficiently at larger distance scales where the gaseous disc was denser and the Toomre's stability criterion plunged below one because of a larger surface density of the disc. On the other hand, the jet-star interactions are clearly the most efficient in removing the atmosphere mass within the S cluster, where the cumulative mass removal is comparable to the one resulting from standard red-giant stellar winds (shaded gray rectangle) as well as the mass removed during star-disc interactions. This is also enhanced by another effect, which is related to the thermal Kelvin-Helmholtz timescale. In Zajaček et al. (2020) we showed that approximately within the S cluster, colliding red giants were not able to cool off before the subsequent collision, which resulted in larger atmosphere cross-sections and hence larger removed mass (warm colliders). Outside the S cluster ($> 0.04\,{\rm pc}$), stars were able to cool off because of longer orbital timescales (cool colliders) and their collisional cross-sections were smaller and therefore also the jet-ablation was further reduced by this effect.

Concerning the probability of an encounter between red giants and the jet with a half-opening angle θ, it is clear that for a spherical stellar cluster, not all the stars will interact

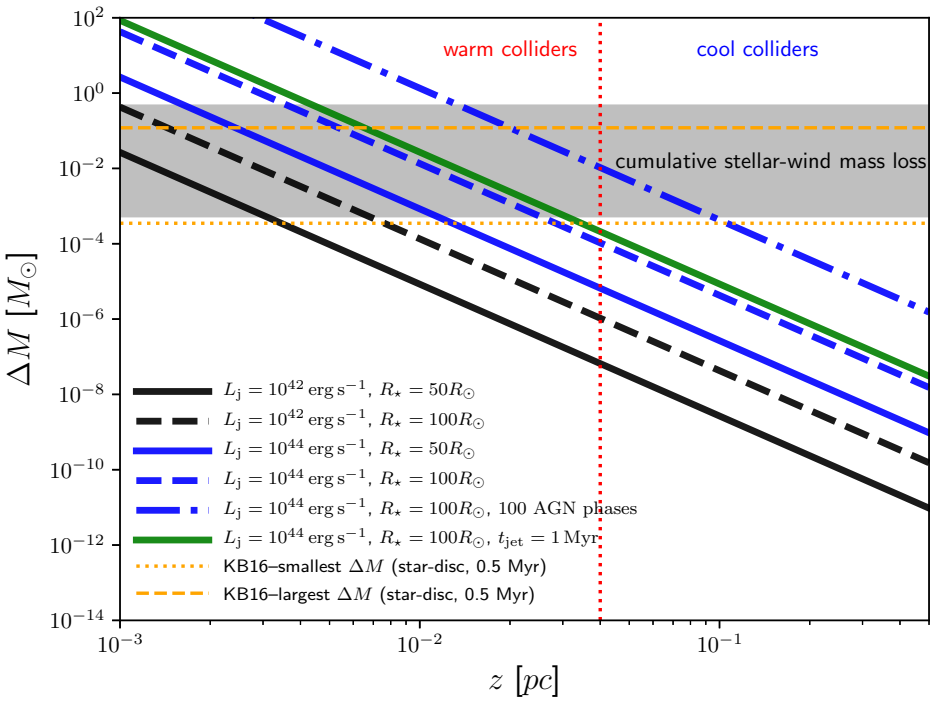

Figure 3. Total mass removed from the red giant atmosphere (in Solar masses) due to the jet ablation as a function of distance from Sgr A* in parsecs. We plot the cases for $L_j = 10^{42}\,\mathrm{erg\,s^{-1}}$ and $L_j = 10^{44}\,\mathrm{erg\,s^{-1}}$ and two different atmosphere radii of 50 and 100 $R_\odot$, see the legend (solid and dashed black and blue lines). These cases are nominally calculated for the jet duration of $t_{jet} = 0.5\,\mathrm{Myr}$. In addition, we also include the case for the longer duration of the jet activity, $t_{jet} = 1\,\mathrm{Myr}$ (solid green line). The cumulative mass removal including 100 AGN phases is depicted by a dash-dotted blue line (for the case with $L_j = 10^{44}\,\mathrm{erg\,s^{-1}}$ and $R_\star = 100\,R_\odot$). For comparison, we also include the cumulative mass removal for star-disc collisions according to Kieffer and Bogdanović (2016) (dashed and dotted orange lines). Furthermore, the cumulative red-giant (RG) stellar-wind loss during 0.5 Myr is shown as a gray rectangle using the observationally inferred mass-loss rates (Reimers, 1987). The red vertical dotted line depicts the outer radius of the S cluster (0.04 pc) and at the same time the approximate dividing radius between the so-called warm and cool colliders (Zajaček et al., 2020).

with the jet at a given moment. In Zajaček et al. (2020), we derive an analytical formula for the mean number of encounters per orbital period in the region with an outer radius $z_{\rm out}$,

$$\overline{N}_{\rm RG} = \frac{4\pi}{4-\gamma} n_0 z_0^{\gamma} \tan\theta z_{\rm out}^{3-\gamma}\,, \tag{7}$$

where n_0, z_0, and γ are the parameters describing 3D number density of late-type stars in the power-law form, $n_{\rm RG} \approx n_0(z/z_0)^{-\gamma}$. For the values inferred by Gallego-Cano et al. (2018), $n_0 \simeq 52\,{\rm pc}^{-3}$, $z_0 \simeq 4.9\,{\rm pc}$, and $\gamma \simeq 1.43$, we obtain $\overline{N}_{\rm RG} \sim 3.5$ within $z_{\rm out} = 0.04\,{\rm pc}$ and $\overline{N}_{\rm RG} \sim 82.6$ within $z_{\rm out} = 0.3\,{\rm pc}$, which is within uncertainties consistent with the number of missing bright giants at these scales (Gallego-Cano et al., 2018; Habibi et al., 2019). Moreover, the number of encounters given by Eq. (7) is a lower limit as the various dynamical processes (resonant relaxation, jet precession) can effectively increase the interaction volume during the jet lifetime.

3 RESULTS: SIMULATED SURFACE-DENSITY PROFILES

The Galactic center stellar population can only be studied in detail in the near-infrared domain, mainly in the $K_{\rm s}$-band at $2.2\,\mu{\rm m}$ (see e.g. Schödel et al., 2014). As the red giant crosses the jet several times, see Fig. 1, its radius will shrink from R_0 to R_1, but its bolometric luminosity $L_\star = 4\pi R_\star^2 \sigma T_\star^4$ will stay constant as it depends on the core mass (Paczyński, 1970; Refsdal and Weigert, 1971), which is not affected. This gives us the basic scaling for the effective temperature after the jet-red giant interactions,

$$T_1 = T_0 \left(\frac{R_0}{R_1}\right)^{1/2}\,. \tag{8}$$

The infrared luminosity $L_{\rm IR} = \pi B_{\rm IR} 4\pi R_\star^2$ will decrease with the decrease in the radius. This can be shown by taking the Rayleigh-Jeans approximation, though very crude in the infrared domain, from which $L_{\rm IR} \approx 8\pi^2(\nu/c)^2 k T_\star R_\star^2$. The ratio between the post- and the pre-collision infrared luminosity can then be expressed as,

$$\frac{L_1^{\rm IR}}{L_0^{\rm IR}} \approx \left(\frac{R_1}{R_0}\right)^{3/2}\,. \tag{9}$$

For illustration of the effect, let us consider the red giant with an initial atmosphere radius of $R_0 = 120\,R_\odot$ that is ablated down to $R_1 = 30\,R_\odot$ after several thousand crossings through the jet. From Eq. (8), the effective temperature will increase to $T_1 = 2T_0$, while the infrared luminosity will decrease to $L_1^{\rm IR} = 0.125 L_0^{\rm IR}$ according to Eq. (9) or the magnitude will increase by 2.26 mag. For an even more profound transition from $R_0 = 120\,R_\odot$ to $R_1 = 4\,R_\odot$, the post-collision values are expected to be $T_1 = 5.5T_0$, $L_1^{\rm IR} = 0.006 L_0^{\rm IR}$, and the magnitude increase is $\Delta K = 5.54$ mag. These changes can already significantly influence stellar counts in individual magnitude bins.

To better evaluate how the red giant–jet interactions could have affected the surface-density profiles of late-type stars in individual near-infrared magnitude bins, we perform

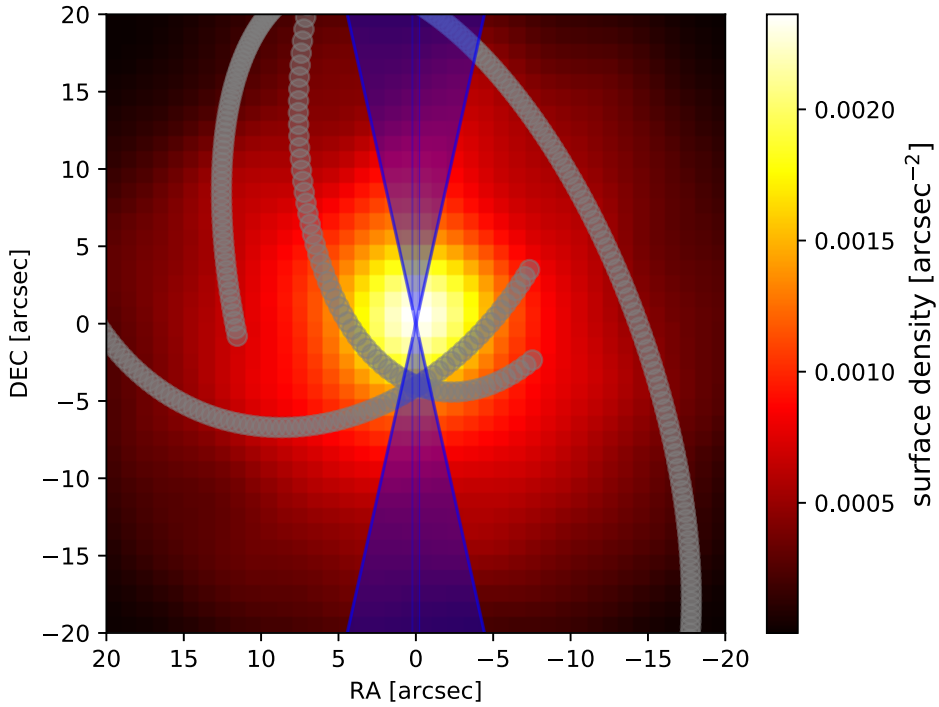

Figure 4. The initial surface-density distribution of the Monte Carlo-generated NSC consisting of 4000 late-type stars, smoothed by the Gaussian kernel on a regular grid of 40×40 points. The blue shaded region represents the jet with a half-opening angle of 12.5°. The three gray streamers represent the three minispiral arms.

a Monte Carlo simulation by generating a mock NSC. The NSC is assumed to be spherical and described by the volume number density of $n_{\rm RG} \approx n_0(z/z_0)^{-\gamma}$ with $n_0 = 52\,{\rm pc}^{-3}$, $z_0 = 4.9\,{\rm pc}$, and $\gamma \sim 1.43$ according to Gallego-Cano et al. (2018). This number density profile implies the presence of ~ 4000 late-type stars inside one parsec, whose properties were generated using the Monte Carlo approach. The surface density distribution of such a cluster is depicted in Fig. 4 including the jet with a half-opening angle of $\theta = 12.5°$ and the three minispiral streamers as currently observed are also plotted for a better orientation.

Each star was assigned a mass in the range between $0.08\,M_\odot$ and $100\,M_\odot$ according to the Kroupa initial mass function (IMF; Kroupa, 2001). The Chabrier/Kroupa IMF seems to be consistent with the IMF of the Galactic center late-type stellar population (Pfuhl et al., 2011). Subsequently, we also assigned the core mass to each star. For the purposes of our analysis, we fixed the core-mass fraction to $\mu_{\rm c}/m_\star = 0.4$, which lies between the value derived from the Schönberg-Chandrasekhar limit and the values expected from the last phase of the stellar evolution, when the white-dwarf core constitutes most of the mass of solar-type stars.

To calculate the magnitude distribution in the near-infrared K_s-band, we followed this procedure,

(1) We calculate the bolometric stellar luminosity and the stellar radius as a function of the core mass, $L_\star(\mu_c)$ and $R_\star(\mu_c)$, according to Eq. (19) in Zajaček et al. (2020).
(2) When the jet is active, we compare $R_\star$ of the entering star with R_{stag} calculated using Eq. (3). When $R_\star \geq R_{stag}$, we set $R_\star = R_{stag}$. For this analysis, we assumed that almost all late-type stars within 0.5 pc could have interacted with the jet for at least several hundred times. This would be possible when the vector resonant-relaxation timescale is shorter than the jet lifetime or the jet would be precessing.
(3) The effective temperature is calculated as $T_\star = T_\odot (L_\star/L_\odot)^{1/4}(R_\star/R_\odot)^{-1/2}$.
(4) From the Planck function $B_\nu(T_\star)$, we calculate the flux density at K_s-band, $F_\nu = \pi B_\nu(T_\star)(R_\star/d)^2$, where d is the distance to the Galactic center. The intrinsic (dereddened) apparent magnitude is then calculated as $m_K = -2.5 \log (F_\nu/653\,\mathrm{Jy})$.

In the next step, to estimate the surface-density distributions, we count the number of stars $N_\star$ in the concentric annuli with the mean radius R and the width ΔR, from which we estimate the surface density as $\sigma_\star = N_\star/(2\pi R \Delta R)$ with the uncertainty of $\sqrt{N_\star}/(2\pi R \Delta R)$. Then we bin the stars into two-magnitude bins, starting at 18 mag and going down to the brightest stars with 10 mag. Initially, without any jet influence, the surface density distribution across all magnitude bins could be described as a single power-law described as $N(R) = N_0(R/R_0)^{-\Gamma}$, hence as a proper cusp, see Table 1. When the jet is switched on with the kinetic luminosity of $L_j = 10^{44}\,\mathrm{erg\,s^{-1}}$, the surface-density profile of the brightest giants (10-12 mag, dereddened) becomes flat up to $\sim$ 0.3 pc, see Fig. 5. The flattening inside 0.04 pc is also apparent for late-type stars in the 12-14 mag bin (dereddened), while fainter stars with larger magnitudes maintain a cusp-like distribution as the most recent observational studies indicate (Gallego-Cano et al., 2018; Habibi et al., 2019; Schödel et al., 2020). The surface-density distribution of bright late-type stars can be fitted by a broken power-law function in the form $N(R) = N_0(R/R_{br})^{-\Gamma}[1 + (R/R_{br})^{\Delta}]^{(\Gamma-\Gamma_0)/\Delta}$, where R_{br} is the break radius, Γ is the slope of the inner cluster part inside R_{br}, Γ_0 is the slope of the outer cluster part, and Δ describes the sharpness of transition. For both the case without any jet and the case with the jet kinetic luminosity of $10^{44}\,\mathrm{erg\,s^{-1}}$, we summarize the slopes and the break radii of the fitted power-law functions in Table 1 for individual magnitude bins.

4 DISCUSSION AND CONCLUSIONS

We presented a novel scenario based on the red giant–nuclear jet interactions to explain the peculiarities of the Milky Way Nuclear Star Cluster – on one hand, the cusp-like distribution of faint late-type stars, which is expected from the two-body relaxation, and on the other hand, the core-like distribution of bright red giants, which requires a mechanism that preferentially acts on stars with more extended atmospheres. The interaction of red giants with the nuclear jet during active phases of Sgr A* can naturally explain the observed surface-density features since the jet removes the envelopes of more extended red giants more efficiently from basic principles. The repetitive mechanical removal of the atmosphere material also ensures that the resulting effect on the late-type star is permanent –

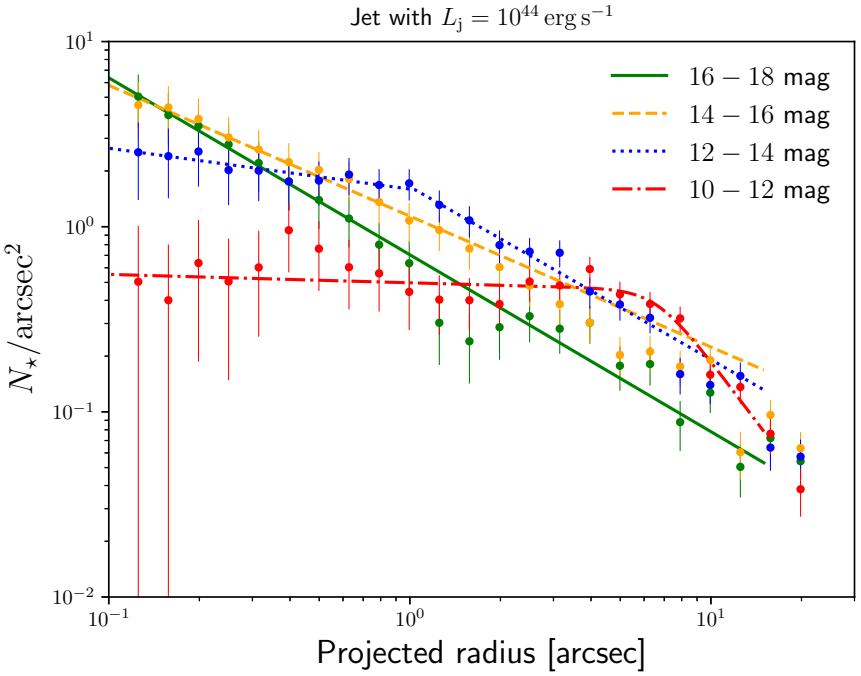

Figure 5. Post-collisional surface-density distributions of late-type stars constructed from an initially cuspy NSC. The jet kinetic luminosity was set to 10^{44} erg s^{-1} and all the stars were assumed to interact with the jet, which for the brightest giants led to the ablation of their envelopes. The brighter late-type stars in the magnitude bins 10-12 mag and 12-14 mag exhibit a broken power-law distribution, while the fainter giants (14-16 mag and 16-18 mag) maintain the cusp-like distribution. The magnitude values are treated as intrinsic or dereddened. For the comparison with the observational results, it is necessary to add ∼ 2.5 mag (Schödel et al., 2010) for the line-of-sight mean extinction in $K_{\rm s}$-band.

its effective temperature will increase, its mass will decrease, and the infrared luminosity will drop. This is an advantage of this model in comparison with the central luminosity source proposed by Sellgren et al. (1990), since after the source luminosity drops, the CO molecule could form again in the extended atmosphere because of the lowered ionizing potential.

In addition, we showed that the jet–red giant interactions are the most efficient in removing the mass inside 0.04 pc or the S cluster region, where the removed mass by the jet ablation is comparable to the cumulative mass loss from stellar winds. Hence, the overall mass loss can effectively be doubled in comparison with the standard stellar evolution during the jet existence. The mass removal in the S cluster could also be enhanced by the fact that red giants are expected to be warm colliders in this region, i.e. stars that are not able to cool off before the subsequent collision with the jet. Therefore their envelopes are more puffed up, which increases the collisional cross-sections and the overall mass loss. For

Table 1. Best-fit slopes and break radii of the power-law distributions that are used to describe the surface-density distributions of the mock NSC at its initial "cuspy" stage (no jet), see Fig. 4, and in the stage after the active phase with the jet, see distributions in Figure 5. Values are listed for different magnitude bins and two cases of the jet activity: no jet and the jet with the kinetic luminosity of $L_{\rm j} = 10^{44}\,{\rm erg\,s^{-1}}$.

Magnitude bin	No jet activity	Jet $L_{\rm j} = 10^{44}\,{\rm erg\,s^{-1}}$
18-16 mag	single: $\Gamma = 0.9$	single: $\Gamma = 1.0$
16-14 mag	single: $\Gamma = 0.6$	single: $\Gamma = 0.7$
14-12 mag	single: $\Gamma = 0.6$	broken: $\Gamma = 0.2$, $\Gamma_0 = 0.9$, $R_{\rm br} = 1''$
12-10 mag	single: $\Gamma = 0.7$	broken: $\Gamma = 0.04$, $\Gamma_0 = 2.2$, $R_{\rm br} = 6.6''$

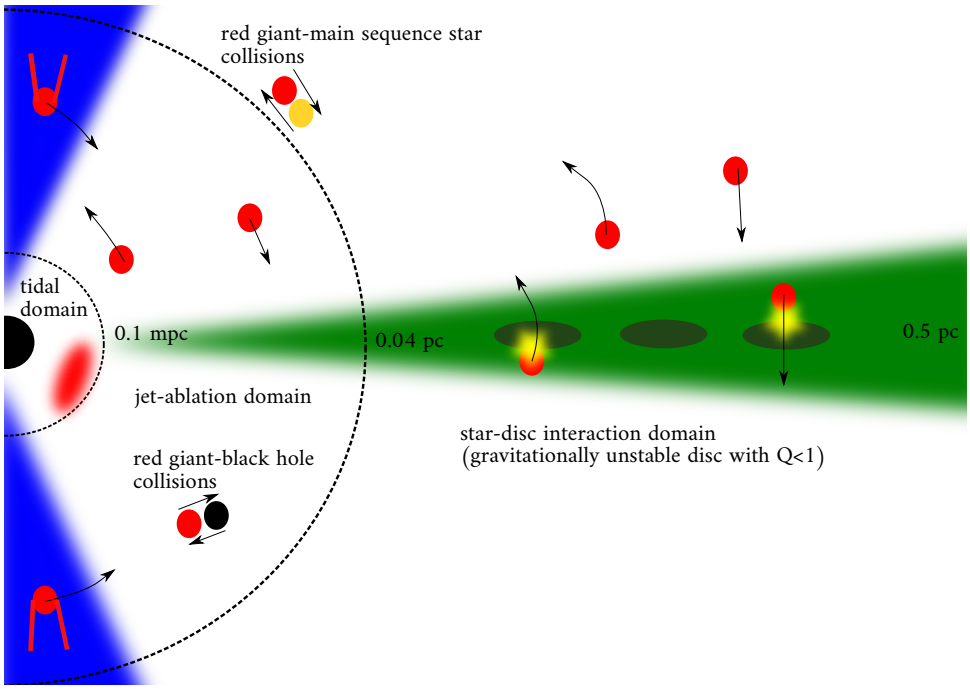

Figure 6. Illustration of the mechanisms that contributed to the depletion of bright red giants in the inner 0.5 pc of the Galactic center. Closest to Sgr A* (0.1 mpc), the tidal stripping of the red giant envelopes operated. Inside the inner 0.04 pc (S cluster), jet-red giant interactions dominated, while outside 0.04 pc, the interaction of red giants with the fragmenting gaseous disc was likely the dominant mechanism. Occasional red giant-black hole and red giant-main sequence star collisions further contributed to the depletion throughout the NSC. Distances are not drawn to the scale.

bright giants with atmosphere radii of the order of $100\,R_\odot$, the increase in the near-infrared magnitude is expected to be $2-6$ mag, which leads to the flattening of their surface-density

profile, while they can turn into fainter gaints in the near-infrared after the ablation and make their profiles even more cuspy.

Outside the S cluster, the efficiency of jet–red giant interactions in terms of the mass removal drops in comparison with star-disc collisions. Therefore, the star-disc collisions likely complemented jet–red giant interactions at larger scales, where the massive gaseous disk fragmented into star-forming clumps with significantly increased density (Levin and Beloborodov, 2003; Milosavljević and Loeb, 2004). On the other hand, at much smaller scales of a fraction of a milliparsec, tidal stripping of envelopes operated. Throughout the NSC, occasional collisions of large red giants with stellar black holes and main-sequence stars could partially have contributed to the depletion, but they cannot alone explain the missing brightest giants (Dale et al., 2009). We illustrate all of these mechanisms and the regions of their largest efficiency in Fig. 6. They likely all contributed to the observed dearth of bright red giants in the inner 0.5 pc.

A limitation of our model is that only a fraction of late-type stars that at a given time cross the jet will suffer the mass removal because of the narrow opening angle of the jet. A wide-angle outflow, e.g. resulting from the accretion disc winds, with a half-opening angle $w\theta$, with $w > 1$, could hit more stars. However, this is at the cost of enlarging the stagnation radius by $\sim w$ and diminishing the mass removal by w^2. Hence, a highly-collimated jet is required for the mechanism to work efficiently enough to create an apparent core in the surface-density distribution. Moreover, discussed dynamical processes, such as the coherent resonant relaxation and the jet precession, can considerably enlarge the interaction volume during the active jet phase. Since there are at least ~ 100 such phases during the Galaxy lifetime, the total number of affected giants is consistent with the number of missing large giants.

ACKNOWLEDGEMENTS

We would like to thank the organizers of RAGtime 22 (dedicated to Prof. Zdeněk Stuchlík) for the smooth and efficient performance of the conference in the online space during the COVID19 pandemic. MZ thanks Robert "Ski" Antonucci (UC Santa Barbara) for input and useful comments. MZ and BC acknowledge the financial support by the National Science Center, Poland, grant No. 2017/26/A/ST9/00756 (Maestro 9). VK thanks MŠMT grant LTI 17018 for support. We are also grateful to the Czech-Polish mobility program (MŠMT 8J20PL037) for support. In addition, MZ also acknowledges the NAWA financial support under the agreement PPN/WYM/2019/1/00064 to perform a three-month exchange stay at the Astronomical Institute of the Czech Academy of Sciences in Prague. VW was supported by European Union's Horizon 2020 research and innovation programme under grant agreement No 894881.

REFERENCES

Alexander, T. (2005), Stellar processes near the massive black hole in the Galactic center [review article], *Physics Reports*, **419**(2-3), pp. 65–142, arXiv: `astro-ph/0508106`.

Alexander, T. (2017), Stellar Dynamics and Stellar Phenomena Near a Massive Black Hole, *ARA&A*, **55**(1), pp. 17–57, arXiv: 1701.04762.

Amaro-Seoane, P. and Chen, X. (2014), The Fragmenting Past of the Disk at the Galactic Center: The Culprit for the Missing Red Giants, *ApJL*, **781**(1), L18, arXiv: 1310.0458.

Amaro-Seoane, P., Chen, X., Schödel, R. and Casanellas, J. (2020), Making bright giants invisible at the Galactic Centre, *MNRAS*, **492**(1), pp. 250–255, arXiv: 1910.04774.

Antonini, F., Capuzzo-Dolcetta, R., Mastrobuono-Battisti, A. and Merritt, D. (2012), Dissipationless Formation and Evolution of the Milky Way Nuclear Star Cluster, *ApJ*, **750**(2), 111, arXiv: 1110.5937.

Araudo, A. T., Bosch-Ramon, V. and Romero, G. E. (2013), Gamma-ray emission from massive stars interacting with active galactic nuclei jets, *MNRAS*, **436**(4), pp. 3626–3639, arXiv: 1309.7114.

Armitage, P. J., Zurek, W. H. and Davies, M. B. (1996), Red Giant–Disk Encounters: Food for Quasars?, *ApJ*, **470**, p. 237, arXiv: astro-ph/9605137.

Bahcall, J. N. and Wolf, R. A. (1977), The star distribution around a massive black hole in a globular cluster. II. Unequal star masses., *ApJ*, **216**, pp. 883–907.

Barkov, M. V., Aharonian, F. A., Bogovalov, S. V., Kelner, S. R. and Khangulyan, D. (2012), Rapid TeV Variability in Blazars as a Result of Jet-Star Interaction, *ApJ*, **749**(2), 119, arXiv: 1012.1787.

Barkov, M. V., Aharonian, F. A. and Bosch-Ramon, V. (2010), Gamma-ray Flares from Red Giant/Jet Interactions in Active Galactic Nuclei, *ApJ*, **724**(2), pp. 1517–1523, arXiv: 1005.5252.

Baumgardt, H., Gualandris, A. and Portegies Zwart, S. (2006), Ejection of hypervelocity stars from the Galactic Centre by intermediate-mass black holes, *MNRAS*, **372**(1), pp. 174–182, arXiv: astro-ph/0607455.

Bland-Hawthorn, J. and Cohen, M. (2003), The Large-Scale Bipolar Wind in the Galactic Center, *ApJ*, **582**(1), pp. 246–256, arXiv: astro-ph/0208553.

Bland-Hawthorn, J., Maloney, P. R., Sutherland, R., Groves, B., Guglielmo, M., Hao Li, W., Curzons, A., Cecil, G. and Fox, A. J. (2019), The Large-scale Ionization Cones in the Galaxy, *ApJ*, **886**(1), 45.

Bogdanović, T., Cheng, R. M. and Amaro-Seoane, P. (2014), Disruption of a Red Giant Star by a Supermassive Black Hole and the Case of PS1-10jh, *ApJ*, **788**(2), 99, arXiv: 1307.6176.

Britzen, S., Fendt, C., Witzel, G., Qian, S. J., Pashchenko, I. N., Kurtanidze, O., Zajacek, M., Martinez, G., Karas, V., Aller, M., Aller, H., Eckart, A., Nilsson, K., Arévalo, P., Cuadra, J., Subroweit, M. and Witzel, A. (2018), OJ287: deciphering the 'Rosetta stone of blazars, *MNRAS*, **478**(3), pp. 3199–3219.

Buchholz, R. M., Schödel, R. and Eckart, A. (2009), Composition of the galactic center star cluster. Population analysis from adaptive optics narrow band spectral energy distributions, *A&A*, **499**(2), pp. 483–501, arXiv: 0903.2135.

Dale, J. E., Davies, M. B., Church, R. P. and Freitag, M. (2009), Red giant stellar collisions in the Galactic Centre, *MNRAS*, **393**(3), pp. 1016–1033, arXiv: 0811.3111.

Ernst, A., Just, A. and Spurzem, R. (2009), On the dissolution of star clusters in the Galactic Centre - I. Circular orbits, *MNRAS*, **399**(1), pp. 141–156, arXiv: 0906.4459.

Gallego-Cano, E., Schödel, R., Dong, H., Nogueras-Lara, F., Gallego-Calvente, A. T., Amaro-Seoane, P. and Baumgardt, H. (2018), The distribution of stars around the Milky Way's central black hole. I. Deep star counts, *A&A*, **609**, A26, arXiv: 1701.03816.

Genzel, R., Thatte, N., Krabbe, A., Kroker, H. and Tacconi-Garman, L. E. (1996), The Dark Mass Concentration in the Central Parsec of the Milky Way, *ApJ*, **472**, p. 153.

Guo, F. and Mathews, W. G. (2012), The Fermi Bubbles. I. Possible Evidence for Recent AGN Jet

Activity in the Galaxy, *ApJ*, **756**(2), 181, arXiv: 1103.0055.

Habibi, M., Gillessen, S., Pfuhl, O., Eisenhauer, F., Plewa, P. M., von Fellenberg, S., Widmann, F., Ott, T., Gao, F., Waisberg, I., Bauböck, M., Jimenez-Rosales, A., Dexter, J., de Zeeuw, P. T. and Genzel, R. (2019), Spectroscopic Detection of a Cusp of Late-type Stars around the Central Black Hole in the Milky Way, *ApJL*, **872**(1), L15, arXiv: 1902.07219.

Heywood, I., Camilo, F., Cotton, W. D., Yusef-Zadeh, F., Abbott, T. D., Adam, R. M., Aldera, M. A., Bauermeister, E. F., Booth, R. S., Botha, A. G., Botha, D. H., Brederode, L. R. S., Brits, Z. B., Buchner, S. J., Burger, J. P., Chalmers, J. M., Cheetham, T., de Villiers, D., Dikgale-Mahlakoana, M. A., du Toit, L. J., Esterhuyse, S. W. P., Fanaroff, B. L., Foley, A. R., Fourie, D. J., Gamatham, R. R. G., Goedhart, S., Gounden, S., Hlakola, M. J., Hoek, C. J., Hokwana, A., Horn, D. M., Horrell, J. M. G., Hugo, B., Isaacson, A. R., Jonas, J. L., Jordaan, J. D. B. L., Joubert, A. F., Józsa, G. I. G., Julie, R. P. M., Kapp, F. B., Kenyon, J. S., Kotzé, P. P. A., Kriel, H., Kusel, T. W., Lehmensiek, R., Liebenberg, D., Loots, A., Lord, R. T., Lunsky, B. M., Macfarlane, P. S., Magnus, L. G., Magozore, C. M., Mahgoub, O., Main, J. P. L., Malan, J. A., Malgas, R. D., Manley, J. R., Maree, M. D. J., Merry, B., Millenaar, R., Mnyandu, N., Moeng, I. P. T., Monama, T. E., Mphego, M. C., New, W. S., Ngcebetsha, B., Oozeer, N., Otto, A. J., Passmoor, S. S., Patel, A. A., Peens-Hough, A., Perkins, S. J., Ratcliffe, S. M., Renil, R., Rust, A., Salie, S., Schwardt, L. C., Serylak, M., Siebrits, R., Sirothia, S. K., Smirnov, O. M., Sofeya, L., Swart, P. S., Tasse, C., Taylor, D. T., Theron, I. P., Thorat, K., Tiplady, A. J., Tshongweni, S., van Balla, T. J., van der Byl, A., van der Merwe, C., van Dyk, C. L., Van Rooyen, R., Van Tonder, V., Van Wyk, R., Wallace, B. H., Welz, M. G. and Williams, L. P. (2019), Inflation of 430-parsec bipolar radio bubbles in the Galactic Centre by an energetic event, *Nature*, **573**(7773), pp. 235–237, arXiv: 1909.05534.

Hills, J. G. (1975), Possible power source of Seyfert galaxies and QSOs, *Nature*, **254**(5498), pp. 295–298.

Ito, H., Kino, M., Kawakatu, N., Isobe, N. and Yamada, S. (2008), The Estimate of Kinetic Power of Jets in FR II Radio Galaxies: Existence of Invisible Components?, *ApJ*, **685**(2), pp. 828–838, arXiv: 0807.1946.

Kieffer, T. F. and Bogdanović, T. (2016), Can Star-Disk Collisions Explain the Missing Red Giants Problem in the Galactic Center?, *ApJ*, **823**(2), 155, arXiv: 1602.03527.

Kim, S. S. and Morris, M. (2003), Dynamical Friction on Star Clusters near the Galactic Center, *ApJ*, **597**(1), pp. 312–322, arXiv: astro-ph/0307271.

King, A. (2020), GSN 069 - A tidal disruption near miss, *MNRAS*, **493**(1), pp. L120–L123, arXiv: 2002.00970.

Kroupa, P. (2001), On the variation of the initial mass function, *MNRAS*, **322**(2), pp. 231–246, arXiv: astro-ph/0009005.

Levin, Y. and Beloborodov, A. M. (2003), Stellar Disk in the Galactic Center: A Remnant of a Dense Accretion Disk?, *ApJL*, **590**(1), pp. L33–L36, arXiv: astro-ph/0303436.

Li, Z., Morris, M. R. and Baganoff, F. K. (2013), Evidence for a Parsec-scale Jet from the Galactic Center Black Hole: Interaction with Local Gas, *ApJ*, **779**(2), 154, arXiv: 1310.0146.

Merritt, D. and Szell, A. (2006), Dynamical Cusp Regeneration, *ApJ*, **648**(2), pp. 890–899, arXiv: astro-ph/0510498.

Miller, M. J. and Bregman, J. N. (2016), The Interaction of the Fermi Bubbles with the Milky Way's Hot Gas Halo, *ApJ*, **829**(1), 9, arXiv: 1607.04906.

Milosavljević, M. and Loeb, A. (2004), The Link between Warm Molecular Disks in Maser Nuclei and Star Formation near the Black Hole at the Galactic Center, *ApJL*, **604**(1), pp. L45–L48, arXiv: astro-ph/0401221.

Morris, M. (1993), Massive Star Formation near the Galactic Center and the Fate of the Stellar Rem-

nants, *ApJ*, **408**, p. 496.

Mužić, K., Eckart, A., Schödel, R., Buchholz, R., Zamaninasab, M. and Witzel, G. (2010), Comet-shaped sources at the Galactic center. Evidence of a wind from the central 0.2 pc, *A&A*, **521**, A13, arXiv: 1006.0909.

Paczyński, B. (1970), Evolution of Single Stars. I. Stellar Evolution from Main Sequence to White Dwarf or Carbon Ignition, *Acta Astronomica*, **20**, p. 47.

Peißker, F., Zajaček, M., Eckart, A., Sabha, N. B., Shahzamanian, B. and Parsa, M. (2019), New bow-shock source with bipolar morphology in the vicinity of Sgr A*, *A&A*, **624**, A97, arXiv: 1903.05986.

Perets, H. B., Hopman, C. and Alexander, T. (2007), Massive Perturber-driven Interactions between Stars and a Massive Black Hole, *ApJ*, **656**(2), pp. 709–720, arXiv: astro-ph/0606443.

Perucho, M., Bosch-Ramon, V. and Barkov, M. V. (2017), Impact of red giant/AGB winds on active galactic nucleus jet propagation, *A&A*, **606**, A40, arXiv: 1706.06301.

Pfuhl, O., Fritz, T. K., Zilka, M., Maness, H., Eisenhauer, F., Genzel, R., Gillessen, S., Ott, T., Dodds-Eden, K. and Sternberg, A. (2011), The Star Formation History of the Milky Way's Nuclear Star Cluster, *ApJ*, **741**(2), 108, arXiv: 1110.1633.

Phinney, E. S. (1989), Manifestations of a Massive Black Hole in the Galactic Center, in M. Morris, editor, *The Center of the Galaxy*, volume 136 of *IAU Symposium*, p. 543.

Ponti, G., Hofmann, F., Churazov, E., Morris, M. R., Haberl, F., Nandra, K., Terrier, R., Clavel, M. and Goldwurm, A. (2019), An X-ray chimney extending hundreds of parsecs above and below the Galactic Centre, *Nature*, **567**(7748), pp. 347–350, arXiv: 1904.05969.

Rees, M. J. (1988), Tidal disruption of stars by black holes of 10^6-10^8 solar masses in nearby galaxies, *Nature*, **333**(6173), pp. 523–528.

Refsdal, S. and Weigert, A. (1971), On the Production of White Dwarfs in Binary Systems of Small Mass, *A&A*, **13**, p. 367.

Reimers, D. (1987), What do binaries teach us about mass-loss from late-type stars?, in I. Appenzeller and C. Jordan, editors, *Circumstellar Matter*, volume 122 of *IAU Symposium*, pp. 307–318.

Schawinski, K., Koss, M., Berney, S. and Sartori, L. F. (2015), Active galactic nuclei flicker: an observational estimate of the duration of black hole growth phases of $\sim 10^5$ yr, *MNRAS*, **451**(3), pp. 2517–2523, arXiv: 1505.06733.

Schödel, R., Feldmeier, A., Neumayer, N., Meyer, L. and Yelda, S. (2014), The nuclear cluster of the Milky Way: our primary testbed for the interaction of a dense star cluster with a massive black hole, *Classical and Quantum Gravity*, **31**(24), 244007, arXiv: 1411.4504.

Schödel, R., Merritt, D. and Eckart, A. (2009), The nuclear star cluster of the Milky Way: proper motions and mass, *A&A*, **502**(1), pp. 91–111, arXiv: 0902.3892.

Schödel, R., Najarro, F., Muzic, K. and Eckart, A. (2010), Peering through the veil: near-infrared photometry and extinction for the Galactic nuclear star cluster. Accurate near infrared H, Ks, and L' photometry and the near-infrared extinction-law toward the central parsec of the Galaxy, *A&A*, **511**, A18.

Schödel, R., Nogueras-Lara, F., Gallego-Cano, E., Shahzamanian, B., Gallego-Calvente, A. T. and Gardini, A. (2020), The Milky Way's nuclear star cluster: Old, metal-rich, and cuspy. Structure and star formation history from deep imaging, *A&A*, **641**, A102.

Sellgren, K., McGinn, M. T., Becklin, E. E. and Hall, D. N. (1990), Velocity Dispersion and the Stellar Population in the Central 1.2 Parsecs of the Galaxy, *ApJ*, **359**, p. 112.

Su, M., Slatyer, T. R. and Finkbeiner, D. P. (2010), Giant Gamma-ray Bubbles from Fermi-LAT: Active Galactic Nucleus Activity or Bipolar Galactic Wind?, *ApJ*, **724**(2), pp. 1044–1082, arXiv: 1005.5480.

Yusef-Zadeh, F., Arendt, R., Bushouse, H., Cotton, W., Haggard, D., Pound, M. W., Roberts, D. A., Royster, M. and Wardle, M. (2012), A 3 pc Scale Jet-driven Outflow from Sgr A*, *ApJL*, **758**(1), L11, arXiv: 1208.1193.

Yusef-Zadeh, F., Royster, M., Wardle, M., Cotton, W., Kunneriath, D., Heywood, I. and Michail, J. (2020), Evidence for a jet and outflow from Sgr A*: a continuum and spectral line study, *MNRAS*, **499**(3), pp. 3909–3931, arXiv: 2008.04317.

Zajaček, M., Araudo, A., Karas, V., Czerny, B. and Eckart, A. (2020), Depletion of Bright Red Giants in the Galactic Center during Its Active Phases, *ApJ*, **903**(2), 140, arXiv: 2009.14364.

Proceedings of *RAGtime 20–22, 15–19 Oct., 16–20 Sept., 19–23 Oct., 2018/2019/2020, Opava, Czech Republic*
Z. Stuchlík, G. Török and V. Karas, editors, Silesian University in Opava, 2020, pp. 375–382

Recurrence analysis of spinning particles in the Schwarzschild background

Ondřej Zelenka,[1,2,a] Georgios Lukes-Gerakopoulos[1,b] and Vojtěch Witzany[1,c]

[1]Astronomical Institute of the Academy of Sciences of the Czech Republic, Boční II 1401/1a, CZ-141 31 Prague, Czech Republic
[2]Institute of Theoretical Physics, Faculty of Mathematics and Physics, Charles University, CZ-180 00 Prague, Czech Republic
[a]ondrzel@gmail.com,
[b]gglukes@gmail.com,
[c]witzany@asu.cas.cz

ABSTRACT
In this work the dynamics of a spinning particle moving in the Schwarzschild background is studied. In particular, the methods of Poincaré section and recurrence analysis are employed to discern chaos from order. It is shown that the chaotic or regular nature of the orbital motion is reflected on the gravitational waves.

Keywords: Black holes – spinning particles – chaos

1 INTRODUCTION

The equations of motion of a small extended test body in curved spacetimes were first derived by Mathisson (1937) and Papapetrou (1951), and later reformulated by Dixon, W.G. (1970a,b, 1974). The study of such bodies is usually reduced to the pole-dipole approximation, in which all the higher-order multipoles are neglected. In this approximation the test body is characterized solely by its mass and spin and it is called a spinning particle. When this particle is subject only to the gravitational interaction, the equations of motion of the particle read

$$\frac{\mathrm{D}P^{\mu}}{\mathrm{d}\tau} = -\frac{1}{2} R^{\mu}{}_{\nu\kappa\lambda} v^{\nu} S^{\kappa\lambda}, \tag{1}$$

$$\frac{\mathrm{D}S^{\alpha\beta}}{\mathrm{d}\tau} = P^{\alpha} v^{\beta} - v^{\alpha} P^{\beta}, \tag{2}$$

where P^{μ} denotes the four-momentum, $S^{\mu\nu}$ denotes the spin tensor, $v^{\mu} = \mathrm{d}x^{\mu}/\mathrm{d}\tau$ denotes the four-velocity (we choose the affine parameter τ to be the proper time), and $R^{\mu}{}_{\nu\kappa\lambda}$ denotes the Riemann tensor. This set of equations is often called the Mathisson-Papapetrou-Dixon (MPD) equations. To be able to evolve the MPD equations, one has to fix the center of the

978-80-7510-432-8

mass of the body x^μ by imposing a so called Spin Supplementary Condition (SSC). The SSC, we have implemented in this work, is the Tulczyjew–Dixon (TD) (Tulczyjew, 1959; Dixon, W.G., 1970a) one

$$S^{\mu\nu}P_\nu = 0. \tag{3}$$

For this SSC the 4-velocity is related to the other variables through:

$$v^\mu = \frac{m}{\mu^2}\left(P^\mu + \frac{2S^{\mu\nu}R_{\nu\kappa\lambda}P^\iota S^{\kappa\lambda}}{4\mu^2 + R_{\alpha\beta\gamma\delta}S^{\alpha\beta}S^{\gamma\delta}}\right), \tag{4}$$

where $\mu^2 = -P_\nu P^\nu$ is the mass defined with respect to the momentum and $m = -P_\nu v^\nu$ is the mass defined with respect to the velocity.

In the case of TD SSC, μ is a constant of motion independently from the spacetime background. This holds also for the measure of the spin $S = \frac{1}{2}S_{\mu\nu}S^{\mu\nu}$. There are, however, some background-dependent constants constructed from Killing vectors. In particular, for a Killing vector ξ^μ the quantity

$$C = \xi^\mu P_\mu - \frac{1}{2}\xi_{\mu;\nu}S^{\mu\nu} \tag{5}$$

remains conserved along the worldline $x^\mu(\tau)$ (Dixon, W.G., 1970a). In the case of the Schwarzschild spacetime the integrals are four. Namely the energy E and the three components of the total angular momentum $J_b = (J_x, J_y, J_z)$. In the case of geodesic motion, which corresponds to the case $S = 0$, the respective system is integrable, since for the respective Hamiltonian $H = g^{\mu\nu}P_\mu P_\nu/(2\mu)$ there are as many degrees of freedom as integrals. In particular, there is the energy, two components of total angular momentum[1] and the preservation of the Hamiltonian function itself $H = -\mu/2$. The introduction of the spin increases the degrees of freedom cancelling the integrability and induces chaotic motion to the system (Suzuki and Maeda, 1997). Witzany et al. (2018) showed that, independent of the space-time background, the spinning particle under the TD SSC has only one additional active degree of freedom as compared to the geodesic problem (the structureless test particle), at least if the conservation of the spin measure as well as the TD constraint itself are taken into account. This implies that by using the remaining constants of motion (E and two components of J_b) in the case of the Schwarzschild background, the degrees of freedom can be reduced to two, i.e., the dynamics of the system can be described in a 4 dimensional phase space.

This work revisits the study of chaos in the case of a spinning particle moving in the Schwarzschild spacetime, which was for the first time performed by Suzuki and Maeda (1997). Since the dynamics of the studied system can be confined to 2 degrees of freedom by fixing the values of the integrals of motion, a 2D Poincaré section is an accurate method to study the dynamics of the system. However, when the number of degrees of freedom is higher than 2, such as for a spinning particle moving in a Kerr background,

[1] The components of the total angular momentum are not mutually in involution, thus from the three components only the two could be taken into account.

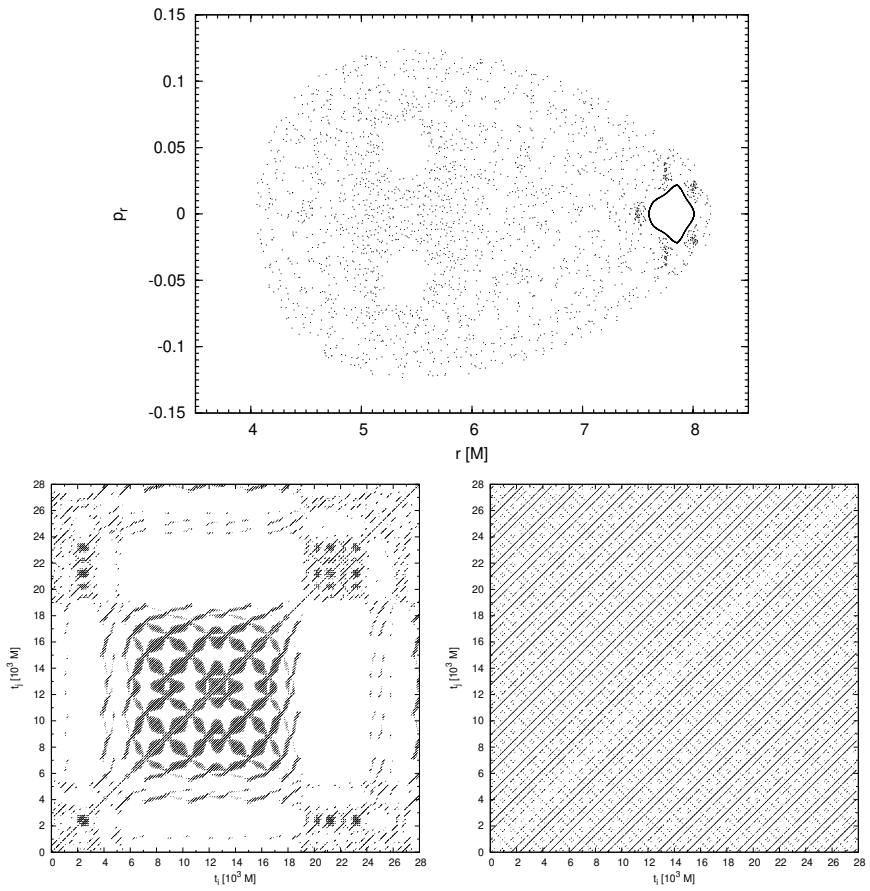

Figure 1. *Top panel*: A Poincaré section on the equatorial plane $\theta = \pi/2$ with $P_\theta > 0$, $E = 0.92292941\mu$, $J_z = 4.0\mu M$, $S = 1.4\mu M$. *Bottom left panel*: The recurrence plot for a chaotic trajectory with initial conditions $r = 4.5M$, $P_r = 0$; recurrence threshold $\varepsilon = 0.87083$. *Bottom right panel*: The recurrence plot for a regular trajectory with initial conditions $r = 7.6M$, $P_r = 0$; recurrence threshold $\varepsilon = 0.49013$.

then a 2D Poincaré section is not a reliable method to study the dynamics (see, e.g., Lukes-Gerakopoulos et al., 2016). For studying systems independently from the number of degrees of freedom *recurrence analysis* is considered to be a more appropriate method (see, e.g., the review of Marwan et al., 2007 and reference therein). Further advantage of recurrence analysis is that it is a method analyzing time series, which is advantageous when we consider signals from gravitational wave strains later on. Thus, in this work we test the performance of the recurrence analysis by comparing it with the standard method of a 2D Poincaré section.

Units and notation: Geometric units are used throughout the article, $G = c = 1$. Greek letters denote the indices corresponding to spacetime, while Latin letters denote indices corresponding only to space. We use the Riemann tensor defined as $R^{\alpha}{}_{\beta\gamma\delta} = \Gamma^{\alpha}_{\gamma\lambda}\Gamma^{\lambda}_{\delta\beta} - \partial_{\delta}\Gamma^{\alpha}_{\gamma\beta} - \Gamma^{\alpha}_{\delta\lambda}\Gamma^{\lambda}_{\gamma\beta} + \partial_{\gamma}\Gamma^{\alpha}_{\delta\beta}$, where the Christoffel symbols Γ are computed from the metric with signature $(-,+,+,+)$. The Levi-Civita tensor is $\epsilon_{\mu\nu\rho\sigma} = \sqrt{-g}\tilde{\epsilon}_{\mu\nu\rho\sigma}$, with the Levi-Civita symbol $\tilde{\epsilon}_{0123} = 1$.

2 COMPARING POINCARÉ SECTION METHOD WITH RECURRENCE ANALYSIS

According to the recurrence analysis, if $\boldsymbol{y}(t)$ is a vector time series in an arbitrary phase space, then a *recurrence* occurs when the distance between the ith point and the jth point of the time series drops below a threshold ε. These recurrences are recorded in the recurrence matrix

$$\mathcal{R}(i, j; \varepsilon) = \Theta\left(\varepsilon - ||\boldsymbol{y}(i) - \boldsymbol{y}(j)||\right), \tag{6}$$

where $||.||$ denotes a norm in the phase space and Θ denotes the Heaviside step-function. A depiction of a recurrence matrix produces a recurrence plot (see, e.g., Marwan et al., 2007). By inspecting a recurrence plot, as by inspecting a Poincaré section, one can tell whether a time series is chaotic or not. On a Poincaré section a chaotic orbit appears as a swarm of scattered points, an example of which can be seen in the top panel of Fig. 1. On the other hand, on a recurrence plot a chaotic orbit can be identified by observing square–like structures, as can be seen in the left bottom panel of Fig. 1. A regular orbit is depicted on a Poincaré section as a smooth zero-width closed curve, as the one lying at $7 \lesssim r \lesssim 8$ in the top panel of Fig. 1, while on a recurrence plot the regularity of the orbit manifests itself by long diagonal lines covering the whole plot.

For the initial conditions of Fig. 1 we have followed the setup suggested by Suzuki and Maeda (1997). Namely, we have chosen J_z to be the only non-zero total angular momentum component, i.e. $J_b = (0, 0, J_z)$; we have fixed the energy E and the spin measure S, which is most conveniently expressed in units of μM, where M is the mass of the central Schwarzschild black hole. Apart from the constants, we always choose initial conditions such that $\theta = \pi/2, P_r = 0$ and r varying from orbit to orbit (t, ϕ, r, θ are the usual Schwarzschild coordinates). From the four components of the SSC (Eq. (3)) only three are linearly independent, and along with the choice of the constants of motion this setup determines the six components of the spin tensor and the remaining three components of the momentum. For more details on how to set up the initial conditions the interested reader is referred to Suzuki and Maeda (1997).

To evolve the MPD equations with TD SSC one has to use Eq. (4) at each integration step and take into account the fact that $v^{\mu}v_{\mu} = -1$. This procedure actually fixes the mass m at each integration step. The time series for the recurrence plots in Fig. 1 were obtained by the method explained in Appendix A.

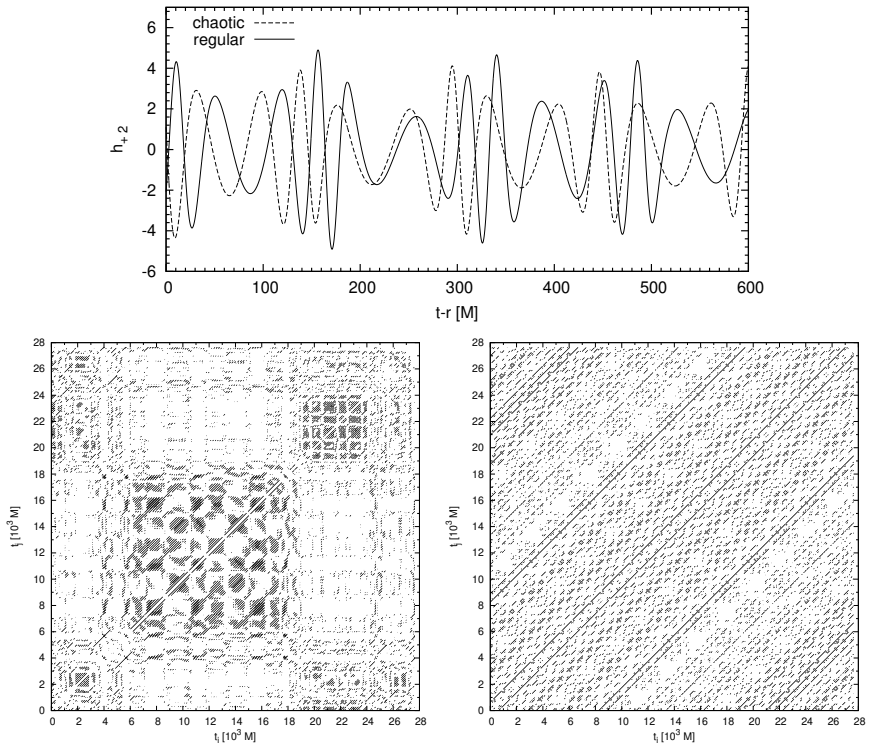

Figure 2. *Top panel*: The gravitational waveforms of the strain mode h_{+2} corresponding to the orbits presented in Fig. 1. *Bottom left panel*: The recurrence plot of the waveform corresponding to the chaotic orbit, using time delay $8.664M$ and embedding dimension 21, $\varepsilon = 8.566$. *Bottom right panel*: The recurrence plot for the waveform corresponding to the regular orbit, using time delay $8.664M$ and embedding dimension 21, $\varepsilon = 6.819$.

3 GRAVITATIONAL WAVE STRAINS

In this section we will discuss whether chaos and order can be discerned in gravitational waves. We shall use gravitational waves emitted from a spinning particle moving in the Schwarzschild background. In a similar study, Kiuchi and Maeda (2004) have used the analytic formula of multipole expansion of gravitational field to calculate the gravitational

waves. In our study, we use a time-domain Teukolsky equation solver called Teukode. Teukode was developed by Harms et al. (2014) and in Harms et al. (2016) the spin of the particle was incorporated.

From Teukode we obtain the strain h_+ decomposed in a spin-weighted spherical harmonic basis

$$h_+ = \sum_{\mathrm{m}=1}^{\infty} h_{+\mathrm{m}} = \sum_{l=2}^{\infty} \sum_{\mathrm{m}=1}^{\mathrm{m}=l} h_{+l\mathrm{m}}. \tag{7}$$

For the purposes of our study we use just h_{+2}. The waveforms of the strain for the two cases in the bottom panels of Fig. 1 are shown in the top panel of Fig. 2. From looking at the shapes of the waveforms alone one cannot tell whether they belong to a chaotic or a regular trajectory, which is in agreement with the findings of Kiuchi and Maeda (2004). To get an answer to the above issue one has to apply an appropriate chaos detection technique. In our work this technique is the recurrence analysis. In the bottom panels of Fig. 2, we see recurrence plots of h_{+2}, the left corresponds to gravitational waves from the chaotic orbit and the right corresponds to gravitational waves from the regular orbit of Fig. 1.

The recurrence plots of Fig. 2 look quite similar to the respective ones in Fig. 1, thus they characterize the orbits in the same way as in Fig. 1. Namely, the left bottom panel is dominated by square-like structures indicating chaos and the right bottom panel is dominated by diagonal lines indicating order. In conclusion, the information about the chaoticity or the regularity of an orbit is encoded in the respective gravitational waves.

In the regular case of the right panel of Fig. 2 a more careful inspection shows that the diagonal lines are slightly diffused. This diffusion is introduced by the numerical accuracy of Teukode. This is similar to what happened when Lukes-Gerakopoulos and Kopáček (2018) polluted the time series with white noise. Moreover, it should be mentioned that this is the first time that Teukode has been tested for off-equatorial orbits. The fact that the orbital and the waveform recurrence plots do not only indicate the same dynamical nature, but actually look alike, confirms that Teukode is performing well also for off-equatorial orbits.

4 SUMMARY

We have employed recurrence analysis to discern chaos from order in the case of a spinning particle moving in the Schwarzschild background. In particular, we have first provided a Poincaré section, on which we identified one regular and one chaotic orbit. For these two orbits we have produced the respective recurrence plots and we have confirmed their nature with respect to chaoticity. Then, we fed these two trajectories to the Teukode to produce the respective gravitational waveforms. Since from just inspecting a waveform one cannot tell whether it comes from a regular or chaotic trajectory (Kiuchi and Maeda, 2004), we have applied recurrence analysis on the gravitational waveforms. The waveform recurrence plots and the respective orbital ones look very similar, which indicates that the information about the chaoticity or not of an orbit can be revealed in the emitted gravitational waves.

ACKNOWLEDGEMENTS

The authors are supported by Grant No. GAČR-17-06962Y of the Czech Science Foundation. G.L.-G. would like to acknowledge networking support by the COST Action CA16104. O.Z. and G.L.-G. would also like to express gratitude for the hospitality of the Theoretical Physics Institute at the University of Jena. Finally, we would like to thank Ondřej Kopáček, Sebastiano Bernuzzi, Enno Harms and Sarp Akcay for useful discussions and comments.

REFERENCES

Dixon, W.G. (1970a), Dynamics of extended bodies in General Relativity. I. Momentum and angular momentum, *Proc.Roy.Soc.Lond.*, **A314**, pp. 499–527.

Dixon, W.G. (1970b), Dynamics of extended bodies in General Relativity. II. Moments of the charge-current vector, *Proc.Roy.Soc.Lond.*, **A319**, pp. 509–547.

Dixon, W.G. (1974), Dynamics of extended bodies in General Relativity. III. Equations of motion, *Philosophical Transactions of the Royal Society of London A: Mathematical, Physical and Engineering Sciences*, **277**, pp. 59–119.

Harms, E., Bernuzzi, S., Nagar, A. and Zenginoğlu, A. (2014), A new gravitational wave generation algorithm for particle perturbations of the Kerr spacetime, *Classical Quantum Gravity*, **31**(24), 245004, arXiv: 1406.5983.

Harms, E., Lukes-Gerakopoulos, G., Bernuzzi, S. and Nagar, A. (2016), Asymptotic gravitational wave fluxes from a spinning particle in circular equatorial orbits around a rotating black hole, *Phys. Rev. D*, **93**(4), 044015, arXiv: 1510.05548.

Kiuchi, K. and Maeda, K.-I. (2004), Gravitational waves from a chaotic dynamical system, *Phys. Rev. D*, **70**(6), 064036, arXiv: gr-qc/0404124.

Lukes-Gerakopoulos, G., Katsanikas, M., Patsis, P. A. and Seyrich, J. (2016), Dynamics of a spinning particle in a linear in spin Hamiltonian approximation, *Phys. Rev. D*, **94**(2), 024024, arXiv: 1606.09171.

Lukes-Gerakopoulos, G. and Kopáček, O. (2018), Recurrence analysis as a tool to study chaotic dynamics of extreme mass ratio inspiral in signal with noise, *International Journal of Modern Physics D*, **27**, 1850010, arXiv: 1709.08446.

Marwan, N., Carmen Romano, M., Thiel, M. and Kurths, J. (2007), Recurrence plots for the analysis of complex systems, *Phys. Rep.*, **438**, pp. 237–329.

Mathisson, M. (1937), Neue mechanik materieller systemes, *Acta Phys.Polon.*, **6**, pp. 163–2900.

Papapetrou, A. (1951), Spinning test particles in general relativity. 1., *Proc.Roy.Soc.Lond.*, **A209**, pp. 248–258.

Suzuki, S. and Maeda, K.-I. (1997), Chaos in Schwarzschild spacetime: The motion of a spinning particle, *Phys. Rev. D*, **55**, pp. 4848–4859, arXiv: gr-qc/9604020.

Tulczyjew, W. (1959), Motion of multipole particles in general relativity theory, *Acta Phys. Pol*, **18**, p. 393.

Witzany, V., Steinhoff, J. and Lukes-Gerakopoulos, G. (2018), Hamiltonians and canonical coordinates for spinning particles in curved space-time, *arXiv e-prints*, arXiv: 1808.06582.

APPENDIX A: RECURRENCE PLOTS

The recurrence plots for the trajectories in Fig. 1 have been produced using the following method: points of the numerically integrated trajectory were sampled at a rate of $\Delta t = 8.664M$ and the data for r, P_r, θ, P_θ, S^t, S^r, S^θ, S^ϕ ($S^\mu \equiv -\frac{1}{2}\epsilon^{\mu\nu\rho\sigma} P_\nu S_{\rho\sigma}/\mu$) were extracted. Each of these 8 time series was rescaled to have zero mean and unit variance. This way, we obtained data in an 8-dimensional space and computed the recurrence matrix using Eq. (6) with the Euclidean metric.

Computation of the recurrence plots of gravitational waveforms in Fig. 2 was slightly more complicated, because in this case there is only limited information available (we used the strain $h_{+\,2}$) as opposed to full phase space vectors when working with trajectories. It is therefore necessary to use some technique of phase space reconstruction, in this case the time delay method. We provide a short description of the method; for more details, the reader is referred to Marwan et al. (2007).

The time delay method has been proven to provide a diffeomorphism between the original and the reconstructed phase space under certain assumptions. Consider a time series $\boldsymbol{x}(t)$. The reconstructed time series vector is then

$$\boldsymbol{y}(t) = (\boldsymbol{x}(t), \boldsymbol{x}(t + \Delta t), \ldots, \boldsymbol{x}(t + (N - 1)\Delta t)) \,, \tag{A1}$$

where Δt is called the time delay and N is the embedding dimension. Both of these are essentially free parameters, but there are methods to fix these for optimal results. The canonical choice of the time delay is the first minimum of the mutual information. To obtain a reasonable embedding dimension one can study the fraction of false nearest neighbors, that is, the fraction of points whose nearest neighbor in the reconstructed phase for the given embedding dimension becomes more distant by a certain factor when the dimension is increased.

Proceedings of *RAGtime 20–22, 15–19 Oct., 16–20 Sept., 19–23 Oct., 2018/2019/2020, Opava, Czech Republic*
Z. Stuchlík, G. Török and V. Karas, editors, Silesian University in Opava, 2020, pp. 383–396

Understanding the iron Kα line emissivity profile with GR radiative transfer code

Wenda Zhang[1,a], Michal Dovčiak[1], Michal Bursa[1], Jiří Svoboda[1] and Vladimír Karas[1]

[1] Astronomical Institute, Czech Academy of Sciences, Boční II, CZ-141 31 Prague, Czech Republic
[a] zhang@asu.cas.cz

ABSTRACT

One of the most promising methods to measure the spin of an accreting black hole is fitting the broad iron Kα line in the X-ray spectrum. The line profile also depends on the geometry of the hard X-ray emitting corona. To put constraints on the black hole spin and corona geometry, it is essential to understand how do they affect the iron Kα line emissivity profile, i.e., the local emissivity of the iron Kα emission as a function of the radius on the accretion disc. In this work, we present calculations of the illumination and the iron Kα emissivity profiles performed with the GR radiative transfer code Monk that employs the Monte Carlo method. In most previous studies the distinction between the illumination and emissivity profiles was not clearly made. For AGN discs, the emissivity profile has a similar shape with the illumination profile, but in the innermost region the former is steeper than the latter; whereas for accretion discs in black hole X-ray binaries, the distinction between the two profiles is more dramatic. We find out that the different behavior between AGN and black hole X-ray binary discs is due to the different energy spectra of the illuminating radiation. This suggests that the emissivity profile of the iron Kα line cannot be determined by black hole spin and corona geometry alone and the energy spectrum of the illuminating radiation has to be taken into account. We also study the dependence of the emissivity profile on the geometry of the corona.

1 INTRODUCTION

X-ray spectra of Active Galactic Nuclei (AGNs) and X-ray binaries (XRBs) exhibit signatures of X-ray reflection, including iron K fluorescent lines and the Compton hump (see the review of Miller, 2007). It is generally believed that they are due to the hard X-ray radiation of the corona illuminating the underlying accretion disc (see Fabian and Ross, 2010 and references therein). The iron line is intrinsically narrow, but the observer at infinity sees broad and asymmetric line profile, due to the gravitational redshift by the strong gravitational field of the black hole and Doppler broadening of the accretion disc (Fabian et al., 1989; Laor, 1991). The shape of the broad iron line depends on the black hole spin, and thus fitting the iron line profile is one of the most promising methods of measuring the spin

978-80-7510-432-8

of accreting black holes (e.g., Miller et al., 2009). For Sgr A*, constraints on the black hole spin can also be put by analyzing the polarization and/or variability of its emission (e.g., Eckart et al., 2006; Trippe et al., 2007; Shcherbakov et al., 2012; Karssen et al., 2017).

To put a constraint on the black hole spin it is important to know the radial emissivity profile of the iron fluorescent lines and the effect of altering black hole spin on the emissivity profile. Martocchia et al. (2000) and Miniutti et al. (2003) studied the emissivity profile of an accretion disc illuminated by a point-like source above the disc and found the profile to be a three-segment broken power-law. Dovciak et al. (2014) investigated in detail the dependence of the emissivity profile on the black hole spin and corona height assuming the lamp-post geometry. Analysis of the emissivity profile of accretion discs irradiated by extended coronae was performed by Wilkins and Fabian (2012) and Gonzalez et al. (2017).

In most of the previous studies, the authors made no clear distinction between the illumination profile (the total energy of illuminating radiation per unit time per unit area) and the emissivity profile of a particular radiative process (the number of photons emitted per unit time per unit area). Also, simple assumptions were made for the spectrum of the illuminating radiation. For example, when calculating the iron Kα emissivity profile the spectrum was usually assumed to have power-law shape in the energy band most relevant for iron K fluorescent lines. Unlike the illumination profile, the emissivity profile also depends on the specific radiative process and is thus sensitive to the local energy spectrum of the illuminating radiation. In this work, we present the illumination and iron Kα emissivity profiles obtained with the general relativistic (GR) Monte Carlo radiative transfer code Monk (Zhang et al., 2019). Thanks to its Monte Carlo nature we are able to calculate not only the flux but also the spectrum of the illuminating radiation as measured in the rest frame of the disc fluid for accretion discs illuminated by extended coronae. As a result, we are able to calculate both the illumination and the emissivity profiles.

2 PROCEDURE

2.1 Calculating the illumination and emissivity profiles

We calculate the illumination and emissivity profiles of a thin Keplerian disc illuminated by an optically-thin extended corona. The thin disc extends down to the innermost circular stable orbit (ISCO). We assume that the thin disc follows Novikov-Thorne temperature profile and there is zero torque at the inner boundary. Following the "superphoton scheme" (Dolence et al., 2009), we sample seed superphotons from the thin disc and propagate the superphotons along null geodesics in the Kerr spacetime (for details see Zhang et al. 2019, submitted). Each superphoton is characterised by its energy at infinity E_∞, weight w, initial position x_0^μ, and initial wave vector k_0^μ. Its weight w has the physical meaning of superphoton generation rate per unit time in a distant observer's frame. If the superphoton is traveling inside the extended corona, we set the step of raytracing to be much less than the scattering mean free path and for each step, we evaluate the Compton scattering optical depth. If the superphoton is scattered, we sample the energy and momentum of the scattered superphoton assuming Klein-Nishina differential cross-section. Finally, we collect superphotons that arrive at the thin disc. For each superphoton, we have the following information: E_∞, w, and its position x^μ and wave-vector k^μ while hitting the disc.

We divide the accretion disc into several radial bins, from ISCO to 100 GM/c^2. The proper area of the i-th bin is

$$\mathcal{S}_i = \int_{r_i}^{r_{i+1}} \frac{2\pi\rho\gamma}{\sqrt{\Delta}} \sqrt{r^2 + a^2 + \frac{2a^2 r}{\rho^2}} \mathrm{d}r, \tag{1}$$

where $\rho^2 \equiv r^2 + a^2\cos^2\theta$, and $\Delta \equiv r^2 - 2r + a^2$, γ is the Lorentzian factor of the disc fluid as measured by a stationary observer, and r_i, r_{i+1} are the lower and upper boundaries of the i-th radial bin. To translate the time from a distant observer's frame to the local frame, we calculate $u^t \equiv dt/d\tau$:

$$u^t = \frac{1}{\sqrt{1 - 2/r + 4\Omega a/r - \Omega^2(r^2 + a^2 + 2a^2/r)}}, \tag{2}$$

where Ω is the angular velocity of the disc fluid. In the i-th radial bin, the flux of the illuminating radiation in the unit of energy per unit time per unit area as measured by the disc fluid is

$$\epsilon_i = \frac{\sum w E_{\rm disc} u_i^t}{\mathcal{S}_i}, \tag{3}$$

where the sum is over all Comptonised photons that strike the thin disc between r_i and r_{i+1}, and $E_{\rm disc}$ is the photon energy measured by the disc fluid. Denoting the four-velocity of the disc fluid U^μ, we have $E_{\rm disc} = -k^\mu U_\mu E_\infty$.

The probability for a hard X-ray photon to produce an iron Kα photon while striking the neutral disc (e.g., George and Fabian, 1991):

$$P(E) \propto \frac{n_{\rm Fe}\sigma_{\rm Fe}(E)}{\sum n_j \sigma_{\rm j,abs}(E) + n_e \sigma_{\rm sca}(E)}, \tag{4}$$

if the energy of the hard X-ray photon is above neutral iron K edge $E_K \sim 7.12$ keV, where $n_{\rm Fe}$ is the number density of neutral iron, n_j is the number density of the j-th ion species, n_e is the number density of electron, σ_{Fe} is the photon-ionisation cross section of neutral iron, $\sigma_{j,abs}$ is the photon-ionisation cross section of the j-th ion species, and $\sigma_{\rm sca}$ is the Compton scattering cross section. As $\sigma_{Fe}, \sigma_{\rm sca} \propto E^{-3}$ while $\sigma_{\rm sca}$ is varying slowly with energy, $P(E)$ decreases with energy rapidly and the photons with energy just above the iron K edge are most essential for the production of iron Kα photons (George and Fabian, 1991).

In the i-th radial bin, the emissivity of iron Kα photon, i.e., the number of iron Kα photons produced per unit area per unit time in the local frame is

$$\varepsilon_i = \frac{\sum w P(E_{\rm disc}) u_i^t}{\mathcal{S}_i}. \tag{5}$$

where the sum is over all superphotons with $r_i \le r \le r_{i+1}$ and $E_{\rm disc} \ge E_K$.

In this paper we assume that the elements in the disc atmosphere are neutral and have solar abundance (Grevesse and Sauval, 1998). The photon ionisation cross sections are calculated with analytical formula by Verner and Yakovlev (1995). For Compton scattering we assume Klein-Nishina scattering cross section.

2.2 Relation between the illumination and emissivity profiles

Let us assume that the spectra of the illuminating radiation at different radii on the disc is different only by different normalisations and redshift (which is the case for an isotropic, lamp-post corona). In this case, we can write the count spectrum of the illuminating radiation as observed by the disc fluid located at radius r as

$$N(E, r) = F(r) f\left(\frac{E}{g(r)}\right) \frac{1}{g(r)}, \tag{6}$$

where $g(r)$ is the dependence of redshift factor $g \equiv E_{\rm disc}/E_{\infty}$ on radius. Then

$$\epsilon(r) = \int_0^{\infty} EN(E, r) dE = F(r) g(r), \tag{7}$$

whatever shape the spectrum has. The iron Kα emissivity profile

$$\varepsilon(r) = \int_{E_K}^{\infty} N(E, r) P(E) dE = \frac{F(r)}{g(r)} \int_{E_K}^{\infty} P(E) f\left(\frac{E}{g(r)}\right) {\rm d}E. \tag{8}$$

For Comptonised spectrum the high energy spectrum can usually be described by a cut-off power-law function. In this case $f(E) = E^{-\Gamma} e^{-E/E_{\rm cut}}$ for $E \geq E_0$, where Γ is the photon index, $E_{\rm cut}$ is the high-energy cut-off energy, and E_0 is the energy of the low-energy cut-off. If $E_0 \leq E_K/max(g(r))$, then

$$\varepsilon(r) = F(r) g^{\Gamma-1}(r) \int_{E_K}^{\infty} P(E) E^{-\Gamma} e^{-E/g(r)E_{\rm cut}} {\rm d}E. \tag{9}$$

For the iron Kα emissivity profile, as $P(E)$ decrease rapidly with energy, the integral is not sensitive to $g(r)$, therefore

$$\varepsilon(r) \propto F(r) g^{\Gamma-1}(r), \tag{10}$$

and

$$\frac{\varepsilon(r)}{\epsilon(r)} \propto g^{\Gamma-2}(r). \tag{11}$$

We can see that whether the emissivity profile is steeper than the illumination profile depends on the value of Γ and the slope of $g(r)$.

3 RESULTS

3.1 Stationary spherical corona in AGNs

In this section, we present the illumination and emissivity profiles of accretion discs illuminated by a spherical corona above the disc. We assume a maximally rotating black hole ($a = 0.998$), to investigate the profiles around a rotating black hole. The effect of the black hole spin will be carried out in a future work. The black hole has a mass of 10^7 $M_{\odot}$ and is

accreting with a mass accretion rate of 4.32×10^{23} g s^{-1}. Assuming the radiative efficiency to be 0.354 for a $a = 0.998$ black hole, the bolometric luminosity is expected to be $\sim 10\%$ the Eddington luminosity, more or less the median Eddington rate of X-ray selected AGNs (Lusso et al., 2012). The spherical corona is stationary, i.e., the fluid has the same angular velocity with a zero angular momentum observer. Although the assumption of a stationary corona is somewhat unphysical, it has been taken in many previous studies where the observations were successfully described. Since in this work we are mainly investigating the effect of the corona geometry on the illumination and emissivity profiles, we still take this assumption, but calculations with more realistic assumptions of the coronae will be carried out in a future work. The temperature of the corona is 100 keV, and the Thomson optical depth of the corona $\tau_{\rm T} \equiv \sigma_T n_e R_c = 0.2$, where $\sigma_{\rm T}$ is the Thomson scattering cross section, and R_c is the radius of the corona.

3.1.1 Dependence on corona size

In Fig. 1 we present the illumination and emissivity profiles for spherical coronae of different sizes. The center of the corona is located on the black hole rotation axis, $10\,GM/c^2$ above the equatorial plane. For all corona sizes the emissivity profile seems to be quite steep at the innermost region of the accretion disc (below $\sim 2-3\,GM/c^2$), and becomes shallower as the radius increases. Then beyond $\sim 10\,GM/c^2$, it becomes steeper again. We fit the emissivity profile in different regions on the accretion disc with a power-law model (i.e., $\varepsilon(r) \propto r^{-q}$) using the least squared method, and summarize the results in Table 1. In the innermost region of the accretion disc ($r \leq 2\,GM/c^2$), the emissivity profile becomes steeper as the corona radius decreases. Far away from the black hole ($r \geq 20\,GM/c^2$), the indices are roughly consistent with the Newtonian value of 3.

Table 1. Measurements of emissivity and illumination indices for spherical coronae of different sizes

Corona radius $[GM/c^2]$	1	2	4	8
Emissivity profile				
q ($r \leq 2\,GM/c^2$)	6.55	6.49	6.32	5.67
q ($r \geq 20\,GM/c^2$)	2.97	3.00	2.98	3.02
Illumination profile				
q ($r \leq 2\,GM/c^2$)	2.92	2.92	2.96	3.27
q ($r \geq 20\,GM/c^2$)	3.06	3.06	3.07	3.09

The illumination profile has a similar three-segment broken power-law profile but in the innermost region it is shallower than the emissivity profile. We also fit the profiles with a power-law model and present the results in Table 1. We measure the photon index of the illuminating radiation in the energy band of 20–100 keV and find it to be ~ 3, greater than 2. According to Dovciak et al. (2014), in the innermost region of the accretion disc

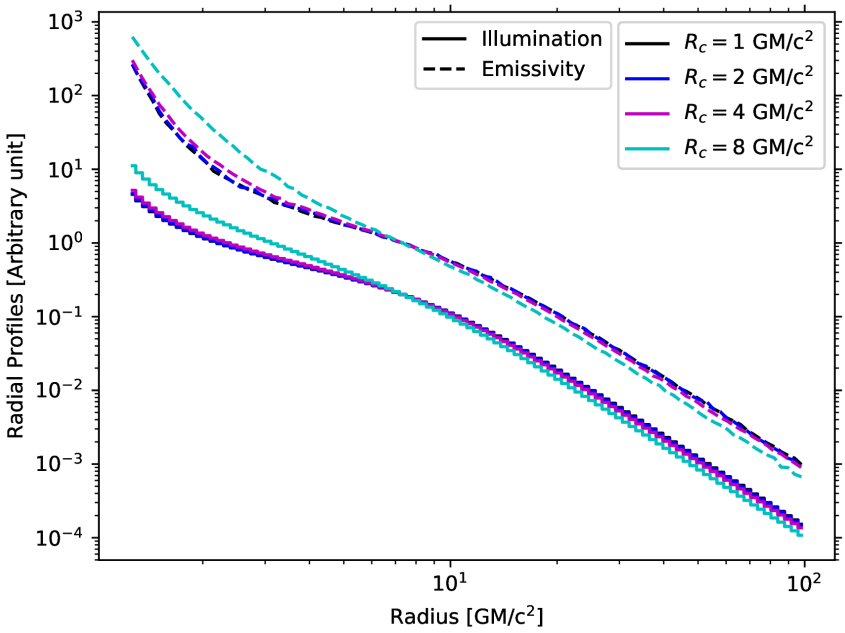

Figure 1. The illumination (solid lines) and emissivity (dashed lines) profiles of accretion discs illuminated by stationary spherical coronae of different sizes.

$g(r)$ increases with decreasing radius. Therefore the result that the emissivity profile is steeper than the illumination profile is consistent with the conclusion drawn in Sec. 2.2.

3.1.2 Dependence on corona height

In Fig. 2 we present the illumination and emissivity profiles for spherical coronae located at different heights above the equatorial plane. The radius of the coronae is 1 GM/c^2. We fit the emissivity and illumination profiles in different regions with a power-law model and summarise the results in Table 2. In the innermost region, as the height increases, the emissivity profile becomes steeper. The illumination profile is shallower than the emissivity profile.

3.2 Co-rotating slab corona in AGNs

In this section we present the results for accretion discs irradiated by slab coronae above the disc. The slab coronae are co-rotating with the underlying accretion disc. The thickness of the slab is 2 GM/c^2. The optical depth of the corona along the vertical direction is $\tau_T \equiv n_e \sigma_T h/2 = 0.2$, and the temperature of the corona is 100 keV. The black hole and thin disc have the same properties as in the previous subsection.

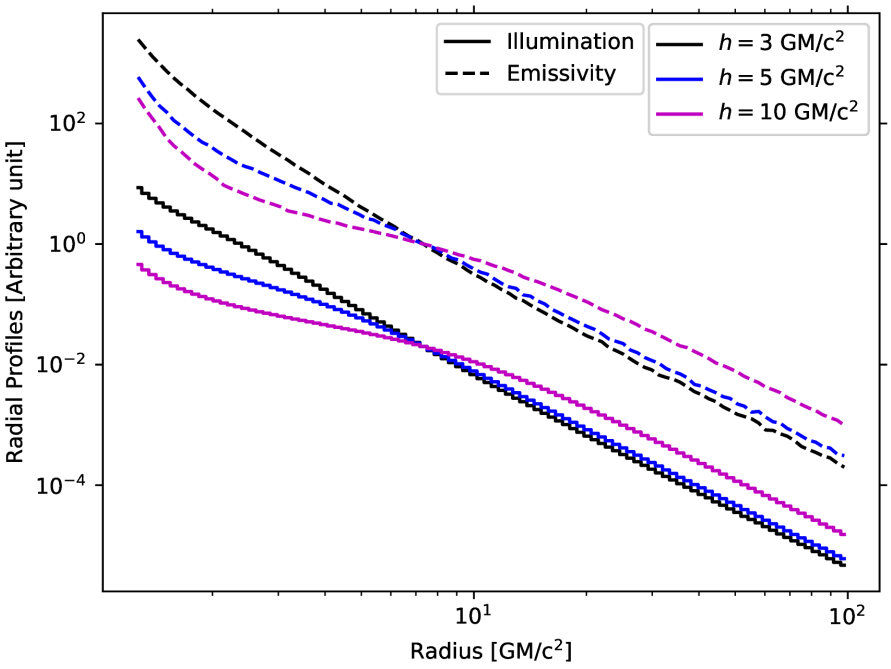

Figure 2. The illumination (solid lines) and emissivity (dashed lines) profiles of accretion discs illuminated by stationary spherical coronae located at different heights above the accretion disc.

Table 2. Measurements of emissivity and illumination indices for spherical coronae of different heights

Corona height $[GM/c^2]$	3	5	10
Emissivity profile			
q $(r \leq 2\ GM/c^2)$	5.80	5.90	6.55
q $(r \geq 20\ GM/c^2)$	3.15	3.13	2.97
Illumination profile			
q $(r \leq 2\ GM/c^2)$	3.52	3.01	2.92
q $(r \geq 20\ GM/c^2)$	3.13	3.12	3.06

3.2.1 Dependence on corona size

In Fig. 3 we present the illumination and emissivity profiles for accretion discs irradiated by slab coronae of different sizes. We measure the emissivity and illumination indices and

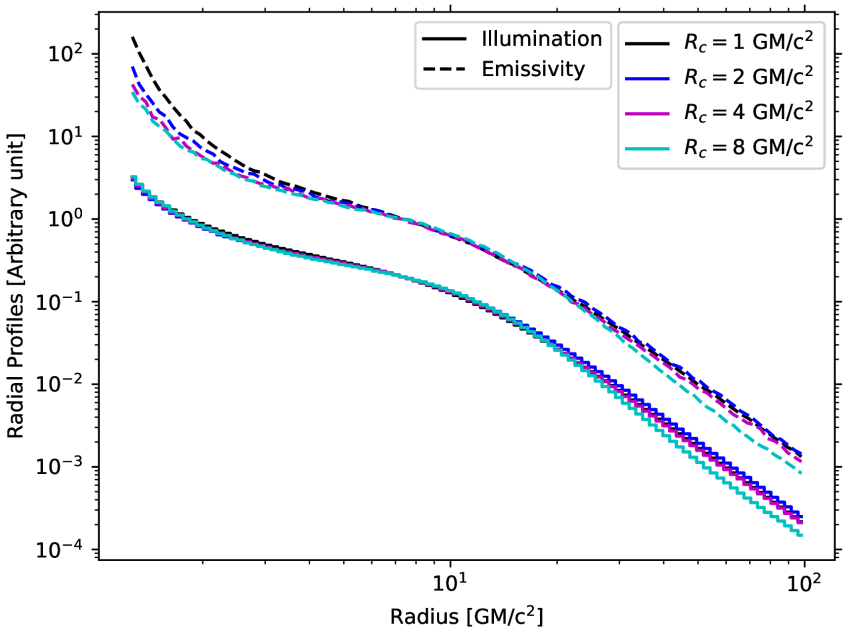

Figure 3. The illumination and emissivity profiles of accretion discs illuminated by co-rotating slab coronae of different sizes.

summarise the results in Table 3. Compared with the spherical coronae, the emissivity profile is more sensitive to the corona size, with shallower emissivity from more extended corona. Similarly with spherical coronae, the illumination profile is shallower than the emissivity profile given the same corona size.

Table 3. Measurements of emissivity and illumination indices for slab coronae of different sizes

Corona radius $[GM/c^2]$	1	2	4	8
Emissivity profile				
q ($r \leq 2\ GM/c^2$)	6.09	4.82	4.42	4.09
q ($r \geq 20\ GM/c^2$)	2.95	2.97	3.00	3.26
Illumination profile				
q ($r \leq 2\ GM/c^2$)	2.84	2.84	2.92	3.00
q ($r \geq 20\ GM/c^2$)	3.06	3.05	3.08	3.31

3.2.2 Dependence on corona height

In Fig. 4 we present the illumination and emissivity profiles for accretion discs irradiated by slab coronae located at different heights above the accretion disc. As the height increases, both the emissivity and the illumination profiles become steeper in the innermost region.

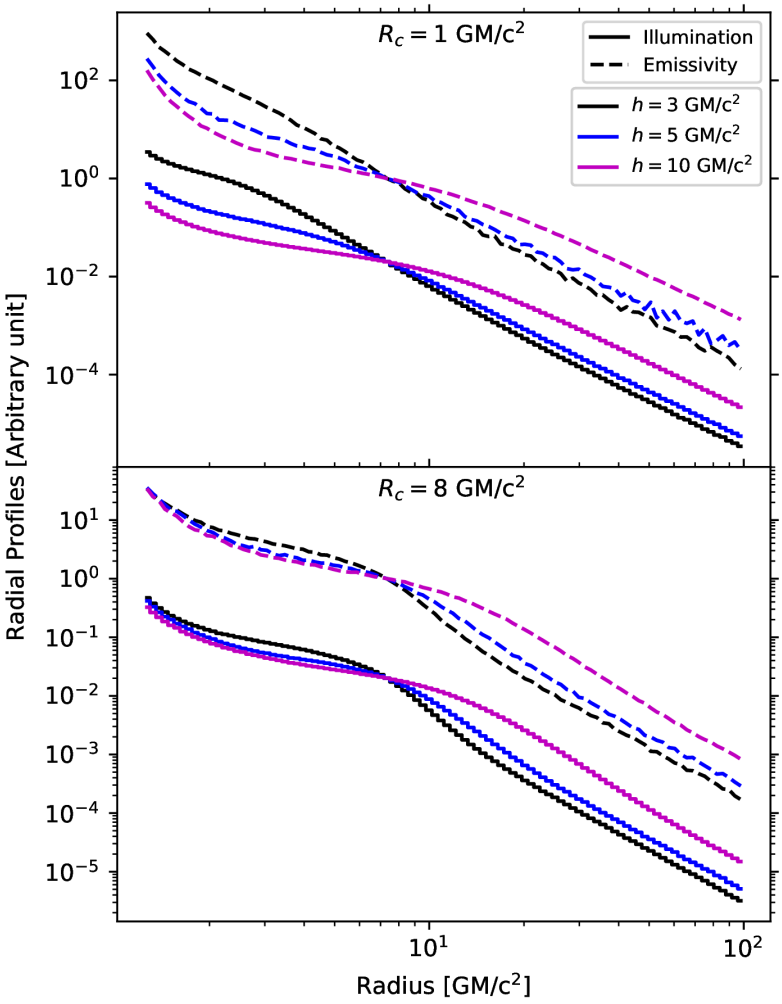

Figure 4. The illumination and emissivity profiles for accretion discs illuminated by co-rotating slab coronae located at different heights above the accretion discs. In the upper and lower panels we present the profiles for corona radii of 1 and 8 GM/c^2, respectively.

Table 4. Measurements of emissivity and illumination indices for slab coronae of different heights

Corona height $[GM/c^2]$	3	5	10
$R_c = 1\ GM/c^2$			
Emissivity profile			
$q\ (r \leq 2\ GM/c^2)$	4.72	5.60	6.09
$q\ (r \geq 20\ GM/c^2)$	3.28	3.11	2.95
Illumination profile			
$q\ (r \leq 2\ GM/c^2)$	2.30	2.78	2.84
$q\ (r \geq 20\ GM/c^2)$	3.19	3.17	3.06
$R_c = 8\ GM/c^2$			
Emissivity profile			
$q\ (r \leq 2\ GM/c^2)$	3.19	3.74	4.09
$q\ (r \geq 20\ GM/c^2)$	2.97	3.02	3.26
Illumination profile			
$q\ (r \leq 2\ GM/c^2)$	2.77	3.15	3.00
$q\ (r \geq 20\ GM/c^2)$	2.98	3.02	3.31

3.3 Stationary spherical coronae in XRBs

In the upper panel of Fig. 5 we present the illumination and emissivity profiles of accretion discs in XRBs illuminated by spherical coronae. The parameters are the same with Sec. 3.1, but for a $M = 10\ \mathrm{M}_\odot$ black hole accretion at a rate of 4.32×10^{17} g s^{-1} (corresponding to 10% Eddington luminosity). The emissivity profile is distinct compared with the emissivity profile of AGNs (Fig. 1) in that the profile is shallower than the Newtonian case below $\sim 10\ GM/c^2$, and the emissivity even decreases towards lower radius below $\sim 1.6\ GM/c^2$.

To highlight the distinction in the emissivity profile, in the lower panel of Fig. 5 we compare the profiles of accretion discs around 10 $\mathrm{M}_\odot$ and 10^7 $\mathrm{M}_\odot$ black holes. The illumination profiles are identical while the difference in the emissivity profile is obvious. To understand the difference, we calculate the spectra of the illuminating radiation as observed by the disc fluid at radii of 1.27, 1.58, and 2.67 GM/c^2, respectively, and present the results in Fig. 6. For $M = 10^7$ $\mathrm{M}_\odot$, the low-energy cut-off is much lower than E_K, as a result a higher redshift simply leads to more X-ray photons above E_K; whereas for the 10 $\mathrm{M}_\odot$ case, the low-energy cut-off of the count spectra is in the range of $2-10$ keV, resulting in a distinct emissivity profile. This indicates that the energy spectra of the hard X-ray radiation could substantially affect the emissivity profile.

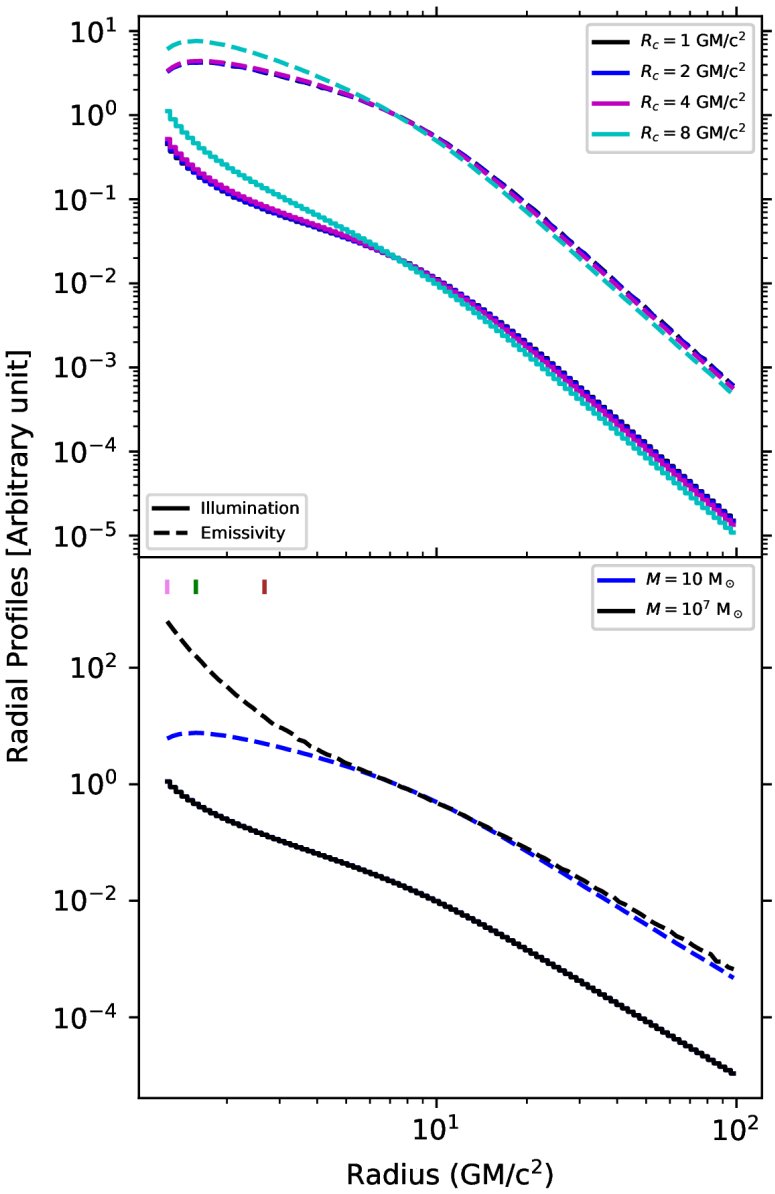

Figure 5. Upper panel: the illumination (dashed lines) and emissivity (solid lines) profiles of accretion discs illuminated by spherical coronae of different sizes. The accretion disc is rotating about a 10 $M_\odot$ black hole. Lower panel: comparison of the profiles between accretion discs around a 10 black hole (black) and a 10^7 $M_\odot$ black hole (blue). The violet, green, and brown vertical bars indicate the locations the spectra of which are plotted in Fig. 6.

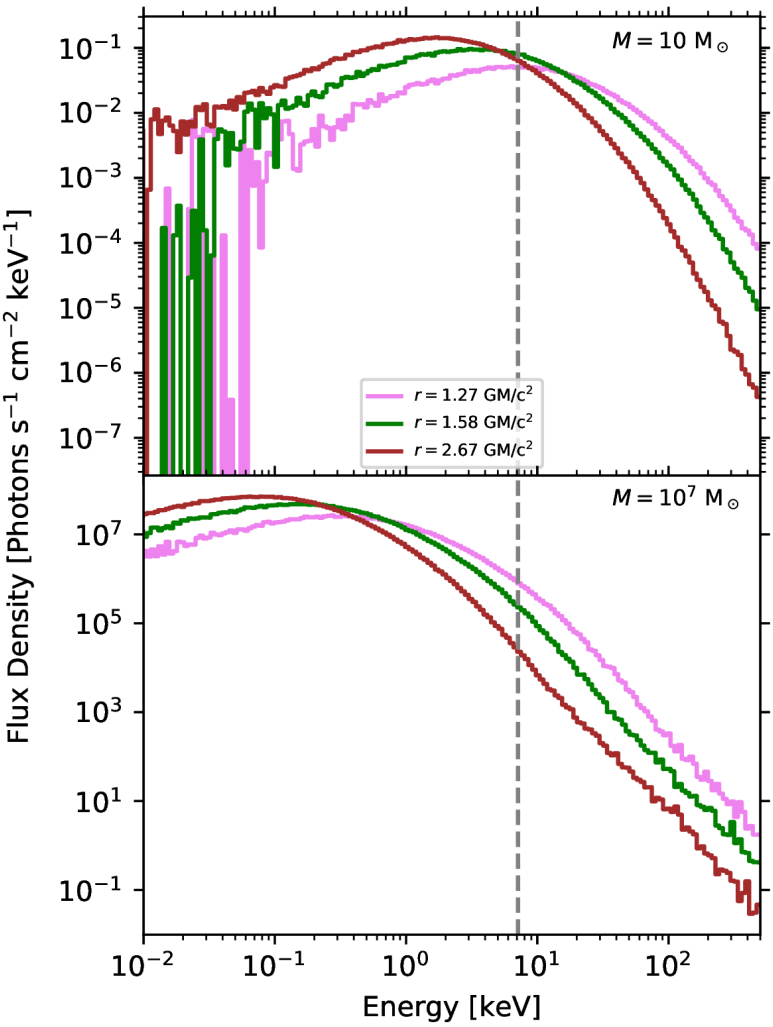

Figure 6. The energy spectra of the illuminating radiation observed by disc fluid located at different radii. The spherical corona is located 10 GM/c^2 above the accretion disc and has radius of 1 GM/c^2. The spectra at different radii are plotted in different colors, while the locations are indicated by the vertical bars in Fig. 5. The vertical dashed line indicates the location of neutral iron K edge at 7.12 keV. In the upper and lower panels we present the spectra for accretion discs around 10 and 10^7 $M_\odot$, respectively.

4 SUMMARY

In this work we present the illumination and neutral iron Kα emissivity profiles of accretion discs irradiated by extended coronae. With our GR Monte Carlo radiative transfer code Monk, we can calculate the energy spectrum of the illuminating radiation in the rest frame of the accretion disc. As a result, we are able to calculate both the illumination and emissivity profiles while in most previous studies the authors did not make a clear distinction between the two. For AGN discs, the emissivity profiles are in general steeper than the illumination profiles for the parameters taken in the calculations; whereas for accretion discs in black hole X-ray binaries, the distinction is more dramatic: the emissivity even decreases with decreasing radius in the innermost region of the disc. We find out that the different behaviors in AGNs and black hole X-ray binaries are due to the difference in energy spectra of the illuminating radiation as seen by the disc. This suggests that the emissivity profile of the iron Kα line cannot be determined by black hole spin and corona geometry alone, and the energy spectrum of the illuminating radiation has to be taken into account. We also study the dependence of the emissivity profile on the geometry of the corona and find the emissivity in the innermost region of the disc steepens as the corona becomes less extended or as the corona has a larger height.

ACKNOWLEDGEMENTS

The authors acknowledge financial support provided by Czech Science Foundation grant 17-02430S. This work is also supported by the project RVO:67985815. This research makes uses of Matplotlib (Hunter, 2007), a Python 2D plotting library which produces publication quality figures.

REFERENCES

Dolence, J. C., Gammie, C. F., Mościbrodzka, M. and Leung, P. K. (2009), Grmonty: A Monte Carlo Code for Relativistic Radiative Transport, *ApJS*, **184**, pp. 387–397, ISSN 0067-0049.

Dovciak, M., Svoboda, J., Goosmann, R. W., Karas, V., Matt, G. and Sochora, V. (2014), An XSPEC model to explore spectral features from black-hole sources - II. The relativistic iron line in the lamp-post geometry, *arXiv:1412.8627*, arXiv: 1412.8627.

Eckart, A., Schödel, R., Meyer, L., Trippe, S., Ott, T. and Genzel, R. (2006), Polarimetry of near-infrared flares from Sagittarius A*, *A&A*, **455**, pp. 1–10, ISSN 0004-6361.

Fabian, A. C., Rees, M. J., Stella, L. and White, N. E. (1989), X-ray fluorescence from the inner disc in Cygnus X-1, *MNRAS*, **238**, pp. 729–736, ISSN 0035-8711.

Fabian, A. C. and Ross, R. R. (2010), X-ray Reflection, *Space Science Reviews*, **157**, pp. 167–176, ISSN 0038-6308.

George, I. M. and Fabian, A. C. (1991), X-ray reflection from cold matter in active galactic nuclei and X-ray binaries, *MNRAS*, **249**, pp. 352–367, ISSN 0035-8711.

Gonzalez, A. G., Wilkins, D. R. and Gallo, L. C. (2017), Probing the geometry and motion of AGN coronae through accretion disc emissivity profiles, *MNRAS*, **472**, pp. 1932–1945, ISSN 0035-8711.

Grevesse, N. and Sauval, A. J. (1998), Standard Solar Composition, *Space Science Reviews*, **85**, pp. 161–174, ISSN 0038-6308.

Hunter, J. D. (2007), Matplotlib: A 2D Graphics Environment, *Computing In Science Engineering*, **9**(3), pp. 90–95, ISSN 1521-9615.

Karssen, G. D., Bursa, M., Eckart, A., Valencia-S, M., Dovčiak, M., Karas, V. and Horák, J. (2017), Bright X-ray flares from Sgr A*, *MNRAS*, **472**, pp. 4422–4433, ISSN 0035-8711.

Laor, A. (1991), Line profiles from a disk around a rotating black hole, *ApJ*, **376**, pp. 90–94, ISSN 0004-637X.

Lusso, E., Comastri, A., Simmons, B. D., Mignoli, M., Zamorani, G., Vignali, C., Brusa, M., Shankar, F., Lutz, D., Trump, J. R., Maiolino, R., Gilli, R., Bolzonella, M., Puccetti, S., Salvato, M., Impey, C. D., Civano, F., Elvis, M., Mainieri, V., Silverman, J. D., Koekemoer, A. M., Bongiorno, A., Merloni, A., Berta, S., Le Floc'h, E., Magnelli, B., Pozzi, F. and Riguccini, L. (2012), Bolometric luminosities and Eddington ratios of X-ray selected active galactic nuclei in the XMM-COSMOS survey, *MNRAS*, **425**, pp. 623–640, ISSN 0035-8711.

Martocchia, A., Karas, V. and Matt, G. (2000), Effects of Kerr space-time on spectral features from X-ray illuminated accretion discs, *MNRAS*, **312**, pp. 817–826, ISSN 0035-8711.

Miller, J. M. (2007), Relativistic X-Ray Lines from the Inner Accretion Disks Around Black Holes, *Annual Review Of Astronomy Astrophysics*, **45**, pp. 441–479, ISSN 0066-4146.

Miller, J. M., Reynolds, C. S., Fabian, A. C., Miniutti, G. and Gallo, L. C. (2009), Stellar-Mass Black Hole Spin Constraints from Disk Reflection and Continuum Modeling, *ApJ*, **697**, pp. 900–912, ISSN 0004-637X.

Miniutti, G., Fabian, A. C., Goyder, R. and Lasenby, A. N. (2003), The lack of variability of the iron line in MCG-6-30-15: General relativistic effects, *MNRAS*, **344**, pp. L22–L26, ISSN 0035-8711.

Shcherbakov, R. V., Penna, R. F. and McKinney, J. C. (2012), Sagittarius A* Accretion Flow and Black Hole Parameters from General Relativistic Dynamical and Polarized Radiative Modeling, *ApJ*, **755**, p. 133, ISSN 0004-637X.

Trippe, S., Paumard, T., Ott, T., Gillessen, S., Eisenhauer, F., Martins, F. and Genzel, R. (2007), A polarized infrared flare from Sagittarius A* and the signatures of orbiting plasma hotspots, *MNRAS*, **375**, pp. 764–772, ISSN 0035-8711.

Verner, D. A. and Yakovlev, D. G. (1995), Analytic FITS for partial photoionization cross sections., *Astronomy Astrophysics Supplement Series*, **109**, pp. 125–133, ISSN 0365-0138.

Wilkins, D. R. and Fabian, A. C. (2012), Understanding X-ray reflection emissivity profiles in AGN: Locating the X-ray source, *MNRAS*, **424**, pp. 1284–1296, ISSN 0035-8711.

Zhang, W., Dovčiak, M. and Bursa, M. (2019), Constraining the Size of the Corona with Fully Relativistic Calculations of Spectra of Extended Coronae. I. The Monte Carlo Radiative Transfer Code, *ApJ*, **875**(2), p. 148.

Title: **Proceedings of RAGtime 20–22:
Workshops on black holes and neutron stars,
15–19 Oct., 16–20 Sept., 19–23 Oct. 2018/2019/2020,
Opava, Czech Republic**

Published by: Silesian University in Opava
Institute of Physics in Opava
Bezručovo nám. 13
CZ-746 01 Opava, Czech Republic

Editors: Z. Stuchlík, G. Török and V. Karas

Cover design: Otakar Karlas

1st edition

Printed by : Profi-tisk group s.r.o.,
Kyselovská 559/125,
783 01 Olomouc - Slavonín, Czech Republic

Published in December 2020

INTER-EXCELLENCE

SLEZSKÁ
UNIVERZITA
FYZIKÁLNÍ ÚSTAV
V OPAVĚ

The publication was supported by the INTER-EXCELLENCE project No. LTI17018 and the internal grant of the Silesian University in Opava No. 07/2015-FPF.

ISBN 978-80-7510-432-8 (Print)
ISBN 978-80-7510-433-5 (Online)
ISSN 2336-5668 (Print)
ISSN 2336-5676 (Online)

Typeset in LaTeX

Název: **Proceedings of RAGtime 20–22:**
Workshops on black holes and neutron stars,
15–19 Oct., 16–20 Sept., 19–23 Oct. 2018/2019/2020,
Opava, Czech Republic

Nakladatel: Slezská univerzita v Opavě
Fyzikální ústav v Opavě
Bezručovo nám. 13
CZ-746 01 Opava, Česká republika

Editoři: Z. Stuchlík, G. Török a V. Karas

Obálka: Otakar Karlas

První vydání

Tisk: Profi-tisk group s.r.o.,
Kyselovská 559/125
783 01 Olomouc - Slavonín, Česká republika

Vydáno v prosinci 2020

The publication was supported by the INTER-EXCELLENCE project No. LTI17018 and the internal grant of the Silesian University in Opava No. 07/2015-FPF.

ISBN 978-80-7510-432-8 (Print)
ISBN 978-80-7510-433-5 (Online)
ISSN 2336-5668 (Print)
ISSN 2336-5676 (Online)

Vysázeno systémem LaTeX

EUROPEAN UNION
European Structural and Investment Funds
Operational Programme Research,
Development and Education

MINISTRY OF EDUCATION, YOUTH AND SPORTS

INTER-EXCELLENCE

SILESIAN UNIVERSITY
INSTITUTE OF PHYSICS IN OPAVA

ISBN 978-80-7510-432-8
ISSN 2336-5668